Titre: Title:	MIL Metal-Organic Frameworks: Synthesis, Post-Synthetic Modifications, and Applications
Auteur: Author:	Mahmoud Yosry Mohamed Zorainy
Date:	2022
Type:	Mémoire ou thèse / Dissertation or Thesis
Référence: Citation:	Zorainy, M. Y. M. (2022). MIL Metal-Organic Frameworks: Synthesis, Post-Synthetic Modifications, and Applications [Ph.D. thesis, Polytechnique Montréal]. PolyPublie. https://publications.polymtl.ca/10306/

Document en libre accès dans PolyPublie
Open Access document in PolyPublie

URL de PolyPublie: PolyPublie URL:	https://publications.polymtl.ca/10306/
Directeurs de recherche: Advisors:	Daria Camilla Boffito, & Serge Kaliaguine
Programme: Program:	Génie chimique

POLYTECHNIQUE MONTRÉAL

affiliée à l'Université de Montréal

MIL Metal-Organic Frameworks: Synthesis, Post-Synthetic Modifications, and Applications

MAHMOUD YOSRY MOHAMED ZORAINY

Département de génie chimique

Thèse présentée en vue de l'obtention du diplôme de *Philosophiæ Doctor*
Génie Chimique

Février 2022

POLYTECHNIQUE MONTRÉAL

affiliée à l'Université de Montréal

Cette thèse intitulée :

MIL Metal-Organic Frameworks: Synthesis, Post-Synthetic Modifications, and Applications

présentée par **Mahmoud Yosry Mohamed ZORAINY**
en vue de l'obtention du diplôme de *Philosophiæ Doctor*
a été dûment acceptée par le jury d'examen constitué de :

Robert LEGROS, président
Daria Camilla BOFFITO, membre et directrice de
recherche **Serge KALIAGUINE**, membre et codirecteur de
recherche **Jean-Philippe HARVEY**, membre
Michael KATZ, membre externe

DEDICATION

To Almighty God, my beloved parents, brothers, and sincere friends...
To everyone who believed in me...
To everyone who ever supported me...

ACKNOWLEDGEMENTS

Writing a scientific thesis is tough. At every failing experiment, you start to lose hope. But, with those people around you, those people who love and support you, you can live it as a dream. This thesis would never have come to light without the help of many people, to whom I am very thankful. Foremost, I would like to express my sincere gratitude to my supervisors:

Prof. Daria C. Boffito, thank you for your kindness, continuous support, encouragement, and motivation. Thank you for being reasonable, for considering your students' mental health, especially during the pandemic. You are the best ship captain one can have; I can never thank you enough.

Prof. Serge Kaliaguine, my co-supervisor, my role model: thank you for accepting me as one of your students. Thank you for making this possible! I will always appreciate our scientific discussions.

Also, I would like to thank my committee members, ***Prof. Robert Legros***, ***Prof. Jean-Philippe Harvey***, and ***Prof. Micheal Katz***, for reviewing and evaluating my thesis.

I would also like to express my deep and sincere gratitude to ***Prof. Mohamed Gobara*** and ***Prof. Sherief Elbasuney*** for their valuable contributions in my studies, I would not have done this without your help.

To my second family, friends, office mates, and co-workers: ***Dalma Schieppati***, ***Hela Laajimi***, ***Nooshin Saadatkhah***, ***Zahra Khani***, thank you for your help, suggestions, and relieving talks. Thank you for being around!

I am also grateful for all EPIC group members and my lab mates, especially ***Dr. Ergys Pahija*** and ***Dr. Mohamed Gar Alalm***, for being a huge source of inspiration and ideas. Also, the unsung heroes of the chemical engineering department of Polytechnique Montreal: ***Martine Lamarche***, ***Claire Cerclé***, and ***Gino Robin***, ***Matthieu Gauthier***, for their devoted assistance.

To my brothers here in Montreal: ***Dr. Hatem Titi***, ***Ramy Sadek***, ***Moustafa Ossman***, ***Micheal Silwanis***, ***Ahmed Bahgat***, and ***Ahmed Emam***, I am in a debt of gratitude to you for your support and presence.

A special thanks to my family: My Dad, Mom, and my Brothers, for their invaluable love, encouragement, and believing in me during this endeavour. My dearest friend ***Nidale Hamouchene***, who was there for me during my toughest moments. I am eternally grateful for what you did for me!

RÉSUMÉ

Au cours des dernières décennies, la communauté scientifique du monde entier a assisté à l'émergence d'une nouvelle classe de matériaux poreux aux caractéristiques structurelles et chimiques incontestablement uniques. La découverte des charpentes organométalliques (MOF) a impressionné la communauté des zéolites et des matériaux poreux. La grande expansion dans ce domaine a comblé une lacune dans les dimensions des solides poreux. Depuis lors, les MOF sont en concurrence avec les zéolites et les oxydes métalliques dans diverses applications, notamment la catalyse, l'adsorption et la séparation de gaz, la photocatalyse et la détection. Dans cette thèse, les travaux de recherche ont été orientés vers la synthèse, la caractérisation, la modification post-synthétique et les applications de charpentes métal-organiques. Ici, nous avons sélectionné trois des MOF de type MIL bien connus. Ils possèdent tous une structure 3D construite à partir d'ions métalliques trivalents et du lieur ditopique de l'acide benzènedicarboxylique-1,4 (H_2BDC); cependant, ils occupent des filets différents.

Parmi ces MOFs, nous allons cibler en premier lieu le MIL-101. Ce dernier est considéré comme étant un type distinctif avec une structure robuste, une surface spécifique, un volume de pores inhabituellement élevés, et une stabilité chimique remarquable dans l'air, l'eau et les acides. Il a brillé en tant que candidat prometteur pour diverses applications depuis sa découverte en 2005. En outre, sa structure robuste a attiré beaucoup d'attention pour d'autres améliorations afin d'accéder davantage à son plein potentiel. A travers notre thèse nous allons contribuer à cet objectif grâce à une compréhension approfondie de la science derrière cette structure. En 2014, S. Bhattacharjee *et al.* est sorti avec une revue détaillée couvrant la synthèse, la caractérisation, la fonctionnalisation et les applications de ce célèbre MOF à cette époque. Cependant, un tel examen s'est concentré sur le MOF de type chrome. Malgré les études étendues sur ce type, l'existence des ions chrome a quelque peu limité l'utilisation de ce MOF. Les autres MOF MIL-101 isostructuraux, fabriqués à partir de différents métaux et leurs applications, n'ont pas été inclus. Notre premier objectif serait de passer en revue les avancées récentes dans la synthèse du chrome MOF et de ses différents analogues métalliques. De plus, le type multivarié de ce MOF (MTV-MIL-101), dans lequel deux métaux ou plus sont utilisés pour mettre en place le cadre, sera discuté. De plus, les polymorphes MIL-101 ou les isomères de charpente construits à partir des mêmes constituants mais de structures et de morphologies différentes seront passés en revue. Cette section peut être considérée comme une version complémentaire de l'examen de Bhattacharjee, y compris d'autres perspectives.

Notre objectif suivant sera penché sur l'un des points très discutables de la synthèse du MTV-MIL-101 à métaux mixtes. La méthode d'échange post-synthétique (PSE), qui est définie comme étant une voie éprouvée pour modifier et ajouter différentes fonctionnalités des MOF, sera examinée en vue de la réalisation du MIL-101 (Cr/Fe) à métaux mixtes. En 2013, Szilágyi *et al.* a signalé la réalisation de plusieurs MIL-101 à métaux mixtes via PSE (c'est-à-dire MIL-101(Cr/Fe), MIL-101(Cr/Al) et MIL-101(Cr/Fe/Al)). Cependant, des études antérieures ont rapporté l'obtention du MIL-101 à métaux mixtes uniquement par synthèse directe. Depuis lors, un débat a eu lieu sur la validité des conclusions de Szilágyi. Dans nos recherches, nous allons régler ce différend tout en enquêtant sur la méthode de Szilágyi afin de pouvoir juger de leurs résultats. Ensuite, nous allons effectuer des expériences dans des conditions de temps étendues et différents précurseurs métalliques. Aussi, nous envisagerons de changer le solvant de la réaction.

En deuxième lieu, nous abordons le type du MOF MIL-88B , ayant la structure flexible à base de fer, l'un des isomères de charpente MIL-101 construits à partir des ions fer trivalents et du lieur BDC. Cependant, il se distingue par sa flexibilité et sa grande stabilité thermique. De plus, une telle structure fournit une teneur élevée en oxygène et en fer qui la désigne comme un catalyseur riche en oxygène pour les systèmes énergétiques. Dans notre étude, le MIL-88B(Fe) a été obtenu via une méthode de synthèse assistée par micro-ondes. Il a ensuite été intégré dans un composite perchlorate d'ammonium (PA)/MOF ciblant une décomposition catalysée du PA (l'oxydant le plus couramment utilisé dans les systèmes énergétiques). De plus, la décomposition du MIL-88B(Fe) entraînerait la formation de particules de Fe_2O_3 qui peuvent encore améliorer la décomposition du PA. Les particules de catalyseur peuvent diminuer le changement de phase endothermique cristallographique AP, agir comme un donneur d'électrons pour les matériaux énergétiques déficients en électrons et soutenir la diffusion hétérogène d'une molécule en phase gazeuse sur la surface du catalyseur. La diminution de l'énergie d'activation de la décomposition AP a été calculée à l'aide des modèles de Kissinger et Kissinger-Akahira-Sunose (KAS).

Dernièrement , nous allons mettre en exergue le troisième MOF intitulé (MIL-47) qui est à base de vanadium. Ce MOF a la même structure et occupe le même groupe spatial que le MIL-53, qui est un autre polymorphe de MIL-101. Tel que synthétisé, le MIL-47 a une structure flexible comme MIL-53. Cependant, lors de l'activation thermique, la structure devient robuste. La synthèse de MIL-47 a été rapportée à partir de divers précurseurs métalliques, dont le chlorure de vanadium (III) (VCl_3) en tant que riche source d'ions métalliques. Dans nos études, nous avons tenté la synthèse de MIL-47 à partir d'autres matériaux de départ via une voie solvothermique facile, recherchant une approche économique et plus verte. Le pentoxyde de vanadium (V_2O_5) a été utilisé dans notre synthèse comme source de métal facile-

ment abondante, peu coûteuse et thermodynamiquement stable. De plus, un tel précurseur fournit un taux contrôlable de production d'ions métalliques en fonction des conditions de réaction appliquées. Les propriétés du MIL-47(V) nous ont orientés vers son application à des fins anti-corrosion, où les cristaux MOF ont été incorporés dans un revêtement époxy/MOF pour protéger la surface de l'alliage d'aluminium AA2024 contre un environnement riche en chlorure.

ABSTRACT

Over the past decades, the scientific community all over the world witnessed the emergence of a new class of porous materials with unquestionably unique structural and chemical features. The discovery of metal-organic frameworks (MOFs) impressed the community of zeolites and porous materials. The great expansion in this field fulfilled a gap in the dimensions of porous solids. Since then, MOFs have been competing with zeolites and metal oxides in various applications, including catalysis, gas-adsorption and separation, photocatalysis, and sensing. In this thesis, research studies were directed towards the synthesis, characterization, post-synthetic modification, and applications of metal-organic frameworks. Here, we selected three of the well-known MIL-type MOFs. They all possess a 3D structure built from trivalent metal ions and the ditopic 1,4-Benzenedicarboxylic acid linker (H_2BDC); however, they occupy different nets.

Among these MOFs, MIL-101 was targeted as a distinctive MOF with a robust structure, unusual high surface area and pore volume, and distinguished chemical stability in air, water, and acids. It sparkled as an up-and-coming candidate for various applications since its discovery in 2005. Besides, its robust structure has drawn much attention for further enhancements to gain more access to its full potential. Here, we will contribute to this goal through a profound understanding of the chemistry behind this structure. In 2014, S. Bhattacharjee *et al.* came out with a detailed review covering the synthesis, characterization, functionalization, and applications of this famous MOF by that time. However, such a review focused on the chromium-type MOF. Despite the extended studies on this type, the existence of the chromium ions somehow limited the use of this MOF. Other isostructural MIL-101 MOFs, made out of different metals and their applications, were not included. Our first goal would be to review the recent advancements in the synthesis of the chromium MOF and its different metal analogues. In addition, the multivariate type of this MOF (MTV-MIL-101), whereby two or more metals are used to set up the framework, will be discussed. Moreover, MIL-101 polymorphs or framework isomers built from the same constituents but of different structures and morphologies will be reviewed. This section can be considered a complementary version of Bhattacharjee's review, including other perspectives.

Moving forward to the next objective, we will consider one of the highly debatable points in the synthesis of mixed-metal MTV-MIL-101, whereby the post-synthetic exchange (PSE) method, as a well-proven route to modify and add different functionalities to MOFs, will be examined towards the achievement of mixed-metal MIL-101(Cr/Fe). In 2013, Szilágyi *et al.*

reported the achievement of several mixed-metal MIL-101s via PSE (i.e., MIL-101(Cr/Fe), MIL-101(Cr/Al), and MIL-101(Cr/Fe/Al)). However, previous studies reported the attainment of mixed-metal MIL-101 only through direct synthesis. Since then, a debate has been taking place about the validity of Szilágyi's findings. In our research, we will settle this dispute by investigating Szilágyi's method to be able to judge their results. Then, we will repeat the experiments at extended conditions of time and different metal precursors. Also, we will consider changing the reaction solvent.

The second selected MOF is the flexible iron-based MIL-88B structure, one of the MIL-101 framework isomers built from the trivalent iron ions and the BDC linker. However, it distinguishes itself for its flexibility and high thermal stability. In addition, such a structure provides a high oxygen and iron content that nominates it as an oxygen-rich catalyst for energetic systems. In our study, MIL-88B(Fe) was obtained via a microwave-assisted synthesis method. It was then integrated into an ammonium perchlorate (AP)/MOF composite targeting a catalyzed decomposition of AP (the most commonly used oxidizer in energetic systems). Also, the decomposition of MIL-88B(Fe) would result in the formation of Fe_2O_3 particles that can further enhance the decomposition of AP. The catalyst particles can decrease AP crystallographic endothermic phase change, act as an electron donor to electron-deficient energetic materials, and support heterogeneous diffusion of a gas-phase molecule on the catalyst surface. The decrease in the activation energy of AP decomposition was calculated using Kissinger and Kissinger–Akahira–Sunose (KAS) models.

The third selected MOF is the vanadium-based metal-organic framework (MIL-47). This MOF has the same structure and occupies the same space group as the MIL-53 framework, which is another polymorph of MIL-101. As-synthesized, the MIL-47 has a flexible structure as MIL-53. However, upon thermal activation, the structure becomes robust. The synthesis of MIL-47 has been reported from various metal precursors, including vanadium(III) chloride (VCl_3) as a rich source of metal ions. In our studies, we attempted the synthesis of MIL-47 from other starting materials via a facile solvothermal route, seeking an economic and greener approach. Vanadium pentoxide (V_2O_5) was utilized in our synthesis as a readily abundant, low-cost, and thermodynamically stable metal source. Furthermore, such a precursor provides a controllable rate of metal ion production depending on the applied reaction conditions. The properties of MIL-47(V) directed us for its application in anti-corrosion purposes, whereby the MOF crystals were incorporated in an epoxy/MOF coating to protect the surface of aluminum alloy AA2024 against a chloride-rich environment.

TABLE OF CONTENTS

LIST OF TABLES

LIST OF FIGURES

LIST OF SYMBOLS AND ACRONYMS

AASBU	Automated assembly of secondary building units
AcOH	Acetic acid
aMOFs	Amorphous metal-organic frameworks
AP	Ammonium perchlorate
AOPs	Advanced oxidation processes
ATR	Attenuated Total Reflectance
BBC, H$_3$BBC	1,3,5-tris(4′-carboxy[1,1′-biphenyl]-4-yl)benzene
BCPBD, H$_2$BCPBD	1,4-bis-p-carboxyphenyl buta-1,3-diene
BDC, H$_2$BDC	1,4-Benzene dicarboxylic acid
BET	Brunauer-Emmett-Teller
BODIPY	Boron dipyrromethene
BPDC, 4,4′-BPDC	4,4′-biphenyldicarboxylic acid
BTB	1,3,5-Tris(4-carboxyphenyl) benzene
BTC, H$_3$BTC	Benzene-1,3,5-tricarboxylic acid or Trimesic acid
BTE	4,4′,4″-(1,3,5-benzenetriyltri-2,1-ethynediyl)trisbenzoic acid
BTP	3,5-Bis(trifluoromethyl)phenyl isocyanate
t-BuONO	*tert*-Butyl nitrite
CAL	Cinnamaldehyde
CAU	Christian-Albrechts University
COL	Cinnamyl alcohol
CoPOM	Cobalt-based polyoxometalate
CPs	Coordination Polymers
CQDs	Carbon quantum dots
CSD	Cambridge structural database
CUS	Coordinatively unsaturated metal sites
DEF	*N*, *N*-diethyl fomamide
DFT	Density functional theory
DMF	*N*, *N*-dimethylformamide
DMSO	Dimethyl sulfoxide
L-Dopa	3,4-dihydroxy-L-phenylalanine
DRS	Diffuse reflectance spectroscopy
DUT	Dresden University of Technology
ED	Electron Diffraction

EDS, EDX	Energy-dispersive X-ray spectroscopy
EIS	Electrochemical impedance spectroscopy
EPR	Electron paramagnetic resonance
ESCP	Ethoxysuccinato-cisplatin
ESR	Electron spin resonance
EtOH	Ethanol
FTIR	Fourier Transform Infrared
HER	Hydrogen evolution reaction
HKUST	Hong Kong University of Science and Technology
HREM	High-resolution electron microscopy
HTXRD	High-temperature X-ray diffraction
ICP-OES	Inductively coupled plasma - optical emission spectroscopy
IEP	isoelectric point
IR	Infrared
IRMOF	Isoreticular Metal-Organic Framework
IUPAC	International union of pure and applied chemistry
LAG	Liquid-assisted grinding
MeOH	Methanol
MIL	Material of Lavoisier Institute
MMM	Mixed matrix membranes
MOFs	Metal-organic frameworks
MOPs	Metal-organic polyhedra
MTN	Mobil thirty-nine
MTV	Multivariate
MW	Microwave
nZVI	Nano zero-valent iron
NDC, 2,6-NDC	2,6-naphthalenedicarboxylic acid
NH_2-BDC	2-Amino terephthalic acid
NHE	Normal hydrogen electrode
NMR	Nuclear magnetic resonance
NU	Northwestern University
OER	Oxygen evolution reaction
OMS	Open metal sites
ORR	Oxygen reduction reaction
PAni	Polyaniline
PCN	Porous Coordination Network

PCP	Porous Coordination Polymer
PDMS	Poly(dimethyl siloxane)
PEBA	Poly(ether-block-amide)
POM	Poloxometalate
PSE	Post-synthetic exchange
PSLE	Post-Synthetic Linker exchange
PSM	Post-synthetic modification
PSE	Post-synthetic exchange
PTA	Phosphotungstic Acid
PVDF	Poly(vinylidene fluoride)
PXRD	Powder X-ray Diffraction
ROS	Reactive oxygen species
SACS	Solvent-assisted cation substitution
SALE	Solvent-assisted linker exchange
SAXS	Small-angle X-ray scattering
SBU	Secondary building unit
SEM	Scanning electron microscopy
SLI	Sequential linker installation
SPES	Sulfonated poly(ether sulfone)
SSA	Specific surface area
ST	Super tetrahedron
TBU	Tertiary Building Unit
TDXRPD	Temperature-dependent X-ray powder diffraction
TEM	Transimission electon microscopy
TGA	Thermogravimetric analysis
THF	Tetrahydrofuran
TMAOH	Tetramethylammonium hydroxide
TOF	Turnover frequency
TPA	Terephthalic acid (also see BDC)
UiO	University of Oslo
UMCM	University of Michigan Crystalline Material
US	Ultrasound
UV	Ultraviolet
UV-Vis	Ultraviolet-Visible
UV-Vis-NIR	Ultraviolet-Visible-Near Infrared
WAXS	Wide-angle X-ray scattering

XRD	X-ray diffraction
XRF	X-ray fluorescence
ZIF	Zeolitic Imidazolate Frameworks

LIST OF APPENDICES

CHAPTER 1 INTRODUCTION

The revolutionary discovery of metal-organic frameworks (MOFs), almost 20 years ago, represented a huge turning point in the life of many researchers. Since then, the number of studies focusing on this interesting field has been increasing exponentially. Moreover, with the endless number of possible structures offered by this category, MOFs have attracted the sights of the scientific community worldwide as unique candidates in various applications. MOFs were considered under the broad class of hybrid materials in the early stages as a simple classification based on the structure constituents. However, the idea of tailoring the structure motivated researchers to focus on the assembly of multiple metal ions and organic linkers, seeking new structures of different properties.[1]

Basic attempts in MOF synthesis adapted primitive techniques, which mostly require a very long reaction time, reaching months. After that, the successful utilization of the solvothermal technique in MOF synthesis had made it the most widely adopted route in every publication by that time. At this stage, researchers were divided into those interested in new structures serving specific applications and others focusing on applying novel synthesis methods to achieve these structures. Among these new techniques, microwave-assisted synthesis is another promising alternative to solvothermal. Such a technique allowed for the achievement of many MOF structures at a much shorter reaction time and higher-quality crystals. Also, it results in products of smaller particle size that, in turn, improve the performance of these materials when incorporated in composites.[2]

In parallel, adding different functionalities to the framework, or MOF functionalization, took part in these research studies. Multivariate structures (MTV-MOFs), including both mixed-metal and mixed-linkers, were also of great interest in providing synergistic effects towards the targeted application. The next stage involved other avenues like heterogeneous MOFs and guest particles encapsulation. At this point, the computational design of MOFs was developed for several frameworks revealing the ability to expect structures that are not yet achieved.[3]

The next chapter will include more about the history of metal-organic frameworks, classification, and basic concepts in this field. Besides, we will discuss the different synthesis methods applied so far to prepare these remarkable structures. Also, a brief discussion about MOF functionalization and the latest advancements in these frameworks will be involved.

CHAPTER 2   LITERATURE REVIEW

2.1   Metal-Organic Frameworks, Brief History

Metal-organic frameworks (MOFs) have aroused great scientific attention in the last decades as a new emerging class of porous materials owing to their noticeable potential in various applications.[4–7] MOFs were sometimes labeled as porous coordination polymers (PCPs) or porous coordination networks (PCNs) in the early stages. They are usually known to be solid crystalline materials of high porosity originally made out of small building units of metal ions or clusters connected to multidentate organic ligands, resulting in multidimensional structures (Figure 2.1).[3,8,9] Such networks are considered large, accessible cages of regular shapes with large specific surface areas and high pore volume. These materials were proven to be extraordinarily beneficial in separation, gas storage, drug delivery, and heterogeneous catalysis.[10–12]
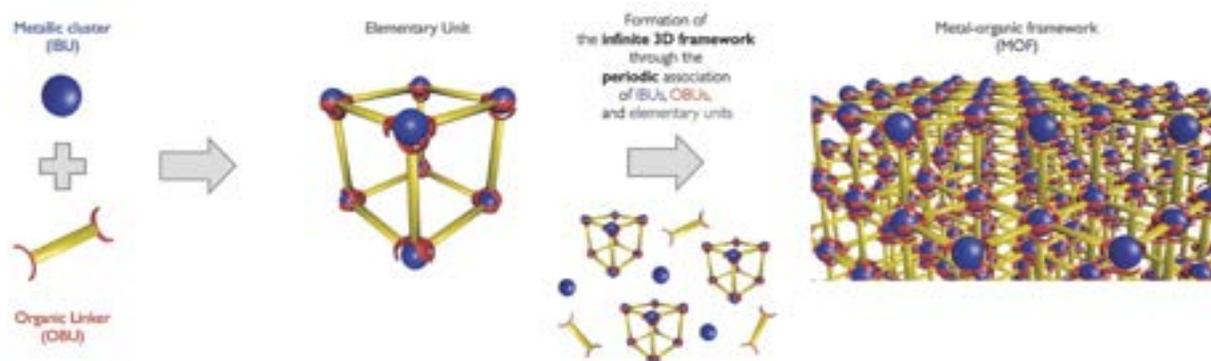
Figure 2.1 Self-assembly of metal-organic frameworks. *Reprinted with permission from ref.[9]*

The recent expansion in MOFs' discoveries has made it clearer that those materials of interest have unintentionally reduced the gap between different disciplines of chemistry. Some have regarded it as an interdisciplinary field related to the basic ones like inorganic and organic chemistry, and those specialized such as coordination, solid-state, computational, and crystal chemistry. However, the more knowledge we get about MOFs, the more confident we are that these materials belong to a new discipline, which motivated a great deal the rise of so-called "Reticular chemistry." Reticular chemistry is now defined as the branch of chemistry that is concerned with studying the linkage and breakage of some specific chemical entities to form extended structures in a controlled manner that can match a pre-designed strategy.[3,13]

The term "MOF" was first introduced by Yaghi *et al.* in 1995.[14] However, by the late 1990s, MOFs gained an exceptional reputation after successfully removing the guest solvent molecules in a process that is now commonly known as "Activation of MOFs." Activation was reported to one of the very first known MOFs called MOF-5 "IRMOF-1" without the loss of porosity through cracking or even collapsing the structure.[15] Such effective activation took place by replacing the solvent with a more volatile one, which would offer less stress on the crystals upon removal to result in a material with permanent porosity. In addition, the reported surface area and pore volume for MOFs surpass that of zeolites and other porous materials.[3]

In August 2009, the international union of pure and applied chemistry (IUPAC) started the "Coordination Polymers and Metal Organic Frameworks: Terminology and Nomenclature Guidelines" project headed by Lars R. Öhrström.[16] The main objective of this task group was to work on proper definitions and classification of these terms that would be acceptable by the researchers within this community.[16, 17] After several meetings, discussions, and surveying, the board of members came out with some recommendations published in the Journal of Pure and Applied Chemistry in 2013 and are supposed to be used as guidelines of unified perspectives.[17] MOFs were classified as a subcategory of coordination networks under the broad main category of coordination polymers in that article (Figure 2.2).
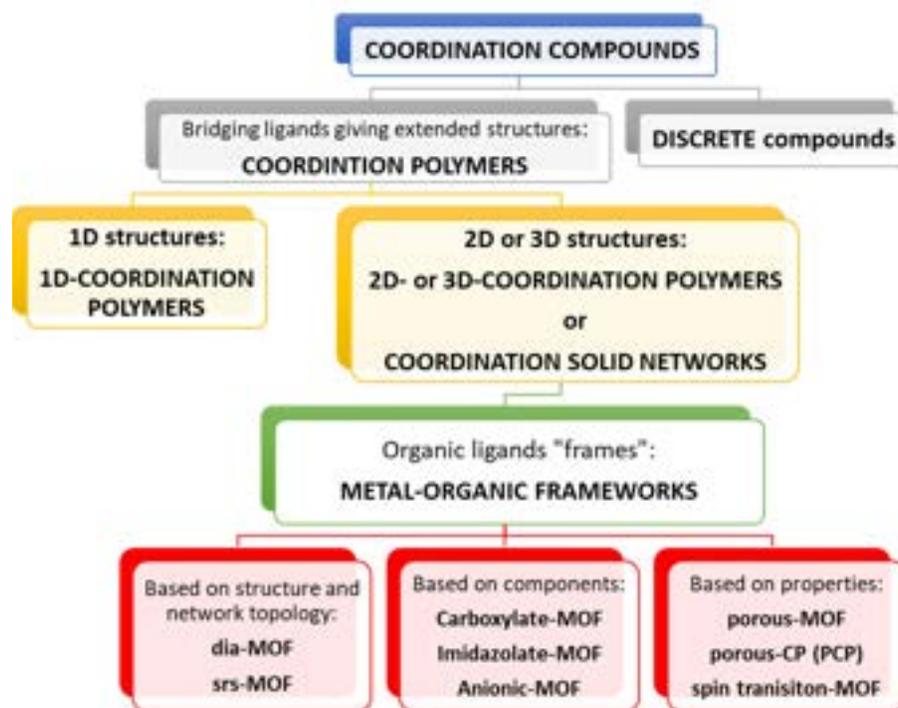
Figure 2.2 IUPAC classification of coordination compounds.

It was also recommended to use the term MOF with the coordination networks of the 2D and 3D extensions only matching their revised definition: "A metal-organic framework, abbreviated to MOF, is a coordination network with organic ligands containing potential voids." More importantly, it was explicitly discouraged the use of the term "Hybrid inorganic-organic materials" on these coordination polymers and to keep it for the sol-gel processed materials to avoid any misunderstanding, where MOFs were sometimes included in the classification of hybrid materials.[17]

2.2   A Closer Look into MOFs

As mentioned before, MOFs are basically formed through an initial step of complex formation by the metal cations with the organic bridging ligands through a covalent (coordination) bonding.[18] Then, a further stage of self-assembly takes place to give frameworks extending from 0D to 3D networks (Figure 2.3). Sometimes, it is much simpler to describe the structure in terms of nodes and linkers (or struts). The nodes represent the central metal ions or the polynuclear metal clusters, while the linkers are those organic molecules that possess moieties capable of bonding with the nodes (Figure 2.4).[3] Interestingly, MOFs were proven to be designable and tailorable based on the degree to which the involved metal is able to coordinate and form complexes and the dimensions or the points of extension of the used ligand (number of connecting groups).
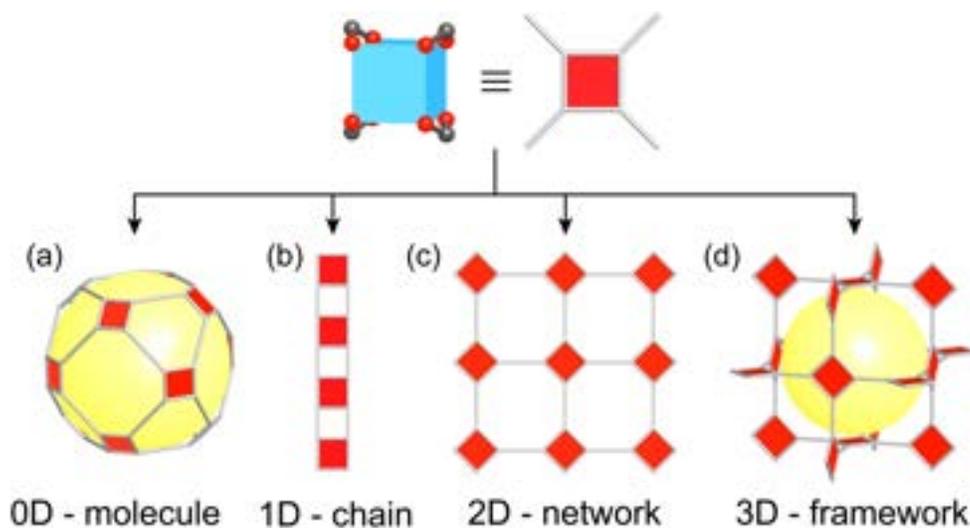
Figure 2.3 Multidimensional connections in MOFs. *Reprinted with permission from ref.[3]*
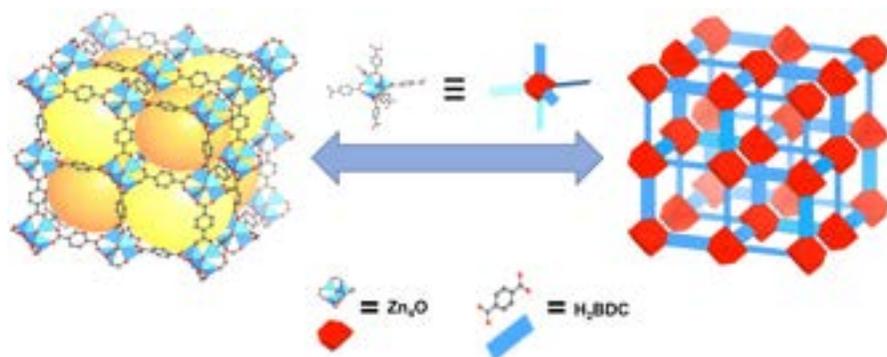
Figure 2.4 MOF-5 represented in nodes and linkers.

Furthermore, the secondary building unit (SBU) is a commonly used term in MOF chemistry, initially used for zeolites to describe their structural richness. The concept of SBUs allowed for the deconstruction of the frameworks of complex structures into limited structural subunits and their description in terms of simple nets of definite arrangements. Using this strategy, the whole network structure is regarded as a set of neighboring repeated SBUs connected to each other.[3] A single SBU is typically an aggregate of metal ions along with the binding groups of the organic anion linker as an integrated unit. SBUs take the shape of a paddlewheel of different extension points ranging from 3 and up to 12 connecting points (Figure 2.4). Usually, they are illustrated in the augmented layout instead of the particular atomic style (inset of Figure 2.4). Implementing such a concept permits the analysis and disassembly of the obtained MOFs for the deep studying and understanding of their topologies, and consequently, the design and prediction of others.[19] In the more sophisticated structures, the term tertiary building unit (TBU) might be used to describe such detailed frameworks.[20]
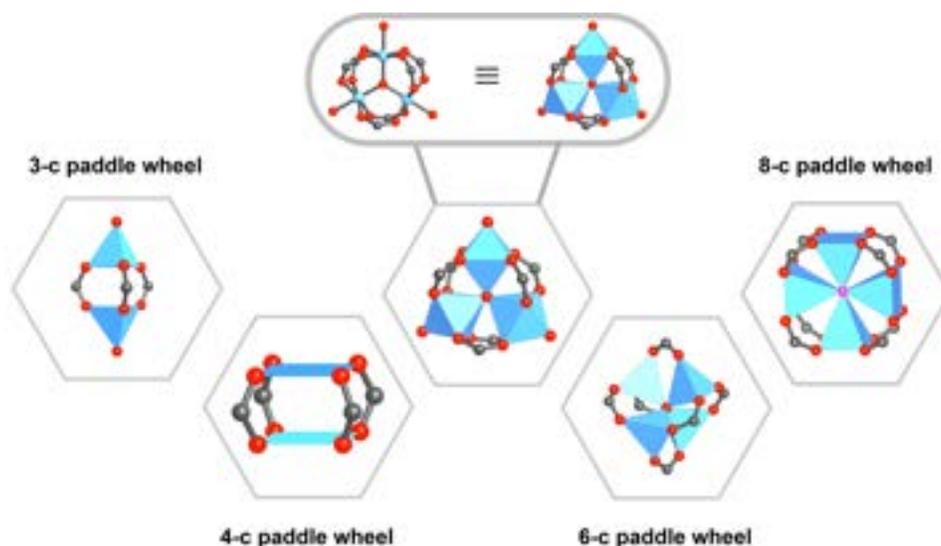
Figure 2.5 SBUs of different points of extension.

Speaking of the nodes, theoretically, any element that is capable of forming complexes can be implemented in MOFs.[21] Starting with the mono-, di-, and trivalent metals of groups I, II, and III, MOFs based on sodium (MOF-705), magnesium (MOF-74), aluminium (MIL-53), and many more of these groups have already been reported (MIL stands for Material of Institute Lavoisier).[22–24] A higher number of MOFs are based on the transition metals since they offer a higher degree of coordination and various oxidation states as a result of the d-orbitals contribution.[19] For this type of nodes, we can find MOF-5 (Zn^{2+}), HKUST-1 (Cu^{2+}), MIL-88 (Fe^{3+}), and UiO-66 (Zr^{2+}); whereby HKUST and UiO stand for Hong Kong University of Science and Technology and University of Oslo, respectively (Figure 2.6). Moreover, lanthanides were found to be able to contribute to the MOF formation; however, controlling their structure was found to be complicated due to the presence of the f-orbitals that have complex interactions.[3] Also, heterometallic MOFs were also reported, in which the framework is made from two or more metals.[25]
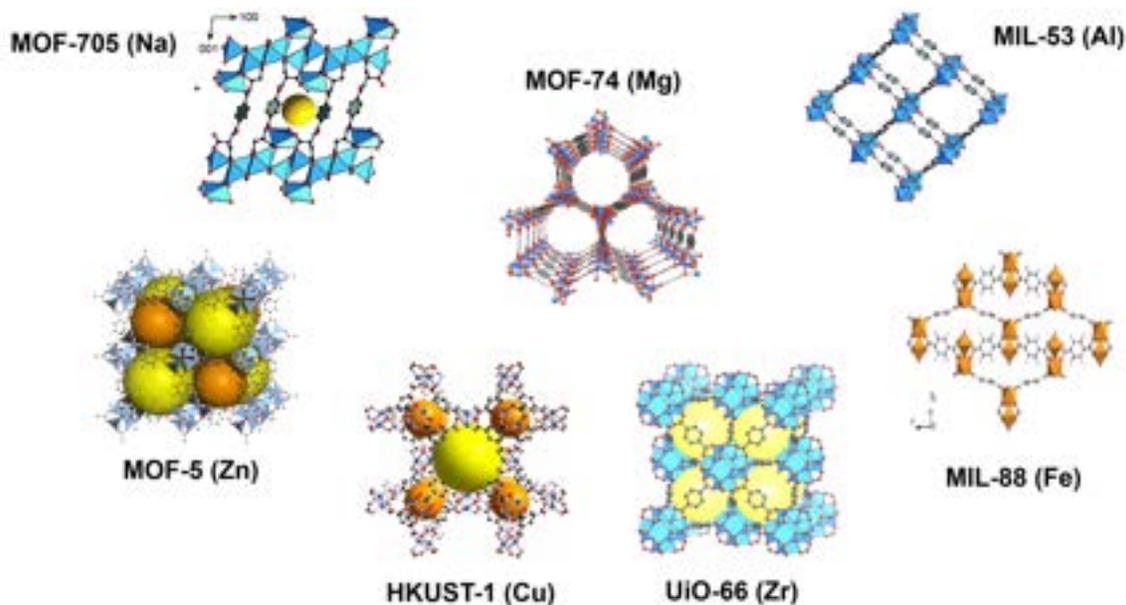
Figure 2.6 Examples of MOFs of various metals.

On the other hand, linkers of multiple binding groups are divided into carboxylate linkers, nitrogen-containing linkers, and mixed linkers (Figure 2.7).[26] Carboxylate linkers are mainly polycarboxylate ligands, in which the electron pair donor sites are the oxygen atoms of the carboxyl groups. They are subdivided into aliphatic and aromatic acids. Aliphatic ligands include short- and long-chain acids like oxalic, fumaric, succinic, and adipic. MOFs with aromatic acid ligands like terephthalic acid (H_2BDC) and trimesic acid (H_3BTC) are the most popular. However, other aromatic linkers with extended lengths are also reported as H_3BTB, H_3BTE, H_3BBC.

In nitrogen-based linkers, bridging takes place between the metal nodes and the nitrogen atoms present in the ligand. N-heterocyclic compounds are the most dominant type of these linkers. It may contain pyridine, imidazole, and triazine, along with their derivatives. The use of such type of linkers has resulted in a whole new type of coordination polymers named zeolitic imidazolate frameworks (ZIFs).[27] Finally, mixed linkers are those ligands that possess both types of binding groups and are capable of binding with the metal centers by both sites. 2,5-diamino terephthalic acid is a very convenient example of the mixed-type linkers.
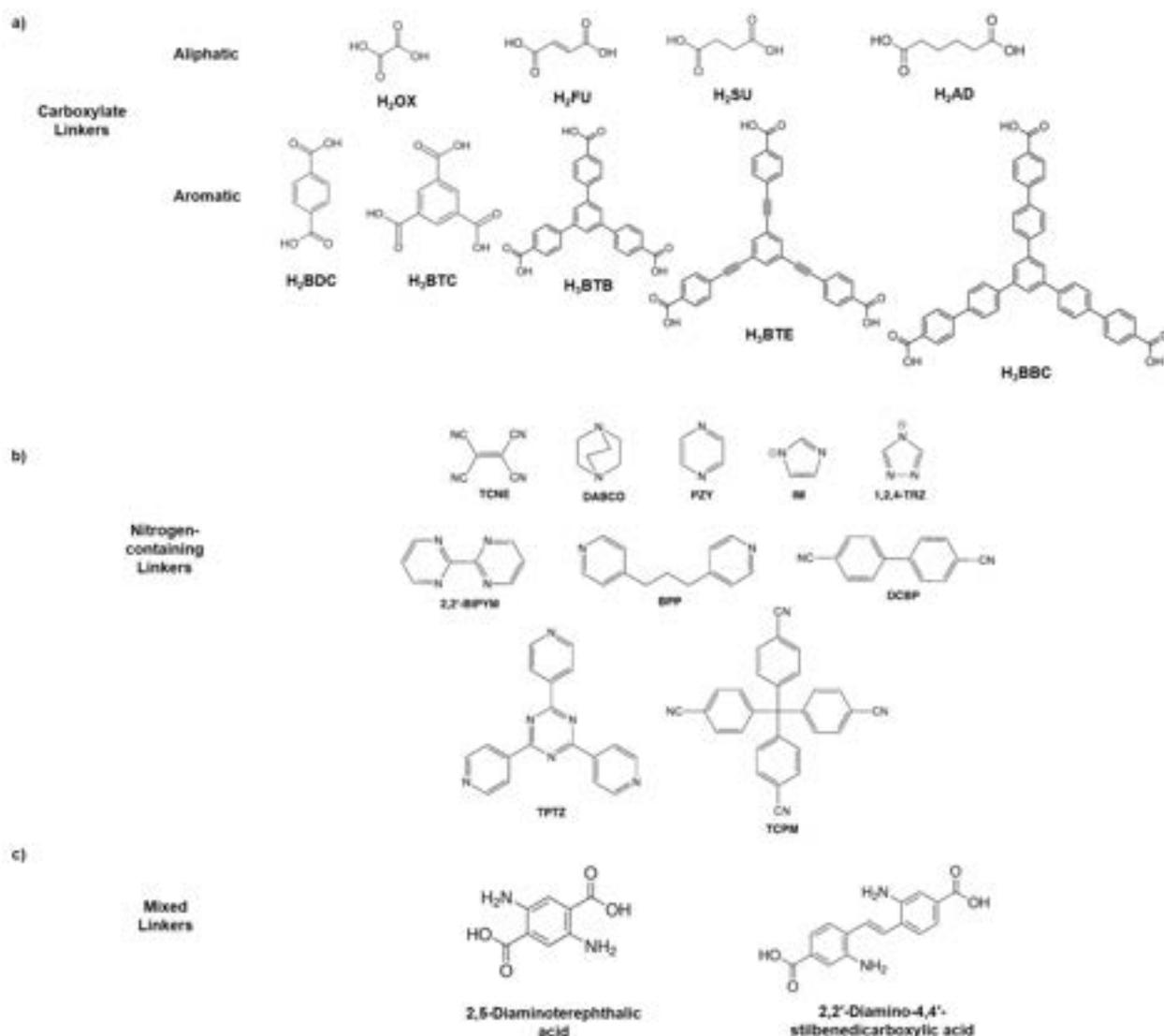
Figure 2.7 Types of Linkers in MOFs a) Carboxylate, b) Nitrogen-containing, and c) Mixed.

2.3 MOFs Synthesis Techniques

2.3.1 Conventional method

For MOFs, the conventional preparation method refers to the hydrothermal/solvothermal synthesis technique, in which a solution of the metal salt and the ligand is prepared and then placed in a closely-tight hydrothermal bomb (Figure 2.8). The reaction takes place under autogenous pressure as a result of heating the mixture at temperatures higher than the boiling point of the solvent. Conventional synthesis results in crystals of good quality and large sizes suitable for further structural determination. Despite being the most common and widely used technique, alternatives have been investigated as it is still considered a less energy-efficient method as it requires high reaction temperatures, long reaction times, and large consumption of energy.[28]

Figure 2.8 Conventional hydrothermal/solvothermal method for MOF synthesis.

2.3.2 Solvent evaporation and Vapour diffusion synthesis

In the solvent evaporation method, the precursors are entirely dissolved in a minimum amount of a solvent that is then allowed to evaporate at ambient temperature. With no external energy source provided, this technique might take place over extended periods of time, reaching months. Variating the concentration of the reactants above the solubility threshold influenced by the slow evaporation induces the MOF crystals precipitation (Figure 2.9).[29].

Vapor diffusion is regarded as an alternative technique for the solvent evaporation method that also takes place at room temperature, in which the metal salt and the ligand are typically dissolved in a suitable solvent. However, in this method, the solution is not covered directly. It is placed in another container that is then sealed. A space between the ends of both vessels should be kept clear to ensure the diffusion of the formed vapors. The surrounding outer vessel should contain a solution of a volatile base that will slowly evaporate over a long time

and diffuse into the inner vessel, resulting in MOF crystals of large sizes (Figure 2.10).[29]

Figure 2.9 Solvent evaporation technique.

Figure 2.10 Vapor Diffusion technique.

2.3.3 Microwave-assisted synthesis

Microwave-assisted synthesis is considered as one of the most promising non-conventional techniques for MOFs production, for being a timesaving and an energy-efficient technique.[30] Microwave (MW) radiations are electromagnetic radiations of frequencies ranging from 0.3 to 300 GHz that corresponds to a wavelength range of 1 mm to 1m (Figure 2.11-a). In this system, a magnetron produces microwaves that are then transferred through waveguides to a confined space called the sample chamber, where the reaction vessel is placed (Figure 2.11-b). Heating takes place in the microwave systems by the dielectric heating effects, where the

sample interacts with the generated electromagnetic field based on two major mechanisms; Dipolar polarization and Ionic conduction.[31]

In the dipolar polarization, the molecules with dipole moments constantly rotate to align with the oscillating field that in turn causes frictions generating heat. On the other hand, the ionic conduction mechanism depends on the ions of the medium that repeatedly vibrate in the alternating field resulting in collisions with the neighboring molecules releasing energy (Figure 2.11-c). The heat production in microwave systems is perfectly homogenous compared to the conventional heating methods as the reaction medium itself is internally heated by its components (Figure 2.11-d).[26]
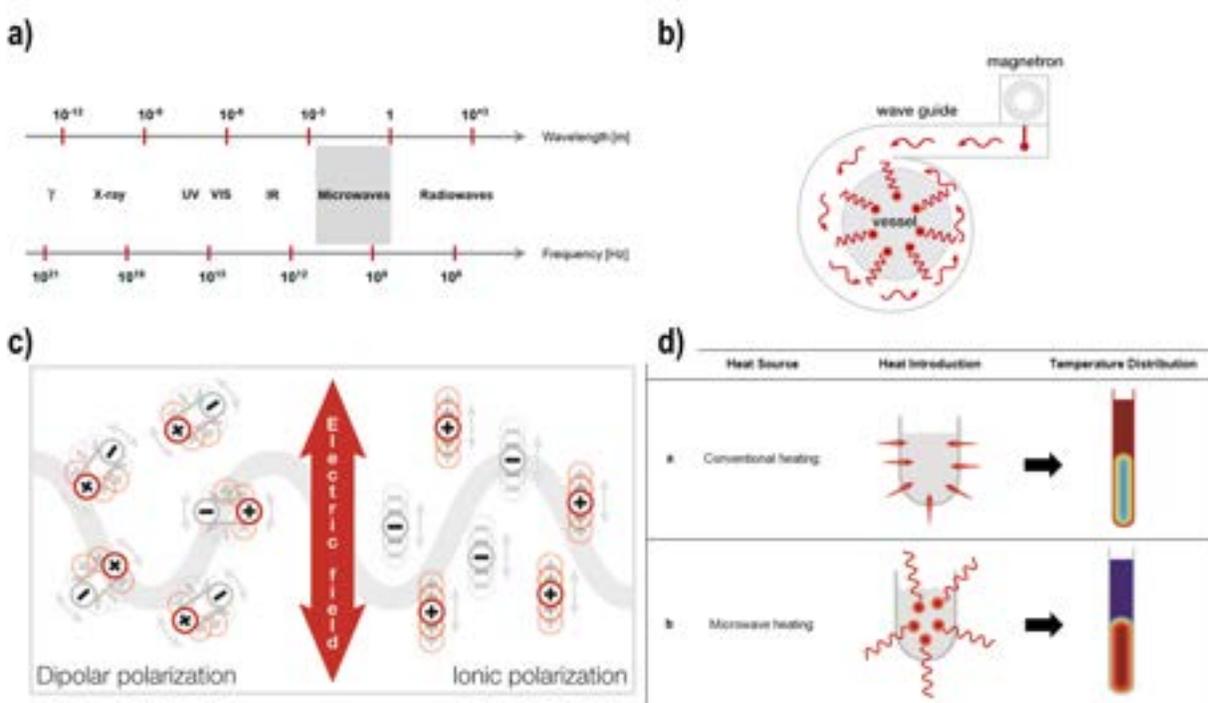
Figure 2.11 Microwave-assisted synthesis. a) Electromagnetic waves spectrum, b) Schematic diagram of the MWs distribution inside a reactor, c) The two main heating mechanisms induced by MWs, d) Temperature distribution inside a vial resulting from different heating methods.

The ongoing research success of the microwave-assisted synthesis of MOFs has resulted in increased utilization of this approach. This approach enabled us to achieve higher reaction temperatures (superheating of the solvents), decrease the energy consumption and the reaction time (by the direct "in-core" heating), and obtaining higher yields and purer compounds (minimizing wall effects and faster heating rates). However, obtaining single crystals that are large enough to undergo successful analysis is still a challenging matter due to the high

nucleation rate resulting from the fast heating at high temperatures.[32]

2.3.4 Mechanochemical synthesis

The mechanochemical synthesis technique for producing MOFs is the most eco-friendly process that belongs to the non-conventional methods of preparation. In this technique, the reaction takes place at room temperature without the involvement of any solvents. This solvent-free method initiates the reaction by the cleavage of the intramolecular bonds as a result of applying some external mechanical forces (i.e., grinding) followed by some chemical transformations leading to the production of the desired MOF (Figure 2.12).[33]
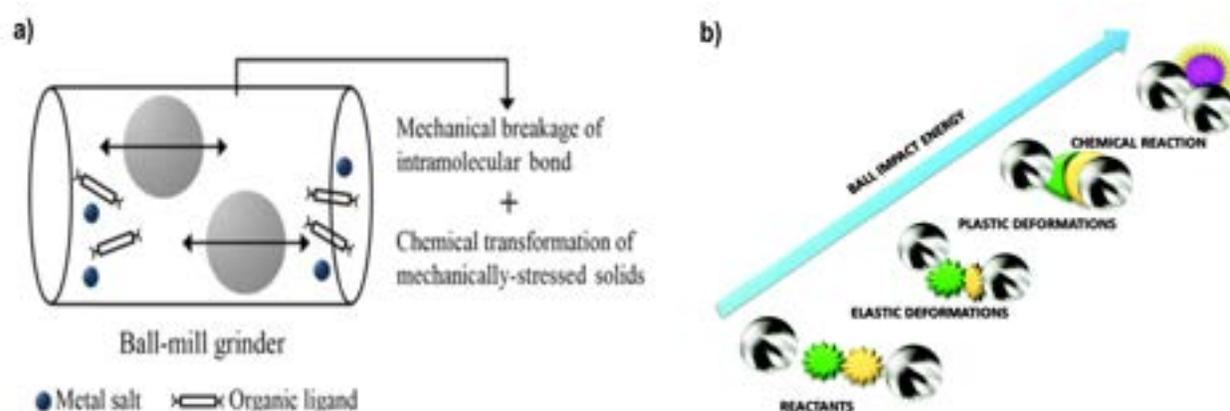
Figure 2.12 Mechanochemical synthesis. a) Schematic diagram of the process, b) Stepwise transformation based on the energy delivered by the balls in a typical mechanochemical synthesis by ball milling.

This method was proved to be advantageous over other techniques as no liquid wastes are produced after the reaction (except for water as a side-product), thus saves many post-treatment steps of purification. Besides, short reaction times, in terms of minutes, are required for this process.[34] Moreover, synthesis of some MOFs was successfully achieved starting with metal oxides instead of the usual metal chloride or nitrate salts. Nevertheless, with this growing reputation, successful investigations of this method are still limited.

Liquid-assisted grinding (LAG), as the second route of mechanochemical synthesis, has been reported for some MOFs, in which a minimal amount of a solvent is introduced with the reaction mixture. The addition of such solvent drops increases the mobility of the reactants on the molecular scale, leading to accelerated reactions of shorter times. Furthermore, the use of different liquids was found to influence the formation of specific topologies, hence considered as structure-directing agents.[35]

2.3.5 Sonochemical synthesis

Continuous interest in non-conventional techniques gave rise to the ultrasound-assisted (sono-chemical) synthesis of MOFs. The sonochemical synthesis was reported to resemble the microwave synthesis approach as it homogeneously heats the reaction mixture resulting in a high rate of nucleation and a concise crystallization time. Ultrasonic (US) waves are used to deliver sufficient energy to the medium, influencing the formation of MOFs.[36] It is considered as one of the energy-efficient methods, in which the ultrasound waves develop a state of what is so-called "acoustic cavitation," where a massive number of bubbles are formed and collapsed, creating hot spots all over the reaction medium. These numerous hot spots of high local temperature and pressure lead to faster heating rates and very fine crystals (Figure 2.13).[28]
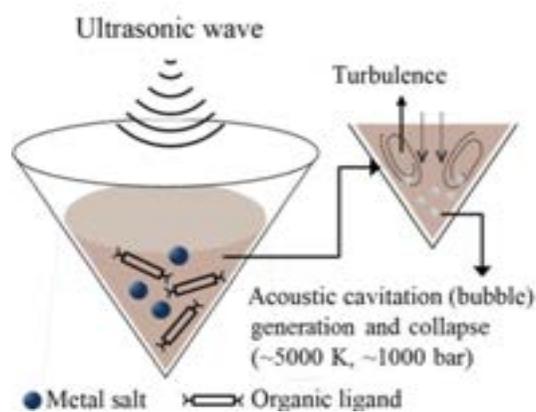
Figure 2.13 Sonochemical synthesis technique. *Adapted with permission from ref.[28]*

2.3.6 Electrochemical synthesis

In electrochemical synthesis, a pure metal source is used instead of a metal salt to obtain the required MOF. A metal rod is connected as the anode in an electric circuit, and the electrolyte used contains the dissolved linker along with a conducting salt (Figure 2.14). This method provides a continuous supply of metal ions, based on the anodic dissolution, that would further react with the involved linker to result in a MOF of high purity due to the absence of any accompanying anions (i.e., chloride, or nitrate). The purity of the obtained MOF and the continuous flow reaction had made this technique favorable in the large-scale production. A drawback of this method is that acid-free synthesis might not be successfully performed; otherwise, metal deposition on the cathode might occur.[28] A protic solvent is usually employed to prevent this deposition by forming hydrogen gas at the cathode instead.
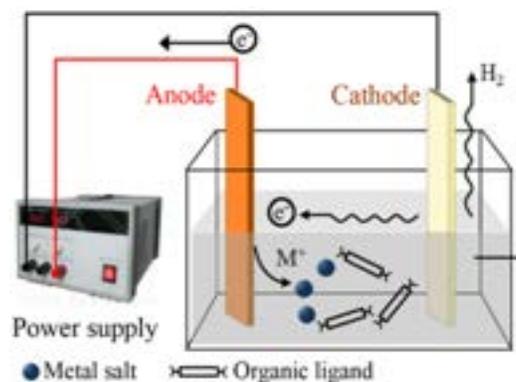
Figure 2.14 Electrochemical synthesis technique. *Adapted with permission from ref.[28]*

2.4 Complexity and heterogeneity in MOFs

Based on the different building units of the metal-organic frameworks, the attempts of implanting more than one linker or SBU in the same structure have given rise to complexity and heterogeneity of MOFs. Complexity in MOFs means the formation of new complex structures as a result of the implication of more than one network topology in one formulation, giving a totally distinct network of different topology.[3] This can be carried out by using either the same SBU (referring to using the same metal) with two or more linkers of different dentation types (e.g., BDC and BTC) or by using different multiple different SBUs with the same linker or even the use of both different SBUs and linkers. Such complex structures are called Multinary structures, in which the position and the identity of each building network block are reserved and could be defined crystallographically (Figure 2.15).[3]
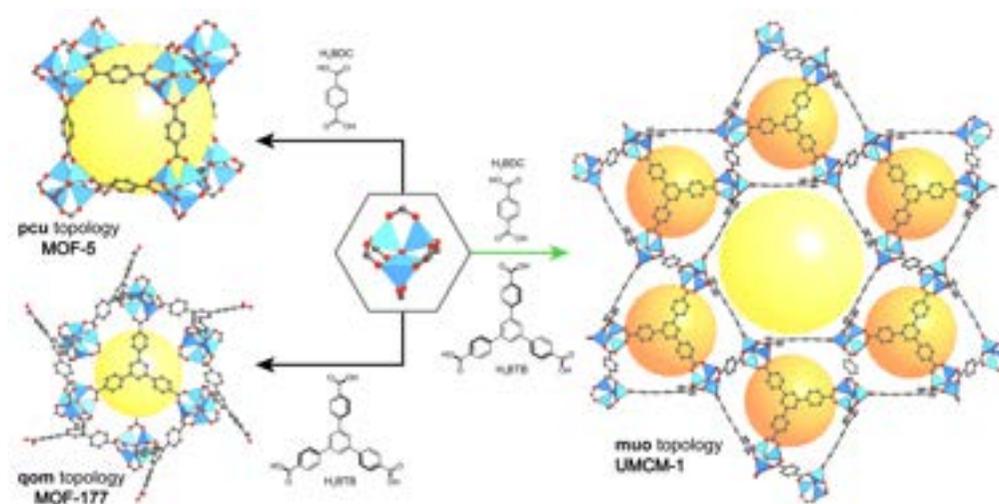
Figure 2.15 UMCM-1 as an example of complexity in MOFs. *Reprinted with permission from ref.[3]*

In contrast, heterogeneity implies the achievement of the same structural type of the parent MOF (i.e., topology), but with comparable building units, preserving identical backbone.[3, 37]. Heterogeneous MOFs, otherwise called Multivariate (MTV) MOFs, are obtained by either the Multi-Metal or the Multi-Linker approach. In the multi-metal approach, various metal ions that form the same SBU are employed with the same linker (Figure 2.16-a). On the contrary, the multi-linker approach involves the introduction of a single-metal-type SBU to linkers of the same structure but with different functional groups (e.g., BDC and NH_2-BDC) (Figure 2.16-b). Hence, MTV-MOFs are isostructural and metrically identical MOFs of distinct chemical compositions.[38]
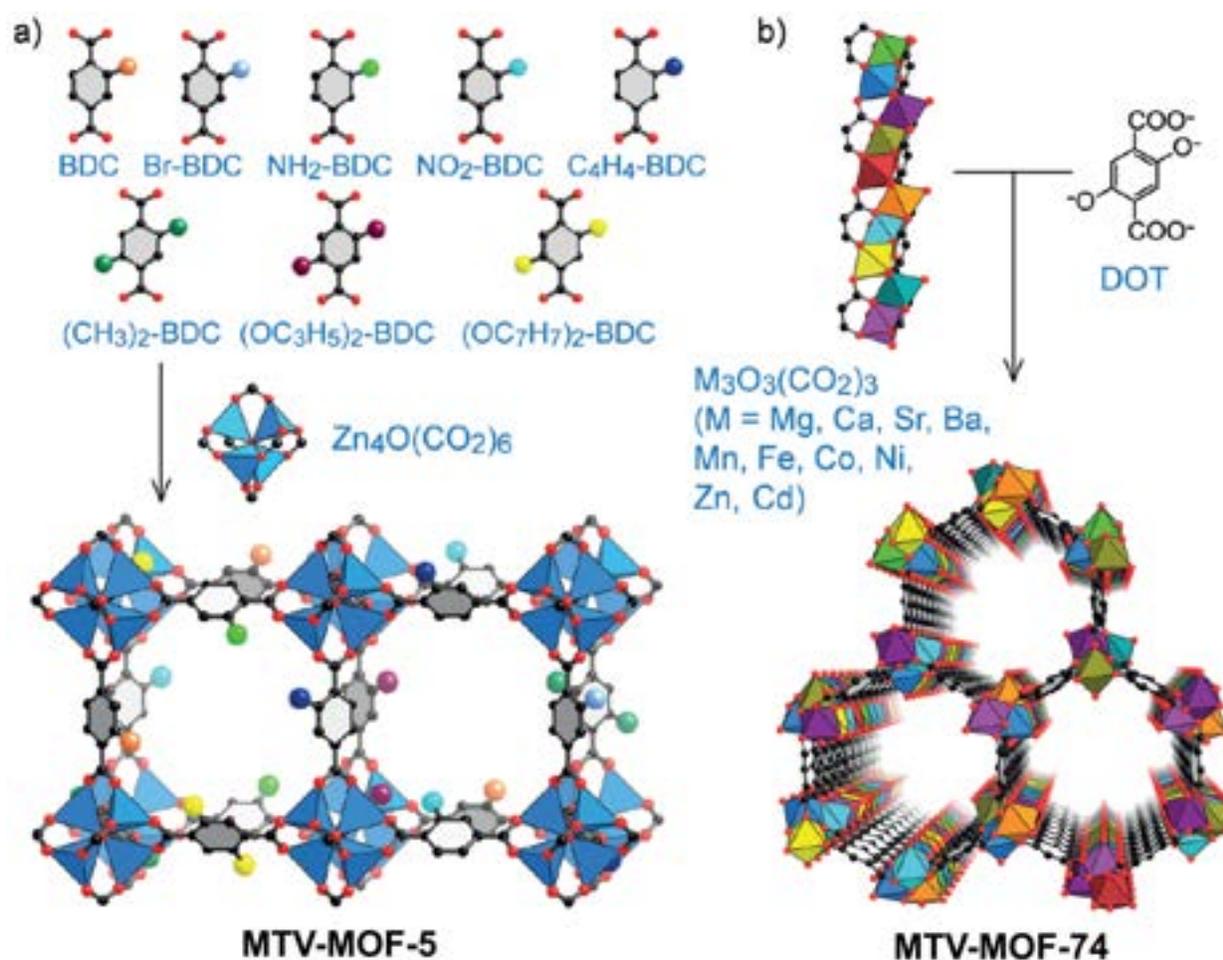
Figure 2.16 Heterogenity in MOFs. a) Multi-linker approach, b) Multi-metal approach. *Reprinted with permission from ref.[39]*

However, in MTV-MOFs, the distribution of the variating building units in the resulting structure does not have a specific topological preference, which means that there will be no

favorable occupation in the crystal and so an undefined spatial arrangement might take place. Hence, various possibilities might exist depending on the chemical nature of the variating constituent and the reaction conditions. In the multi-linker approach, the distribution of the main linker along with its derivatives may follow one of the following scenarios:

a) A random distribution scenario.
b) A well-ordered alternating pattern.
c) Clustering of functionalities.

However, in the multi-metal approach, the variation in the position of the metal is restricted to the SBU itself, as a building block, resulting in a limited number of possibilities:

a) Domain scenario, in which SBUs of a single metal type are formed first and then connected to the other metal type SBUs (Figure 2.16-a).
b) Well-mixed scenario, in which the whole SBUs involved in the MOF formation consist of heterometallic (i.e., bimetallic) clusters (Figure 2.16-b)
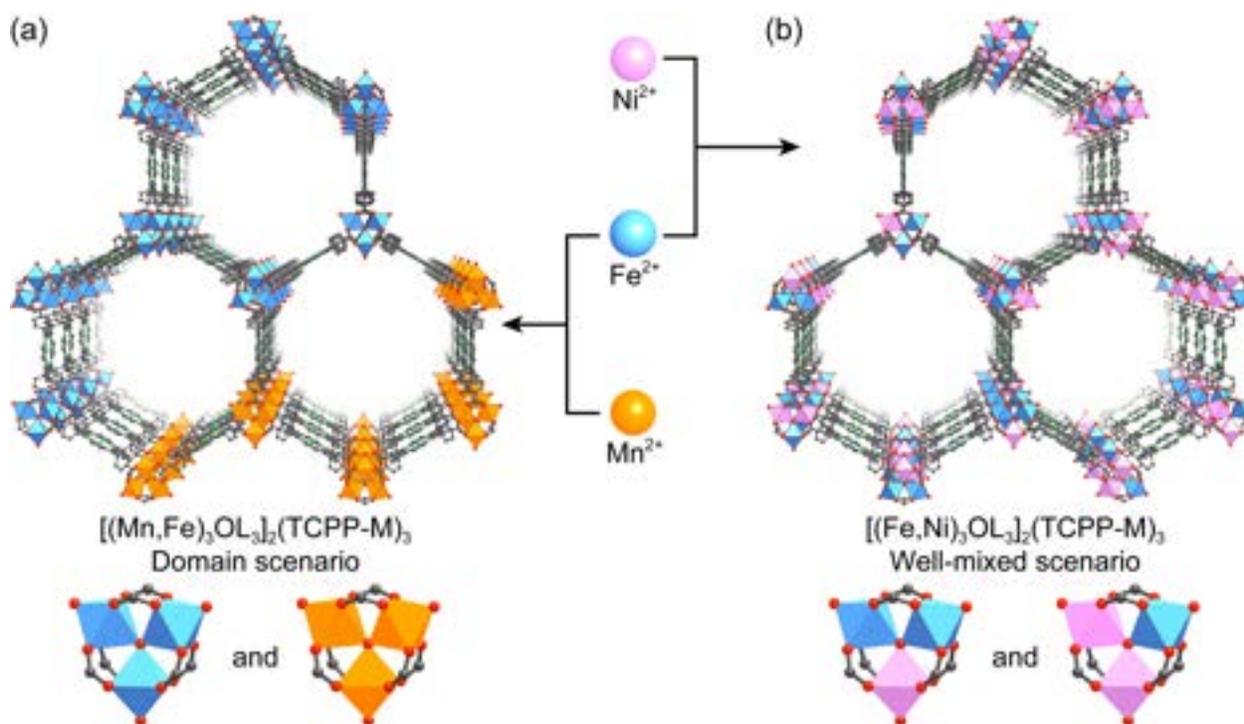
Figure 2.17 Multi-metal MOF. a) Domain scenario, b) Well-mixed scenario. *Reprinted with permission from ref.[3]*

2.5   Functionalization of MOFs

The infinite variations in the structure and composition of metal-organic frameworks based on the synthesis method and the building units have made them highly studied material lately. Besides, the noticeable expansion in MOFs' chemistry has proven them to be designable and tailorable to serve the purpose of use perfectly. Direct and indirect modifications performed on MOFs have been reported to further increase the impact of MOFs in their different fields of application.[40]

Functionalization of MOFs includes those modifications that might take place prior, during, or even after preparation. In other words, functionalization is classified into pre-synthetic, in situ, and post-synthetic modifications. Post-Synthetic Modification (PSM) may also subdivide into weak, strong, and covalent, based on the nature and strength of interactions (Figure 2.18).[3].
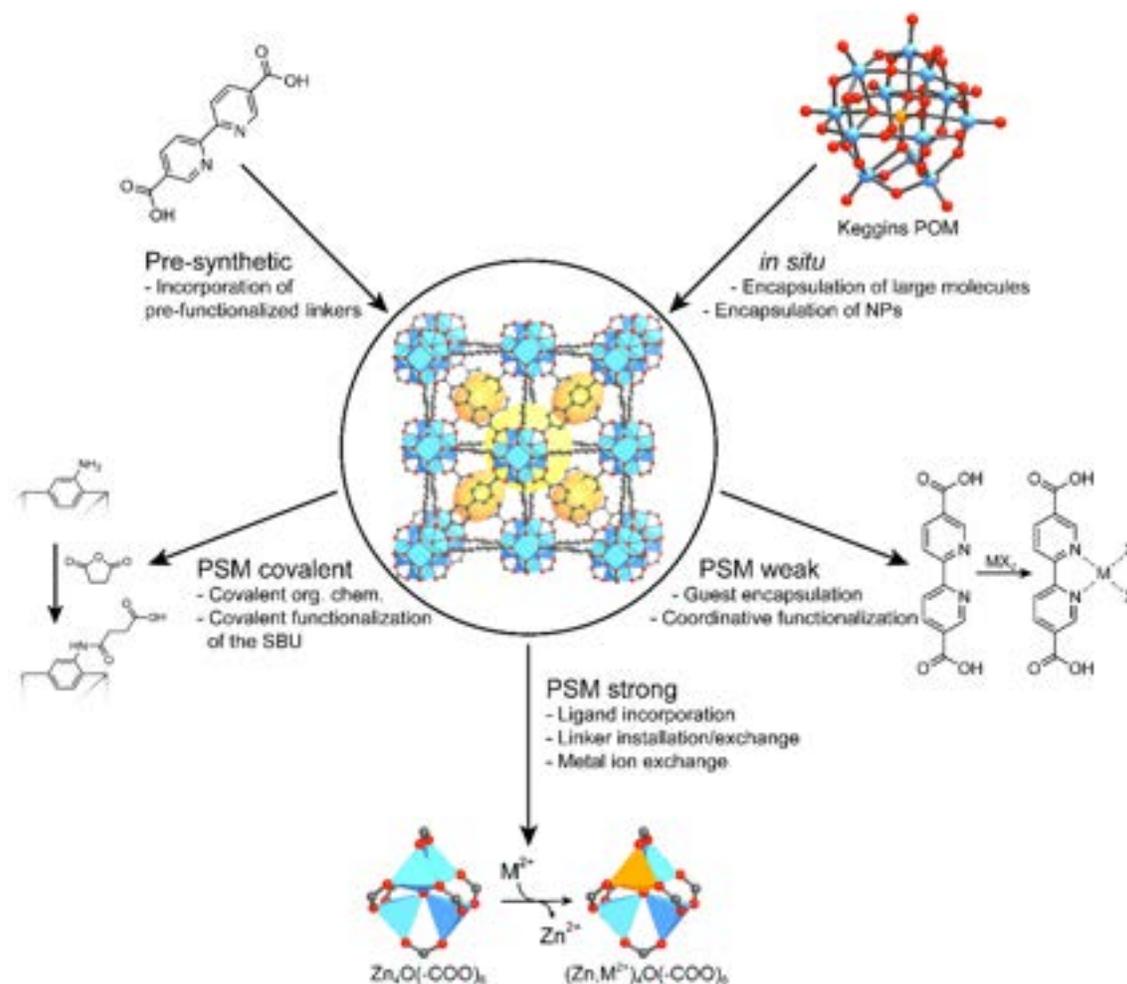
Figure 2.18 Functionalization of MOFs. *Reprinted with permission from ref.[3]*

Pre-synthetic modifications include the employment of linkers with suitable functional groups to the backbone of the targeted MOF so that they would not affect the structure; however, they are susceptible to further processing after preparation. In situ modifications comprise the encapsulation of either large molecules or metal nanoparticles within the pores of the MOF. Trapping of such molecules can take place during the framework formation, in which the molecules are immobilized in the pores of a small aperture window.[41]

PSM is generally the most widely used method of functionalization as it provides a facile route of modification without risking any interference with the formulation of the intended MOF. Moreover, it gives direct access to structures that were not achievable by the direct route. PSM of weak interactions covers processes of guest molecules substitution as the case for the reaction solvent (mother liquor) replacement for activation. In addition, further coordination with pre-synthetically modified MOFs or MOFs with open metal sites (OMS) is also included in this weak-PSM category. Covalent PSM might also include the further reaction of a functional group that is already contained within the MOF structure (usually amino groups); however, in this case, the reaction takes place through covalent bonding, but not just coordination.[3, 18]

PSM of strong interactions is considered as a powerful tool for MOF manipulation. It is regarded as the second-chance or the backdoor of modifying the inherent structural properties. It also allowed for the addition and exchange of one of the constituents of the main framework. It was proven to be an alternative way for the introduction of heterogeneity in MOFs and the achievement of multivariates MTVs that can not be prepared through one-pot (direct) synthesis. Strong-PSM had made it possible for reticulation by linker-exchange through a process named post-synthetic linker exchange (PSLE) or solvent assisted linker exchange (SALE), in which a MOF is refluxed with a concentrated solution of the linker in a suitable solvent for a prolonged time at elevated temperature. In the same manner, MOFs can undergo a metal ion exchange to achieve MTV-MOFs of mixed-metal SBUs, which would be very beneficial in catalytic applications. Moreover, PSM can offer complexity in MOFs through a post-synthetic linker installation process named sequential linker installation (SLI), in which the network structure is converted from one topology to another through single-crystal to single-crystal transformation due to the introduced linker after preparation.

CHAPTER 3   COHERENCE OF THE ARTICLES

The following four chapters comprise the publications output based on the main findings of this research and represent the core of the thesis. Each chapter presents a separate peer-reviewed journal paper.

Chapter 4 consists of a comprehensive critical review of MIL-101 metal-organic framework *"Revisiting the MIL-101 Metal–Organic Framework: Design, Synthesis, Modifications, Advances, and Recent Applications"* that was published in *Journal of Materials Chemistry A* (Vol. 9, P. 22159-22217, 2021). In this review, we covered the design, structure, synthesis, and characterization of MIL-101(Cr) since its discovery by Férey *et al.* in 2005. Also, we present the first profound review study on currently known MIL-101 metal analogues in the literature (e.g., Fe, Al, V, Sc, Ti, and Mn). Furthermore, we compared all the synthesis routes introducing the impediments, merits, and influence on the final structures. Furthermore, we reviewed mixed-metal MIL-101 structures, especially those made from Cr, Fe, and Al combinations. Finally, recent advances of this remarkable MOF and its applications in different disciplines, including adsorption, catalysis, photocatalysis, membranes, sensors, and drug delivery.

Chapter 5 addresses the results of the first article *"Multivariate Metal-Organic Framework MTV-MIL-101 via Post-Synthetic Cation Exchange: Is It Truly Achievable?"* that was published in *Dalton Transactions* (Vol. 51, P. 3280-3294, 2022). In this article, we arbitrated the dispute of whether or not the SACS method applies to MIL-101(Cr) to obtain the mixed-metal MTV-MIL-101s. Szilágyi's method that recurs to aqueous solutions of metal(III) chloride yielded a mixture of α-Fe$_2$O$_3$ with the pristine MOF crystals, instead of promoting metal-ion substitution. Therefore, the post-synthetic cation exchange for MIL-101(Cr) cannot be performed in aqueous media, confirming the stability and kinetic inertness of the chromium ion sphere in water. On the other hand, the cation substitution was successful by changing the refluxing solvent to DMF. Hence, mixed-metal MIL-101s are achievable via the simple PSE technique; however, the used solvent is the most crucial factor to consider.

Chapter 6 encloses the results of the second article *"Microwave-Assisted Synthesis of the Flexible Iron-Based MIL-88B Metal-Organic Framework for Advanced Energetic Systems"* that was published in *Journal of Inorganic and Organometallic Polymers and Materials* (2022). In this article, the flexible MIL-88B structure was obtained via a rapid microwave-assisted technique, whereby the reaction took place at 150 °C for 10 min. Such conditions influenced the production of uniform hexagonal diamond-like crystals. These crystals were

then incorporated in an oxidizer/MOF composite for an enhanced catalytic decomposition behavior beneficial in energetic systems. The results showed that the MOF contributes to the overall decomposition of the composite, giving a higher energy output at a lower decomposition temperature. Also, activation energy calculations were performed to prove the decrease in the activation energy of the ammonium perchlorate oxidizer as a result of the MOF incorporation.

Chapter 7 presents the results of the third article "*Facile Solvothermal Synthesis of MIL-47 (V) Metal-Organic Framework for a High-Performance Epoxy/MOF Coating with Improved Anticorrosion Properties*" that was published in *RSC Advances* (Vol. 12, P. 9008-9022, 2022). In this article, MIL-47(V) was successfully synthesized from V_2O_5 via a solvothermal method, whereby the reaction did not require the addition of any modulators/mineralizers. Moreover, the reaction took place at a lower reaction temperature and duration than other studies reported before (180 °C/20 h instead of 220 °C/72 h). The prepared MOF was then added to epoxy to produce an advanced coating that applies to aluminum alloy AA2024 for corrosion protection in a harsh chloride-rich environment. Investigation via SEM-EDX for the MOF/epoxy coating revealed a uniform coating with a constant thickness of 10 ± 2 μm and a homogeneous distribution of the MOF crystals within the thermoset epoxy matrix. The epoxy/MOF coating was more hydrophilic than the neat-epoxy coating. However, the inclusion of the MOF extended the lifetime protection of the metal surface three folds. Besides, we proposed an interaction mechanism between the corrosive species and the epoxy/MOF composition. The corrosive species diffuse into the coating and interact with MOF crystals to release vanadate ions and develop a protective film at the intermetallic particles.

Additionally, **Appendix A** presents our contribution in another publication concerning the synthesis of a coordination polymer (CMCP) and its use anticorrosion applications. Appendix A encompass the results of the solvothermal synthesis of a Ce/Melamine coordination polymer (CMCP) and in application to provide anticorrosion protection for aluminum alloy AA2024 against a chloride-rich environment. The article "Synthesis of a novel Ce(III)/melamine coordination polymer and its application for corrosion protection of AA2024 in NaCl solution" was published in *RSC Advances* (Vol. 11, P. 6330-6345, 2021).

CHAPTER 4   ARTICLE 1 - REVISITING THE MIL-101 METAL-ORGANIC FRAMEWORK: DESIGN, SYNTHESIS, MODIFICATIONS, ADVANCES, AND RECENT APPLICATIONS

Mahmoud Y. Zorainy,[1,2] Mohamad Gar Alalm,[1,3] Serge Kaliaguine,[4] Daria. C. Boffito[1]

4.1   Abstract

Metal-organic frameworks (MOFs) have expanded into a burgeoning topic in materials science and engineering. Their success mostly stems from the versatility of their structure that can be diversely designed by precise control over the assembly. We conduct a critical review on the design and synthesis of MIL-101 MOFs, assessing the viability and applications of its diversified structures. Previous reviews are limited to the MIL-101(Cr). On the contrary, this study presents the synthesis strategies, the merits, and the limitations of the different MIL-101 metal analogues, including Fe, Al, V, Ti, Sc, and Mn. Furthermore, we review the literature on the multivariate type of MIL-101 (MTV-MIL-101), whereby pairwise combinations of metals are involved in the framework. We discuss how the synthesis parameters such as temperature, medium pH, and ratios of precursors intimately influence the final product characteristics. This study moreover presents the effects of changes in these parameters on the final framework structure. For instance, other polymorphs like MIL-88, MIL-53, MOF-235, MIL-47, and MIL-67 were detected in the final product. Finally, the recent applications of MIL-101 in adsorption, catalysis, photocatalysis, membrane preparation, sensor design, and drug delivery are presented and discussed.
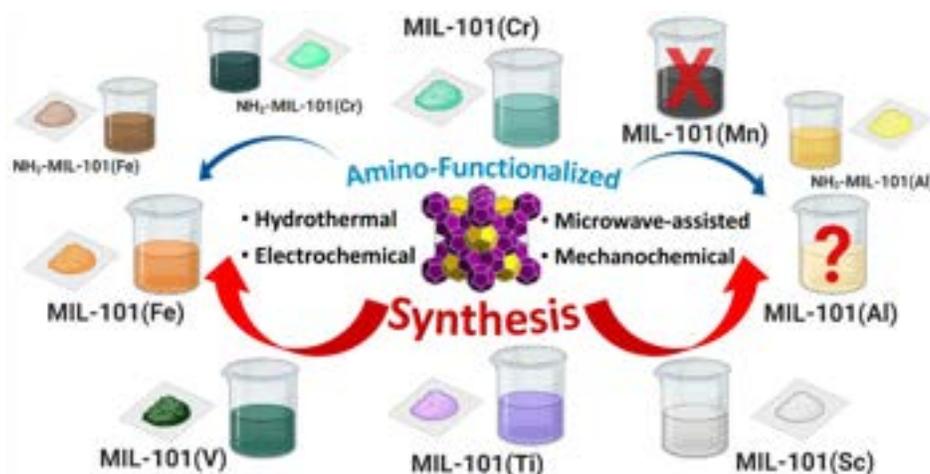
[1]Chemical Engineering Department, Polytechnique Montréal, Montréal, QC H3C 3A7 (Canada)
[2]Chemical Engineering Department, Military Technical College, Cairo (Egypt)
[3]Department of Public Works Engineering, Faculty of Engineering, Mansoura University, 35516 (Egypt)
[4]Chemical Engineering Department, Laval University, Québec, QC G1V 0A6 (Canada)

4.2 Introduction

Metal-organic frameworks (MOFs) are highly porous crystalline compounds comprising an infinite array of repeating small building units. These units include metal ions or clusters connected to polydentate organic ligands through covalent or iono-covalent bonds forming multidimensional networks. They were designated by the international union of pure and applied chemistry (IUPAC) as a subclass of coordination polymers (CPs) that contain "potential voids."[16, 17] Nevertheless, MOFs are also referred to as structures varying from 0D (also called metal-organic polyhedra "MOPs"), 1D, 2D, and up to 3D frameworks. These are considered as having large, accessible cages of regular shapes. They possess remarkably high surface area and pore volumes, and they are capable of trapping different molecules within these cavities. These materials were proven to have substantial benefits in a wide range of applications, including gas storage, separation, and heterogeneous catalysis.[3]

Prior to discussing recent advances related to MIL-101 as a particular MOF structure, some general features of MOFs will be recalled in order to illustrate the reasons to select MIL-101 as the object of this review. Describing MOFs as crystalline materials does not necessarily imply the solid, robust structure of their ordinary powder form. Amorphous metal-organic frameworks (aMOFs) in which the crystallinity of the basic building blocks is maintained over short distances are possible, whereas the long-range periodic order has been of major interest in this discipline.[42] Controlling the degree of periodicity to middle- and short-ranged networks has given rise to glass and liquid CPs (4th generation).[43, 44] Furthermore, soft, flexible, or dynamic MOFs are also a new subclass of these materials (3rd generation). In this subclass, a reversible flexing (crystal-to-crystal transformation) of the framework takes place under the effect of external chemical/physical stimuli such as guest encapsulation/elimination, temperature, pressure, light, or electric field.[45] In addition, by taking the time evolution into account as another dimension while studying these dynamic networks, 4D-MOFs have been defined.[46] Advances in synthesis and characterization led to a plethora of different MOFs, which led to a wide range of applications like sensing, drug delivery[47], and many more.[48]

In 3D-MOFs of permanent porosity (2nd generation), the robustness of these structures imparts constant lattice parameters and a preserved pore volume as long as the structure is kept intact, and no guest molecules are included. Over the past decades, Férey's group has profoundly investigated the different topologies and synthesis procedures of such porous materials belonging to this type.[13, 49–58] Among their notable contributions is the MIL-101 chromium(III) terephthalate MOF that held the world's record of the highest surface area and largest pore volume of $S_{BET} \approx$ 4230 m^2 g^{-1} ($S_{Langmuir} \approx$ 5900 m^2 g^{-1}) and $V_{pore} \approx$ 2.15 cm^3 g^{-1} for years until the advent of other MOFs of comparable or even ex-

ceeding values (Table 4.1).[13] Nevertheless, with this outstanding progress, obtaining the theoretical simulated surface area is still elusive. For instance, the structures based on the infinite benzene rings (poly-p-phenylene) have a theoretical surface area $\geq 10,577$ m^2 g^{-1} (Figure 4.1).[59]

Table 4.1 Some recent MOFs of high BET surface areas and pore volumes

MOF	S_{BET} (m^2 g^{-1})	V_{pore} (cm^3 g^{-1})	Ref.
MIL-101	4230	2.15	[13]
UMCM-2^a	5200	2.32	[60]
MOF-200	4530	3.59	[61]
MOF-210	6240	3.60	[61]
NU-109^b	7010	3.75	[62]
NU-110	7140	4.40	[62]
DUT-60^c	7839	5.02	[63]

^{a}UMCM (University of Michigan Crystalline Material), ^{b}NU (Northwestern University), ^{c}DUT (Dresden University of Technology)
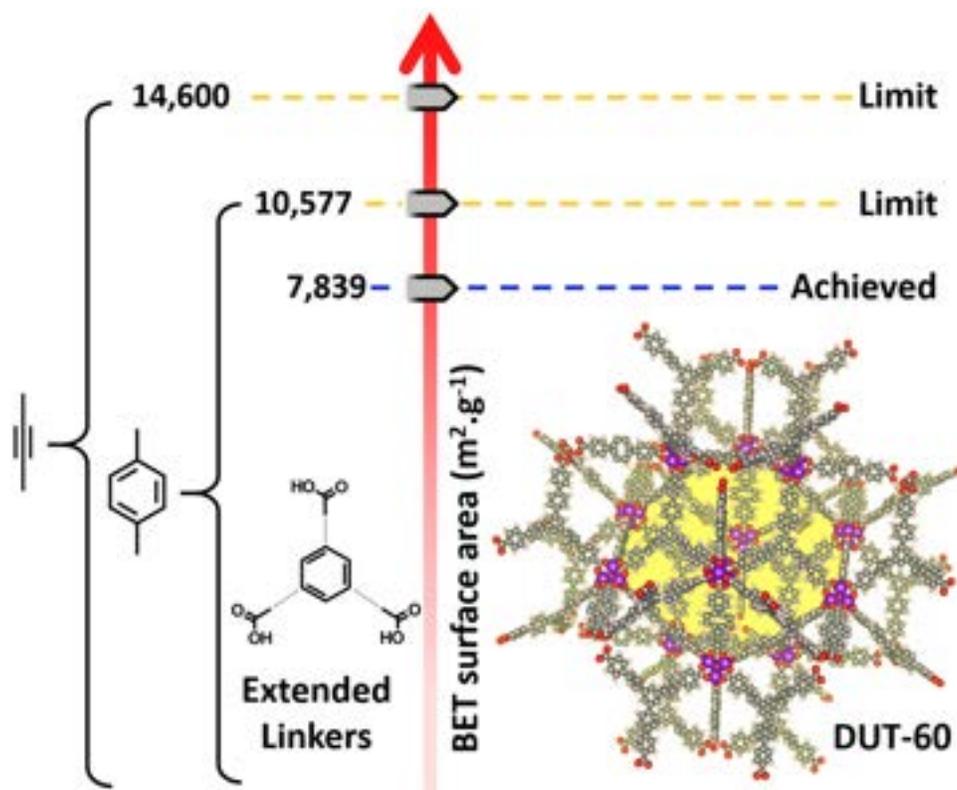
Figure 4.1 The surface area of DUT-60 compared to the maximum achievable simulated surface area. *Modified with permission from Ref.[63]*

It is believed that high surface areas can be obtained by introducing larger linkers within the structure through the involvement of more benzene-ring-containing linkers (e.g., the tritopic 1,3,5-tris(4′-carboxy[1,1′-biphenyl]-4-yl)benzene "H_3BBC" and ditopic 1,4-bis-p-carboxyphenyl buta-1,3-diene "H_2BCPBD" linkers, in case of DUT-60).[63] Other simulations revealed a new ceiling, surpassing this surface area limit regarding MOFs ($\geq$ 14600 m^2 g^{-1}) that would be attainable by replacing the linkers of repeating phenyls with the more "area-efficient" acetylene extended ones (as in the case of NU-109 and NU-110).[62]

However, while approaching this limit, these MOFs become highly susceptible to collapse upon activation (solvent molecules removal from the pores) unless supercritical fluid extraction is involved. In such a method, the pores of the material are evacuated, and the included solvent molecules are removed from the material matrix by using a flow of supercritical fluid (usually carbon dioxide) as the extracting solvent. The supercritical solvent is them evacuated from the pores without formation of an interphase meniscus which would impose constraints on the pore walls.[64–66] Nevertheless, only a few MOFs with these highly extended linkers were reported because of their sophisticated syntheses that in turn would make them costly materials.[62, 67]

Among all MOFs, MIL-101 MOFs are distinguished with both a rigid architecture and high porosity. Furthermore, they show higher chemical and hydrothermal stabilities than other MOFs. The incorporation of different metal ions in the lattice structure of MIL-101 MOFs revealed different properties that could be useful in a variety of applications. MIL-101(Cr) synthesis and applications were reviewed elsewhere,[68] whereas other metal MIL-101 analogues were not covered in previous reviews so far. Considering the toxic nature of chromium, limiting the utilization of MIL-101 in practical applications, further attention should be paid to other metal MIL-101 frameworks.

Herein, we review the MIL-101 isomorphs prepared from other metal ions besides chromium, including their functionalized forms and chemical and thermal stability. Mixed-metal structures of two or more metal types are also reviewed. The chromium-type MOF design history and most recent advancements in their synthesis and modifications will be briefly presented.

4.3   Design of MIL-101 metal-organic framework

Férey *et al.* confirmed the concept of a priori design and tailoring of MOFs through targeted chemistry [52] and computational modeling [69], which predicted the existence of one of the most remarkable MOFs; MIL 101(Cr).[13] MIL stands for Materiau de l'Institut Lavoisier. This MOF shows excellent stability against air, water, and acids, along with extremely high

surface area and pore volume ($S_{BET} \geq 4000$ m^2 g^{-1}, $V_{pore} \geq 2.0$ cm^3 g^{-1}).[13]

As designed, the unit cell of MIL-101 consists of metal-(III) trimers (Figure 4.2) crosslinked by terephthalic acid [1,4-benzene dicarboxylate (H$_2$BDC)] to give a super tetrahedron (ST), marked as the secondary building unit (SBU) of this MOF (Figure 4.2-b). Each trimer includes three octahedra with the metal atom to be in the center of every octahedron (Figure 4.2-a); two of them have a water molecule bonded to it, while the third one is bonded to a halide or hydroxide ion, depending on the preparation conditions (Figure 4.2-i). Each octahedron is connected laterally to another one by the carboxylic groups of two BDC molecules on both sides, yielding four connections with the other two and a total of six bidentate carboxylic linkers in each trimer (Figure 4.2-ii, iii). All octahedra are connected through the same μ_3-oxo atom found on the one vertex directed towards the center of the trimer (Figure 4.2-a, i).

The trimers occupy the four vertices of the SBU tetrahedron, whereas the organic ligands represent the six edges of the super tetrahedron to give a microporous structure ($\sim$8.6 Å free aperture) as depicted in (Figure 4.2-b). The connection of the SBUs propagates through the vertices (Figure 4.2-iii) to give two types of mesoporous cages delimited by 20 and 28 STs, respectively (Figure 4.2-c, d). The smaller cages enclose $\sim$29 Å-diameter pores of pentagonal-shaped windows of $\sim$12 Å aperture size. In comparison, the larger cages possess internal diameters of $\sim$34 Å that exhibit hexagonal-shaped windows of $\sim$14.5 Å$\times$16 Å openings.

Thus, two mesoporous cages are contained within this structure with a ratio of 2:1 and accessible pore volumes of $\sim$12,700 Å^3 and $\sim$20,600 Å^3, respectively. The resulting crystalline solid is a 3D corner-shared network with an augmented Mobil thirty-nine (MTN) zeotype architecture (Figure 4.2-e), showing a cubic system cell with a volume of 702,000 Å^3.

Other Cr-based MOFs viz., MIL-88, and MIL-89 were reported by Serre *et al.* whereby the chromium trimers were condensed with various ditopic carboxylate linkers (fumaric and muconic acid, respectively).[52] Unlike MIL-101, the conventional ab initio structural determination methods have been successfully implemented to solve the structures of these already-synthesized MOFs from their powder patterns. On the contrary, the same procedures did not apply to the crystal structure determination of MIL-101. Its powder diffraction pattern was ruled out for being too complex in spite of its high crystallinity.[69]

The computational approach was undertaken to predict the MIL-101 structure based on the experimental data of the chemical composition and dimensionality.[69] Its chemical formula was found to be Cr$_3$F·(H$_2$O)$_2$·O·[(O$_2$C)-C$_6$H$_4$-(CO$_2$)]$_3$ revealing a metal-to-ligand ratio of 1:1.[13] Furthermore, a notably high surface area (around 4000 m^2 g^{-1}, BET) was obtained by nitrogen sorption measurement techniques suggesting a 3D structure.[13, 69]
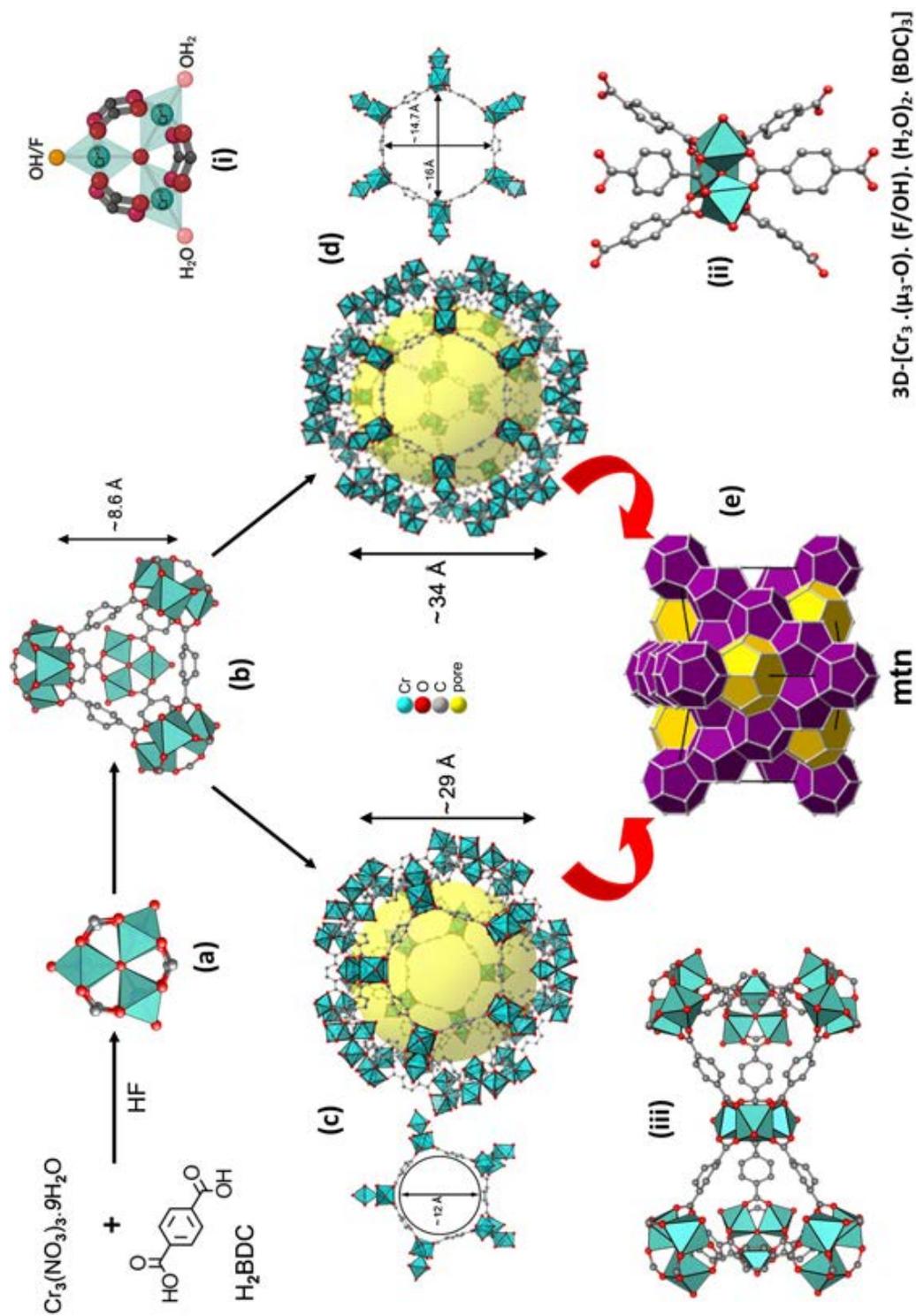
Figure 4.2 Schematic representation of the MIL-101(Cr) metal-organic framework. a) Trimeric SBU. b) Structural supertetrahedron (ST). c) Smaller pentagonal cage. d) Larger hexagonal cage. e) Mobil Thirty-Nine (MTN) topology. i) The elaborated form of the MOF basic trimer. ii) A single SBU/linkers unit connection. iii) The corner-sharing connection of STs within the MOF. *Adapted from Ref.[68, 70, 71] with permission from The Royal Society of Chemistry.*

Following this strategy, several candidates of 3- to 6-ring connections were produced through the direct-space assembly of the building units using the automated assembly of secondary building units (AASBU) method. In this method, numerous combinations of pre-defined SBUs are explored concerning auto-assembly in the 3D space.[69] The nodes were considered as rigid bodies and the linkers "or struts" as flexible ones. They were modeled as $(M_xL_y)^{inorg}$ and $(C_nL_m)^{org}$, where M, C, and L represent the metal centers, carbon skeleton, and the ligand atoms (oxygen atoms of the connecting carboxylate groups), respectively. The L^{org} ... L^{inorg} were chosen as the "Sticky-atoms" pairs responsible for holding the linkers and the nodes together as well as the propagation of the assembly, where L^{org} and L^{inorg} are defined as equally possible linkage points with a high priority of overlapping.

Applying a series of simulated Monte Carlo annealing and energy-minimization steps has limited the number of candidates to two candidates (the 5- and 6-ring assemblies), which were compatible with the periodicity and symmetry of these infinite arrangements. These connections were derived from similar networks in other MOFs and zeolites, complying with the geometrical constraints. The assembly of the supertetrahedra is believed to propagate through the "corner-sharing" route conserving the 5-rings and 6-rings constructions into the MTN zeotype architecture of space group *Fd-3m*. The calculated powder pattern obtained from these simulations was compared to the pattern achieved experimentally to verify the matching of both structures. Hence, the MIL-101 framework was confirmed to follow these connections and assemblies, resulting in the development of pentagonal and hexagonal cages within the structure and occupying the MTN topology (Figure 4.2).

4.4 Synthesis, Activation, and Characterization of MIL-101(Cr)

The preparation route and reaction conditions are crucial to the growth of the targeted structure. The conventional synthesizing of MOFs usually involves solvothermal/hydrothermal procedures. However, other methods were developed to fulfill other requirements, such as controlling the crystal size, obtaining defect-free crystals, facilitating and accelerating the growth, and increasing the production yield. Among these innovative and faster methods are the microwave-assisted [30, 31], sonochemical [30, 72, 73], mechanochemical [74–76], and electrochemical methods [77, 78].

Other methods were developed to achieve specific purposes at the expense of preparation time. For instance, the solvent evaporation and vapor diffusion methods require very long preparation times that may reach several weeks or months to avoid elevated reaction temperature.[79, 80] Other routes may include ionic liquids, microfluidic synthesis, and dry-gel conversion techniques.[28]

4.4.1 Conventional Solvothermal/Hydrothermal synthesis

G. Férey reported for the first time the synthesis of the MIL-101(Cr) metal-organic framework employing the conventional hydrothermal technique.[13] Briefly, chromium(III) nitrate non-ahydrate $(Cr(NO_3)_3 \cdot 9H_2O)$ was dissolved in water, and an equivalent amount of terephthalic acid and hydrofluoric acid were added following the chemical formula stated in (Figure 4.2-ii, Table 4.2). Since the chromium salt is highly soluble in water and the BDC ligand is sparingly soluble, a dark blue suspension was obtained. The suspension was then transferred into a hydrothermal bomb and kept for 8 h at 220 °C, yielding a light sea-green-colored suspension containing the targeted crystals (Figure 4.3). The resulting products were octahedral particles of the MIL-101 metal-organic framework (Figure 4.4) along with some other needle-shaped ones resulting from the unreacted and recrystallized BDC linker.
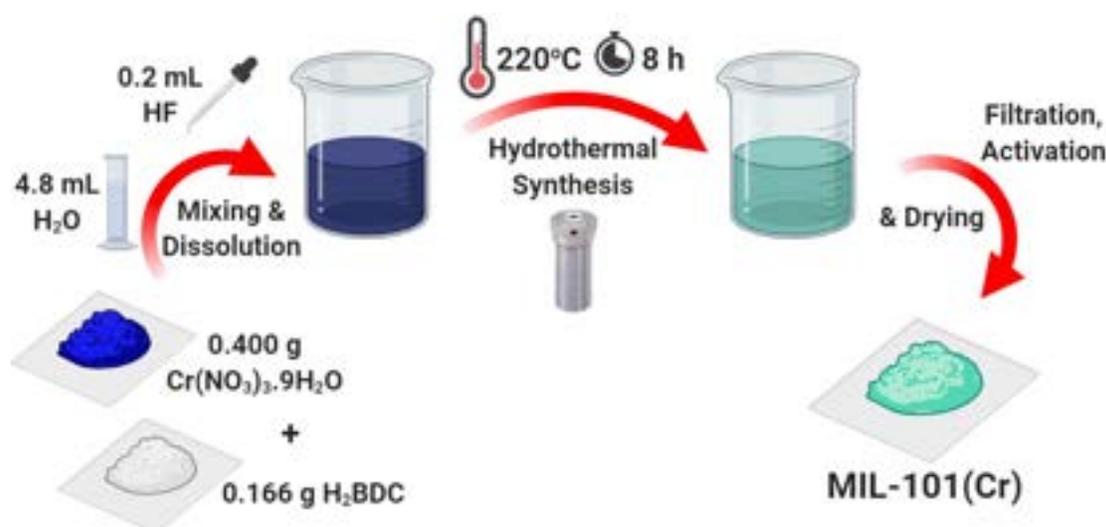
Figure 4.3 The hydrothermal synthesis of MIL-101(Cr) expressing the color change between different stages.

The products were then filtered to separate the recrystallized H_2BDC particles and collect the fine MOF crystals. Usually, after the MOF synthesis and separation, an activation process takes place, in which the undesirable molecules of the solvent, linker, and side-products within the pores are removed. In the case of MIL-101, it was activated by a solvothermal treatment using ethanol at 100 °C for 20 h to evacuate the free acid molecules clogging the pores.

The activated powder showed a high crystallinity product with a calculated low-density of 0.62 g cm^{-3}. Nitrogen sorption measurements showed a large surface area and pore volume of $S_{BET} \approx 4230$ m^2 g^{-1} ($S_{Langmuir} \approx 5900$ m^2 g^{-1}) and $V_{pore} \approx 2.1$ cm^3 g^{-1}. Besides, a characteristic type-I isotherm was given with two secondary uptakes at P/P$_0$= 0.1 and 0.2, representing the two microporous windows in agreement with simulations. It is worth noting

that the activated sample revealed a 20% higher surface area compared to the "as-synthesized" one, confirming that activation is a mandatory step.
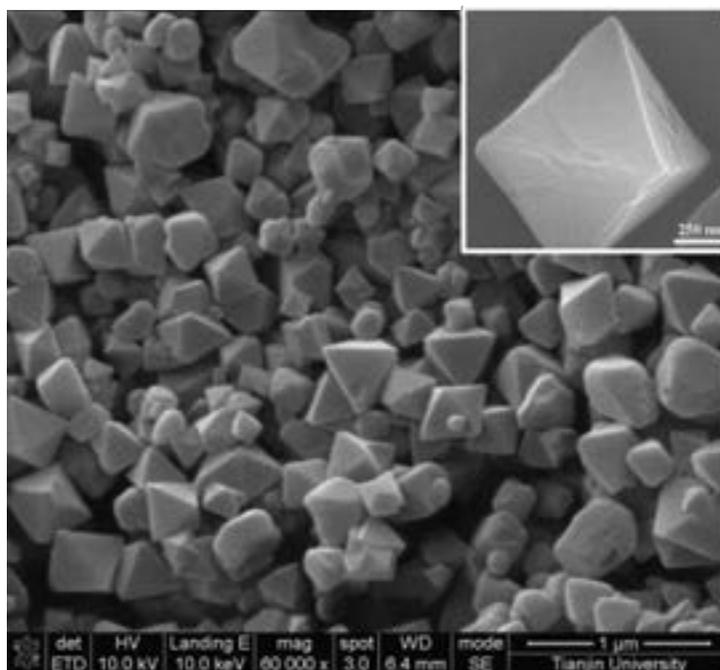
Figure 4.4 The octahedral-shaped crystals of MIL-101 produced by the hydrothermal route.[81] (inset: a submicron MIL-101 octahedron, representing the average (common) outcome of the conventional method)[82] *Reprinted with permission from Ref.[81, 82]*

This MOF shows good thermal and chemical stabilities in the air, retaining its chemical identity for months, whereby the thermogravimetric analysis (TGA) confirmed the structure was kept intact at temperatures up to 275 °C.[13] Moreover, further structural and morphological analyses were performed and reported separately.[83] Depending on electron diffraction (ED), high-resolution electron microscopy (HREM), and transmission electron microscopy (TEM), imaging was done at low magnification due to the sensitivity of the crystals to the electron beam.[83] TEM allowed getting images of the octahedral-shaped crystals of MIL-101 at different orientations (Figure 4.5).[83]
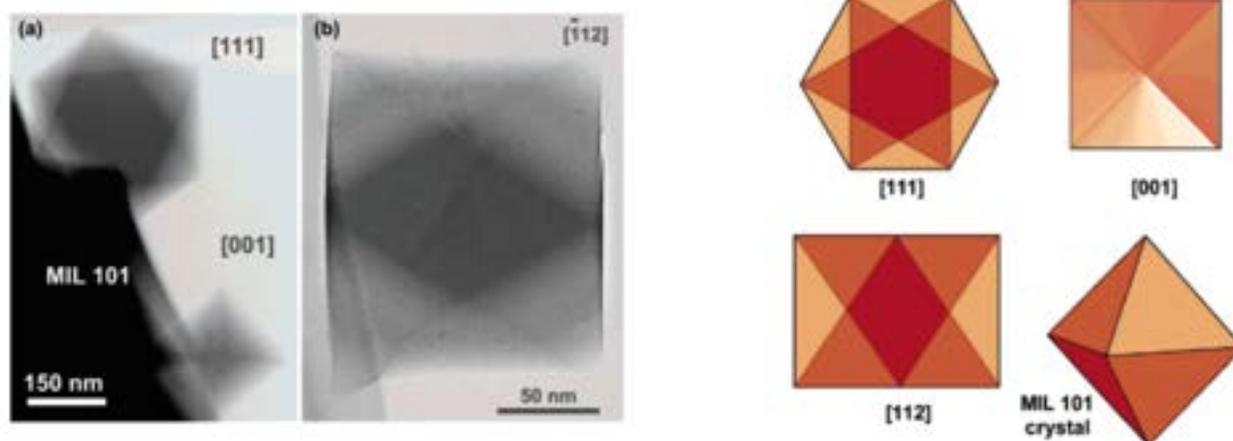
Figure 4.5 TEM images of the octahedral MIL-101 crystals at different orientations versus a graphical representation of a perfect crystal at the same orientations. *Reprinted with permission from Ref.[83]. Copyright © 2005, American Chemical Society.*

At this point, a brief overview of recent advances in the synthesis and functionalization of MIL-101(Cr) will be reported. For a thorough presentation of this topic, the reader is referred to the review of Ahn *et al.*.[68] MIL-101(Cr) was found to be obtainable over a wide range of parameters. Nevertheless, the synthesis process is still considered sensitive to the applied reaction conditions. Consequently, modifications to the reported procedures, even what has been deemed a "minute change," may result in some inconsistency. In some cases, the hydrothermal bomb's size, which is not usually reported, can cause variations in the results. It was therefore found useful to highlight the prominent boundaries (limitations) of the reaction parameters that directly affect the properties of the produced MIL-101(Cr). Table 4.2 summarizes some of the recent advances in the synthesis of MIL-101(Cr).

In attempts to get higher quality crystals at shorter reaction time and lower temperature, different synthesis parameters were investigated including, the type of chromium salt, reactants molar ratios, dilution, acidic/basic medium, additives, temperature, and time of reaction. These works can be summarized as follows:

- regarding the synthesis:

i) (Type of salt): It was found that chromium chloride hexahydrate ($CrCl_3 \cdot 6H_2O$) and chromium trioxide (Chromium(VI) oxide, CrO_3) can replace the nitrate salt as the starting metal ions source to prepare MIL-101(Cr) and its functionalized derivatives.[84–88]

ii) (Molar ratio): The usual practice of using the stoichiometric equimolar ratio of reactants has been questioned as the optimal ratio in acidic media. Some reports have found such

an equivalent ratio to be the perfect match [89], whereas others suggested a slightly higher ratio of Cr to BDC would yield better results.[90, 91] On the other hand, attempts based on a double linker to metal ratio reported better properties.[92] Hence, the ideal ratio is still a matter of discussion.

iii) (Dilution): The amount of water added to the reaction mixture or the degree of dilution can definitely drive the formation of the MIL-101 structure or one of its framework isomers.[93] The MIL-101 phase was found to be favored when using higher water content at low acidity.[93] In addition, the amount of added water controls the size of the produced crystals, whereby doubling the amount of water would decrease the particle size almost to half of its initial value.[84, 90, 91]

iv) (Acidic/Basic medium): Controlling the pH of the reaction medium is crucial to the crystallization, growth, and purity of MOFs.[94] Originally, MIL-101(Cr) was synthesized under the influence of HF.[13] However, other syntheses involving acidic media focused on the achievement of the same stable structure without incorporating hydrofluoric acid (HF-free) as a highly toxic, eco-hostile, and corrosive chemical. The impact of using other less hazardous inorganic acids as mineralizers was also investigated. Nitric acid (HNO_3), as well as hydrochloric acid (HCl), seem to be more promising alternatives, whereby a comparable particle size was achieved but with a 20% higher surface area [95] and 70% better yield.[96]

v) On the other side, syntheses investigating the influence of basic conditions were explored. Initial dissolution of the salt and the linker would result in a low pH (2.6 - 3.3). By adding different inorganic and organic alkalis, the reaction would be adjusted for a more basic medium.[84] Under such conditions, the dissolution and deprotonation extent of the BDC linker would increase, motivating the coordination between the metal ion and the carboxylic ligand.[94] Increasing the pH (4.0 - 5.0) through NaOH addition was found to decrease the particle size and the surface area as well.[84, 97] However, incorporating tetramethylammonium hydroxide (TMAOH, pH= 6.0 - 6.5) would recover a 100% pure MIL-101(Cr) phase as it prevents the recrystallization of BDC.[89] Moreover, synthesis using TMAOH would provide an equivalent surface area and a high yield of 88% at a lower reaction temperature.

vi) (Additives): Organic monocarboxylic acids, like acetic acid, stearic acid, and benzoic acid with some of its derivatives, were reported to replace HF in the reaction medium and successfully producing the MIL-101 phase at a slightly lower reaction temperature.[70, 98, 99] When present, monocarboxylic acids act as modulators for the reaction. They contribute to the structure formation as competitive linkers, regulating nucleation and growth rates and controlling the particle sizes of the produced MIL-101.[100] Replacing up to 30%(mol.) of the introduced BDC with a monocarboxylic acid can result in smaller particles with half

the size of the unmodulated samples.[99] Moreover, monocarboxylic acid molecules can also function as phase-selector, offering kinetic control to the self-assembly of the MOF.[100] At lower concentrations of monocarboxylic modulators, the reaction is directed to forming the MIL-101 framework. Increasing the concentration would shift the reaction towards the production of another framework isomer.[100, 101]

vii) Acid/Additive-free synthesis was examined as a more environment-friendly process, in which the MIL-101 was synthesized without the incorporation of acids or any other additive, just the three main components: the metal ion source, the linker, and the solvent. These trials were reported to be successful; however, excessive washing and activation treatments are required to evacuate the MOF pores.[84, 89, 92, 97, 102, 103]

viii) (Temperature and time): The synthesis temperature and time are considered the most critical parameters when it comes to MOF synthesis. Both parameters greatly influence driving the reaction towards different products, whereby various Cr-BDC networks would result and coexist depending on these two factors.[104] Hence, achieving pure crystals of a single phase at a lower reaction temperature and a shorter reaction time has been the leading research trigger for energy-saving purposes. Hydrothermal synthesis of MIL-101(Cr) based on other reaction conditions (discussed above) can extend the reaction time from 4 h up to 120 h, at temperatures between 180 °C – 220 °C.[88, 99] However, the temperature and time of reaction are mainly dependent on the source of energy applied, the efficiency of energy delivery, and its interactions. Thus, other synthesis methods and techniques were developed for better results, as will be presented in the following subsections.

- for post-synthesis treatment (activation process):

viii) Alkaline media were found to help the dissolution of the organic acid linker during the post-synthesis purification step (activation) to eliminate the recrystallized linker from the MOF pores.[105] Inorganic hydroxides were shown not to be as effective as the organic amines and amides, which brought the N, N-dimethylformamide (DMF) as one of the most used solvents in the activation process, especially when using ultrasound waves.[97, 105]

ix) Also, for the activation, fluoride-containing salts like ammonium fluoride (NH_4F) are effective when applied in a consecutive sequence of washing steps by hot water, ethanol, and an aqueous solution of NH_4F, whereby the surface area was significantly enhanced by almost 50%.[106, 107] Such alkaline halide exchange solutions are believed to be essential for removing any organic and inorganic species trapped within the pores. Moreover, the fluoride anion is also believed to provide the nuclei formation and promote crystallinity and crystal growth.[106, 108]

- Scaling up:

x) Departing from the usual laboratory scale, Janiak *et al.* scaled up the synthesis of MIL-101(Cr) by performing it in a 3 L autoclave.[70] Upon scaling up, they investigated the changes in the effect of various parameters, including different acidic modulator/additive types and concentrations, washing procedure, stirring, and reaction temperature and time on the resulting products. They could obtain more than 100 g MIL-101 per batch with a yield of 70% and a surface area of $S_{BET}=$ 4000 m^2 g^{-1} in a large-scale fluoride-free process.[70]

- Mixed-solvothermal synthesis:

Based on previous results, especially on conducting the reaction in basic media and aiming at the achievement of the MOF synthesis at a lower reaction temperature, Tan *et al.* reported the growth of MIL-101(Cr) crystals in a mixed-solvent environment.[109] DMF was added to the aqueous reaction medium to improve the dispersion of the H$_2$BDC linker. As a cosolvent, DMF was chosen for its high miscibility in water, besides its ability to dissolve the organic linker creating a homogeneous mixture. Different ratios of DMF/H$_2$O were studied, and MIL-101 was reported to be achievable in the range of 0 - 0.5, and a ratio of 0.2 resulted in uniform crystals of average particle size of 200 nm. Synthesis at this ratio effectively lowered the reaction temperature to (140 °C - 180 °C) compared to 220 °C for conventional synthesis. However, the highest crystallinity was obtained at 160 °C. The sample also exhibited the highest surface area, pore size, and adsorption properties compared to the other HF and HF-free samples prepared in the same study (Table 4.2). A yield of around 50% is usually achieved in similar preparations. Nevertheless, in this study, a remarkable yield of 83% was reached at a lower temperature. All these advantages would make this method a less energy-consuming route and a further step towards the industrial production of MOFs.

Table 4.2 Summary of some MIL-101(Cr) studies that investigate different synthesis parameters

Method	Precursor		Synthesis conditions			Activation			Textural Properties		Yield[a] (%)	Ref.
	Metal Salt	Metal:Linker ratio	Medium	Temp. (°C)	Time	Solvent	Temp. (°C)	Time (h)	S_{BET} (m² g⁻¹)	V_{pore} (cm³ g⁻¹)		
Hydrothermal	$Cr(NO_3)_3$	1:1	H_2O/HF	220	8 h	EtOH	100	20	4230	2.1	50	[13]
	$Cr(NO_3)_3$	1:1	H_2O/HF	220	8 h	— EtOH/H_2O	85	— 3	4000[b] 5500[b]	n.a. 1.9	n.a.	[85]
	$Cr(NO_3)_3$	1:1	H_2O/HF	220	8 h	— H_2O/EtOH NH_4F	85 60	— 3 10	2800 3780 4230	1.37 1.74 2.15	n.a.	[110]
	$CrCl_3$	1:1	H_2O H_2O/NaOH	210	24 h	DMF	70	1	3160 n.a.	1.54 n.a.	42 [74]	[84]
	$Cr(NO_3)_3$	1:1	H_2O	218	18 h	DMF	[104]	12	3460	n.a.	64	[97]
	$Cr(NO_3)_3$	0.75:1 1:1 1.25:1 1.5:1 1.75:1	H_2O/HF	200	8 h	EtOH	—	12	1582 2328 2946-3586[c] 2642 2414	0.79 1.23 1.53-1.85[c] 1.41 1.28	n.a.	[90, 91]
	$Cr(NO_3)_3$	1:1 1:2	H_2O H_2O/HF H_2O/HNO_3 H_2O H_2O/HF H_2O/HNO_3	220	8 h	DMF EtOH NH_4F	80 80 60	8 18 5	1758 2132 3129 4293 2794 3597	0.85 1.18 1.41 2.42 1.43 1.65	n.a.	[92]
	$Cr(NO_3)_3$	1:1	H_2O H_2O/HF H_2O/TMAOH	180	24 h	—	—	—	2250 3184 3197	1.24 1.53 1.55	n.a. n.a. 88	[89]
	$Cr(NO_3)_3$	1:1	H_2O/HF	220	8 h	DMF MeOH	80 r.t.	8 120	3609	1.55	46	[96]

Table 4.2 Summary of some MIL–101(Cr) studies that investigate different synthesis parameters (Cont.)

Method	Precursor		Synthesis conditions			Activation			Textural Properties		Yield[a] (%)	Ref.
	Metal Salt	Metal:Linker ratio	Medium	Temp. (°C)	Time	Solvent	Temp. (°C)	Time (h)	S_{BET} (m² g⁻¹)	V_{pore} (cm³ g⁻¹)		
Hydrothermal	$Cr(NO_3)_3$	1:1	H_2O/HNO_3	220	8 h	EtOH NH₄F	80 60	18 5	3814[c]	1.72[c]	78[c]	[96]
	$Cr(NO_3)_3$	1:1	H_2O/HF H_2O/HCl	220	8 h	EtOH	120	15	2533 3090	1.28 1.64	n.a.	[95]
	$Cr(NO_3)_3$	1:1	H_2O/CH_3COOH	200	8 h	EtOH	—	1	2736	1.50	n.a.	[98]
	$Cr(NO_3)_3$	1:1	H_2O $H_2O/benzoic$ $acid$ $H_2O/stearic$ $acid$ $H_2O/4$-methoxybenzoic acid $H_2O/4$-nitrobenzoic acid $H_2O/perfluorobenzoic$ acid	220	4 h	EtOH	—	—	2944 2923 2691 2646 2692 2893	2.57 2.93 2.95 2.68 2.53 2.33	49 n.a. n.a. n.a. n.a. n.a.	[99]
	$Cr(NO_3)_3$	1:1	H_2O H_2O/HF H_2O/HNO_3 H_2O/HCl H_2O/H_2SO_4 $H_2O/HCOOH$ H_2O/CH_3COOH H_2O/CF_3COOH $H_2O/fumaric$ acid $H_2O/citric$ acid $H_2O/succinic$ acid $H_2O/benzoic$ acid $H_2O/phenylphosphonic$ acid	200	15 h	DMF EtOH	—	16 16	2410 2620 3450-3870[c] 1560 1750 590 2750 2650 760 740 2510 1760 2460	1.30 1.82 1.66 0.79 0.81 0.56 1.55 1.34 0.69 0.58 1.28 0.93 1.49	56 47 82 36 48 27 24 73 28 37 59 39 51	[70]
	$Cr(NO_3)_3$ $CrCl_3$ CrO_3	1:1	H_2O H_2O/HCl	180	96 h 120 h	H_2O EtOH	—	—	990-2280	0.45-1.20	n.a.	[88]
Mixed-solvothermal	$Cr(NO_3)_3$	1:1	DMF/H_2O H_2O	160	24 h	DMF	65	4	2453 2318	1.16 1.12	83 53	[109]

34

Table 4.2 Summary of some MIL-101(Cr) studies that investigate different synthesis parameters (Cont.)

Method	Precursor		Synthesis conditions			Activation			Textural Properties		Yield[a] (%)	Ref.
	Metal Salt	Metal:Linker ratio	Medium	Temp. (°C)	Time	Solvent	Temp. (°C)	Time (h)	S_{BET} (m² g⁻¹)	V_{pore} (cm³ g⁻¹)		
Microwave (MW)	$Cr(NO_3)_3$	1:1	H_2O/HF	210	40 min	EtOH	100	20	3900	2.3	n.a.	[111]
	$CrCl_3$	1:1	H_2O H_2O/NaOH	210	1 h 15 min	DMF	70	1	3196 3223	1.55 1.57	38 37	[84]
	$Cr(NO_3)_3$	1:1	H_2O	220	15 min	DMF	70	12	4004	n.a.	55	[97]
	$Cr(NO_3)_3$	1:1	H_2O/HF	220	1 h	EtOH	120	20	3054	2.01	n.a.	[112]
MW/hydrothermal	$CrCl_3$	1:1	H_2O H_2O/NaOH	210	4 min(MW)/12 h 4 min(MW)/3 h	DMF EtOH	70	1	1819 1897	1.47 1.54	35 39	[113]
Mechanochemical	$Cr(NO_3)_3$	1.5:1 1:1 1:1	— H_2O/HF H_2O	220	4 h	EtOH	60	6	2764[c] 3439 3517	1.7 2.3 2.2	n.a.	[114]

[a]Based on chromium. [b]Langmuir surface area. [c]Maximum reported at optimized conditions, r.t.= room temperature, n.a.= not available.

4.4.2 Microwave-assisted Synthesis

Microwave-assisted synthesis is considered one of the most promising non-conventional techniques for MOF production as it critically reduces the overall processing time and provides tight control of energy consumption. Besides, the yield is often comparable to that of the traditional methods.[84,97] Microwave technology allows fine-tuning of various MOF properties, including particle size, morphology, and phase selectivity.[30,115]

Microwave as an alternative synthesis route was recently found to produce MOFs that are not achievable by any other route owing to the selective heating of the reaction components. The heat production in microwave systems is volumetric as the reaction medium itself is internally heated by the rotation of the dipoles in the molecules composing the system, compared to the conventional heating methods, in which energy is delivered by conduction, convection, and radiation.[31,115] This approach enables the utilization of higher reaction temperatures (superheating of the solvents) with low energy consumption and reaction time (by the direct "in-core" heating). Furthermore, it allows particle size control with a narrower crystal size distribution thanks to the separate control of crystal nucleation and growth rates. Microwave synthesis also distinguishes for the higher yields and purer-phase materials owing to gradientless temperature fields and faster heating rate.[116,117]

MIL-101(Cr) was first synthesized utilizing microwave irradiation by Jhung *et al.*, following the same procedure as in the hydrothermal method, namely using an equimolar solution of precursors in the presence of HF at a slightly lower reaction temperature (210 °C instead of 220 °C).[111] The preparation took place at a constant power of 600 W and different reaction times. Increasing the time over 60 min resulted in the formation of a different phase. Heating via microwave showed a great ability to control the dimensions of the produced crystals in the nanoscale range (40 nm - 90 nm for short crystallization times of a few minutes) while maintaining their monodispersed size. The optimized crystals obtained at the reaction time of 40 min were of a surface area of 3200 m^2 g^{-1} (BET) and pore volume of 2.3 cm^3 g^{-1}.

Many other attempts were further made to enhance the properties of the resulting MIL-101 crystals and study the interaction of different synthesis parameters with microwaves.[84, 97,106,112,118–122] Moreover, phase selectivity of the microwave-assisted synthesis over the conventional method was established by Khan *et al.*, whereby the MIL-101 phase was favored over any other Cr-BDC phases at the optimized heating route.[104,123] In such a study, MIL-101 crystals were still produced at reaction times exceeding 1 h (up to 3 or 4 h), which contradicts the findings of Jhung *et al.* discussed earlier.[104,111] However, the preparation was initiated from a chloride salt of chromium instead of the usual nitrate. The irradiation took place at a constant power of 400 W, which is lower than that used previously, indicating

the high dependence of the resulting particles on the process conditions. In addition, it was found that the phase transformation occurs at extended reaction times due to the degradation of the MIL-101 structure under these conditions.

In general, adopting MOFs in the industry is still limited because of the problems facing their large-scale production. Despite being of obvious potential interest for large-scale MOF production, microwave synthesis industrial deployment faces some resistance as the process is not yet fully understood. Thomas-Hillman and Laybourn *et al.* discussed the knowledge gaps in this production technology.[123] They clearly stated the importance of studying the penetration depth, in addition to any other available information like the dielectric properties, frequency of the electromagnetic waves, and the power-energy dissipation. Incorporating these points in future studies would help in comprehending the interactions of the operating parameters in the long run.

In another study, Soltanolkottabi *et al.* followed a combination of both synthesis methods (microwave and hydrothermal) to control the morphology of the resulting MOF and study the effect of microwaves versus the conventional heating on particle size.[113] Reaction initiation (nucleation) took place rapidly under microwaves, and then the resulting nuclei were transferred into an electrically heated oven, where crystal growth can proceed separately. Following the same procedures of nucleation and propagation based on the heating method, they were able to produce nanoparticles in the range of (60 nm - 155 nm) while controlling the final particle shape. They also found an optimized water content (degree of dilution) to attain a higher nucleation rate. In this work, they tackled the higher dissolution of the BDC linker and the conflicting trend of reducing the concentration of reactants on nucleation and growth rates. However, they pointed out the contradiction with Jhung *et al.* expressed by the smaller particle sizes at higher pH that was not observed in their case.[111]

4.4.3 Mechanochemical Synthesis

Among other non-conventional synthesis techniques, the mechanochemical method is considered the most eco-friendly process, as the reaction takes place at room temperature without the involvement of any solvent (solvent-less technique). Reaction initiates through the cleavage of the intramolecular bonds as a result of applying external mechanical forces (i.e., grinding) followed by chemical transformations leading to the production of the desired MOF.[124] As a solvent-free method, it was proven to be advantageous over other techniques as no liquid wastes are produced after the reaction (except for water as a side-product), thus saves many post-treatment steps of purification. Besides, short reaction times, in terms of minutes, are required for this process.[34] Nevertheless, despite the growing interest and successful in-

vestigations of this method, it is still limited for its different variables that can affect the properties of the obtained results.

To this end, Leng *et al.* synthesized a MOF through a semi-mechanochemical process.[114] In their study, chromium nitrate salt was ground and mixed with the H_2BDC linker for 30 min at room temperature; then, the resulting mixture was transferred to a Teflon-lined autoclave. The solid-phase reaction took place at 220 °C for 4 h (Table 4.2). Among their worthy findings, good MOF crystals of a slightly lower surface area and pore volume compared to other solvent-included ones were obtained. However, it turns out that the resultant solids were nitrated-MOF crystals (MIL-101-NO_2) instead of the targeted MIL-101(Cr), which somehow explains the slight drop in the mentioned properties. They also reported that such results are not achievable by any other chromium-type precursor (oxide or chloride). Moreover, different reactant ratios were studied along with different reaction times and implied that the MIL-101 crystals are still achievable with a ratio of Cr/BDC higher than or equal to 0.7, but not 2.0, and a reaction time of more than 2 h until 40 h. Nevertheless, the best reaction conditions were determined to be of reactants ratio of 1.5 (Cr/BDC) and a reaction time of 4 h. Longer times would result in more nitro-groups bonded to the structure and thus a lower surface area structure.

In the mechanochemical synthesis, owing to the solid-solid reaction taking place under grinding, the degree of the product crystallinity, the density of crystal defects, and the resulting particle size would be a matter of discussion. In the above-cited method of Leng *et al.*, MIL-101(Cr) was synthesized hydrothermally with and without the addition of HF for comparison purposes.[114] The SEM images of the hydrothermally-synthesized samples revealed the formation of the recognizable octahedral crystals of the MIL-101 framework with an average particle size around 300 nm – 500 nm (Figure 4.6-b and c). Smaller crystals are still observed, maintaining the same octahedral shape. By contrast, the product of the mechanochemical synthesis did not show any definite crystal shape (Figure 4.6-a). It was rather an aggregate of smaller particles of irregular granular shape, expressing a particle size much smaller than 200 nm (reaching 40 nm). However, such results were from the microscope data analysis, and no other particle size analysis technique was implemented to confirm these findings.

On the other hand, the SEM images can definitely confirm that the degree of crystal deformation in the samples synthesized hydrothermally is much lower than that of the materials produced by the mechanochemical technique (Figure 4.6).[114] In the hydrothermal synthesis, the dissolution of the precursors prior to reaction, results in the free metal ions hydration spheres formation, and the used solvent facilitates the movement of these ions. Hence, the

nucleation and growth of the MIL-101 crystals can proceed, resulting in the definite octa-hedral shape. In the mechanochemical method, however, the metal ions are bound to the initial metal-salt crystals, and in a solvent-free (neat-grinding) technique, the interactions of these metal ions with organic linkers will be limited to those in direct contact.[75, 125] As a result, the mechanochemically-produced MIL-101 crystals would show higher ill-formation than those of the hydrothermal route.[114]
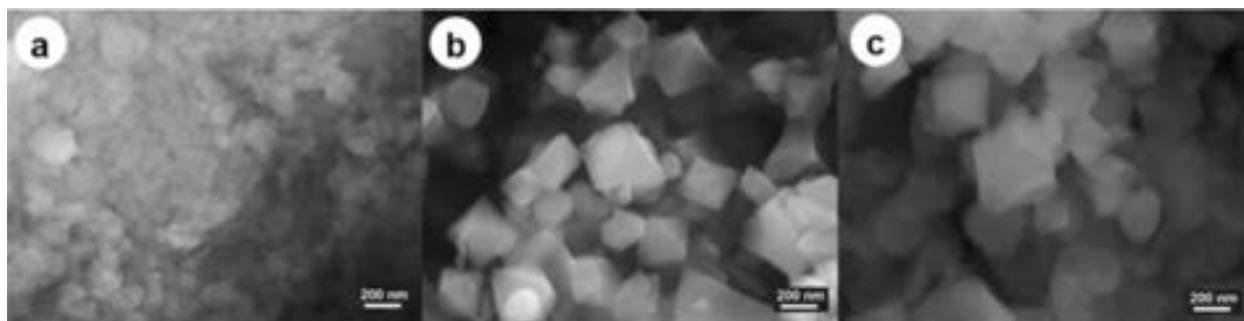
Figure 4.6 SEM images of the obtained MIL-101 crystals. a) mechanochemically-synthesized, b) conventionally-synthesized (with HF), c) without HF. *Reprinted with permission from Ref.[114]. Copyright © 2016, American Chemical Society.*

With the high defect density resulting from this neat grinding mechanochemical technique, the products were expected to show lower crystallinity compared to hydrothermal samples. However, the given XRD diffraction patterns showed a fairly good crystallinity agreeing with the simulated one.[114] Thus, the MOF structure is still formed on the molecular scale. Nevertheless, the XRD pattern showed broader peaks corresponding to smaller crystal domains.

Research on mechanochemical synthesis is still very trending, especially with the recent liquid-assisted grinding (LAG) technique, in which a minimal amount of solvent is introduced with the reaction mixture to increase the mobility of the reactants on the molecular scale.[75] This leads to accelerated reactions in shorter times.[125] Furthermore, the use of different liquids that can dissolve and coordinate with the metal precursor (e.g., DMF, ethanol, or water) was found to influence the formation of specific topologies, hence considered as structure-directing agents.[35]

4.5 Isomorphic MIL-101 frameworks

Based on the above-mentioned properties of MIL-101, several promising approaches were reported to produce the same structural morphology, but with different compositions, a characteristic referred to as "isomorphism."[126] Simply, the term implies equal forms, which technically points out the existence of some compounds with the same crystalline structure. Isomorphous MOFs share an identical space group, and so they deserve the same general empirical formula based on nodes and linkers.[127]

Re-building an isostructural MIL-101 framework, but with different trivalent metal ions rather than chromium, or other ditopic ligands than the BDC, has been studied, aiming for new and hopefully better chemical and physical properties. Nevertheless, the term isomorphic is usually adopted in the field of MOFs to refer to those recreated MOFs having different equivalent metal centers. However, those built from the H_2BDC linkers of different functional groups (Figure 4.7) -despite being of the same morphology- are rather designated as functionalized MIL-101.[68, 88] Herein, we introduce the MIL-101 isomorphs and their functionalized forms only, excluding the chromium as its functionalized structures were covered elsewhere.[68]
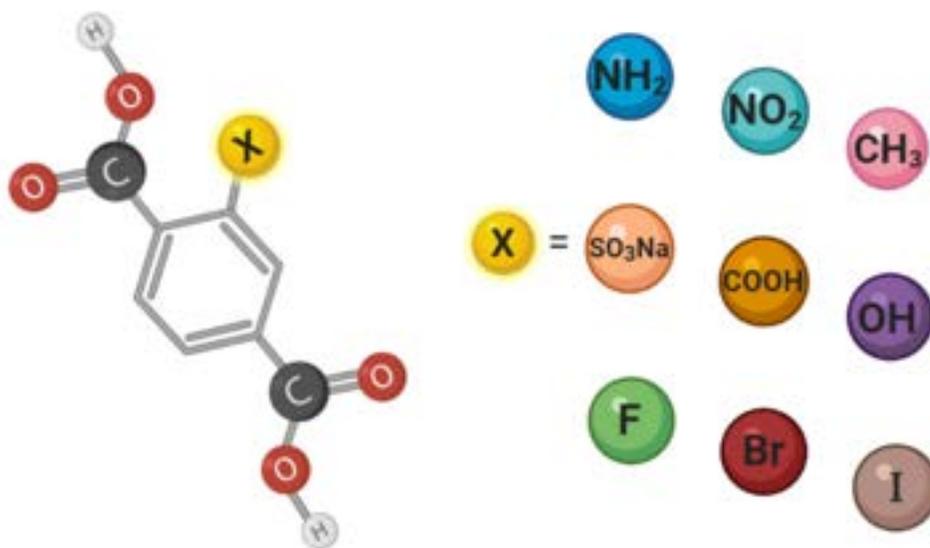
Figure 4.7 Examples of the functional groups on the terephthalic acid linker reported for chromium-type MIL-101 metal-organic frameworks.[68, 88]

4.5.1 MIL-101(Fe), iron isomorph

The most popular candidate elements are those around Cr in the first transition series (3d-series, Z= 21-30), as they possess stable trivalent ions of comparable size and chemistry. Starting with iron, the very early study by Bauer *et al.* resulted in the successful production of amino-functionalized MIL-101(Fe) (NH$_2$-MIL-101(Fe)).[128] This study aimed at investigating the effect of different preparation conditions on three isoreticular MOFs based on comparable trivalent metal ions and BDC bi-dentate linkers, one of which is MIL-101(Fe). Furthermore, the transformation of the MIL-101 structure to other equivalent forms of totally different crystal structures was studied, expressing a phenomenon known as "polymorphism," which will be discussed in the next section. It is worth mentioning that this study is the pioneering one for the synthesis of iron MOFs. In this study, the amino-functionalized MIL-101(Fe) was prepared from a 2:1 molar solution, in which ferric chloride hexahydrate (FeCl$_3$·6H$_2$O) was mixed with 2-amino terephthalic acid (NH$_2$-BDC), then dissolved in DMF (Table 4.3). Heating in a stainless-steel autoclave at 110 °C for 24 h resulted in a dark-brown suspension of the targeted product (Figure 4.8-a).

On the other hand, Taylor-Pashow *et al.* first synthesized MIL-101(Fe) as a pure phase, whereby the whole same structure was obtained with the ferric ions replacing the chromium cations.[129] It was prepared from an "equimolar" solution of ferric chloride hexahydrate and H$_2$BDC linker dissolved in DMF (Table 4.3). The solution was held for 10 min at 150 °C in a microwave oven. The particles were centrifuged and washed with DMF and ethanol to remove any unreacted components. In that case, the activation process was not essential as the synthesis was initialized from a solution, not a suspension like in the chromium case. This method resulted in Fe-MOF of particle size around 200 nm and a yield of 20%. The surface area was reported to be in the range of ∼4000 m^2/g (Langmuir).[129]

In the same study, partly amino-functionalized MIL-101 (NH$_2$-MIL-101(Fe)) was also prepared by replacing a portion of the terephthalic acid with 2-amino terephthalic acid in a one-pot synthesis. The preparation was reported to be successful when the percentage of the amino-functionalized linker was less than 20%. Higher percentages would result in a different MOF morphology. Combining the advantages of this remarkable structure, along with an ion safer than chromium, encouraged more investigations on the Fe-based MOFs. Besides, the addition of amino groups to the MIL-101(Fe) structure was intended to increase the attachment of some biological guest molecules covalently. Due to their biodegradability, both the MIL-101(Fe) and its amine-functionalized counterparts were efficient platforms for delivering imaging contrast agents and slow release of drugs and prodrugs.[129]

In other studies, Kholdeeva *et al.* prepared a MIL-101(Fe) framework based on the previ-

ous procedures of Taylor-Pashow; however, solvothermally in a Teflon-lined stainless steel bomb.[130, 131] In agreement with Bauer's findings, the MIL-101(Fe) was prepared from a "2:1 molar ratio" solution in DMF at 110 °C for 20 h (Table 4.3). The initial clear orange solution of the precursors turns into an orange suspension after the synthesis. Then, upon washing with hot ethanol, filtration, and drying, the powder of MIL-101(Fe) of the same color was obtained (Figure 4.8-b). The products had a BET-specific surface area (SSA) in the range of 3200 m^2 g^{-1} – 3400 m^2 g^{-1}. The ferric analogue of the MIL-101 framework showed superior catalytic activity in the solvent-free allylic oxidation of alkenes with molecular oxygen.
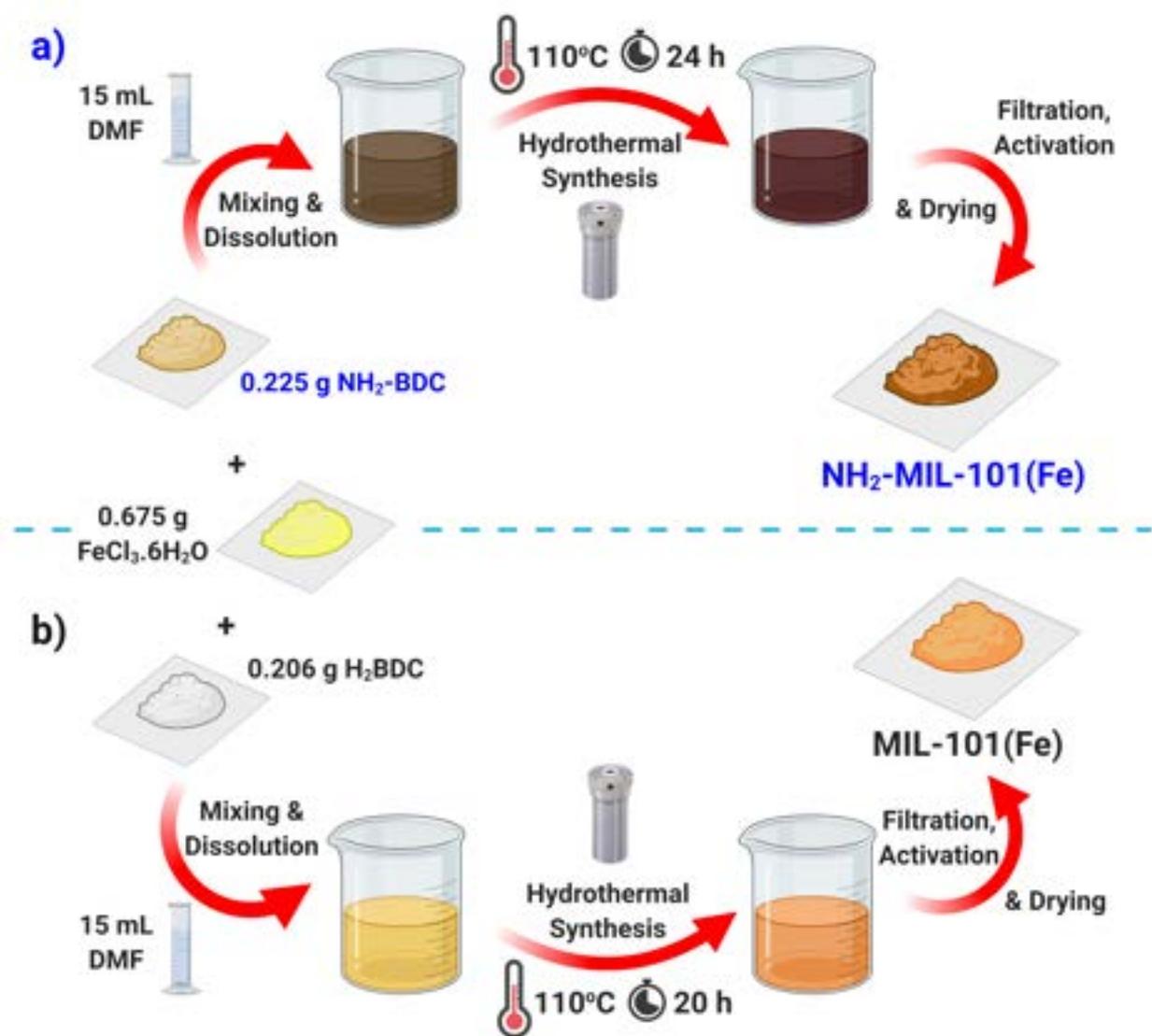
Figure 4.8 Hydrothermal synthesis of the iron isomorph expressing color changes at different stages. a) Amino-functionalized MIL-101(Fe). b) Unfunctionalized MIL-101(Fe).

MIL-101(Fe) is considered the second most studied MIL-101 analogue after chromium. However, its synthesis is far more challenging than that of the chromium isomorph as the reaction is more sensitive to slight variations in any of the synthesis parameters, and it can be easily converted to another MOF type. Moreover, a single pure phase is not usually produced, as a mixture of two or more phases may be obtained.[128, 132, 133] For instance, Metzler-Nolte *et al.* reported the production of dissimilar structure despite following the same procedure of Taylor-Pashow.[129, 132] Nevertheless, by diluting the initial solution, the MIL-101 phase became the major phase.[132] The presence of some crystals of the other phase was still noticeable, even at higher dilution. On the other hand, doubling the metal ions concentration, in line with Bauer's findings, would favor a purer phase of MIL-101, even at a higher temperature of 150 °C instead of 110 °C.[128, 132]

Synthesis of the iron analogue and its functionalized derivatives have also been reported from iron(III) nitrate nonahydrate ($Fe(NO_3)_3 \cdot 9H_2O$) and iron(III) perchlorate hydrate ($Fe(ClO_4)_3 \cdot nH_2O$) as metal ion sources.[134, 135] The attempt of using acetic acid as a monocarboxylic acid modulator was furthermore reported to be successful, and the produced MIL-101(Fe) had a surface area around (S_{BET}= 2670 m^2 g^{-1}) and pore volume of (V_{pore}= 0.75 cm^3 g^{-1}).[136] Variations in synthesis conditions with the successful achievement of MIL-101(Fe) and many of its functionalized forms are listed in Table 4.3. The stability of the iron isomorph in moist air and water has been doubted, and it was sometimes mentioned that it would not last for long in such conditions and may degrade quickly.[137, 138] Comparatively, some Fe-BDC MOFs were reported to have very low stability in water, while others that occupy the same structure were of higher stability.[132, 139, 140] However, this point was not studied in depth so far. Furthermore, the synthesis of such compounds was found to be highly sensitive to the reaction solvent. Nevertheless, studies focusing on the pristine unfunctionalized form (MIL-101(Fe)) are not plentiful. On the other hand, phase transition in the synthesis of the amino-functionalized form (NH$_2$-MIL-101(Fe)) is more often reported in literature.[133]

Horcajada, Serre *et al.* were able to incorporate a series of functionalized BDC linkers, whereby pristine, 2-amino, 2-bromo, 2-chloro, 2-trifluoromethyl, and 2,5-dimethyl functionalized-MIL-101(Fe) were successfully obtained.[134] In parallel, a set of elongated ditopic carboxylates (2,6-naphthalene dicarboxylate "NDC" and 4,4′-biphenyl dicarboxylate "BPDC") was used to replace the BDC linker into the main framework for extra-large pore apertures (Figure 4.9). All structures were reported to be achieved solvothermally at temperatures around 100 °C and 150 °C and reaction time from 2 h to 16 h, except for the amino- and trifluoromethyl- functionalized ones which were obtainable via microwave at a holding time of 5 min (Table 4.3).

The XRD patterns of all powders confirmed the formation of the MIL-101 structure. The surface area measurements did not however meet expectations, as the measured values were in the range of hundreds (except NH_2- and Cl-MIL-101(Fe)) compared to the predicted thousands of m^2 g^{-1}. Such differences in the measured surface area were ascribed to the instability of the obtained products in some solvents, in which the conservation of the formed structure was highly dependent on the preserving solvent. Dissociation and single-crystal to single-crystal transformation might take place depending on the nature of this solvent. Most of the products were found to be stable for months in ethanol, DMF, and toluene, whereas in solvents like water and tetrahydrofuran (THF), degradation or phase transformation may take place in hours.
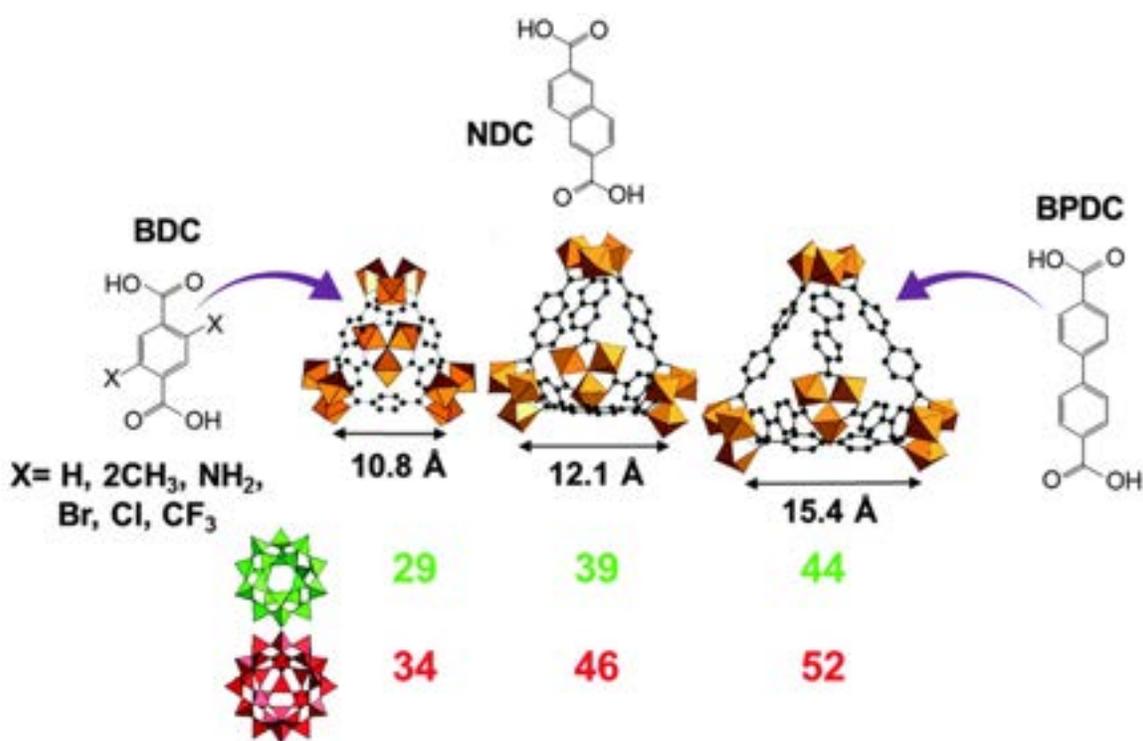
Figure 4.9 Subset of the functionalized and extended MIL-101(Fe) analogues studied with the size (in Angstrom) of the small and large cages represented in light green and red, respectively. *Adapted from Ref.[134] with permission from The Royal Society of Chemistry.*

The studies targeting the synthesis and application of the iron isomorph have been rapidly increasing lately, and usually, only one of the above-mentioned synthesis procedures is adopted in these investigations.

Table 4.3 Synthesis of the MIL-101(Fe) analogue

Method	Functionalization	Precursor		Synthesis conditions			Textural Properties		Application and comments	Ref.
		Metal Salt	Metal:Linker ratio	Medium	Temp. (°C)	Time	S_{BET} (m² g⁻¹)	V_{pore} (cm³ g⁻¹)		
Conventional	2-amino	$FeCl_3$	2:1	DMF	110	24 h	—	—	-Phase-selectivity and synthesis conditions optimization.	[128]
Microwave	Pristine 2-amino	$FeCl_3$	1:1	DMF	150	10 min	4000[a]	—	-Drug delivery: BODIPY dye & ESCP prodrug. -Mixed-linker synthesis.	[129]
Conventional	Pristine	$FeCl_3$	2:1	DMF	110	20 h	3200-3400	1.4	-Catalysis: Solvent-free allylic oxidation of cyclohexene and α-pinene.	[130, 131]
Conventional	Pristine 2-amino	$FeCl_3$	2:1	DMF	110	24 h	3739 3438	1.75 1.64	-Catalysis: basic catalysts for Knoevenagel condensation of benzaldehyde. -Synthesis as in ref.[128]	[137]
Conventional Microwave	Pristine 2-amino 2-chloro 2-bromo 2-trifloromethyl 2,5-dimethyl	$FeCl_3$ $Fe(ClO_4)_3$	1:1	DMF H₂O EtOH	100 150	5 min- 16 h	300 1840 1975 440 245 370	—	-Synthesis of extended and functionalized Fe-MOFs with MTN topology. -Use of ferric hypochlorite in the synthesis of MIL-101(Fe). -Replacement of the BDC linker with NDC and BPDC as ditopic linkers.	[134]
Conventional	Pristine	$FeCl_3$	1:1	DMF/AcOH	110	24 h	2670	0.75	-Catalysis: acetalization of aldehydes with methanol and enamination of β-dicarbonyl compounds.	[136]
Conventional	Pristine 2-amino 2-nitro 2-carboxy 2-hydroxy	$FeCl_3$	2:1	DMF	110	24 h	3753 2810 2331 2289 2998	—	-Effect of functionalized ligand on the photodegradation of phenanthrene.	[141]
Conventional	Pristine	$Fe(NO_3)_3$	1:1.5	DMF	130	72 h	2240	1.3	-Gas adsorption: methane and hydrogen. -Use of ferric nitrate in the synthesis of MIL-101(Fe).	[135]
Microwave	2-amino	$FeCl_3$	1:1	H₂O EtOH DMF	100 100 150	5 min 20-30 min 30 min	—	—	-Phase-Selective microwave-assisted synthesis of iron amino-terephthalate MOFs.	[133]

[a]Langmuir surface area.

4.5.2   MIL-101(Al), aluminum isomorph

Notwithstanding aluminum not being a transition metal, it has shown the ability to develop the trimeric μ_3-oxo cluster, well-known for the 3d-block elements.[142, 143] Hence, it was reported to have a great potential to form similar MOFs based on the trivalent metal ions, like chromium and iron.[144–149] Pure unfunctionalized MIL-101(Al) was however never obtained through direct synthesis up to now; only functionalized forms of this isomorph have been obtained.

The amino-functionalized MIL-101(Al) was first observed in Ahnfeldt *et al.* investigations about some other type of Al-MOF. The MIL-101 configuration coincidentally resulted within their experimental procedure to prepare another targeted MOF.[150] Throughout the followed set of experiments, two types of aluminum salts (nitrate and chloride) were employed in different combinations with the NH_2-BDC linker, and a set of protic and aprotic solvents (DMF, methanol, ethanol, and acetonitrile). The NH_2-MIL-101(Al) structure was only formulated when the chloride salt and DMF were used, in addition to a precursor molar ratio of 1:1 or greater in favor of the metal salt. Any other combination would result in a different MOF or none at all. Moreover, a reaction temperature of 125°C over a duration of 5 h was not sufficient to produce any single MOF phase. A mixture of different phases was always obtained even under these conditions of precursor ratio and solvents.

Serra-Crespo *et al.* were the first to report the successful synthesis and isolation of the amino-functionalized MIL-101(Al) structure both solvothermally and via microwave in direct-synthesis procedures.[151] In such a procedure, aluminum chloride hexahydrate ($AlCl_3 \cdot 6H_2O$) was used as the metal precursor, 2-amino terephthalic acid (NH_2-BDC) as the linker, and DMF as the solvent (Table 4.4). Then, the solution was placed in a Teflon-lined autoclave and heated in an oven at 130 °C for 72 h or 6 h under microwave irradiation. The resulting yellow powder was filtered under vacuum and washed with acetone (Figure 4.10). The produced MOF was activated in boiling methanol overnight (nearly 12 h) to remove any undesired species trapped within the pores. The final product was stored at a temperature of 100 °C to prevent moisture capture.

In contrast, all attempts to obtain MIL-101(Al) in its pure unfunctionalized phase following the exact same steps and reaction conditions resulted in the formation of another Al-MOF of different structure and properties (MIL-53(Al), see Figure 4.10). Besides, using the chloride source of aluminum instead of nitrate was emphasized as any attempts at using the nitrate source always failed.[152–154] The reported surface area for the activated NH_2-MIL-101(Al) was 2100 m^2 g^{-1} (BET), and the pore volume was 0.77 cm^3 g^{-1}.[151] This Al-framework showed good thermal stability in the air, whereby no signs of decomposition were observed

until above 375 °C. However, MeOH and DMF were released around 65 °C and 150 °C, respectively. The amino-functionalized MILs of Cr and Fe usually show a lower decomposition temperature than the pristine structure due to the degradation of the amino group before the linker itself.[128, 155, 156] Hence, introducing Al within the structure of the MIL-101 metal-organic framework would result in a more thermally stable compound compared to the MIL-101(Cr) and MIL-101(Fe), but only if MIL-101(Al) is obtained as a pure phase.
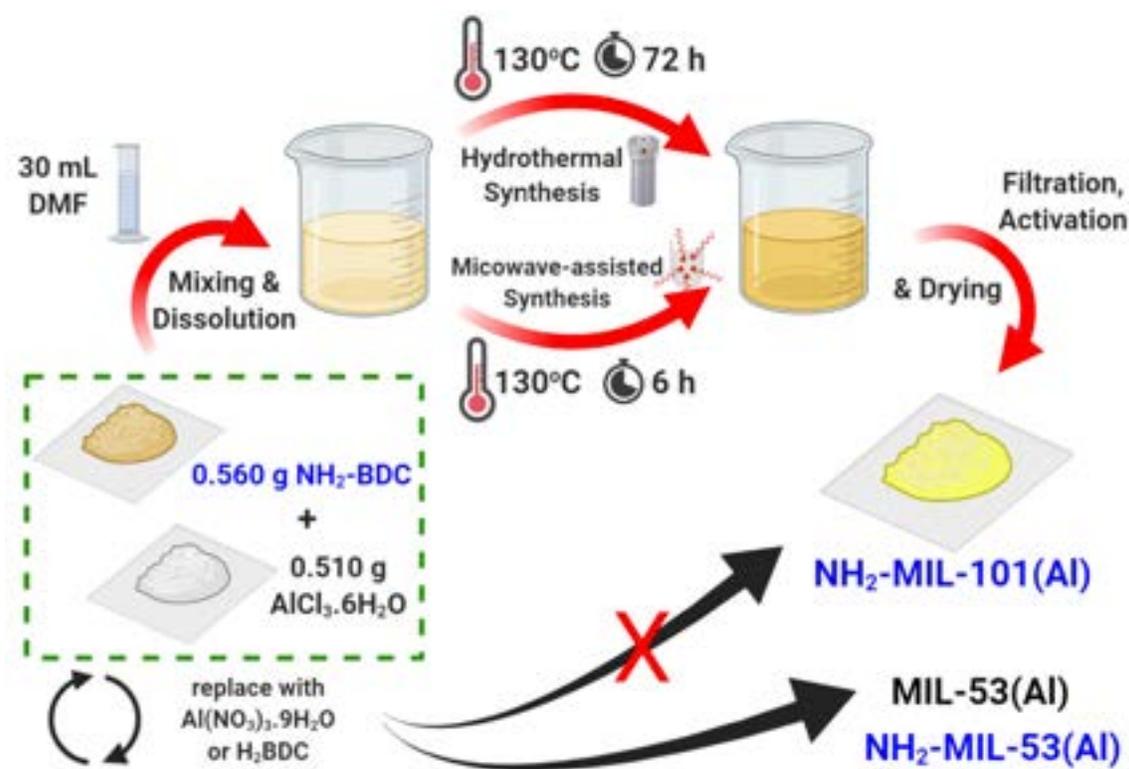
Figure 4.10 Synthesis of the amino-functionalized aluminum isomorph expressing color change between the different steps.

The application of NH_2-MIL-101(Al) in the separation of carbon dioxide from a CO_2/CH_4 mixture showed a higher affinity for adsorbing carbon dioxide rather than methane and nitrogen gases.[151] In addition, its performance as a basic catalyst in the Knoevenagel condensation of benzaldehyde with ethyl cyanoacetate in DMF at 40 °C was tested.[151] The yield of ethyl(E)-α-cyanocinnamate as the main targeted product of the condensation reached 80% over a reaction time of 3 h with a selectivity close to 100%. Attempts to synthesize the pristine and functionalized derivatives of the MIL-101(Al) analogue are reported in Table 4.4.

Table 4.4 Selected publications on the synthesis and application of the MIL-101(Al) functionalized derivatives

Method	Functionalization	Precursor		Synthesis conditions			Textural Properties		Application	Comments	Ref.
		Metal Salt	Metal:Linker ratio	Medium	Temp. (°C)	Time (h)	S_{BET} (m² g⁻¹)	V_{pore} (cm³ g⁻¹)			
Conventional Microwave	2-amino	AlCl₃	1:1.5	DMF	130	72 / 6	2100	0.77	Synthesis, gas adsorption, and catalysis	- First to report	[151]
Conventional	2-amino	AlCl₃	2:1	DMF	110	21	3099	1.53	Catalysis: basic catalysts for Knoevenagel condensation of benzaldehyde	- Simple setup - Low temp. synthesis	[137]
Conventional	2-amino	AlCl₃	1:1.5	DMF	130/110	72/21	2303	—	Achievement of the pristine MIL-101(Al) via post-synthetic deamination of NH₂-MIL-101(Al)	- Synthesis as in ref. [137,151] - Achievement of the unfunctionalized MIL-101(Al) through PSM is confirmed	[157]
	Pristine		2:1		—	—	2445	—			
Conventional	2-amino 2-methyl 2-nitro 2-oxymethyl 2-difluoro 2-dimethyl 2-dioxymethyl 1,4-naphthalene dicarboxylic acid	Al(ClO₄)₃	1:1	DEF	130 170	3-12 10 min	2230 2398 1725 1928 1328 1728 1906 1350	—	Synthesis and gas-adsorption applicable for all derivatives	- Failed to prepare MIL-101(Al), Cl-MIL-101(Al), and F-MIL-101(Al) - Microwave syn. was not	[158]

In the same manner, Hartmann and Fischer synthesized the amino-functionalized MIL-101(Al) to use as a basic catalyst for the Knoevenagel condensation of benzaldehyde with malononitrile and with ethyl cyanoacetate to produce benzylidene malononitrile and ethyl α-cyanocinnamate, respectively. A selectivity of 99% and a yield of over 90% were achieved in a timeframe of 3 h. However, they were capable of preparing the NH_2-MIL-101(Al) framework following a much simpler strategy at a lower reaction temperature and much smaller time (almost one-third).[137]

In a typical process, a 2:1 molar ratio solution was prepared in a 100-mL round bottom flask, in which the NH_2-BDC linker was dissolved in DMF. The solution was then heated to 110 °C under stirring in an oil bath. Equal portions of the hexahydrated chloride salt of aluminum were added to the hot solution over a period of 2 h. The mixture was kept under reflux for a reaction duration of 19 h. The yellow solid powders formed after cooling down were collected and separated by filtration, then washed with DMF and ethanol. Thereafter, it was activated by Soxhlet extraction with ethanol over 24 h. A higher SSA of 3099 m^2 g^{-1} (BET) and pore volume of 1.53 cm^3 g^{-1} were obtained. In addition, the Al-based structure proved remarkable stability over the Fe-based one in moist air over an extended period, reaching 96 h, with no change in neither the porosity nor the crystallinity.[126]

Putting more effort into understanding the reasons behind this successful achievement of the NH_2-MIL-101(Al) MOF, Goesten and Stavitski investigated the formation of this topology through small- and wide-angle scattering (SAXS/WAXS) studies.[159, 160] Their studies confirmed that the reaction kinetics is highly dependent on the type of solvent involved, whereby the reaction could be shifted towards the production of NH_2-MIL-101(Al) with the use of DMF as the reaction solvent solely. The presence of H_2O in small amounts would result in a different assembly and another form of Al-MOFs.[159] Higher concentrations of aluminum precursor, with its high moisture content, can provide sufficient water molecules that hinder the formation of the MIL-101 topology.[159,160] The same group continued their studies through in-situ nuclear magnetic resonance (NMR) and density functional theory (DFT). They established that the synthesis of the MIL-101(Al) framework requires not only using metal chloride precursor and DMF as the solvent but also NH_2-BDC as the linker.[161]

In their study, electronic structure DFT calculations were performed on an appropriate charge-neutral structure motif containing three Al centers equivalent to the trinuclear metal clusters found in Al-MOFs. The calculations showed that the development of the trimeric μ_3-oxo cluster is a kinetically favored step and that the MIL-101 is not the thermodynamically stable phase regardless of the linker type (Figure 4.11). However, computations based on replacing the aqua ligands at the unsaturated sites of the metal trimer with DMF, in the

case of MIL-101(Al) (Figure 4.11, left), revealed a significant decrease in the energy gap to $+8$ kJ mol^{-1}. Despite this small energy difference, the successful synthesis of the pristine unfunctionalized Al analogue physically is not reported yet. Moreover, a lower energy barrier of -6 kJ mol^{-1} was determined in the case of the amino-functionalized linker, NH$_2$-MIL-101(Al) (Figure 4.11, right). Such a decrease in the activation energy explains the possible achievement of MIL-101's node experimentally when DMF was employed as the reaction solvent instead of water.[151, 159–161] This agreement between the computational calculations and the experimental data elaborates the pivotal role of DMF as a promoter and stabilizer in combination with NH$_2$-BDC linker for the μ_3-O-centered cluster existence in the medium. Accordingly, in all compared species, it is shown that the energy barrier for the formation of the MOF lattice is systematically lower when the Al cluster is complexed with DMF rather than water (88 vs. 112 kcal "unfunctionalized," and 86 vs. 124 kcal "Amino-functionalized").
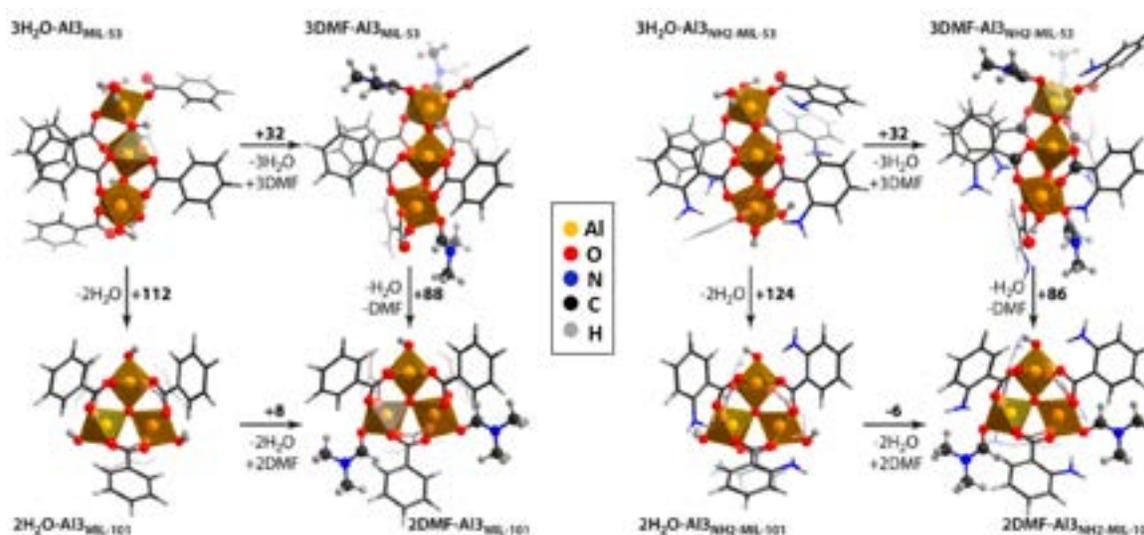
Figure 4.11 Chemical representation of the trinuclear-Al-clusters transformations influenced by the solvent-ligand interactions based on DFT calculations. *Reprinted with permission from Ref.[161]. Copyright © 2014, American Chemical Society.*

Liquid-state NMR experiments were also used to look into the coordination chemistry around the metal ion and trace the large chemical complex structures of Al-DMF during the synthesis. The results revealed that the coordination between Al and DMF occurs initially. The dissociation of this complex starts upon heating the medium to 130 °C. At this temperature, the dissociated (free) aluminum ions bond with the less-favorable BDC linker molecules, and an HCl-DMF complex starts forming. Signals of NH$_2$-MIL-101(Al) and the produced water molecules were detected after 30 min at 130 °C. In line with the DFT studies, the reaction of the chloride ion with water and DMF to produce the HCl-DMF complex was not developing

due to the hydroxide ion (OH$^-$) not being any more stabilized in the coordination sphere of Al^{3+}. The binding of the produced hydroxido ligand to the third unsaturated site of the trimer is a key step to finalize the desired topology of MIL-101(Al). This report provided a reliable explanation for the topology dependence on the solvent and the reaction precursors. Dimethyl sulfoxide (DMSO) was moreover suggested as an alternative solvent for this synthesis due to its ability to form complexes with HCl. What makes this interesting is the ability to investigate the chemistry of aluminum coordination as a p-block element apart from the transition d-block elements.[162, 163]

Since the parent member of this isomorph (MIL-101(Al)) was reported not to be possible to obtain by the conventional methods, Chmielewski *et al.* reported the successful synthesis of the missing metastable MIL-101(Al) via an indirect technique, whereby the deamination of the amino-functionalized derivative took place through post-synthetic modification.[157] First, NH$_2$-MIL-101(Al) was synthesized as reported, then treated with tert-butyl nitrite (*t*-BuONO) at room temperature for 60 min, followed by heating in methanol. This process resulted in the full conversion of all amino groups. However, heating in methanol was found to contaminate the products extensively. Fortunately, conducting the same procedures at a temperature of -20 °C suppressed the formation of such contaminants. Therefore, the ideal conditions for small-scale experiments are treating the functionalized MOF at -20 °C, followed by adding methanol after 1 h at the same temperature for 18 h. Finally, the products were washed and heated with methanol at 60 °C for 4 h.

The complete deamination of the products was established by ^{1}H NMR, ATR-FTIR, and nitrogen sorption.[157] The non-functionalized MIL-101(Al) showed a single peak at 7.87 ppm in the ^{1}H NMR also found in the spectrum of the H$_2$BDC linker. Besides, the vibrational peaks of the amino group at 1621 cm^{-1} and 1339 cm^{-1} were disappeared in the ATR-IR spectrum. Moreover, the processed products revealed a slightly higher surface area of 2445 m^2 g^{-1} compared to the 2303 m^2 g^{-1} value of its functionalized form. For larger-scale processes, methanol was not found as much effective as at a small scale, whereas dichloromethane was proven to be an appropriate alternative. An almost 100% conversion was attained when starting with 50 mg - 100 mg MOF and following the same procedures but using dichloromethane instead of methanol.

Buragohain *et al.* synthesized the amino-functionalized structure along with seven other derivatives, namely (methyl-, nitro-, oxymethyl-, difluoro-, dimethyl-, dioxymethyl-, and naphthalene-) dicarboxylate-linked frameworks as depicted in Figure 4.12.[158] However, in their method, aluminum perchlorate was used instead of the chloride salt, while *N, N*-diethyl formamide (DEF) was the primary solvent. The solvothermal synthesis included the mix-

ing and dissolution of the intended linker with an equimolar amount of aluminum perchlorate nonahydrate (Al(ClO$_4$)$_3$·9H$_2$O) in DEF. The mixture was heated to 130 °C for 3 to 12 h depending on the used linker. However, this method failed to prepare the pristine fluoro-MIL-101(Al) and chloro-MIL-101(Al). Exploring other synthesis methods, they were able to reproduce four of these derivatives (-CH$_3$, -OCH$_3$, -C$_6$H$_4$, -(OCH$_3$)$_2$) by the microwave-assisted route. Using microwaves, these derivatives were prepared at a higher temperature of 170 °C, but with a shorter reaction time of 10 min. The measured BET surface area of the collected powders varied from 1328 m^2 g^{-1} to 2398 m^2 g^{-1}, showing the highest area for the methyl-functionalized and the least for the difluoro (Table 4.4).

Figure 4.12 Various functionalized H$_2$BDC linkers successfully incorporated in the synthesis of the MIL-101(Al) framework.[151, 158] *Adapted with permission from Ref.[151, 158]*

Investigations on possible applications of the Al analogue have been increasing, whereby applying such material in catalysis, gas adsorption, and many others was found to be promising. Attempts at achieving the pristine type are still ongoing through the bimetallic incorporation.

4.5.3 MIL-101(V), vanadium isomorph

Back to transition metals and seeking new assorted properties, vanadium was also employed in the synthesis of the MIL-101 framework by Biswas *et al.*[164] MIL-101(V) was predicted to be obtainable since the construction of other types of vanadium-MOF possessing the same trimeric oxo-centered [V$_3$(μ_3-O)(H$_2$O)$_3$]$^{7+}$ building units has been reported.[51, 165, 166] In this feature, Biswas *et al.* synthesized the vanadium isomorph by incorporating the chloride salt of vanadium, H$_2$BDC, and DMF in a 2:1 molar ratio solution at 150 °C for 24 h (Table 4.5). First, a mixture of VCl$_3$ and the linker was weighed in a nitrogen-filled glove box due to the sensitivity of the vanadium salt to ambient air. Thereafter, they were dissolved in DMF inside a 10-mL Pyrex tube, followed by heating to the specified t emperature. After

24 h, a dark-green powder was collected. Likewise, the amino-functionalized analogue was prepared using the same procedures, except for replacing the BDC linker with NH_2-BDC to obtain a bright-green powder. Both products showed a moderate crystallinity that required a second step of thermal activation. MIL-101(V) and NH_2-MIL-101(V) were activated at 130 °C and 100 °C for 12 h, respectively. Activation took place under vacuum, and the activated products were kept in an inert atmosphere due to their sensitivity be air and moisture as they could be decomposed within a few hours in the ambient temperature.

It is worth mentioning that with the high crystallinity of the activated MIL-101(V), its XRD pattern showed additional peaks imputed to an impure phase. On the other hand, all the attempts to collect the patterns for the functionalized form failed due to its lower stability compared to the pristine one. The N_2 sorption measurements revealed a specific surface area of 2118 m^2 g^{-1} (BET) and 3032 m^2 g^{-1} (Langmuir) for MIL-101(V), whereas the amino-functionalized framework recorded a lower surface area of 1623 m^2 g^{-1} (BET). The lower SSA of the vanadium isomorph to that of chromium was ascribed to the occlusion of some species within the pores, as the usual activation process in a solvent was not applicable in this case. Besides, the presence of a secondary phase may reduce the overall surface area. The thermal studies showed moderate thermal stability of both frameworks up to 320 °C for MIL-101(V) and 240 °C for NH_2-MIL-101(V) in a helium atmosphere, producing residuals of V_2O_5. The CO_2 uptake for these products was also measured and found to be higher compared to other V-MOFs suggesting the gas storage to be a convenient application for such compounds.

In a recent comparative study, Xu *et al.* prepared similar MIL-101(V) and NH_2-MIL-101(V) through a favorable solvothermal procedure, whereby purer-phase products were fabricated at a lower temperature.[167] In this procedure, a 2:1 molar ratio solution of the vanadium chloride (VCl_3) metal precursor along with the linkers (H_2BDC or NH_2-BDC) were completely dissolved in DMF (Table 4.5). The solution was then sonicated and heated in a Teflon-lined autoclave to a temperature of 120 °C (a lower temp. than the 150 °C previously reported) for an equivalent reaction time of 24 h. The products were subjected to spontaneous cooling, filtered, and washed by DMF and ethanol. Finally, the product was dried in a nitrogen flow for 12 h. A typical XRD pattern similar to that simulated for the original chromium structure was acquired with no signs of any interfering impure phases. The measured BET-specific surface areas of the products were 2623 m^2 g^{-1} for the MIL-101(V) and 2340 m^2 g^{-1} for the NH_2-MIL-101(V), which is the highest for any reported vanadium metal-organic framework. Such enhancement in the synthesis method was reflected in a better CO_2 uptake for both products than Biswas's approach.[164, 167]

Despite being air- and water-sensitive, the vanadium analogue and its functionalized derivatives are still studied for many available applications like gas adsorption, catalysis, and guest-encapsulation for catalytic and electrochemical purposes (Table 4.5).[164,167–169] Moreover, they are considered amongst the structures having the highest surface area of all vanadium MOFs so far.[164,166]

Table 4.5 Literature on the MIL-101(V) isomorph

Synthesis method	Precursor			Synthesis conditions			Textural Properties		Application	Comments	Ref.
	Metal salt	Linker	Metal:Linker ratio	Medium	Temp. (°C)	Time (h)	S_{BET} (m² g⁻¹)	V_{pore} (cm³ g⁻¹)			
Conventional	VCl₃	H₂BDC NH₂-BDC	2:1	DMF	150	24	2118 1623	—	Synthesis and gas sorption properties of MIL-101(V)	- Pyrex tube	[164]
	VCl₃	H₂BDC NH₂-BDC	2:1	DMF	120	24	2623 2340	—	Enhanced properties of gas sorption and separation of MIL-101(V)	- Synthesis in DMF - Lower reaction temp. (120 °C)	[167]
	VCl₃	H₂BDC	1:1	EtOH	120	48	3600	—	Framework isomerism in vanadium MOFs	- Synthesis in EtOH - Lower reaction temp. (120 °C)	[170]
	VCl₃	H₂BDC NH₂-BDC	2:1	DMF	150	24	—	—	Nanoparticles incorporation and catalysis: epoxidation of allyl alcohols and alkenes	- Synthesis as in ref. [164]	[168]
	VCl₃	H₂BDC	1:1	EtOH	120	48	—	—	Functionalized carbon material as a cathod for lithium-ion batteries	- Synthesis as in ref. [170]	[169]

4.5.4 MIL-101(Ti), titanium isomorph

Other studies reported the titanium isomorphs of the MIL-101 MOF as potential adsorbents for gas storage and separation applications (Table 4.6). Long *et al.* were the first to report and discuss the synthesis and processing of the MIL-101(Ti), whereby the synthesis was performed in an anaerobic and moisture-free atmosphere to avoid the instability of the framework in ambient conditions.[171, 172] An equimolar solution was prepared in an N_2-filled glovebox, in which the anhydrous chloride salt of Titanium(III) ($TiCl_3$) and the H_2BDC linker were placed in a Schlenk flask connected to a vacuum line system. Then, a 10:1 anhydrous DMF/ethanol volumetric solution was transferred into the flask by the cannula-transfer technique. The obtained solution was held at 120 °C, under stirring and inert conditions, for 18 h to yield a dark-purple powder of the titanium MOF analogue. The resulted powders were washed with anhydrous DMF and dried under vacuum. Different activation methods were tried, but the highest SSA was attained by solvent exchange with anhydrous tetrahydrofuran (THF) followed by drying under vacuum at 150 °C for 12 h.

Activation at these specified conditions could induce some coordinatively unsaturated metal sites (CUS), otherwise denoted as open metal sites (OMS), to the titanium(III)-oxo cluster, causing distortion at these sites (Figure 4.13-b). This activated analogue was of a BET-specific surface area of 2970 m^2 g^{-1} ($S_{Langmuir}$= 4440 m^2 g^{-1}) and a pore volume of 1.50 cm^3 g^{-1}. Adsorption capabilities of the unfunctionalized MIL-101(Ti) were measured against different gases such as N_2, H_2, CO, and CO_2. However, it revealed no remarkable adsorption to any of them as designed, and only weak physisorption was observed.

Table 4.6 Studies targeting the synthesis of the MIL-101(Ti) isomorph

Synthesis method	Precursor		Textural Properties		Comments	Ref.
	Metal salt	Linker	S_{BET} (m^2 g^{-1})	V_{pore} (cm^3 g^{-1})		
Conventional	$TiCl_3$	H_2BDC	2970	1.5	- Synthesis and structure analysis - Gas adsorption of N_2, H_2, CO, CO_2, and O_2	[171]
Conventional Electrochemical	$TiCl_4$	H_2BDC BPDC	3285 3263	1.49 2.2	- Synthesis and structure analysis, and gas adsorption	[173]

In another attempt based on the very high affinity of the Ti^{3+} sites to coordinate with oxygen, adsorption against oxygen was measured. It showed irreversible chemical adsorption of the O_2 molecules to the metal sites. Those oxygen molecules were tightly bonded to the framework causing a slight reduction in the measured SSA. All attempts to release these molecules, and regenerate the original framework, were in vain. Thorough investigations via electron paramagnetic resonance (EPR), IR, UV-Vis-NIR spectroscopies, and magnetic susceptibility confirmed the charge-transfer reactions between the species. Such reactions caused overall framework oxidation and Ti^{4+} superoxide and peroxide formation within the structure (Figure 4.13-c and d). Closer examinations showed that the Ti(IV)-peroxide species prevail over time on account of the superoxide, while the primary Ti(III)-oxo species remain after the exposure to oxygen.
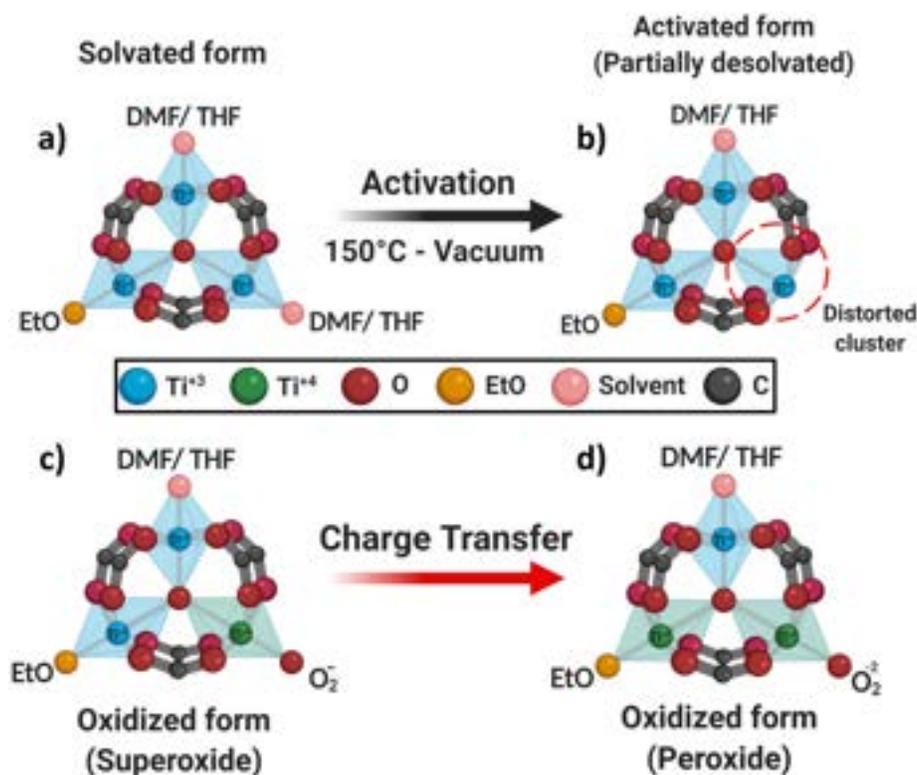
Figure 4.13 Transformations in the titanium-oxo cluster of the MIL-101(Ti) analogue at different stages.[171,172] *Modified with permission from Ref.[171]. Copyright © 2015, American Chemical Society.*

In another study, Antonio *et al.* obtained the MIL-101 structure electrochemically.[173] More challenging, they were able to utilize this route to synthesize the intended MOF from dissolved metal ions instead of a metallic anode. MIL-101(Ti) was synthesized from the commercially available titanium tetrachloride liquid precursor ($TiCl_4$) rather than the expensive and air-sensitive titanium trichloride salt ($TiCl_3$). In such an electrosynthetic strategy, $TiCl_4$

and H_2BDC were dissolved in anhydrous DMF/ethanol 10:1-solution, and 0.1 M $TBAPF_6$ as a supporting electrolyte into the cathodic compartment. The Ti^{4+} ions were completely reduced to the trivalent cation over a nickel foam working electrode at an applied potential of E= -1.2 V for 4 h versus $Ag/AgNO_3$. These conditions generated a bright blue/purple Ti^{3+} containing electrolyte, which was heated at a typical temperature of 120 °C under N_2 atmosphere for 18 h to provide the targeted MIL-101(Ti) framework. The measured BET surface area for this electrochemically-synthesized titanium analogue was found to be 3285 m^2 g^{-1} ($S_{Langmuir}$= 4360 m^2 g^{-1}), which was almost identical to that previously reported.[171]

Taking a step further, and thanks to this method, they were able to prepare the isoreticular MIL-101(Ti) metal-organic framework (MIL-101(Ti)-BPDC), whereby the BDC linker was replaced by the ditopic linker 4,4𝘭-biphenyl dicarboxylic acid (H_2BPDC). The same procedures were followed except that a 2:1 molar ratio solution was used, resulting in bigger STs and a larger overall structure (Figure 4.14). In comparison, the MIL-101(Ti)-BPDC was also prepared solvothermally.
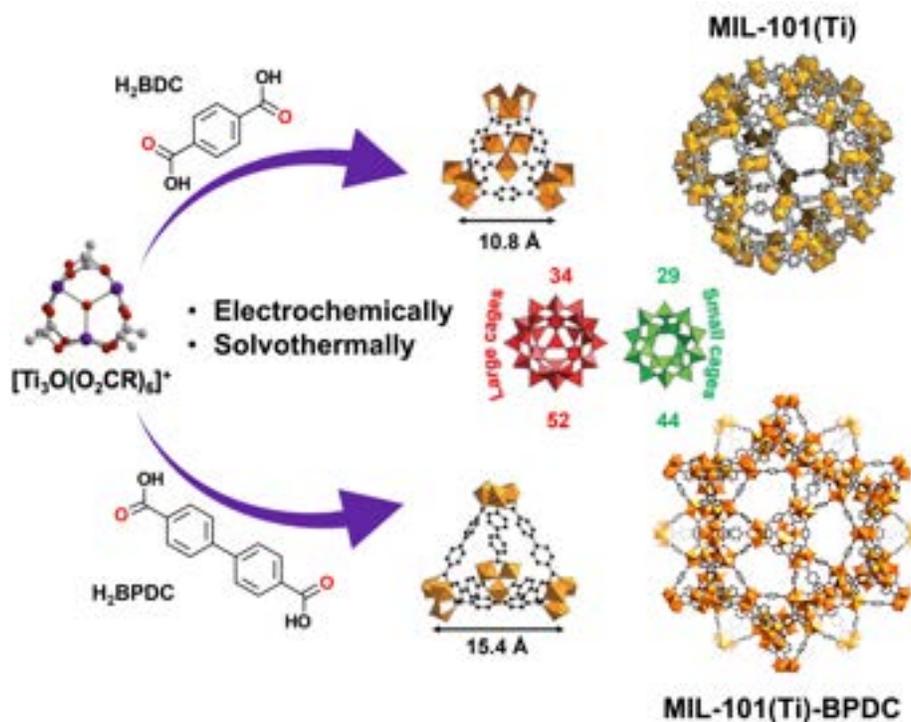
Figure 4.14 Electrochemically- and solvothermally-synthesized isomorphic MIL-101(Ti) and isoreticular MIL-101(Ti)-BPDC. Red numbers indicate the size of the large cages in the corresponding structure, and the green ones represent the smaller cages.[134,174,175] *Adapted with permission from Ref.[134, 174, 175]*

The solvothermally-prepared isoreticular framework exhibited a BET surface area of 2139 m^2 g^{-1} and pore size of 1.32 cm^3 g^{-1}. On the other side, the electrochemically synthesized one was of a higher surface area of 3263 m^2 g^{-1} and pore size of 2.20 cm^3 g^{-1}. The MIL-101(Ti)-BPDC also showed an irreversible binding behavior similar to that of MIL-101(Ti), whereby oxidation of the Ti(III) sites into Ti(IV) superoxides and peroxides was observed.[171]

Finding other reports that include the synthesis, or the application of the MIL-101(Ti) framework, was elusive. So, to the best of our knowledge, these are the only reports of the titanium isomorph.

4.5.5   MIL-101(Sc), scandium isomorph

Scandium, as the lightest rare-earth/transition metal with a very stable (+3) oxidation state, was also examined to develop the μ_3-oxo-centered trimer as the main building block of the MIL-101 framework. This trinuclear SBU was already detected in some scandium 2D MOFs.[175,176] The 3D MIL-101(Sc) isomorph was firstly reported by Mowat *et al.*, presenting the different scandium 3D MOFs with the ditopic and tritopic carboxylate linkers.[177] Throughout a series of experiments, the MIL-101(Sc) analogue resulted from the reaction of the hydrated scandium nitrate salt (Sc(NO$_3$)$_3$·3H$_2$O) with the H$_2$BDC linker in a solvothermal reaction. The precursors were dissolved in DMF then heated at 100 °C for 24 h - 48 h. At these conditions, the MIL-101 phase was obtained; however, it was highly contaminated with another type of Sc-MOFs. Thermal applications showed that the structure, along with the included contamination, breaks down between 400 °C - 500 °C. Nevertheless, and despite being a major phase, MIL-101(Sc) did not show an equivalent large pore size as observed for other metal isomorphs. A pore size of 0.16 cm^3 g^{-1} was measured, indicating unfree pores resulted from the interfering phase.

Meanwhile, MIL-101(Sc) was reported to be fully synthesized mediating solvothermal conditions.[178] In this study, hydrated scandium nitrate was mixed with H$_2$BDC and dissolved in anhydrous DMF at ambient temperature. The use of anhydrous DMF was reported to be crucial since the presence of small amounts of water has resulted in other Sc-MOF structures. After complete dissolution of the components, the solution was transferred into a Teflon-lined autoclave and heated at 90 °C for 24 h to yield a white powder of MIL-101(Sc). The resulting powders were then filtered, washed with DMF, activated in ethanol at 100 °C for 16 h. The recorded BET surface area of the activated MIL-101(Sc) was about 3490 m^2 g^{-1} ($S_{Langmuir}$= 4970 m^2 g^{-1}) with pore sizes of 1.55 nm and 2.21 nm. TGA analysis showed some agreement with the previous study, whereby the structure collapses within the temper-

ature range of 340 °C - 540 °C, leaving a residual of Sc_2O_3 behind. Unfortunately, no other attempts using the same preparation procedures were reported to produce the MIL-101(Sc) framework.

Nevertheless, in another approach of Mitchell *et al.*, MIL-101(Sc) was synthesized from an aqueous chloride salt ($ScCl_3$) solution.[179] On the other side, terephthalic acid was dissolved in a DMF/ethanol mixture. Solutions were mixed, transferred to Teflon-lined autoclave, and heated to 80 °C for 24 h. The resulted white powder of the scandium isomorph was then collected, washed with DMF, and finally dried. Exposure to moist air or drying at a high temperature reaching 100 °C - 120 °C may cause a remarkable loss in crystallinity. Consequently, evacuation of the pores took place at ambient or slightly elevated temperature of 60 °C under vacuum. The nitrogen adsorption measurements showed that the highest surface area was around 640 m^2 g^{-1} (BET) and a pore volume of 0.33 cm^3 g^{-1}, which is remarkably low compared to the expected values of any MIL-101 framework.

In a recent study, the same procedures were followed, but no data about the properties of the achieved MIL-101 structure were mentioned.[180] The catalytic performance of MIL-101(Sc) among other various MOFs of different divalent and trivalent metal centers was measured in multiple reactions as Lewis-acid active catalysts.[179,180] Scandium-containing MOFs showed a noticeable activity; however, the MIL-101 framework did not exhibit the best effectiveness owing to its instability at the reaction conditions and the low surface area in comparison with the chromium analogue. Besides, it was evidenced that such activity was not induced by the surface metal sites, and the reactants may be adsorbed inside the pores to react with the available open metal sites. The low catalytic activity of the MIL-101(Sc) framework in that study was expected as a result of its low thermal stability as well as its use in its as-synthesized form, whereby the structure was not fully activated, and the pores were still occupied with the solvent molecules, yielding low surface area.

4.5.6 General features

Based on what was stated above regarding the different analogues of the MIL-101 framework, they all seem to show some common features resulting from their common crystallographic structure. However, being built from different trivalent metal ions induces some inner differences among these isomorphs. Some of these features are discussed below.

Crystallinity and lattice parameters:

Powder X-ray diffraction (PXRD) is the main characterization technique to confirm the formation of the targeted MOF structure and identify its phase purity. Their high crystallinity results in high-intensity peaks. The calculated pattern derived from the original simulation of the chromium-type MIL-101 framework showed a high density of miller indices at higher 2θ angles and a lower density at lower ones. On the contrary, and in agreement with the powder pattern collected experimentally, the pattern revealed high-intensity peaks at small angles of 2θ range = 0° - 20°, and almost no other noticeable peaks at higher angles (Figure 4.15).

MIL-101 isomorphs comprise different trivalent metal ions, replacing Cr in the same crystal structure yielding similar patterns consistent with the simulated one, as confirmed experimentally.[13,129,131,164,171,178] Different bond lengths would however owing to the various metal ions having different covalent radii.[181] Different lattice parameters, inducing slight shifts and intensity variations in the XRD patterns are observed (Table 7). Linker functionalization would also result in comparable XRD patterns.[128,137,151,167] Nevertheless, functionalization will have substantial effects on other properties like the pore size, chemical, and thermal stability, as will be discussed below. Mixed-metal and mixed-linker MIL-101 will also follow the same trend.
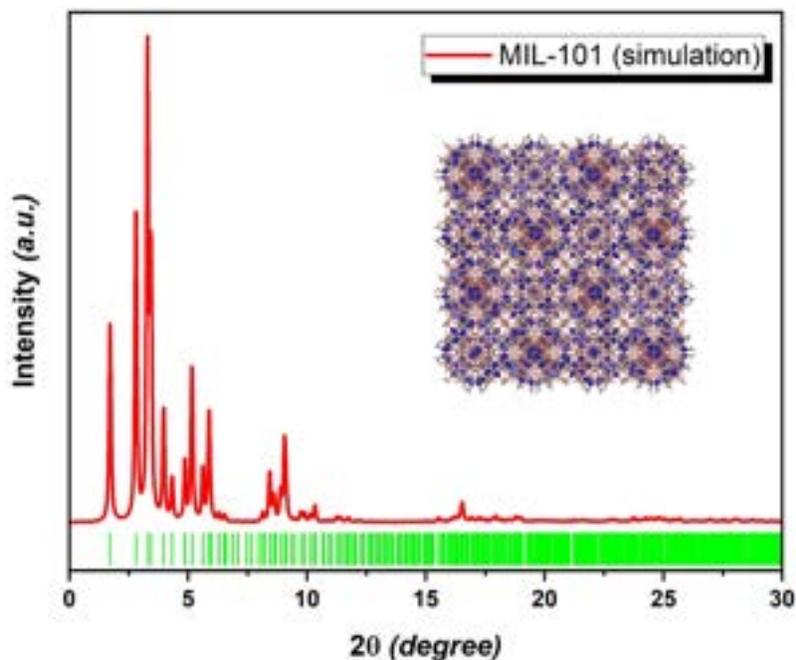
Figure 4.15 Simulated XRD pattern for the original MIL-101(Cr) "red" in comparison with the calculated miller indices "green."[13,69] (Inset: simulated structure reproduced via Mercury/CSD File: "OCUNAC")

Table 4.7 Elements reported in the synthesis of the MIL-101 framework with their covalent radii and their measured change in the lattice parameters based on the synchrotron refinements

Element	Covalent radius (Å)	MOF	a (Å)	V (Å^3)	Ref.
Al	1.21(4)	NH$_2$-MIL-101(Al)	87.7^b 88.01(1)	681,820.5(2)^c	[182, 183]
Sc	1.70(7)	MIL-101(Sc)	90.032(1)	729,790.1(1)^c	[178]
Ti	1.60(8)	MIL-101(Ti)	89.78(2)	723,600(500)	[171]
V	1.53(8)	MIL-101(V)	88.77(3)	699,548.8(48)	[164]
Cr	1.39(5)	MIL-101(Cr)	88.869(1)	701,806.3(1)	[13]
Fe	1.32(3)^a	MIL-101(Fe)	89.781(3) 90.196(2)	728,732.2(5)^c	[134, 184] [134, 184]

^{a} Low-spin configuration,^{b} Simulation data, ^{c} Calculated based on the averaged a values.

Nitrogen adsorption and textural properties:

As discussed above, MIL-101(Cr) gives a characteristic type-I isotherm with two secondary uptakes between P/P$_0$= 0.1 and 0.2, representing micropore filling (Figure 4.16).[13] Despite having a high surface area, MIL-101(Cr) is usually found to have lower measured values than first reported by Férey in the original publication.[68] As illustrated in the previous sections, various synthesis parameters, along with the synthesis activation technique used, can cause a noticeable decrease in the measured surface area and pore volume due to the inclusion of some side products, linker or solvent residuals in the pores. Commonly, a specific surface area in the range of $S_{BET} = 2300$ cm^3 g^{-1} – 3500 cm^3 g^{-1} is found to be acceptable, based on the previous studies (Table 4.2).[68] Other MIL-101 analogues and their functionalized derivatives also give the typical MIL-101 isotherm and an equivalent surface area (Tables 4.3 - 4.6). Structures built from functionalized linkers show a much lower surface area than pristine because of the volume occupied by the functionalizing group.[185]

Generally, in resembling materials of similar isotherm, the Langmuir model, corresponding to monolayer adsorption, is used to interpret the data for relative pressure points P/P$_0$< 0.4

(usually in the range of 0.05 to 0.35).[186–188] Particularly, in the case of MIL-101, for P/P_0 in the range 0.05 to 0.2, models agree well with experimental data.[13] However, since the gas-adsorption in MOFs having large accessible cages takes place through weak interactions (physisorption), the multilayer adsorption is more reliable. Hence, the surface area based on the Brunauer–Emmett–Teller (BET) model is mostly preferred.[3]
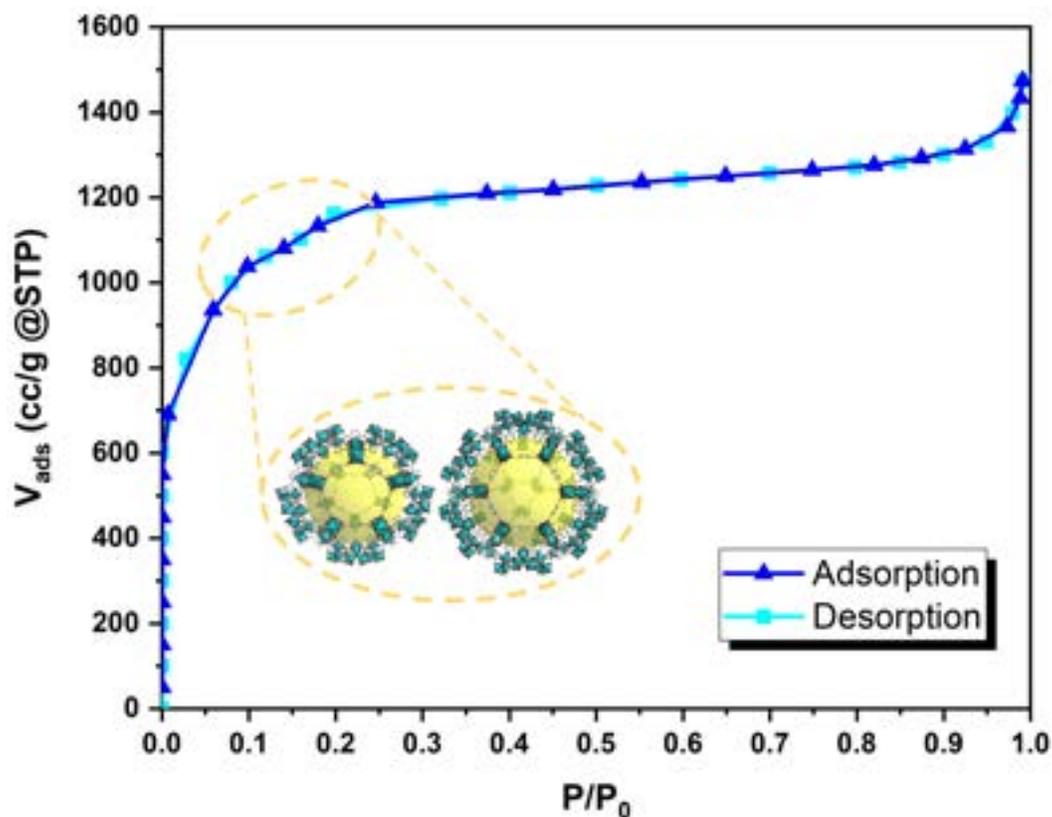
Figure 4.16 Representative N_2 adsorption isotherm reported for MIL-101(Cr), with the secondary uptake corresponding to pore filling.[13, 97]

Structural stability:

Another important feature to be discussed would be the stability of the MIL-101 structure. The term "Stability" usually refers to the ability of a MOF to avoid irreversible chemical and physical changes upon exposure to various operating conditions.[189] At the early stages of MOFs discovery, synthesizing frameworks with a very high surface area and pore volume was the main research interest. However, designing more stable structures that would withstand harsh operation conditions became the core of many recent studies. Generally, in MOFs, each type is assigned for some recommended applications based on its given properties. These properties emerge from its chemical composition and crystal structure. For a specific application, the stability of a MOF's structure is important for applications whereby the

framework should remain unchanged, preserving its original properties during the whole course of the process.[189] Hence, the stability of a MOF should include both its thermal and chemical stability.

Thermal stability: Thermal stability indicates the structural resistance to degradation at relatively high temperatures. However, the available techniques to evaluate this type of stability on MOFs are still limited, and TGA is the most used approach of assessment.[190] For MIL-101, routine measurements are conducted at temperatures ranging from room temperature to 600 °C or 800 °C. A typical TGA plot (Figure 4.17) would show three distinctive stages as follows:

- First, a small weight loss is observed at low temperatures (up to 150 °C), corresponding to the desolvation of the framework, whereby evaporation of the solvent molecules within the pores takes place along with the removal of the water molecules (immobilized liquid moieties) bound at the vertices of the metal trimers (Figure 4.17-a).[13,191] The size and the temperature of this step rely on the type of solvents used during synthesis and activation.[190] By the end of the first stage, a plateau region should be witnessed, in which the solvent-free evacuated framework remains standing with some open metal sites.[190]

- At higher temperatures, an extensive steep weight loss should be recognized equivalent to the departure of the remaining OH^-/X^- ions, detachment of the organic linker, followed by the decomposition of the whole framework (Figure 4.17-b).[13,191] This sharp step represents the main degradation stage of the framework, whereby 45% or higher weight loss is detected at this point.[13,97,111]

- Finally, a second plateau comes after, indicating the constant weight of the residuals, which are mainly the left-behind metal oxide clusters (Figure 4.17-c). At this temperature, the metal oxide crystals reorganize to occupy their most stable form. Usually, about 20% - 30% of the original weight remains after the structure decomposition, corresponding to the persisting bulk mass of the metal oxide. In the case of measurements undergoing higher temperatures (up to 1000 °C), a tertiary weight-loss step may exist, marking the fusion and decomposition of the metal oxide.[97]

The original chromium-type MIL-101 was initially stated to show moderate thermal stability up to 275 °C in air.[13,111,192] Nevertheless, the reported decomposition temperature may slightly vary from one study to another depending on the synthesis method, activation procedures, and preservation conditions. Also, experimentally, the type of gas used during analysis (air, nitrogen, or argon), the heating rate, and the purge gas flow rates may take part in these variations. Thus, later studies sometimes report higher decomposition temperatures between 300 °C - 350 °C.[193–196]
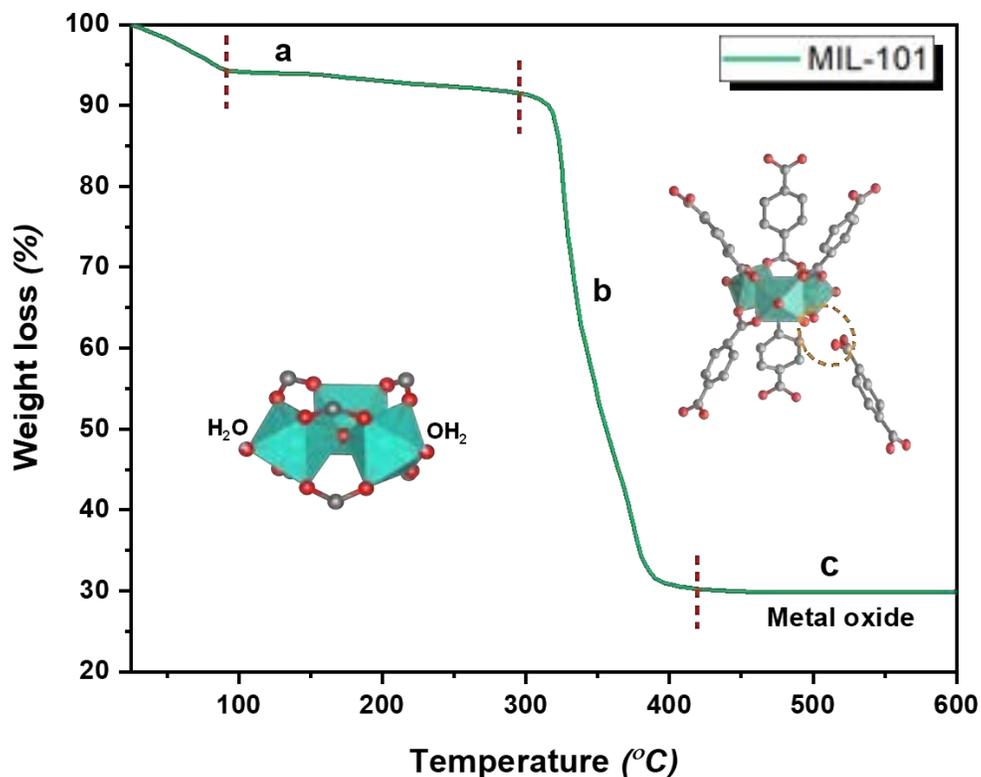
Figure 4.17 A typical TGA plot for the MIL-101 framework, expressing different weight loss stages within each temperature range. (a= solvent evaporation, b= framework decomposition, c= metal-oxide formation) [13, 197]

Critically identifying the decomposition temperature of a MOF based on TGA data solely will probably provide less accurate results. Besides, TGA focuses on the framework deteri-oration disregarding any changes in the crystallographic structure that might occur before degradation. Utilizing high-temperature XRD (HTXRD), close tracking of the crystal disintegration, and any probable phase transformation can provide more information about the different events during breakdown. HTXRD investigations on MIL-101(Cr) showed some minor alterations to the prominent diffraction peaks around $4°$ and $8.7°$ during the temperature rise to 200 °C, which was interpreted to the loss of water and solvent molecules. At higher temperatures, the structure crystallinity was still maintained until a sudden drop of all peaks between 350 °C and 375 °C, corresponding to the framework destruction. Hence, the actual decomposition temperature of MIL-101(Cr) might be higher than those reported previously in the TGA studies.[97]

Since MOF is built through coordination of a metal cluster and an organic linker, its thermal stability is related to factors affecting both components and their interaction. For the metal cluster, the type of the SBU formed as well as the oxidation state of the included metal ions, bond strength, and preferred coordination number would significantly determine its degree

of interaction with the organic linker, affecting the framework thermal withstanding. On the other hand, the nature of the organic linker (aliphatic/aromatic) and the type of its donor heteroatoms are also contributing.

All the metal centers in pristine MIL-101 isomorphs hold the same bonding with the organic linker, secondary building unit, and the same oxidation state. Most of them are *3d*-transition elements, sharing comparable chemical and physical properties. Nevertheless, they differ internally depending on the stability of their ions' oxidation state, covalent radius, and local coordination environment. Hence, all MIL-101 isomorphs follow the same degradation sequence at elevated temperatures, but their decomposition temperature would slightly differ depending on the metal type present. Technically, MIL-101(Cr) and its various analogues show framework degradation temperature within the range of 250 °C to 400 °C. Air- and water-sensitive analogues like MIL-101(V) follow the same trend, showing a decomposition temperature under inert gas between [320 °C (TGA) - 400 °C (TDXRPD)].[164]

Functionalized MIL-101s would start decomposing over a broader temperature range, depending on the functional group on the organic linker.[99] Amino-functionalized frameworks were found to show lower decomposition temperatures than unfunctionalized ones, regardless of the metal type.[99, 164] In spite of their lack of certainty, these trends would allow the prediction of the decomposition temperatures for some functionalized and non-functionalized structures. For example, NH_2-MIL-101(Al) was reported to show structural degradation around 375 °C (TGA) under air.[151, 183] Considering this trend, pristine MIL-101(Al) would be of higher thermal stability than its amino-functionalized form, thus higher than all other analogues. Related studies on similar MOFs confirmed this trend.[198] Thermal studies on the deaminated NH_2-MIL-101(Al) are still required to either confirm or reject such a hypothesis.[157] Keeping in mind that a loss of crystallinity was recorded for NH_2-MIL-101(Al) over 300 °C under air, using time-resolved XRD, this loss may result from a low chemical stability at high temperature.

Chemical and hydrothermal stability: Chemical stability is another important criterion to take into account when selecting a MOF for a particular application. In similar contexts, chemical stability implies the durability of a given MOF for a considerable period of time against the ambient atmosphere. This concept goes beyond the reactivity of the MOF with the surrounding moisture to include its structural changes when it comes in full contact with water. Real-life applications may also require stability against more aggressive environments. For example, MOFs in drug delivery shall have chemical stability in aqueous solutions of different pH. In other applications, like catalysis, both chemical and thermal stability are essential for the framework to survive the reaction with limited degradation.

Owing to their highly crystalline structures, PXRD is the primary characterization technique used to assess the chemical stability of MOFs. Comparing the resulting patterns before and after the exposure to the environment under study gives a basic idea of the degree of the framework deterioration. Nevertheless, quantification based on XRD results is not sufficient to judge the framework's stability. Partial degradation may happen, so that other techniques should be involved to get realistic conclusions. Gas sorption measurements would be an adequate and complementary method in this regard. Inert gas adsorption can reflect the decay in surface area of the inner pore walls and the overall loss in porosity. Also, water adsorption is another efficient way to study the chemical interactions between the water molecules and the MOF pores, and therefore its stability in water.

Among the 100,000 entries registered under the MOF subset in the Cambridge structural database (CSD), only a few are considered of potential use in industrial applications as a result of their reasonable chemical stability. These "stable" MOFs hold their structural integrity under oxidative atmosphere. MIL-101 is usually mentioned among those chemically stable MOFs. However, the chromium-based structure is the one referred to in most cases. MIL-101(Cr) was originally reported to show considerable chemical and solvothermal stability over months.[13] The structure was found to remain intact in air and many organic solvents under these prolonged periods. These initial stability investigations were not detailed enough so that more recent experimental and computational studies were conducted in order to define the stability limits of this framework.

Relying on XRD data and N_2 adsorption measurements, the chemical stability of MIL-101(Cr) in the air was further confirmed.[106] In some cases, slight diminishing of some XRD peaks intensity was recognized at long exposure times, reaching one year.[90] MIL-101(Cr) was also found to show remarkable solvothermal stability when subjected to various organic solvents at boiling temperatures for 8h.[90, 106, 199] No change in the peak intensity or structural porosity was noticed in the case of exposure to boiling water over a week, indicating the high hydrothermal stability of the structure.[106, 199, 200] Water stability of MIL-101(Cr) was verified by utilizing water adsorption.[139, 200] The framework was reported to be hydrophilic, expressing a heat of adsorption (45.13 kJ mol^{-1}) close to the molar enthalpy of evaporation for water (40.69 kJ mol^{-1}), suggesting that adsorption takes place at first as a monolayer around the metal centers. Other layers are then formed by coordination to the monolayer through hydrogen bonding, resulting in water clusters inside the pores.[139]

In another interesting study, Low *et al.* investigated the hydrothermal stability of MIL-101(Cr) experimentally in a high throughput experiment, in which the resistance of a MOF to hydrolysis by water was investigated at high temperatures.[201] Samples were tested for a

duration of 2 h in a 48-quartz cell high throughput unit, whereby steaming at different water partial pressures was introduced to each row, and each column was treated at a different temperature (Figure 4.18). Results showed that MIL-101(Cr) has high hydrothermal stability reaching a limit of 50% steam at 325 °C.[201] Steamed samples showed severe deterioration in their morphology and overall physical properties. An evident drop in the framework's surface area along with most of its XRD peaks decrease confirmed these results.

A recognizable color change could be noticed for all samples conditioned over the temperature range of 250 °C to 300 °C, in which the known sea-green color of MIL-101(Cr) turned brownish.[201] The color gradient was sensible in the direction of temperature increase (right to left) across all steaming levels and not the direction of higher steaming levels for each temperature (Figure 4.18). Hence, it seems that the framework itself was resistant to hydrolysis regardless of the amount of steam applied. However, approaching temperatures close to decomposition temperature catalyzed such a reaction on all levels, whereby partial decomposition of the structure or detachment of the linker facilitated the interaction and bondage of the metal center to the introduced water molecules.
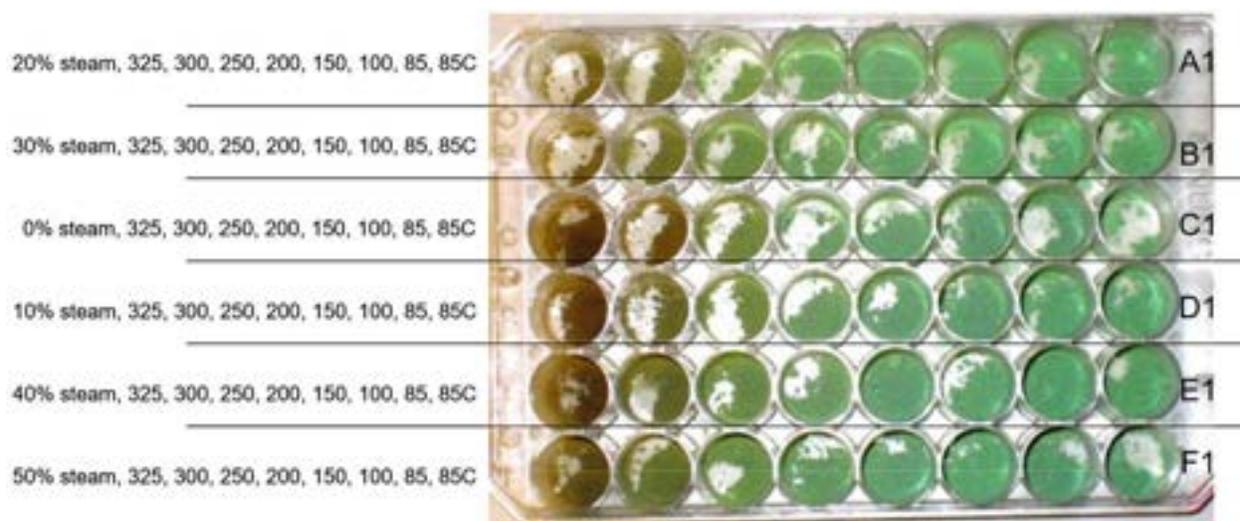
Figure 4.18 The high throughput test employed to evaluate the hydrothermal stability of MIL-101(Cr). Temp. range= 85 °C – 325 °C, Steaming percentage= 0% - 50%. A color change from green to brown was observed for all samples at high temperatures (≥ 250 °C). *Reprinted with permission from Ref.[201]. Copyright© 2009, American Chemical Society.*

Nevertheless, the limitation of these experimental investigations lies in two points. First, and most importantly, the XRD patterns presented for MIL-101(Cr) showed a sharp diffraction peak around 10.8°, together with other peaks of lower intensities around 18° and 25°. Some of these peaks were defined by the authors as associated to a linker impurity.[201] However, close

reviewing of this pattern would show a great similarity with that of MIL-88B (a framework isomer to MIL-101(Cr), see section 4.6).[52, 54] MIL-88B crystals can also be witnessed in the SEM images, with their distinct hexagonal crystals different from the octagonal MIL-101 ones.[132, 201] Hence, the samples were rather a mixture of two phases (i.e., MIL-101 and MIL-88B) than a single pure MIL-101 phase. MIL-88B shares the same trimeric SBU as that in MIL-101. MIL-88, however, has a different crystal structure with a higher decomposition temperature and different chemical stability.[52, 54] The presence of the MIL-88 phase within the samples may have induced a different response in the applied tests.

Second, in the conducted experiments, all samples were loaded to the cells, activated overnight under a nitrogen flow, then heated to the specified temperature assigned to each column before the steam introduction.[201] As a result, the samples heated to high temperatures (250 °C - 325 °C) were forced to go through partial decomposition first before reacting with steam, ignoring the synergistic effect of the two factors taking place simultaneously. The decomposition temperature of the samples was not measured or identified before the run. Consequently, the intensity decrease in the measured diffraction peaks for the steamed MIL-101 sample at 300 °C could have resulted from the thermal decomposition of the sample only aside from the influence of the steam.[13]

Finally, the color change observed does not necessarily mean the hydrolysis of the framework, especially as it also occurred in samples with 0% steaming (Figure 4.18-C1).[201] This change may refer to the amorphization of the MIL-101 framework or, most probably, the phase transformation to the MIL-88 structure as the peaks belonging to this phase have become more pronounced. Also, a similar phenomenon was detected during the microwave-assisted synthesis of MIL-101(Cr) at high reaction times reaching 240 min and 360 min. The resulting powders turned from green to brown, revealing the presence of the MIL-88B crystals.[202]

In the same publication, computational calculations based on quantum mechanics and molecular modeling of the MIL-101(Cr) trimeric cluster compared to other SBUs were performed.[201] The model followed a stepwise reaction, in which the water molecule approaches the metal cluster at the point of connection of the metal center and the ligand (Figure 4.19-a). The water molecule then causes the bond breakage between the metal center and the carboxylate linker, leaving the cluster with an open metal site (Figure 4.19-b). Hydrolysis takes place, and the oxygen atom of the water molecule bonds with the metal cluster and redirects its protons towards the oxygen atom of the carboxylate group (Figure 4.19-c). In the last stage, the carboxylate ligand changes from η_2 to η_1 coordination state, and hydrogen bonds become effective between the metal cluster, bonded water molecules, and the dissociated carboxylate ligand.

These calculations introduced the basic concepts in predicting the chemical stability of existing MOFs and for designing new chemically stable structures. Similar to thermal stability, the chemical stability of a given MOF would depend on the type of the metal ions, their valency, preferred oxidation state, and degree of coordination within an SBU.[201] Likewise, the type of hetero atoms found in the linker and its affinity to form complexes with the metal ions also contribute to the overall chemical stability.[201] In this context, the metal type, preferred oxidation state, and bond strength between the metal center and the ligand atoms are considered the most influential factors in this case.
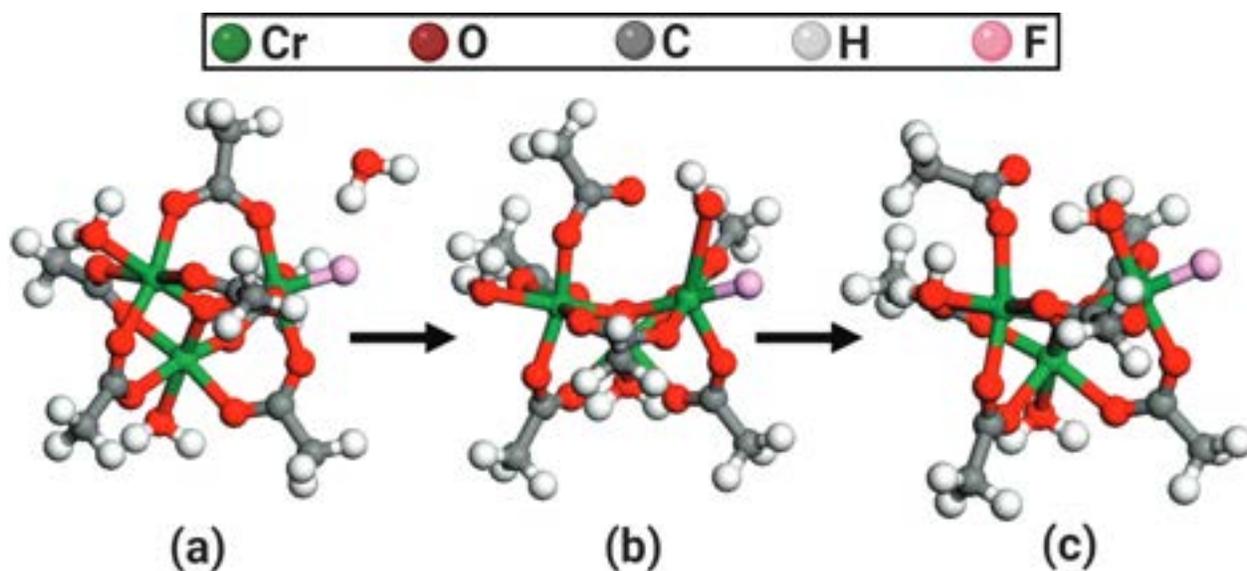
Figure 4.19 Molecular modeling of the trimeric oxo cluster resembling that of MIL-101(Cr), expressing different stages of interaction during hydrolysis. a) water molecule existence (initiation), b) Ligand-metal bond breakage/ water molecule bonding (transition), c) protons redirection and hydrogen bond formation (product). *Adapted with permission from Ref.[201]. Copyright © 2009, American Chemical Society.*

All MIL-101 isomorphs share the same oxidation state, trimeric SBU, topology, and organic linker (H_2BDC). They are all built from comparable transition metals, showing a trivalent oxidation state, whereas this may not be the most stable state for all these elements. According to Low's findings, the bond strength in the equivalent metal oxides can give a rough estimation concerning the chemical stability of the studied MOFs.[201] Following this concept, the metal-oxygen bond strength in Cr_2O_3 is higher than that of Fe_2O_3 (447 kJ mol^{-1} vs. 400.4 kJ mol^{-1}, respectively).[201] So, MIL-101(Cr) is to be more chemically stable than its iron analogue (i.e., MIL-101(Fe)), which agrees with the actual situation.[137, 138, 183] Al_2O_3 has a much higher bond strength (513.9 kJ mol^{-1}).[201] This would allow expecting

pristine MIL-101(Al) to show higher chemical stability than the chromium and iron analogues. However, this information is not yet available for the unfunctionalized MIL-101(Al). Even though MIL-101(Al) was synthesized through PSM, its chemical stability is not well studied so far.[157] On the contrary, the amino-functionalized aluminum isomorph (NH$_2$-MIL-101(Al)) has shown lower stability than MIL-101(Cr), but in this case, the functional group might be contributing to overall stability.[137, 138, 183]

V$_2$O$_3$ has a bond strength of 499.5 kJ mol^{-1}, compared to Cr$_2$O$_3$, MIL-101(V) would be predicted to express higher chemically stability than MIL-101(Cr). MIL-101(V) was, however reported to be sensitive to moist air and water. Its structure would decompose within a few hours when exposed to humid air.[164] Trivalent vanadium ion (V^{3+}) is not the most stable oxidation state for most vanadium compounds.[198] Based on the TGA studies concerning V-MOFs, different vanadium oxides with different oxidation states of the vanadium ion may appear in the original structure.[49, 203] V$_2$O$_5$ is the given residual in the case of the MIL-101(V) framework.[164, 167] The M-O bond strength in the stable oxide was suggested to provide closer results. Hence, V$_2$O$_5$ with a bond strength of 382.7 kJ mol^{-1} (lower than Cr$_2$O$_3$) can explain this instability.[198]

MIL-101(Ti) was also reported to be an air-sensitive MOF that is easily oxidized when exposed to ambient atmosphere.[171] Nevertheless, the bond strength of all titanium oxides is higher than Cr$_2$O$_3$ (e.g., Ti$_2$O$_3$= 535.75 kJ mol^{-1}).[201] Hence, the mere energy of the metal-oxygen bond is not uniquely correlated to the stability of all these analogues. The oxidation state of the metal ion in the cluster is also to be considered, since the (+3) oxidation state is not always the most stable state for several of these elements. Hence, the possible change in oxidation state is also playing an effective role in determining the chemical stability of a MOF. MIL-101(Sc) might be a counterexample for being unstable despite having a very stable (+3) oxidation state.[179] Some studies regarding the effect of different metal ions on the chemical stability of a particular MOF structure also suggested considering the inertness and lability of the metal ion.[198, 204] The chemical stability of isotypic MOFs was proved to correlate well with an increase in inertness or a decrease in lability of the central metal ion.[198]

In another study, Leus *et al.* systematically investigated and compared the chemical and hydrothermal stability of a series of famous MOFs known to be stable, including MIL-101(Cr) and NH$_2$-MIL-101(Al).[138] The hydrothermal stability test was conducted through exposure to saturated steam at 200 °C for 5h. The chemical stability against air, water, acidic (HCl, pH= 0 and 4), basic (NaOH, pH=12), and oxidizing (5%wt. H$_2$O$_2$) media was studied considering both short-term (3 days) and long-term exposure (60 days) at room temperature.

Stability evaluation was made through XRD and surface area measurements. Once again, MIL-101(Cr) showed remarkable overall hydrothermal and chemical stability, except under oxidizing environment for longer exposure times. XRD results revealed no phase transformation, and the structure was kept intact, preserving its high crystallinity in most cases. In addition, surface area measurements showed no signs of internal decomposition of the framework. The measured surface area was almost similar to (if not exceeding) that of the as-synthesized sample. Moreover, MIL-101(Cr) samples tested in different acidic or basic media expressed a close to 30% increase in surface area. Under these conditions, the dissolution of the free linker becomes more accelerated, which would facilitate the evacuation of the MOF pores, resulting in a higher SSA. In the presence of peroxides (H_2O_2 test, oxidizing environment), the chemical endurance of the structure is still maintained in the short term. However, extended exposure to this hostile environment would force the MOF transformation to the thermodynamically stable phase, MIL-53 (a framework isomer to MIL-101(Cr), see section 4.6).

In contrast, NH_2-MIL-101(Al) did not show equivalent stability, and in most tests, transformation to the MIL-53 phase is to arise. Short-term exposure to water would drastically reduce the framework crystallinity indicating internal fragmentation of the structure, causing about 50% decrease in the measured surface area.[138] Nevertheless, a complete phase transformation to the more stable MIL-53 structure was identified in contact with the ambient atmosphere and after the steaming test. Also, the amino-functionalized framework was found to show similar chemical change when subjected to acidic or basic media. In highly acidic media (pH= 0), complete dissolution of the structure was detected over both the short and long terms, with no signs of any phase transformation. Hence, the amino-functionalized aluminum analogue was reported to have very low chemical and hydrothermal stability.[138]

4.5.7   Case study: MIL-101(Mn), manganese isomorph

So far, five out of the ten elements in the first row of the d-block transition metals were used to prepare the MIL-101 framework viz., scandium, titanium, vanadium, chromium, and iron. Manganese, as the midst element among chromium and iron, is believed to be able to form the MIL-101 structure under appropriate conditions. Especially since Mn was reported in the synthesis of MIL-100 metal-organic framework, which is an equivalent MOF discovered after MIL-101. It is however built from the same metal trimer and the tritopic linked benzene-1,3,5-tricarboxylic acid (H_3BTC or Trimesic acid) (Figure 4.20), exhibiting the same MTN topology.[205, 206] Also, Mn was recently involved in the synthesis of the MIL-88B, which is a framework isomer built from trivalent metal ions and the H_2BDC linker.[207]

Recently, Songolzadeh *et al.* reported the synthesis of the MIL-101(Mn) isomorph along with other analogues (i.e., MIL-101(V) and MIL-101(Cr)) for the adsorption and separation of quinoline.[208] All MOFs were prepared solvothermally from their metal oxide (chromium trioxide "CrO_3", vanadium pentoxide "V_2O_5", and manganese(III) oxide "Mn_2O_3") at different precursors ratios of (0.33, 0.67, and 1.00) with respect to the BDC linker. A wide range of reaction temperatures (120 °C, 150 °C, and 180 °C) and times (10 h, 15 h, and 20 h) were selected to synthesize these isomorphs. In a typical synthesis, the metal oxide was mixed with an appropriate amount of linker according to the assigned ratios and then dissolved in DMF. Heating to the desired temperature for a certain time took then place in a Teflon-lined autoclave. Finally, the collected powders were filtered, washed with DMF, water, and acetone before drying at 160 °C under vacuum.
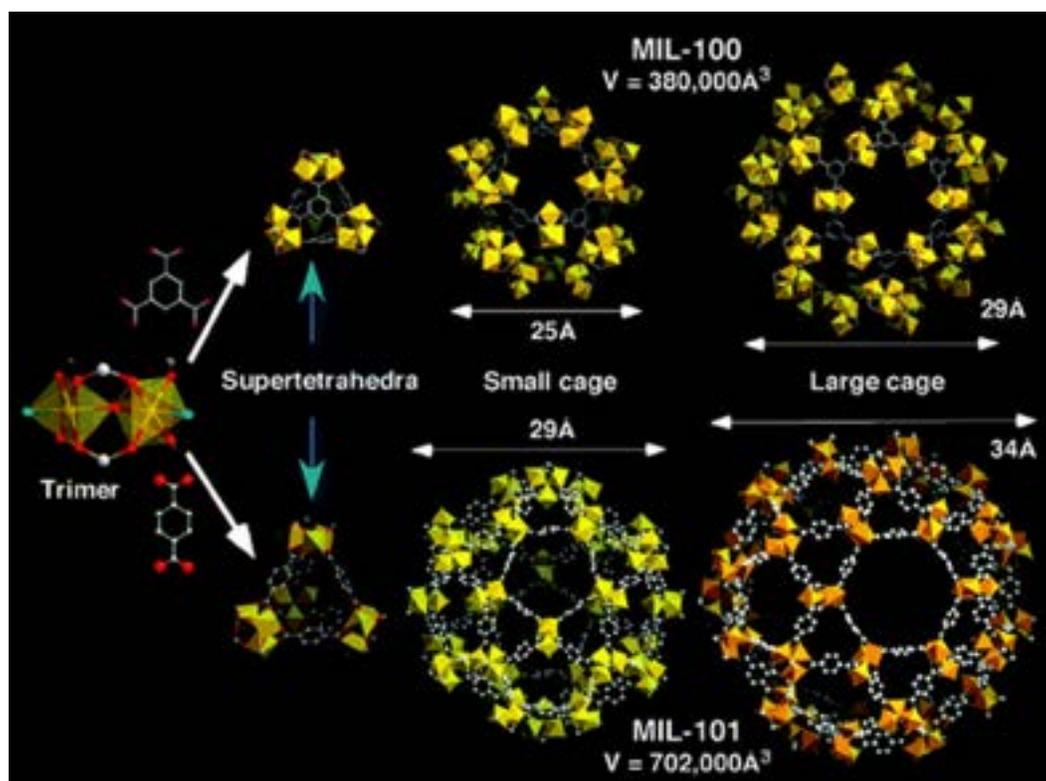
Figure 4.20 Synthesis and coordination of the metal trimer with different linkers yielding both MIL-100 and MIL-101. *Reprinted with permission from Ref.[110]. Copyright © 2008, American Chemical Society.*

Some contradictions were however noticed in the results, leaving some doubts over the fact that MIL-101(Mn) was achieved. Firstly, according to the paper, all MOFs were obtained over the whole range of applied temperature, which somehow contradicts the above-mentioned results, implying that the MIL-101(Cr) was not obtainable at a low synthesis temperature

of 120 °C and with DMF as a solvent.[109] Using DMF as the only solvent (water-free medium), as was done in this work, is known to result in a different product but not in the MIL-101 structure.[109] In addition, equivalent MOFs are usually prepared from equimolar solutions, and sometimes even with metal precursor being in excess, but in this work the optimal molar ratio was for an excess linker. No discussion about the stability or sensitivity of the obtained MOFs in the air (especially the vanadium and manganese analogues) was reported.[164, 167, 205]

Most importantly, the collected and displayed XRD pattern for the MIL-101(Mn) showed many diffraction peaks in the 2θ range of 10° - 80° with no referring to smaller angles. This is totally contrasting to the simulated pattern of the MIL-101(Cr), with most of the high-intensity peaks being at small angles and almost no peaks over this range, as shown in Figure 4.15 and Figure 4.21. Substituting the chromium atom with manganese (or any other metal) in the same given computational crystal model results in the same pattern but with different intensities. Hence, achieving this MOF structure with different metal types should give a comparable pattern but not as different as observed.
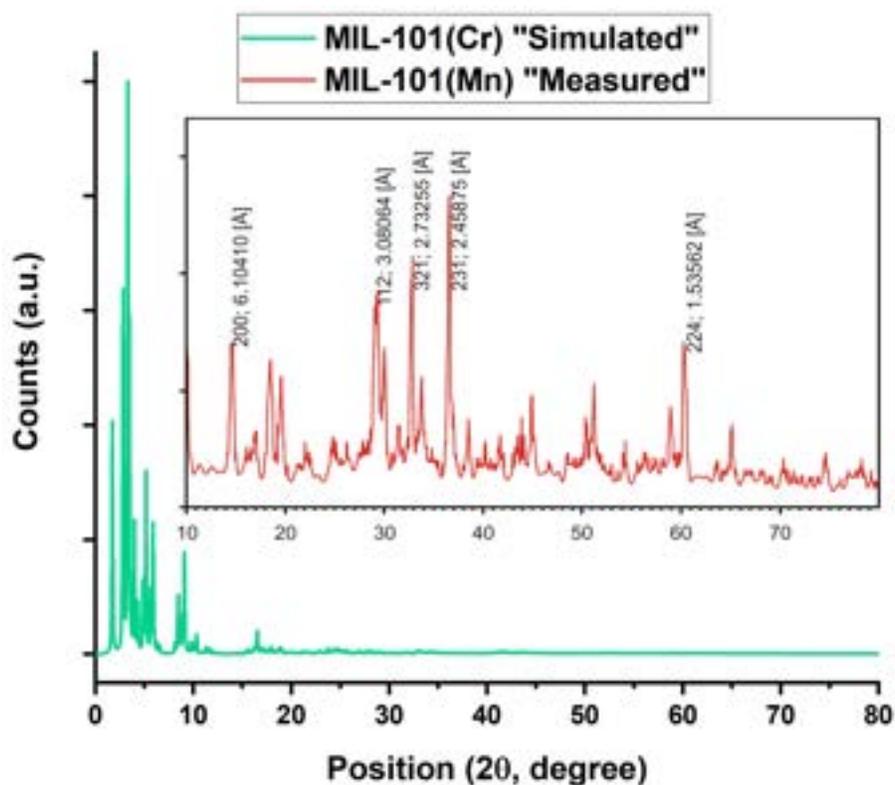
Figure 4.21 XRD pattern for the reported MIL-101(Mn) isomorph "inset-red" in comparison with the simulated pattern for the original MIL-101(Cr) "green."[208] (reproduced via Mercury/CSD File: OCUNAC)

Furthermore, despite the high surface area (S_{BET}= 4204 m^2 g^{-1}) and the large pore size (35Å) reported for this Mn-analogue, the measured N$_2$ isotherm was clearly identified by the authors as a type-II isotherm. Nevertheless, the presented isotherm was almost linear. On the contrary, the reported isotherms of the original MIL-101(Cr) or any of its isomorphs (pristine and functionalized) were consistently found to exhibit a type-I isotherm with two secondary uptakes at the relative pressure of 0.05 and 0.2 (Figure 4.16 and Figure 4.22). Hence, it is likely that the compound achieved in this work is not of MIL-101 structure.
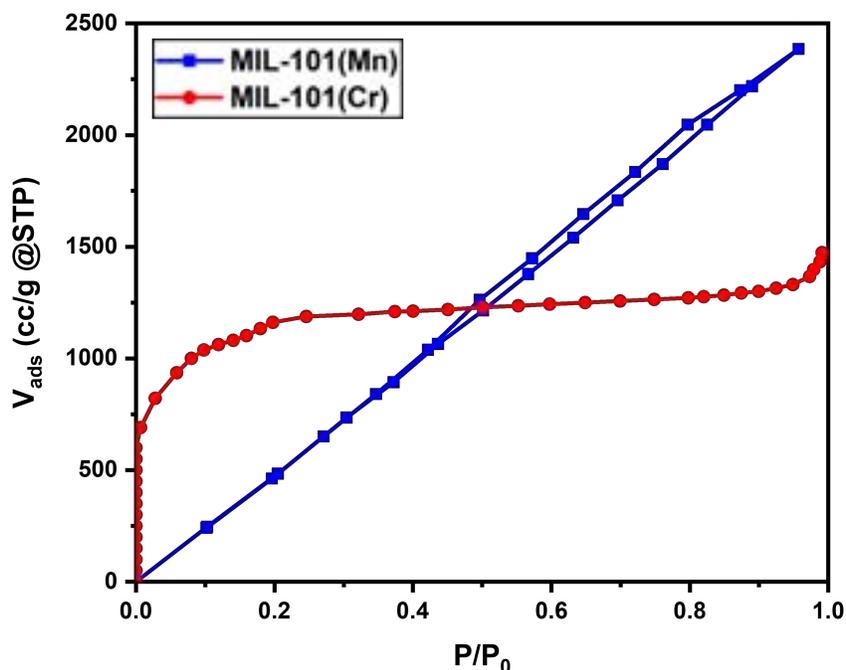
Figure 4.22 N$_2$ adsorption isotherms reported for both the Manganese analogue (blue/semi-linear) compared to that of Chromium or any other MIL-101 isomorph/derivatives.[13,97,208]

Accordingly, since the mentioned work is the only publication reporting the synthesis of the manganese analogue MIL-101 framework, it is believed that MIL-101(Mn) is not yet a demonstrated materials and that further work is still needed to establish a synthesis procedure of this new MOF.

4.6   Polymorphism of MIL-101

As a matter of fact, the MIL-101 framework is not the only MOF that is built from the trinuclear metal cluster and ditopic organic linker. In addition to isomorphism, polymorphism, or framework isomerism, is another commonly-known phenomenon in the field of MOFs. [170] Polymorphism is defined as "the ability of a compound to crystallize in more than one distinct crystal structure," whereas it denotes diverse arrangements of rigid molecules in the

solid-state.[209, 210] Many MOFs of different structures come out from the reaction of the same initial precursors based on the reaction conditions. The interaction of such precursors leads to different SBUs with various connections to produce MOFs of multiple morphologies. This structure variation reflects many different physical and chemical properties.

The trigonal prismatic metal cluster of the MIL-101 framework along with the H_2BDC linker was reported to face polymorphism, whereby different assemblies were observed, resulting in different MOF topologies. Just before MIL-101 was reported, another 3D MOF, built from the same trinuclear oxo-centered chromium cluster and the dicarboxylate linker, was obtained, namely, MIL-88 (Figure 4.23-a).[50] In this feature, MIL-88B was used to denote the structure built from the terephthalate linker since the structure of the MIL-88 was reported to be obtainable from many dicarboxylates such as fumaric acid (MIL-88A), 1,4-BDC (MIL-88B), 2,6-NDC (MIL-88C), and 4,4′-BPDC (MIL-88D).[52,54] The XRD studies illustrated a structural formula of $[M_3^{III}O·(BDC)_3·F/OH·(8H_2O)·solvent]$, and a distinct diffraction pattern different from that of the MIL-101 (Figure 4.24-a,b).[54] Compared to the MTN topology of the MIL-101 framework, MIL-88 was reported to occupy the less transitive topology of the acs net with the *P-62c* space group (Figure 4.23-a,b), making it the default structure and the thermodynamic isomer for many trivalent metal ions like Sc [175–177], V [170], Mn [207], Cr, and Fe [52, 54, 211]. Besides, the MIL-88 framework was found to exhibit channels rather than the cages of the MIL-101 structure (Figure 4.23-a, b). However, other investigations proved that the structure of the MIL-88 MOF is flexible, in which the size of its channels changes depending on the surrounding medium (solvent), represented as the framework "breathing" (Figure 4.23-a). [132, 211, 212] This renowned difference between the framework rigidity of the MIL-101 structure and the flexibility within the MIL-88 structure has played a vital role in redirecting studies for different applications.

MOF-235 is another framework isomer to MIL-101 that is frequently reported as a formed intermediate during the synthesis of other structures using the same precursors.[159, 161, 213] Further, MOF-235 was found to result from the assembly of the trivalent metal trimer and the H_2BDC linker, giving the formula of $[M_3O·(1,4\text{-}BDC)_3·(DMF)_3]·[FeCl_4]·(DMF)_3]$.[214] Therefore, by comparing the structures of MOF-235 and MIL-88, and aside from the type of solvent included, it could be stated that both structures are identical, underlying the exact *P-62c* topology. Nevertheless, the MOF-235 structure has an overall cationic character balanced by the tetrahalide metal $[M^{III}X_4]^−$ counterion, located in its hexagonal pores (Figure 4.23-c).[214] Moreover, MOF-235, with its metal halide inclusion, is usually obtained through quenching and mostly in the cases whereby a metal trichloride is used initially in the synthesis.[213]The XRD pattern for MOF-235 is shown in Figure 4.24-c.[214]
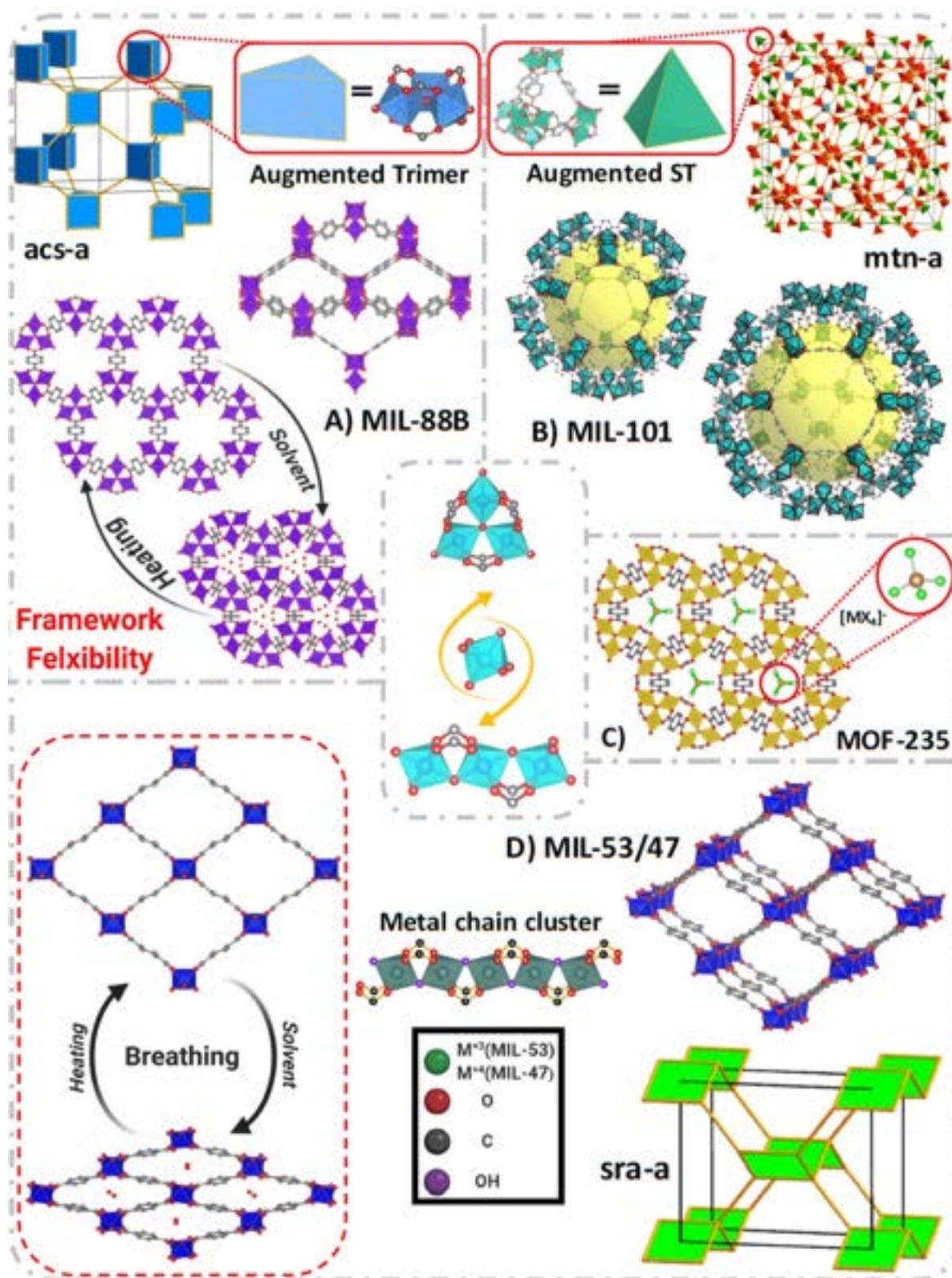
Figure 4.23 Schematic representation of the different polymorphs built up from the same metal octahedron. a) MIL-88, b) MIL-101, c) MOF-235, and d) MIL-53/47.[70,211,214–216]
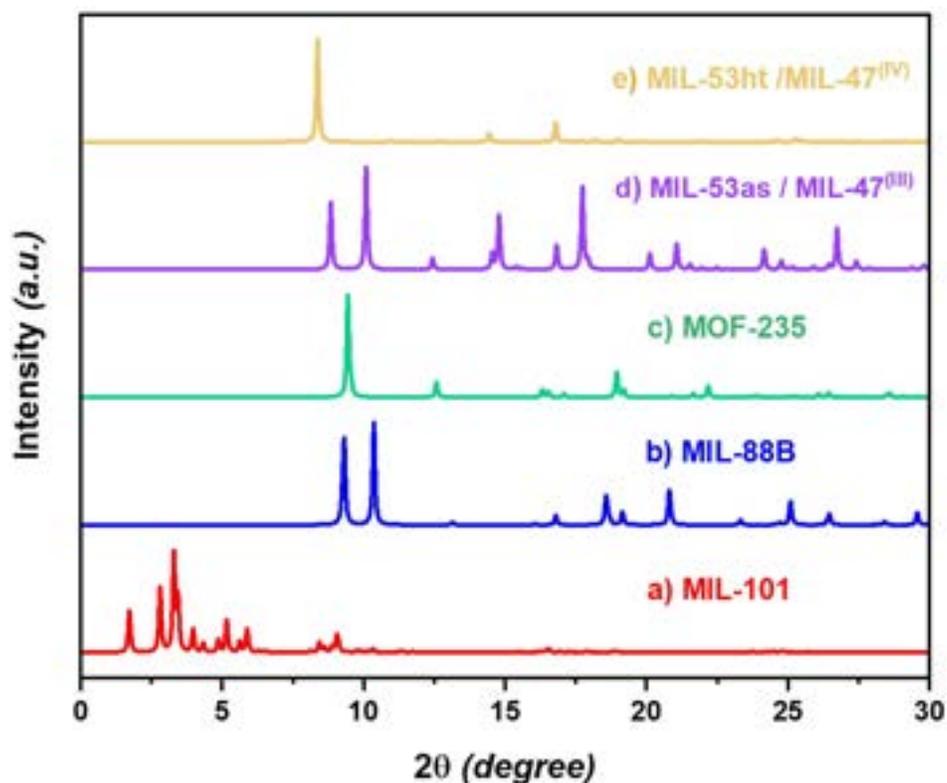
Figure 4.24 Diffraction patterns of the MIL-101 polymorphs. a) MIL-101, b) MIL-88B, c) MOF-235, d) MIL-53 (as-synthesized) / MIL-47as (M^{III}), e) MIL-53 (high-temp.)/ MIL-47 (M^{IV} calcinated). (Calculated patterns reproduced via Mercury/CSD simulated files: "OCUNAC," "YEDKOI," "DANWOF," "MINVOU01/IDIWIB," "MINVUA01/IDIWOH," respectively)

On the other hand, MIL-53 is another member of this three-dimensional MOF family that is routinely produced during the synthesis of MIL-101, MIL-88, and MOF-235. It is formed by the reaction of the BDC linker with the metal(III) octahedron but not in the shape of the trinuclear μ_3O-trimer. However, in this structure, the metal octahedra are connected to form infinite metal chain clusters through a corner-sharing assembly (Figure 4.23-d).[50] Despite not being a framework isomer to MIL-101, It is essential to include such a structure since it is closely related to these isomers.[159,170] The activated MIL-53(ht) has the chemical formula of M^{III}(OH).(BDC), whereby the OH represents the ligand by which the metal octahedra are linked to form the trans-chain cluster.[50] Like the MIL-88 isomer, the MIL-53 framework was found to have channel-shaped pores that exhibit the same flexibility and breathing behavior for different adsorbates (Figure 4.23-d).[24,217] This framework flexibility would cause some variations in the resulting diffraction pattern depending on the solvent; however, the XRD patterns for MIL-53(as) and MIL-53(ht) are shown in Figure 4.24-d,e.

MIL-47 is a framework isomer for MIL-53, in which they share the same linker, structure, and

topology. However, MIL-47 is made out of tetravalent metal ions (particularly vanadium) rather than the trivalent of the MIL-53 (Figure 4.23-d).[49] They were both reported to occupy the sra topology with the space group of Pnam. In contrast, MIL-47 was found to express a relatively rigid structure compared to MIL-53, keeping the same space group at different stages.[49, 166] Nevertheless, MIL-53 was proved to show some structural changes between its as-synthesized state (space group *Imcm*) and its dried one (that is identical to MIL-47 *"Pnam"*). MIL-53 was synthesized using different transition metals of stable (+3) oxidation state (Sc, Cr, and Fe) [50,177,218] besides others of the p-block (Al, Ga, and In).[217,219,220] On the other hand, MIL-47 was basically built from V, and recent investigations were made to incorporate Mn.[49,51,221] The diffraction patterns of the as-synthesized MIL-47(V^{III}) and the calcinated MIL-47(V^{IV}) are shown in Figure 4.24-d,e. Other polymorphs may include MIL-68 and CAU-1 (CAU=Christian-Albrechts University).[150,180,222]

This close relation between these frameworks (MIL-101, MIL-88, MOF-235, MIL-53, and MIL-47) was investigated and illustrated in different studies. [170, 223–225] Generally, they were prepared from the same precursors, but the growth of a specific structure was dependent on the accompanying reaction conditions, kinetics, and thermodynamics. As mentioned earlier, Stavitski and Goesten were able to track these different structural transformations for Al-based MOFs using various characterization and computational techniques (Figure 4.11).[159–161] NH_2-MIL-53(Al) was found to be the default thermodynamic phase at high temperatures. On the other hand, NH_2-MOF-235(Al), as a transient phase, would be formed instantaneously at low temperatures in the presence of DMF within the medium (Figure 4.25). However, at anhydrous conditions (DMF only), the NH_2-MOF-235(Al) intermediate transforms into NH_2-MIL-101(Al) at higher temperatures.[161] Increasing the temperature would force the dissociation and further transformation into the MIL-53 structure.[159]

In this account, Carson *et al.* studied similar issues on vanadium.[170] Experimental investigations suggested that such transformations are imputed to the reaction time, temperature, solvent, and pH, as the thermodynamic state directed by these conditions affects the growing structure. The thermodynamic studies revealed that MIL-101(V) is the kinetically favored product obtained by the reaction of VCl_3 with the BDC linker in ethanol at 120 °C for 48 h (Table 4.5, Figure 4.26). MIL-88(V), as the thermodynamic isomer, was produced under the same reaction procedures and conditions but in the presence of HCl. At higher temperatures, the MOFs may be dissociated into their building blocks regardless of the presence of HCl. Furthermore, the vanadium sites may be oxidized, and finally, re-assemble into the thermodynamic phase of MIL-47. Moreover, changing the solvent to water may not influence the MOF structure except for the MIL-47 framework.
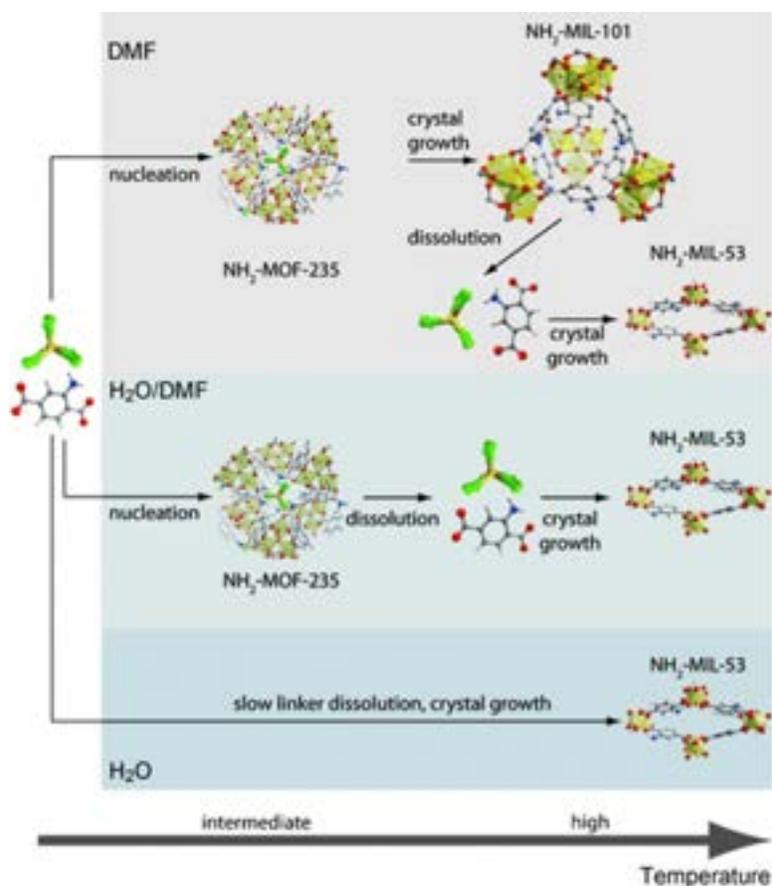
Figure 4.25 Crystallization of different Al-terephthalate MOFs depending on the precursors' concentration, temperature, and the reaction medium. *Reprinted with permission from Ref.[159]*
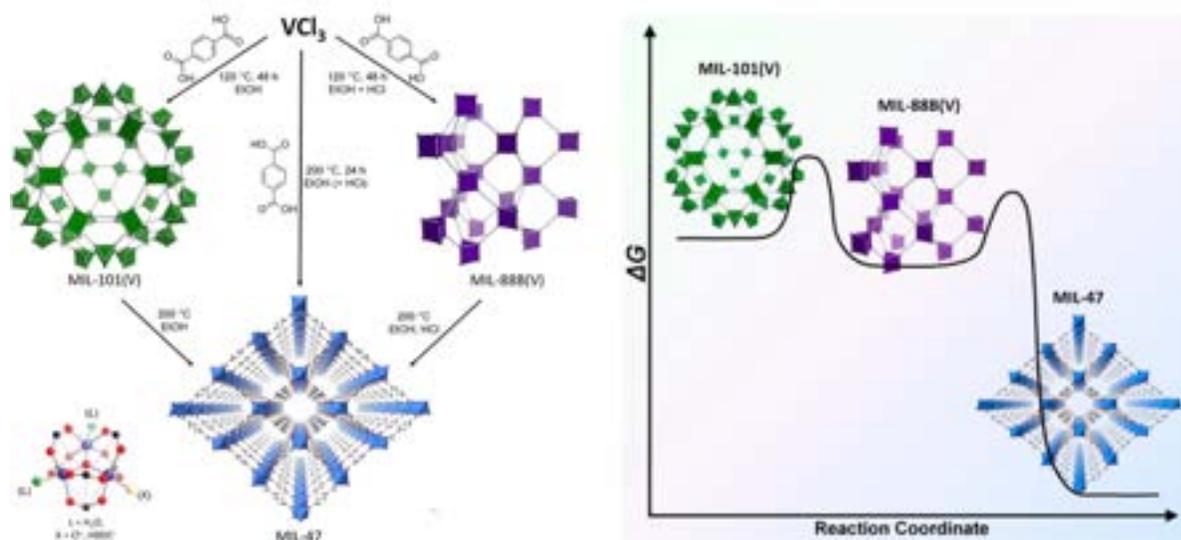
Figure 4.26 The influence of the reaction conditions on the polymorphism of the vanadium isomorph. *Reprinted with permission from Ref.[170]. Copyright © 2013, American Chemical Society.*

Bauer *et al.* came out with comparable results in their study concerning the NH_2-MIL-101(Fe) analogue, whereby the initial precursors' molar ratio and scaling up were found to have a great impact on the product.[128] Besides, reactions underwent solvothermally in different solvents and several pHs, which led to remarkable results. Using acetonitrile as the main solvent, NH_2-MIL-88(Fe) was the only obtainable MOF at a high pH or elevated temperature. Otherwise, a totally amorphous product was produced. Methanol would also direct the reaction into the MIL-88 phase at lower temperatures regardless of the pH. However, at a higher temperature, either an amorphous or unidentified phase of Fe-BDC was detected. Synthesis in DMF enables the growth of the MIL-101 as the favorable major phase, especially at a low temperature of 110 °C and a precursors' molar ratio of 2:1 metal ion to linker. However, raising the pH may promote the growth of the MIL-88 phase. Finally, water shifts the reaction to the thermodynamically favored MIL-53 phase, and at some points, the three phases co-existed.

In a similar study, Horcajada *et al.* investigated the phase-selectivity of the amino-functionalized derivative of the iron isomorph but in a microwave-assisted synthesis.[133] In agreement with Bauer's findings, synthesis in water promoted the growth of thermodynamic MIL-53 phase, whereas synthesis in alcohol (ethanol) fostered the MIL-88 phase. However, NH_2-MIL-101(Fe) could be obtained in both solvents with a very limited adjustment. Furthermore, the syntheses using DMF as the main solvent were the prevalent ones, which were more likely to produce the MIL-101 phase. The experiments involved HCl as a mineralizer failed to result in this kinetic phase, except with water, but in those cases, it was always a mixture of MIL-101 and MIL-53 phases.[128, 133]

4.7 Heterogeneity and multivariate (MTV) MIL-101

Based on the different building units of the MOFs, the attempts of involving more than one linker or SBU in the same structure have gain concern in a quest for complexity and heterogeneity. Complexity refers to the formation of new complex structures due to the implication of more than one network topology in one formulation, producing a totally distinct network. In contrast, heterogeneity implies the growth of the same structural type of the parent MOF (i.e., topology) but with comparable building units, preserving identical backbone.[3] Heterogeneous MOFs, also called multivariate (MTV) MOFs, are obtained by either the multi-metal or the multi-linker approach. In the multi-metal approach, various metal ions that form the same SBU are employed with the same linker. On the contrary, the multi-linker approach involves the introduction of a single-metal-type SBU to linkers of the same structure but with different functional groups. Hence, MTV-MOFs are isostruc-

tural and metrically identical MOFs of distinct chemical compositions. Herein, likewise the previous context, we will review the mixed-metal MTV-MIL-101, the mixed-linker, and the interfering with Bhattacharjee's functionalization.[68, 88, 129]

Mixed-metal MIL-101 can be obtained either through direct synthesis or post-synthetic modifications (PSM). PSM is the most widely used method for functionalization of a pre-synthesized MOF, as it provides a facile route and powerful tool for MOF manipulation without risking any interference with the formulation of the targeted MOF. Moreover, it allows direct access to structures that are not achievable by the direct route. The PSM, which permits the addition and exchange of one of the main framework constituents, is classified as PSM of strong interactions. Therefore, it is considered as the second-chance or the back-door of modifying the inherent structural properties. Furthermore, it was proven to be an efficient alternative for introducing heterogeneity into MOFs and the achievement of MTVs that are elusive to obtain by one-pot synthesis. Therefore, it is considered an economically and ecologically recommended procedure for large-scale synthesis with minimum waste.

4.7.1 MTV-MIL-101s through PSM

As a proof of concept, Szilágyi *et al.* obtained MIL-101(Cr/Fe), (Cr/Al), and (Cr/Fe/Al) via post-synthetic solvent-assisted cation substitution (SACS) method.[226] First, MIL-101(Cr) was synthesized according to Férey's original recipe. Then 100 mg of MIL-101(Cr) was cation-exchanged through refluxing with 5 mg of $AlCl_3$ or 10 mg of $FeCl_3$ solution in 100 mL of deionized water at 100 °C for 72 h. Metal-ion substitution was confirmed through Mössbauer spectroscopy and UV-Vis spectroscopy utilizing the Kubelka-Munk function for all Fe-containing samples (Figure 4.27). Besides, the amount of the metal replaced was observed by ICP-OES, whereby it was almost around 5% or less in MIL-101(Cr/Fe) and MIL-101(Cr/Fe/Al) for iron and reached 10% or more in MIL-101(Cr/Al) and MIL-101(Cr/Fe/Al) for aluminum.
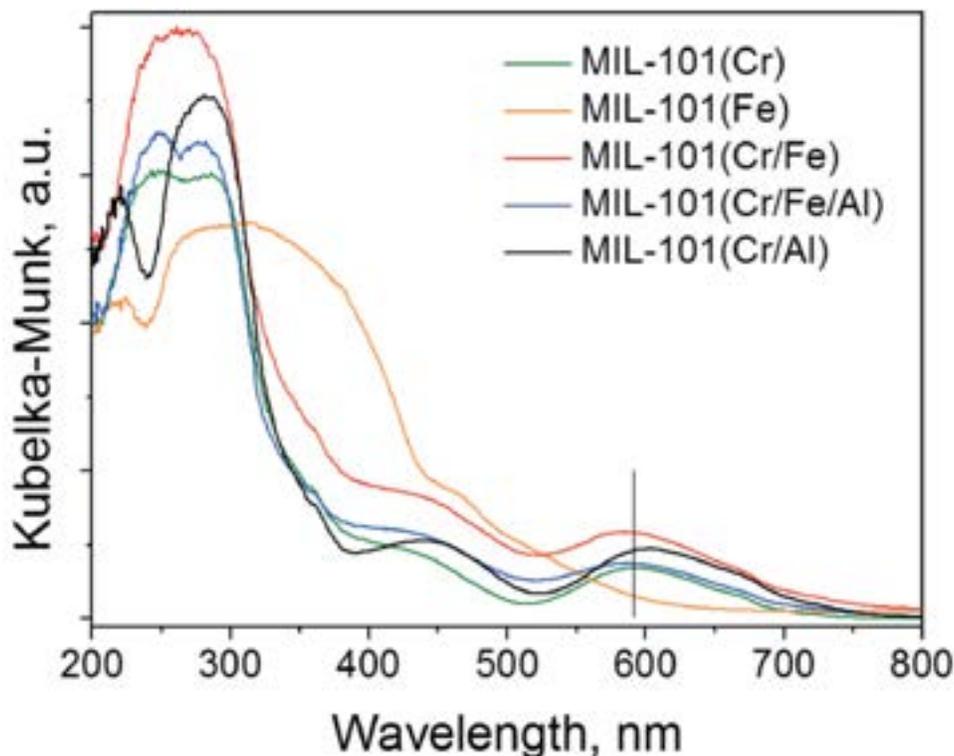
Figure 4.27 UV-Vis spectra of mixed-metal MIL-101s achieved via PSM. *Reproduced from Ref.[226] with permission from The Royal Society of Chemistry.*

XRD was employed to study the structural integrity. All samples showed the same pattern of pristine MIL-101(Cr). Furthermore, BET surface area measurements revealed a drop in the surface area from 2230 m^2 g^{-1} of MIL-101(Cr) to 1830 m^2 g^{-1} and 1838 m^2 g^{-1} for (Cr/Fe) and (Cr/Fe/Al), respectively. However, MIL-101(Cr/Al) showed a slight increase in SSA to 2644 m^2 g^{-1}. Application of these different mixed-metal MIL-101 samples in the adsorption of H_2 was carried out at cryogenics and ambient temperature. Nevertheless, they all did not show a noticeable enhancement compared to the original MIL-101(Cr). However, due to the changes taking place in the electronic environment, such compounds are highly suggested for catalytic application as active Lewis acids.

4.7.2 MTV-MIL-101s by Direct synthesis

In addition to Szilágyi's study that validated the cation-exchange in MIL-101(Cr) via PSM, other reports followed their footprints to support the metal-sites substitution.[227] However, others believed that post-synthetic ligand and metal-ion exchange (PSE) processes in MIL-101(Cr) are not achievable due to the kinetic inertness of the Cr(III) ion, and it can be only prepared through direct synthesis techniques.[228, 229]

MIL-101(Cr/Fe)

Vu *et al.* synthesized MIL-101(Cr) via the conventional hydrothermal method, with 25% of the Cr atoms superseded by Fe.[229] MIL-101(Cr/Fe) was prepared by the addition of 16 g of chromium and iron salts (3:1 wt%) and 6.56 g (3.95 mmol) H_2BDC to a 200-mL aqueous HF solution. The mixture was then stirred for 3 h and heated in a Teflon-lined autoclave at 220 °C for 9 h. The product was then collected, washed with hot ethanol, and finally dried. It is worth mentioning that using higher percentages of incorporating iron into the MIL-101(Cr) framework failed to obtain the targeted structure. The XRD pattern for MIL-101(Cr/Fe) was found to be identical to the simulated pattern of MIL-101(Cr) with no other peaks of the metal oxides, MIL-88, or MIL-53. In addition, the produced MIL-101(Cr/Fe) particles were uniform and of an average size of 1 μm. Besides, Fe was detected to be homogeneously distributed over the whole sample.

The measured BET surface area for MIL-101(Cr/Fe) was around 2997 m^2 g^{-1}, which was lower than that of MIL-101(Cr) prepared by the same procedures. Furthermore, the total pore volume and the pore size of the iron-substituted framework were 0.9958 cm^3 g^{-1} and 2.01 nm, while that for pristine Cr were 1.7526 cm^3 g^{-1} and 1.99 nm, respectively. Thus, by incorporating Fe into the structure, MIL-101(Cr/Fe) was clearly efficient as a heterogeneous photo-Fenton catalyst for the degradation of reactive organic dyes. A photo-induced reaction by the surface iron atoms in the presence of H_2O_2 was able to decompose the dye within 90 min with high reusability and limited iron leaching.

Later on, Bureekaew *et al.* studied the influence of Fe(III) ions as a metal-cationic competitor for MIL-101(Cr) formation in a hydrothermal synthesis.[230] However, in their study, synthesis was carried out in an HF-free environment, in which samples of MIL-101(Cr/Fe) with different iron to chromium percentages were formulated. Samples were prepared as follows: First, MIL-101(Cr) was synthesized using the typical preparation steps, whereby equal amounts (5 mmol) of H_2BDC and $Cr(NO_3)_3.9H_2O$ were mixed in 24 mL of deionized water and placed into a Teflon-lined autoclave. Thereafter, it was heated in an oven at 220 °C for 8 h. Finally, the products were washed with DMF, and activated by ethanol at 80 °C for 24 h. Seeking different percentages of MIL-101(Cr/Fe), a portion of the 5 mmol chromium salt was replaced by an equivalent amount of ferric nitrate nonahydrate. Five percentages (5%, 10%, 15%, 25%, and 33.3 mol% Fe) were assigned along with 100% Fe in a quest for comparison of the final products.

The XRD patterns of the samples with Fe $\leq$ 15% were comparable with that of MIL-101(Cr), while that of 25% exhibited a mixed pattern of MIL-101 and MIL-88. However, a higher percentage of Fe= 33.3% was totally corresponding to the MIL-88. Moreover, the pattern

of the 100% sample was not matching with any of these samples or other known phases. This finding may be attributed to the synthesis of most Fe-MOFs in DMF. Accordingly, the mixed-metal medium was the reason behind these formations and polymorphs. Nevertheless, SEM analyses revealed the presence of a small amount of the MIL-88 phase within the sample of Fe= 15%, which was not detected by the XRD. This phase is distinguished by its long hexagonal rods (red arrows in Figure 4.28-d) rather than the octahedral-shaped particles of MIL-101. Besides, in the three samples showing pure MIL-101 phase (0%,5%, and 10% Fe), relatively larger particles from 100 nm (0% Fe sample) to 600 nm (10% Fe sample) were observed.
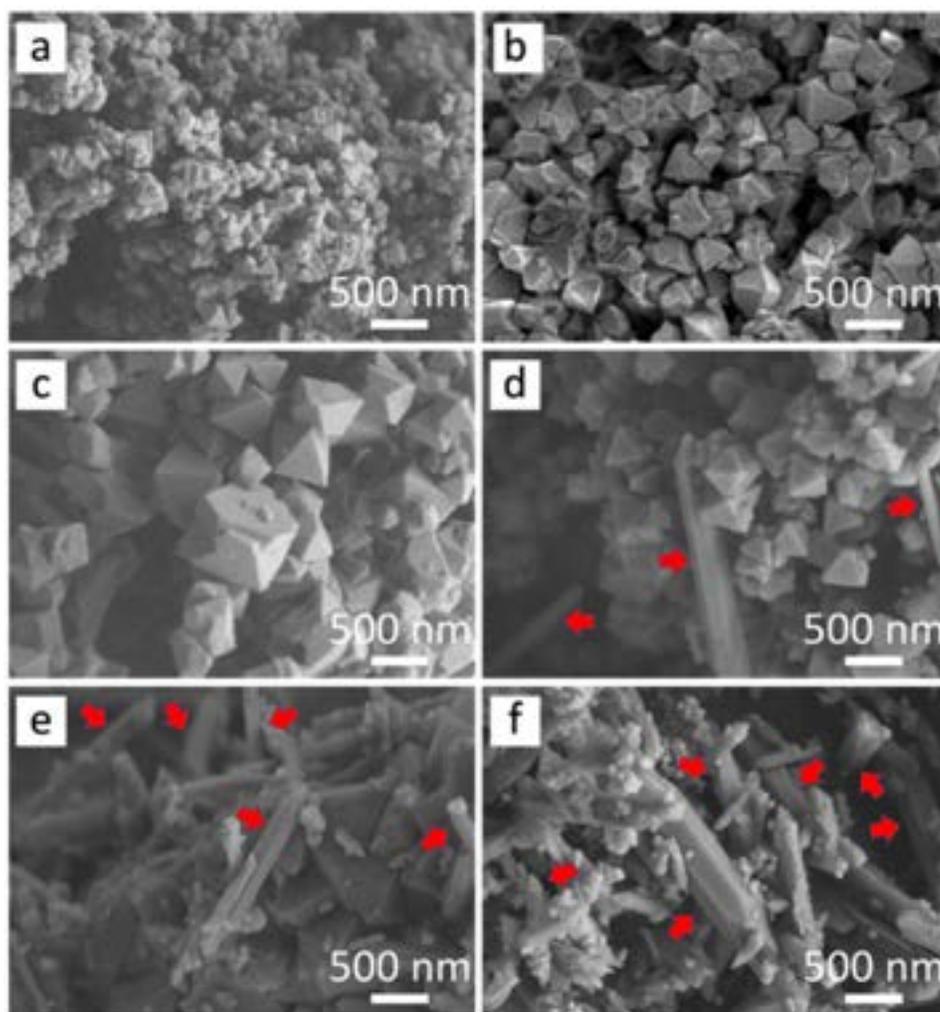
Figure 4.28 SEM images of MIL-101(Cr/Fe) at different molar percentages of Fe. a) 0%, b) 5%, c) 10%, d) 15%, e) 25%, and f) 33.3%. Red arrows point to the hexagonal crystals of the MIL-88 framework. *Adapted with permission from Ref.[230]. Copyright © 2018, American Chemical Society.*

Unexpectedly, this 15% Fe sample, with the small MIL-88 contamination, showed the highest BET surface area of 2864 m^2 g^{-1} compared to other samples and the pristine MIL-101(Cr). In contrast, a drastic reduction in the surface area in the range of hundreds was measured for other samples due to the domination of the MIL-88 phase. This reduction may also be imputed to the framework flexibility and the presence of small amounts of Fe_2O_3. Interestingly, elemental analysis for the samples with the identified MIL-101 phase (5%, 10%, and 15% Fe) showed higher actual percentages of iron incorporation within the structure than the initially targeted. The actual percentages were found to be around 17.5, 24.0, and 31.5, respectively. Obviously, the presence of ferric ions within the reaction medium induces not only the formation of different structural morphologies but also influences the formation of iron-MOFs. Surprisingly, under such conditions, the formation of the MIL-101 is more favored from the iron species rather than the chromium.

Digging deeper, Bureekaew's group continued their investigations on the mixed-metal synthesis of MIL-101 at higher percentages of incorporated Fe. However, they employed the microwave route instead of the conventional procedure.[202] Since MIL-101 was found to be the kinetically favored phase, microwave heating was chosen for its ability to heat the system rapidly and homogeneously at the molecular scale. By overcoming the heat transfer issue of the hydrothermal route, the phase transformation into the MIL-101 can be controlled. Therefore, MIL-101(Cr/Fe) of a constant Fe molar percentage (33.3% mol) was prepared at different reaction times of 5, 10, 30, 60, 120, and 240 min. In typical procedures, 1 mmol of H_2BDC was mixed with 1 mmol of the combined metal precursors $(Cr(NO_3)_3 \cdot 9H_2O$ "66.7% mol Cr" + $Fe(NO_3)_3 \cdot 9H_2O$ "33.3% mol Fe" and dissolved in deionized water into a microwave vial. The reaction mixture was then heated to 200 °C at a constant power of 300 W for the assigned time intervals. After the reaction, the products were centrifuged, washed with DMF and ethanol, and finally dried under vacuum at room temperature. The same procedures were applied to prepare the single metal-type MIL-101(Cr) at a similar timespan. At first glance, the XRD analysis showed that all samples of both single- and mixed-metal basis exhibited the pattern of the MIL-101 framework, emphasizing that fast heating via microwave radiation drives the reaction to that kinetic phase. However, at these reaction conditions, all samples of MIL-101(Cr) exhibited broader peaks corresponding to their smaller particles (~40 nm). On the other side, samples of MIL-101(Cr/Fe) were of larger particle sizes (~150-200 nm), and hence, their patterns were of sharper peaks. Closer looking into all these patterns showed no implications of any accompanied phases, except for the mixed-metal sample at a very long reaction time (240 min), which showed other peaks belonging to the MIL-53 "thermodynamic" phase. With its known structure flexibility, the presence of the MIL-53 particles within the 240-min MIL-101(Cr/Fe) sample has reduced

the measured specific surface area to S_{BET}= 1100 m^2 g^{-1} ($S_{Langmuir}$= 1477 m^2 g^{-1}) and the pore volume to 0.46 cm^3 g^{-1}. Unlike the hydrothermal synthesis, the initial assessment did not show any signs of the MIL-88 polymorph, but the more stable MIL-53 phase existed. Regardless, further investigations via SEM and TEM showed some traces of the hexagonal-shaped rods of MIL-88 resided in MIL-101(Cr) samples at 240 min. MIL-88 traces also appeared in most MIL-101(Cr/Fe) samples starting from 10 min and up to 240 min. Besides, the orthorhombic phase of MIL-53 did not only exist in the mixed-metal system at a longer duration of 240 min, but also traces were detected at 120 min. It is worth mentioning that pure phase MIL-88 or MIL-53 were not obtained in the single-and mixed-metal systems with increasing the reaction time to 360 min (for Cr) and 720 min (for Cr/Fe), and still mixtures of these polymorphs are collected.[202]

In the mixed-metal system, the amount of iron influences the formation of different building blocks. Besides, the iron content in the final products is dependant on the reaction time (Figure 4.29). At shorter reaction times, Fe ions are consumed in the formation of the MIL-101 framework, and it keeps decreasing steadily up to 60 min, whereby Cr ions get more involved in the structure formation, and the MIL-88 starts to grow. At 120 min, the concentration of Fe with respect to Cr increases again, which seems to be the point when the MIL-101 particles dissociate, and the MIL-53 structure manifests. In addition, at shorter time ranges, the presence of Fe as an efficient cationic competitor was believed to urge the formation of the trinuclear oxo-centered metal cluster in a faster manner than Cr, leading to the formation of a cluster with two parts Fe and one part Cr. In this sense, and despite having an apparent well-defined shape, particles of the short-time-heated MIL-101(Cr/Fe) samples were found to comprise an interiorly distorted structure, in which the Fe-O bonds in the M$_3$O cluster were shorter in length than that of Cr-O, causing this deformity (Figure 4.30).
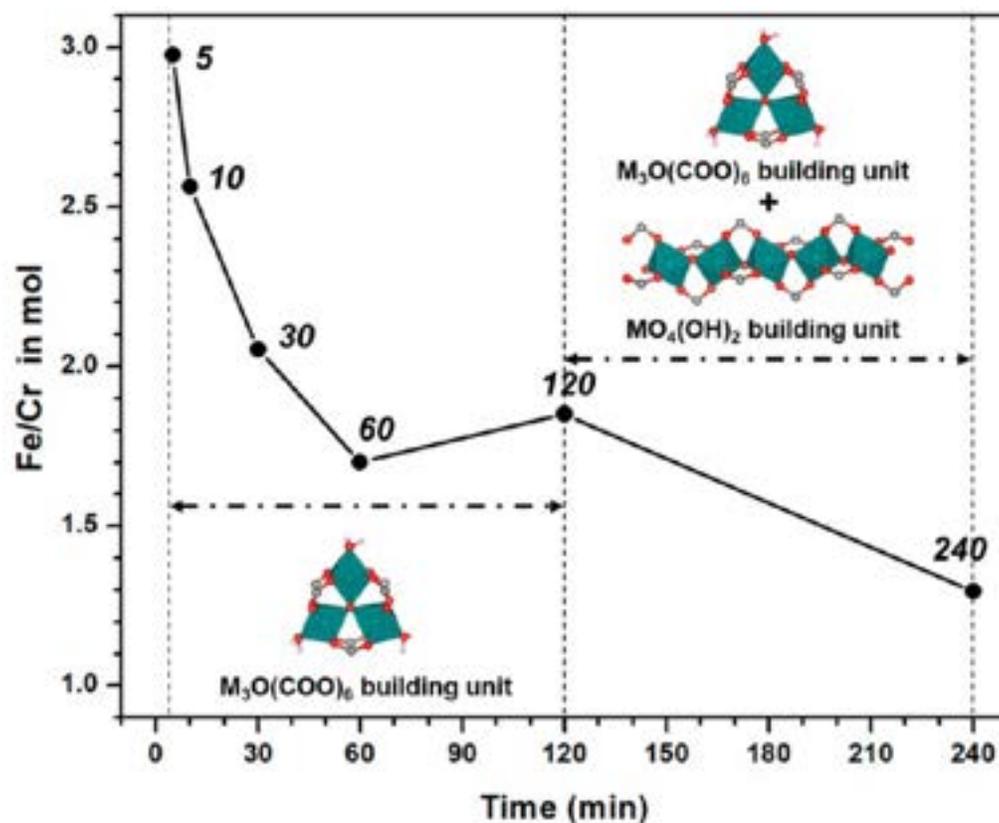
Figure 4.29 The formation of different SBUs based on the metal ratios and the reaction time. *Reprinted with permission from Ref.[202]. Copyright © 2019, American Chemical Society.*
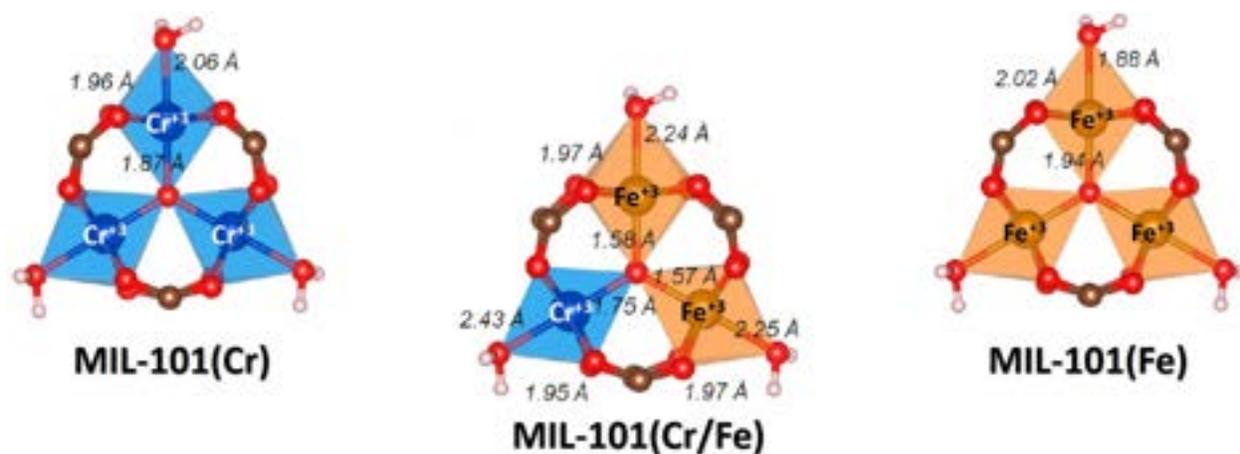
Figure 4.30 Change in the bond lengths of the trinuclear oxo-clusters depending on the trivalent metal type involved. *Reprinted with permission from Ref.[202]. Copyright © 2019, American Chemical Society.*

In a recent study to obtain a mixed-metal structure by a hydrothermal procedure, Fe was incorporated with Cr to prepare a MIL-101 framework for some catalytic applications.[231] Unlike Vu's,[229] different iron sources were adopted along with chromium nitrate as the metal precursors in an HF-free synthesis. Furthermore, higher percentages of Fe were targeted compared to those obtained elsewhere.[230] First, iron nitrate was tried, but at a high temperature of 220 °C for 8 h, it ended up with a mixture of MIL-101 and MIL-88 polymorphs, even in the presence of an organic mineralizing agent like acetic acid (AcOH) at low concentrations. Replacing the iron nitrate by Fe^0 has significantly reduced but did not completely prevent the formation of the MIL-88 phase regardless of introducing AcOH. On the other hand, synthesis in a basic medium of TMAOH was also investigated to enhance the solubility of the H_2BDC linker, which may promote the growth of the MIL-101 structure. Therefore, the synthesis in a lower temperature medium of TMAOH may obtain a pure-phase of MIL-101(Cr/Fe). However, the purity of the product was dependant on the concentration of TMAOH, whereby lower concentrations than 0.06 M led to traces of MIL-53, while higher concentrations may form an amorphous structure.

In their study, MIL-101(Cr/Fe), with two different percentages, was prepared ($\sim$15% mol Fe & 20% mol Fe) in TMAOH solution. The synthesis took place in an autoclave at a reaction temperature of 150 °C for 48 h. Then, the products were activated by a KF (0.1 M) solution for 1 h. The XRD analyses were in line with the simulated pattern of MIL-101(Cr), revealing a pure MIL-101 phase. Furthermore, EDS and ICP-OES analyses confirmed equivalent amounts of Fe to that initially added to reaction medium (MIL-101(Cr/Fe) of 15% mol Fe & 20% mol Fe). Moreover, the comparable particle size of both samples was observed (around 100 nm). The surface areas for the samples were S_{BET}= 2700 m^2 g^{-1} and 3040 m^2 g^{-1} for the (20% mol Fe) and (15% mol Fe), respectively. However, similar pore sizes were observed, including the two types of pore sizes equal to 19 nm and 25 nm. It is worth mentioning that the thermal stability for both samples remained unchanged, regardless of the Fe content, whereby a structural degradation was detected around 300 °C in an oxygen atmosphere. Furthermore, ^{57}Fe Mössbauer spectroscopy confirmed the incorporation of the iron atoms in the lattice structure of the MIL-101 framework. Application of the mixed-metal MIL-101 MOF as a Lewis acid catalyst was evaluated in the Prins addition reaction of β-pinene and formaldehyde to produce Nopol [2-(7,7-dimethyl-4-bicyclo[3.1.1]hept-3-enyl)-ethanol]. The reaction at 80 °C in the presence of acetonitrile and MIL-101(Cr/Fe) exhibited an improved catalytic activity than MIL-101(Cr) and enhanced the chemical stability compared to MIL-101(Fe).

MIL-101(Fe/Al)

Finally, aside from all the attempts to synthesize the mixed-metal MIL-101 structure of chromium and iron basis, other attempts to achieve MIL-101(Fe/Al) were also reported.[232, 233] In one attempt, pristine MIL-101(Fe/Al) was prepared solvothermally, whereby three molar ratios (1:1, 2:1, and 4:1) were explored.[232] The reaction took place at 110 °C for 20 h in DMF as the main reaction solvent. The nitrogen sorption measurements showed a high BET surface area of all MTV samples in the range of $\sim$1300 m^2 g^{-1} except for MIL-101(Fe) (S_{BET}= 374 m^2 g^{-1}), which is too low compared to that usually obtained. The thermal stability studies displayed a higher decomposition temperature with increasing the Al content in the structure. On the other hand, the SEM images showed octahedral-shaped particles for pristine MIL-101(Fe) but totally different morphologies for all MIL-101(Fe/Al) samples. Furthermore, in some of these images, the long hexagonal-shaped particle of MIL-88 can be witnessed. Furthermore, the authors claimed the achievement of the pristine MIL-101(Al) framework along with the MIL-101(Fe/Al) samples. However, the intense peaks presented in the XRD patterns around 5°, 8.5°, 10°, 15°, 18°, and 21° for the MIL-101(Al) sample and all other MIL-101(Fe/Al) suggest the formation of the MIL-53 structure instead of the MIL-101 topology.

In another attempt to achieve the MIL-101 structure from Fe and Al, amino-functionalized MIL-101(Al/Fe) was synthesized via a rapid-reflux method.[233] First, NH$_2$-MIL-101(Al) and NH$_2$-MIL-101(Fe) were prepared following the previously reported methods [234], then small amounts of Fe were to replace Al in the same procedures. The added amounts of Fe were around (5%, 6.67%, 10%, and 20%). The authors reported that the obtained crystals were of a size range around 30 nm, and the XRD patterns measured for all samples showed a great agreement with the simulated one. Besides, the TGA curves revealed an equivalent dissociation behavior for all samples before 300 °C, similar to that usually reported for MIL-101(Cr) and its analogues. In addition, ATR-FTIR, EPR, and elemental mapping via EDX confirmed the incorporation of both Al and Fe into the lattice structure. However, the authors mentioned that the produced crystals were not of the same octahedral shape as that of the monometallic basis. Moreover, the N$_2$ sorption measurements exhibited a type-IV isotherm for all bimetallic samples, which is different from the type-I isotherm measured for the monometallic ones.

Hence, with all these investigations in the achievement of the mixed-metal type MIL-101 framework, it seems that the Cr/Fe studies are of higher progress than that of Fe/Al. However, such investigations on the Fe/Al-type MOF, despite being out of accuracy, seem to be inspiring and encouraging for more profound studies on this type.

4.8 Recent applications

The remarkable advances in tuning the characteristics of MIL-101 MOFs by grafting different functional groups and/or incorporation with co-materials in composites have widened the applications of MIL-101 in different disciplines. The improved characteristics reported in the recent literature include porous architecture, surface area, absorption spectra, adsorption selectivity, and thermal stability.[13,68] In the present work, repetition and overlapping with the previous studies were avoided by limiting this review to recent MIL-101 applications. To this end, we performed a network analysis for the MIL-101 reports published in 2019 or later by VOS viewer© (Figure 4.31) to sort out the most prevalent applications issued over this period (Only recognized by Web of Science©). Modified surface area, porous structure, and light absorption range attracted interest towards environmental applications of MIL-101 MOFs in water and air pollution control, including but not limited to adsorption in gas and liquid environments [235], photocatalysis [236], and membrane separations [237]. MIL-101 MOFs were moreover found to effectively affect the characteristics of several materials, which encouraged their utilization in other sectors such as pharmaceutical industry, analytical and sensing materials. For the sake of brevity, this review was focused on the five applications shown in Figure 4.32.
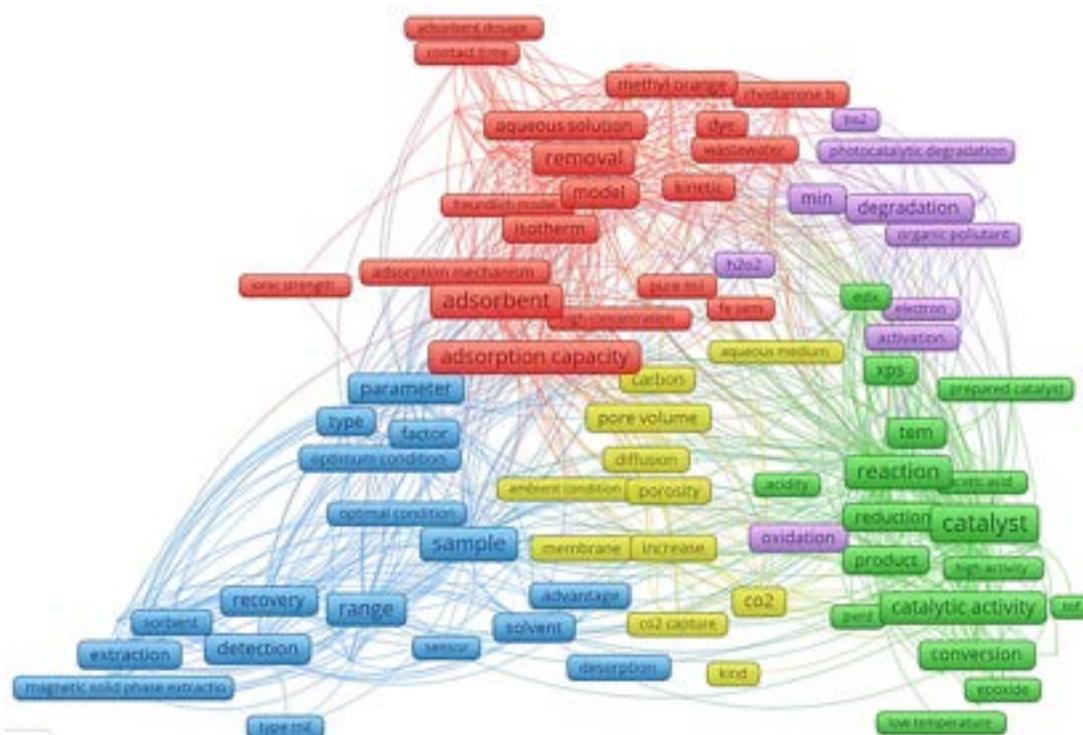
Figure 4.31 The network analysis of the recent MIL-101 applications in the latest literature (2019-2021).

Figure 4.32 The most prevalent applications of MIL-101 MOFs in the recent literature.

4.8.1 Pollutant adsorption

In general, the high surface area and special pore structure of MOFs incite to explore their adsorbability for different pollutants in water. Recently, MIL-101 MOFs with different metal analogues were frequently employed either in composites or as pristine materials for the removal of toxic metals or organic pollutants. Despite the toxicity of chromium, MIL-101(Cr) based MOFs were the most ubiquitous in recent literature. None of the reviewed studies, however, investigated the possible leaching of chromium in water or other solvents. Several studies claimed the stability of MIL-101(Cr) in water, but this claimed stability was only supported by the TGA analysis without monitoring the chromium content in the reactors.[238, 239] Pristine MIL-101 analogues were frequently used in earlier studies revealing promising results.[68, 240] In more recent studies, novel composites and/or functionalized MIL-101 MOFs were employed to enhance the adsorption capacity through different mechanisms, as illustrated in Table 4.8. Zuo et $al.$ used functionalized MIL-101(Cr)–SO$_3$H for removal of three fluoroquinolone antibiotics and compared its performance to the MIL-101(Cr)-NH$_2$ and pristine MIL-101(Cr).[241] For instance, the adsorption capacity was improved from 274 mg g^{-1} to 434 mg g^{-1} for the removal of ofloxacin, whereas it was reduced to 28 mg g^{-1} by using MIL-101(Cr)–NH$_2$. The improved adsorption by MIL-101(Cr)–SO$_3$H was attributed to the electrostatic attraction between the negatively charged ionized sulfonate group and the protonated piperazinyl group in the ofloxacin molecule. On the contrary, the aminated

MIL-101(Cr) acquired positive charges from the protonation of nitrogen atoms in the NH_2 group, which induced repulsive forces with the ofloxacin resulting in a reduced adsorption capacity. Nevertheless, MIL-101(Cr)–NH_2 showed high adsorption capacity for other pollutants such as bisphenol, whereby the adsorption capacity reached 400 mg g^{-1} for several cycles of reuse. This high capacity was due to the π-π interaction with MIL-101 and the H-bonding with NH_2.[242] In another study, three anionic dyes were adsorbed with high capacity to MIL-101(Cr)–NH_2 and compared to pristine MIL-101.[243] A remarkable improvement in the adsorption capacity (about 117%) was obtained upon amination of MIL-101, which was imputed to the H-bonding between the anionic molecules and NH_2. Furthermore, MIL-101(Cr)–NH_2 was used for the removal of hexavalent chromium of a concentration of 140 mg L^{-1} with an adsorption capacity of 44 mg g^{-1}.[244] Aminated MIL-101(Al) has also shown a higher adsorption capacity than aminated MIL-53 for removal of methotrexate, which has been imputed not only to the surface area but the higher positive zeta potential with the appropriate polar amino functional groups.[245] MIL-101(Cr) was also functionalized by the amidoxime group to improve the selective adsorption of hexavalent uranium.[246] Doping with metal ions the lattice structure of MIL-101 is another strategy to enhance the adsorbability of MIL-101 through the electrostatic interactions between the adsorbent and adsorbate. For instance, copper and cobalt were doped in MIL-101(Cr) for enhanced adsorption of tetracycline to the bimetallic MOF.[247] It is worth noting that in most cases of functionalization or metal doping in MIL-101 structure, the surface area was reduced. However, the adsorption capacity was improved due to electrostatic interactions which facilitate the diffusion of the targeted molecules on the surface of MOF and into the pores.[240]

The adsorption capacity of MIL-101 was also improved by incorporating other materials in composites. Adding different porous materials may provide additional functional groups that contribute to the adsorption of complicated molecules and/or increase the surface area. For instance, the surface area of MIL-101(Cr) increased from 2980 m^2 g^{-1} to 3450 m^2 g^{-1} by introducing graphite oxide with 6.0% wt.[239] Furthermore, the addition of graphite oxide improved the stability and reusability as it kept 89% and 86% of its efficiency for adsorption of methyl orange and reactive blue 198 in five consecutive adsorption-desorption cycles, respectively. In another study, Fe_3O_4 was loaded on MIL-101(Fe) using 3,4-dihydroxy-L-phenylalanine (L-Dopa) as an environmentally friendly binder.[248] The composite showed a very high adsorption capacity for removal of methyl red and malachite green (1250 mg g^{-1} and 853 mg g^{-1} respectively), besides it could be easily collected for reuse due to its magnetic properties and remarkable stability by keeping more than 95% of its efficiency in five consecutive cycles. Nano zero-valent iron (nZVI) was also merged with MIL-101(Cr) for the removal of tetracycline but with no comparison with pristine MIL-101.[249] The composite was further

used for Fenton-like oxidation of tetracycline to reduce the required dose of the adsorbent. In a different approach, Wang *et al.* reported the incorporation of 3,5-Bis(trifluoromethyl)phenyl isocyanate (BTP) with MIL-101(Cr) for removal of acetochlor from water.[250] The composite showed a high adsorption capacity due to the H bonding and π-π interaction. A toxicity assessment study showed no acute toxicity of the composite towards two species of microorganisms. In another interesting study, polyethylene glycol was incorporated with MIL-101(Cr) to act as a hydrophobic barrier that hinders the water molecules from diffusion into the MIL-101 pores while allowing the toluene molecules to diffuse into the pores with less competition.[250] The adsorption capacity of toluene of the composite was improved by about 31% compared to pristine MIL-101(Cr).

It can be noticed from Table 4.8 that the thermodynamic equilibria of adsorption of MIL-101 followed the Langmuir isotherm in most cases. This finding indicates that most MIL-101 based MOFs and their composites and derivatives possess homogeneous monolayer of active sites, and the adsorption occurs as a monolayer on the surface.[240, 246]

Table 4.8 Different MIL-101-based materials applied in the adsorption studies

MOF	Surface area ($m^2\ g^{-1}$)	Pollutant	Equilibrium time (min)	Adsorption capacity ($mg\ g^{-1}$)	Followed isotherm	Ref.
MIL-101(Cr)–SO$_3$H	1760	norfloxacin ofloxacin enoxacin	65 55 55	49.4 49.6 49.2	Langmuir Langmuir Langmuir	[241]
MIL-101(Fe)/Fe$_3$O$_4$	N/A	methyl red malachite green	30 60	1250 833	Langmuir Langmuir	[248]
MIL-101(Cr)/NH$_2$	2000	Cr(VI)	10	45	Dubinin–Radushkevich	[244]
CuCO/MIL-101(Cr)	2423	tetracycline	180	80	Freundlich	[247]
3,5-Bis(trifluoromethyl) phenyl isocyanate/MIL-101(Cr)	1113	acetochlor	120	313	Langmuir	[250]
MIL-101(Cr)/NH$_2$	2304	bisphenol	60	400	Langmuir	[242]
MIL-101(Cr)–NH$_2$	2865-3113	Congo red methyl orange chrome blue	N/A	2967 462 260	Langmuir	[243]
ZVI/MIL-101(Cr)	786	tetracycline	180	625	Langmuir	[249]
MIL-101(Al-NH$_2$)	1936	methotrexate	40	458	Langmuir	[245]
polyethylene glycol/ MIL-101(Cr)	2939	toluene	N/A	387	N/A	[238]
graphite oxide/ MIL-101(Cr) hybrid	3540	methyl orange reactive blue 198	30 60	235 175	Langmuir	[239]
Amidoxime MIL-101(Cr)	913	U (VI)	N/A	586	Langmuir	[246]

Table 4.8 Different MIL–101-based materials applied in the adsorption studies (Cont.)

MOF	Surface area ($m^2 g^{-1}$)	Pollutant	Equilibrium time (min)	Adsorption capacity ($mg g^{-1}$)	Followed isotherm	Ref.
Phytic acid- MIL–101(Cr)	2213	Indole quinoline	N/A	543 549	Langmuir	[251]
Polyethyleneimine-MIL–101(Al)–NH$_2$	N/A	methyl orange direct red	N/A	894 998	N/A	[252]
MIL–101(Fe)–NH$_2$	1652	triphenyl phosphate	2880	24.8	Freundlich	[253]
MIL–101(Cr)	3560	triphenyl phosphate	720	101.7	Freundlich	[253]
TiO$_2$/MIL–101(Cr)	2223	methyl orange	80	242	N/A	[254]

4.8.2 Catalysis

Oxygen Reduction Reaction (ORR) is the electrocatalytic reaction occurring at the cathode of a PEM fuel cell. Replacing the Pt by a non-precious metal would significantly diminish the cost of this technology. One possible strategy in doing so, is to pyrolyze a MOF material in order to generate a graphitic carbon mass loaded with a finely dispersed transition metal (usually Fe) located in a C/N environment.[255, 256] Recently, MIL-101 was proposed as the MOF precursor in this catalyst preparation. In [257], a composite of MIL-101(Fe) and polypyrrole was carbonized yielding an active ORR catalyst (see Table 9). Some good ORR performances were also obtained in [258], in which a carbon black loaded with MIL-101(Fe) was pyrolyzed in the presence of melamine. A similar concept was applied in [259, 260], where a MIL-101(Fe) was blended with polyaniline (PAni) and pyrolyzed at 800 °C - 1000 °C.

The same idea of pyrolyzing a MOF precursor was implemented in [261] to generate a highly dispersed Fe phosphide on a N-grafted carbonaceous support. The precursor was a P-loaded NH_2-MIL-101(Fe) and the resulting material was shown to be a good hydrogen evolution reaction (HER) electrocatalyst for water splitting. Also related to water splitting, a photo-catalyst active in both water oxidation and water reduction was proposed in [262]. However, in the latter work, the semiconducting properties and porous structure of MIL-101(Fe) were modified at synthesis by partially substituting the H_2BDC ligand with vanillin. The effect was to introduce some mesoporosity and some partial mixed valence Fe^{3+}/Fe^{2+}. The latter effect was enhanced by the presence of some Fe_3O_4 added to this catalyst.

A different problem was tackled using MIL-101(Cr) in [263]. Replacing noble metals in ORR and OER electrocatalysts (oxygen evolution reaction) by cheaper materials like α-MnO_2 in rechargeable aqueous lithium-air batteries, would also be commercially significant. In this work, it was shown that embedding α-MnO_2 in MIL-101(Cr) enhanced the activity and stability of this material as an ORR and OER electrocatalyst in basic media. Also, taking advantage of the semiconducting properties of MIL-101, a photo-electrocatalyst of water oxidation was designed in [264] whereby a cobalt phosphotungstate (CoPOM) was immobilized in finely dispersed form in the pore structure of MIL-101(Cr). Similarly, in [265], vanadium phosphomolybdate inserted in MIL-101(Cr) yielded an efficient electrocatalyst for the oxidation of ascorbic acid. Besides its use as a precursor for an electrocatalyst, MIL-101 was also used as a catalyst or catalyst support. In [231], for example, a 21% substitution of Fe^{3+} in MIL-101(Cr) was shown to enhance the inherent Lewis acidity of MIL-101(Cr), which resulted in an increase of reaction rate in the Prins condensation of β-pinene with benzaldehyde. Similar substitution of 25% Fe into a MIL-101(Cr/Fe) MTV yielded an active and reusable photo-Fenton oxidation catalyst.[229]

Catalytic activity may also be generated by functionalizing a MOF linker. In [266], a grafted ferrocene group was generated by the reaction of ferrocene carboxaldehyde with NH_2-MIL-101(Fe). The resulting material was shown active in oxidation by potassium persulfate of bisphenol-A in aqueous solution. Similarly, strong sulfonic acid centers were generated by reacting NH_2-MIL-101(Cr) with propane sultone.[267] The product, a RSO_3-NH-MIL-101 (Cr), was found very active in the synthesis of a variety of quinoxalines by condensation of a 1,2-diamine with 1,2-dicarbonyl compounds. In [268], three catalysts were generated by first anchoring $RuCl_3$ in NH_2-MIL-101(Cr) through coordination to the nitrogen atom. Two of them were obtained by further reacting the amine group of $RuCl_3$@NH_2-MIL-101(Cr) with salicylaldehyde ($RuCl_3$@MIL-101(Cr)sal.) or with diphenyl phosphine benzaldehyde ($RuCl_3$@MIL-101(Cr)DPPB). All three catalysts were found active in the hydrogenation of CO_2 to formic acid. The mere encapsulation of phosphotungstic acid in MIL-101(Cr) was shown possible in [269]. The resulting PTA@MIL-101(Cr) was an active and reusable catalyst in a whole series of Biginelli condensation reactions.

The concept of generating a composite material by simultaneous synthesis of MIL-101 with some iron oxidic compound was implemented in [239] [270] and [271]. In [271], a Fe_3O_4-MIL-101(Fe) was used as a catalyst for Fenton-type oxidation of rhodamine B by H_2O_2. The effect of MIL-101 was through its Lewis acid properties, keeping the reaction medium neutral. In [270], a $CoFe_2O_4$ mixed oxide was compounded with MIL-101(Cr) and used as a catalyst for sonocatalytic oxidation of rhodamine B by H_2O_2. The most frequently reported use of MIL-101 in catalysis seems however to be as a support for finely dispersed metal particles. This is not only related to the MOF textural properties and stability of the MIL-101 crystal structure. All these would make it comparable to zeolites in terms of stabilization of highly dispersed nanoparticles. In addition, MOFs allow controlling the chemical environment of the dispersed metal. For example, in [272], Pd particles were created in a sulfonic acid functionalized MIL-101(Cr). The material was intended as a catalyst for the hydroxygenation of vanillin in aqueous solution. The sulfonic acid groups made the solid hydrophilic, which significantly enhanced the reaction rate and selectivity to the secondary product 2-methoxy-4-methyl phenol. The reaction of CO_2 hydrogenation to formic acid is of current interest as providing a way for the chemical storage of hydrogen in the liquid phase [273]. In [274], a good catalyst for this reaction was obtained by grafting triethylene diamine (TEDA) in NH_2-MIL-101(Cr) and dispersing PdAg alloy nanoparticles in the resulting solid. A similar concept was applied in [275] to develop a catalyst for the reverse reaction producing hydrogen from formic acid. In that work, a diamine such as ethylene diamine was also coordinated to the Cr ions of MIL-101(Cr) and Pd nanoparticles were then inserted in the ED@MIL-101(Cr). For this same reverse reaction, the work in [276] demonstrated that a

high TOF (848 h^{-1}) can also be reached using an optimized alloy composition Ag$_{20}$Pd$_{80}$ in a simple AgPd@MIL-101(Cr).

Other hydrogen-generating reactions were dealt with in [277] (aqueous hydrazine, RhNi@ MIL-100(Cr), and [278] (methylamine borane, Cu@MIL-100(Cr)). A technique of in situ reduction of a silver salt by sodium borohydride in MIL-101(Fe) was proposed in [279] to generate silver nanoclusters in MIL-101(Fe). The produced AgNC@MIL-101(Fe) was shown to be active in 4-nitroaniline hydrogenation. It was also said to be fluorescent and magnetically separable.

Selective hydrogenation reactions of α,β unsaturated aldehydes such as cinnamaldehyde or furfural require heterogeneous catalysts bearing Lewis acid sites such as the Cr(III) of MIL-101(Cr) for adsorption of these aldehydes. In [280], a remarkably selective catalyst was obtained by adjusting the composition of Pt-Co nanoparticles dispersed in a MIL-101(Cr). Additional Lewis acid sites were shown to be formed at the interface between the MOF and the metal particle leading to high TOF in addition to unsaturated alcohol selectivity.

In [281], an epoxidation catalyst was designed by dispersion Au nanoparticles in a NH$_2$-MIL-101(Cr) support. This solid was found active, selective, and reusable (four times) in the epoxidation of styrene by using tert-butylhydroperoxide (TBHP) as the oxidizing agent.

The carboxylation of terminal alkynes, such as phenyl acetylene by CO$_2$ forming propiolic acids, would be a fine addition to the various methods of CO$_2$ valorization in Carbon Capture and Utilization (CCU) strategies. In [282], Pd-Cu nanoalloys were dispersed in the framework of MIL-101(Cr). The optimum alloy composition was established to be Pd$_{0.62}$Cu$_{0.8}$. The catalyst was found to be active, selective, and reusable in the carboxylation of a variety of terminal alkyne compounds.

The problem of converting a powdered MOF into a form of catalyst usable in a large-scale reactor, is very seldom dealt with in literature. The authors of [283] used a technique developed by Gascon *et al.* [284] by which particles of MIL-101(Cr) were coated on an alumina pellet. They used this material as a catalyst for methanation of CO$_2$ after inserting Ni particles in the MOF porous structure. This catalyst was shown to be active and selective up to 320 °C.

Table 4.9 Different MIL-101-based materials applied in catalytic processes

MOF	Application	Remarks	Ref.
carbonized polypyrrole coated MIL-101(Fe)	Non-precious metal oxygen reduction reaction (ORR) electrocatalyst.	• ORR performance ($\Delta E_{1/2}$ = -22 mV). • It showed good stability (87.8%). • It revealed high methanol tolerance.	[257]
Composite of MIL-101(Fe) with iron and iron carbide encapsulated in nitrogen-enriched carbons	Oxygen reduction reaction (ORR).	• The onset and half-wave potentials of 0.85 and 0.70 V vs. RHE, respectively. • The composite was compared to Pt/C. • It exhibited higher stability and methanol tolerance.	[258]
Composite of MIL-101(Fe) and polyaniline/Fe_3O_4/Fe_3N@graphite carbon	Oxygen reduction reaction (ORR).	• It exhibited a half-wave potential of 0.916 V vs. RHE. • The electron transfer number was 4.0 at 0.4 V vs. RHE. • It showed excellent stability in an alkaline solution.	[259]
NH_2-MIL-101(Fe)- Fe_xP	electrocatalytic hydrogen evolution reaction (HER).	• It exhibited high electrocatalytic activity HER with only 227 mV overpotential at 10 mA cm^{-2}. • It showed high stability in acidic media in a water-splitting cell. • The water-splitting cell showed hydrogen production with a Faradaic efficiency of near 100%.	[261]
NC@Fe_3O_4- MIL-101(Fe)	Oxygen reduction reaction (ORR).	• It showed onset potential close to that of Pt/C. • It exhibited high long-term cycle stability in alkaline media. • Carbon coating hindered the agglomeration of the iron-based particles eliminating the need of protective layers. • Carbon coating facilitated the fabrication process.	[260]
MIL-101(Cr)-$[Co(H_2O)_2(PW_9O_{34})_2]^{10-}$	Photocatalytic and electrocatalytic water oxidation.	• The photocatalytic activity was examined by visible light (λ > 420 nm) in a 40 mM borate buffer. • The composite was recovered and reused, exhibiting stable photocatalytic activity. • The catalytic current due to water oxidation for occurs at ca. 1.1 V vs. NHE. • The over-potential was estimated 493 mV at the current density of 1 mA/cm^2.	[264]
$\alpha - MnO_2$/MIL-101(Cr)	Oxygen reduction reaction (ORR).	• The ORR onset potential was -0.14 V. • The current density at -0.3 V was -1.31 mA cm^{-2}. • The ORR activity of the $\alpha - MnO_2$/MIL-101(Cr) catalyst was notably better than pristine $\alpha - MnO_2$ and MIL-101(Cr).	[263]
$PMo_{10}V_2$@MIL-101(Cr)	electrocatalytic oxidation of ascorbic acid.	• MIL-101(Cr) revealed one redox process due to chromium metal centers. • $PMo_{10}V_2$ exhibited five redox processes, one ascribed to vanadium centers and four to Mo centers. • The modified electrodes showed higher efficiency toward ascorbic acid oxidation. • The electrodes showed high selective determination of ascorbic acid in the presence of dopamine and vice-versa.	[265]

Table 4.9 Different MIL–101-based materials applied in catalytic processes (Cont.)

MOF	Application	Remarks	Ref.
Phosphotungstic acid@ MIL-101(Cr)	Biginelli condensation reaction.	• The composite was effectively used for the solvent-free synthesis of bioactive 3,4-dihydropyrimidin-2(1H)-ones through Biginelli reaction of benzaldehyde, urea and ethylacetoacetate. • The catalyst was reused several cycles without considerable loss.	[269]
Salen- Zr(IV) complex/ MIL-101(Cr)	• Esterification of oleic acid (with methanol producing biodiesel). • Knoevenagel condensation reaction of aldehydes. • Friedel–Crafts acylation of anisole.	• High efficiency of those reactions was imputed to the high surface area, which allows a good distribution of Zr(IV) species suggesting a high contact with the reactants. • The composite was compared to Pt/C.	[285]
N-heterocyclic carbene- MIL-101(Cr)-NH$_2$	Cross-coupling reactions of phenylboronic acid and aryl halides.	• The catalyst was recovered from the reaction mixture by filtration and reused for 15 times without leaching into solution or loss of activity.	[286]
MIL-101(Fe)/SiO$_2$	Generation of hydrogen by the catalytic reduction of nitro organics.	• The generation of H$_2$ was higher than NaBH$_4$ hydrolysis under the same conditions.	[287]
PdAg/ triethylenediamine- MIL-101-NH$_2$	Hydrogenation of CO$_2$ to formic acid.	• Similar composites with different organic amines, but they showed lower performance. • The recycling tests were performed five times with 23% loss of catalytic activity compared to the initial activity.	[274]
RuCl$_3$@MIL-101(Cr) MIL-101-NH$_2$	Hydrogenation of CO$_2$ to formic acid.	• The MOF was further modified by salicylaldehyde and 2-diphenylphosphino-benzaldehyde.	[268]
Ni/MIL-101-Al$_2$O$_3$	Methanation of CO$_2$.	• The catalyst exhibited better thermal stability as compared to its homologues MIL-101 and Ni/MIL-101. • The maximum CO$_2$ conversion was 85.8%, and CH$_4$ selectivity was 93.2% at 350 °C.	[283]
Co/MIL-101(Cr)	Selective hydrogenation of the carbonyl bond in α, β-unsaturated aldehydes.	• Co-modified MIL-101(Cr) composites enhanced the hydrogenation of cinnamaldehyde (CAL) to cinnamyl alcohol (COL) with higher selectivity than the monometallic Pt/MIL-101(Cr). • 95% conversion of CAL with 91% selectivity to COL was attained by Co/MIL-101(Cr). • The catalyst showed a high conversion of furfural (97%) along with high selectivity to furfural alcohol (94%).	[280]
Fe$_3$O$_4$/ auxiliary ligand vanillin@MIL-101(Fe)	Water splitting.	• Auxiliary ligand vanillin improved the porous structure of MIL-101(Fe) to adsorb more water molecules. • The O$_2$ and H$_2$ production rates were 360,000 and 584 μmol g^{-1} h^{-1}, respectively. • The magnetic recovery was possible due to Fe3O4, and the catalyst was efficiently reused for 5 cycles.	[262]

Table 4.9 Different MIL-101-based materials applied in catalytic processes (Cont.)

MOF	Application	Remarks	Ref.
MIL-101(Cr)/CoFe$_2$O$_4$	Sonocatalytic degradation of organic dyes.	• The degradation of Rhodamine B and methyl orange were 96% and 88%, respectively. • The sonocatalytic activity of the composite was about 12 and 4 times higher than that of the pristine MIL-101(Cr) and CoFe$_2$O$_4$, respectively. • The enhanced sonocatalytic activity of the composite was imputed to the high specific surface area of MIL- 101(Cr) and magnetic property of CoFe$_2$O$_4$, as well as the fast generation and separation of charge carriers.	[270]
MIL-101(Cr/Fe)	Prins reaction.	• It was found that the predominant role of Cr^{3+} ions was to maintain the crystal structure, whereas Fe^{3+} ions to improve the catalytic activity.	[231]
Pd@(ethylene diamine)/ Cr-MIL-101, and Pd@(propyl diamine)/ Cr-MIL-101	Dehydrogenation of formic acid and production of hydrogen at ambient temperature.	• Pd@(ethylene diamine)/Cr-MIL-101 showed a turnover frequency (TOF) of 583 h^{-1} at 328 K.	[275]
NH$_2$-MIL-101(Fe)	Activation of persulfates for the degradation of bisphenol A.	• The active iron sites played the main role in the activation of persulfates. • The catalyst was actively reused for 6 cycles. • The degradation efficiency of 60 mg L^{-1} of bisphenol A exceeded 99%.	[266]
Cu/MIL-101(Cr)	Hydrolytic dehydrogenation of methylamine borane.	• The turnover frequency =257 mol H$_2$/mol Cu×h) and conversion (> 99%) under air at ambient temperature. • It revealed high durability against sintering and leaching. • It retained about 83% of its inherent activity at complete conversion for 10 cycles of of hydrolytic dehydrogenation of methylamine borane. • Leaching of iron was the main motor of the Fenton reaction.	[278]
Fe$_3$O$_4$/ MIL-101(Fe)	Degradation of Rhodamine B in Fenton-like system	• Complete degradation of Rhodamine B was attained under the optimized conditions. • Leaching of iron was the main motor of the Fenton reaction.	[271]
Pd−Cu/MIL-101(Cr)	Chromium reduction and conversion of carbon dioxide.	• The catalytic reduction of Cr(VI) to Cr(III) and the conversion of terminal alkynes into propiolic acids was faster by 3–5 times faster than Pd–Cu nanocrystals.	[282]
MIL-101-Cr−NH-RSO$_3$H	Synthesis of quinoxaline and derivatives.	• The catalyst exhibited high performance in the preparation of quinoxaline derivatives by the condensation of benzene-1,2-diamines with 1,2-dicarbonyl compounds. • It also showed high good stability and good recycling performance.	[267]
Au/NH$_2$-MIL-101(Cr) exhibited	Epoxidation of styrene	• The catalysts worked with low dose and high turnover frequency (TOF) and reusability. • The high catalytic activity was imputed to the high surface area of the parent MOF with a high isoelectric point value (IEP) and the presence of Brønsted basic sites.	[281]

Table 4.9 Different MIL-101-based materials applied in catalytic processes (Cont.)

MOF	Application	Remarks	Ref.
Ag NC@MIL-101(Fe)	Catalytic hydrogenation of 4-nitroaniline.	• A fluorescent Ag nanocluster deposited iron MIL-101 was synthesized. • It showed highly efficient blue luminescence with a narrow emission, a larger Stokes shift, and high photostability at 330 nm. • It achieved a heterogeneous reduction of 4-nitroaniline to 4-phenylenediamine under green and ambient conditions. • The catalyst kept more than 90% of its performance in five cycles or reuse.	[279]
Pd/SO$_3$H-MIL-101(Cr)	Conversion of vanillin.	• The catalyst showed highly dispersed Pd nanoparticles with a uniform size distribution, sufficient reactant contact in aqueous media, and rapid activation of the reactants induced by the Brønsted acid coordination sites. • Complete conversion of vanillin with exclusive selectivity for the 2-methoxy-4-methylphenol product was achieved.	[272]
RhNi-MIL-101(Cr)	Hydrogen generation from hydrous hydrazine.	• High activity and 100% selectivity remained for five cycles.	[277]
AgPd-MIL-101(Cr)	Dehydrogenation of formic acid.	• Among all the catalysts, the Ag$_{20}$Pd$_{80}$@MIL-101 catalyst revealed the highest catalytic activity. • The conversion of formic acid to high-quality hydrogen was achieved at 80 °C with a TOF value of 848 h^{-1}. • The degradation efficiency of 60 mg L^{-1} of bisphenol A exceeded 99%.	[276]
Cr/Fe MIL-101	heterogeneous photo-Fenton catalyst for reactive dye RR195 degradation.	• High adsorption and high photo-Fenton activity were attained.	[229]

4.8.3 Photocatalysis

Photocatalytic reactions show advantages compared to other advanced oxidation processes (AOPs), especially in the sector of water treatment, due to their high efficiency with minimum solid waste (i.e., sludge production and possible utilization of solar energy).[288] Theoretically, photocatalysts are not consumed during the photocatalytic reaction, and they are expected to work infinitely if employed under appropriate conditions. However, the accumulation of surrounding molecules adsorbed on their surface detracts their photocatalytic performance after some periods of operation.[289] Despite the abundant literature on metal oxides and carbonaceous photocatalysts, many of these reveal significant limitations such as a limited absorption of visible light, fast recombination of opposite charge carriers, and fast surface accumulation due to the low surface area, which limit the reusability.[290–293] MIL-101 MOFs could overcome some of the concerns associated with the conventional photocatalysts due to their low bandgap and high surface area. As illustrated in Table 10, most pristine MIL-101 MOFs and their modified forms showed bandgaps lower than 2.9 eV which allows to slightly harvest more energy from the visible light spectra compared to the benchmark photocatalyst TiO_2, which has a bandgap $\approx$ 3.2 eV.[294] To confirm activity under visible light, many researchers used Xenon (Xe) lamps with a cut-off filter for UV light, so the MOF particles were illuminated by only visible light.[295,296] However, pristine MIL-101 MOFs revealed fast recombination of the photogenerated electrons and holes inhibiting their photocatalytic activity.[297] To overcome these limitations, MIL-101 was coupled with other semiconductors in different heterojunctions so the electrons can move from the organic linkers and metal nodes to the merged semiconductor reducing the recombination rate.[298,299] In most of the reported MIL-101 heterojunctions, both levels of the valance and conduction bands of MIL-101 were either higher than the corresponding levels of the cocatalysts or both were lower than the corresponding levels of the cocatalysts, which generated a reduced bandgap of the heterojunction in the form of staggered band as shown in Figure 4.33.[236,297,298,300–305] For instance, Abdpour *et al.* synthesized a composite of NH_2-MIL-101(Cr) and CuS with conduction bands of –0.50 eV and -0.65 eV (vs. NHE) and valence bands of +2.10 eV and +1.15 eV (vs. NHE) respectively.[300] This band structure formed what is known by a Z-scheme charge separation mechanism whereby the photo-generated electrons in the conduction band of NH_2-MIL-101(Cr) interact with the holes in the valence band of CuS, leading to higher redox capacity and more efficient electron-hole separation. It can be noticed that the positions of the MIL-101 band in different studies were not the same (Figure 4.33), which may be related to the percentage of the metal element in MIL-101. For instance, Vu *et al.* reported a Cr mass ratio of 17.8% in their pristine MIL-101(Cr) determined by energy-dispersive X-ray spectroscopy (EDX) [229], whereas Chang *et al.* reported a Cr mass ratio

of 25.5% for a similar MOF.[235] The graphical approximation and assumptions in Mott-Schottky and Tauc diagrams may also lead to further variations in the determination of the band structure.

Furthermore, the porous structure of MIL-101 is appropriate to host other metal oxides as co-catalysts which can act as electron mediators or acceptors helping to facilitate the separation of charges and reduce the overall bandgap.[298] For instance, Zhang *et al.* modified MIL-101(Fe) with TiO_2 for enhancing the degradation of pharmaceutical pollutants under visible light.[298] The composite showed a smaller arc radius of electrochemical impedance spectroscopy (EIS) than both TiO_2 and pristine MIL-101(Fe), which indicated the improved electron-hole separation. In another study, CdS nanoparticles were introduced to MIL-101(Cr) to enhance the reduction of CO_2 to CO under visible light.[306] The composite possessed a reduced bandgap (2.28 eV) and higher sensitivity to visible light than the pristine MIL-101(Cr). In addition, the transient photocurrent responses in multiple on-off cycles of visible light indicated clearly higher photocurrent intensity than the pristine components confirming the efficiency of transfer and separation of charges. This finding corresponds to the significantly enhanced CO production yield observed when the composite was illuminated. Li *et al.* introduced AgBr and $CuFe_2O_4$ to MIL-101(Cr) for efficient reduction of nitrate to nitrogen under UV irradiation.[307] The different valance and conduction potentials of the three incorporated materials formed a useful direct dual Z-scheme that facilitates the transfer of electrons. The long electron path in this dual Z-scheme provided a higher opportunity for the nitrate conversion into nitrite, nitrate, and ammonium. The stability of the composite was confirmed by the stable conversion of nitrate in four consecutive cycles. In a different approach, $NaGdF_4$:Yb,Er nanoparticles were attached to MIL-101(Cr) to exploit the natural luminance of the lanthanide metals in tuning the absorbed light into more harvestable wavelengths.[308] The composite could completely degrade Rhodamine B, whereas less than 50% of the initial Rhodamine B concentration was removed by pristine MIL-101(Cr).

Carbonaceous co-catalysts were also anchored to the porous MIL-101 MOFs to improve their photocatalytic activity. For instance, graphitic carbon nitride (g-C_3N_4) was introduced to MIL-101(Fe) for the reduction of Cr(VI) and oxidation of bisphenol-A.[309] In this study, the photocatalytic performance of the composite was higher than those of solely MIL-101(Fe) and g-C_3N_4, which was attributed to the direct Z-scheme formed by the different band alignments of both components. Furthermore, the composite revealed a reduced bandgap (2.28 eV) which improved the absorption of visible light. In a different study, a similar composite was used as a photocatalyst for the activation of persulfate under visible light.[303] The electron spin resonance (ESR) signals of the composites and pristine components indicated that MIL-101(Fe) was mainly responsible for producing sulfate radicals, whereas g-C_3N_4

generated superoxide radicals and catalyzed the generation of sulfate radicals. Trapping experiments using different scavengers of reactive oxygen species (ROS) ascertained the same finding as to the ESR analysis. A similar approach was adopted to utilize MIL-101(Fe)-g-C$_3$N$_4$/NH$_2$ in photocatalytic heterogeneous Fenton-like reaction under visible light.[310] Unlike the conventional photocatalysts, it can be noticed that superoxide radicals and holes were the main significant ROS in most MIL-101 photocatalytic reactions, whereas hydroxyl radicals were rarely found to be the dominant species, except for some composites where the co-catalysts were anchored to the porous structure of MIL-101. This finding indicates that MIL-101 could be a useful alternative photocatalyst for applications that require special ROS generation.
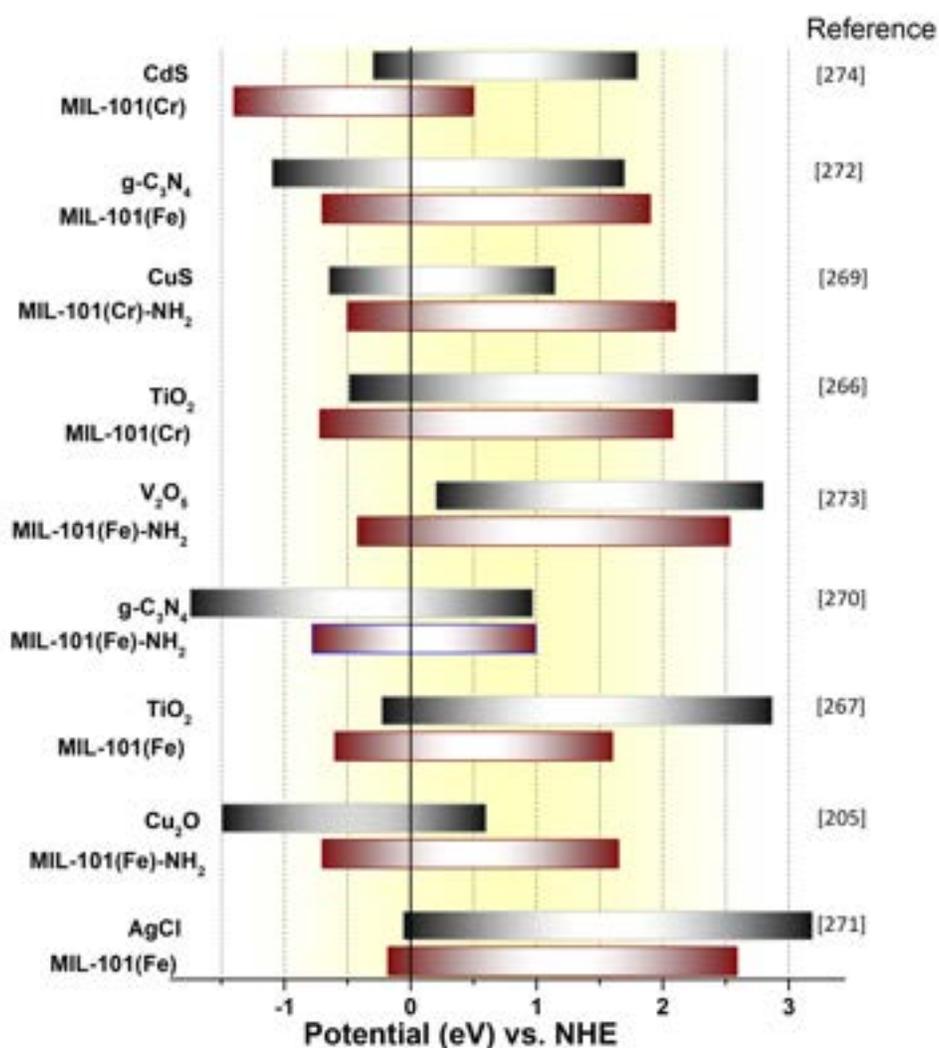
Figure 4.33 The energy band structure for some of the reported heterostructures.

4.8.4 Membrane filtration

In general, MOFs are of special interest as a dispersed phase in designing mixed matrix membranes (MMM). This is because they can be synthesized in functional form with intrinsic porosity. With other microporous materials such as for example zeolites, the post-synthesis grafting of functional groups on the particles external surface, which is necessary to secure interaction with the polymeric continuous phase, is likely to result in pore blockage.[311,312] The controllable pore size and structure, along with the high surface area rich in metal sites, made the MIL-101 MOFs promising for fabrication or modifications of MMMs. Notwithstanding the limited number of publications reporting the employment of MIL-101 MOFs in membrane technology, the applications and roles of MIL-101 in these reports are of high diversity. Sharma *et al.* prepared a composite membrane of MIL-101(Cr)-sulfonated poly(ether sulfone) to utilize the unsaturated Cr sites and the acidic functional groups ($-SO_3H$) in the selective electrodialytic removal of bi-valent lead.[313] Interestingly, the fabricated membrane showed high permeability for monovalent (Na^+) and bi-valent (Zn^{2+}, and Ni^{2+}) ions, whereas it was impervious for the Pb^{2+} ions under the optimum electrodialytic conditions. In addition, the thermal, mechanical, oxidative, and hydrolytic stabilities of the composite membrane were significantly higher than those of pristine sulfonated poly(ether sulfone) (SPES) membrane. In another study, Fang *et al.* introduced MIL-101(Cr) nanoparticles to poly(dimethylsiloxane) (PDMS) hybrid membranes to enhance the gas permeance and the selective separation of hydrocarbons.[314] The propylene permeance was improved by more than 50% and the diffusion rate was faster by 236% compared to pristine PDMS membranes. The unique surface area and pore architecture of MIL-101 also led to propylene sorption selectivity over nitrogen. Rajati *et al.* fabricated a mixed matrix membrane of MIL-101(Cr) microparticles, poly(vinylidene fluoride) (PVDF), and a commercially available polyimide designated as "Matrimid".[315] The product comparison with a neat Matrimid membrane revealed an improvement in CO_2 permeability by 29% and increased selectivity over methane by 23%. Song *et al.* modified the poly ether-block-amide (Pebax 1657) membrane with MIL-101 and NH_2-MIL-101 under different temperatures.[316] They found that the modified membranes could be more effective for the separation of CO_2/N_2 at sub-ambient temperature. Besides, the selectivity of CO_2 was improved at -20 ℃ by 96.5% and 145.1% compared to ambient temperature. In a similar approach, Rodrigues *et al.* fabricated mixed membranes of UiO-66 (Zr) or MIL-101 (Cr) and polyurethane for O_2/N_2 and CO_2/N_2 gas separation.[317] The modified MIL-101 (Cr)/polyurethane membrane showed the highest CO_2/N_2 separation, whereas the selectivity and permeability of O_2/N_2 were not enhanced. Furthermore, the mixed matrix membranes showed better thermal stability than the pristine polyurethane membrane. MIL-101 was also used to facilitate the water perme-

ability in desalination membranes. For instance, Song *et al.* fabricated a reverse osmosis membrane by the polymerization of MIL- 101(Cr) polyhedral particles on graphene oxide sheets.[318] By such modification, the water flux was improved from 20.5 to 38.0 L m^{-2} L^{-1}, with a slight improvement of NaCl rejection. In another study, MIL-101 was merged into poly- ether-block-amide (PEBA) polymer to obtain an effective mixed matrix membrane for the selective ethyl acetate pervaporation.[319] The modified membrane showed a separation factor of 208 and a normalized flux of 52 kg μm m^{-2} h^{-1}, which were better than the MIL-101 free membrane by 206% and 130%, respectively. In another interesting study, Khdhayyer *et al.* fabricated different mixed matrix membranes using a polymer of intrinsic micro-porosity with different structures of MIL-101(Cr) to study the effects of particle size, functional groups, and different precursors.[320] The permeability, diffusivity, and selectivity of He, H_2, O_2, N_2, CH_4, and CO_2 through the different membranes revealed that the aminated and ethylene diamine MIL-101 enhanced the permeability of O_2 and N_2, but did not improve the performance for the CO_2/N_2 and CO_2/CH_4 separation. Incorporating MIL-101 of nano-scale particles led to a remarkable increase in the permeability of all gases without significant change in the selectivity. For a different objective, Ni *et al.* anchored a composite of CdS/MIL-101 on a polyvinylidene fluoride (PVDF) membrane to employ it in an anammox membrane bioreactor.[237] The produced mixed membrane was illuminated by visible light to establish the effect of the composite on biofouling. In the long-term operation, the modified membranes maintained their performance for 26 d compared to 10 - 14 d for pristine membranes. Furthermore, the analysis of the biofilms on the fouled membranes indicated an improved degradation of organic foulants and inactivation of bacteria. Other antibacterial tests exhibited the ability of the composite for the destruction of the cell walls of both Gram-negative and Gram-positive bacteria.

4.8.5 Sensitive detection

The unique porous structure of MOFs, their extreme surface area, and the abundance of functional groups make them ideal candidates for the detection of different analytes. These features lead to significant diffusion of the analytes into the pores allowing several reactions with the functional groups.[321] The detection of analytes by MOFs could be attained either by inserting them in chemically modified electrodes or by modulation of luminescence of a probe. A luminescence detection system includes an excitation source, a luminescent MOF probe, a detector and signal output.[322] Notwithstanding the luminescence detection is a low-cost technology that is distinguished with easy operation and low detection limits, it suffers from limited selectivity and multiple analyte detection. The chemical detection by MOFs is dependent on the accumulation of the targeted analyte on the surface and pores

of a MOF electrode which can be more selective.[321] MIL-101 as one of the predominant MOFs has been reported in many applications of detectors and sensors as a pristine material or mixed with other materials. For instance, Yang *et al.* prepared a fluorescent composite sensor from amino carbon quantum dots (CQDs) and MIL-101-SO_3H nanoparticles for detecting 2,4-dinitrophenol.[323]In this system, the MIL-101-SO_3H encapsulated the CQDs by hydrogen bonding between the SO_3H and NO_2 groups. It also acted as a selective adsorbent to capture the targeted analyte. The composite exhibited a remarkable selectivity towards the 2,4-dinitrophenol with a detection limit of 0.041 μM. Mousavi *et al.* also used amino-CQDs with MIL-101(Fe) to fabricate a hybrid fluorescent probe sensor for the detection of 6-mercaptopurine.[324] In their approach, the interaction between the MIL-101(Fe) functional groups and 6-mercaptopurine was converted into detectable fluorescence signals. The produced sensor displayed high selectivity toward 6-mercaptopurine in the presence of a variety of organic and inorganic interfering substances. Moreover, it showed detection and quantification limits of 55.7 and 202.06 ng L^{-1}, respectively.

In a similar approach, a quartz crystal microbalance was coated by MIL-101(Cr) by the drop-casting method for the sensitive detection of formaldehyde.[325] The detector showed high sensitivity to formaldehyde with a detection limit of 1.79 ppm. Interestingly, the sensor revealed remarkable selectivity to formaldehyde against a variety of volatile organic compounds, including acetone, methanol, and ethanol, which was attributed to the hydrogen bonding between formaldehyde molecules and carboxylate groups in MIL-101(Cr). The same system was reported in another study for detecting various volatile organics such as methanol, ethanol, isopropanol, n-hexane, acetone, dichloromethane, chloroform, tetrahydrofuran, and pyridine in an N_2 environment.[326] The system showed higher sensitivity to pyridine, than chloroform, isopropanol, ethanol, methanol, and tetrahydrofuran in this order, whereas it revealed moderate response for other studied substances. The limits of detection of these substances varied according to the sensitivity to each analyte. For instance, they were 1.60, 3.06, 8.86, 14.17, and 18.40 ppm for pyridine, isopropanol, ethanol, dichloromethane, and tetrahydrofuran, respectively.

In a different approach, Guo *et al.* proposed an innovative sensitive fluorescence sensor using MIL-101(Fe) loaded with nanozyme for the detection of choline and acetylcholine.[327] Their method was dependent on the reaction of acetylcholinesterase to hydrolyze acetylcholine into chlorine which further reacts with choline oxidase to form H_2O_2. The MIL-101(Fe) nanozyme as a catalyst decomposes H_2O_2 in hydroxyl radicals forming highly fluorescent 2-hydroxy terephthalic acid as a product of the oxidation of organic ligand terephthalic acid in the MIL-101(Fe) structure. Through this mechanism, chlorine and acetylcholine could be sensed with detection limits of 20.0 nM and 8.9 nM, respectively. In another study, Zhang *et al.*

developed an ultrasensitive electrochemical immunosensor for the detection of microcystin-LR in aquatic solutions.[328] The sensor comprised MIL-101(Cr) and Au nanoparticles, which revealed high catalytic oxidation potential to ascorbic acid. The developed sensor showed a detection limit of 0.02 ng.mL^{-1} with a linear relationship in the range of 0.05 ng mL^{-1} to 75 μg mL^{-1}. Gan *et al.* developed a voltammetric sensor of MIL-101(Cr) modified by consecutive acid etching in a quest for better hierarchical hollow cages.[329] The produced hollow sensor showed a remarkable voltammetric response for the detection of nitrofurazone in food samples with a linear relation in the range of 0.03 μM to 55 μM and a detection limit of 10 nM. For a different objective, Zhang *et al.* developed a MIL-101(Cr) sensor for humidity sensing properties.[330] The sensor covered a humidity range of (33% to 95%) with a response time of 17 s and a recovery time of 90 s. With further advancements in MIL-101 synthesis and modifications to obtain different tailor-made designs, a significant potential for developing more MIL-101 sensors for various applications is predicted.

4.8.6 Drug delivery

In addition to the aforementioned applications, MIL-101 was recently employed in various products and systems to exploit its unique characteristics in the improvement of various functions. For instance, MIL-101 was recently used in drug delivery for tuning the properties of some pharmaceuticals through interaction with the metal or organic linker. MIL-101 allows large drug loading and encapsulation of different pharmaceuticals.[331] Almasi *et al.* synthesized MIL-101(Fe)-NH$_2$ and modified it with ethylenediamine and 1,2-bis(3-aminopropylamino)ethane to study its performance in the delivery of the non-steroidal anti-inflammatory naproxen.[332] The naproxen delivery from the synthesized amine MIL-101 was observed in simulated body fluids. In another study, Gordon *et al.* utilized different MOFs including MIL-101 for prolonging the administration of acetaminophen, progesterone, and stavudine.[331] The adsorption of drugs into the caves and pores of MIL-101 led to prolonged release time reached 5 days, which is very beneficial in some medical applications. Cabrera-García *et al.* developed amine-functionalized MIL-101(Fe) and MIL-100(Fe) as platforms for the delivery of camptothecin.[333] The delivery by MIL-101(Fe) revealed enhanced cell internalization at positive Zeta- potential and improved intracellular release by the endosomolytic activity. MIL-101 MOFs was not reported to be toxic or dangerous when administered orally. On the contrary, Liu *et al.* found that there is no acute oral toxicity or 28-day oral toxicity of MIL-101(Cr) nanoparticles on mice.[334] The results indicated that a dose of 2000 mg/kg body weight did not reveal any mortality or changes in feed consumption, body weight, organ weight, or behavior. Furthermore, the histopathology assessment revealed no acute or subacute toxicity after oral administration for 28 days.[334]

4.9   Conclusions

To sum up, MIL-101 framework is still one of the highly researched MOFs so far for combining many sought for features of interest in several applications. For instance, MIL-101 MOFs possess: i) mesoporous rigid structure. ii) notably high surface area. iii) remarkable chemical stability in numerous organic solvents, acids, and hydrogen peroxide. iv) Moderate thermal stability up to 300 °C. Hence, numerous research groups are now investigating this framework. However, the reproducibility of the achieved properties, which depend on the synthesis conditions and the preparation method, is still being doubted, and research is ongoing to gain a complete comprehension of its chemistry. As discussed in this review, MIL-101(Cr) was originally synthesized hydrothermally in acidic medium, using HF. Synthesis in a fluoride-free environment has shown HNO_3 to be the second-best choice. Acid-free synthesis was also reported. Nevertheless, synthesis in a basic medium using TMAO resulted in a completely pure product with a yield of 88%. Later, other synthesis techniques, such as the microwave-assisted technique, the mechanochemical method, the dry-gel route, along with a combination of theses, have been explored. The hydrothermal one is still the most utilized technique.

Further studies explored exceptional structures with different trivalent ions and various functionalized linkers, to widen the MIL-101 field of application. This review also presented the other analogues to the chromium framework that involved Fe, Al, V, Ti, Sc, and Mn. Most of them were prepared using the corresponding metal chloride and DMF as the reaction solvent. The iron isomorph, as the second most studied analogue after chromium, has found a wider range of applications, especially in the biomedical field, for being made using a safer ion. However, the iron-type structure showed lower stability than the chromium-type. On the other hand, the direct preparation of aluminum isomorph was limited to the amino-functionalized derivative, whereas the other forms could be obtained indirectly via the deamination of the amino-functionalized structure. The vanadium and titanium analogues were more sensitive to air and moisture. The isostructural isomorphs of scandium and manganese need more investigation as there is no clear information about their preparation, activation, and applications.

Furthermore, other framework isomers or polymorphs were obtained by deviation from the mainly targeted structure MIL-101. MOFs like MIL-88, MIL-53, MOF-235, MIL-47, and MIL-67 with totally diverse characteristics were found to grow from the same precursors of the trivalent metal ion and the ditopic linker. The growth of these unintended products was dependant on time and additives. Structures and highlights of these different MOFs were discussed concisely.

Finally, multivariate frameworks (MTV-MOFs) of a mixed-metal source to obtain the MIL-101 structure with synergistically enhanced properties were presented. Post-synthetic modification and direct synthesis as the main techniques to reach such a goal were discussed and the known attempts were reviewed. The chromium and iron-based MIL-101 have recorded far more progress than any other, and their structure was obtained by various methods and under different conditions. However, MTV-MIL-101s synthesized from iron and aluminum are still under investigation, and they were reported in a limited number of publications. It seems that there is much more to study about the improvement of these interesting MOFs and their applications.

Adsorption, catalysis, photocatalysis, membranes technology, detecting sensors, and drug delivery are the most reported fields of application of MIL-101 in the recent literature. Most of the MIL-101 adsorbents were modified by functional groups to improve the adsorbability and the selectivity towards specific adsorbates. Pyrolyzing MIL-101, either pure or in combination with other materials, was found useful in producing various carbon-based electrocatalysts. The MIL-101 photocatalysts showed improved photocatalytic activity due to their low bandgaps. Besides, the high surface area led to better stability and reusability for longer cycles. Some MIL-101 photocatalysts were merged in composites with metal oxides to improve their performance by Z-scheme bandgaps. MIL-101 was incorporated in the membrane industry to exploit the controllable pore size for the regulation of liquid or gas flow. Furthermore, the utilization of functionalized MIL-101 allowed the design of highly selective membranes. The functionalization of MIL-101 was useful in the design of sensors and probes due to the improved selectivity of the targeted analytes. MIL-101 was employed in drug delivery as a metal or organic linker and for encapsulation of several drugs.

4.10 Conflicts of interest

There are no conflicts to declare.

4.11 Acknowledgements

CHAPTER 5   ARTICLE 2 - MULTIVARIATE METAL-ORGANIC FRAMEWORK MTV-MIL-101 VIA POST-SYNTHETIC CATION EXCHANGE: IS IT TRULY ACHIEVABLE?

Mahmoud Y. Zorainy,[1,2] Hatem M. Titi,[3] Serge Kaliaguine,[4] Daria. C. Boffito[1]

5.1   Abstract

The post-synthetic exchange (PSE) method is a well-proven route to replace, modify, and add different functionalities to metal-organic frameworks (MOFs). Particularly, the solvent-assisted cation substitution (SACS) technique has been reported to prepare mixed-metal multivariate metal-organic frameworks (MTV-MOFs). However, such a technique does not apply to all types of MOFs. In 2013, Szilágyi *et al.* reported the achievement of the mixed-metal MTV-MIL-101 framework via PSE. Since then, a debate has been taking place about the validity of these findings. On the other hand, the attainment of the mixed-metal MIL-101 was reported to be obtainable through the direct synthesis, which is, to some, the only way to achieve it. Here, we settle this dispute by investigating Szilágyi's method not only as described, but also at extended conditions of time and different metal precursors: all attempts were vain. However, by reconsidering the refluxing solvent (Dimethylformamide "DMF" instead of water) and the applied reaction conditions (110 °C – 20 h), mixed-metal MIL-101(Cr/Fe) was achieved via a simple PSE method.
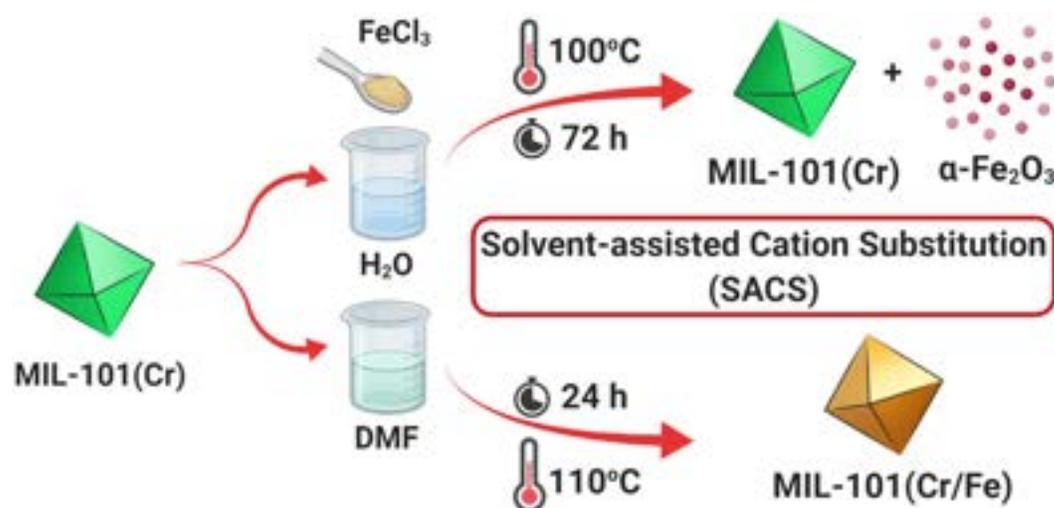
[1]Chemical Engineering Department, Polytechnique Montréal, Montréal, QC H3C 3A7 (Canada)
[2]Chemical Engineering Department, Military Technical College, Cairo (Egypt)
[3]Department of Chemistry, McGill University, Montréal, QC H3A 0B8 (Canada)
[4]Chemical Engineering Department, Laval University, Québec, QC G1V 0A6 (Canada)

5.2 Introduction

Metal-Organic Frameworks (MOFs) are materials whose application in fields including catalysis, gas adsorption and separation, drug delivery, and many more have recently expanded. [7, 335–338] MIL-101 is considered one of the most enticing MOFs due to its robust structure, high specific surface area (SSA, $S_{BET} \geq 4000$ m^2 g^{-1}) and pore volume ($V_{pore} \geq 2.0$ cm^3 g^{-1}), remarkable chemical stability in air, water, acids, and bases, besides its moderate thermal stability (around 300 °C).[13, 68, 339] The properties of MOFs depend on the nature of their active components as well as their structure. Hence, the reconstruction of the MIL-101 framework with different compositions modifies its properties and may contribute to tailoring them towards desired structure and morphology for enhanced performance.

MIL-101 was originally built from the trivalent chromium ion (Cr^{3+}) along with the ditopic 1,4-benzene dicarboxylic acid linker (H$_2$BDC, commercially called terephthalic acid or TPA), yielding a mesoporous structure of mobil thirty-nine (MTN) zeolite topology.[13] Later on, isostructural analogues were synthesized using other trivalent metal cations like Fe^{3+} [128–131], Al^{3+} [137, 151, 157], V^{3+} [164, 167, 170], Ti^{3+} [171, 173], and Sc^{3+} [177, 178]. On the other side, several BDC linkers with different functional groups were incorporated in these syntheses targeting various functionalities[88, 134, 158] Extended structures based on the MIL-101 morphology by replacing BDC with other elongated ditopic linkers such as 2,6-naphthalene dicarboxylate (NDC) and 4,4′-biphenyl dicarboxylate (BPDC) were also studied.[134, 173, 340] These extended structures were investigated, hoping for a higher SSA, thermal stability, and in some cases, improved chemical characteristics. Results did not however meet expectations.[134]

Lately, our group has reviewed the synthesis of the single-metal MIL-101 structure from different metal sources and their recent application in different fields.[339] Attempts to achieve mixed-metal MIL-101 from multiple metal bases were also reported several times in the literature. Such mixed-metal frameworks, mostly bimetallic ones, were proven to have an improved/synergistic performance over monometallic structures.[341] For example, in photocatalysis, MIL-101(Cr/Fe) was reported to express higher photo-Fenton catalytic activity compared to MIL-101(Cr), while maintaining stability, towards commercial reactive dye RR195 degradation.[229] Also, MIL-101(Cr/Ce) promoted the photocatalytic production of hydrogen gas from ammonia borane (NH$_3$BH$_3$) under visible-light irradiation, especially when doped with Pd nanoparticles.[342] In gas-adsorption, MIL-101(Cr/Mg) showed a 40% increase in CO$_2$ adsorption, and 4-times better CO$_2$/N$_2$ selectivity than MIL-101(Cr).[343] In heterogenous catalysis, MIL-101(Cr/Fe) was employed in the Prins reaction of β-pinene and formaldehyde for Nopol production.[231] The incorporation of the Fe^{3+} ions increased

the Lewis-active sites within the structure, yielding an enhanced catalytic activity, while the Cr^{3+} ions maintained the structure stability of the MOF as a heterogenous catalyst.

Multivariate (MTV) frameworks refer to those heterogeneous MOFs made out of mixed components (mixed-metals or linkers), preserving however the same parent MOF topology.[341, 344–346] Usually, MTV-MOFs are obtained either through direct synthesis or post-synthetic exchange (PSE).[39, 339, 341, 347] Direct synthesis includes mixing the desired components prior to reaction and heating the mixture at a specific temperature and for a specific time, which are the same as those for the parent MOF synthesis. Alternatively, PSE encompasses the synthesis of the desired MOF first, followed by a set of processes to exchange one of the main components with another of a similar nature. The direct synthesis, therefore, includes fewer steps and is more straightforward and time-saving. Nevertheless, controlling the formation of the targeted structure through direct synthesis is cumbersome and needs a profound comprehension of the chemistry involved. On the contrary, PSE adopts more steps and requires a longer time; however, it is considered a safer and more controlled approach since modifications occur on an already-existing structure. Hence, PSE can be considered a backdoor, giving access to structures that cannot be achieved by direct synthesis.[3, 348]

Mixed-linker MTV-MIL-101s were reported to be highly attainable via direct synthesis, resulting in structures of textural properties (SSA and pore volume) comparable to MIL-101, which facilitates comparisons in investigations in which the functionality is the only variable.[88, 129, 158] On the contrary, the direct synthesis of single-metal MIL-101s does not yield comparable textural properties: MIL-101s of different metal bases did not exhibit matching SSAs due to the sensitivity of each metal type to the applied reaction conditions.[13, 129, 151, 339] Moreover, changes in the reaction conditions can give rise to other untargeted structures (polymorphs or framework isomers) rather than MIL-101.[170] In conclusion, the formation of MIL-101 polymorphs of the same chemical components but of different networks, like MIL-88 and MIL-53, are highly influenced by the synthesis environment.[170] Hence, the direct synthesis does not seem to be the best route to synthesize multi-metal MIL-101, and PSE appears as a more convenient approach.

As a proof of concept, Szilágyi *et al.* attempted the synthesis of some mixed-metal MTV-MIL-101s via PSE, namely MIL-101(Cr/Fe), (Cr/Al), and (Cr/Fe/Al).[226] MIL-101(Cr) was first synthesized according to Férey's original recipe.[13] Then, by utilizing the solvent-assisted cation substitution (SACS) technique, the Cr^{3+} ions were supposed to be exchanged with the other trivalent metal ions. Experimentally, the MOF was refluxed with aqueous solutions of other metal chlorides to permit the cation replacement. At this point, the achievement of mixed-metal MIL-101s was claimed to be successful, with the result-

ing SSA equivalent or even higher than the original framework. However, other researchers doubted the applicability of PSE solvent-assisted techniques for ligand and cation exchange to MIL-101(Cr).[228, 229] The main reason lies in the presence of the Cr(III) ion sphere within the structure, which makes it not labile, thus resulting in kinetic inertness opposing these modifications.[228] This belief would leave direct synthesis as the only available option to prepare MTV-MIL-101s.

In order to shed light on this dispute and validate whether or not cation-substitution via PSE applies to MIL-101(Cr), we repeated Szilágyi's method to prepare the mixed-metal MIL-101 (Supporting Information, section 5.7).[226] Here, we will only focus on the bimetallic MIL-101(Cr/Fe). In addition, extreme conditions of refluxing time and concentration were applied to verify the limits of such a process. Furthermore, other metal salts (e.g., $Fe(NO_3)_3$) and reaction solvents (e.g., DMF) were also investigated to study their abilities to perform the desired exchange.

5.3 Results and Discussion

5.3.1 Post-synthetic exchange in aqueous solution

The SACS technique involves incubating the MOF in a boiling aqueous solution for 72 h. Thus, it is key to check whether both the initial and the final forms of the MOF (i.e., MIL-101(Cr) and MIL-101(Cr/Fe)) can withstand these conditions. Their hydrothermal stability ensures that the Fe^{3+} ions retain their coordination within the framework, and the structure does not degrade. The chemical and hydrothermal stability of MIL-101(Cr) has already been investigated, confirmed, and reported several times, with the conclusion that it remains intact in boiling water for up to 14 days.[90, 106, 200, 349] On the other hand, the stability of MIL-101(Fe) has been doubted as some Fe-BDC MOFs deteriorate in moist air and in water in less than one hour.[132,134,137,140,346] Thus, we investigated MIL-101(Fe)'s stability via XRD after activation (EtOH – 60 °C/12 h) and exposure to humid atmosphere for 72 h. Results were then compared to samples soaked in boiling water for the same duration. All the patterns confirmed that the crystallinity of the MIL-101(Fe) framework was still preserved (Supporting Information (section 5.7), Figure 5.12).

In Szilágyi's publication, the color change was the main parameter to track the degree of cation substitution.[226] The change in the (d-d) transition of the metals incorporated within the MIL-101 structure and in connection with the BDC linker develops a noticeable visible change in the color of the products. MIL-101(Cr) is a light sea-green powder, while MIL-101(Fe) is of an orange-red ochre color (Table 5.3 - Col. 6 row 6). Thus, MIL-101(Cr/Fe) exhibits an in-between color.[202, 230]

Following the method mentioned above [226], 100 mg of MIL-101(Cr) was added to a 100 ml aqueous solution of iron(III) chloride (ca. 10 mg), and the solution was kept at 100 °C under reflux for 72 h, resulting in a yellowish-green suspension different from the original one (Sample "PSM-10-Cl", Table 5.3 - Col. 2 row 3 & 4). After washing and drying, the product was also darker compared to pristine MIL-101(Cr) (Table 5.3 - Col. 2 row 6), suggesting successful cation exchange. Increasing the concentration of the initial solution to 25 mg, 50 mg, and 100 mg $FeCl_3$ per 100 ml of D.I. water resulted in suspensions and products of a more intense orange color (Table 5.3 - row 4 & 6, Figure 5.13). At a concentration of 100 mg $FeCl_3$, the dried powders were rather ochre red/brown in color (Table 5.3 - Col. 5 row 6).

The XRD analysis of the 10 mg $FeCl_3$ sample (PSM-10-Cl) in the $2\theta = 3°$ - $30°$ range displayed a diffraction pattern typical of MIL-101(Cr), with a nearly flat background and high-intensity peaks (Figure 5.14). Thus, the process preserves the MIL-101 structure integrity along with its high crystallinity. Similarly, the FTIR spectrum of the same sample compared to that of pristine MIL-101(Cr) and MIL-101(Fe) also confirmed the structure consistency, whereby all the absorption bands related to the MIL-101 framework were identified (Figure 5.19). Furthermore, the characteristic peak of the Cr-O bond around 589 cm^{-1} was detected in both spectra of MIL-101(Cr) and PSM-10-Cl.[229,350] In contrast, the spectrum of the PSM-10-Cl sample displayed a shoulder at around 550 cm^{-1} in the same region of the vibrational peak of the Fe-O bond in MIL-101(Fe), thus confirming the presence of the ferric ions.

Also, in agreement with Szilágyi's findings, the UV-Vis diffuse reflectance spectrum of the PSM-10-Cl powders showed a comparable spectrum to that of MIL-101(Cr) (Figure 5.18). The absorption peak around 593 nm in the MIL-101(Cr) spectrum was slightly shifted to shorter wavelengths ($\sim$ 588 nm, blue-shift) in the corresponding spectrum of the PSM-10-Cl sample.[226] Despite being small, this shift was ascribed to the successful substitution of the Cr^{3+} ions with the desired Fe^{3+} ions in the original article. The low shifting was attributed to the minute percentage of Fe^{3+} incorporated as a result of using a dilute solution during the PSE process.[226] In our case, a more significant shift would be expected when using more concentrated solutions (PSM-25-Cl, PSM-50-Cl, and PSM-100-Cl samples). It is worth mentioning that a higher absorption in the visible and near UV range between 330 nm and 750 nm was also witnessed in the PSM-10-Cl sample, similar to the previous results (Figure 5.18).[226] Moreover, by utilizing XRF and scanning electron microscopy – energy-dispersive X-ray spectroscopy (SEM-EDX), a considerable amount of Fe (around 15 wt%) was found to be present in the PSM-10-Cl sample, in spite of using a dilute solution of ferric chloride salt in the initial step (Table 5.8).

Despite initially the results seemed to agree with those of Szilágyi, i.e., the successful sub-

stitution of the Cr^{3+} ions with the Fe^{3+} cations, after collection and centrifugation at high speed (10,000 rpm), the product was separated into different components (Table 5.3 - row 5). Noticeable regions of green and brown colors were distinguishable by the naked eye, with the brown products consistently collecting at the bottom, indicating a higher density product. When viewed from the top of the centrifuge tube, the collected powders showed a bright green color of MIL-101(Cr) (Table 5.3 - Col.6 row 5). That is, the collected products were a mixture of the light-density powders of MIL-101(Cr) (ρ= 0.62 g cm^{-3}) [13, 351] with a higher-density Fe oxide (around 4 - 5 g cm^{-3}), rather than a mixed-metal MTV-MIL-101(Cr/Fe).[352]

To dive deeper into this matter, we pursued the characterization of all the other PSM-Cl samples obtained with a higher concentration of $FeCl_3$ and compared them to the PSM-10-Cl sample. XRD patterns in the $2\theta = 3°$ - 100° range showed a gradual increase in the measured background (from PSM-10-Cl to PSM-100-Cl), along with some noticeable diffraction peaks around $2\theta = 24.1°$, 33.2°, 35.6°, 49.4°, 54.3°, 62.4°, and 63.9° (Figure 5.1). The increase in the measured background was accompanied by the increase in the hump height at lower angles, which can be recognized in the figure by the increasing space between the plotted data and the zero-background dashed line, indicating the presence of an amorphous product.[353] The peaks at $2\theta > 20°$ angles (inset of Figure 5.1) signal the presence of hematite (α-Fe_2O_3) in a semi-crystalline phase.[354, 355]

To further investigate the nature of the obtained products in the PSM-Cl samples, a set of control experiments was reconducted adopting the same refluxing procedures but without the MOF addition (Table 5.4). By the end of these experiments, the initial clear solutions of $FeCl_3$ turned into darker orange/red ones with slight turbidity (Table 5.4 - row 2 and 3). Centrifuging these solutions to collect the suspended particles yielded very small quantities of dark red/brown powders in samples PSM-50-Cl and PSM-100-Cl, while nothing was collectible in samples PSM-10-Cl and PSM-25 Cl. The analysis of the collected powders via XRD gave a typical (α-Fe_2O_3) pattern (Figure 5.15). Hence, the formation of (α-Fe_2O_3) particles can be achieved by the PSE method with high $FeCl_3$ concentrations.

As indicated by Szilágyi *et al.*, other generic characterization techniques such as UV-Vis, IR, and Raman cannot undoubtedly prove the incorporation of the ferric ions into the structure of the MIL-101 framework.[226] However, such techniques can detect the presence of a mixture of MIL-101(Cr) with other materials of different nature, according to our data. Similar to XRD, Raman spectroscopy is another non-destructive structure-sensitive technique that can differentiate between various phases of metal oxides based on their different vibrational and scattering responses.[356] In addition, Raman spectroscopy is usually utilized in similar investigations to confirm the coexistence of iron oxides within the MOF matrix.[357, 358]
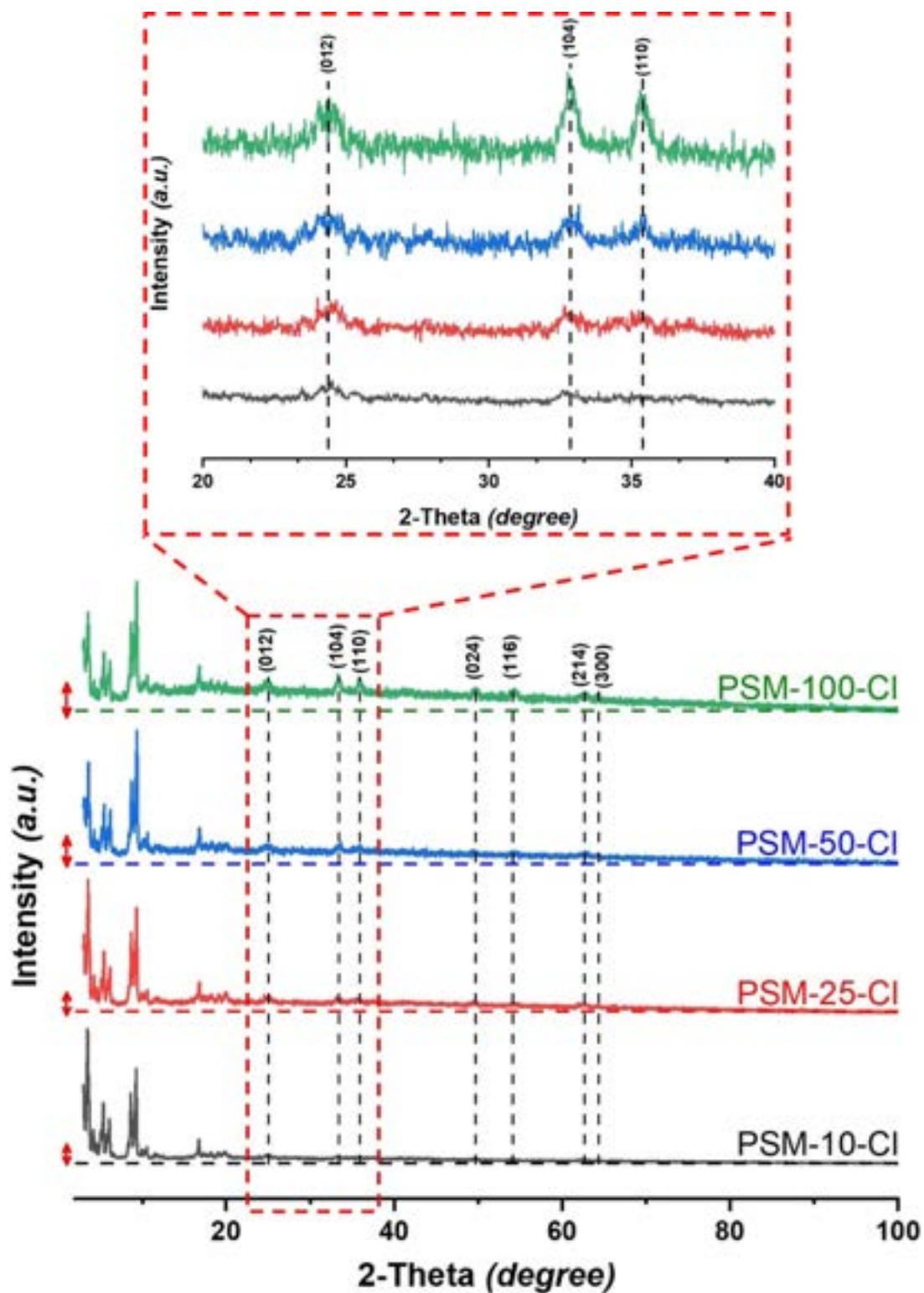
Figure 5.1 XRD patterns of the PSM-Cl samples (PSM-10-Cl "Black" to PSM-100-Cl "Green"). Red arrows on the left side represent the increase in hump height for each sample. Inset: diffraction peaks belonging to α-Fe_2O_3 in the $2\theta = 20°$- $40°$ range.

All images obtained for the MIL-101(Cr) sample through the Raman microscope at different zooming ranges exhibited bright green crystals with no other interfering material (Table 5.9 - row 2). Likewise, the MIL-101(Fe) sample images showed clear crystals of darker color (Table 5.9 - row 3), and measurements performed at different spots confirmed the presence of the MIL-101 phase (Figure 5.2). The vibrational bands at 873 cm^{-1}, 1149 cm^{-1}, 1461 cm^{-1}, and 1618 cm^{-1} correspond to the aromatic and dicarboxylate groups of the H_2BDC linker.[358]
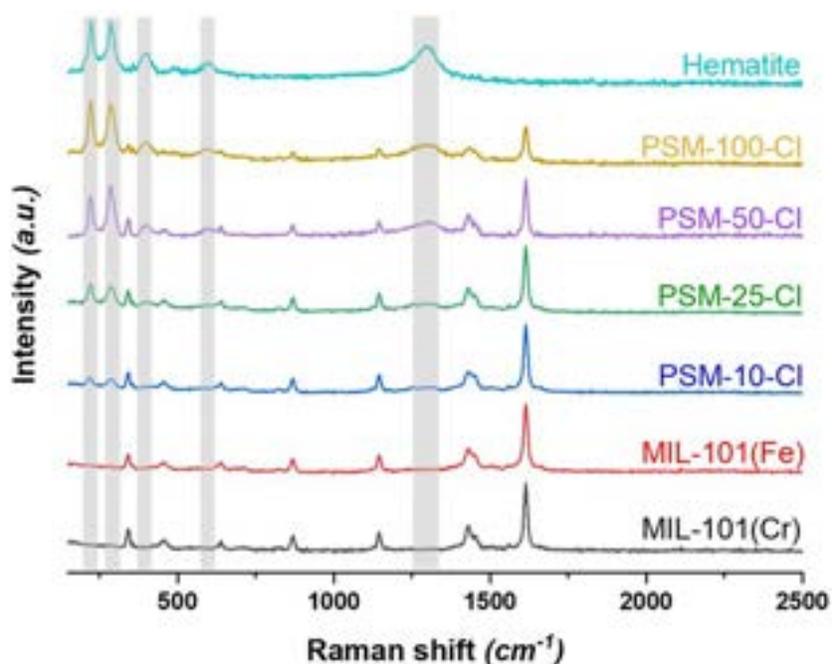
Figure 5.2 Raman spectra (area measurements) of the PSM-Cl samples compared to MIL-101(Cr), MIL-101(Fe), and hematite. Grey shaded regions highlight the bands of α-Fe_2O_3.

On the other side, Raman microscopy images of the PSM-10-Cl sample displayed some dark red/brown particles in combination with the pristine green crystals of MIL-101(Cr) (Table 5.9 - row 4). Measurements performed around these particles recorded the characteristic vibrational bands of the MIL-101 framework along with those of hematite (α-Fe_2O_3) at 227 cm^{-1}, 293 cm^{-1}, 412 cm^{-1}, 610 cm^{-1}, and 1322 cm^{-1} (shaded areas in Figure 5.2).[356] That is, the iron oxide particles are also formed in the samples treated with the diluted solutions. In the PSM-Cl samples obtained at higher $FeCl_3$ concentration, completely separate green and brown regions were observed under the microscope (Table 5.9 - row 5, 6, and 7). Spot analysis within these regions provided different responses (Figure 5.22), emphasizing the formation of discrete ferric oxide particles among the MIL-101 crystals. Area measurements of all samples are presented in Figure 5.2, showing increased signals of Fe_2O_3 over MIL-101 with increasing

the concentration of the initial solution.

Although the (α-Fe$_2$O$_3$) particles were confirmed to be present in all samples, the possibility of the cation exchange is still not excluded. The formation of an iron oxide phase within the reaction medium does not primarily reject or hinder cation substitution, especially since the oxides can be used to prepare MIL-101 in the first place.[86, 87] Thus, depending on the considerable difference in the densities between the MIL-101(Cr) framework and the (α-Fe$_2$O$_3$) particles, SEM operated on the back-scattered electron mode (detector) was selected to screen all the PSM-Cl samples.

The SEM images of the PSM-10-Cl sample also proved the existence of some large foreign particles of different nature and higher density (Figure 5.3). The EDX elemental mapping of such areas revealed that chlorine was present and homogeneously distributed all over the sample. This can be attributed to the replacement of the hydroxide ions (OH$^-$) of the structure with the chloride ions (Cl$^-$) released as a result of the dissolution of FeCl$_3$.[359] On the other hand, Fe, Cr, O, and C were also detectable. However, the detected Fe species were not distributed. They were rather concentrated over the foreign particles. The mapping analysis of the other elements showed that oxygen is also dispersed over the whole sample, but it is excessively masking the foreign particles. Conversely, the Cr and C species were deficient in that particular spot. Hence, this confirms that these higher-density particles are, in fact, (α-Fe$_2$O$_3$) particles that exist within the sample without any interference with the original MIL-101(Cr) crystals. Once again, similar findings were obtained for other PSM-Cl samples of higher concentration (Section 5.7, Figure 5.23 - 5.28). However, with increasing FeCl$_3$ concentration in the initial solutions, the presence of the α-Fe$_2$O$_3$ particles becomes more pronounced (Figure 5.28).Consequently, the achievement of a mixture of MIL-101(Cr) and α-Fe$_2$O$_3$ instead of a mixed-metal MIL-101(Cr/Fe) was confirmed, together with the tendency of this process to form metal oxides rather than promoting cation substitution.

Correspondingly, upon the measurement of the SSA, and considering that the MIL-101 structure is still conserved in all samples, they are expected to display the typical type-I isotherm with its two characteristic secondary uptakes around a relative pressure of 0.05 - 0.20.[7, 8] However, the inclusion of the α-Fe$_2$O$_3$ particles, with their low SSA compared to MOFs, would affect the average SSA. Moreover, with the increasing amount of iron oxide in each sample (XRF & EDX, Table 5.8), the measured SSA is expected to follow an opposite trend. In agreement, the isotherms of all samples were as expected. Furthermore, the measured SSA of the samples treated with concentrated solutions (i.e., PSM-25-Cl, PSM-50-Cl, and PSM-100-Cl) followed the expected trend, whereby the SSA were lower than that of pristine MIL-101(Cr) (Table 5.1).
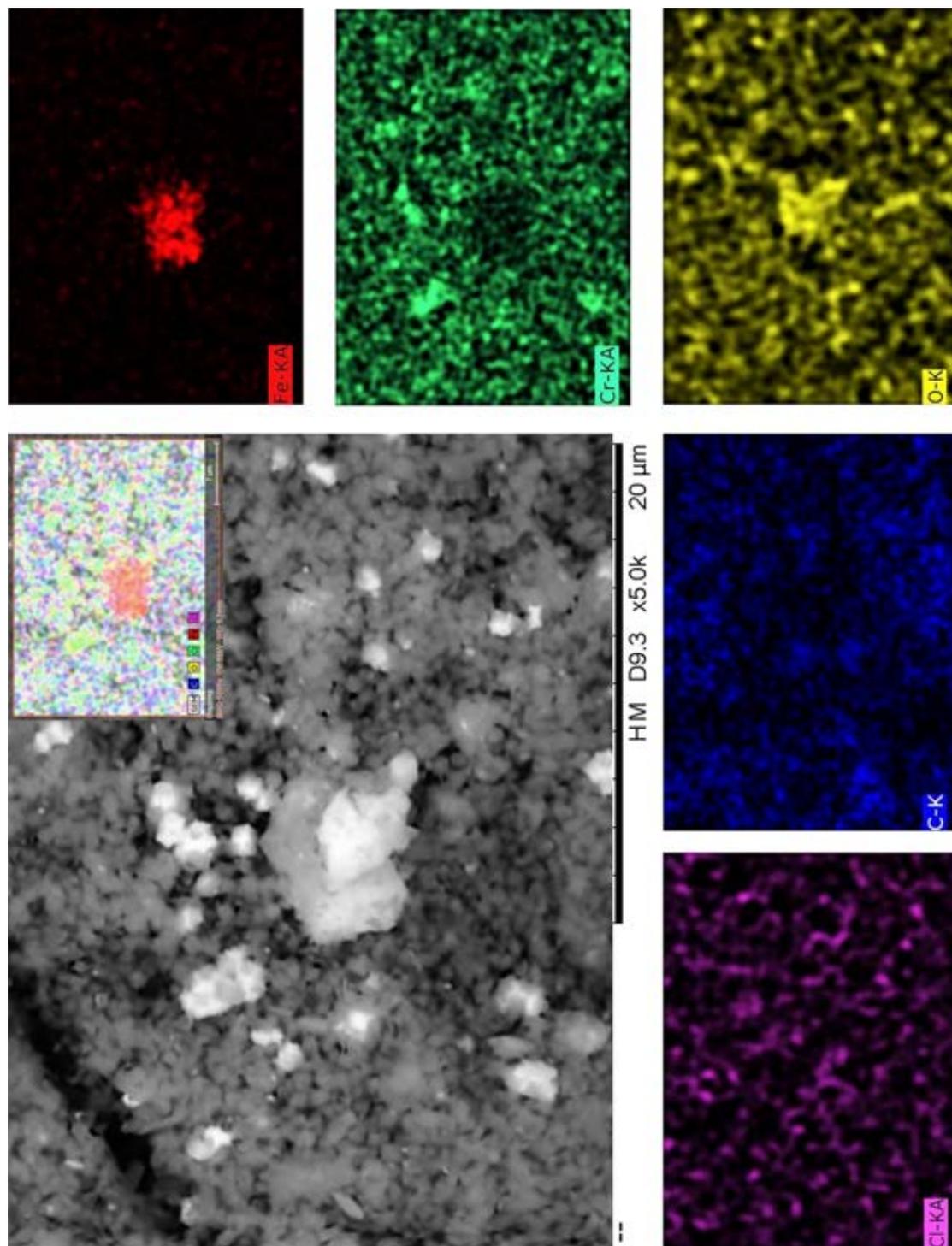
Figure 5.3 Elemental mapping of the PSM-10-Cl sample, revealing the formation of the α-Fe$_2$O$_3$ particles as the major reaction product and the inclusion of the chloride ion within the MOF structure. Color mapping: Cr-green, Fe-red, O-yellow, C-blue, and Cl-purple.

Table 5.1 BET SSA and pore volume of the PSM-Cl samples treated with aqueous solutions of FeCl$_3$ of different concentrations

Sample	MIL-101(Cr)	PSM-0-Cl	PSM-10-Cl	PSM-25-Cl	PSM-50-Cl	PSM-100-Cl
$\mathbf{S}_{BET}$ $\mathbf{(m^2\ g^{-1})}$	2497	2789	2618	2305	2083	2041
$\mathbf{V}_{pore}$ $\mathbf{(cm^3\ g^{-1})}$	1.49	1.77	1.60	1.42	1.35	1.32

Surprisingly, the SSA and pore volume of sample PSM-10-Cl had the highest values compared to all other samples, especially pristine MIL-101(Cr). Notwithstanding, the PSE method, which involves refluxing with a solvent at its boiling temperature, resembles the activation process of MOFs but with the inclusion of a metal salt. Activation of MOFs, in general, is a post-synthesis process that takes place to evacuate the framework pores from any recrystallized linker or reaction side product.[65] Previous studies of the chemical and hydrothermal stability of MIL-101(Cr) confirmed that keeping it in similar conditions would conserve the structure crystallinity and result in a higher SSA as a further activation step.[138] Hence, one more control sample was prepared: differently from the previous control experiments, this sample was expected to elucidate the effect of the PSE method on the MOF without the addition of FeCl$_3$ (i.e., sample PSM-0-Cl).
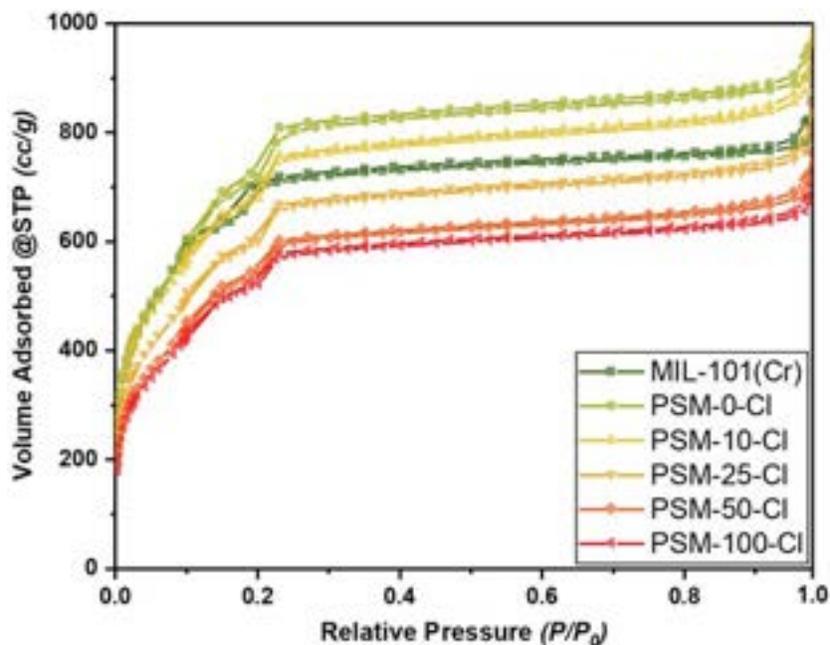
Figure 5.4 N$_2$ sorption isotherms of the PSM-Cl samples compared to pristine MIL-101(Cr), showing a gradual decrease in the measured SSA with the increase of FeCl$_3$ in the synthesis solution.

As expected, the PSM-0-Cl sample had a higher SSA than PSM-10-Cl and pristine MIL-101 (Cr) (Table 5.1). Moreover, compared to the MIL-101(Cr) sample, the isotherm of the PSM-0-Cl sample exhibits a noticeable shift in the position of the secondary uptake points towards a higher relative pressure (Figure 5.4). On the other hand, the position of the secondary adsorption points was the same for the other PSM-Cl samples, similar to that of PSM-0-Cl. That is, the PSE process works as an additional activation step that further evacuates the structure pores, resulting in a higher SSA and larger pore volume. However, with increasing the $FeCl_3$ concentration in the synthesis solution and the consequent formation of α-Fe_2O_3 particles, a gradual decrease in the average SSA happens along.

Back to the initial assessment results, the UV-Vis DRS spectra of the PSM-25-Cl, PSM-50-Cl, and PSM-100-Cl samples did not follow the expected blue-shift as found in the PSM-10-Cl sample.[226] Instead, it resulted in an increased absorption in the 330 nm - 750 nm range (Figure 5.5). Besides, PSM-50-Cl and PSM-100-Cl samples showed a distinctive peak in the near IR range at 874 nm, different from that found in MIL-101(Fe) at 957 nm. The UV-Vis spectra of the PSE samples at high concentrations did not resemble either pristine MIL-101(Cr) or MIL-101(Fe). Comparing these spectra to that of α-Fe_2O_3 obtained from the control samples conducted without the incorporation of the MOF, they follow its general pattern indicating that such iron oxide phase has become the major phase.[360]
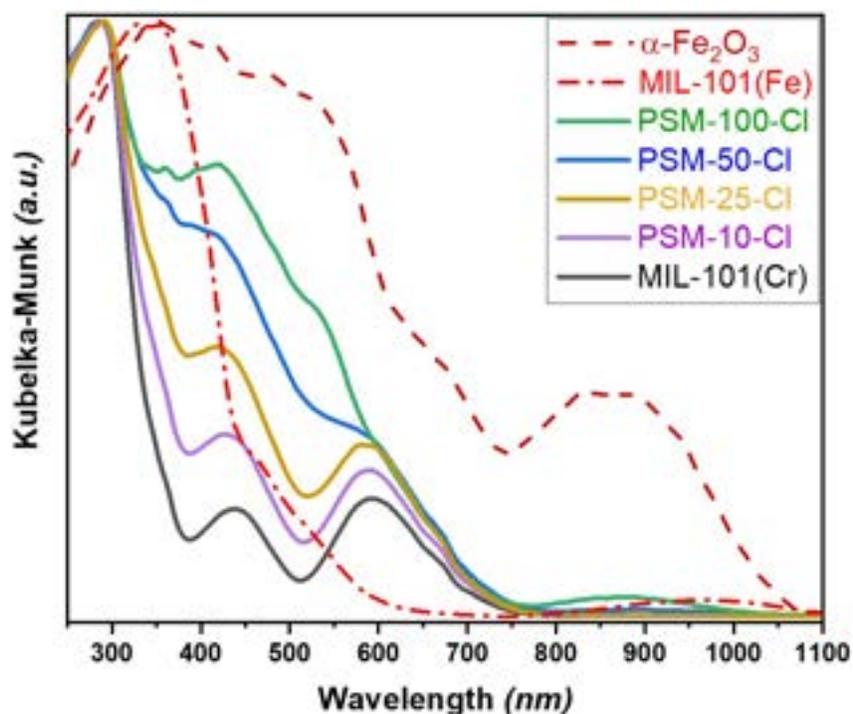
Figure 5.5 UV-Vis DRS spectra of the PSM-Cl samples compared to MIL-101(Cr), MIL-101(Fe), and α-Fe_2O_3 highlighting the great similarity of the obtained spectra to hematite with increasing $FeCl_3$ concentration in the synthesis solutions.

Also, for the obtained FTIR spectra of all PSM-Cl samples, they were almost identical (Figure 5.6) with the shoulder around 550 cm^{-1} that was ascribed to the vibrations of Fe-O bonds. However, with respect to other results that prove the inclusion of the α-Fe$_2$O$_3$ particles instead of the mixed-metal MIL-101 formation, this shoulder was misinterpreted by the involvement of the ferric ions in the structure of the MOF. Nevertheless, the presence of these vibrational peaks should be attributed to the existence of another iron compound among the products that contain the Fe-O bonds, producing the same response.[361]
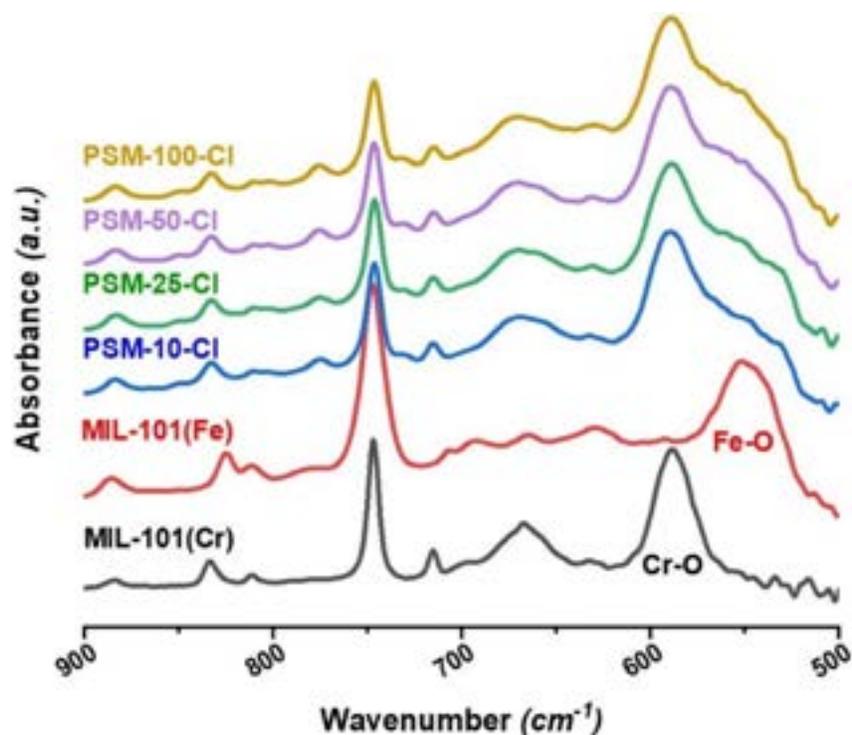
Figure 5.6 FTIR spectra of the PSM-Cl samples compared to MIL-101(Cr) and MIL-101(Fe), expressing the Cr-O and the Fe-O bonds absorption.

So far, our results highlight how an aqueous solution of FeCl$_3$ is unsuitable in the SACS process to achieve the mixed-metal MIL-101(Cr/Fe). This would oppose Szilágyi's findings and leaves the direct synthesis route as the only available option. In additional tests, we investigated the possibility of performing the cation exchange and achieving the mixed-metal framework by either increasing the refluxing time or using another type of iron salt. Unfortunately, extending the duration of the experiments to seven days instead of three or replacing the metal chloride salt with the nitrate yielded the exact same results (samples "PSM-NO$_3$", Table 5.5). Hence, the use of an aqueous solution of trivalent metal ions, in general, is unsuitable for exchanging ferric ions in the MIL-101(Cr) framework.

Post-synthetic exchange in DMF

On the other side, reconsidering the type of solvent involved has been one of the key parameters for the synthesis of other single-metal MIL-101s from many trivalent metals other than chromium.[128, 133, 151, 159, 170] Other studies dealing with the synthesis of mixed-metal MOFs through PSE have carefully considered the used solvent and the conditions applied during the process to match those applied during direct synthesis.[362, 363] For our case, MIL-101(Fe) has often been reported to be prepared from a $FeCl_3$ solution in N,N-Dimethyl-formamide (DMF) at a temperature ranging from 110 °C to 150 °C.[129–131] Synthesis at higher temperatures usually takes place for a shorter period of time (150 °C/10 min – microwave-assisted synthesis); however, lower temperatures require more prolonged periods (110 °C/20 h – solvothermal synthesis). Also, DMF has been proven to take part during the MOF synthesis as a complex-forming medium, essential to allow such a structure formation.[161] Thus, DMF can replace water ideally in the process at 110 °C for 20 h, according to Kholdeeva *et al.* solvothermal method of MIL-101(Fe) synthesis.[130, 131]

Thus, 100 mg of MIL-101(Cr) was added to a solution of $FeCl_3$ at the same concentrations of 10 mg, 25 mg, 50 mg, and 100 mg per 100 ml DMF. The mixture was then kept under reflux for 24 h at 110 °C. Similar to the aqueous solution experiments, the resulting suspensions showed a gradual color change. However, in the case of DMF, all samples were darker and mostly of a golden-brown color (Table 5.6, Figure 5.13-c). Moreover, upon a visual inspection of the products during collection and centrifugation, the color appeared uniform, thus indicating the absence of a side-product as found in the PSM-Cl and PSM-NO$_3$ samples (Table 5.6 - row 6). Also, in contrast to the results of the PSM-Cl samples, the XRD patterns of the PSM-DMF were alike (Figure 5.7, Figure 5.16). They all displayed the pattern of the MIL-101 framework with its high-intensity peaks at lower angles and with no increase in the measured background or presence of other diffraction peaks at higher angles.[13] Hence, the applied process preserves the structural integrity of the framework and prevents the amorphization or the phase transformation of the MOF to one of its polymorphs. In addition, so far, the formation of iron oxides was not observed.

XRF and SEM-EDX investigated the elemental percentage of Fe in each sample. The results showed a progressive increase in the Fe percentage from 18 wt% for sample PSM-10-DMF to 31 wt% for sample PSM-25-DMF, 46 wt% for sample PSM-50-DMF, and 60 wt% for sample PSM-100-DMF (Table 5.8). Hence, the applied procedure, despite being shorter and at a slightly higher temperature, seems to be efficient towards such cation exchange.
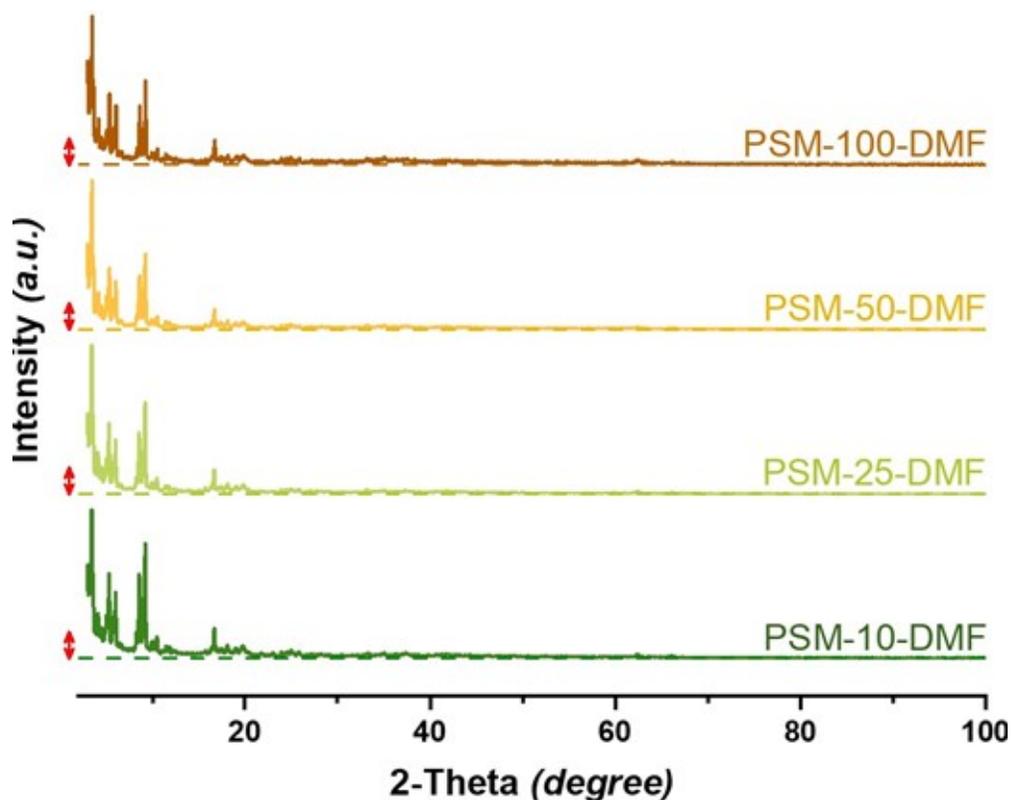
Figure 5.7 XRD patterns of the PSM-DMF samples (PSM-10-DMF "Dark green" to PSM-100-DMF "Brown"). Red arrows of equal length on the left side indicate that an increase in the measured background did not occur, opposite to the results of the PSM-Cl samples.

The UV-Vis DRS spectra of the PSM-DMF samples showed a different behavior compared to PSM-Cl samples, whereby no shifts in the position of the absorption peaks appeared. However, an abrupt increase in the absorption of all PSM-DMF samples occurred in the 250 nm – 450 nm range (Figure 5.8), even for the lowest Fe-cation exchange (sample PSM-10-DMF). Such an increase in the absorption complies with the spectrum of MIL-101(Fe), masking one of the characteristic peaks of MIL-101(Cr) in the visible range at 439 nm. Moreover, in the UV range, the peaks of MIL-101(Cr) and MIL-101(Fe) at 288 nm and 328 nm were identified in the spectra of PSM-10-DMF, PSM-25-DMF, and PSM-50-DMF (Figure 5.8). Nevertheless, the spectra of the PSM-100-DMF sample showed a general absorption over the UV and visible range between 250 nm – 750 nm, with a maximum centered at 328 nm, matching with the MIL-101(Fe) spectrum, and covering up all the MIL-101(Cr) peaks. This change in the absorption behavior of PSM-DMF samples in comparison with the spectra of the PSM-Cl, MIL-101(Cr), and MIL-101(Fe), clearly indicates the successful cation substitution of the Cr^{3+} ions in the MOF structure with the Fe^{3+} ions from the medium.
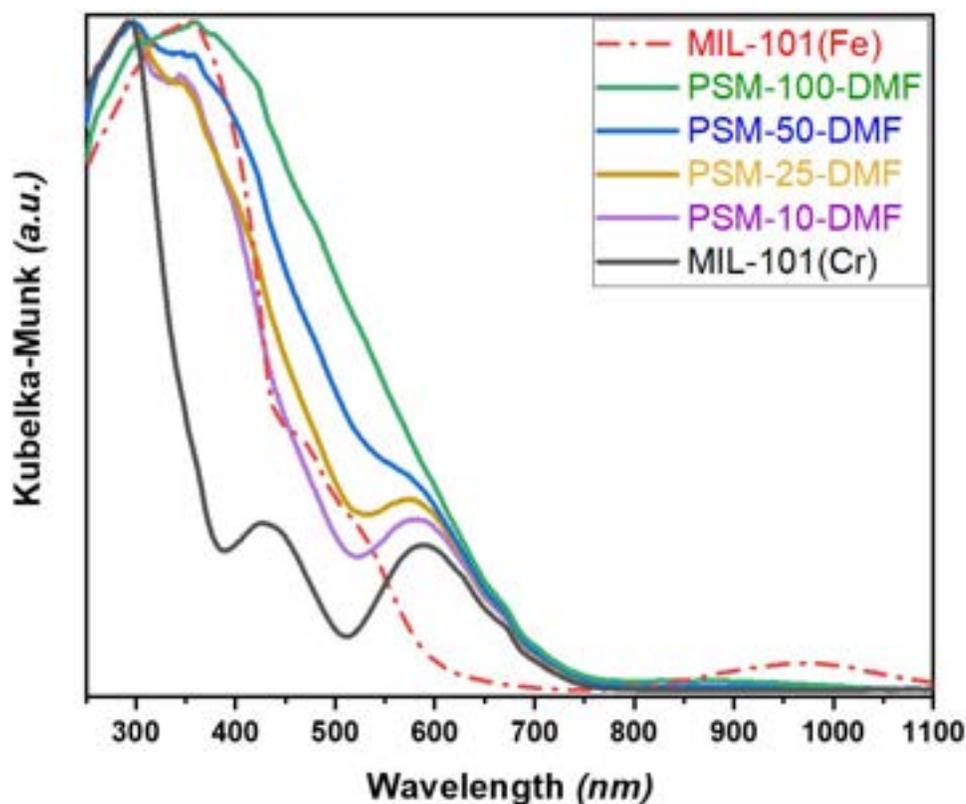
Figure 5.8 UV-Vis DRS spectra of the PSM-DMF samples compared to MIL-101(Cr) and MIL-101(Fe), emphasizing the conformity of the obtained spectra to that of MIL-101(Fe) with the increasing concentration of the exchanged cations.

The N_2 sorption isotherms for the PSM-DMF samples were identical to that of pristine MIL-101(Cr). As discussed above, a control sample "PSM-0-DMF" was also prepared for comparison, whereby the MOF was treated with DMF under similar reaction conditions but without the addition of any Fe salt. Once again, this control sample was of a higher SSA and pore volume than pristine MIL-101(Cr). However, such an increase was not as much as found in the PSM-0-Cl sample (Figure 5.29). Moreover, the shift in the position of the secondary uptake points was not as much pronounced as for the sample refluxed with boiling water. The measured SSA and pore volume for the samples treated with solutions of low concentration (i.e., PSM-10-DMF and PSM-25-DMF) were higher even when compared to the PSM-0-DMF sample (Figure 5.9 and Table 5.2). Nevertheless, at higher concentrations, SSA and pore volume suddenly decreased. Such a drop in SSA may indicate the presence of some foreign particles at high solution concentration, which requires further investigations.

Table 5.2 BET SSA and pore volume of the PSM-DMF samples obtained with different $FeCl_3$ concentrations in DMF

Sample	MIL-101(Cr)	PSM-0-Cl	PSM-10-Cl	PSM-25-Cl	PSM-50-Cl	PSM-100-Cl
S_{BET} $(m^2\ g^{-1})$	2497	2789	2618	2305	2083	2041
V_{pore} $(cm^3\ g^{-1})$	1.49	1.77	1.60	1.42	1.35	1.32
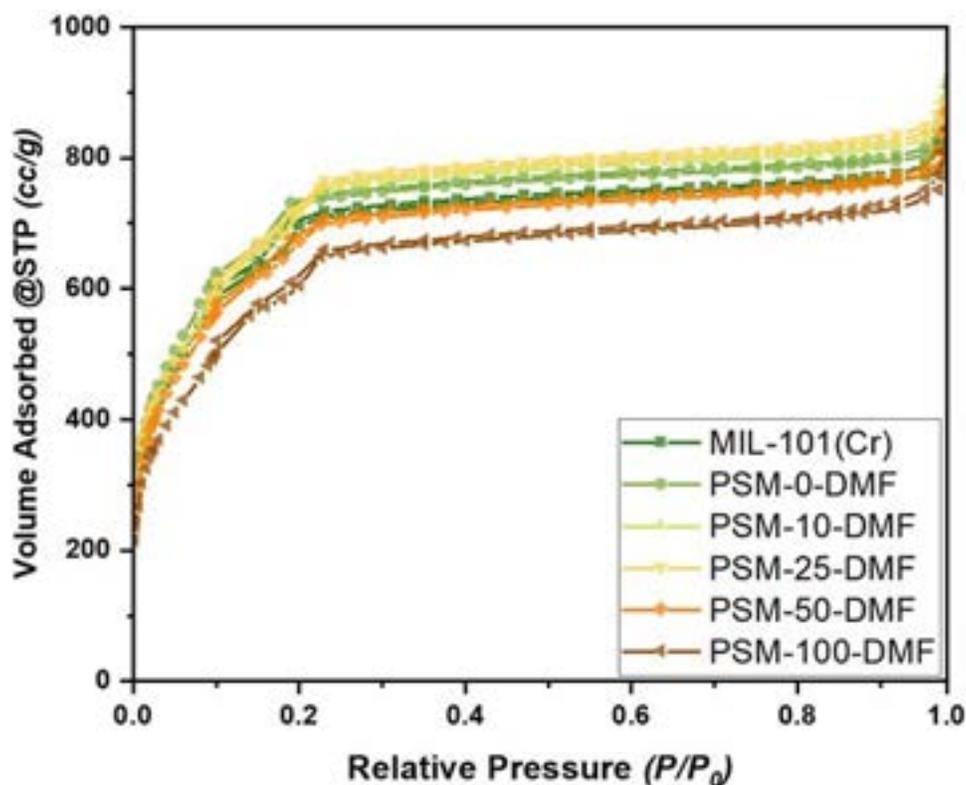
Figure 5.9 N_2 sorption isotherms of the PSM-DMF samples in comparison with the pristine MIL-101(Cr), showing an increased SSA for the samples at lower concentration followed by a noticeable decrease for the samples of higher concentration of $FeCl_3$ in the synthesis solution.

Other characterization techniques were employed to confirm the cation exchange in samples PSM-10-DMF and PSM-25-DMF, and to study more in-depth the samples with a higher Fe concentration (i.e., PSM-50-DMF and PSM-100-DMF) and their decrease in SSA. Also, the mechanism and the reason behind the successful cation substitution using DMF rather than H_2O is still questionable. Raman spectroscopy was once more used to screen all samples, whereby the images obtained from its optical microscope showed an overall change in the color of the PSM-DMF samples (Table 5.10). A gradual colorizing from green to orange

was witnessed parallel to the increase in the Fe concentration: samples PSM-10-DMF and PSM-25-DMF appeared as light orange crystals with no other interfering foreign particles. Their spectra matched the ones of pure MIL-101(Cr), MIL-101(Fe), and PSM-0-DMF, with peaks at 873 cm^{-1}, 1149 cm^{-1}, 1461 cm^{-1}, and 1618 cm^{-1} (Figure 5.10).[358]

Samples PSM-50-DMF and PSM-100-DMF also gave a response typical of the MIL-101 framework. However, the Raman microscope highlighted the presence of some bright red/brown spots (Table 5.10). At these spots, a vibrational response was detected at 227 cm^{-1}, 293 cm^{-1}, 412 cm^{-1}, and 1322 cm^{-1}, comparable to that of the hematite phase (α-Fe$_2$O$_3$, grey-shaded regions in Figure 5.10).[356] The peak at around 610 cm^{-1} of the hematite phase could not be distinguished due to the presence of a broad peak in the 576 cm^{-1} to 785 cm^{-1} range. In this range, only two peaks were recognizable. The first broad peak at around 670 cm^{-1} is similar to that found in the magnetite phase (Fe$_3$O$_4$), with a second sharp one at 738 cm^{-1} usually present in the akageneite phase (β-FeOOH).[356, 364] Besides, other small peaks of inadequate response were recorded at 500 cm^{-1} and 600 cm^{-1} (yellow-shaded regions in Figure 5.10). Hence, samples refluxed with highly concentrated solutions are still prone to the formation of metal oxides. The inclusion of these iron oxide particles explains the minor drop in the measured SSA for samples PSM-50-DMF and PSM-100-DMF. It is worth mentioning that both samples were sensitive to the applied laser, as found in many iron-oxide phases. Increasing the laser power or the collection time at low power leads to a phase change of the oxides to the thermodynamically stable one (hematite).[365]

To better understand the different iron oxide phases formed under the applied conditions, control samples were prepared by refluxing the different FeCl$_3$ solutions in DMF without adding the MOF (Table 5.7). At first, all samples were of bright yellow color, and after refluxing, they all turned into dark orange. Solutions at low concentrations (10 mg and 25 mg FeCl$_3$) were clear, and no product was collected. At higher concentrations, fine particles were suspended in the solutions, and when centrifuged, small traces of a dark red powder for sample PSM-50-DMF and a dark brown one for sample PSM-100-DMF separated (Table 5.7). Despite being of different colors, both powders showed similar vibrational responses using Raman spectroscopy (Figure 5.10). The spectrum of these control samples suggested the formation of multiple iron oxide phases under the applied conditions (mainly hematite "α-Fe$_2$O$_3$", magnetite "Fe$_3$O$_4$", and akageneite "β-FeOOH"), instead of a single one as found when using aqueous solutions.
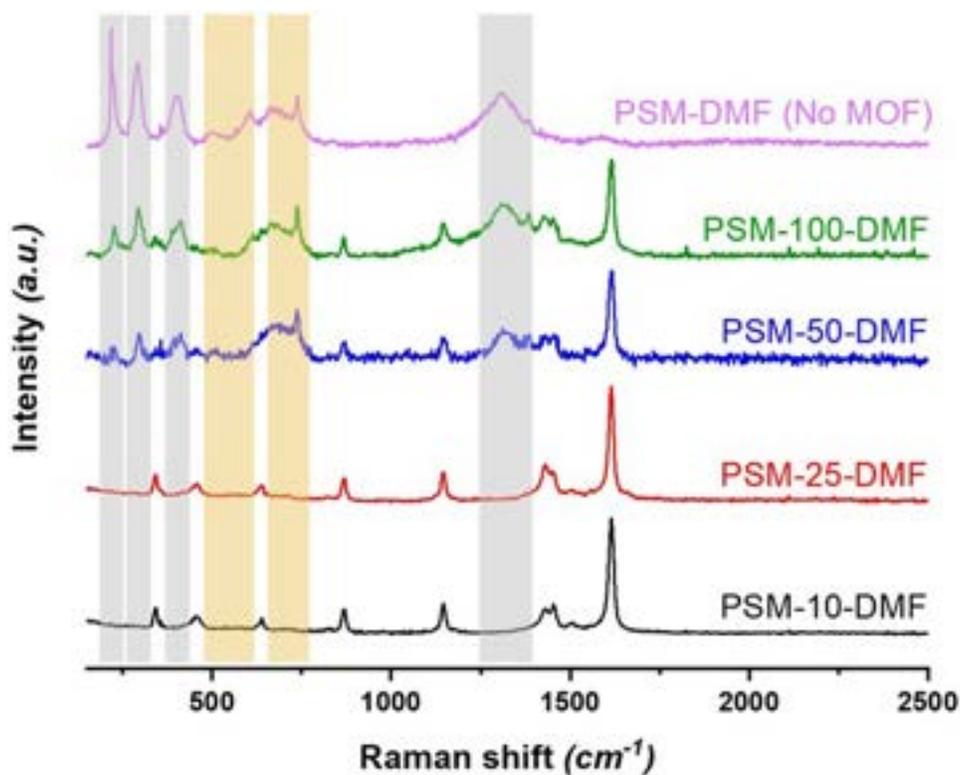
Figure 5.10 Raman spectra of the PSM-DMF samples compared to the spectrum of the control samples (refluxing without incorporating the MOF). Grey shaded regions highlight the bands of α-Fe$_2$O$_3$, while the yellow regions highlight those of magnetite and akageneite.

Surprisingly, the XRD pattern for the control samples was very similar to the 2-line ferrihydrite phase (5Fe$_2$O$_3 \cdot$ 9H$_2$O) with its two broad peaks in the $2\theta = 25°$ - $40°$ and $50°$ - $65°$ range (Figure 5.17).[361, 366] However, a high-intensity sharp peak at around $18.2°$ was also found in the pattern. This peak is usually of low intensity in the diffractograms of magnetite and ferrihydrite (Figure 5.17).[367] It may also belong to the akageneite phase at a slightly shifted position, and the formation of this phase is more probable in such conditions, especially with the presence of the chloride ions within the medium.[368, 369] Over and above, these control samples expressed the ferromagnetic character of the magnetite phase, whereby the powders were attracted when placed in the field of an external neodymium magnet. Therefore, FeCl$_3$ in DMF at 110 °C for 24 h resulted in a mixture of different iron oxide phases, some of which have a distorted structure. However, the formation of one or more of these oxide-hydroxides in the reaction medium may be the reason behind the successful cation exchange in the MIL-101 framework, which shall be studied separately.

SEM was used to screen the PSM-DMF samples, looking for the composition and presence of any foreign particles. At the same magnification level used for the PSM-Cl samples (around 5kx), no foreign particles were noticed in the PSM-DMF samples obtained at low FeCl$_3$

concentration (sample PSM-10-DMF and PSM-25-DMF, Figure 5.11). However, in agreement with the Raman results, samples at higher $FeCl_3$ concentrations (PSM-50-DMF and PSM-100-DMF) included some bigger particles of a different density. Focusing on sample PSM-10-DMF and PSM-25-DMF, electron microscopy at higher magnification (60kx) only detected the octahedral crystals of the MIL-101 framework (Figure 5.11).[83] As in the PSM-Cl samples, elemental mapping of the PSM-DMF samples detected the same five elements Cr, C, O, Cl, and Fe; in addition, nitrogen was also detected. However, they did not follow the same distribution. Reasonably, chromium, carbon, and oxygen were the main structural components introduced initially. As explained earlier, chloride ions were able to perform the anion exchange with the hydroxide ions in the crystals, reflected in the homogenous distribution of the chlorine species throughout the sample. The presence of the nitrogen species, on the other hand, can be attributed to an adsorbed amount of DMF within the pores during the PSE process, or simply due to the replacement of the water molecules at the vertices of the MOF trimer with those of DMF. In contrast, the Fe species were found to be abundantly and homogenously present all over the studied particle, perfectly masking all other species (Figure 5.11). That is, the crystals of the PSM-DMF samples share both metals, and the mixed-metal MIL-101(Cr/Fe) was indeed obtained.

In conclusion, only PSM-DMF samples can be considered a good outcome: their XRD, SSA, Raman, FTIR (Figure 5.21), and SEM results are all matching those of the MIL-101 framework. Hence, the modified PSE method, involving the use of an organic solvent instead of water at the stated conditions, seems to be a working route (up to a limit). Nevertheless, at a high concentration of the metal salt solution, the reaction is also driven towards the formation of different metal oxide phases parallel to the cation substitution (samples PSM-50-DMF and PSM-100-DMF). This would come against Szilágyi's findings in favor of the opposing researchers. However, with the improved method of PSM-DMF, the post-synthetic cation exchange is applicable to MIL-101(Cr). It is also worth mentioning that in Szilágyi's study, and after treating the MOF with the aqueous solution for 72 h, the products were filtered and refluxed with anhydrous tetrahydrofuran (THF) overnight at 100 °C as a secondary activation step.[226] In our case, this step was not performed. Considering that MIL-101(Cr) would be stable in THF as an organic solvent, their process may have helped in dissolving the hematite particles and performing the cation substitution with Fe. This might be the reason behind the successful results of Szilágyi. However, in such a stepwise process, the obtained products would still be contaminated with the metal oxide particles.

The post-synthetic exchange route (PSE), as a subclass of post-synthetic modifications (PSM) of MOFs, is then proved to be another promising and competing technique to prepare mixed-
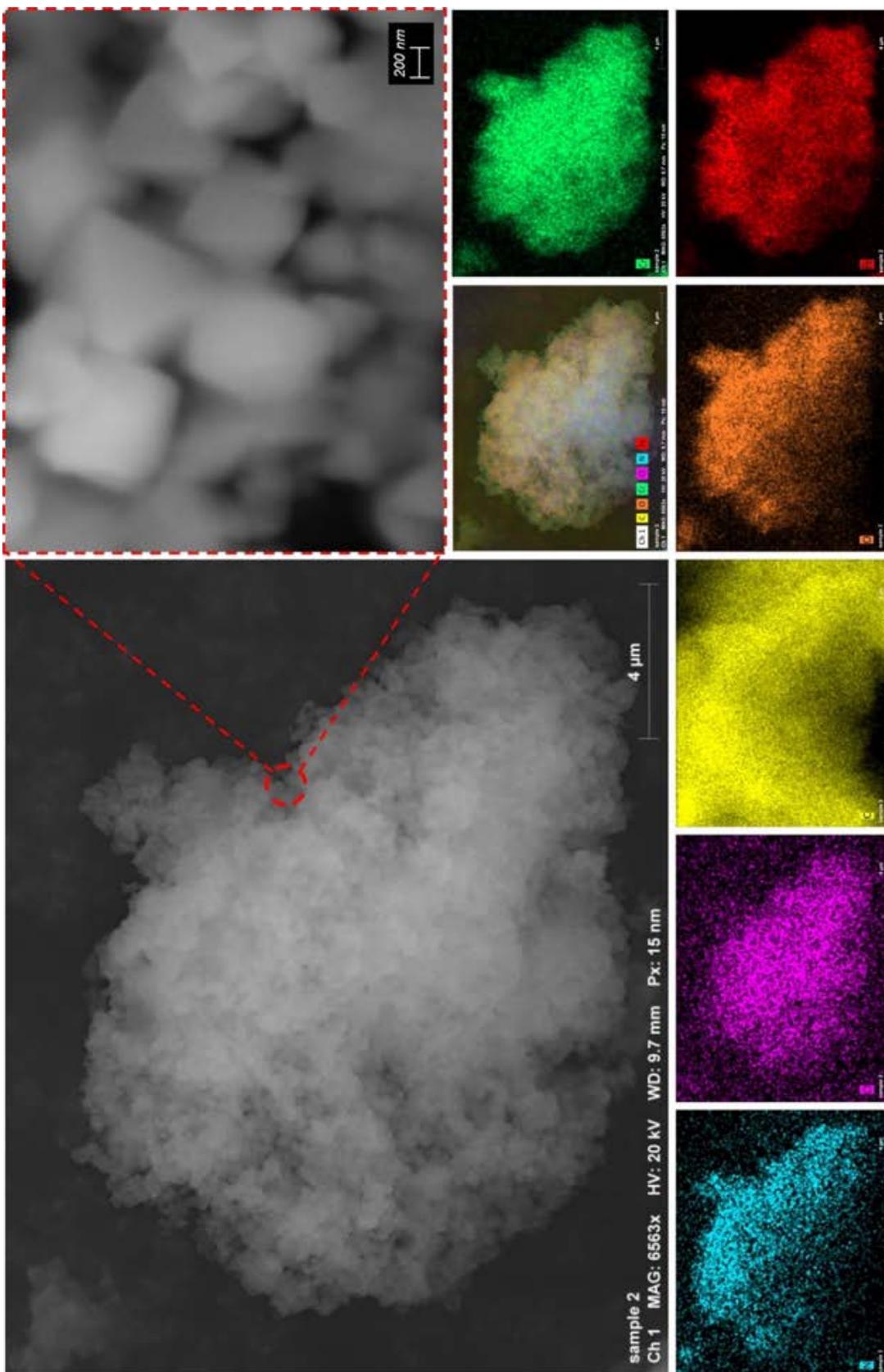
Figure 5.11 Raman spectra of the PSM-DMF samples compared to the spectrum of the control samples (refluxing without incorporating the MOF). Grey shaded regions highlight the bands of α-Fe_2O_3, while the yellow regions highlight those of magnetite and akageneite.

metal structures compared to direct synthesis. Among its advantages, such a route prevents the transformation of the used MOF to one of its framework isomers as well as producing a higher cation-exchanged product. For example, in Bureekaew's et al. attempt to synthesize MIL-101(Cr/Fe) via the hydrothermal route, the SEM images of the sample with 15 mol% initial Fe concentration revealed the presence of some hexagonal MIL-88 crystals among the products.[202, 339] Also, PSE provides more control on the exchanged percentage of the metal cations corresponding to the initially introduced one. For instance, in the attempt of synthesizing MIL-101(Cr/Fe) via the microwave-assisted technique [202], the final product ended up containing < 70 mol% Fe despite being introduced in a much lower percentage around 33 mol% since the applied conditions favored the formation of the product from Fe rather than Cr.[202,339] In addition, the adopted experimental procedure of the PSE process is usually simple. It does not require any sophisticated setup or special tools. Moreover, the exchange process occurs at temperatures lower than that of the synthesis.

Nevertheless, PSE is still known for some of its disadvantages and limitations. Most obviously, it requires longer times versus direct synthesis. Also, at high concentrations of the exchanged metal cations, the formation of metal oxides takes place rather than contributing to the MOF structure. In general, both PSE and direct synthesis are sensitive to the applied reaction conditions and require careful selection of the type of the added metal salt, solvent, reaction temperature, and duration.

5.4 Conclusions

In summary, we arbitrated the dispute of whether or not the SACS method applies to MIL-101(Cr) to obtain the mixed-metal MTV-MIL-101s. Szilágyi's method that recurs to aqueous solutions of metal(III) chloride (samples PSM-Cl) yielded a mixture of α-Fe_2O_3 with the pristine MOF crystals, instead of promoting metal-ion substitution, regardless of the initial Fe precursor ion concentration. Moreover, increasing the process time from three to seven days or using different metal salt (nitrate as an alternative to chloride) yielded the same result. Therefore, the post-synthetic cation exchange for the MIL-101(Cr) framework cannot be performed under such conditions in aqueous media. Supported by characterization techniques (Raman, XRD, SEM-EDX, N_2 sorption), our data align with the findings of the opposing studies, confirming the stability and kinetic inertness of the chromium ion sphere in water. On the other hand, by changing the refluxing solvent to DMF, the cation substitution was successful. As a result, mixed-metal MIL-101(Cr/Fe) was obtained through refluxing MIL-101(Cr) with a solution of $FeCl_3$ in DMF at 110 °C for 24 h. Adopting these modified conditions results in a bimetallic MIL-101(Cr/Fe) with a maximum percentage of 31 wt%

metal ion substitution. A higher concentration induces the formation of different metal oxides simultaneously with the cation exchange process. These results prove that mixed-metal MIL-101s are achievable via the simple PSE technique; however, the used solvent is the most crucial factor to consider, together with the reaction conditions.

5.5 Conflicts of interest

There are no conflicts to declare.

5.6 Acknowledgment

5.7 Supporting Information

5.7.1 Experimental details

All synthetic manipulations were performed under ambient atmosphere, unless otherwise stated.

Materials

Chromium(III) nitrate nonahydrate ($Cr(NO_3)_3 \cdot 9H_2O$, 99%), 1,4-Benzenedicarboxylic acid "terephthalic acid" (H_2BDC, 98%), Iron(III) chloride hexahydrate ($FeCl_3 \cdot 6H_2O$, 97%), Iron(III) nitrate nonahydrate ($Fe(NO_3)_3 \cdot 9H_2O$, 98%), and N,N-dimethyl formamide (anhydrous DMF, 99.8%) were purchased from Sigma-Aldrich, Canada. Acetone ($\geq 99.5\%$) and Ethanol (EtOH, 98%) were purchased from Fischer Scientific, USA.

All chemicals were used as received with no further processing. All glassware was washed with conc. HCl or aqua regia after each experiment to get rid of any metal oxide contamination present.

Methods

Synthesis of MIL-101(Cr):

MIL-101(Cr) was synthesized hydrothermally following Bromberg's method with slight modifications.[97] The hydrothermal HF-free synthesis took place in a Parr's 200-ml large capacity acid digestion vessel (Parr Instrument Company, Model# 4748A) to provide a sufficient MOF amount for the whole process of post-synthetic modification (PSM) and to ensure that all samples were from the same batch. First, 10 g $Cr(NO_3)_3 \cdot 9H_2O$ (25 mmol) and 4.15 g H_2BDC (25 mmol) were mixed and added to 100 ml of deionized water. The solution was then stirred for 15 min resulting in a dark blue-colored suspension of a pH around 2.5. Next, the suspension was transferred into the Teflon-lined autoclave bomb and then heated to 218 °C in a conduction oven. The reaction was held at this temperature for 18 h without stirring. After this time, the bomb was left to cool down gradually to room temperature inside the oven over a period of 5 h - 6 h.

The reaction yielded a sea green-colored suspension of a pH around 0.5. The powders were collected through centrifugation at a speed of 10,000 rpm for 10 min. The separated solids were then washed with water, ethanol, and DMF. Activation took place by keeping the MOF in DMF overnight at 75 °C. After that, the activated MOF was washed with ethanol and acetone before drying at 60 °C overnight.

Synthesis of MIL-101(Fe):

MIL-101(Fe) was synthesized via the microwave-assisted technique for the purposes of comparison. Following Metzler-Nolte's findings, a diluted solution of iron(III) chloride and H_2BDC in DMF with a ratio of 1:1:565, respectively, would drive the reaction towards the formation of the MIL-101 phase.[132] In addition, with the metal ion in excess with respect to the organic linker, the MIL-101 phase would be predominant. The synthesis took place in a 30 ml glass vial of Anton Paar's Monowave 400 microwave (MW) reactor. In a typical procedure, 0.675 g $FeCl_3 \cdot 6H_2O$ (2.45 mmol) and 0.206 g H_2BDC (1.24 mmol) were directly weighed into the reaction vials. Then, 15 ml DMF was added to the vial, and it was magnetically stirred for 30 min at room temperature until the complete dissolution of the precursors, resulting in a pale orange-colored solution. The vial was then covered with a Teflon-lined silicon septum and placed into the reaction chamber of the MW reactor. The reaction proceeded, holding a temperature of 150 °C for 10 min under constant stirring (500 rpm). After the reaction, the synthesis vessel was cooled to room temperature by air circulation at 6 bar inside the MW reactor. The reaction yielded an orange-colored suspension. The powders were collected through centrifugation at a speed of 10,000 rpm for 10 min. The separated

solids were then washed with DMF and ethanol and then dried at 80 °C.

Post-synthetic cation exchange:

Following Szilágyi's procedure, PSM of the activated MOF was achieved through the solvent-assisted cation substitution method (SACS).[226] In such a process, 100 mg MIL-101(Cr) was refluxed with 100 ml of $FeCl_3 \cdot 6H_2O$ aqueous solutions at 100 °C for 72 h. The amount of $FeCl_3 \cdot 6H_2O$ in 100 ml deionized water was 10 mg for the initial experiments. Then, we increased the concentration to 25, 50, and 100 mg to probe the maximum achievable exchanged capacity. Samples were then centrifuged, washed with deionized water and ethanol. Drying took place at 85 °C overnight. The process was repeated for a longer refluxing time of seven days. Besides, we also adopted $Fe(NO_3)_3 \cdot 9H_2O$ instead of the chloride to investigate the effect of a different precursor.

In addition to the process duration and the type of precursors, the reaction solvent was also varied. We selected DMF as a refluxing solvent adopting Kholdeeva's conditions for MIL-101(Fe) synthesis. 100 mg MIL-101(Cr) was refluxed with 100 ml DMF at the same concentration of $FeCl_3 \cdot 6H_2O$ (10 mg, 25 mg, 50 mg, and 100 mg). Then, the solution was kept for 24 h at 110 °C. The same separation and washing steps were followed as before, whereby the products were centrifuged at 10,000 rpm for 10 min, then washed with DMF and ethanol. The samples were dried at 80 °C overnight.

All samples were kept in a desiccator under vacuum until characterization.

5.7.2 Characterization

Powder X-ray diffraction (PXRD) patterns were recorded on a Bruker D8 Advance X-ray diffractometer equipped with LYNXEYE linear position-sensitive detector (Bruker AXS, Madison, WI). Data was collected over a 2θ= 3 ° - 100 ° range at increments of 0.02 ° and a scanning rate of 0.2 ° s^{-1}. In the diffractometer, a Cu-Kα source (λ= 1.5406 Å) was operated at a tube voltage and a current of 40 kV and 40 mA, respectively. Samples for PXRD were prepared by placing a thin layer of samples on a zero-background silicon crystal plate supported on a cup. For multiscan experiments to test MOF stability, we conducted 350 scans in which data was collected over a 2θ= 3 ° - 50 ° range at increments of 0.02 ° each for 12 min.

Fourier-transform Infrared (FTIR) spectra were collected using the Perkin Elmer 65 spectrophotometer equipped with an ATR diamond. With the high-efficiency ATR technique, a full range scan (4000 cm^{-1} - 450 cm^{-1}) was performed with a resolution of 4 cm^{-1}, and the data were averaged over 32 scans.

UV-Vis spectra were collected using a Thermo Scientific Evolution 220 UV-Vis spectropho-tometer equipped with the integrated sphere accessory for powder samples diffuse reflectance measurements. A full wavelength scan (220 nm - 1100 nm) was performed on all samples. The blank sample holder covered with Spectralon® was used as the reference. 50 mg of each sample was weighed into the equivalent sample holder with a spring to press the sample powders homogeneously. All samples were measured in the specular excluded (SPEX) mode with the sample holder window to be in direct contact with the walls of the integration sphere. The embedded Kubelka-Munk setting was used to convert reflectance measurements into equivalent absorption spectra.

X-ray fluorescence analysis (XRF, Benchtop Epsilon 4 - Malvern Panalytical) was employed to detect the elemental composition of all samples. Cr and Fe were the elements specified to be detected, and results were given in the normalized elemental percentage. For each sample, 100 mg was weighed into the 35-mm P1 cup assembled with the circular Mylar film of 3.5 μm thickness.

Raman spectra were obtained using a WITec alpha300R access confocal Raman microscope equipped with a motorized stage, CCD detector, and 1800 grooves mm^{-1} optical grating. In addition, the instrument was equipped with a green Co laser source of a 532 nm wavelength. Measurements were done using three collecting lenses (10x, 50x, and 100x). Powder samples were pressed against a glass microscope slide. Spot analysis was performed over some selected area in each sample with an accumulating response of 20 scans, each of a signal integration time of 10 s to differentiate between different phases included. Spectra were collected in the region from 100 cm^{-1} to 3500 cm^{-1}, with a resolution of 1 cm^{-1}. Besides, area analysis over a square area of a side length of 10 μm was also recorded to get a collective response for the whole sample. The laser power was in the range of 0.5 mW - 0.7 mW to avoid any local heating induced by the laser.

N$_2$ sorption experiments were carried out to measure the textural properties of the samples. Measurements took place at 77 K on the Autosorb iQ analyzer supplied from Quantachrome Instruments (USA). We used 100 mg of each sample. Sample outgassing took place at 170 °C for 20 h under dynamic vacuum. Finally, the multi-point Brunauer-Emmett-Teller (BET) and the Langmuir methods were applied to estimate all samples' specific surface area (S$_{BET}$, S$_{Langmuir}$) in the P/P$_0$ range $\leq$ 0.25. On the other hand, the Barrett-Joyner-Hallender (BJH) and the Density-functional theory (DFT) calculations were used for the pore volume estimation at the point of P/P$_0$= 0.95.

A scanning electron microscope (SEM, Benchtop Hitachi TM 3030 Plus) equipped with the energy-dispersive X-ray (EDX) detector screened the surface structure and the compositions

of all the products. Samples were dispersed on double-sided carbon tape and mounted on an aluminum stub. Mainly, the instrument was operated on the back-scattered electron mode to distinguish between the different densities among the powders. A Carl Zeiss scanning electron microscope (Model: EVO MA 10, Germany) operated on the secondary electron mode was used to inspect the morphology of the obtained crystals at a higher magnification. The instrument detected the elements automatically, as well as their distribution and percentage abundance with respect to the mass ratio.

5.7.3 Results
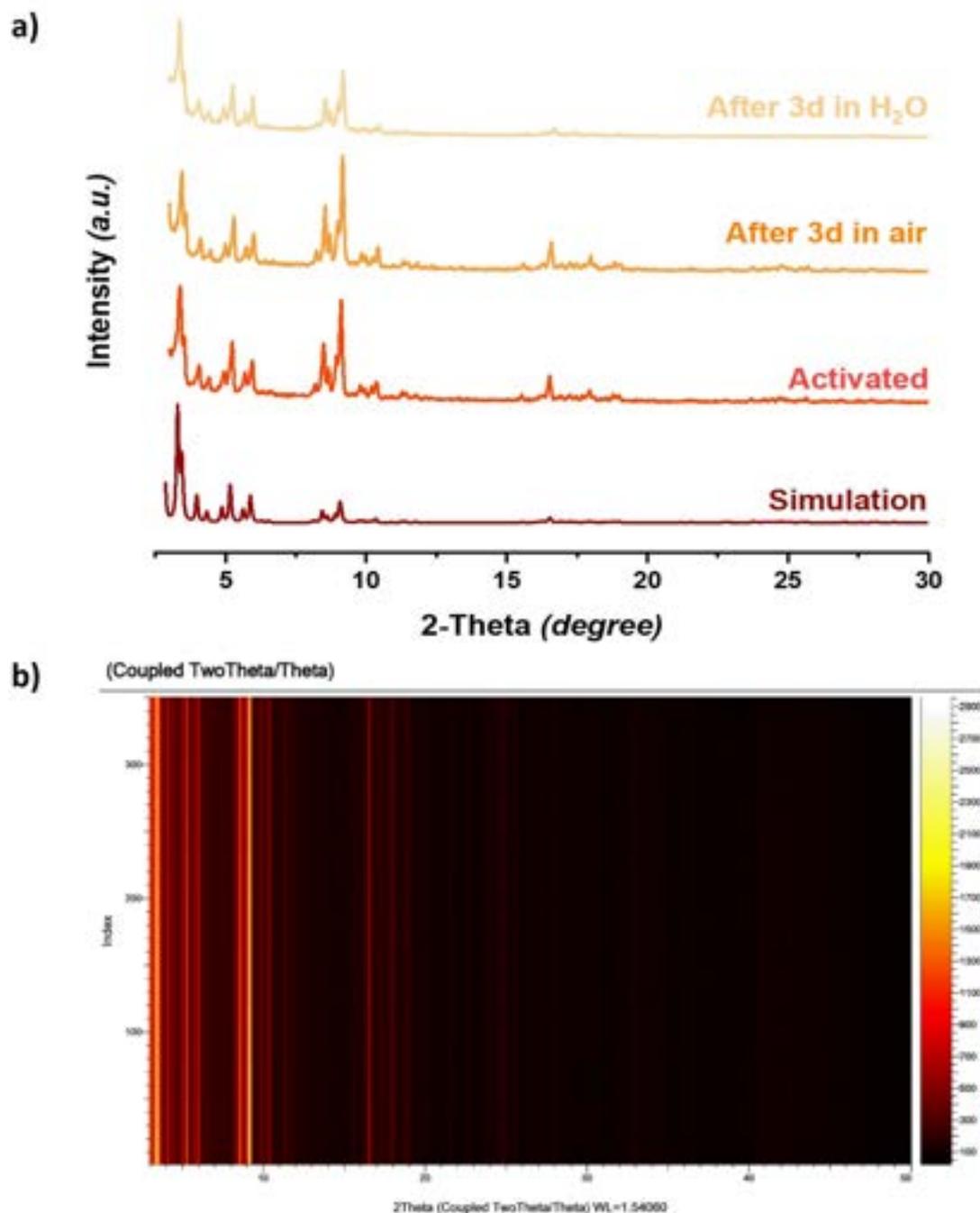
Figure 5.12 Chemical stability investigation on the MIL-101(Fe) framework. a) XRD patterns of the MIL-101(Fe) framework after prolonged exposure to air and water. (Maroon: Simulation "reproduced From CCDC file: OCUNAC", Dark Orange: as-synthesized/ acti-vated MIL-101(Fe), Light Orange: subjected to ambient atmosphere for 72 h, Beige: soaked in boiling water for 72 h). b) Two-dimensional XRD pattern for the MIL-101(Fe) sample after treatment with boiling water, followed by consecutive XRD stability scans for 72 h under air. Brighter lines indicate high-intensity accumulations at the corresponding 2θ.

Table 5.3 Application of the Post-synthetic modification (PSM) method on MIL-101(Cr) using aqueous solutions of FeCl$_3$

	10 mg FeCl$_3$ (PSM-10-Cl)	25 mg FeCl$_3$ (PSM-25-Cl)	50 mg FeCl$_3$ (PSM-50-Cl)	100 mg FeCl$_3$ (PSM-100-Cl)	Notes
Aqueous Sol.					____
+ 100 mg MOF					____
After reflux (72 h)					____
After Washing					Top view of the centrifuge tube
After Drying					MIL-101(Cr) / MIL-101(Fe)

Table 5.4 Refluxing aqueous solutions of FeCl$_3$ without the addition of MIL-101(Cr)

	10 mg FeCl$_3$	25 mg FeCl$_3$	50 mg FeCl$_3$	100 mg FeCl$_3$
Aqueous Sol.				
After reflux (72 h) No MOF				
After Drying	———	———		

Table 5.5 Application of the Post-synthetic modification (PSM) method on MIL-101(Cr) using aqueous solutions of $Fe(NO_3)_3$

	10 mg $Fe(NO_3)_3$ (PSM-10-NO$_3$)	25 mg $Fe(NO_3)_3$ (PSM-25-NO$_3$)	50 mg $Fe(NO_3)_3$ (PSM-50-NO$_3$)	100 mg $Fe(NO_3)_3$ (PSM-100-NO$_3$)
Aqueous Sol.				
+ 100 mg MOF				
After reflux (72 h)				
After Washing				
After Drying				
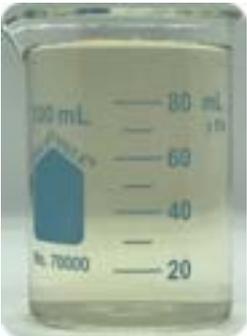
Table 5.6 Application of the Post-synthetic modification (PSM) method on MIL-101(Cr) using solutions of FeCl₃ in DMF

	10 mg FeCl₃ (PSM-10-DMF)	25 mg FeCl₃ (PSM-25-DMF)	50 mg FeCl₃ (PSM-50-DMF)	100 mg FeCl₃ (PSM-100-DMF)
Solution in DMF				
+ 100 mg MOF				
After reflux (24 h)				
After Washing				
After Drying				
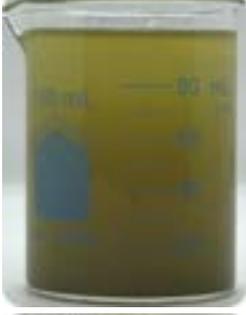
Table 5.7 Refluxing solutions of FeCl$_3$ in DMF without the addition of MIL-101(Cr)

	10 mg FeCl$_3$	25 mg FeCl$_3$	50 mg FeCl$_3$	100 mg FeCl$_3$
Solution in DMF				
After reflux (24 h) No MOF				
After Drying	———	———		

a)

b)

c)
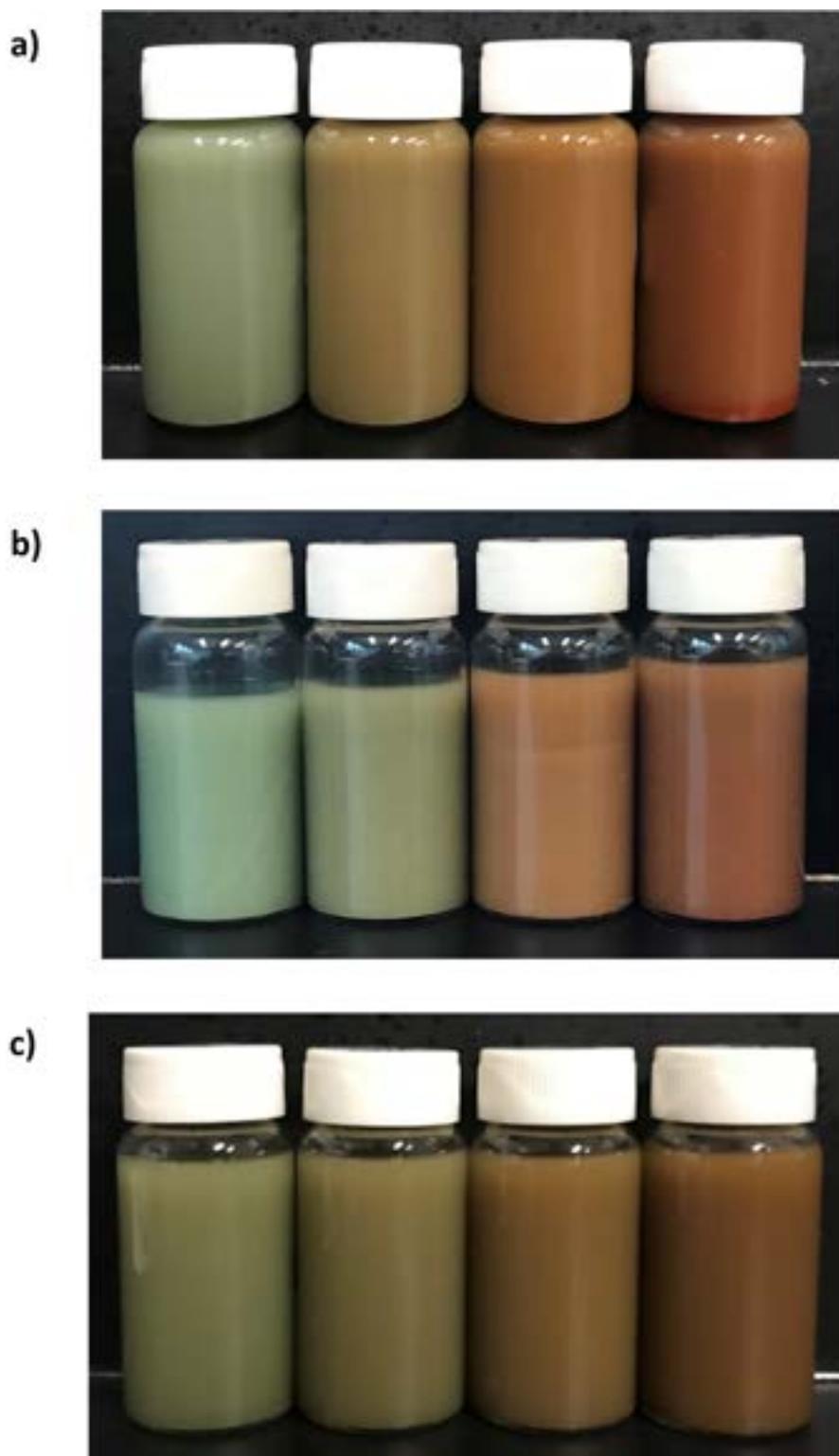
Figure 5.13 PSE samples before drying, showing a different color each. a) PSM-Cl samples. b)PSM-NO$_3$ samples. c) PSM-DMF samples.

5.7.4 Other results

PXRD

First, characterization via PXRD was performed to ensure the achievement of the MIL-101(Cr) framework by the HF-free method of Bromberg, whereby the resulting pattern (Figure 5.14, "Red") was very similar to the simulated one (Figure 5.14, "Black"). Then, PXRD was applied to the obtained powders of the PSE method to ensure that the MIL-101 structure is still preserved with no transformation to any other framework isomer.

Starting with the 10 mg $FeCl_3$ sample (PSM-10-Cl), the pattern of this sample (Figure 5.14, "Blue") showed a nearly flat background, and all the high-intensity peaks were recognized in the 2θ= 3 ° - 10 ° range. The pattern was very similar to that of the prepared MIL-101(Cr) with the main diffraction peaks at around 2θ = 3.2 °, 3.9 °, 5.1 °, 5.8 °, 8.3 °, and 9.0 °.
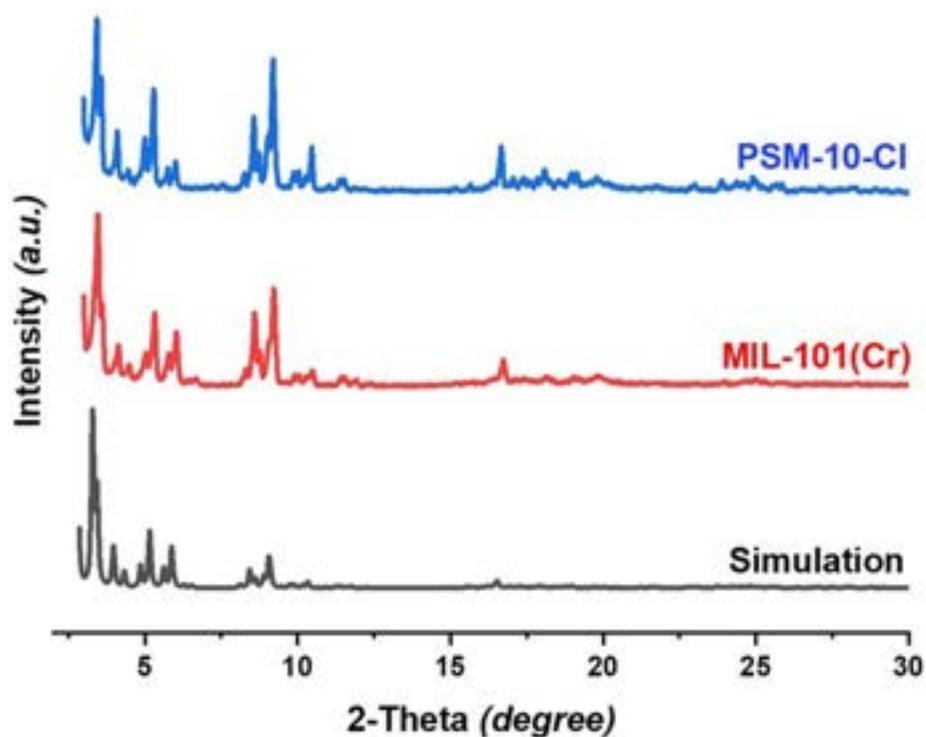
Figure 5.14 XRD patterns of the MIL-101(Cr) before and after reflux. (Black: simulation "reproduced From CCDC file: OCUNAC", Red: as-synthesized MIL-101(Cr), Blue: products after refluxing with an aqueous sol. of 10 mg $FeCl_3$ for 72 h at 100 °C.)
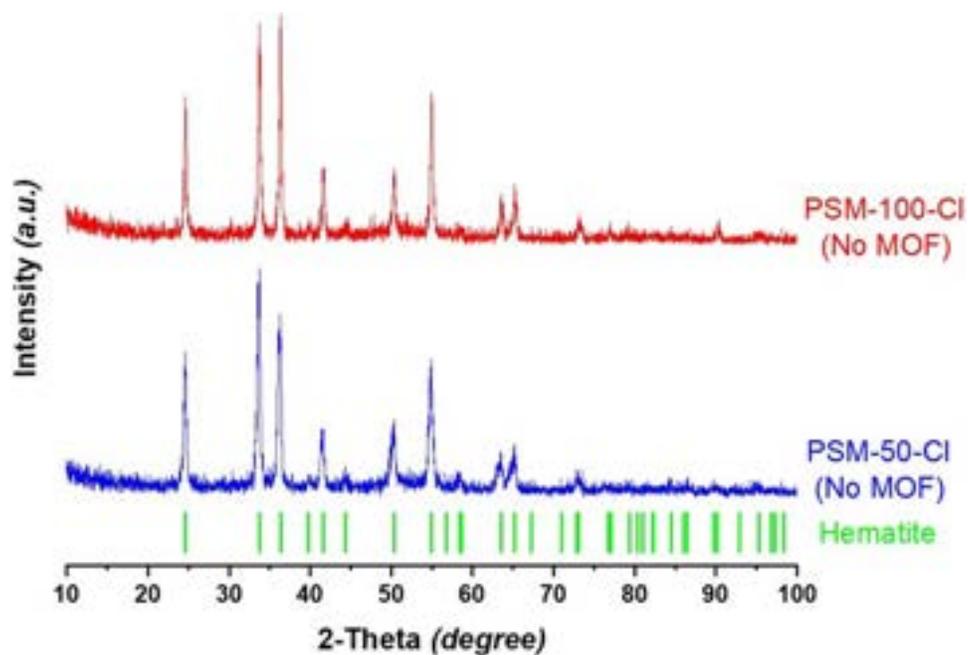
Figure 5.15 XRD patterns of the PSM-Cl control samples refluxed without adding the MOF compared to the diffraction peaks of hematite "light-green".
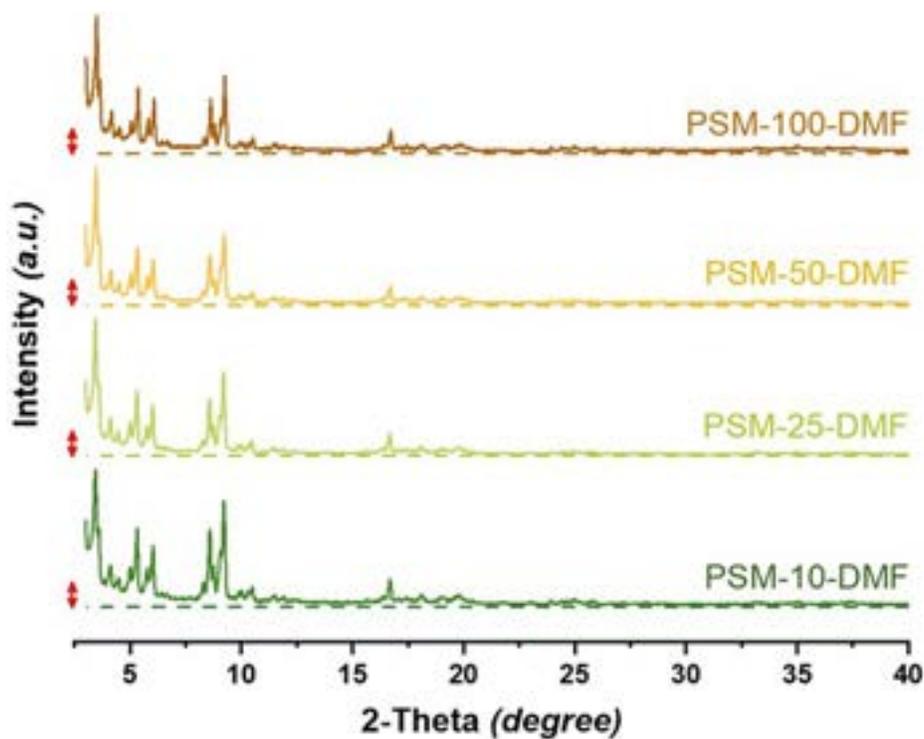
Figure 5.16 XRD patterns of the PSM-DMF samples in the $2\theta = 3\,°$- $40\,°$ range (PSM-10-DMF "Dark green" to PSM-100-DMF "Brown").
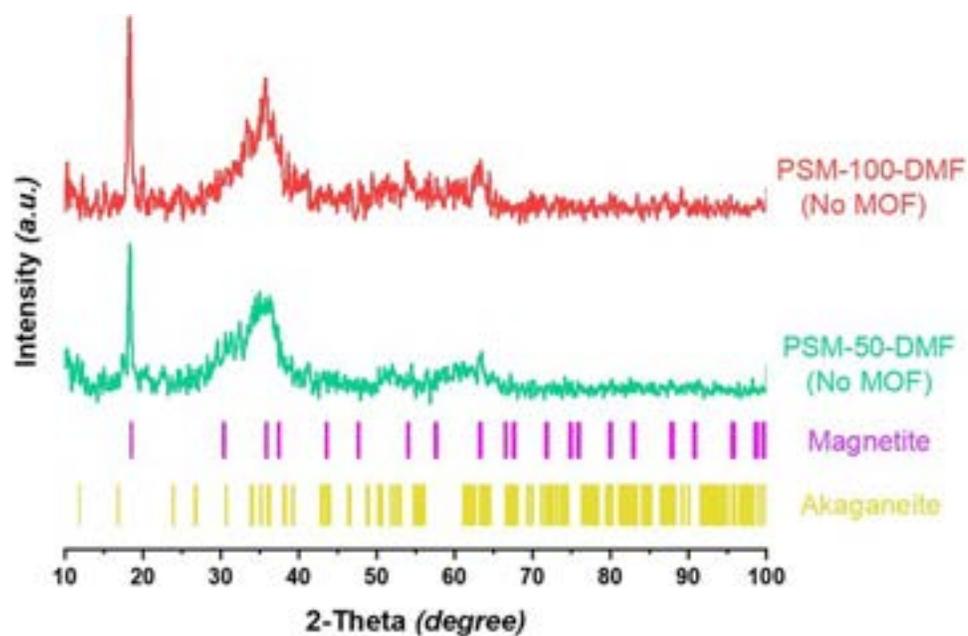
Figure 5.17 XRD patterns of the PSM-DMF control samples refluxed without adding the MOF compared to the diffraction peaks of magnetite "magenta" and akaganeite "yellow".

UV-Vis DRS

UV-Vis diffuse reflectance spectroscopy (DRS) is a sensitive characterization technique in the case of mixed-metal MOFs built from different 3d elements in their powder form.[226,341] In such a technique, transition-metal MOFs show characteristic absorption in the visible range corresponding to the metals' d-d electrons excitation, which is the main reason for the various colors acquired by these MOFs based on their different metal centers. Thus, such a technique can be used to qualitatively detect the substitution of the structure's main metal constituent with other cations of similar nature.

The UV-Vis spectrum of MIL-101(Cr) showed three absorption bands in the UV and visible regions (Figure S3). The absorption peak in the UV range around 288 nm results from the internal ligand $\pi - \pi^*$ charge transition (ILCT). The other two peaks in the visible range around 439 nm and 593 nm are attributed to electronic transitions between the internal energy levels of Cr trimer, expressing its light sea-green color. On the other hand, the absorption bands of MIL-101(Fe) in the UV and visible range (220 nm - 600 nm) were convoluted showing a broad peak. However, a weak absorption could be witnessed around 957 nm within the near IR range.
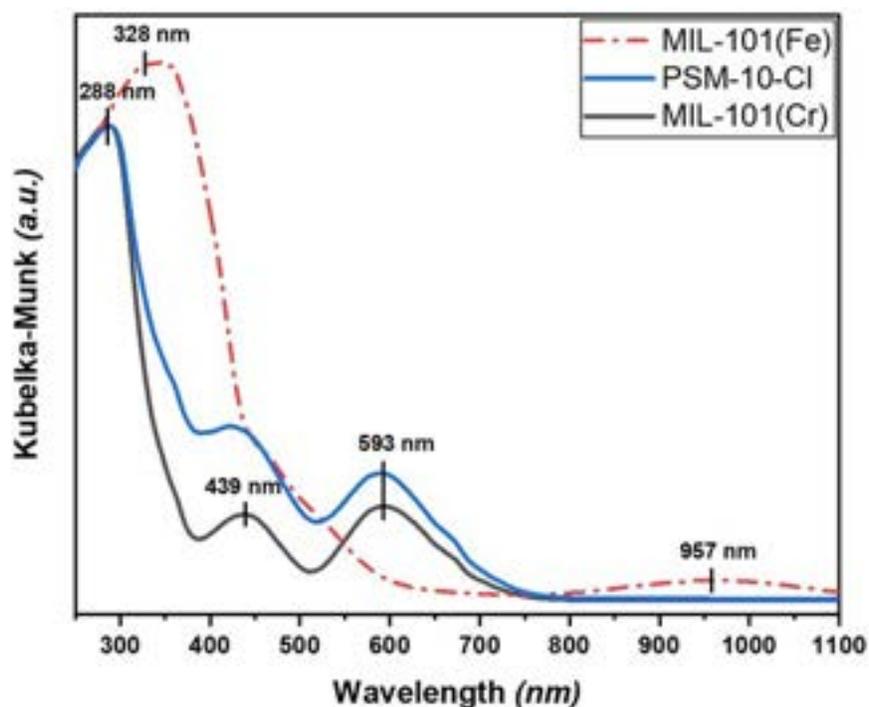
Figure 5.18 UV-Vis spectrum of the PSM-10-Cl (blue solid line) in comparison with the as-synthesized MIL-101(Cr) (black solid line) and MIL-101(Fe) (red dashed line).

The spectrum of the PSM-10-Cl sample was comparable to that of MIL-101(Cr), with its distinguishable absorption in the UV-Vis range and no other absorption at longer wavelengths. Nevertheless, the spectrum revealed a higher absorption in the visible and near UV range between 330 nm and 750 nm. In addition, the peak at around 439 nm showed some broadness compared to the pristine sample, and the peak around 593 nm was slightly shifted (blue-shift) towards shorter wavelengths.

FTIR

FTIR was used to confirm that the composition of the MIL-101 structure is still maintained after reflux and the incorporation of Fe(III) into the structure through PSM. The vibrational spectrum of the 10 mg FeCl$_3$ sample (PSM-10-Cl) was almost typical to that of pristine MIL-101(Cr).[229, 253, 350, 370] First, the vibrations of the carboxylate group bonds and the aromatic ring were recognized within the 1750 cm^{-1} - 1250 cm^{-1} range. Peaks in the 1250 cm^{-1} to 600 cm^{-1} region are attributed to the C-H bonds of the ring. In the region below 600 cm^{-1}, the metal-O bonds' vibrations were detected.

The antisymmetric and symmetric stretching of the dicarboxylate groups matched the absorption bands at around 1631 cm^{-1} and 1398 cm^{-1}, respectively.[88, 370] The stretching of the aromatic ring (C=C) bonds was assigned to the peak at 1507 cm^{-1}.[229, 350, 371] In addition, the peaks at around 1017 cm^{-1}, 744 cm^{-1}, 1166 cm^{-1}, and 883 cm^{-1} are attributed to the in-plane and out-of-plane bending of the (C-H) bond.[229, 253, 350, 371] In both spectra of pristine MIL-101(Cr) and PSM-10-Cl, the Cr-O bonds' absorption could be detected at around 589 cm^{-1}.[229, 350] On the other hand, the spectrum of the PSM-10-Cl sample showed a recognizable shoulder at around 550 cm^{-1} matching with the Fe-O peak in pristine MIL-101(Fe).[229, 372, 373]
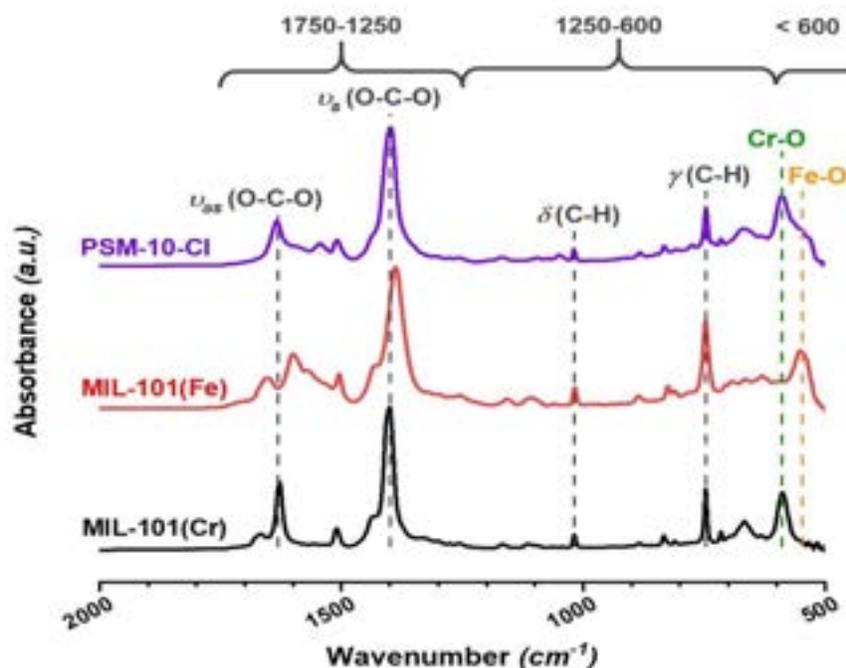
Figure 5.19 FTIR spectra of the as-synthesized MIL-101(Cr) (black) and MIL-101(Fe) (red) compared to that of the PSM-10-Cl sample (magenta), showing the shoulder at around 550 cm^{-1}, corresponding to the Fe-O bond vibrations.
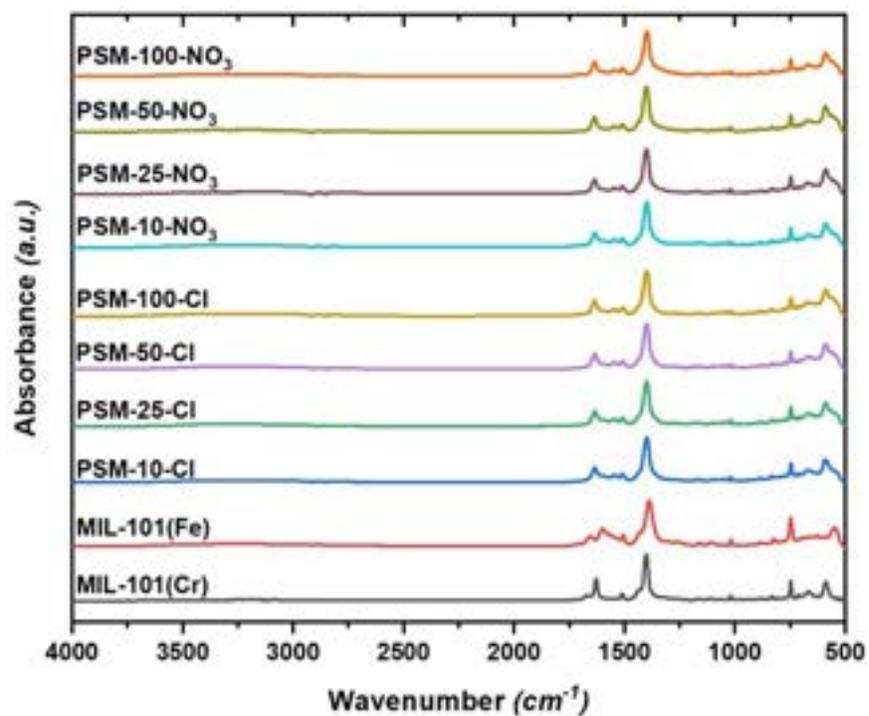
Figure 5.20 FTIR spectra of the PSM samples in aqueous solutions.
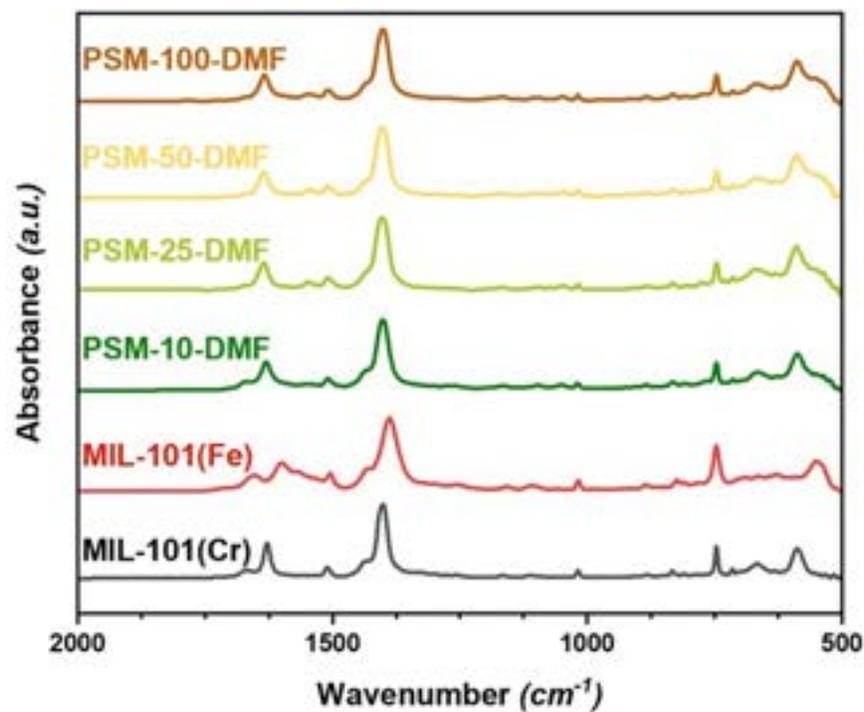
Figure 5.21 FTIR spectra of the PSM-DMF samples.

Table 5.8 Elemental composition of all samples after the PSE process

Sample	PSM-0-Cl		PSM-10-Cl		PSM-25-Cl		PSM-50-Cl		PSM-100-Cl	
Technique	XRF	SEM	XRF	SEM	XRF	SEM	XRF	SEM	XRF	SEM
Cr	99.9	99.9	82.9	85.9	71.1	76.8	55.8	59.5	43.9	46.4
Fe	0.1	0.1	17.1	14.1	28.9	23.2	44.2	40.5	56.1	53.6

Sample	PSM-0-NO$_3$		PSM-10-NO$_3$		PSM-25-NO$_3$		PSM-50-NO$_3$		PSM-100-NO$_3$	
Technique	XRF	SEM	XRF	SEM	XRF	SEM	XRF	SEM	XRF	SEM
Cr	99.9	99.9	86.6	88.8	75.2	78.1	54.7	58.3	43.9	47.1
Fe	0.1	0.1	13.4	11.2	24.8	21.9	45.3	41.7	56.1	52.9

Sample	PSM-0-DMF		PSM-10-DMF		PSM-25-DMF		PSM-50-DMF		PSM-100-DMF	
Technique	XRF	SEM	XRF	SEM	XRF	SEM	XRF	SEM	XRF	SEM
Cr	99.9	99.9	81.1	82.4	68.2	69.6	53.2	54.9	39.3	41.8
Fe	0.1	0.1	18.9	17.6	31.8	30.4	46.8	45.1	60.7	58.2

Raman

Table 5.9 Raman microscope images of PSM-Cl samples at different magnifications

Sample	10x	50x	100x
MIL-101(Cr)			
MIL-101(Fe)			
PSM-10-Cl			
PSM-25-Cl			
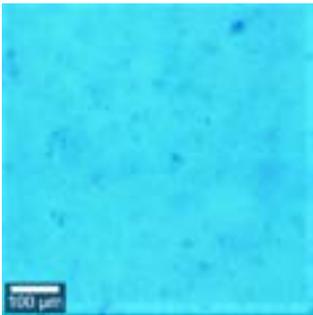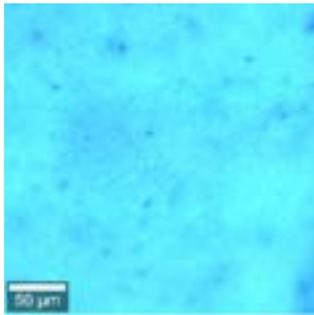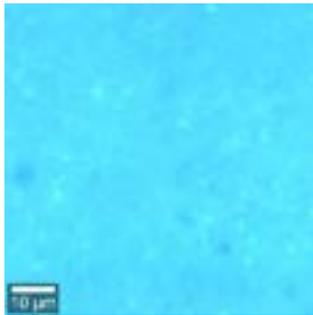
	100 μm	50 μm	10 μm
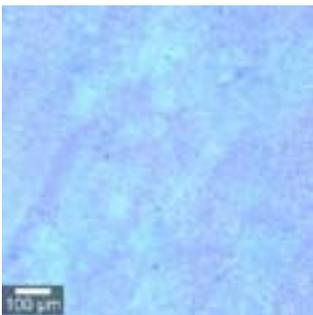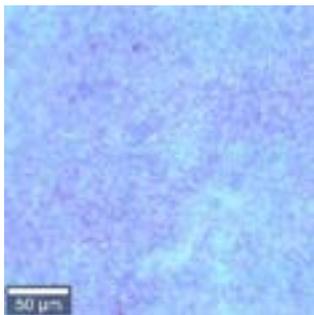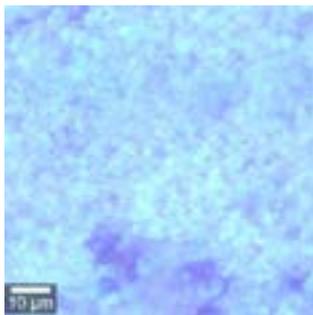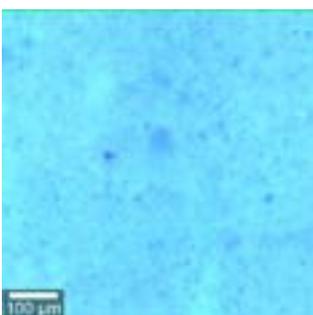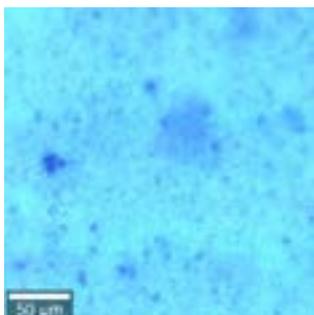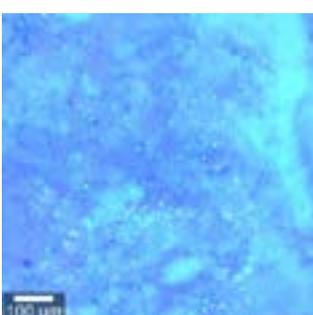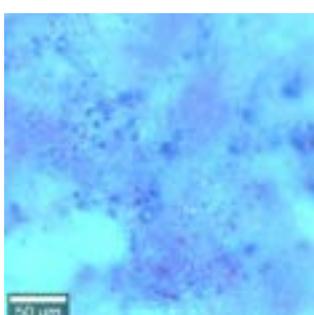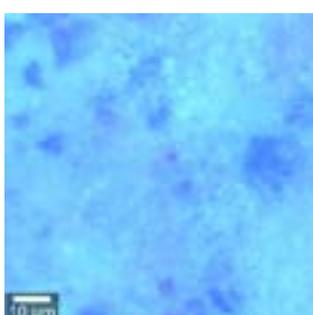
PSM-50-Cl
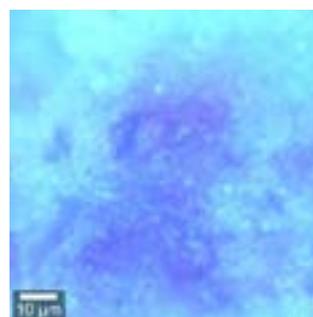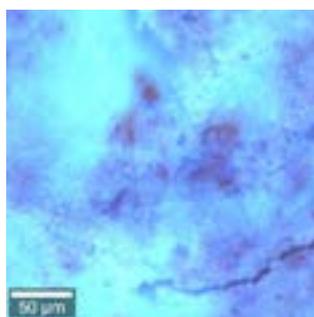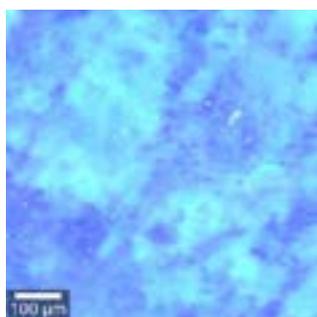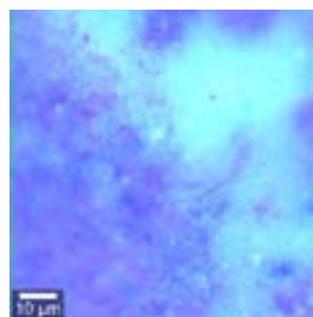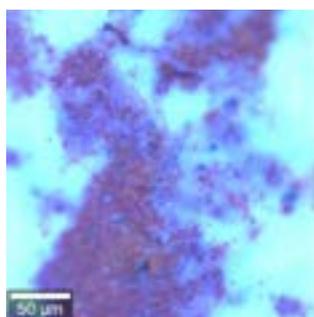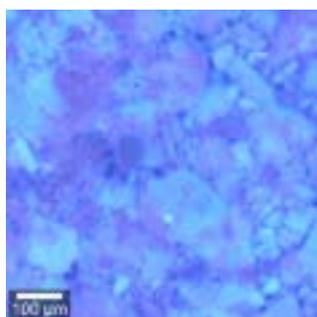
PSM-100-Cl

**PSM-Cl
No MOF
(Hematite)**
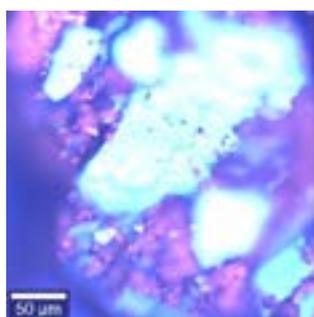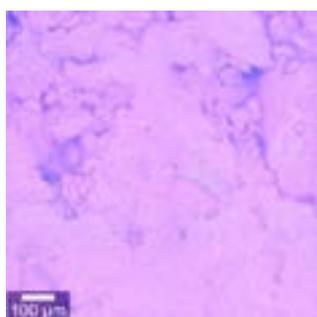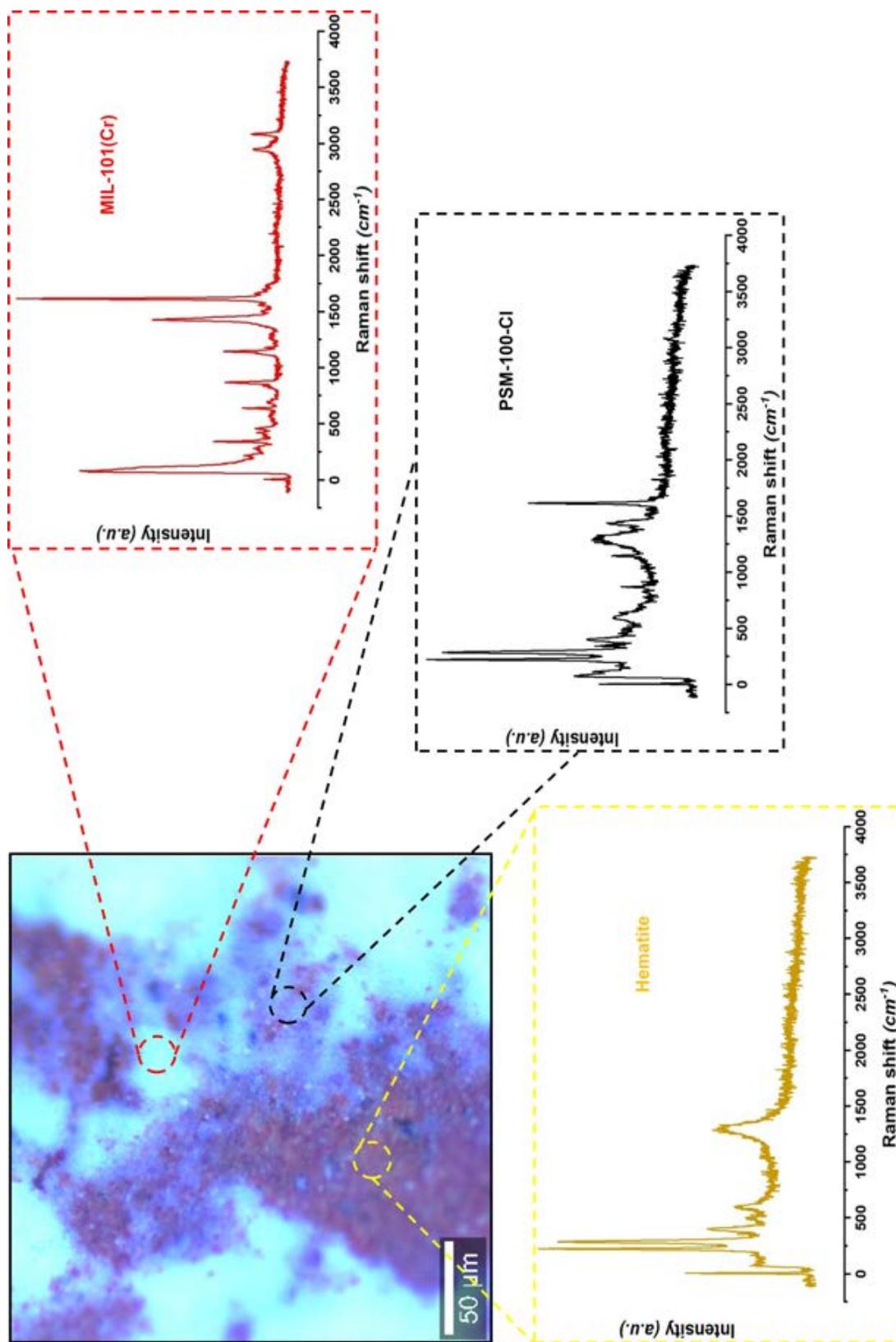
Figure 5.22 Spot analysis of different regions within sample PSM-100-Cl.

Table 5.10 Raman microscope images of PSM-DMF samples at different magnifications

Sample	10x	50x	100x
PSM-0-DMF			
PSM-10-DMF			
PSM-25-DMF			
PSM-50-DMF			
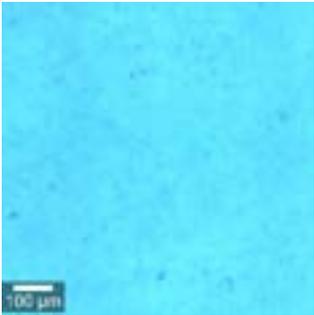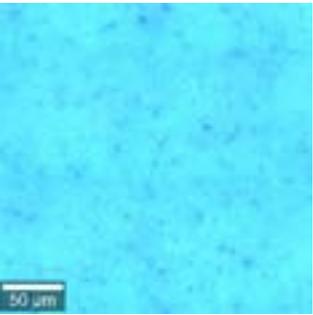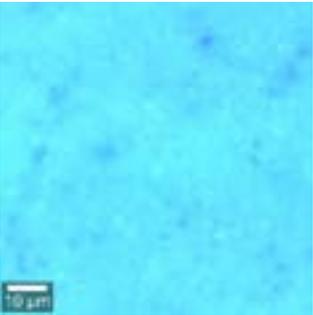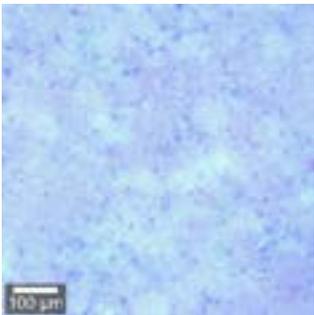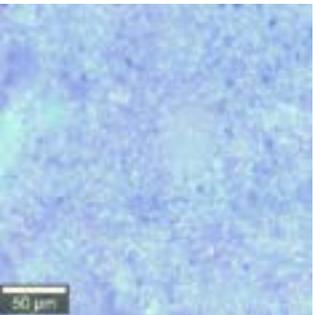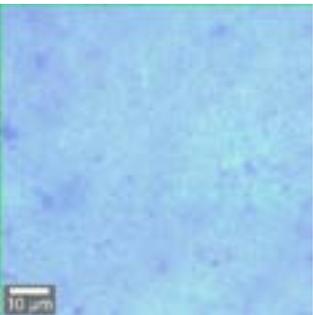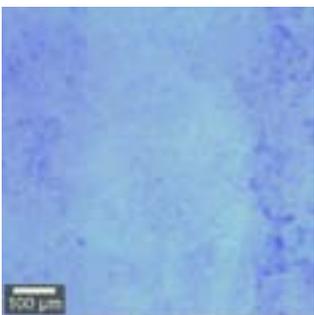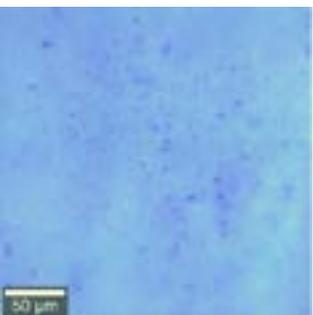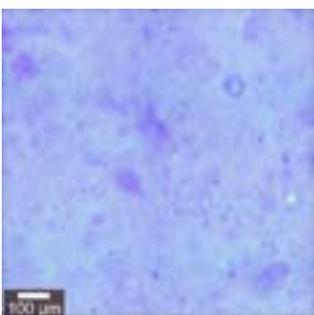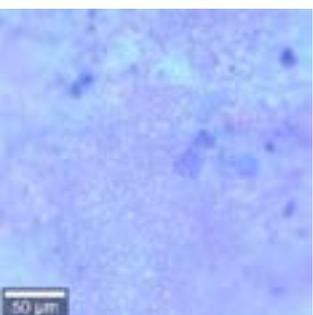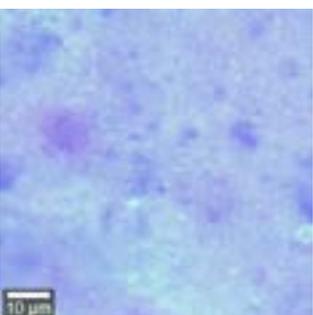
PSM-100-DMF
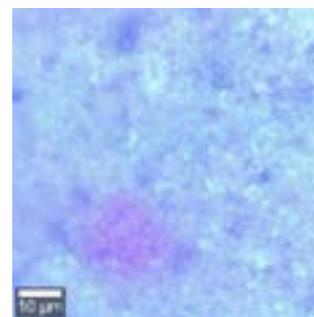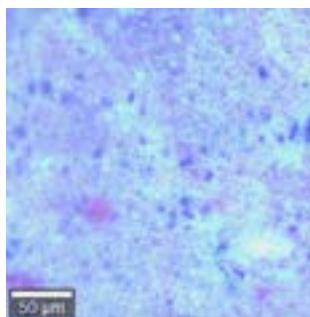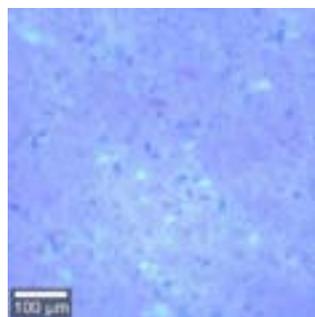
PSM-DMF No MOF
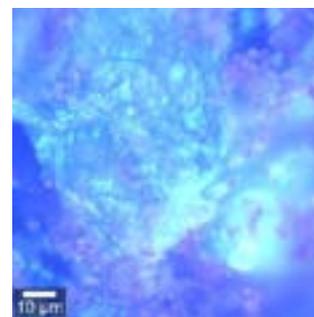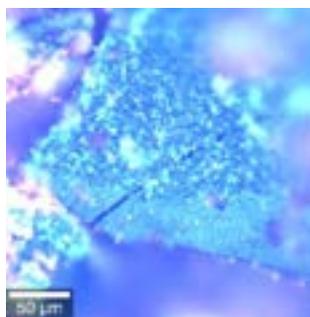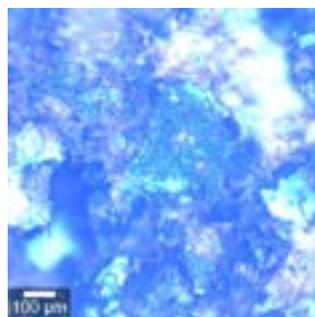
SEM
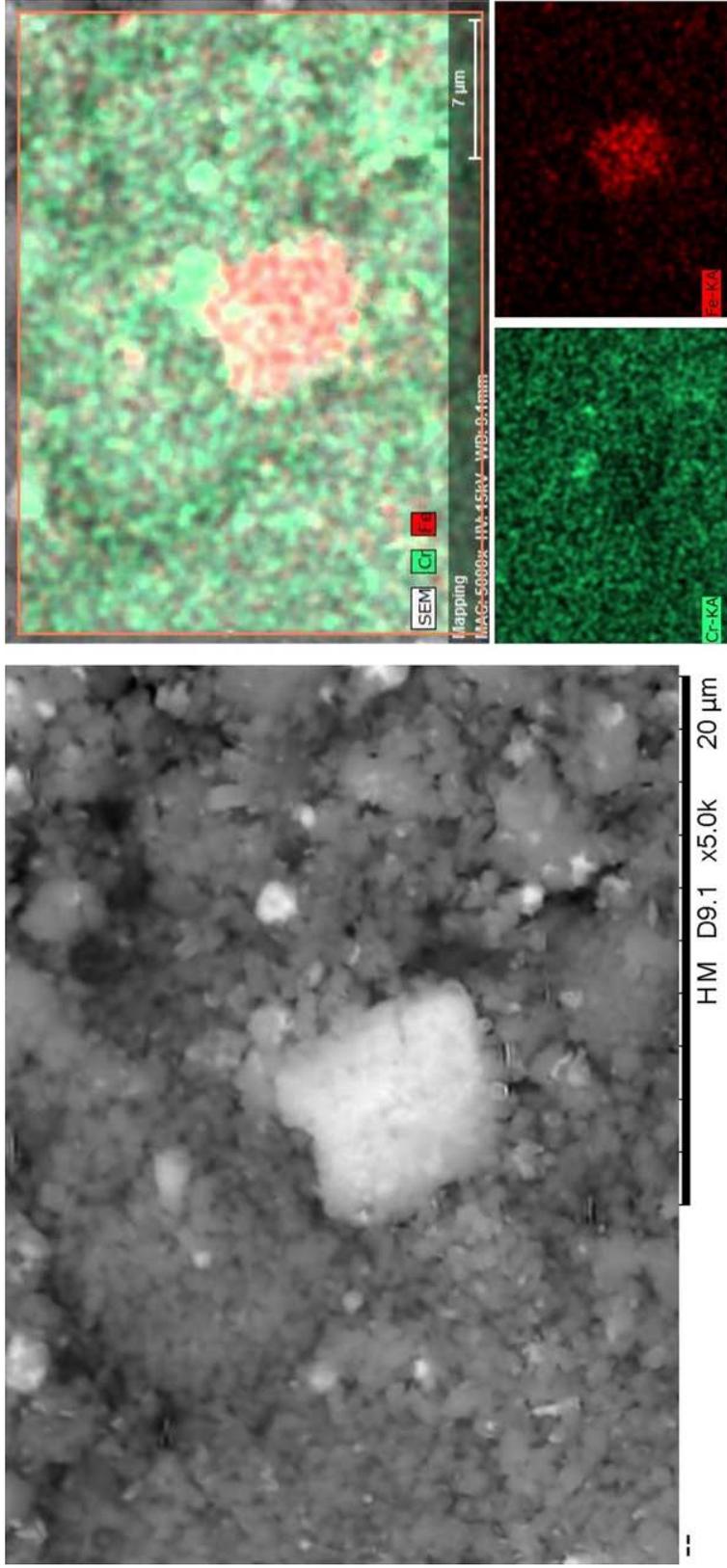
Figure 5.23 SEM image of the PSM-25-Cl sample with the mapping of the Cr and Fe distribution over the sample.
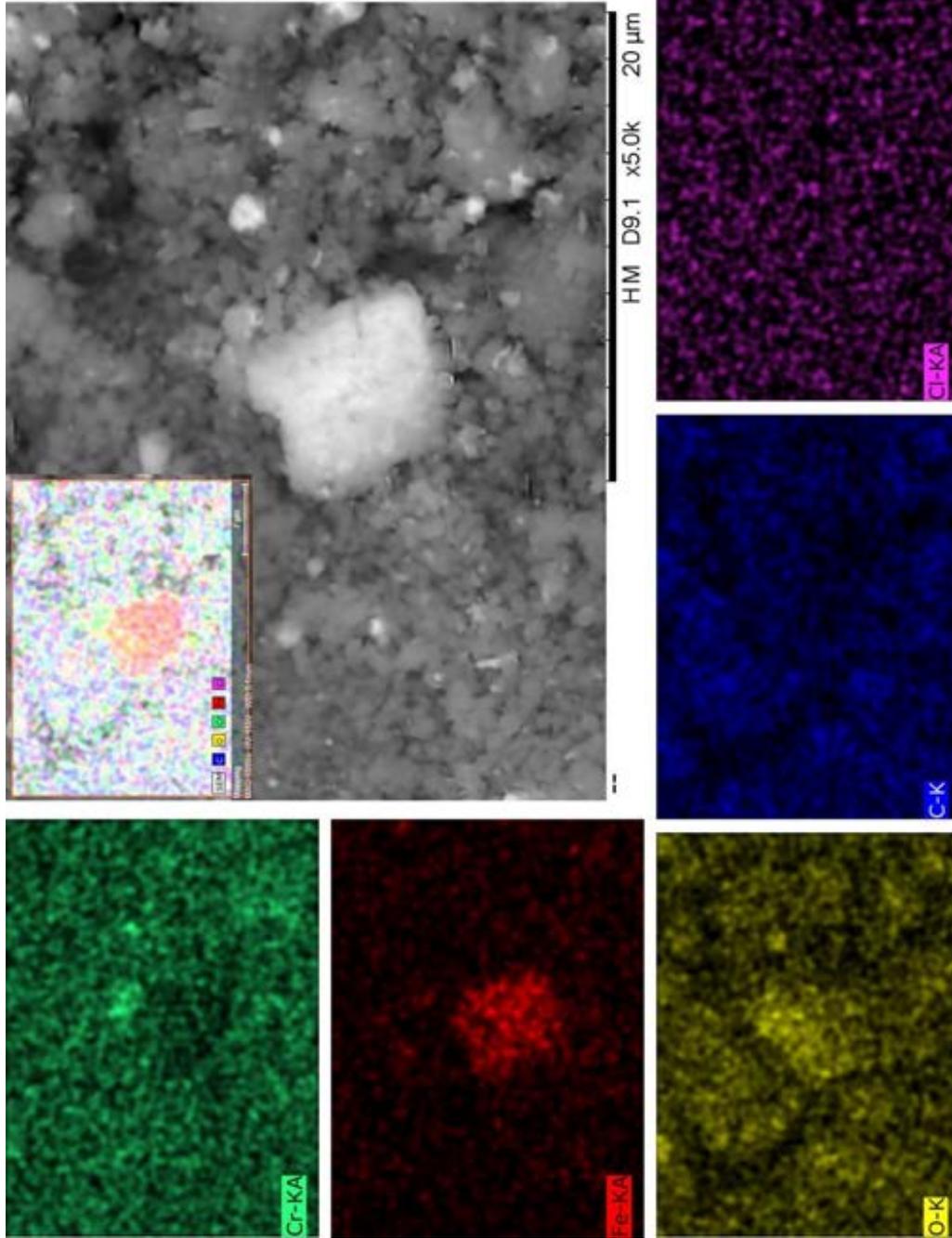
Figure 5.24 SEM image of the PSM-25-Cl sample with its whole elemental mapping distribution over the sample.
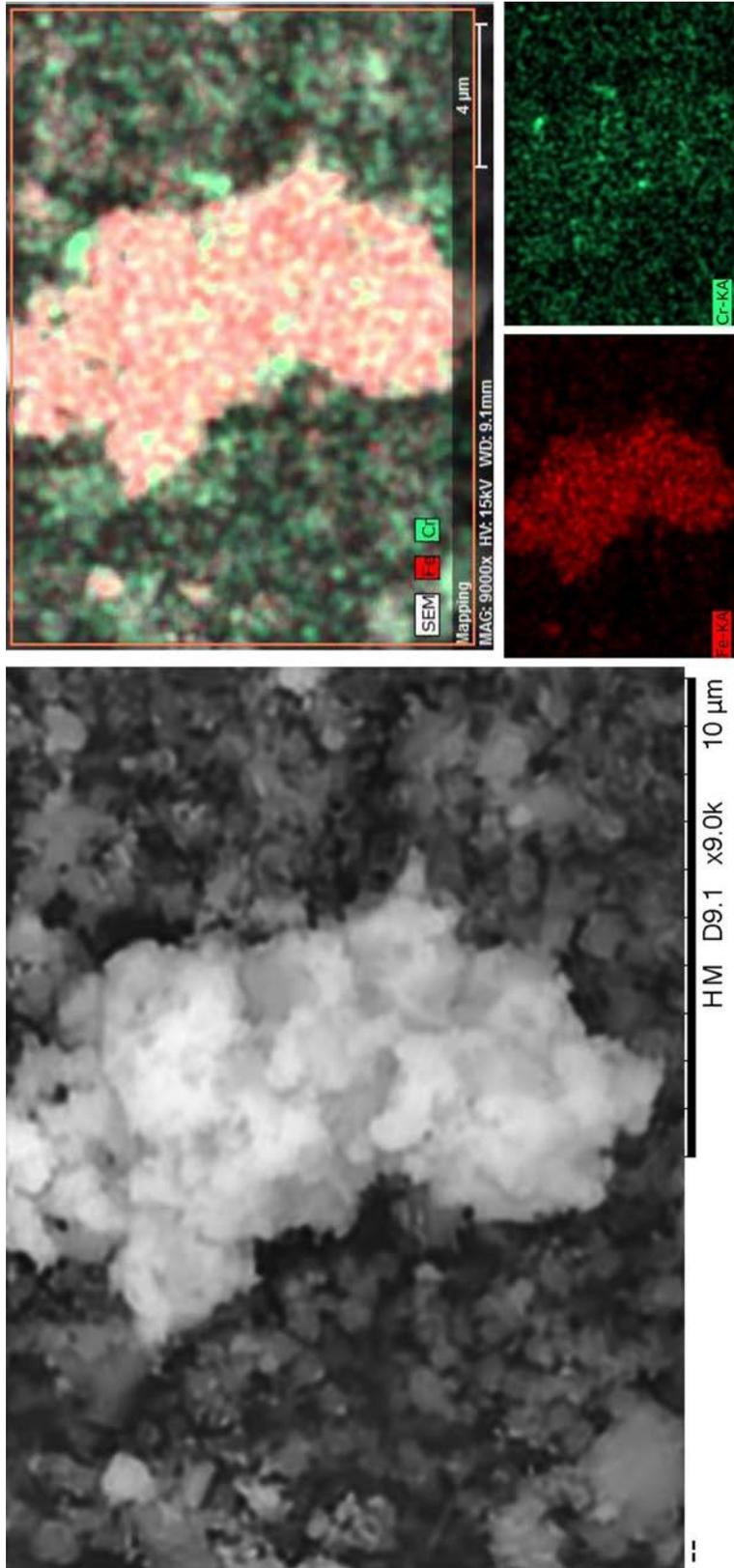
Figure 5.25 SEM image of the PSM-50-Cl sample with the mapping of the Cr and Fe distribution over the sample.
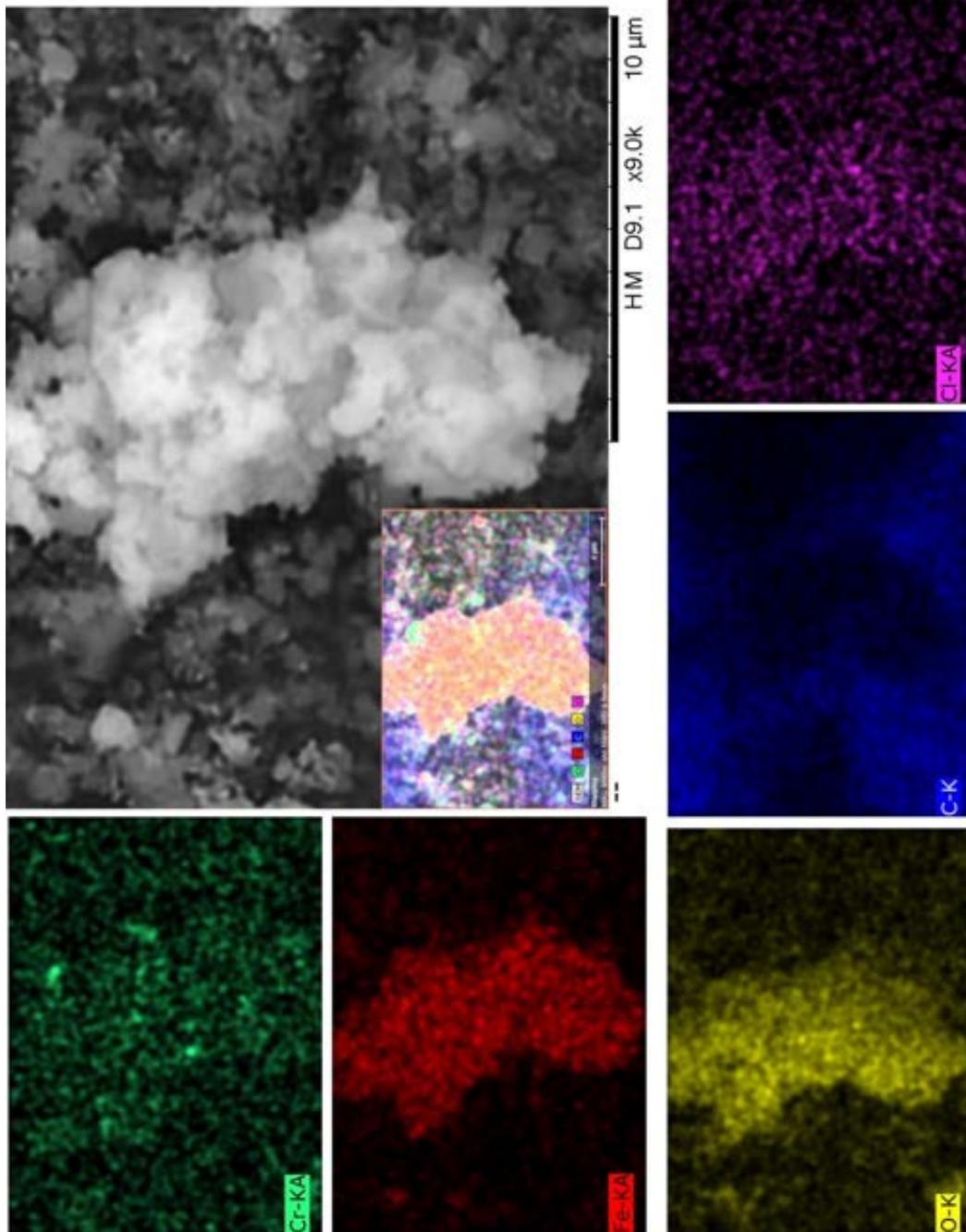
Figure 5.26 SEM image of the PSM-50-Cl sample with its whole elemental mapping distribution over the sample.
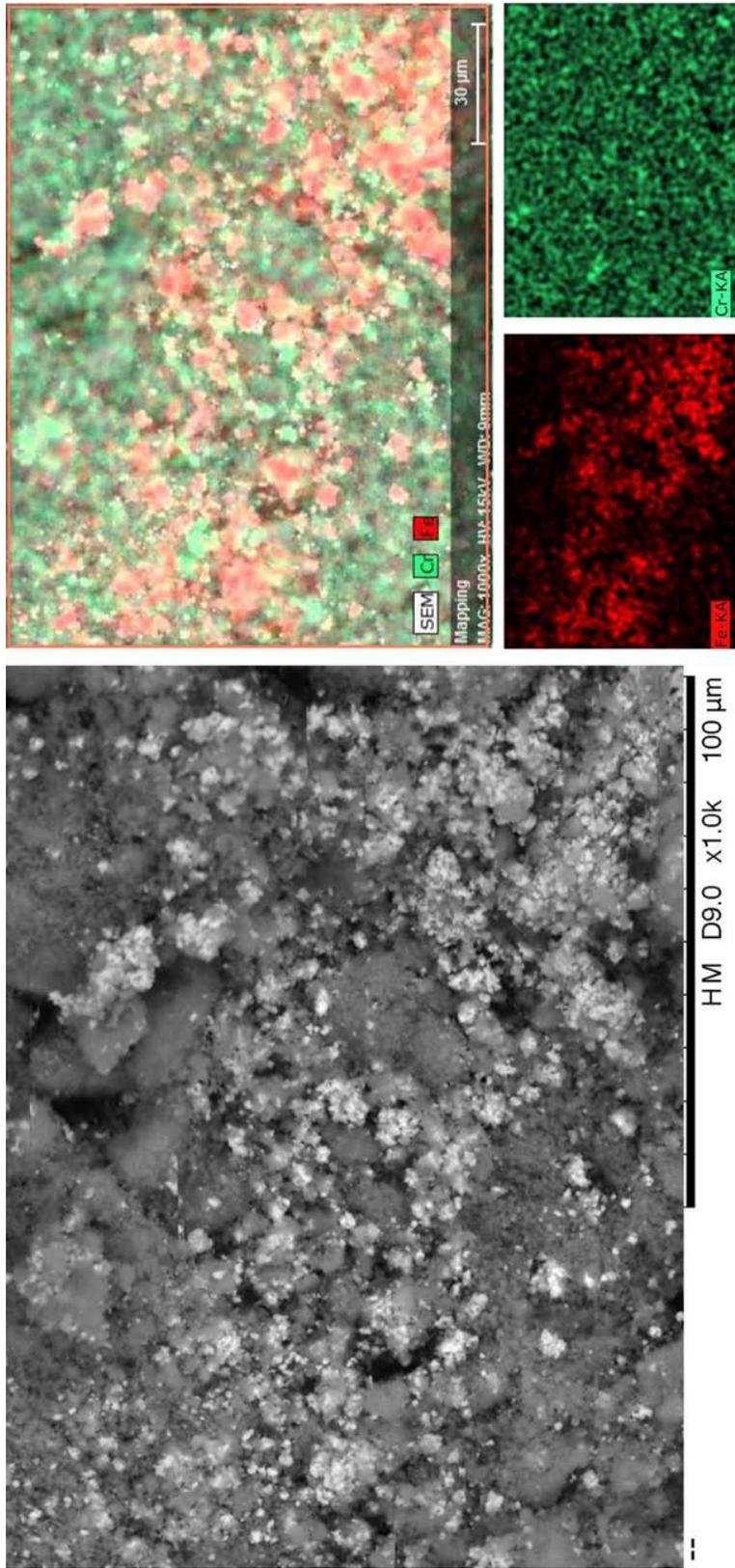
Figure 5.27 SEM image of the PSM-100-Cl sample with the mapping of the Cr and Fe distribution over the sample.
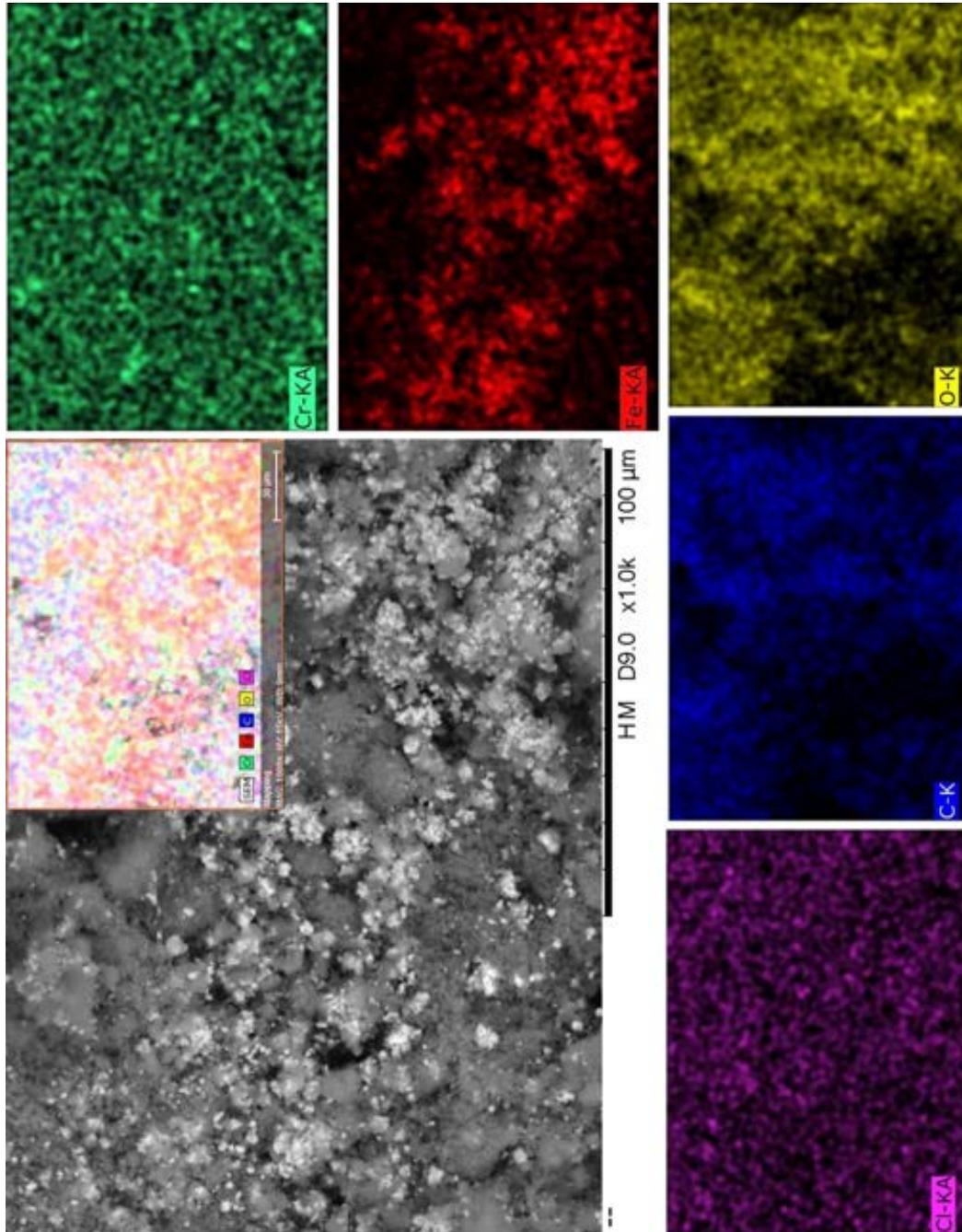
Figure 5.28 SEM image of the PSM-100-Cl sample with its whole elemental mapping distribution over the sample.

BET

Table 5.11 Specific surface area and pore volume of all PSM samples

Sample	MIL-101(Cr)	PSM-0-Cl	PSM-10-Cl	PSM-25-Cl	PSM-50-Cl	PSM-100-Cl
$\mathbf{S}_{BET}$ $(\mathbf{m^2\ g^{-1}})$	2497	2789	2618	2305	2083	2041
$\mathbf{S}_{Langmuir}$ $(\mathbf{m^2\ g^{-1}})$	3852	4127	3971	3663	3429	3398
$\mathbf{V}^{\dagger}_{pore}$ $(\mathbf{cm^3\ g^{-1}})$	1.49	1.77	1.60	1.42	1.35	1.32
$\mathbf{V}^{\ddagger}_{pore}$ $(\mathbf{cm^3\ g^{-1}})$	1.14	1.46	1.37	1.11	1.07	1.05
Sample	MIL-101(Cr)	PSM-0-Cl	PSM-10-NO$_3$	PSM-25-NO$_3$	PSM-50-NO$_3$	PSM-100-NO$_3$
$\mathbf{S}_{BET}$ $(\mathbf{m^2\ g^{-1}})$	2497	2789	2654	2570	2121	2033
$\mathbf{S}_{Langmuir}$ $(\mathbf{m^2\ g^{-1}})$	3852	4127	4014	3917	3476	3372
$\mathbf{V}{\dagger}_{pore}$ $(\mathbf{cm^3\ g^{-1}})$	1.49	1.77	1.62	1.53	1.38	1.31
$\mathbf{V}{\ddagger}_{pore}$ $(\mathbf{cm^3\ g^{-1}})$	1.14	1.46	1.38	1.27	1.10	1.05
Sample	MIL-101(Cr)	PSM-0-DMF	PSM-10-DMF	PSM-25-DMF	PSM-50-DMF	PSM-100-DMF
$\mathbf{S}_{BET}$ $(\mathbf{m^2\ g^{-1}})$	2497	2605	2647	2686	2589	2306
$\mathbf{S}_{Langmuir}$ $(\mathbf{m^2\ g^{-1}})$	3852	3959	4006	4058	3950	3667
$\mathbf{V}{\dagger}_{pore}$ $(\mathbf{cm^3\ g^{-1}})$	1.49	1.52	1.73	1.75	1.51	1.46
$\mathbf{V}{\ddagger}_{pore}$ $(\mathbf{cm^3\ g^{-1}})$	1.14	1.27	1.40	1.43	1.26	1.12

†= Barrett-Joyner-Hallender (BJH) method, ‡= Density-functional theory (DFT) method.
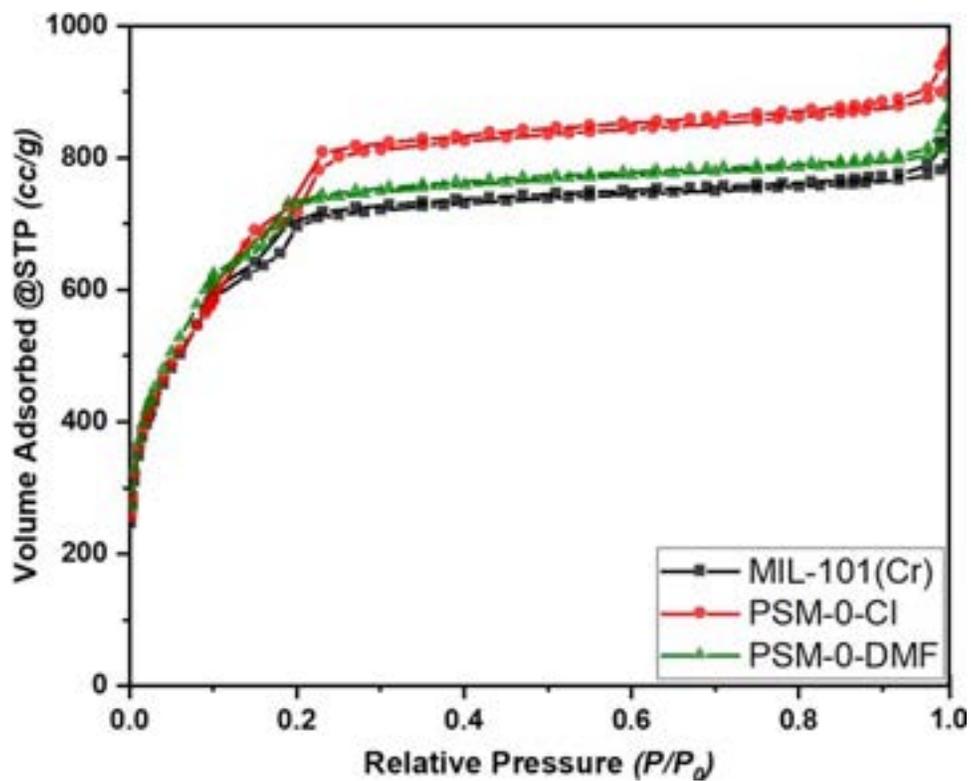
Figure 5.29 N_2 sorption isotherms for pristine MIL-101(Cr), PSM-10-Cl, and PSM-10-DMF samples.

CHAPTER 6   ARTICLE 3 - MICROWAVE-ASSISTED SYNTHESIS OF THE FLEXIBLE IRON-BASED MIL-88B METAL-ORGANIC FRAMEWORK FOR ADVANCED ENERGETIC SYSTEMS

Mahmoud Y. Zorainy,[1,2] Serge Kaliaguine,[3] Mohamed Gobara,[2] Sherif Elbasuney,[2,4] and Daria C. Boffito[1]

6.1   Abstract

The 3D metal-organic framework(MOF), MIL-88B, built from the trivalent metal ions and the ditopic 1,4-Benzene dicarboxylic acid linker (H_2BDC), distinguishes itself from the other MOFs for its flexibility and high thermal stability. MIL-88B was synthesized by a rapid microwave-assisted solvothermal method at high power (850 W). The iron-based MIL-88B [$Fe_3.O.Cl.(O_2C-C_6H_4-CO_2)_3$] exposed oxygen and iron content of 29% and 24%, respectively, which offers unique properties as an oxygen-rich catalyst for energetic systems. Upon dispersion in an organic solvent and integration into ammonium perchlorate (AP) (the universal oxidizer for energetic systems), the dispersion of the MOF particles into the AP energetic matrix was uniform (investigated via elemental mapping using an EDX detector). Therefore, MIL-88B(Fe) could probe AP decomposition with the exclusive formation of mono-dispersed Fe_2O_3 nanocatalyst during the AP decomposition. The evolved nanocatalyst can offer superior combustion characteristics. XRD pattern for the MIL-88B(Fe) framework TGA residuals confirmed the formation of α-Fe_2O_3 nanocatalyst as a final product. The catalytic efficiency of MIL-88B(Fe) on AP thermal behavior was assessed via DSC and TGA. AP solely demonstrated a decomposition enthalpy of 733 J g^{-1}, while AP/MIL-88B(Fe) showed a 66% higher decomposition enthalpy of 1218 J g^{-1}; the main exothermic decomposition temperature was decreased by 71 °C. Besides, MIL-88B(Fe) resulted in a decrease in AP decomposition activation energy by 23% and 25% using Kissinger and Kissinger–Akahira–Sunose (KAS) models, respectively.

---

[1]Chemical Engineering Department, Polytechnique Montréal, Montréal, QC H3C 3A7 (Canada)

[2]Chemical Engineering Department, Military Technical College, Cairo (Egypt)

[3]Chemical Engineering Department, Laval University, Québec, QC G1V 0A6 (Canada)

[4]Nanotechnology Research Center, Military Technical College (MTC), Cairo (Egypt)

6.2   Introduction

Metal-organic frameworks (MOFs) are highly porous crystalline materials with large, accessible cages of regular shapes that confer unusually high surface area and pore volume. Such structures are capable of entrapping different molecules within their cavities for multiple purposes.They were found to be beneficial in a wide range of applications, whereby gas storage [374, 375], separation [376–378], and heterogeneous catalysis [379, 380] are the most significant.[381]

Among the different generations of MOFs, the second and third generations (2G and 3G, respectively) recently attracted more attention. MOFs belonging to the 2G are known to be robust structures that extend in the two- or three- dimensions to provide a permanent porosity with potential for various applications such as guest capture and release as well as sensing.[44, 382] The 3G MOFs are more attractive as their structures were proved to be soft and dynamic. Materials comprised in this subclass display reversible flexing (breathing) that takes place due to the presence of external chemical or physical stimuli such as guest encapsulation/elimination, temperature, pressure, light, or electric field.[374, 382]

In March 2021, the Cambridge Crystallographic Data Centre (CDCC) announced the existence of more than 100,000 registered entries under the MOF subset.[383] The highly flexible MIL-88B framework has attracted numerous research groups' attention for its distinctive capability of expressing crystal transformation depending on the surrounding environment. MIL-88 refers to the formation of a 3D structure, whereby the trigonal prismatic metal cluster is formed from three trivalent metal centers and is connected to a ditopic linker, preserving the same parent topology.[52, 54] The letter in the designation indicates the type of this ditopic linker, whereby A denotes the use of fumaric acid (MIL-88A), B stands for 1,4-Benzenedicarboxylic acid (BDC, MIL-88B), C for 2,6-naphthalene dicarboxylic acid (NDC, MIL-88C), and D for 4,4′-biphenyl dicarboxylic acid (BPDC, MIL-88D).[54]

MIL-88B was initially reported to be built from the trinuclear oxo-centered chromium cluster and the dicarboxylate linker, giving a structural formula of $[M_3^{III}O.(BDC)_3.X$, where M represents the trivalent metal cation, and X can be either F, Cl, or OH depending on the synthesis conditions].[52, 54] In its unit cell, the metal(III) trimers are crosslinked by the BDC linker to give a super tetrahedron (ST), the secondary building unit for such a framework (Supporting information (section 6.7), Figure 6.19). For each trimer, the metal atom is centered in each octahedral, whereby two of these octahedra are bonded to a water molecule while the third one is bonded to either a halide or hydroxide ion. Each octahedron is connected laterally to another one by the carboxylic groups of two BDC molecules on both

sides, yielding four connections with the other two and a total of six bidentate carboxylic linkers in each trimer. All octahedra are connected through the same μ_3-oxo atom found on the one vertex directed towards the center of the trimer.

The trimers occupy the four vertices of the SBU tetrahedron, whereas the organic ligands represent the six edges of the super tetrahedron to give a microporous structure ($\sim$8.6 Å free aperture, Figure 6.19), and the connection of the SBUs propagates through the vertices to result in the flexible structure of the MIL-88 metal-organic framework. It was reported that this framework occupies the topology of the acs net with the $P - \bar{6}2C$ space group, in which the voids within such a structure are composed of channels and not cages. Figure 6.1-a displays the structure of MIL-88B along the a-axis, and Figure 6.1-b displays the channels within the framework, whereby the structure is viewed along the c-axis.

The MIL-88B framework, with its known flexibility, expresses what is known as the "Breathing effect," in which the MOF crystals are capable of shrinking and swelling reversibly.[132, 211, 212, 384] This change modifies the unit cell capacity of the framework, thus affecting the size of the channels without destruction or decomposition of the structure (6.1-c).[132, 384] Such a phenomenon is rarely found in solid crystals, making this MOF's capability an exciting research subject. Furthermore, on the macroscopic scale, the resulting MIL-88B(Fe) crystals may occupy different forms ranging from hexagonal bipyramids (diamond-like crystals) to hexagonal prisms (rod-like crystals), depending on the synthesis conditions (6.1-d).[385, 386]

As mentioned above, MIL-88B was first synthesized from the trivalent chromium ions; other metals were, however, incorporated in the preparation of this material, such as Sc [175–177], V [170], Mn [207], and Fe [52, 54, 211]. Recently, with the increasing numbers of studies on other flexible MOF materials, Fe-based MOFs have been sought for many applications because of their advantages as nontoxic, biocompatible metal sources with outstanding physicochemical features with their raw materials being readily available and inexpensive.[387, 388]
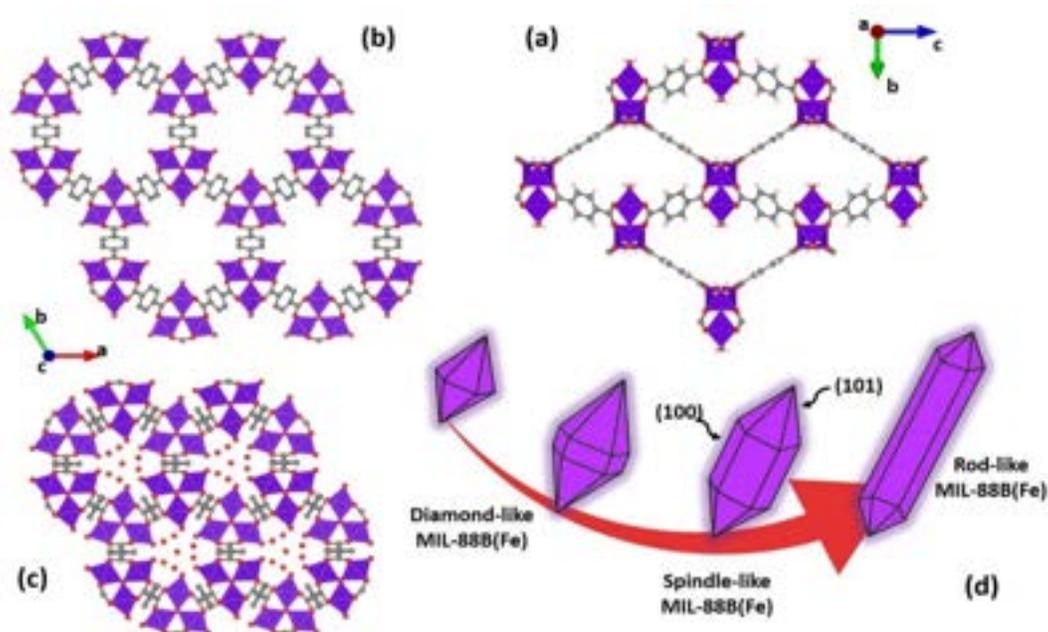
Figure 6.1 The crystalline structure of the flexible MIL-88B framework. a) the view of the structure along the a-axis. b) along the c-axis. c) breathing effect due to chemical inclusion. d) different crystal shapes resulting from variations in the synthesis parameters.

In highly energetic systems and solid fuel propellants, ammonium perchlorate (AP) is one of the most commonly used oxidizers.[389, 390] AP comprises fuel and oxidizing elements in the same molecule; with high active oxygen content. The decomposition of AP follows an initial endothermic process, whereby a phase transition takes place from the orthorhombic structure to the cubic, which experiences high activation energy.[391, 392] At higher temperatures, its crystals become unstable and degrade before melting, similar to other ammonium salts. This degradation is accompanied by a dissociative sublimation and the release of ammonia gas (NH_3) and perchloric acid ($HClO_4$), which accounts for 30%wt. of the whole decomposition process.[393, 394]

On the other side, the combustion of AP has been widely studied; AP decomposition was found to be a complex process. During combustion, its reactive species undergo a sequence of chain reactions with the production of free oxygen and other gaseous products (i.e., O_2, NO, and NO_2), yielding a high oxidizing power. Generally, combustion reactions are spontaneously propagating exothermic reactions that require specific activation energy to start the reaction. In the case of energetic materials containing AP, the highly endothermic changes of its dissociation and sublimation have high activation energy and hence could result in a low burning rate.[395]

A catalyzed combustion process can decrease the required activation energy and sustain the

whole combustion process at a high propagation index.[396] In the case of AP, this catalysis affects the endothermic decomposition of the oxidizer. Transition metal oxides can catalyze AP thermal decomposition, with significant changes in combustion characteristics.[397–400] Ferric oxide is the most active of these catalysts, mainly if used in the nano-scale range.[401, 402] Nanostructured energetic systems can experience smaller critical diameters, high reaction rate, high heat output, as well as high heat release rate.[397, 400, 403]

Here, the iron-based MIL-88B was synthesized following a rapid microwave-assisted solvothermal method. The highly efficient microwave method provided high-quality MIL-88B(Fe) crystals in high yield and excellent phase purity. It represented an energy-saving route for the rapid synthesis of the targeted MOF crystals.[31] In addition, the microwave-assisted technique provided smaller crystals than the conventional method.[30] The MIL-88B(Fe) was characterized with XRD, FTIR, SEM, TEM, TGA, and DSC. It was then integrated into an AP matrix to control the thermal decomposition of the entire matrix. During combustion, the organic linker of the MIL-88B(Fe) framework decomposes first with the release of CO_2 and H_2O molecules.[387, 404] The decomposition of MIL-88B(Fe) gives a high content of Fe_2O_3 nanoparticles as residuals homogeneously dispersed into the AP matrix resulting in the exclusive formation of mono-dispersed nano-catalysts.[405–407] It is expected that further combustion of the AP/MIL-88B(Fe) matrix significantly changes the decomposition of AP, yielding a higher burning rate.

6.3 Experimental

All synthetic manipulations were performed under ambient atmosphere unless otherwise stated.

6.3.1 Materials

For the MOF synthesis, Iron(III) chloride hexahydrate ($FeCl_3.6H_2O$, 97%), 1,4-Benzenedicarboxylic acid "terephthalic acid" (H_2BDC, 98%), *N,N*-dimethyl formamide (anhydrous DMF, 99.8%), Ethanol (EtOH, 98%), and Acetone (CH_3COCH_3, 97%) for the nanocomposite were all purchased from Sigma-Aldrich (Canada). In addition, ammonium perchlorate (NH_4ClO_4, 99%) was purchased from Alpha Chemica (India). All chemicals were used as received with no further processing.

6.3.2 Synthesis of MIL-88B(Fe)

The iron-based MIL-88B crystals were synthesized following the reported Metzler-Nolte method with slight modifications, in which the microwave-assisted technique was adopted.[132, 384] The synthesis took place in the 30 ml-glass vial of Anton Paar's Microwave reactor (Monowave 400). In a typical procedure, as shown in Figure 6.2, an equimolar mixture of FeCl$_3$.6H$_2$O (0.69 mmol, 0.187 g) and H$_2$BDC (0.69 mmol, 0.115 g) was weighed directly in the reaction vial. Then, 15 ml DMF was added to the mixture, and the solution was magnetically stirred for 30 min at room temperature to ensure complete dissolution of the components. Later on, the vial was covered with a Teflon-lined silicon septum and placed into the reaction chamber of the microwave reactor. The reaction proceeded after heating the reaction medium to 150 °C and maintaining the temperature for 10 min under constant stirring (500 rpm). After the reaction, the reactor chamber was cooled to room temperature by the circulation of air introduced to the instrument under the pressure of 6 bar. (Detailed reaction progress and variation of the parameters during synthesis are reported and plotted in the supporting information (Supporting information(section 6.7), Table 6.2, Figure 6.20 and 6.21)).

The reaction yielded an orange-colored suspension that was centrifuged at a speed of 10,000 rpm for 10 min. The separated solids were washed with DMF (×2), ethanol (×3) and then dried at 80 °C overnight. The dried powders were kept under vacuum until further use.

Figure 6.2 Schematic diagram for the MIL-88B(Fe) synthesis procedures via microwave-assisted technique.

6.3.3 Material Characterization

Powder X-ray diffraction (PXRD) data were recorded on a Bruker D8 Advance diffractometer equipped with Bragg-Brentano geometry and Ni-filtered Cu-Kα radiation (wavelength, $\lambda_{K\alpha} = 1.5406$ Å). Samples were prepared by placing a thin layer of the powder directly on a low-zero background silicon wafer supported on the sample holder. The pattern was collected in the 2θ-range of 3°- 40° with a step size of 0.02°.

Fourier-transform infrared spectroscopy was applied using the attenuated total reflection (ATR) Perkin Elmer spectrum 65 spectrometer equipped with a diamond crystal. Characterization took place over the wavenumber range of 4000 cm^{-1} - 450 cm^{-1} , with a resolution of 4 cm^{-1}, and an accumulation of 32 scans in absorption mode.

Adsorption isotherms were measured using a Quantachrome autosorb-1 analyzer with N$_2$ as adsorbate at 77 K. Prior to adsorption experiments, outgassing of the samples was performed in vacuo at 250 °C for 12 h with a heating ramp of 5 °C min^{-1}. The specific surface area was determined by applying the Brunauer–Emmett–Teller (BET) equation on the nitrogen adsorption-desorption isotherms at a relative pressure (P/P$_0$) between 0.05 and 0.15.

Thermogravimetric analysis(TGA) was performed to establish the thermal stability of the produced MOF on a TGA Q50 instrument by utilizing 5 mg of each sample. Samples were heated at a controlled heating rate of 10 °C min^{-1} from ambient temperature to 800 °C under flowing air. The balance and flows rates were both of 20 mL min^{-1}.

Scanning Electron Microscopy (SEM) was used to investigate the crystalline morphology and topology of the MIL-88B MOF. Images were obtained using a Carl Zeiss scanning electron microscope (Model: EVO MA 10, Germany). Samples were suspended in methanol and deposited onto carbon tape. Transmission electron microscopy (TEM, JEOL JEM-2100F) was also employed to record images of the material at 200 kV in bright field imaging mode.

Differential Scanning Calorimetry (DSC) was conducted in closed-pan type experiments via the TA Instruments Q2000 Modulated-DSC©. Approximately 5mg of each sample was weighed in airtight-sealed aluminum pans. Samples were then cooled to 0 °C, before heating at a heating rate of 10 °C min^{-1} until a temperature of 400 °C. A constant nitrogen purging of 50 mL min^{-1} was maintained during the experiments. The TGA and the DSC data were analyzed using the Universal Analysis software version 2000 from the TA instruments website.

6.3.4 Integration of MIL-88B(Fe) MOF into AP matrix

For the matrix preparation, MIL-88B(Fe) was first dispersed in acetone and then sonicated for 30 minutes using an ultrasonic probe homogenizer (400 W - 24 kHz, 50% Amp. , Hielscher - Germany). Ammonium perchlorate was dissolved in the acetone colloid, and dichloromethane was employed as a proper anti-solvent. Finally, the precipitated particles were filtered and dried at 80 °C for SEM imaging and TGA.

6.3.5 Thermal behavior of AP nanocomposite

The catalytic effect of the synthesized MIL-88B(Fe) and its decomposition residue on AP's thermal decomposition was investigated via DSC. The tested sample was heated to 500 °C at a controlled heating rate of 10 °C min^{-1} under N$_2$ flow of 50 ml min^{-1}. The impact of the MOF structure and iron oxide nanocatalyst on AP's weight loss with temperature elevation was further investigated using TGA.

6.3.6 Kinetic study of AP nanocomposite

The impact of MIL-88B(Fe) on AP's decomposition rate was evaluated by TGA. The AP nanocomposite sample was heated at a rate of 2, 4, 6, 8, and 10 °C min^{-1}. Kissinger and Kissinger–Akahira–Sunose (KAS) models were employed for kinetic analysis and activation energy calculations.[408, 409]

The Kissinger's model was employed to calculate the activation energy (E_a) of AP nanocomposite (Equation 6.1).[410, 411]

$$-\frac{Ea}{R} = \frac{dln(\frac{\beta}{T_p^2})}{d(\frac{1}{T_p})}$$

(6.1)

where, Ea is the activation energy, R is the gas constant, β is the heating rate. and Tp is the peak temperature, corresponding to the position of the rate peak maximum. The peak temperature (Tp) is determined as the temperature of the peak signal (maximum or minimum) measured by DSC, DTA or derivative thermogravimetry (DTG).

The Kinetic parameters of Kissinger's model were evaluated using Kissinger–Akahira–Sunose (KAS) model (Equation 6.2).[412]

$$ln\frac{\beta_i}{T_{\alpha,i}^{1.92}} = Const. - 1.00008\frac{E\alpha}{RT\alpha}$$

(6.2)

6.4   Results and Discussion

6.4.1   Characterization of MIL-88B(Fe) MOF

Powder X-ray Diffraction (PXRD):

According to the microwave-assisted method of Metzler-Nolte, heating a solution of Fe^{3+} and H_2BDC in DMF with a molar ratio of 1:1:140 at 150 °C for 10 min would result in a MIL-88B(Fe) structure with diamond-like and short spindle-like crystals.[132] Characterization via PXRD confirmed the achievement of the MIL-88B(Fe) framework by the adopted synthesis method. The resulting pattern (Figure 6.3, "Blue") showed a nearly flat background, and high-intensity peaks were recognized in the 2θ range of 5° - 30°.[132, 384] The experimental pattern agreed with the calculated one (Figure 6.3, "Red"), revealing that the [101] plane is the dominant one while the [100] plane is the least intense.[132, 385, 386] Additional XRD calculations can be found in the supporting info. (Table S2).
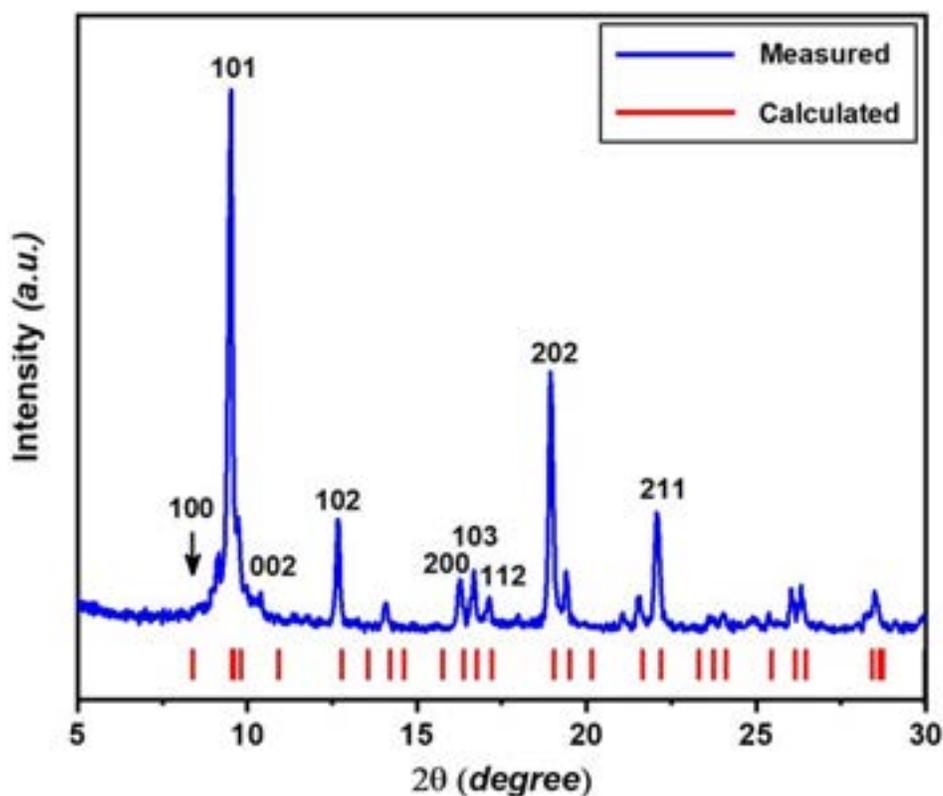
Figure 6.3 The XRD pattern for the microwave-synthesized MIL-88B(Fe) metal-organic framework compared to the calculated peaks of the simulated structure. (The original simulation file was obtained from Cambridge Crystallographic Data Centre "CCDC" under the identifier name of "YEDKOI")

Scanning Electron Microscopy (SEM):

Scanning electron microscopy (SEM) confirmed the findings of PXRD, whereby the hexagonal bipyramidal-shaped (diamond-like) crystals of MIL-88B(Fe) were the major type of crystals produced (Figure 6.4). Furthermore, scanning the obtained MOF crystals at three to five different spots demonstrated a uniform crystal size in the range of a few microns (as represented in the size histogram, Figure 6.4) with a preferential growth of the 101 facets rather than that of the 100 ones.[132,386] The presence of smaller crystals of the same shape could also be detected, resulting from the fast heating rate and the high microwave power adopted during synthesis. (Supporting information (section 6.7), Figure 6.20).
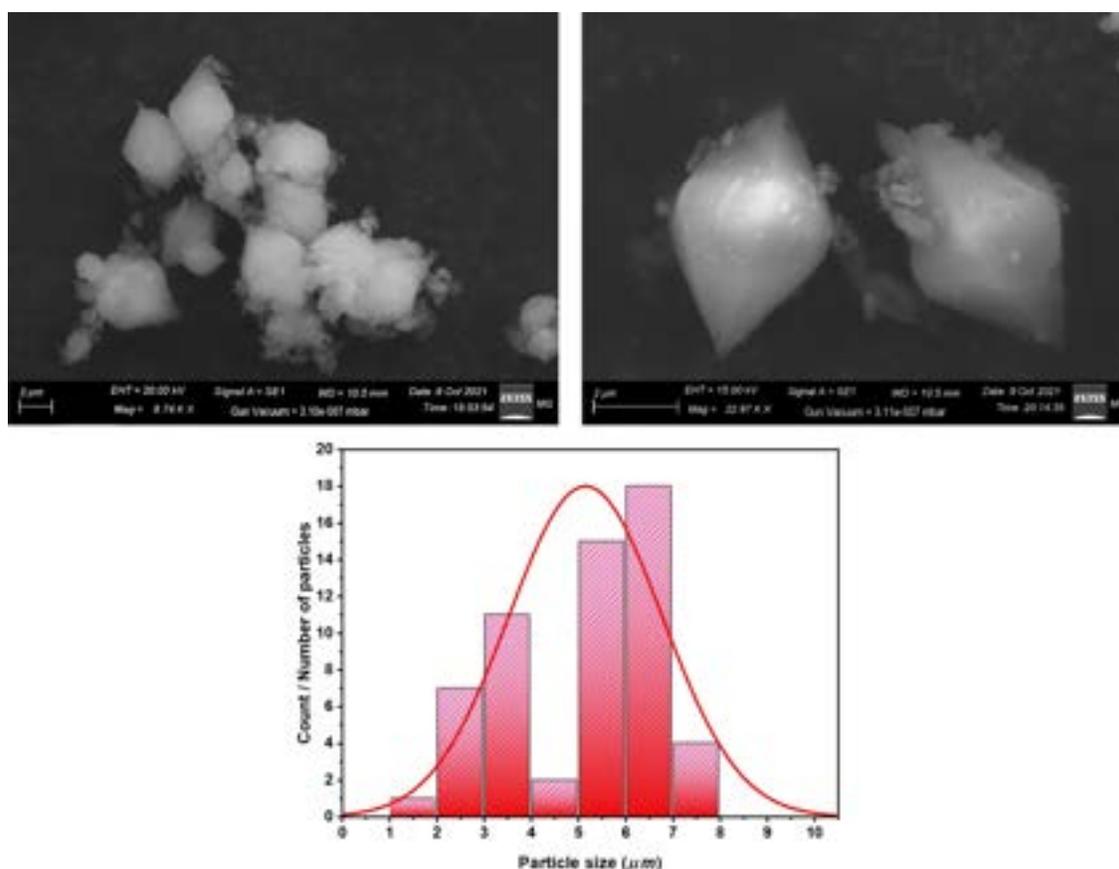
Figure 6.4 SEM micrographs and particle size histogram of the as-synthesized MIL88-B(Fe) hexagonal bipyramidal-shaped crystals.

Elemental mapping was conducted using the EDAX detector of the SEM to assess the dispersion of the main elements within the framework (Figure 6.5). As explained earlier, in the MIL-88B(Fe) framework structure, each metal trimer comprises three metal ions connected through central oxygen and six linker molecules. Besides, at the outer vertices of the trimer, either a water molecule or a hydroxyl group is attached to the metal ion satisfying its coor-

dination. The negative hydroxyl ions are sometimes replaced by the chloride ions provided by the initial precursors. Hence, detecting most of these elements in the mapping is reasonable, including Fe, O, C, and Cl (Figure 6.5). The mapping confirmed the uniform elemental dispersion within the sample. Moreover, the obtained elemental composition confirmed the chemical formula of the MIL-88B MOF ($C_{24}H_{12}O_{13}Fe_3Cl$) with respect to the atomic and mass percentages indicated (Figure 6.6).
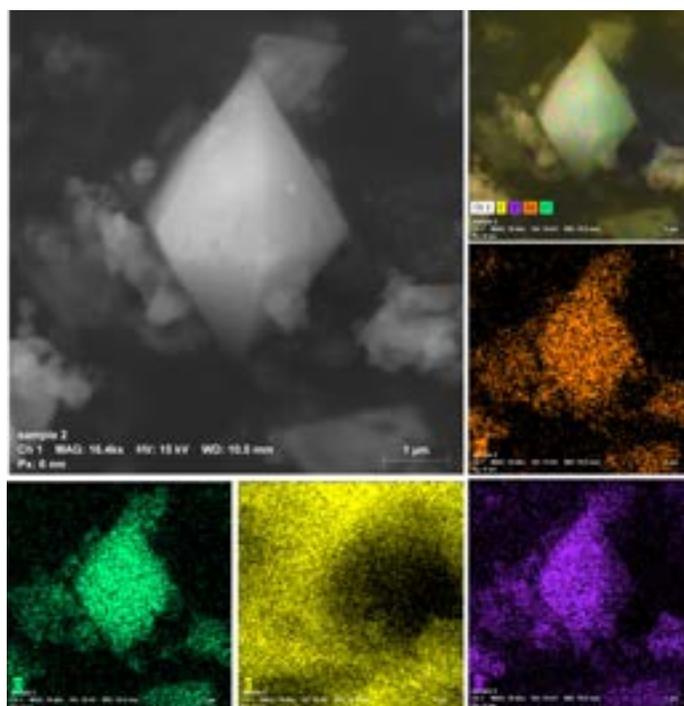
Figure 6.5 Elemental mapping of the as-synthesized MIL88-B (Fe) MOF.

Element	Mass %	Mass Norm. %	Atom %
Carbon	28.0	48.4	63.2
Oxygen	15.8	27.1	26.8
Chlorine	9.9	16.9	7.7
Iron	4.7	7.6	2.3
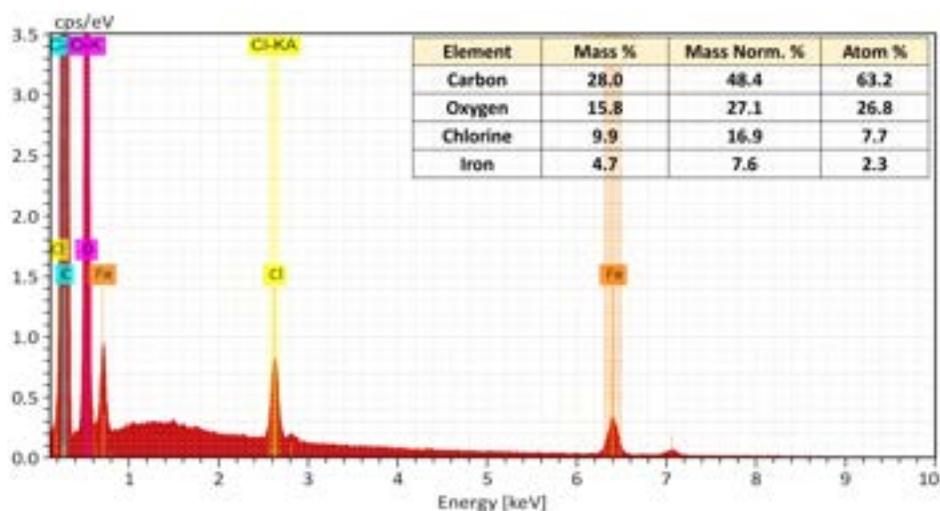
Figure 6.6 Elemental composition of the MIL88-B (Fe) framework.

Transmission Electron Microscopy (TEM):

As reported above, the SEM images showed that the majority of the crystals produced have a diamond-like shape and a particle size of few microns. Nevertheless, the TEM micrographs (Figure 6.7) allowed establishing the existence of smaller particles with an aspect ratio (length/width) around two. These particles are of spindle-like shapes and 400 nm in length and 200 nm in width (Figure 6.7). The reaction medium was heated uniformly under constant microwave power of 300 W in the original recipe.[132] In the present work, a higher heating rate was applied under an initial high-power pulse reaching a maximum of 850 W (Supporting information (section 6.7), Figure 6.20). The fast-heating rate applied would result in a higher nucleation rate. This could yield changes in the morphology of the produced crystals depending on the precursors' concentrations at this reaction location. Secondly, no sudden cooling (quenching) was employed at the end of the reaction, as reported in Ref. [132]. On the contrary, in our case, a slow cooling followed (Supporting information (section 6.7), Figure 6.21), which would force the reaction to proceed at a lower temperature. This would favor the growth of already formed crystals and the formation of smaller ones of different (deformed) shapes.
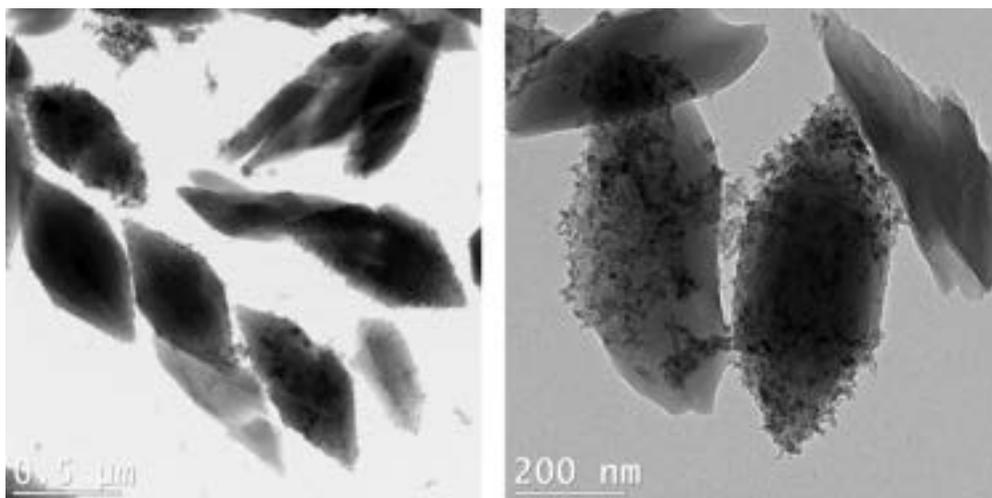
Figure 6.7 TEM micrographs of MIL-88B(Fe) expressing the presence of some short spindle-like crystals.

Fourier-Transform Infrared spectroscopy (FTIR):

FTIR confirmed the formation of the desired MOF structure (Figure 6.8) and the connection of the trivalent Fe^{3+} ions to the ditopic H_2BDC linker. Indeed, the vibrational spectrum of the obtained crystal agreed with that of Fe-BDC metal-organic frameworks (i.e., MIL-53 and MIL-101), with the high-intensity peaks in the range of 2000 cm^{-1} - 400 cm^{-1}.[229, 253, 350,

370] First, the range from 1750 cm^{-1} - 1250 cm^{-1} corresponds mainly to the vibrations of the carboxylate group bonds and, to some extent, the aromatic ring. The second region in the range between 1250 cm^{-1} - 600 cm^{-1} is ascribed to the C-H bonds of the ring. Finally, in the region below 600 cm^{-1}, the metal-O bonds' vibrations are detected.

In the first region, the absorption bands around 1631 cm^{-1} and 1398 cm^{-1} are assigned to the antisymmetric and symmetric stretching of the dicarboxylate groups, respectively.[88,253] The peak related to the aromatic ring (C=C) bonds stretching is recognized at 1507 cm^{-1}.[229, 350,371] In the second region, the peaks at 1017 cm^{-1}, 744 cm^{-1}, 1166 cm^{-1}, and 883 cm^{-1} are attributed to the in-plane/out-of-plane bending of the (C-H) bonds.[229, 253, 350, 371] Most importantly, the absorption of Fe-O bonds could be recognized around 545 cm^{-1}.[229,372,373]
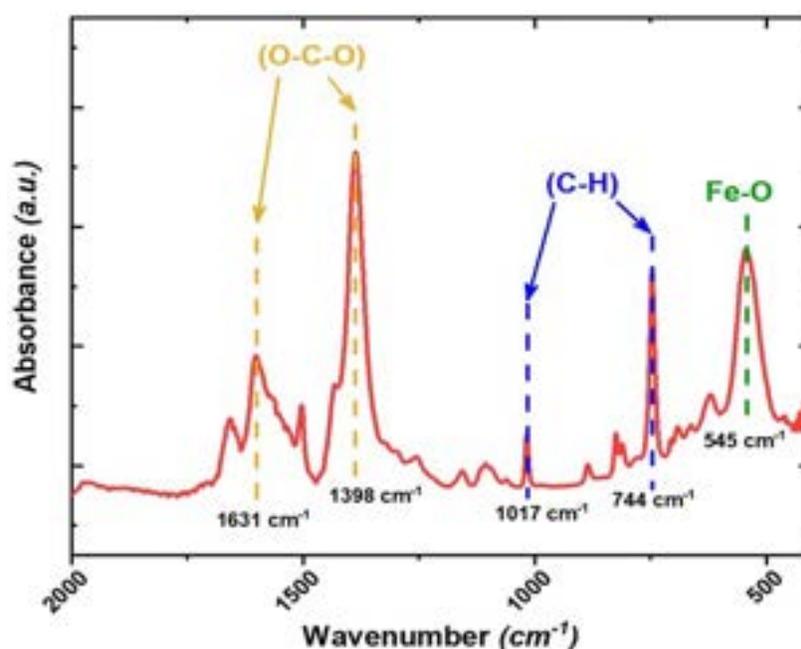
Figure 6.8 FTIR absorption spectrum of the activated MIL-88B(Fe).

Surface area measurement:

The textural properties of the synthesized MIL-88B(Fe) were measured using N$_2$ sorption over a relative pressure (P/P$_0$) range between 0.01 and 0.99. According to simulations, the 3D structure of the MIL-88B framework at its maximum expansion should exhibit a high surface area of 3040 m^2 g^{-1}.[413] However, due to the high flexing character of its structure, and it low affinity towards the adsorption of nitrogen gas, a low specific surface area was measured.[413,414] The experimental N$_2$ adsorption-desorption curve is shown in Figure 6.9, showing the type-I isotherm, usually obtained for microporous solids.
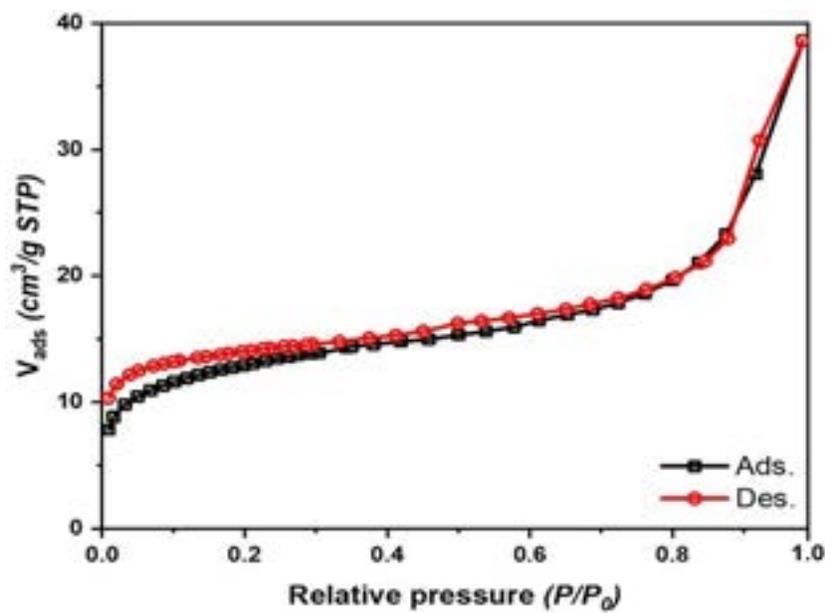
Figure 6.9 Adsorption/desorption isotherm of the MIL-88B(Fe) MOF.

For MOFs, the BET analysis is commonly used for determining surface areas from nitrogen adsorption isotherms.[415] It was originally derived for multilayer gas adsorption onto flat surfaces. However, in the case of metal-organic frameworks, gas adsorption usually takes place through pore-filling instead of layer formation.[416] Nevertheless, It is reported that the BET method is still applicable in the case of microporous structures at a low-pressure range, whereby a linear fitting of the BET plot is achieved with a positive y-intercept.[415–417] Within this range, the measured surface area usually agrees with the accessible surface area calculated through simulations.

Hence, the specific surface area of the obtained MIL-88 crystals was calculated using the BET method, at a relative pressure between 0.05 and 0.15 [415], expressing a specific surface area of 47 m^2 g^{-1}. The fitting for the data obtained within this range matched perfectly with the BET plot ((Supporting information(section 6.7), Figure 6.22)). A hysteresis loop was observed on the desorption curve associated with the known breathing effect of the MIL-88 framework. The pore volume and the pore size would vary due to the swelling and the shrinkage of the pores at different stages. Nevertheless, the low SSA reported for the MIL-88B framework has been highly dependent on the residual adsorbed solvent.[418–422] It is discussed in terms of the low affinity of the structure towards the adsorption of nitrogen besides the steric hindrance of the terminal ligands.[341, 418, 419] In addition, due to the flexing character of the MIL-88 structure, degassing the adsorbed solvent from the pores at high temperature would transform the framework from the narrow-pore (np) structure to the closed-pore (cp) structure, resulting in a low-measured SSA.

Thermal gravimetric analysis (TGA):

The thermogravimetric profile of the as-produced MIL-88B(Fe) MOF was investigated. Samples were subjected to the airflow of 20 ml min^{-1} with a constant temperature ramp of 10 °C min^{-1} from room temperature up to 800 °C. The obtained thermogravimetric curve is presented in Figure 6.10, demonstrating the structure's high thermal stability.
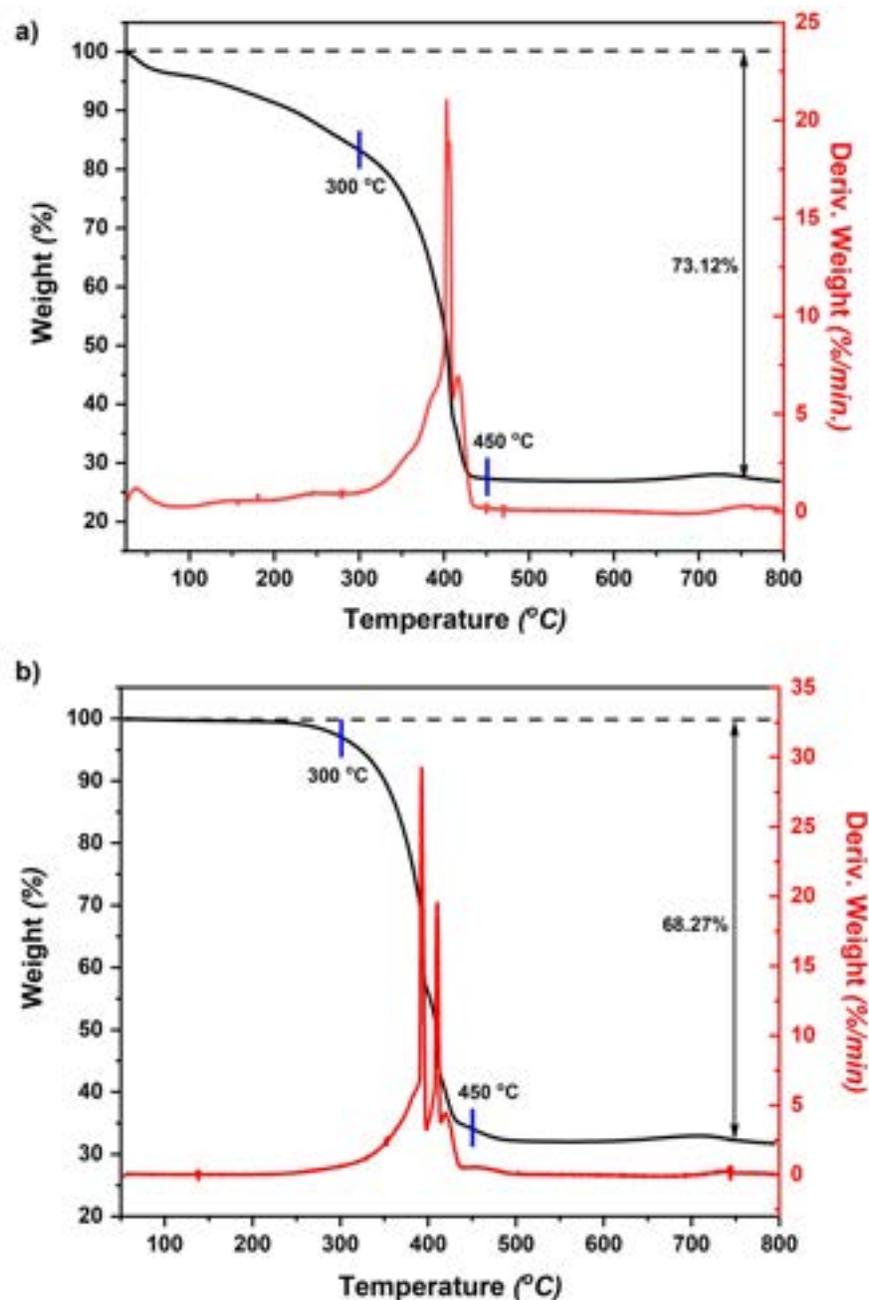
Figure 6.10 TGA thermograms of the DMF-treated MIL-88B(Fe) MOF, as-synthesized (a), after thermal treatment at 170 °C for 3 h (b).

The TGA curve of the as-synthesized MOF showed a continuous weight loss as the temperature went up to 500 °C, in which one main step was observed around 400 °C as indicated by the DTG thermogram (Figure. 6.10-a). According to previous studies in the literature, such a weight-loss step is related to the thermal decomposition of the MOF structure. On the other hand, the continuous weight loss occurring below 300 °C is mostly related to the desorption and evaporation of the guest solvents (EtOH and DMF) within the pores adsorbed during synthesis and activation steps. In order to confirm these results, a small amount of the as-synthesized MOF was thermally treated at 170 °C for 3 h before the TGA analysis (Figure 6.10-b). The curve of the thermally treated sample showed almost no weight loss (plateau) in the region below 300 °C, followed by a significant weight loss step (equivalent to ca. 68%) in the next temperature range between 300 °C - 450 °C. In this range, the detachment of the BDC linker and decomposition of the whole framework takes place, displaying the high thermal stability of MIL-88B(Fe). In the region above 500 °C, no significant weight loss was witnessed with residual solids of an ochre-red color remaining after decomposition.

As planned, the thermal decomposition of the MIL-88B(Fe) crystals would end up giving smaller particles of α-Fe$_2$O$_3$ in the nano-range size that would eventually interact with the AP matrix to catalyze its decomposition. The XRD pattern for the TGA test residuals was measured (Figure 6.11), validating the formation of the α-Fe$_2$O$_3$ with its recognizable diffraction peaks at $2\theta = 24.1°$, $33.2°$, $35.6°$, $49.4°$, $54.0°$, $62.5°$, and $63.9°$. Hence, the targeted in-situ sequential formation of the nanostructured oxide particles would be achieved during thermal decomposition during the AP combustion process.
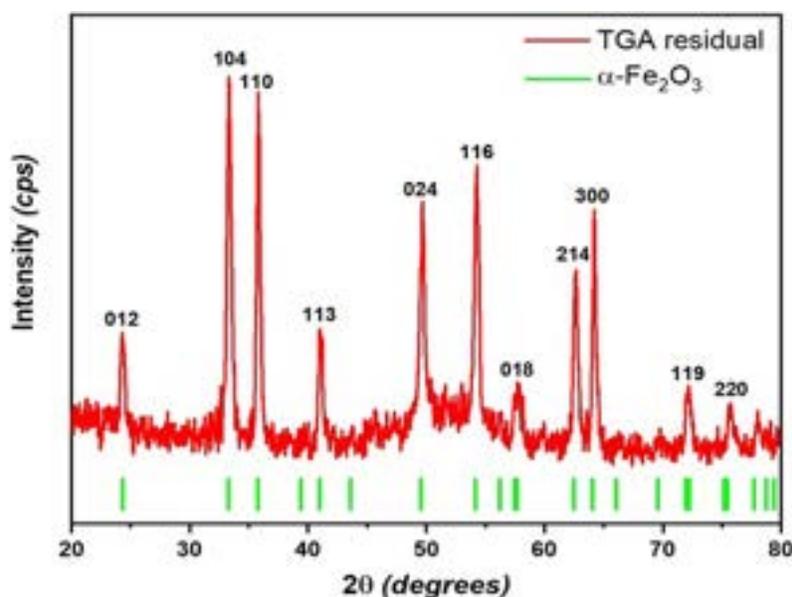
Figure 6.11 The XRD pattern for the TGA residuals confirming the formation of the α-Fe$_2$O$_3$ particles as a final product after the calcination of the MIL-88B(Fe) framework.

6.4.2 Characterization of MIL-88B(Fe)/Ammonium perchlorate(AP) nanocomposite

As shown in Figure 6.12, introducing the small MIL-88 particles into an AP composite resulted in a significant dispersion of AP, with the composite particle size ranging around 2 μm - 3 μm compared to the 150 μm - 200 μm size of the initial AP particles.
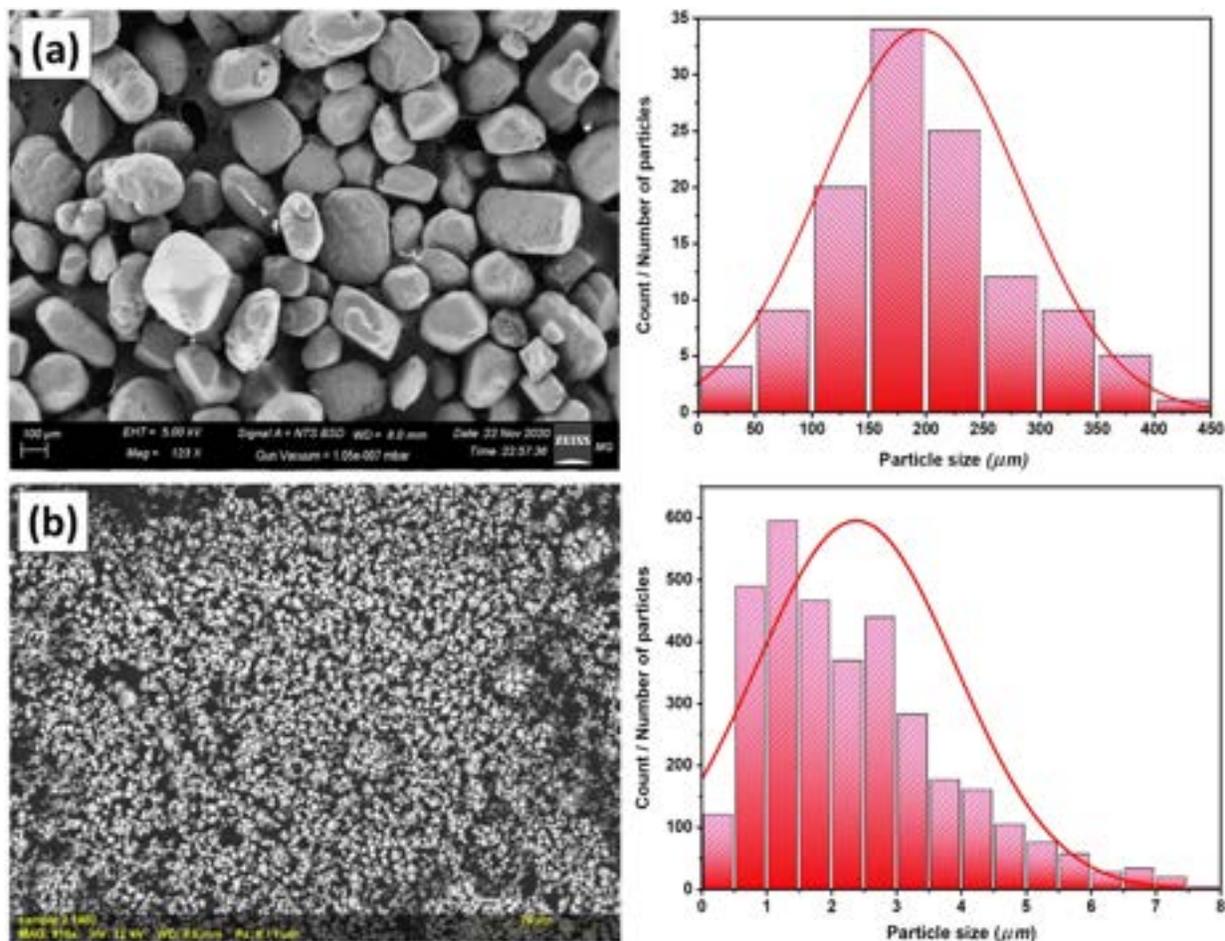
Figure 6.12 SEM micrographs and particle size histogram of pure AP (a), MIL-88B(Fe)/AP nanocomposite (b).

Visual inspection of the MIL-88B(Fe) MOF/AP nanocomposite demonstrated uniform dispersion of MIL-88B(Fe) MOF particles into the oxidizer matrix. Initially, AP demonstrated a white color, whereas the MOF/AP nanocomposite acquired an orange color at only 1%wt. added MOF (Figure 6.13).
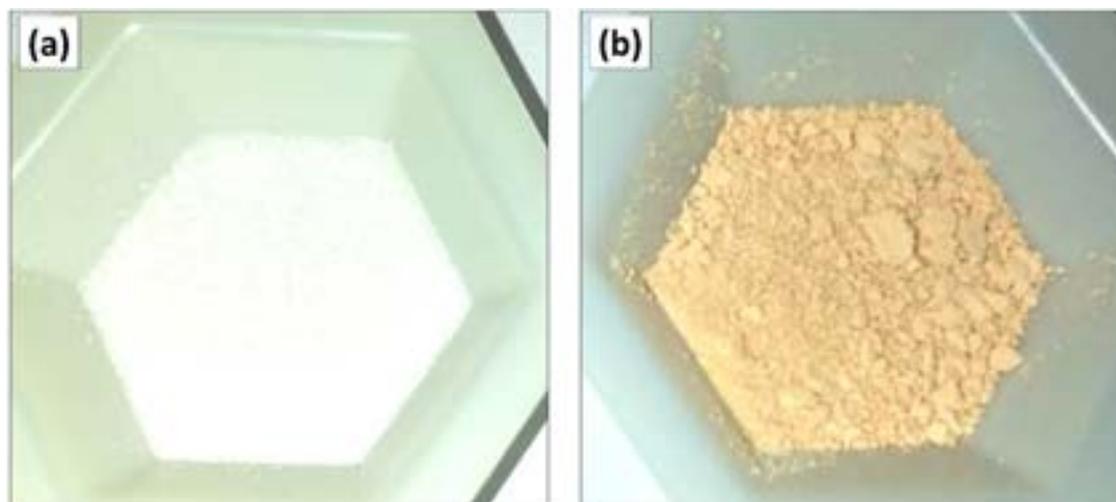
Figure 6.13 Appearance of pure AP particles (a), MIL-88B(Fe) MOF/AP nanocomposite (b).

The dispersion of MIL-88B(Fe) MOF into the energetic matrix was further investigated via elemental mapping using an EDX detector. Satisfactory uniform elemental dispersion was verified from the EDX micrographs (Figure 6.14).
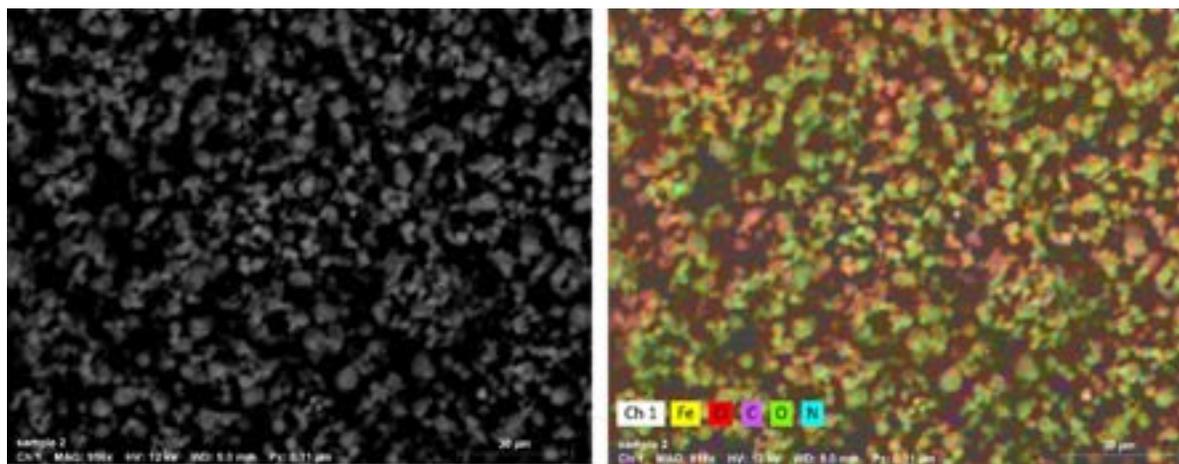
Figure 6.14 Elemental mapping of MIL-88B(Fe) MOF/AP nanocomposite.

6.4.3 Thermal behavior of MIL-88B(Fe) MOF/AP nanocomposite

The catalytic efficiency of MIL-88B(Fe) MOF on AP thermal behavior was investigated using DSC. While AP demonstrated a total heat release of 733 J g^{-1}. MIL-88B(Fe) MOF resulted in an enhanced heat output by 66%, the AP/MOF composite resulted in a 66% enhanced heat output of 1218 J g^{-1}, and the main exothermic decomposition temperature was decreased by 71 °C (Figure 6.15).
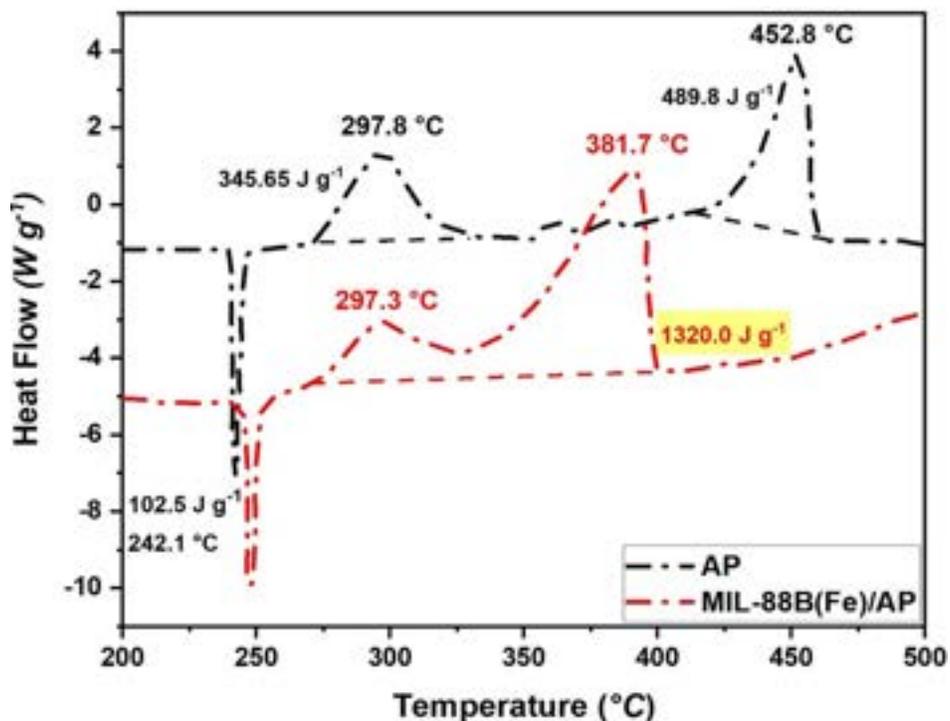
Figure 6.15 Impact of Mil-88B(Fe)MOF on AP thermal behavior using DSC.

The MIL-88B(Fe) MOF ($C_{24}H_{12}O_{13}Fe_3Cl$) contributed to the AP/MOF composite decomposition through the organic linker decomposition, resulting in higher heat output. Besides, it exhibits a catalytic effect via the Fe content and boosts the combustion enthalpy thanks to the O_2 content. MIL-88B(Fe) exhibited an O_2 and Fe content of 29% and 24%, respectively; therefore, it resulted in a high catalytic activity with improved interfacial surface area and reactivity. Furthermore, the exclusive evolution of a Fe_2O_3 nanocatalyst during the decomposition process supports this catalytic ability, facilitating the decomposition of more AP present in the sample and yielding an enhanced decomposition enthalpy of the composite by 66%. The impact of MIL-88B(Fe) MOF NPs on AP thermal behavior was further evaluated using TGA (Figure 6.16).
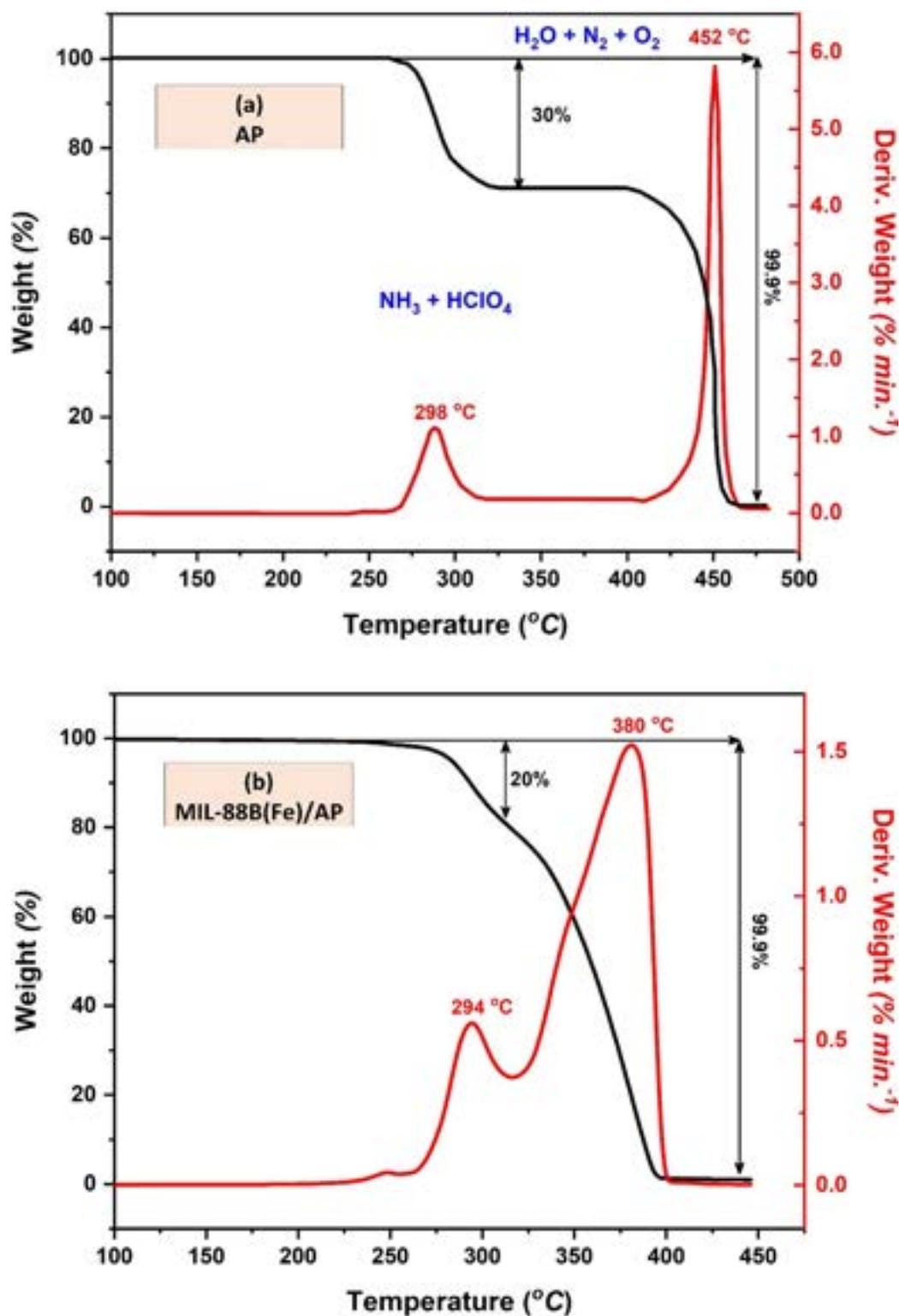
Figure 6.16 Impact of MIL-88B(Fe) MOF on AP thermal behavior using TGA.

TGA results demonstrated a decrease in AP main decomposition temperature by 72 °C; this result agreed with the DSC outcomes.

6.4.4 Kinetic study of MIL-88B(Fe) MOF/AP nanocomposite

Kinetic parameters obtained by the Kissinger method:

Kissinger's model is based on the highest decomposition peak temperature; this temperature was obtained from the DTG thermogram (Figure 6.17).
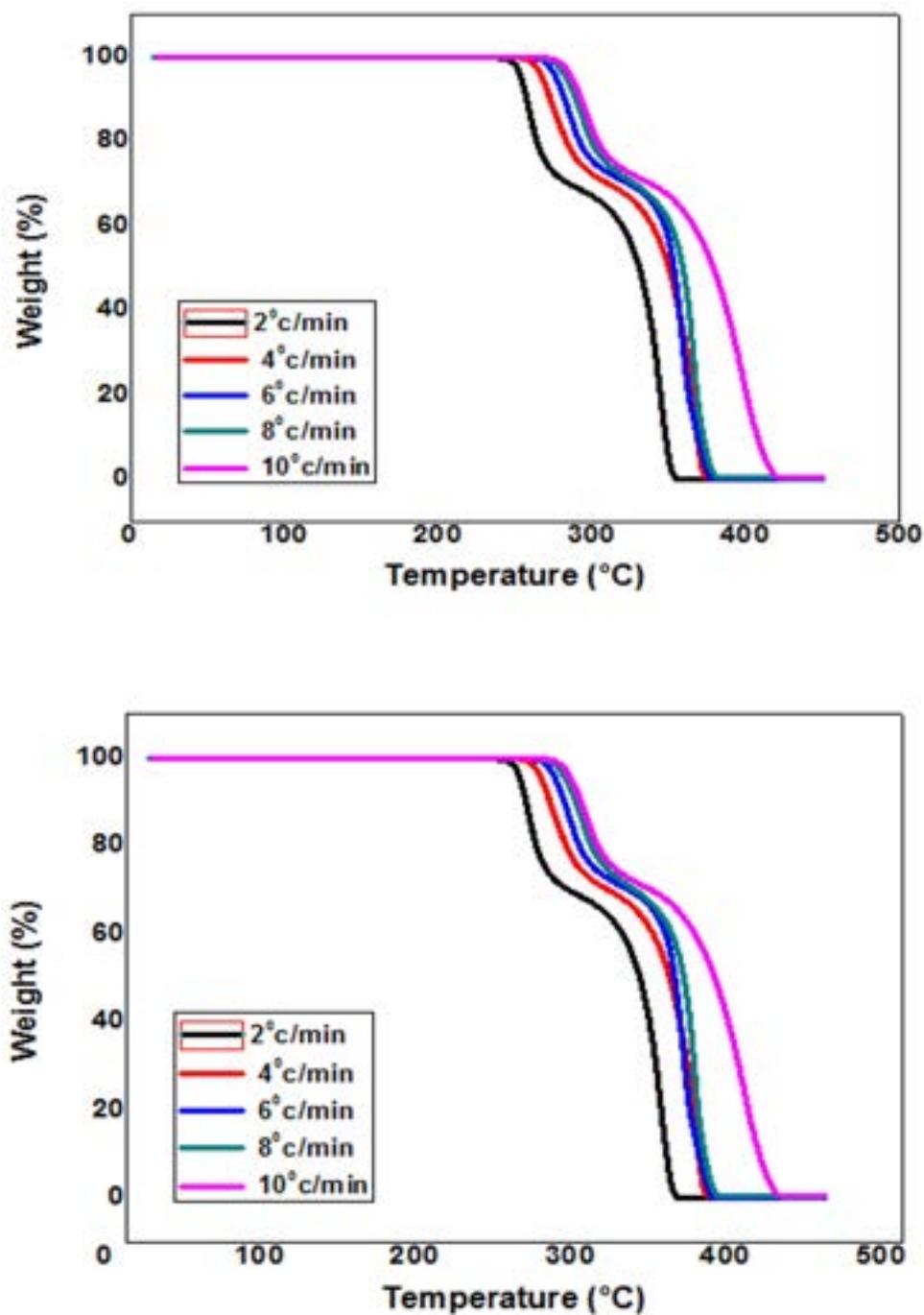
Figure 6.17 TGA thermogram of AP(a), MIL-88B(Fe)/AP(b).

The activation energy was obtained from the slope of the straight-line $ln(\frac{\beta}{T_2})$ versus $\frac{1}{T}$ at the five selected heating rates.
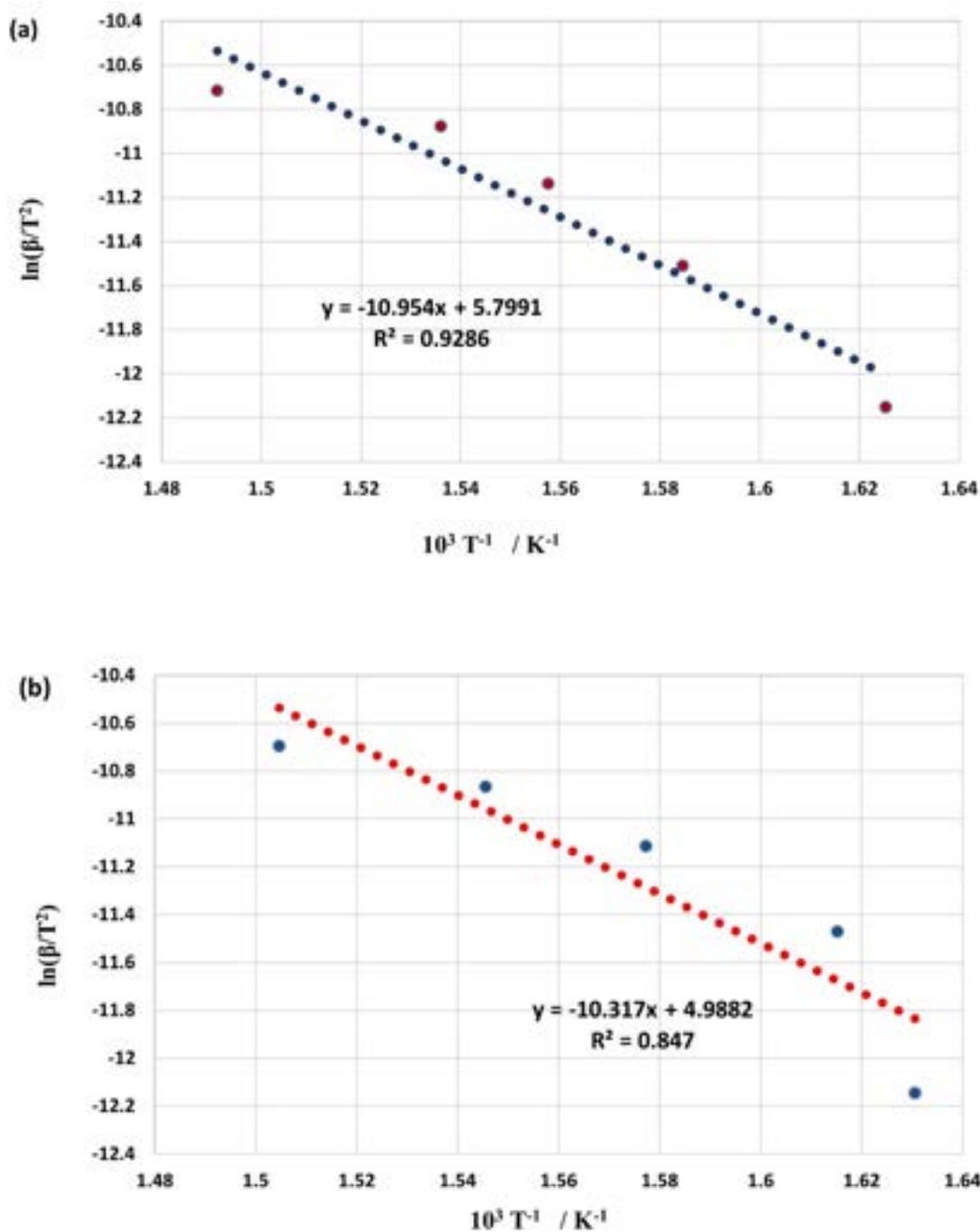
Figure 6.18 Activation energy of AP (a), MIL-88B(Fe)/AP (b), using the Kissinger method.

The activation energy of AP to MOF/AP were found to be 92.1 kJ mol^{-1} and 85.8 kJ mol^{-1}, respectively.

Kinetic parameters obtained by the Kissinger – Akahira – Sunose (KAS) method:

Activation energy at different fractional conversion was determined using the modified Kissinger-Akahira-Sunose (KAS) method. The kinetics parameters, including pre-exponential factor (A), kinetic model (f(α)), the activation energy (E_a), and a regression factor (r) of AP and MOF/AP, are tabulated in Table 6.1.

Table 6.1 Kinetic data of un-activated AP and activated AP using the (KAS) method

α reacted	AP			MIL-88B(Fe) MOF /AP		
	E_a (kJ mol^{-1})	Log A (s^{-1})	r	E_a (kJ mol^{-1})	Log A (s^{-1})	r
0.05	90	15	0.982	85	19	0.993
0.10	92	17	0.993	86	18	0.997
0.15	93	13	0.987	87	17	0.998
0.20	95	14	0.989	88	18	0.995
0.25	96	17	0.992	87	17	0.987
0.30	89	15	0.992	87	17	0.998
0.35	90	16	0.988	85	19	0.998
0.40	95	14	0.995	86	18	0.997
0.45	92	13	0.996	87	18	0.998
0.50	93	14	0.998	87	17	0.997
0.55	94	15	0.996	86	17	0.988
0.60	95	16	0.995	85	19	0.997
0.65	92	17	0.998	87	17	0.996
0.70	93	18	0.998	88	19	0.997
0.75	94	19	0.999	86	17	0.996
0.80	95	14	0.998	87	18	0.998
0.85	94	15	0.999	87	19	0.997
0.90	94	14	0.999	86	19	0.998
Mean	93.1	15.3		87.2	16.8	

The mean value of the activation energies of AP and MOF/AP were found to be 93.1 kJ mol^{-1} and 87.2 kJ mol^{-1}, respectively. Activation energy using the KAS method was found to be in good agreement with the Kissinger method.

6.5 Conclusions

Iron-based MIL-88B metal-organic framework was synthesized following a facile microwave-assisted method with high power input at 850 W, resulting in uniform size distribution in the range of few microns for a total synthesis time of 15 min. The structure of the achieved flexible MOF was confirmed via XRD, SEM-EDX, TEM, N_2 adsorption. Furthermore, the results showed that most of the produced MOF crystals were of a hexagonal bipyramidal diamond-like shape with the presence of some short spindle-like ones. The MIL-88B(Fe) structure showed high thermal stability above 300 °C and high Fe and O_2 content of 24% and 29% respectively, suggesting the potential use of such a MOF in catalytic applications in the field of energetic materials. The XRD pattern for the MIL-88B(Fe) framework TGA air oxidation products confirmed the formation of an α-Fe_2O_3 nanocatalyst as a final product. The catalytic efficiency of MIL-88B (Fe) on AP thermal behavior was assessed via DSC and TGA. AP solely has a decomposition enthalpy of 733 J g^{-1}, while the AP/MIL-88B(Fe) composite offered an increased decomposition enthalpy by 66%; the main exothermic decomposition temperature was decreased by 71 °C. Besides, MIL-88B(Fe) resulted in a decrease in the AP activation energy by 23% and 25% according to the Kissinger and KAS models, respectively.

6.6 Acknowledgment

6.7 Supporting Information

6.7.1 Structure of MIL-88B(Fe) SBU

The overall structure of the iron-based flexible MIL-88B metal-organic framework is shown in the main text in Figure 6.1. However, its secondary building unit, the smallest building block in the framework, is not fully illustrated. As explained, in the MIL-88B(Fe) structure, the trinuclear metal μ_3-oxo cluster is formed at the reported reaction conditions, whereby the three metal centers are connected through a central oxygen atom (Figure 6.19).[52] Each metal ion forms an octahedral complex with the four connecting linkers around the central

ion in its square plane. At the outer vertex of the complex, a solvent molecule bonds to the metal center through an oxygen atom or an individual halide anion present from the initial precursors.[54, 211]
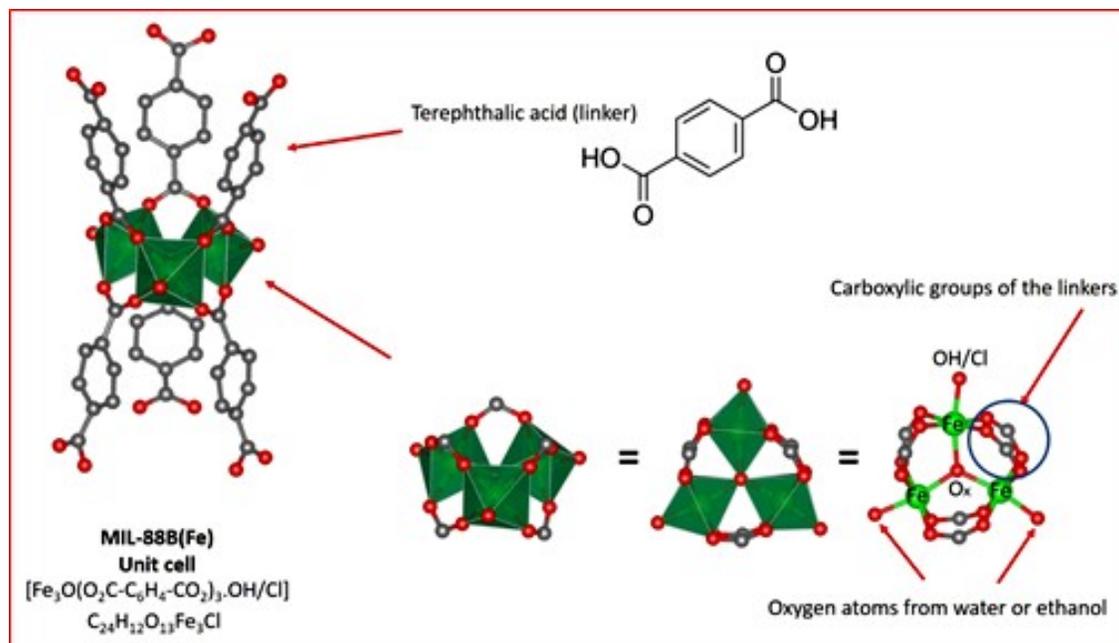
Figure 6.19 The trimetallic μ_3-O cluster of the MIL-88B(Fe) metal-organic framework.

6.7.2   Microwave synthesis of MIL-88B(Fe)

- Model: Microwave Synthesis Reactor Monowave 400.

- Company: Anton Paar (Canada).

- Vial type: Glass vial G30.

- Vial volume: 30 ml. - Filled volume: 15 ml.

- Temperature control: Ruby thermometer + IR sensor

Table 6.2 The applied method for the microwave-assisted synthesis of MIL-88B(Fe)

Step	Program	Temp. (°C)	Time (hh:mm:ss)	Actual step time (hh:mm:ss)	Powder (W) [limit]	Cooling	Stirrer speed (rpm)
1	Heat as fast as possible	150	—	00:00:55	850	Off	500
2	Hold	150	00:15:00	00:15:00	850	Off	500
3	Cool down	55	—	00:04:05	—	On	500
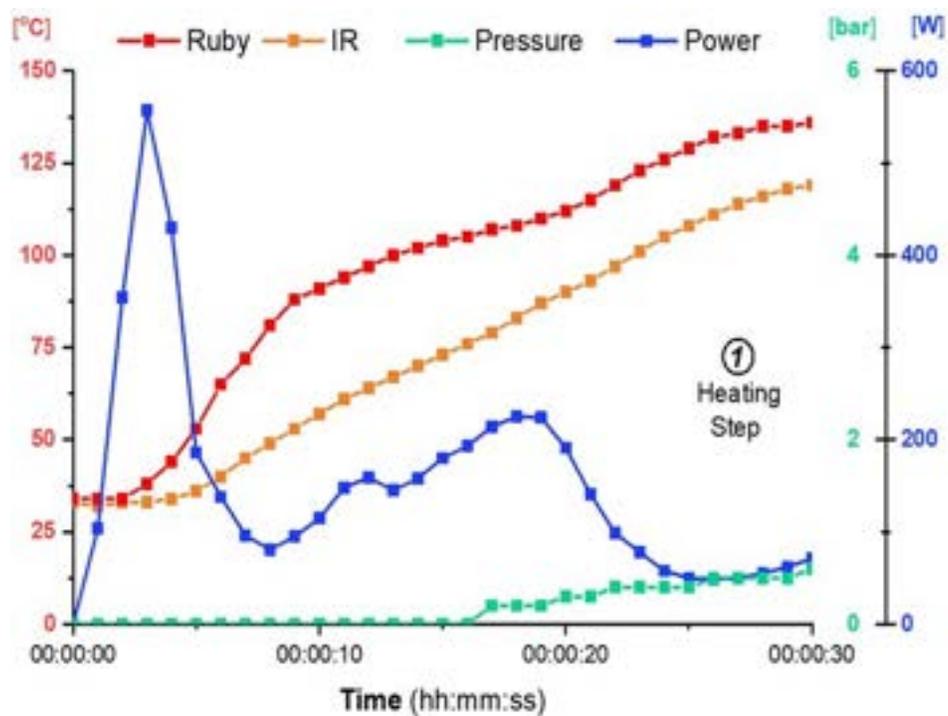
Figure 6.20 Detailed demonstration of the initial heating step during the MIL-88B(Fe) preparation
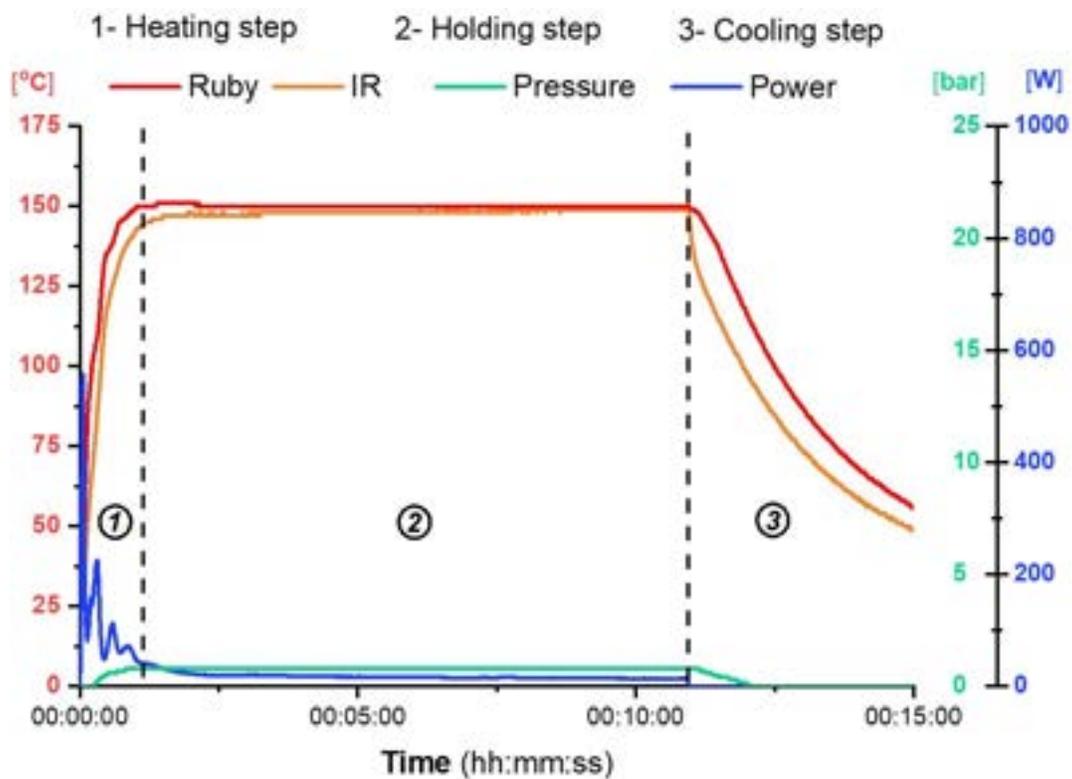
Figure 6.21 Graphical representation of the reactor conditions at each step during the MW synthesis process for MIL-88B(Fe).

6.7.3 X-ray Diffraction calculations

Based on the XRD data, calculations were made to investigate more about the prepared MIL-88B(Fe) crystals via microwave-assisted techniques (Table 6.3). Bragg angles were identified among these calculations, and the interplanar spacing (d-spacing) was deduced.[423] Besides, the calculated crystallite size was averaged to be around 50 nm. Compared with the TEM images, the small crystals detected are MOF grains composed of smaller crystallites. Similarly, the larger crystals in the SEM images are MOF particles of smaller grains found in the TEM images, where the crystallite size calculations by applying Scherrer's equation would fail as the particle size is definitely greater than 200 nm.

Moreover, it is clear that the calculated values of the crystallite size are of a wider range to be consistent, indicating that the microstrain is not the only component affecting the peak broadening and that the crystallite size contributes to the broadening as well. Finally, the instrumental broadening was also reviewed both from the X-ray source ($K_{\alpha 1}$ and $K_{\alpha 2}$ overlap) and the machine optics (LaB_6 standard), the $\beta_{inst.}$ was rounded to 0.05° reflected in decrease in the calculated crystallite size by almost 7 nm.

Table 6.3 Different calculations performed based on the XRD data

Parameters		Bragg's angle		d-spacing (Å) $d_{hkl}=\lambda/(2sin\theta)$	FWHM β (°)	D (nm) $=\frac{K\lambda}{\beta cos\theta}$	Average D (nm)	Microstrain $\epsilon=\frac{\beta}{4cos\theta}$	Microstrain (ϵ) $\times10^{-3}$
K	λ (Å)	2θ (°)	θ (°)						
0.87[424]	1.5406	9.49677	4.748385	9.3054	0.16868	45.68	49.42	8.86×10^{-3}	8.86
		12.66948	6.33474	6.9813	0.13091	59.02		5.15×10^{-3}	5.15
		14.07583	7.037915	6.2868	0.12889	60.03		4.56×10^{-3}	4.56
		15.86276	7.93138	5.5824	0.16207	47.84		5.08×10^{-3}	5.08
		16.2722	8.1361	5.4429	0.17989	43.12		5.49×10^{-3}	5.49
		16.66066	8.33033	5.3168	0.19005	40.84		5.66×10^{-3}	5.66
		17.10361	8.551805	5.1801	0.2041	38.05		5.92×10^{-3}	5.92
		18.94681	9.473405	4.6801	0.15352	50.71		4.01×10^{-3}	4.01
		19.39821	9.699105	4.5722	0.13107	59.44		3.35×10^{-3}	3.35
		21.05935	10.529675	4.2152	0.09555	81.75		2.24×10^{-3}	2.24
		21.54412	10.77206	4.1214	0.16083	48.61		3.69×10^{-3}	3.69
		22.08101	11.040505	4.0224	0.17716	44.17		3.96×10^{-3}	3.96
		26.05347	13.026735	3.4174	0.14537	54.22		2.74×10^{-3}	2.74
		26.32926	13.16463	3.3822	0.18149	43.46		3.39×10^{-3}	3.39
		28.49522	14.24761	3.1299	0.28104	28.19		4.83×10^{-3}	4.83

6.7.4 Surface area measurement

The specific surface area of the obtained MIL-88 crystals was calculated using the BET method, at a relative pressure between 0.05 and 0.15 [415], expressing a specific surface area of 47 m^2 g^{-1}. The fitting for the data obtained within this range matched perfectly with the BET fitting (Figure 6.22). Nevertheless, the low SSA reported for the MIL-88B framework has been reported to be highly dependent on the adsorbed solvent.[418–422]
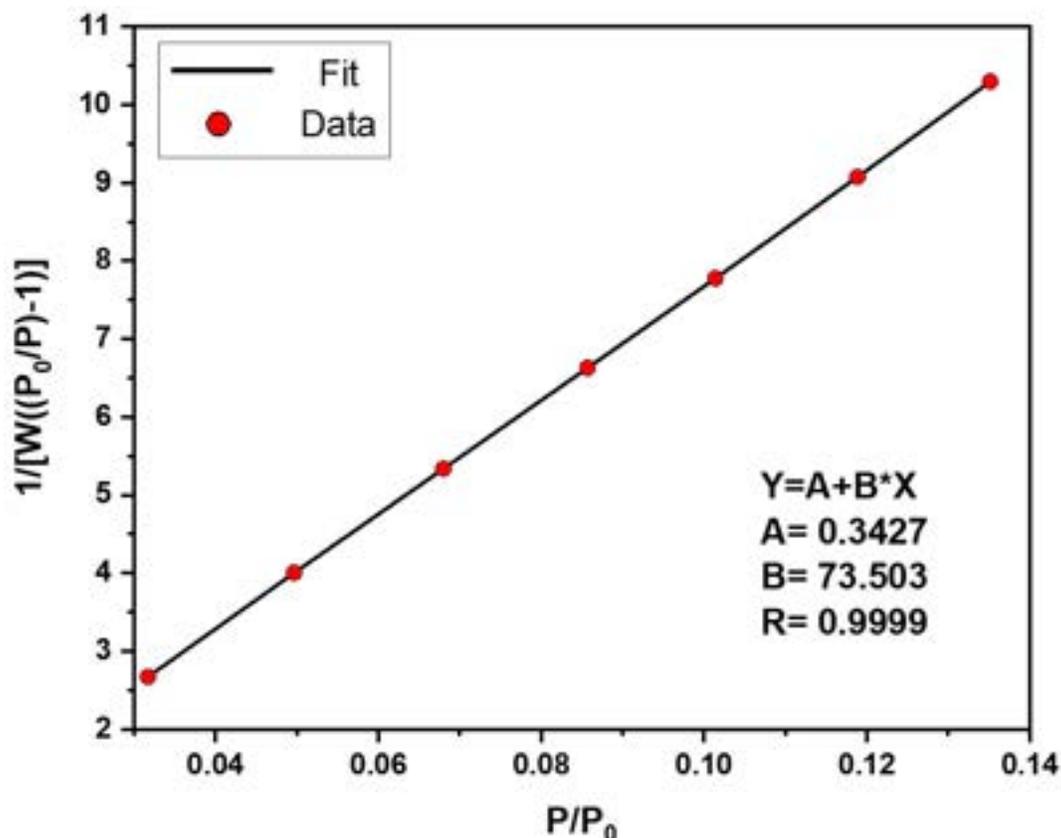
Figure 6.22 BET fit for the adsorption isotherm of MIL-88B(Fe).

We dug deeper to find the reason behind the low SSA measured for the MIL-88 framework. The MIL-88 framework possesses a flexible structure similar to that of the framework isomer MIL-53. They are both built from the trivalent metal ions and the ditopic H_2BDC linker. However, their breathing character comes as a result of different stimuli. The MIL-53 structure comprises infinite chains of metal oxo-clusters. These chains are corner linked to each other through the BDC linker. In the as-synthesized form MIL-53-as (cell volume = 1440 Å^3), the tunnels are occupied by structurally disordered molecules of neutral terephthalic acid. They leave the structure by heating at 300 °C and create the structure MIL-53-ht, with empty tunnels (cell volume = 1486 Å^3). By cooling in air, the structure reabsorbs water,

which leads to the third form MIL-53lt (cell volume = 1012 Å^3).[425] Hence, thermal treatment would make the framework swell, and adsorbing polar molecules would make it shrink again. During SSA measurement of the MIL-53 framework via nitrogen sorption, the powders are degassed at high temperatures, and high SSA is measured due to the structure expansion.

Unlike MIL-53, evacuating the pores of the as-synthesized MIL-88 framework forces the structure to shrink, and the original space group is preserved. As a result, a drastic increase in the length between the two non-equatorial trimers of the framework's cages is observed, correlated with a decrease in the distance between the equatorial ones. Upon solvent adsorption, the bipyramidal cages flatten, increasing the cell volume, resulting in the framework swelling.[425]

Hence, the dry (solvent-free) MIL-88 has small pores, while MIL-53ht has expanded ones. Moreover, the swelling of the MIL-88 structure is highly dependent on the type of adsorbate and the steric hindrance of the terminal ligands.[341,418,419] Its low affinity towards nitrogen adsorption (very minute swelling) also contributes to the measured SSA. In addition, the adsorption kinetics is to be considered, in which the time taken by the structure to express its flexing character varies from seconds to hours or days depending on the incorporated solvent. All these reasons interpret why the reported SSA for the MIL-88 framework is usually low compared to the very high SSA known for MOFs.[418–422]

CHAPTER 7   ARTICLE 4 - FACILE SOLVOTHERMAL SYNTHESIS OF MIL-47(V) METAL-ORGANIC FRAMEWORK FOR A HIGH-PERFORMANCE EPOXY/MOF COATING WITH IMPROVED ANTICORROSION PROPERTIES

Mahmoud Y. Zorainy,[1,2] Mohamed Sheashea,[2] Serge Kaliaguine,[3] Mohamed Gobara,[2] and Daria. C. Boffito[1]

7.1   Abstract

The vanadium-based metal-organic framework (MIL-47) distinguishes itself among other MOFs for its distinctive structure and unique properties (e.g., flexible structure, high thermal stability, and high surface area). The synthesis of MIL-47 has been reported from various metal precursors, including vanadium(III) chloride (VCl_3) as a rich source of metal ions. Attempts have been made to include other starting materials, a step forward towards large-scale production. Synthesis from various solid materials is encouraged, seeking an economic and greener approach. In this study, vanadium pentoxide (V_2O_5), a readily abundant low-cost and thermodynamically stable metal source, was used to synthesize the MIL-47(V) framework via a facile solvothermal route. Such a precursor provides a controllable rate of metal ion production depending on the applied reaction conditions. In our method, the synthesis took place at a low temperature and reaction time (180 °C for 20 h, instead of 220 °C for 72 h), yielding MIL-47 microrods. Moreover, among its unique properties, the metal centers of MIL-47 oxidize under the influence of thermal or chemical treatments, preserving the framework structure. This unusual character is not commonly witnessed in comparable MOF structures. Such a property can be leveraged in anti-corrosion applications, whereby a redox reaction would sacrifice the framework components, protecting the metal in contact. However, the chemical stability of MIL-47 is doubted against the corrosive medium. Thus, an epoxy coating with 10 wt% MOF loading was incorporated in our investigation to extend the aluminum alloy (AA2024) surface protection for prolonged exposure duration. The uniformity of distribution of the prepared MOF within the epoxy matrix was confirmed using SEM/EDX. Electrochemical impedance spectroscopy (EIS) was used to evaluate the corrosion performance of the coated samples. The results showed that the inclusion of V-MOF offers extended corrosion prevention, over 60 days, for the AA2024 alloy against artificial

[1]Chemical Engineering Department, Polytechnique Montréal, Montréal, QC H3C 3A7 (Canada)
[2]Chemical Engineering Department, Military Technical College, Cairo (Egypt)
[3]Chemical Engineering Department, Laval University, Québec, QC G1V 0A6 (Canada)

seawater. The neat epoxy coating could not prevent the corrosion of AA2024 over two weeks of immersion, whereby pitting corrosion was clearly observed. The V-MOF could induce a series of redox reactions leading to the precipitation of vanadium on the cathodic sites of metal surfaces.
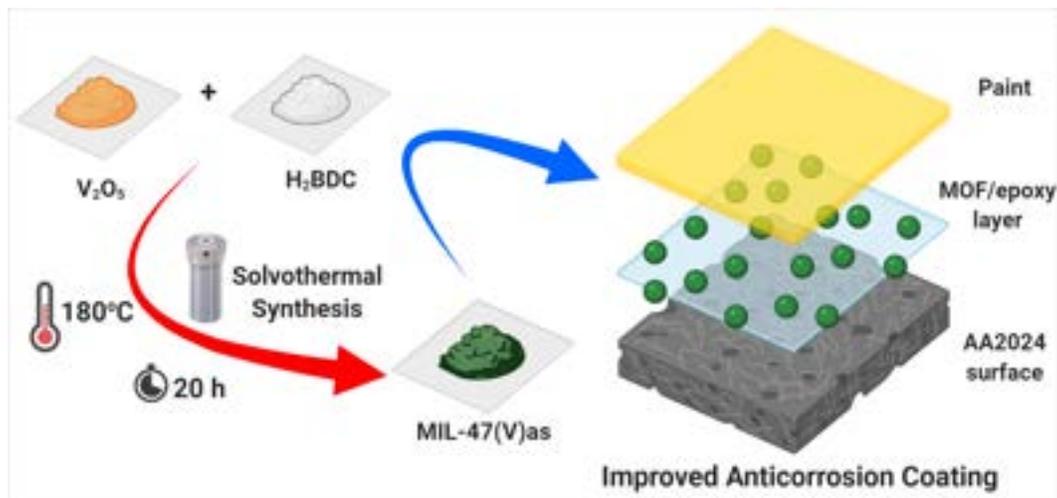
7.2 Introduction

Metal-organic frameworks (MOFs) have been applied in catalysis [426], gas adsorption and separation[427, 428], sensing [429], and drug delivery [430]. MOFs comprise both inorganic and organic moieties, whereby the metal ions or the metal oxo-clusters are connected to polytopic organic linkers resulting in multidimensional frameworks.[3] The synthesis of MOFs has been developing over the last decades targeting alternative, non-conventional approaches for faster reaction times, higher production yields, and controlled morphology.[77] On the other hand, hydrothermal/solvothermal synthesis is still the most commonly used synthesis technique, in which a metal source reacts with an organic linker and a convenient solvent under specific reaction conditions of temperature and time, resulting in distinct arrangements of frameworks.[431]

Among all MOFs discovered until now, those made out from vanadium are still limited.[166] MIL-47(V) was the first vanadium framework synthesized and reported in the literature.[49] It has drawn attention as a result of its large specific surface area ($S_{Langmuir}$= 1320 m^2 g^{-1}), high thermal stability in air (400 °C), as well as its derived superior catalytic properties.[49, 166] Such a structure is built from infinite (V-O-V)$_n$ chains linked with benzene-1,4-dicarboxylic acid (H$_2$BDC, also known as terephthalic acid or TPA), yielding a porous 3D orthorhombic structure (Figure 7.1).[166] In these chains, each two vanadium atoms share an oxygen atom and two carboxylic groups of separate linker molecules (Figure 7.1-a). The formed pores

within the structure are rather channels and not cages, whereby each tunnel is bounded by four benzyl units of the H_2BDC linker and four chains of corner-shared VO_6 octahedra (Figure 7.1-c,d).[49, 166, 339]

As synthesized, the MIL-47 framework is isostructural to MIL-53 with its flexible structure and the trivalent metal ions, whereby the bridged oxygen atoms between the metal octahedra belong to terminal hydroxide ligands.[418] They both occupy the sra topology and the *Pnma* space group.[49, 432] However, the metal ions of the MIL-53 structure maintain their valency regardless of the surrounding conditions. The synthesis of MIL-53 has been reported from different transition metals (e.g., Sc, Cr, Fe) of stable (+3) oxidation state.[50, 177, 218] In addition, it was successfully obtained from other p-block elements (e.g., Al, Ga, and In).[217, 219, 220] On the contrary, MIL-47 was basically built from vanadium, and recent investigations reported the potential incorporation of manganese.[49, 221, 433]

Upon the synthesis of these MOFs, the as-synthesized structure was found to be soft and dynamic, whereby reversible flexing (breathing) takes place in the presence of external chemical or physical stimuli.[49, 166, 418] The as-synthesized MIL-47 "MIL-47as" occupies the narrow pores (np) arrangement due to the inclusion of unreacted BDC molecules inside the pores (Figure 7.1-b). During the thermal activation of the framework in the air, evacuation of the pores takes place and the structure swells, similar to MIL-53ht, occupying the large pore (lp) arrangement (Figure 7.1-d). Unlike MIL-53, throughout the activation process, the V^{3+} ions oxidize to V^{4+}, and the μ_2-OH bonds with the metal centers turn into μ_2-O (i.e., vanadyl group (V=O)), but the topology remains unchanged. After calcination, the MIL-53lt keeps its breathing character depending on the transitions between the large-pore (lp) and the closed-pore (cp) arrangements (Figure 7.1-c,d). In contrast, MIL-47 expresses a relatively rigid structure compared to MIL-53lt, whereby permanent porosity is achieved.[49, 166, 339, 418] Hence, the lp $\rightarrow$ cp transitions were prohibited, and the cp arrangement was not obtainable in the activated form of MIL-47.

Later on, investigations of this distinctive structure confirmed that despite the relative structural rigidity of MIL-47, the framework is still responsive to external mechanical pressure towards the cp transition.[434] In addition, guest encapsulation or liquid adsorption were found to induce some structural deformation and twisting.[435] Other alternative activation methods (e.g., vacuum) were developed to stabilize MIL-47 in its trivalent oxidation state, conserving its structural flexibility.[436] Nevertheless, partial oxidation to the tetravalent state results in an intermediate product containing both oxidation states, and with the increase in the V^{4+} ions, the structure regains its rigidity towards the lp form.[436]
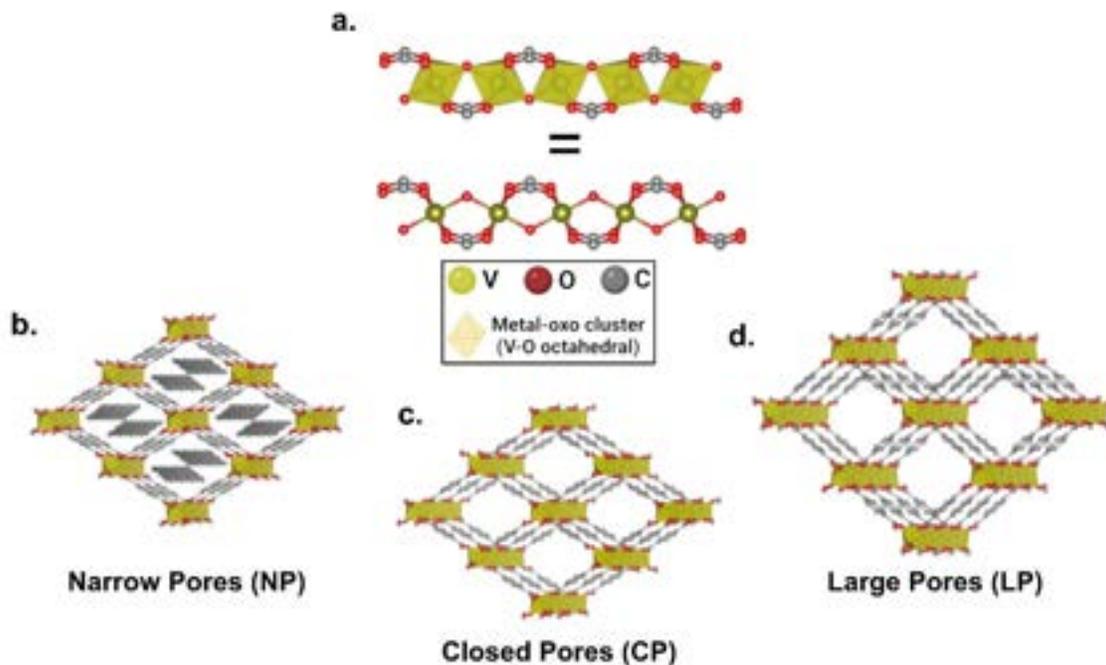
Figure 7.1 The structure of the vanadium MOF, MIL-47, expressing its flexibility under the effect of external stimuli. a) Infinite (V-O-V) one-dimensional chains. b) Narrow pores. c) Closed pores. d) Large pores. Color code: yellow-vanadium, red-oxygen, grey-carbon, hydrogen atoms were omitted for clarity.

In a typical MOF synthesis, different metal salts are incorporated as a source of metal ions, usually soluble ones such as metal chloride, nitrate, or acetate. Recent studies focusing on this approach offered other metal-salt-free choices, for instance, pure metals and alloys, metal oxides, hydroxides, and carbonates.[437] Such solvent-insoluble solids hardly release metal cations in common solvents, and when used as metal precursors, they supply ions at different rates depending on the reaction conditions; hence, controlling the MOF formation rate. Besides, employing these materials can offer a greener, economical, and sustainable route to tune the size and shape of the targeted MOF. For example, Kitagawa *et al.* have adopted using these solid materials, especially oxides, as a strategy to obtain MOF templates.[437,438]

When it comes to MIL-47, vanadium (III) chloride (VCl_3) has been the most commonly used metal precursor as it is the most reactive.[49, 434–436, 439–442] Nevertheless, VCl_3 is expensive and air-sensitive. It is unstable and easily decomposes when it comes in contact with the ambient atmosphere; thus, extra caution has to be paid while handling this material. As a result, weighing is usually taking place in a nitrogen-filled glove box, which is inconvenient when scaling up the process. Recent investigations have also involved the use of ammonium metavanadate (NH_4VO_3) as a less expensive, more stable, and readily available vanadium

precursor.[443] On the other hand, upon thermal decomposition of MIL-47, a mixture of vanadium(IV) and vanadium(V) oxides (VO$_2$ & V$_2$O$_5$) is left as a residue after the decomposition of the organic linker. Vice-versa, vanadium dioxide (VO$_2$) was successfully employed in the synthesis of MIL-47.[444, 445] However, to our best knowledge, V$_2$O$_5$ has not been reported as a precursor to MIL-47 yet,but only in the synthesis of another framework isomer using the 1,4-naphthalenedicarboxylic acid linker (i.e., [V(OH)ndc]$_n$ MOF).[446]

Metal corrosion is a major problem in the industrial and manufacturing fields. Its spontaneous nature resulting from the surrounding interactions with the metal surface leads to a significant loss in the metal physicochemical properties.[447] Aluminum alloy (AA2024) is extensively applied in the aircraft industry because of its high strength-to-weight ratio, high fatigue resistance, and toughness.[448] However, this alloy does not stand against corrosion in atmospheric conditions. Consequently, cladding or coating along with an inhibitor is usually applied. Organic coatings, such as epoxy, are an effective, practical, and cost-effective approach that can be applied to protect most metal substrates.[449] In order to achieve a prolonged protection lifetime, researchers have applied various strategies in which the incorporation of nanoporous materials, like carbon nanotube, graphene oxide, and nano-silica, comes on top. Recently, research considering reinforcing epoxy with MOFs and achieving advanced organic coatings of multi-functions is highly expanding.[450–452] Moreover, functionalization of MOFs for bonding with the nanofillers and the barrier coating has also been researched for a more advanced coating, providing a long-term protection for the metal-surface.[453–459]

Generally, metal corrosion is inhibited, reduced, or controlled by either adsorption-blocking or electrochemical actions.[460] An inhibitor prevents a metal or an electrolyte from coming into contact with the other side of a porous substrate. This barrier is formed by a combination of physisorption and chemisorption. Inhibitors usually interact through the adsorption mechanism by forming a protective film or layer by physisorption at the metal/electrolyte interface. They can also interact chemically to form an insoluble complex barrier hindering the direct contact between the metal surface and the corrosive electrolyte.[460] For MOFs, recent studies reported that the inhibition follows the adsorption-blocking mechanism[459,461,462]: Indeed, in MOFs, the organic linker confers different functional groups that are electron donor heteroatoms with π bonds.[460] Corrosion inhibition by coordination polymers or MOFs through electrochemical action is less common. Studies considering the anti-corrosion properties of MOFs are still scarce.

The presence of organic linkers within the structure of MOFs makes them compatible with the polymeric matrices.[450] Also, they can be functionalized to increase their interaction for more advanced MOFs/polymer nanocomposites. Moreover, the metal centers can accelerate

the cross-linking of these networks as active Lewis-acid sites, catalyzing the epoxy ring-opening reaction. For example, MIL-101(Cr), with its high surface area and highly active metal centers, facilitates the curing of thermoset polymers used as organic corrosion barriers. Such a porous structure significantly increases the amount of heat released during curing even at very low loadings.[463] Our group has previously studied the anti-corrosion performance of a cerium (III)/melamine coordination polymer and the mechanism behind the interactions taking place.[464, 465]

Here, we studied the solvothermal synthesis of the MIL-47 framework from V_2O_5 as an inexpensive, widely available, and thermodynamically stable precursor, a step forward towards scaling up the production of this MOF. In similar syntheses from oxides, one of the main drawbacks is the inclusion of unreacted metal oxide among the product as a contaminant, which we could avoid with the method proposed. The narrow-pore MIL-47(V^{III})as was fully characterized before its incorporation in the epoxy coatings for the anti-corrosion experiments. Moreover, the performance of the MOF/epoxy coating was evaluated, compared to neat epoxy coating, as an improved corrosion barrier to aluminum alloy AA2024 in a chloride-rich environment.

7.3 Results and Discussion

7.3.1 MIL-47 characterization

The recorded PXRD diffractogram was very similar to the simulated pattern of as-synthesized MIL-53 and MIL-47 (Figure 7.2). The pattern showed recognizable high-intensity peaks in the 5° - 30° 2θ-range, with the major diffraction peaks at around 2θ= 8.8°, 10.1°, 14.8°, 17.7°, 24.1°, and 26.7°.[49, 466] Moreover, in comparison with the pattern of the original vanadium precursor, the main diffractions of V_2O_5 at 2θ= 15.4°, 20.3°, 21.7°, and 26.2° were not detected in the recorded pattern, indicating a pure MOF product without any residual oxide.[466] Hence, the adopted synthesis technique (solvothermal method) was able to induce the release of the required metal cations from V_2O_5 as a precursor under the selected reaction conditions. The simple washing procedure applied was sufficient to remove unreacted precursors. On the other hand, upon thermal activation of the MIL-47 framework, the structure occupies the less flexible large-pore form. The XRD pattern for the activated MOF form was identical to the simulation of the reported MIL-47, whereby the prominent diffraction peaks were recognizable in the 5° - 20° 2θ-range, specifically at 8.3°, 14.4°, and 16.8° (Figure 7.2).[49] Once again, no diffractions of the metal oxide occurred in the activated MOF pattern.
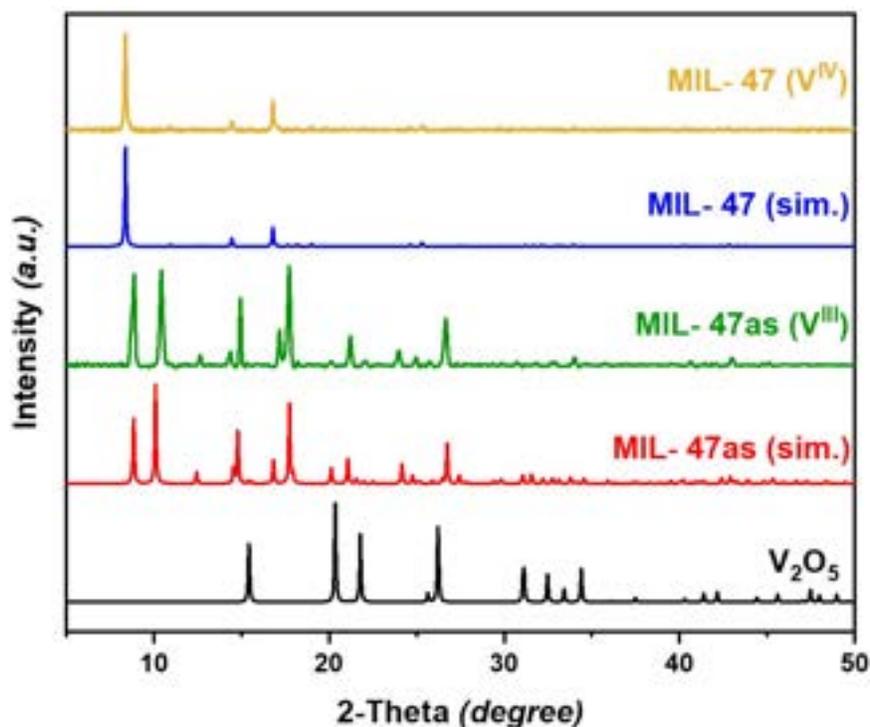
Figure 7.2 The XRD patterns for the MIL-47(V) metal-organic framework compared to simulations. V_2O_5 – "black"; MIL-47as (simulation) – "red"; MIL-47as (V^{III}) – "green"; MIL-47 (simulation) – "blue"; MIL-47(V^{IV}) – "yellow"; (Calculated patterns reproduced via Mercury/CSD simulated files: "IDIWIB" and "IDIWOH," respectively).

Fourier-transform infrared spectroscopy (FTIR) was employed to confirm the formation of the targeted MOF and the linkage between the vanadium cations and the organic ditopic H_2BDC ligands. The vibrational spectrum of the obtained crystals agreed well with that reported for the MIL-47 framework (Supporting Information (section 7.7), Figure 7.15). In order to ensure that the synthesized MOF is metal-oxide free, Raman spectroscopy was used as a selective technique to investigate such possible inclusion of other materials within the MOF crystals (Supporting Information (section 7.7), Figure 7.16). It clearly showed that despite being prepared from a metal oxide precursor, the synthesis technique reported here produced pure MOF crystals without any oxide residue.

The thermogravimetric analysis (TGA) technique was utilized to investigate the thermal stability of the MOF product. This technique can also indicate the inclusion of metal oxide residue based on the increase in the final weight percentage. Heating the MIL-47as sample from room temperature to 800 °C resulted in three weight-loss steps (Figure 7.3). The first step corresponds to the evaporation of residual solvents, whereby a gradual weight loss (equivalent to 5% - 7%) occurs at temperatures $\leq$ 200 °C. The second step of almost 30% weight-loss is in the region between 200 °C – 350 °C, originating from the oxidation of the

V^{3+} metal centers and the loss of the hydroxide groups bonded to the vanadium oxo-chains. At these temperatures, the thermal activation of the MOF occurs, whereby heat removes the unreacted H_2BDC linker from the framework's pores. Finally, the detachment of the organic linker and decomposition of the framework structure takes place in the third step between 375 °C – 425 °C, showing a weight loss of 40% with a mixture of VO_2 and V_2O_5 remaining as residue after the experiment.[49, 439]
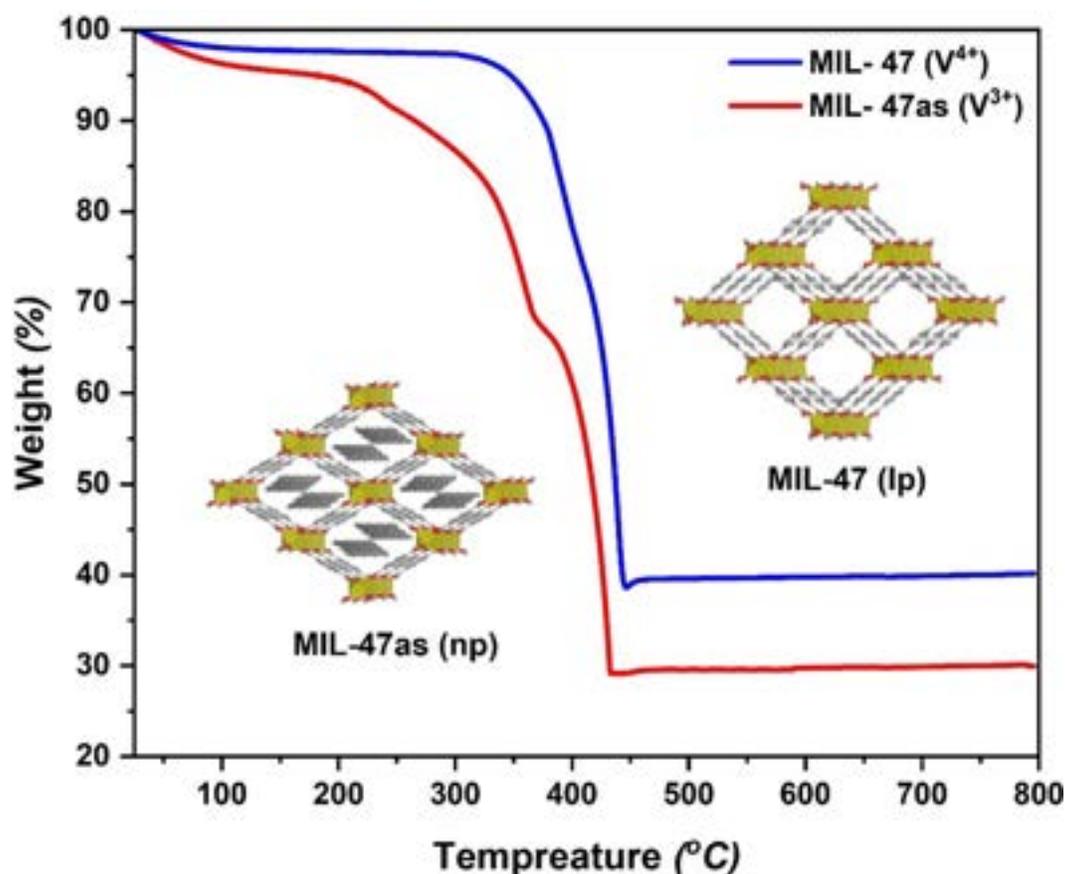
Figure 7.3 TGA curves of the as-synthesized MIL-47 "MIL-47as" powder compared to the thermally activated sample (MIL-47), showing the different weight loss steps and the transformation from the np to the lp forms of the structure.

Overall, the MIL-47as sample lost ca. 70% of its initial weight, comparable to published TGA data.[49, 166, 198, 434, 436, 439, 442, 443] Hence, confirming the purity of the obtained MOF and the absence of any residuals from the metal precursor. However, the separation and washing steps significantly affect the quality of the MOF product. Excessive washing can lead to partial decomposition as a result of its low chemical stability.[198] The TGA results confirmed that the above-reported washing procedures were convenient to achieve a pure product without decomposition.

On the other hand, the thermally activated sample (MIL-47) showed a single dominant weight-loss step (Figure 7.3) aside from the initial weight loss of 2% - 3% below 100 °C resulting from the evaporation of the adsorbed water.[217] After this slight weight loss, a plateau follows, skipping the metal centers' oxidation and the pore evacuation step until the decomposition of the framework between 350 °C – 450 °C, expressing a large-pore (lp) arrangement.[49] Once again, the TGA curve of this sample agreed with the previous studies, whereby a total weight loss of ca. 60% was witnessed (10% less than MIL-47as) as a result of the framework activation and oxidation.[49]

The thermally activated sample of MIL-47 showed no difference compared to the as-synthesized one, whereby the crystal had almost the same rod-like shape and average particle size. However, the MIL-47 powder appeared to have yellow color at low magnification, but the crystals seemed to be slightly greenish at higher magnification. Moreover, the recorded spectrum of MIL-47 was similar to the one of MIL-47as (Figure 7.16) with very minute changes. For example, in the spectrum of the thermally activated sample, the peaks related to the metal-O vibrations at lower wavenumbers were more pronounced (sharper peaks of higher intensity). In the 850 cm^{-1} - 950 cm^{-1} range, the small peak at around 891 cm^{-1} in the spectrum of MIL-47as shifted to a higher wavenumber to appear as a shoulder in the spectrum of MIL-47. On the contrary, in the 1400 cm^{-1} – 1500 cm^{-1} range, the shoulder appearing in the MIL47as spectrum around 1450 cm^{-1} was shifted to lower wavenumber in the MIL-47 spectrum. Similar shifts were noticed in the study of Yot *et al.* while studying the breathing behavior of MIL-47(V) under the effect of external mechanical forces, marking the transformations of these frameworks between different forms.[434]

The SEM images of the MOF samples confirmed the results reported above. Owing to the considerable difference in density between the as-synthesized crystals of MIL-47(V) framework and the V_2O_5 particles, SEM operated on the back-scattered electron mode (detector) was selected to screen the sample, whereby no traces of any foreign particles were found among the MOF crystals. On the other hand, the morphology of the crystals was studied using the secondary electron detector (Figure 7.4). The images showed the rod-like shape of the obtained crystals with a length of a few microns (< 10 μm, Figure 7.4-a and b). Furthermore, the images of the thermally activated samples showed typical crystals with no change in the morphology compared to the as-synthesized sample (Figure 7.4-c).
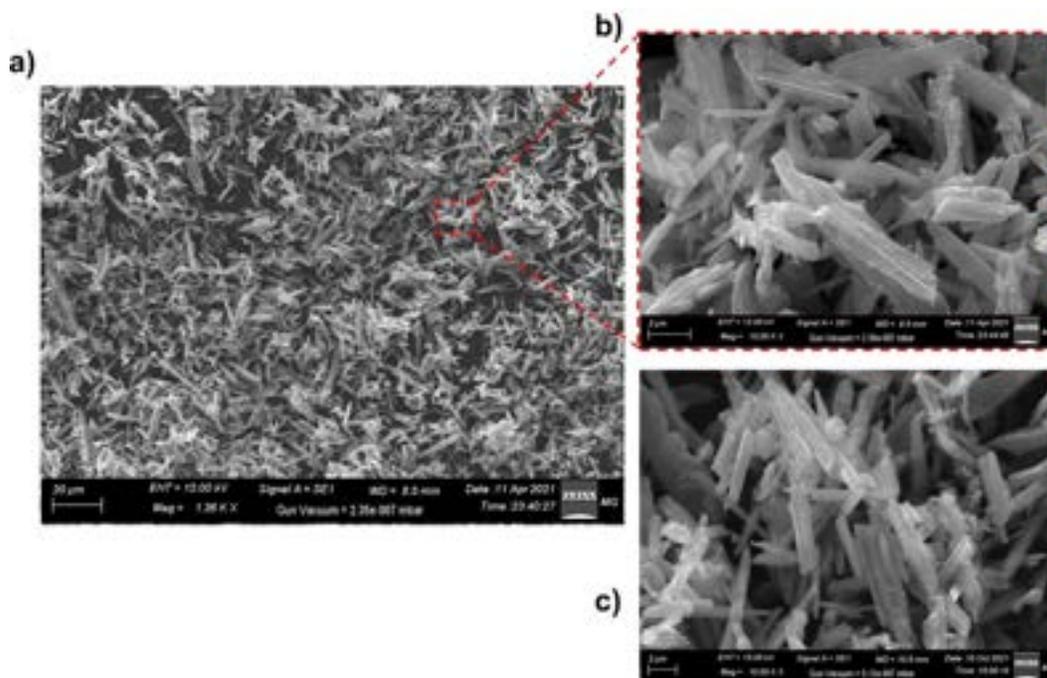
Figure 7.4 The SEM images of the MIL-47 samples at different magnifications.
a) and b) as-synthesized MIL-47, c) thermally activated MIL-47.

The EDX elemental analysis and mapping of the as-synthesized sample confirm the main composition of the MOF structure, whereby the three main elements V, O, and C were detected. These three elements were homogeneously distributed all over the sample (Figure 7.5). Also, the measured concentration of each element agreed with the reported formula of the MIL-47 MOF, whereby the abundance of each element was found as (at.%): C 49%, O 37%, and V 14%.[49]
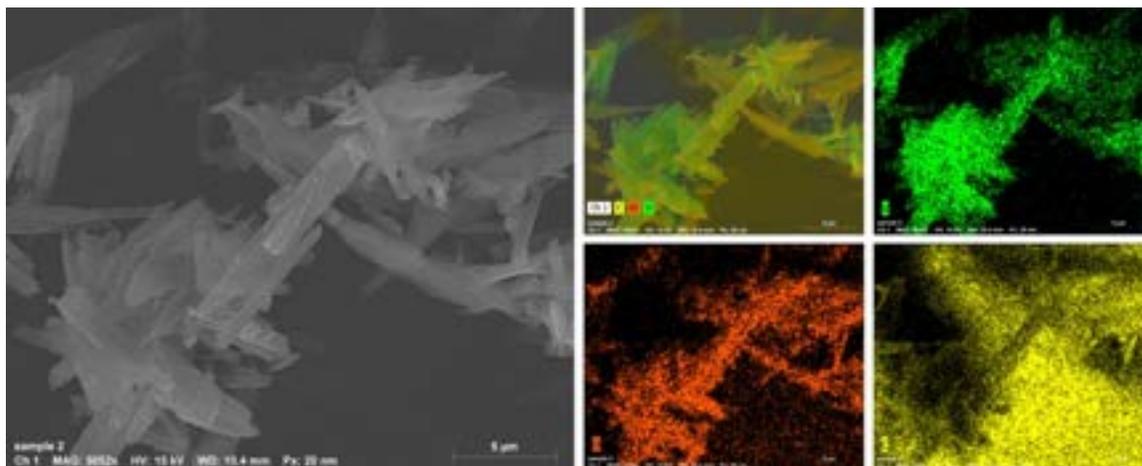
Figure 7.5 Elemental mapping of the as-synthesized MIL-47 sample obtained through the solvothermal technique, expressing the homogeneous distribution of the elements over the whole MOF crystals. Color mapping: V – bright green, O – orange, C – yellow.

7.3.2 Corrosion performance

Before testing the corrosion resistance of the prepared coatings, the adhesion and the thickness of both the neat epoxy and the MOF/epoxy coatings were investigated. The results of the crosshatch adhesion test, applied to evaluate the adhesion of both types of coating, revealed an excellent adhesion of the coating to the surface of the substrate (Figure 7.17). Next, using SEM/EDX microscopy, the thickness of each coating was investigated. The cross-section images showed uniform coating with a constant thickness of around $\approx 10 \pm 2$ μm (Figure 7.6).

Also, the surfaces of the coatings were free from cracks and contained no voids in between layers. Both coatings displayed excellent adhesion to the AA2024 substrate, whereby there is no sharp edge between the coating and the metal substrate (C represents the epoxy matrix in both samples). Furthermore, the cross-section image of the MOF/epoxy coated sample depicts a uniform distribution of the vanadium-MOF within the epoxy matrix; however, the epoxy-coated AA2024 sample did not show any vanadium. Due to the low thickness of the MOF/epoxy layer, it can be used as a pre-treatment layer applied before applying the subsequent paint topcoats.

The surfaces of the coatings were free from cracks and contained no voids in between layers. Moreover, both coatings displayed excellent adhesion to the AA2024 substrate, whereby there is no sharp edge between the coating and the metal substrate (C represents the epoxy matrix in both samples). Furthermore, the cross-section image of the MOF/epoxy coated sample depicts a uniform distribution of the vanadium-MOF within the epoxy matrix; however, the epoxy-coated AA2024 sample did not show any vanadium. Due to the low thickness of the MOF/epoxy layer, it can be used as a pre-treatment layer applied before applying the subsequent paint topcoats.

Moreover, the homogeneity of the MOF/epoxy coating was thoroughly investigated. The uniform distribution of the MIL-47as crystals within the epoxy matrix was monitored and validated using SEM/EDX (Figure 7.7-a). The SEM images of the coating surface obtained from the back-scattered detector showed that the V-MOF crystals were fully integrated into the organic matrix, preserving the same particle size presented in Figure 7.4. Based on the density difference between the MIL-47as microrods and the hardened epoxy matrix, the MOF crystals appear as white particles randomly dispersed over the darker grey/black colored epoxy coating (Figure 7.7-a). Furthermore, the elemental spot analysis of the coating confirmed the homogeneous distribution of vanadium all over the organic epoxy matrix in agreement with the previous results. However, nitrogen and aluminum were also detected in addition to the main MOF elements reported above (Figure 7.7-b). Nitrogen results from the
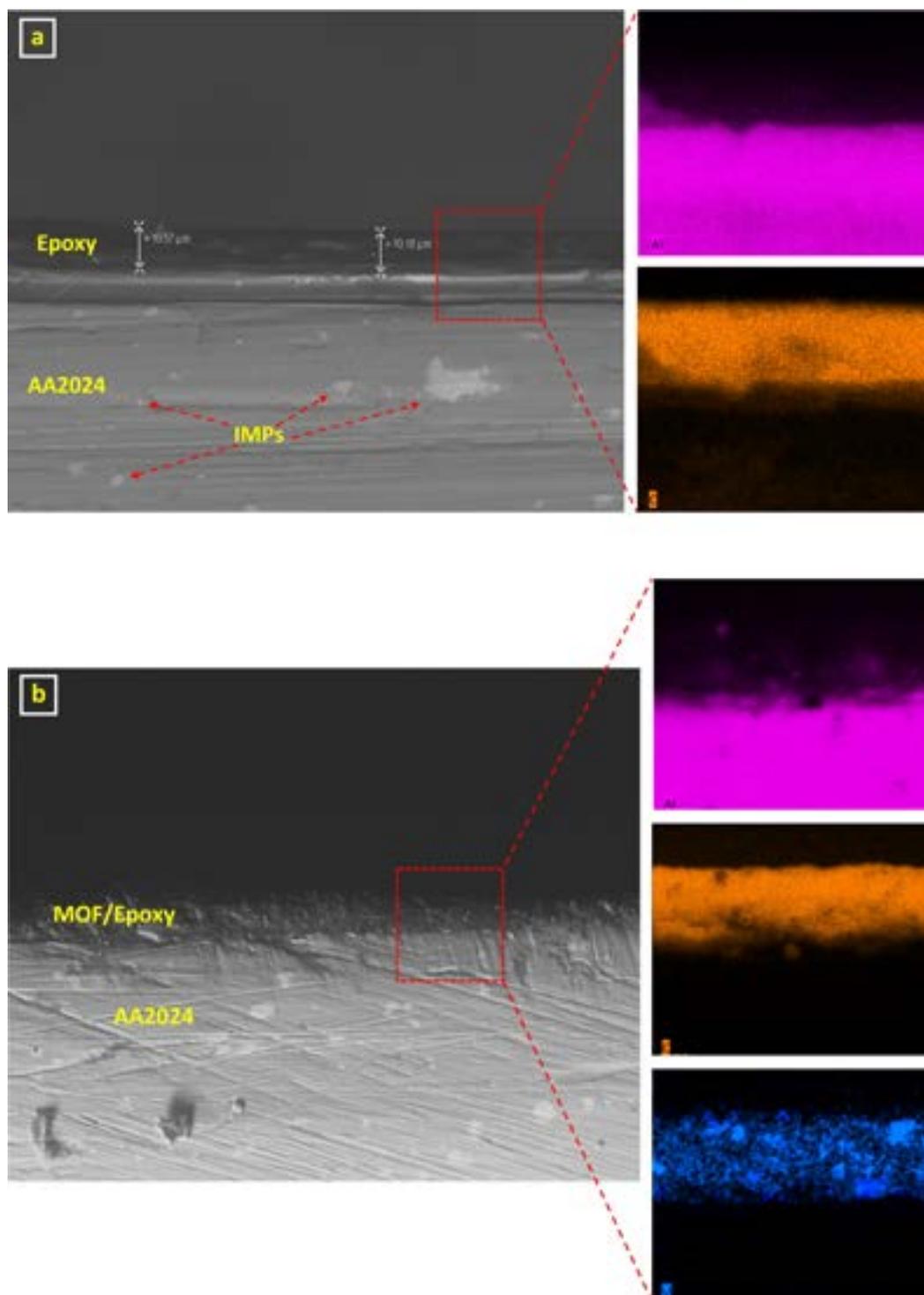
Figure 7.6 Side view for the cross-section of (a) neat epoxy (b) MOF/epoxy coated AA2024 samples under the SEM with their elemental EDX mapping. Color mapping: Al – purple, C - orange, V – blue.

DETA hardener as a tertiary amine responsible for the epoxy ring-opening and the initiation of the polymerization process, while the noticeable aluminum peak belongs to the substrate as a result of the small coating thickness employed in this case.
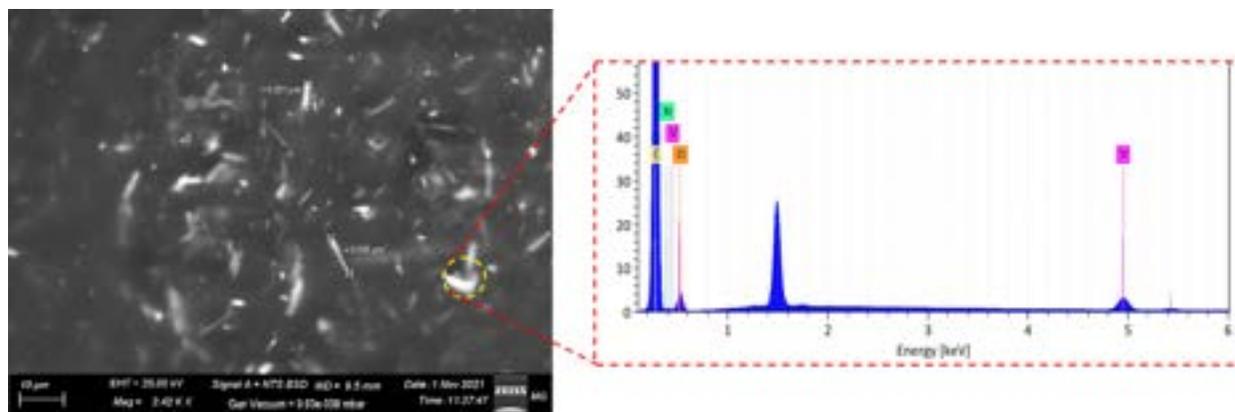
Figure 7.7 Figure 10. (a) SEM image of the MOF/epoxy coating surface (Top view) (b) EDX spot analysis of the selected area, with the peak between 1 keV – 2 keV belonging to the aluminum substrate. Color code: V – pink, C – yellow, N – light green, O – orange.

The corrosion prevention behavior of the coated samples was assessed via electrochemical impedance spectroscopy (EIS). Such a technique offers computable data reflecting both the corrosion and coating degradation processes throughout the whole course of immersion in the corrosive environment. Starting with the neat epoxy-coated AA2024 sample, the trend is linear with a slope approaching -1, expressing a general capacitive behavior at high and mid-range frequencies (Figure 7.8-a) that maintained over the 3-week immersion period in the corrosive electrolyte, 3.5%wt NaCl.[467] This epoxy coating acts as a barrier showing an initial high impedance of 6 MOhm cm^2 at 0.01 Hz after 3 days of immersion, whereby the corrosive solution would not effectively diffuse into the coating/surface interface during this early stage. However, the impedance gradually decreases through the end of the immersion test, losing more than an order of magnitude of impedance to about 0.3 MOhm cm^2 after 21 days of immersion.

In addition, the total impedance (|Z| at 0.01 Hz) showed a continuous decrease throughout the immersion test with the rise of a new time constant at the low-frequency range after 14 days of immersion. This time constant slightly increases afterward, as indicated by the phase angle plot (Figure 7.8-b). The figure clearly shows that the coating sustained the high phase angle at the high-frequency range during the immersion time. Nevertheless, the decrease in the impedance at the low-frequency range along with the existence of this new time constant indicate the degradation of the organic epoxy coating and the deterioration

of its properties as a barrier. This time constant is usually attributed to the relaxation of the mass transport process due to the formation of the corrosion products.[468] This activity is accompanied by pitting corrosion in different spots, observed after 14 days of immersion, which clearly confirms the breakdown of the epoxy coating. This behavior takes place in similar physical, non-active barrier coating systems.
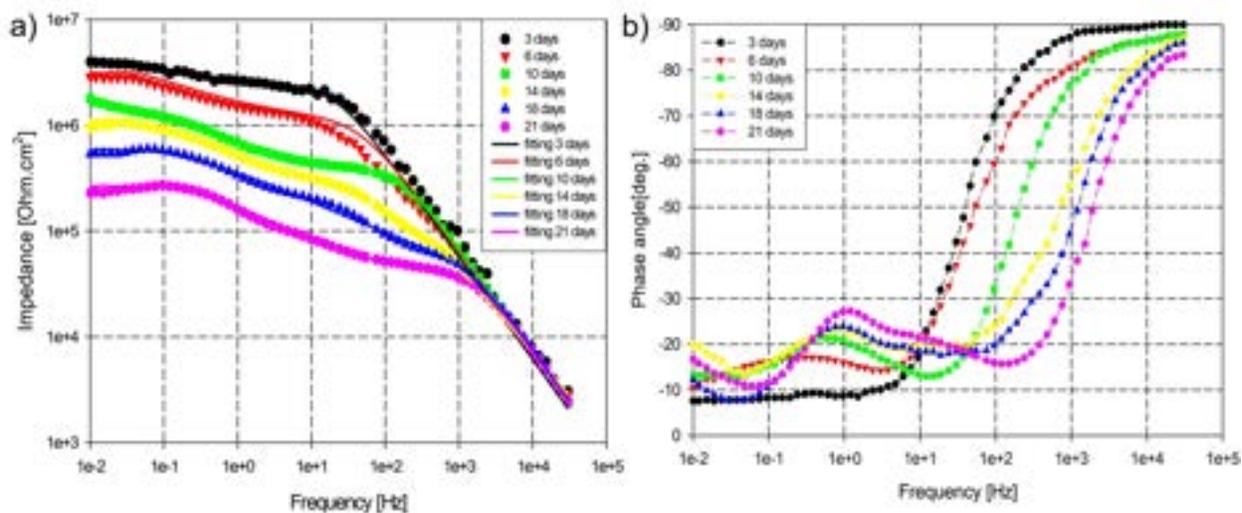
Figure 7.8 Bode plots of the epoxy coated AA2024 samples in 3.5% NaCl solution at room temperature. a) Impedance, b) phase angle.

The pitting corrosion formed in the neat epoxy-coated sample was investigated by the EDX elemental mapping (Figure 7.18). According to the mapping, aluminum, carbon, copper, magnesium, and oxygen were all detected. All the detected metals represent the different components of the aluminum alloy, while carbon mainly belongs to the epoxy coating. Over the scanned area, several spots were found to be of a different nature (red circles in Figure 7.18). Closer inspection of these spots revealed a recognizable decrease in the carbon content and a corresponding increase in the other metals in the same area, indicating the degradation of the coating around these pitting centers. Also, the images clearly show the presence of several cracks within the coating matrix.

The corrosion process starts when the electrolyte diffuses through the coating to the inner metallic surface. Aluminum/copper alloys, AA2xxx, are subjected to pitting corrosion in an aerated chloride-containing environment due to surface inhomogeneities. The intermetallic particles containing copper and magnesium (such as $AlCu_2$, AlCuMnFe, and Al_2CuMg) have a higher potential to corrode than the aluminum matrix.[469] In aerated NaCl solution, these intermetallic particles act as a cathode with respect to the matrix, at which the cathodic

reaction (reduction of oxygen) takes place on the surface of these intermetallic particles. Consequently, the most affected areas are those adjacent to these intermetallic particles.[470, 471] In addition, the surface of AA2024 alloy contains up to 3% of intermetallic particles. Although these particles enhance the mechanical properties (mainly the strength) of the alloy, they would increase its susceptibility to localized corrosion resistance (mainly pitting corrosion).[472–475]

Unlike the neat epoxy coating, the corrosion performance of the MOF/epoxy coating expressed a different behavior (Figure 7.9-a). The impedance clearly showed a slight decrease in the early stage of immersion (around 2 MOhm cm^2 at 0.01 Hz after 3 days of immersion) compared to that of the neat epoxy sample. In addition, this coat did not display the capacitive behavior measured in the high and mid-range of frequencies for the neat epoxy coating. This behavior change can be attributed to the variation in the hydrophilic character of epoxy as a result of the MOF crystals and their highly porous nature.[476] The impedance curve also shows a continuous decrease in the measured values during the first three weeks of immersion (similar to the neat epoxy coating). However, the impedance seems to be stable after that period, showing no sign of corrosion or delamination over the rest of the 60 days immersion course. During this period, and despite the slight decrease in the impedance at high and mid-range frequency, the total impedance (|Z| at 0.01 Hz) remained stable. This maintained impedance stability without the observation of any new time constant indicated the stability of the coating/metal interface, proving the ability of the MOF/epoxy coating to prevent AA2024 oxidation in 3.5%NaCl solution.
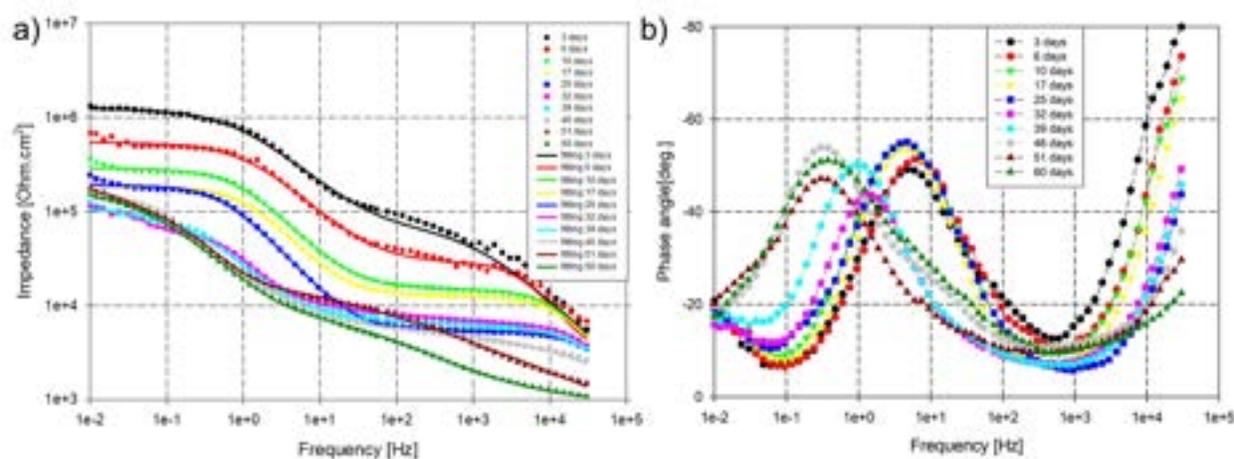
Figure 7.9 Bode plots of the MOF/epoxy coated AA2024 samples in 3.5% NaCl solution at room temperature. a) Impedance, b) phase angle.

The phase angle plot of the MOF/Epoxy coating (Figure 7.9-b) showed a sharp reduction in

phase angle values at the high-frequency range (3×10^5 Hz) during the first three weeks of immersion. After this period, the coating becomes stable for the rest of the 60 days. The curve also reveals two time constants around 10^4 and 6 Hz corresponding to the coating/electrolyte and coating/metal interfaces, respectively. In addition, the latter time constant gradually shifts from 6 Hz to 0.4 Hz, while the maximum of this time constant peak seems to be stable during the immersion test. Such behavior suggests the formation of an interfacial layer that can protect the metal from corrosion.[471] The test was terminated once the delamination of the coating began to appear after 65 days (Figure 7.19). Although the coating was delaminating (red circles in Figure 7.19), the sample's surface did not show any evident corrosion after 65 days of immersion in 3.5%wt NaCl solution.

The Nyquist plots of the epoxy coated AA2024 sample (Figure 7.10-a) in the corrosive 3.5% NaCl solution clearly showed two time constants that characterize a typical physical barrier coating. Both the capacitance and resistance components of the impedance continue to decrease with the immersion time, as indicated by the shrinkage of the time constant radii. This decrease in the corrosion impedance was accompanied by the observation of pitting corrosion, indicating the failure of the coating. Contrarily, the Nyquist plots of the MOF/epoxy coated AA2024 sample (Figure 7.10-b) revealed two impeded semicircles covering both high- and low-frequency ranges. The semicircles at the low-frequency range clearly display irregularity due to the inhomogeneity of the metal surface and/or the frequency dispersion.[477] The plots feature the presence of a capacitive loop at the low-frequency range with a radius decreasing with the immersion time during the first 10 days. The most noticeable observation from this figure is that after the initial period of immersion, 10 days, the diameter of the capacitive loop at the low-frequency range seems to be stable over the rest of the immersion period. This stability at low frequencies is related to the corrosion resistance of the metal substrate.[478] This behavior indicates that the MOF/epoxy coating can provide corrosion protection for AA2024 in the 3.5% NaCl solution over an extended period of time. Such an event agrees and confirms the optical observations, whereby the coating does not show any sign of delamination or blistering.

The change in hydrophobicity of these coatings plays a significant role in their corrosion protection performance and influences the behavior of these samples. Hence, the contact angle of both neat and MOF/epoxy coatings was measured at the beginning of immersion (test) using distilled water. Contact angles of 86° and 53° (Figure 7.20) were measured for the neat epoxy and the MOF/epoxy samples, respectively, suggesting a considerable change in the impedance behavior of both coatings in the high-frequency range being related to the increase in hydrophilicity of the coating.
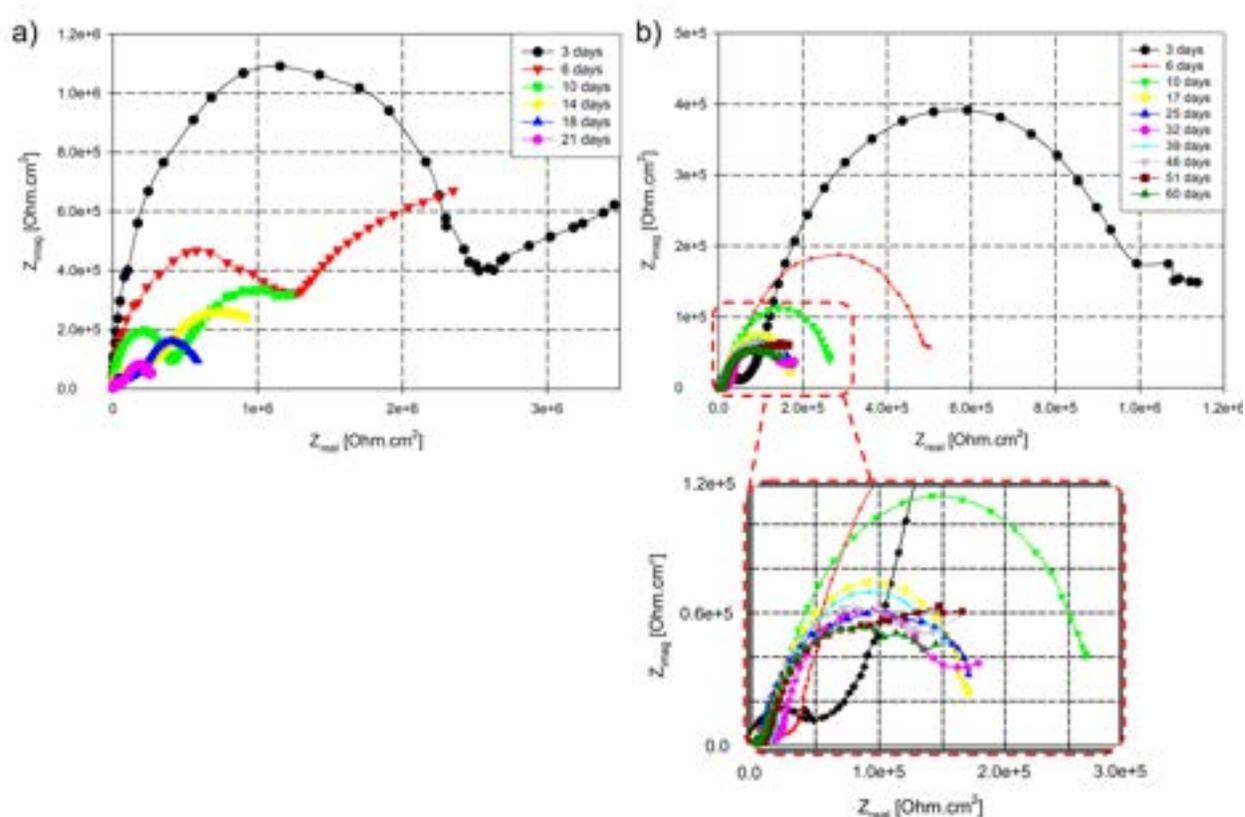
Figure 7.10 Temporal Nyquist plots for the coated AA2024 samples in 3.5% NaCl solution at room temperature a) neat epoxy, b) MOF/epoxy coating.

For a better understanding of the corrosion behavior of the coated samples, the EIS data for both epoxy coating systems were fitted to equivalent circuits, as presented in Figure 7.11. Figure 7.11-a represents the equivalent circuit of the neat epoxy during the first week of immersion. This figure consists of electrolyte resistance (R_s), coating capacitance (C_{coat}), and coating pore resistance (R_{coat}). In comparison, Figure 7.11-b shows a typical equivalent circuit of an organic coating, representing both the neat epoxy after a week of immersion and the MOF/epoxy coating during the entire immersion course. In Figure 7.11-b, two time constants were observed during immersion in the corrosive solution for both epoxy coatings. The first time constant at high frequencies is assigned to the capacitance (C_{coat}) and pore resistance (R_{coat}) of the coating, while the other in the low-frequency range one represents the double-layer capacitance (C_{dl}) and the charge transfer resistance (R_{ct}) of the corrosion areas. In these circuits, constant phase element (CPE) was used as a replacement for pure capacitance to attain more accurate results from experimental data fitting due to the non-ideal behavior of pure capacitors.[479] The capacitance can be calculated from CPE parameters according to the following equation,[480] and the electrochemical parameters are

reported in Table 7.1 and 7.2.

$$C_{dl} = \frac{Y_o.\omega^{(n-1)}}{sin(\frac{n\pi}{2})} \tag{7.1}$$

Where Y_o is the *CPE* constant, ω is the angular frequency (rad s^{-1}), and n is the *CPE* exponent where n=1 for an ideal capacitor.
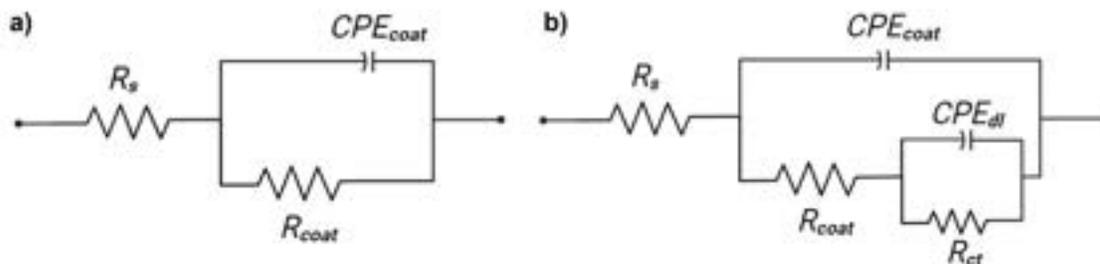
Figure 7.11 The equivalent circuits applied in the fitting of the impedance data for a) neat epoxy until 3 days of immersion, b) neat epoxy after 3 days and MOF/epoxy.

Figure 7.12-a shows the coating capacitance and resistance changes over the immersion time for the neat epoxy coated AA2024 sample. The figure shows a slight decrease in R_{coat} during the course of immersion in the corrosive electrolyte, while the values of the C_{coat} show a kind of stability during the first two weeks of immersion followed by an increase in its value. This behavior reflects the hydrophobic properties of the epoxy coating. The R_{ct} of the epoxy coated AA2024 sample continuously decreases during the immersion period, as depicted in Figure 7.12-b, in which C_{dl} gradually increases with immersion time. The behavior is attributed to the diffusion of the corrosive electrolyte to reach the coating/metal interface followed by the interaction with the metal surface forming corrosion products. These results specify the rapid degradation of the neat epoxy coated AA2024 in this Cl^{-}-containing solution forming pitting corrosion.

Table 7.1 The electrochemical parameters extracted from the fitting of the EIS results of the neat epoxy sample after immersion in a corrosive 3.5% NaCl solution at various immersion times

Sample	Time [day]	R_s [$\Omega.cm^2$]	Q_{coat} [10^{-9} $F.cm^2.s^{n-1}$]	n_1	R_{coat} [10^4 $\omega.cm^2$]	Q_{dl} [10^{-7} $F.cm^2.s^{n-1}$]	n_2	R_{ct} [10^5 $\Omega.cm^2$]
Epoxy	3	3.2	2.91	1.00	61.42	—	—	—
	6	4.9	2.59	0.95	49.31	5.49	0.97	34.12
	10	2.3	1.98	0.92	45.54	9.26	0.94	29.81
	14	1.8	2.65	0.88	29.18	10.9	0.93	9.21
	18	1.3	5.29	0.87	5.31	14.71	0.87	7.51
	21	1.3	27.18	0.76	2.70	69.16	0.79	4.22

Table 7.2 The electrochemical parameters extracted from the fitting of the EIS results of MOF/epoxy sample after immersion in a corrosive 3.5% NaCl solution at various immersion times

Sample	Time [day]	R_s [$\Omega.cm^2$]	Q_{coat} [$10^{-9}\ F.cm^2.s^{n-1}$]	n_1	R_{coat} [$10^4\ \omega.cm^2$]	Q_{dl} [$10^{-7}\ F.cm^2.s^{n-1}$]	n_2	R_{ct} [$10^5\ \Omega.cm^2$]
MOF/epoxy	3	3.2	2.08	0.75	7.12	0.94	0.74	11.81
	6	4.9	3.92	0.79	2.60	1.62	1.00	5.22
	10	2.3	8.78	0.85	1.48	1.86	0.95	2.74
	17	1.8	11.25	0.88	1.25	2.07	0.93	1.74
	25	1.3	18.03	0.89	0.54	4.01	0.88	1.85
	32	1.3	77.16	0.76	0.64	69.38	0.79	1.66
	39	2.4	89.15	0.77	0.65	91.72	0.76	1.21
	46	3.1	90.48	0.72	0.61	48.41	0.45	2.08
	51	1.8	63.28	0.97	1.24	44.51	0.36	2.97
	60	2.1	79.92	0.85	1.03	69.92	0.52	1.91
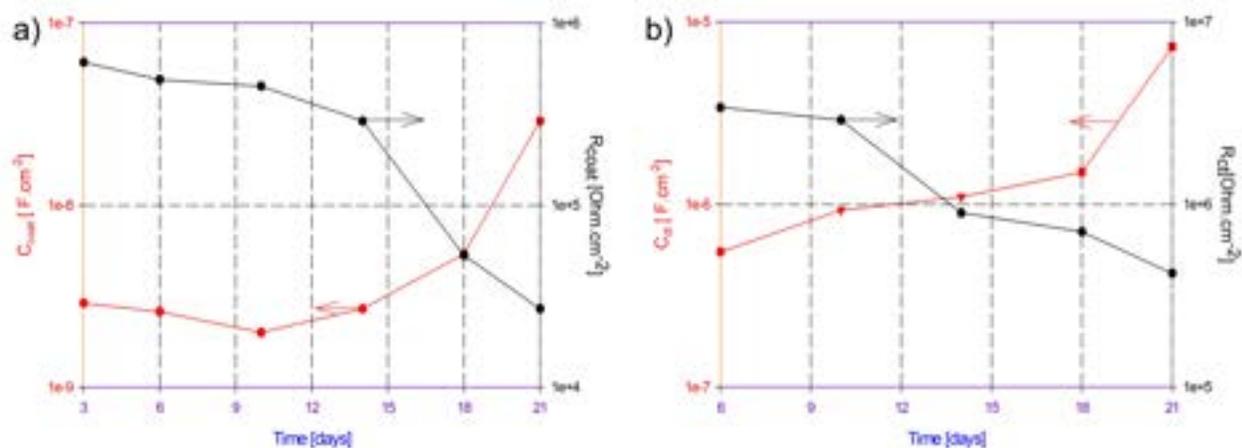
Figure 7.12 The change in a) C_{coat} and R_{coat} and b) C_{dl} and R_{ct} values regarding the epoxy coated AA2024 sample in 3.5% NaCl solution versus the immersion time.

Figures 7.13-a and 7.13-b show the experimental EIS data fitting results related to the MOF/epoxy coating on the equivalent circuit. Both figures have the same trend of changing parameters; the C_{dl} and C_{coat} increase at the beginning of immersion then seem to be steady while R_{ct} and R_{coat} decrease at the beginning then seem to have plateau values. In contrast to the continuous change in the coating/metal interface' parameters (R_{ct} decreases and C_{dl} increases) of epoxy coating with the observation of pitting corrosion, the MOF/epoxy coating shows higher stability of these interface parameters after 4 weeks of immersion. The stability of the coating/metal interface resistance and capacitance indicates a considerable enhancement of the resistance to the corrosive electrolyte diffusion, which can be attributed to the presence of the MIL-47as crystals within the epoxy coating.[467] This behavior is usually presented upon the development of a protective layer formed as a result of the presence of the V-MOF within the epoxy matrix.
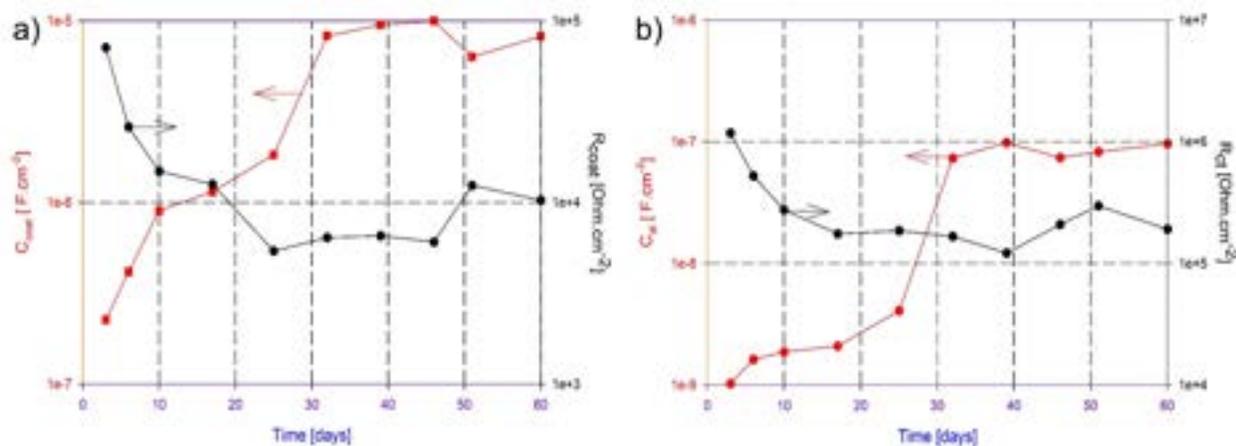
Figure 7.13 The change in a) C_{coat} and R_{coat} and b) C_{dl} and R_{ct} values regarding the MOF/epoxy coated AA2024 sample in 3.5% NaCl solution versus the immersion time.

7.3.3 Mechanism of interaction

AA2024 is an aluminum alloy with a high mechanical strength owing to the intermetallic particles (IMPs). These IMPs decrease the corrosion resistance of the alloy by altering the corrosion potential of the alloy's surface.[472, 473] Such an alloy is usually susceptible to localized corrosion, mostly pitting, in an aerated Cl^--containing solution, and the degree of pitting depends on the nature of these IMPs.[469] Generally, under free corrosion conditions, IMPs of AA2024 (such as the S-phase) are active species compared to the Al matrix due to the presence of magnesium. Magnesium will then dissolve, leaving copper behind, which acts as a local cathode assisting oxygen reduction reaction. In this aerated solution, the main reduction reaction would be that of oxygen reduction resulting in the creation of some intermediates as follows:

$$\frac{1}{2}O_2 + H_2O + 2e^- \rightarrow 2OH^- \tag{7.2}$$

$$O_2 + H_2O + 2e^- \rightarrow H_2O_2 + OH^- \tag{7.3}$$

The oxygen reduction occurs on the cathodic areas in which IMPs exist, representing almost 3% of the total alloy surface area.[465] The oxidation reaction takes place by the dissolution of the Al matrix existing around these IMPs, developing pitting. The Al matrix dissolution (oxidation reaction) undergoes a series of reactions that finally forms the $Al(OH)Cl^+$ complex, which is easily dissolved in the aqueous solution.[465]

$$Al + 3H_2O \rightarrow Al(OH)_3 + 3H^+ + 3e^- \tag{7.4}$$

$$Al + 2H_2O \rightarrow AlO(OH) + 3H^+ + 3e^- \tag{7.5}$$

$$Al + \frac{3}{2}H_2O \rightarrow Al_2O_3 + 3H^+ + 3e^- \tag{7.6}$$

$$Al(OH)^{2+} + Cl^- \rightarrow Al(OH)Cl^+ + 3H^+ + 3e^- \tag{7.7}$$
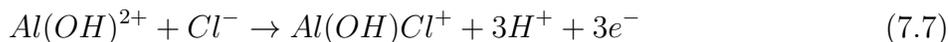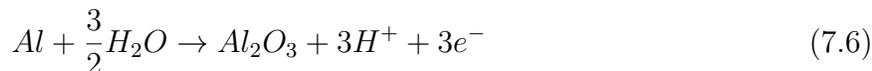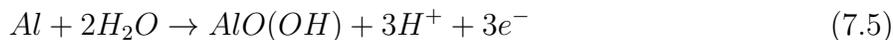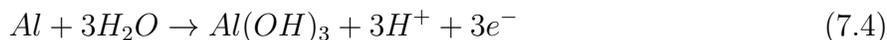
In the previous section, the results clearly showed that the presence of the V-MOF (MIL-47as) particles within the epoxy matrix significantly reduced the corrosion rate of AA2024 in an aerated NaCl solution. Generally, the vanadate treatment can reduce the oxygen reduction reactions similar to that of chromate. This interaction with the AA2024 alloy can be attributed to the reduction in the galvanic current of the metal surface, in which the vanadate species selectively cover the cathodic sites (i.e., precipitating on the IMPs forming a stable film).[481] The rate-determining step of this film formation is the diffusion of vanadate species from the bulk to the IMPs.[482] In this context, the presence of a vanadate layer over the IMPs hinders the oxygen adsorption on the surface, effectively reducing corrosion in an aerated aqueous solution.[483, 484]

Similar studies based on the X-ray photoelectron spectroscopic (XPS) investigations showed that the corrosion prevention of an aluminum alloy by vanadate is achieved via a complex series of redox reactions on the cathodic IMPs sites.[482, 485] In vanadate treatments, many forms of vanadium ions can be introduced, referring to an anionic coordination complex of vanadium (usually oxoanions) that mostly exists in one of the high oxidation states +3, +4, or +5.[486] These vanadate species are usually unstable and quickly hydrolyzed in aerated aqueous solutions. For example, in anticorrosion treatments, the V^{5+} species would be reduced to V^{4+} and/or V^{3+} on the cathodic site followed by subsequent oxidation, forming a vanadium-rich film, where the V^{4+} and/or V^{5+} oxidation states abundantly exist.[482, 485] This film would develop over a prolonged immersion time, whereby its thickness increases with the immersion time and temperature.

Based on these results, it can be postulated that in our case, oxygen is first reduced according to the above equations (7.2 and 7.3). On the other side, the MOF crystals within the epoxy matrix slowly dissociate, releasing V^{3+} ions, which are then dissolved into the solution.[198] Generally, the V^{3+} ions are readily oxidized in the air or aerated solutions.[487] These ions

would be reacting with the oxidizing species at the cathodic sites forming V^{4+} and/or V^{5+} as follows:

$$2V^{3+} + \frac{3}{2}H_2O_2 \rightarrow V^{4+} + 3V^{5+} + 3OH^- \tag{7.8}$$
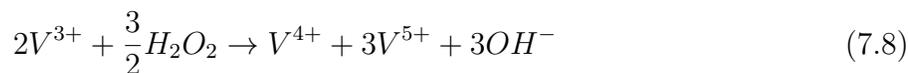
Finally, the produced V^{4+}/ V^{5+} ions would precipitate on the IMPs forming a stable film that goes against any further oxygen reduction, consequently reducing the corrosion rate of AA2024 in aerated NaCl solution.[465] The development of this vanadate film proceeds during the first three weeks of immersion, explaining the initial decrease in the impedance of the MOF/epoxy coating reported above (Figure 7.9-a).

The strategy of applying corrosion inhibitors in this type of alloys is to reduce the inhomogeneity of the surface potential, hence decreasing the galvanic corrosion. The addition of any inhibitor needs to be controlled and targeted towards specific areas.[488] Thus, the presence of the V-MOF (MIL-47as) crystals not only controls the leaching of vanadium within the matrix but also influences homogeneity among the layers. These MOF crystals interact with the aqueous solution molecules along with their accompanying oxidizing species that slowly diffuse from the medium to the metal surface through the MOF/epoxy matrix. The MIL-47as particles are slightly soluble in similar aqueous media, governing the leaching of the vanadate ions from MOF structure into the epoxy matrix and targeting the surface areas where the corrosive solution would diffuse.[198] The released V^{3+} ions would directly move and precipitate at these cathodic sites, IMPs, to decrease oxygen reduction reaction.

7.4 Conclusions

In summary, the vanadium MIL-47 metal-organic framework was successfully synthesized via a solvothermal method. Such a synthesis combines several advantages: a) the reaction does not require the addition of modulators/mineralizers like monocarboxylic acids, which makes it a simple, direct, and straightforward route. b) The reaction occurs at a lower reaction temperature and duration than other studies reported before (180 °C/20 h instead of 220 °C/72 h). c) Vanadium pentoxide (V_2O_5) was employed as a suitable metal precursor; it is inexpensive and highly available. Moreover, the characterization of the products showed that the achieved MOF was pure without any metal-oxide contamination. In addition, the as-synthesized MOF had the same thermal stability compared to those obtained via other synthesis techniques. The prepared MOF was then added to epoxy to produce an advanced coating that applies to aluminum alloy AA2024 for corrosion protection in a harsh chloride-rich environment. Investigation via SEM-EDX for the MOF/epoxy coating revealed a uniform

coating with a constant thickness of 10 ± 2 μm and a homogeneous distribution of the MOF crystals within the thermoset epoxy matrix. Compared to the neat-epoxy coating, the inclusion of small loading of the MOF particles (10 wt%) increases the hydrophilicity of the coating. However, they can extend the lifetime protection of the metal surface 3 folds. According to the results of the EIS experiments, the MOF/epoxy coating would have the same behavior as the neat epoxy one for the first three weeks, whereby the corrosive species diffuse into the coating. Nevertheless, the MIL-47as crystals would then interact with these diffusing molecules releasing vanadate ions and developing a protective film at the intermetallic particles. Such a protective film provides extended cathodic protection.

7.5 Conflicts of interest

There are no conflicts to declare.

7.6 Acknowledgment

7.7 Supporting Information

7.7.1 Materials and Methods

Materials

Vanadium(V) oxide (V_2O_5, $\geq$ 98%), 1,4-Benzenedicarboxylic acid "terephthalic acid" (H_2BDC or TPA, 98%), and *N, N*-dimethyl formamide (anhydrous DMF, 99.8%) were used to synthesize the MIL-47(V)as framework. They were all purchased from Sigma-Aldrich, Canada. Ethanol (EtOH, 98%) was purchased from Fischer Scientific, USA, and was applied in the washing and activation process.

Diglycidyl ether of bisphenol A, commonly known as Epoxy or component A, with an equivalent weight of 450–500 g/equiv. (Huntsman, China) was applied as the main coating. Diethylenetriamine (DETA), a tertiary amine acting as a curing agent or hardener (component B), was purchased from CDH, India. Acetone as the coating thinner, in addition to

sodium chloride (NaCl, $\geq$ 99.0%) for the corrosive medium preparation, were purchased from Sigma-Aldrich, Canada.

All chemicals were used as received with no further processing, and all aqueous solutions were prepared with deionized water. All experimental procedures were performed under ambient atmosphere unless otherwise stated.

Synthesis of MIL-47(V) metal-organic framework

The MIL-47(V) metal-organic framework was solvothermally-synthesized in a Parr's 200-ml large capacity acid digestion vessel (Parr Instrument Company, Model# 4748A) to provide a sufficient amount of MOF for all experiments, ensuring that all samples are the same. In a typical procedure, a 1:1 metal-to-linker ratio mixture was prepared, whereby 4.55 g V_2O_5 (25 mmol) and 4.15 g H_2BDC (25 mmol) were weighed, mixed, and dissolved in a 100 ml DMF (Figure 7.14-A). The mixture was then stirred for 30 min. Since V_2O_5 is not completely soluble in DMF, a bright-orange colored slurry of a pH around 5.3 was formed (Figure 7.14-B). Next, the slurry was transferred into the Teflon-lined autoclave bomb and heated to 180 °C in a conduction oven. The reaction was held at this temperature for 20 h without stirring. The bomb was then left to cool down gradually to room temperature inside the oven

The reaction yielded a deep green colored suspension of a pH around 7.7 (Figure 7.14-C). Powders of a greenish-yellow color were collected through centrifugation at a speed of 10,000 rpm for 10 min (MIL-47as, Figure 7.14-D).[439] The separated solids were thoroughly washed with DMF ($\times$3) and ethanol ($\times$3). After each wash, the powders were rinsed and vortexed for 1 min at 3000 rpm. The as-synthesized product (MIL-47as) was thermally activated at 300 °C for 12 h to remove any unreacted BDC linker within the pores, yielding the oxidized non-flexible form (MIL-47) of a yellow color (Figure 7.14-D).[49]
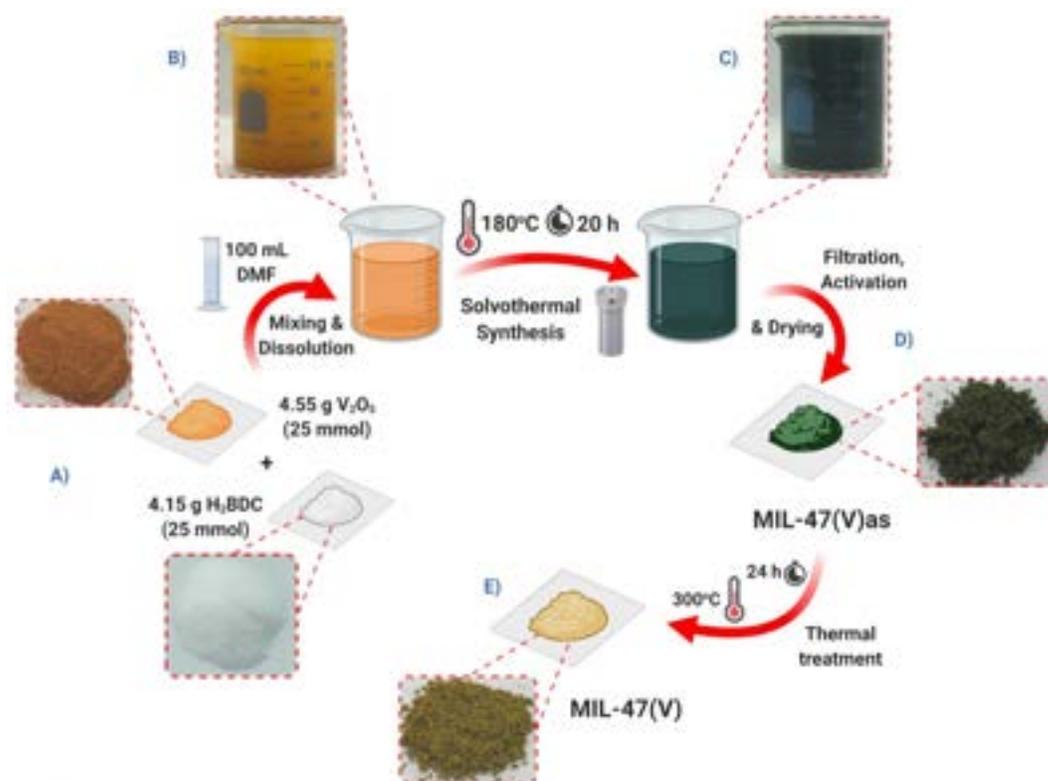
Figure 7.14 The solvothermal synthesis of the MIL-47 metal-organic framework. A) Mixing of the metal and organic precursors, B) Orange slurry before synthesis, C) Deep-green suspension after synthesis, D) Greenish-yellow powder of as-synthesized MIL-47 "MIL-47as", E) MIL-47 as a final product after thermal activation.

Aluminium alloy specimen, epoxy coating, and corrosive medium preparation

Aluminum alloy AA2024, Cu-rich as the main alloying component, was employed as the working electrode. Rectangular-shaped coupons with dimensions of [L×W×H= 12.5 cm × 2.5 cm × 0.1 cm] and a typical composition of wt.%: Cu(3.8-4.9), Mg(1.2-1.8), Si(0.50), Fe(0.50), Mn(0.3-0.9), Cr(0.10), Zn(0.25), Ti(0.15), and Al(balance) were obtained from Q-panel™, USA. The surface of the coupons was sanded with 320, 600, and 1200 grit abrasive SiC paper to remove the outer layer containing any scale or contamination and prepare the metal surface for the next step of coating. These coupons were then cleaned with ethanol, followed by deionized water before drying at room temperature through a compressed air stream for 1 min. After drying, the coupons were stored in a dry environment, desiccator with silica gel, until use in the corrosion evaluation experiments.

For comparison, a neat epoxy coating was prepared side-by-side to the MOF/epoxy one. The preparation of the neat epoxy included the following steps: 2 g of component A (untreated epoxy resin) was weighed and dissolved in 5 ml acetone. Then, the solution was stirred

for 5 min until the complete dissolution of the resin. An equivalent amount of the DETA hardener (component B) was then added to the solution and left to stir in a closed flask for another 5 min at room temperature. For the MOF/epoxy coating, 0.2 g of the as-synthesized MOF (MIL-47as) was sonicated with the epoxy solution for 5 min using an ultrasonic probe homogenizer (400 W - 24 kHz, 50% Amp. , Hielscher - Germany), before adding the hardener. Finally, the obtained solution was applied to the aluminum coupons through spray coating using an airbrush to obtain a uniform coat with a thickness of 10 ± 2 μm.

An aqueous solution of 3.5 wt.% NaCl was prepared to simulate the artificial seawater corrosive medium and the chloride-rich environment. Such an aggressive electrolyte is able to destroy the superficial passive aluminum oxide layer and develop a localized corrosion attack. This solution is the standard corrosive electrolyte for the AA2xxx series in corrosion evaluation standards, like ASTM G44 and G47.

Characterization

Powder X-ray diffraction (PXRD) patterns were recorded on a Bruker D8 Advance X-ray diffractometer equipped with LYNXEYE linear position-sensitive detector (Bruker AXS, Madison, WI). Data was collected over a 2θ-range of 3° - 50° at an increment of 0.02° and a scanning rate of 0.2° s^{-1}. The diffractometer, with a Cu-Kα source (λ= 1.5406 Å), operated at a tube voltage and current of 40 kV and 40 mA, respectively. Samples for PXRD were prepared by placing a thin layer of samples on a zero-background silicon crystal plate supported on a cup.

Fourier-transform Infrared (FTIR) spectra were collected using the Perkin Elmer spectrum 65 spectrophotometer equipped with an ATR diamond. With the high-efficiency ATR technique, a full range scan (4000 cm^{-1} - 450 cm^{-1}) was performed with a resolution of 4 cm^{-1}, and the data were averaged over 32 scans.

Thermogravimetric analysis (TGA) was performed on the TA Instruments Q50 analyzer. Experiments were conducted in an oxidative flow of air (50 mL min^{-1}) in a platinum pan. Heating took place in the range of 25 °C - 800 °C at a rate of 10 °C min^{-1}.

Raman spectra were obtained using a WITec alpha300R access confocal Raman microscope equipped with a motorized stage, CCD detector, and 1800 grooves mm^{-1} optical grating. In addition, the instrument was equipped with a green cobalt laser source of a 532 nm wavelength. Measurements were done using three collecting lenses (10x, 50x, and 100x). Powder samples were first pressed against a glass microscope slide. Spot analysis was then adopted over some selected spots in each sample with an accumulating response of 20 scans,

each of a signal integration time of 10 s to ensure that the obtained MOF is free from any metal oxide phases. Spectra were collected in the region from 100 cm^{-1} to 3500 cm^{-1}, with a resolution of 1 cm^{-1}. Area analysis over a square area of a side length of 10 μm was also recorded to get a collective response for the whole sample. Finally, the laser power was adjusted to be as low as possible to avoid any local heating induced by the laser.

A scanning electron microscope (SEM, Carl Zeiss EVO MA 10 - Germany) equipped with the energy-dispersive X-ray (EDX) detector was utilized to screen the surface structure and the compositions of all the products. Samples were dispersed on double-sided carbon tape and mounted on an aluminum stub. Mainly, the instrument was operated in the secondary electron mode to inspect the morphology of the obtained crystals at a higher magnification. The instrument was left to detect the present elements automatically and their distribution and percentage abundance with respect to the mass ratio.

Electrochemical characterization studies

The electrochemical corrosion experiments were performed at room temperature on a potentiostat/galvanostat, reference 600 Gamry™, with a standard three-electrode type cell. In all experiments, the aerated corrosive solution volume ratio to sample surface area was adjusted to be 50 ml cm^{-2}. A saturated calomel electrode was used as a reference electrode, platinum as a counter electrode, and the coated AA2024 specimen was the working electrode. The EIS tests were performed over a frequency range of 10^5 to 10^{-2} Hz with an amplitude of 10 mV peak-to-peak, using AC signal at OCP.

7.7.2   Further results.

FTIR:

Fourier-transform infrared spectroscopy (FTIR) was employed to confirm the formation of the targeted MOF and the linkage between the vanadium cations and the organic ditopic H_2BDC ligands (Figure 7.15). The vibrational spectrum of the obtained crystals agreed well with that reported for the MIL-47 framework, whereby the high absorption bands related to the antisymmetric and symmetric stretching of the dicarboxylate groups were easily recognized at 1533 cm^{-1} and 1394 cm^{-1}, respectively.[489] The peak at 893 cm^{-1} was assigned to the bending vibrations of the conjugated aromatic ring carbons (C=C–C), while those at 1018 cm^{-1} and 740 cm^{-1} were attributed to the in-plane stretching and out-of-plane wagging of the aromatic ring (C-H) bonds, respectively.[489]
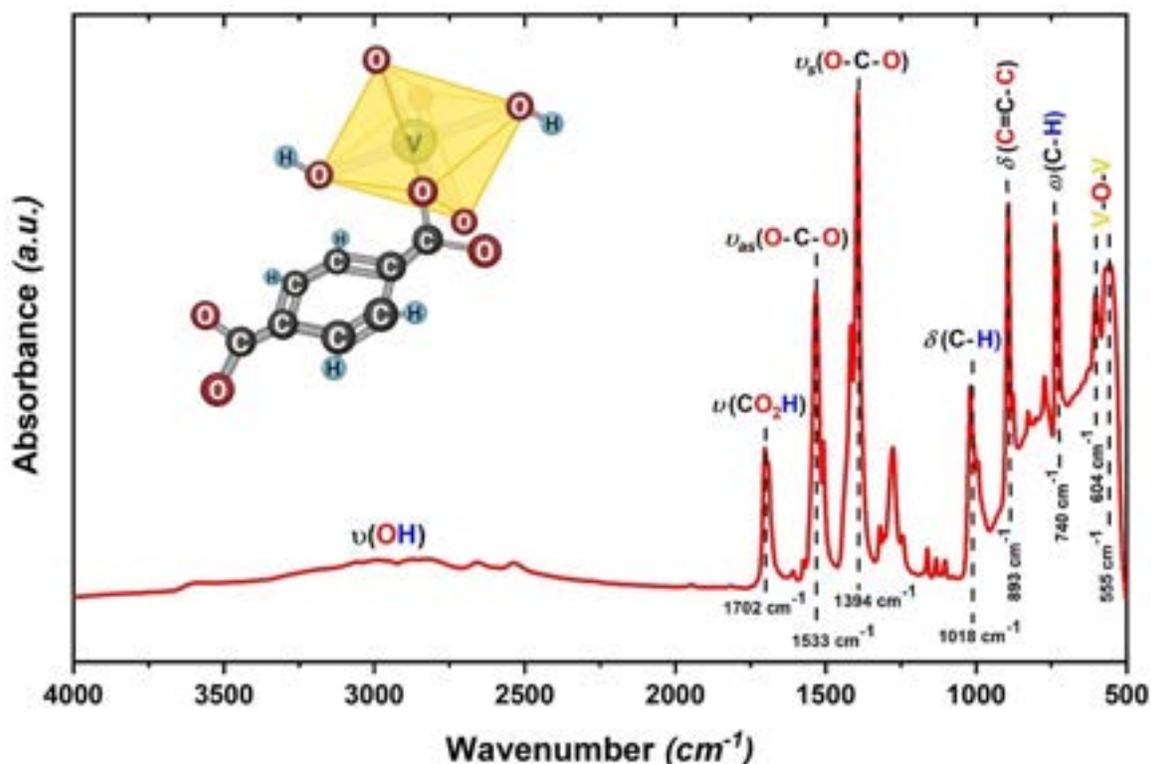
Figure 7.15 FTIR spectrum of the as-synthesized MIL-47 expressing the narrow-pore form and the inclusion of unreacted H_2BDC molecules within the pores. Inset: the connection of the vanadium oxo-cluster with the linker, showing different types of bonding all over the MOF structure.

Most importantly, the metal oxo-chains (V-O-V) vibration was detected in the far IR region around 555 cm^{-1} and 604 cm^{-1} that was ascribed to the symmetric and antisymmetric

stretching, respectively.[490–492] In addition, the broad absorption around 3000 cm^{-1} confirmed the presence of OH groups within the as-synthesized MIL-47 structure, referring to a narrow-pore arrangement.[489] Moreover, the peak at 1702 cm^{-1} corresponding to protonated carboxylic groups verified the presence of unreacted linker molecules within the pores of the MOF, which is unavoidable during synthesis even after the partial pore evacuation during the washing step by DMF.[217, 439]

Raman:

In order to ensure that the synthesized MOF is metal-oxide free, Raman spectroscopy was used as a selective technique to investigate such possible inclusion of other materials within the MOF crystals. As shown in Figure 7.16, actual images obtained through the instrument microscope for the vanadium pentoxide powder, at different zooming levels, exhibited large block-like crystals of a particle size > 50 μm and deep orange color. Raman spectra performed around these crystals recorded the characteristic vibrational bands of V_2O_5 at 151 cm^{-1}, 201 cm^{-1}, 288 cm^{-1}, 308 cm^{-1}, 412 cm^{-1}, 488 cm^{-1}, 532 cm^{-1}, 707 cm^{-1}, and 999 cm^{-1}.[492] Most importantly, the bands at 151 cm^{-1} and 201 cm^{-1} correspond to the lattice vibrations, while those at 288 cm^{-1}, 412 cm^{-1}, and 993 cm^{-1} are assigned to the vanadyl (V=O) bending and stretching vibrational modes. Also, the vibrations at 488 cm^{-1} and 707 cm^{-1} are attributed to the V-O-V bending and stretching, respectively.[493]

Investigating the powder of the as-synthesized MIL-47 framework showed greenish rod-like crystals of smaller particle size (in the range of a few microns) compared to the crystals of V_2O_5. The given spectra at different spots were alike, with the vibrational bands measured at 870 cm^{-1}, 1154 cm^{-1}, 1460 cm^{-1}, and 1622 cm^{-1} corresponding to the aromatic and dicarboxylate groups of the H_2BDC linker.[489] The bands at lower wavenumbers belong to the vibrations of the V-O chain bonds.[434, 489] The sample was screened, searching for any foreign particle, but none was found. Also, the area analysis of a large portion of the sample did not show any different signal compared to the spot analysis. Hence, we can conclude that, despite being prepared from a metal oxide precursor, the synthesis technique reported here produced pure MOF crystals without any oxide residue.
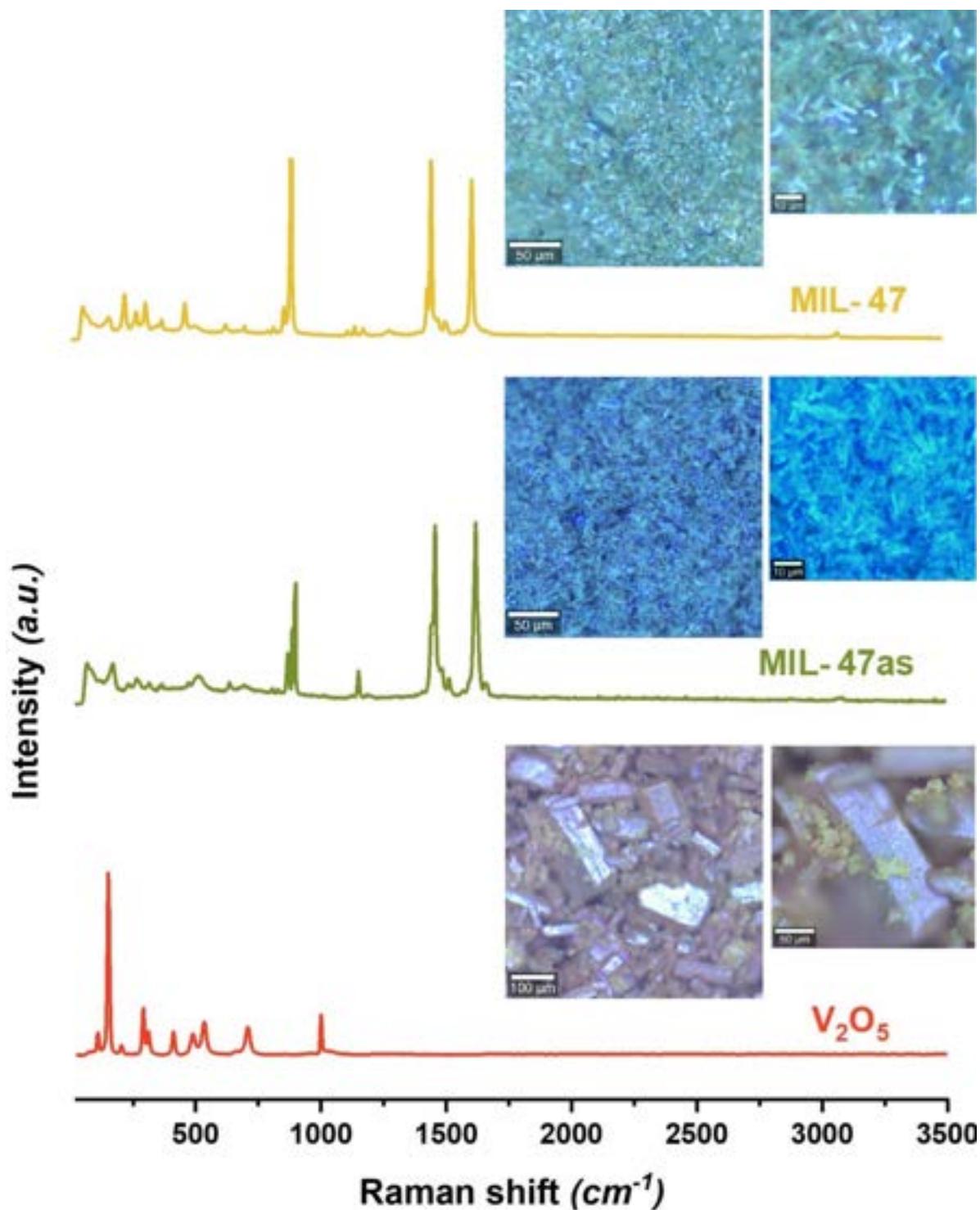
Figure 7.16 Raman spectra of V_2O_5 "red"; as-synthesized MIL-47 "green"; and thermally activated MIL-47 "yellow". Inset: actual optical microscopic images of the investigated spots/areas in each powder.

Coating Adhesion:

The crosshatch adhesion test was applied to both coating types (neat epoxy and MOF/epoxy) in order to evaluate their adhesion performance, both before and after immersion in the corrosive electrolyte (i.e., 3.5% NaCl solution) for 24 h. Conducting the wet adhesion was intended to assess the influence of water uptake on the adhesion properties of coatings. The crosshatch cut test of the dry samples did not show any signs of delamination after performing the test ten times on the same area, whereby the edges of the cuts were completely smooth with none of the squares detached (i.e., 5B rating). Similarly, performing the test on the wet samples was of the same results, in which the MOF/epoxy samples did not exhibit any distinguishable differences in behavior when compared to the neat epoxy ones as shown in Figure 7.17.
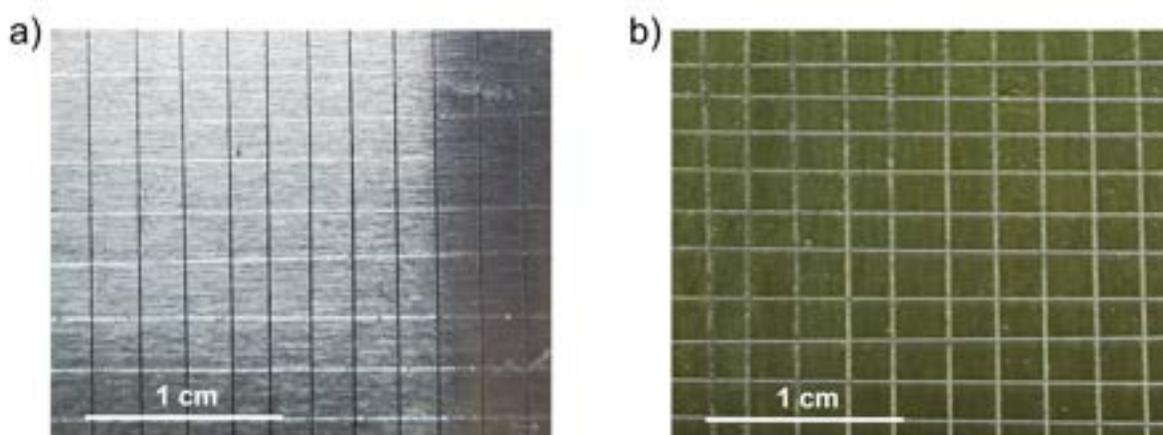
Figure 7.17 Adhesion test results (a) neat epoxy and (b) MOF/epoxy samples.

From these results it can be concluded that the addition of the MIL-47 MOF to the epoxy coating has not significantly changed the adhesion properties of the coating.

Corrosion performance:

- Pitting corrosion within the neat epoxy coating:
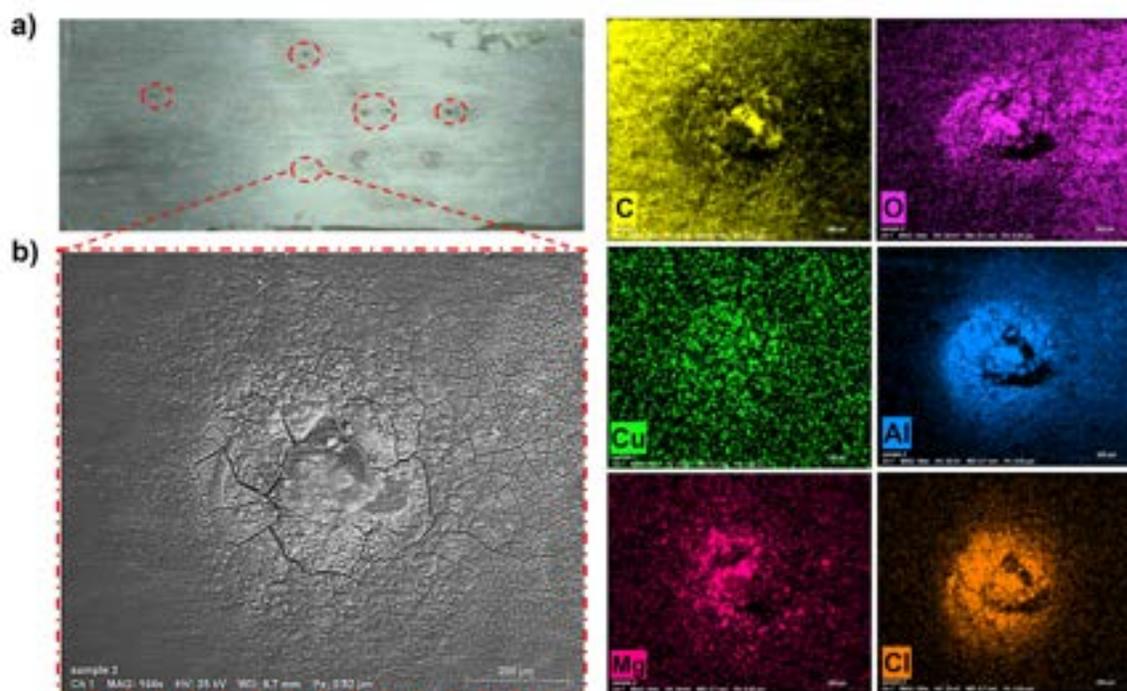
Figure 7.18 Optical image of epoxy coated AA2024 (a) and EDX mapping of the pitting corrosion after 25 days immersion (b). Color mapping: C – yellow, O – purple, Cu – light green, Al – blue, Mg – pink, Cl – orange.

- Coating delamination in the MOF/epoxy coating:
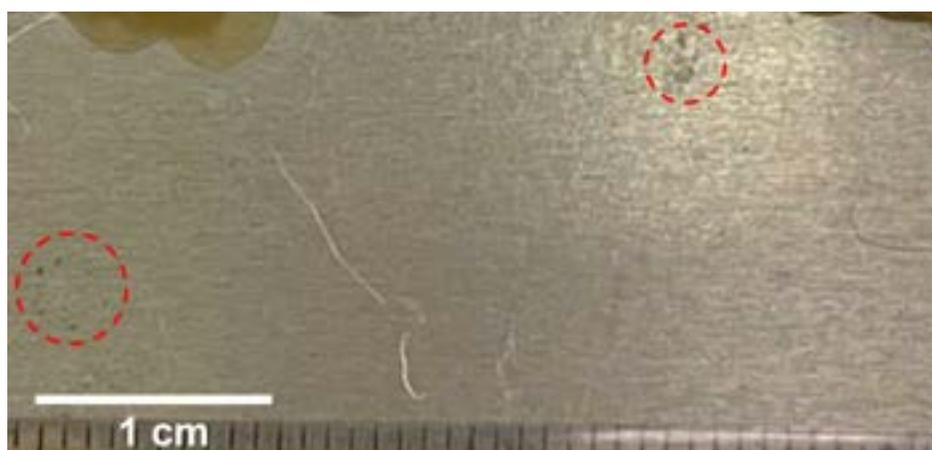
Figure 7.19 Optical images of the MOF/epoxy coated AA2024 samples after 65 days of immersion in 3.5%NaCl, showing slight coating delamination at the marked spots (red circles)

- Contact angle measurement:
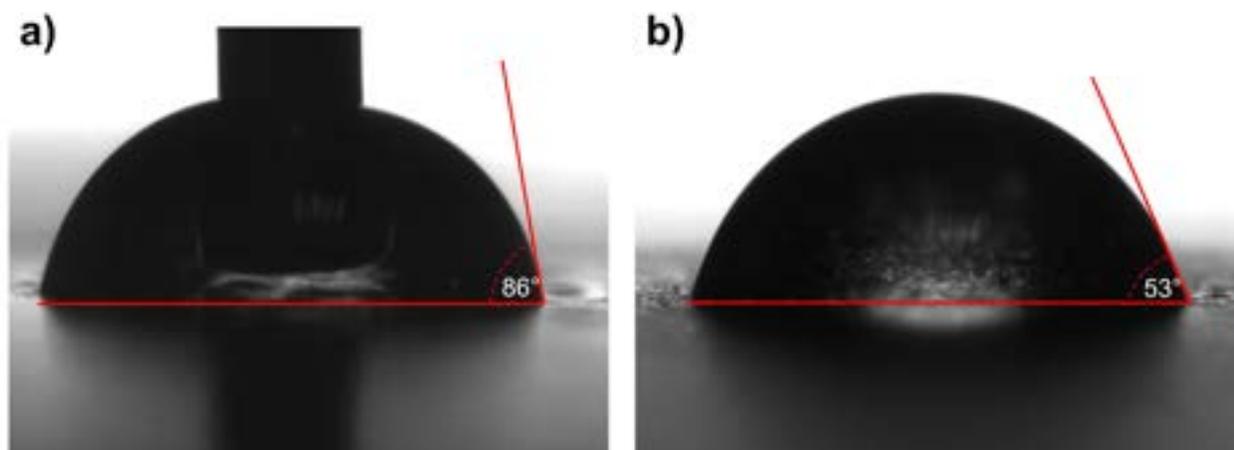
Figure 7.20 Optical images of the contact angle measurements of (a) epoxy (b) MOF/epoxy coatings.

CHAPTER 8   GENERAL DISCUSSION

This work concerns the synthesis and applications of metal-organic frameworks as an emerging class of porous materials. Three well-known MOFs, belonging to those structures discovered at Lavoisier institute (MIL series), were targeted in our research (namely, MIL-101, MIL-88B, and MIL-53/MIL-47). The synthesis and structures of this series were deeply investigated by the group of Gérard Férey over the past decades. They widely focused on transition metals as a result of their ability to form complexes and high-coordination compounds. In this research, the selected MOFs are closely related since they are all built from trivalent metal ions and the ditopic carboxylic linker, H_2BDC, yielding a highly porous 3d structure. These framework isomers or polymorphs share some common features. However, they behave differently because of the different connections within their structures. For example, MIL-101 and MIL-88 have the same trimeric SBUs, while MIL-53 and MIL-47 are built from metal-oxo chains. On the other hand, the structure of MIL-53/MIL-47 and MIL-88 were reported to be flexible, expressing the breathing character of the 3G MOFs, while the structure of MIL-101 is robust, whereby its pore size does not change by the effect of external stimuli. Hence, studying these MOFs' synthesis, characterization, and post-synthetic modification would be beneficial in various industrial and engineering applications.

In this regard, we started our research by filling a literature gap, whereby MIL-88 and MIL-53 are extensively covered in reviews interested in flexible MOFs. However, those including the MIL-101 structure are not comprehensive enough to cover the tremendous research focusing on this interesting framework. Throughout the first phase of this research, we conducted a critical review of the design and synthesis of MIL-101 MOFs, assessing the viability and applications of its diversified structures. We discussed how the synthesis parameters such as temperature, medium pH, and ratios of precursors intimately influence the final product characteristics. In addition, we presented the synthesis strategies, the merits, and the limitations of the MIL-101(Cr) analogues, including Fe, Al, V, Ti, Sc, and Mn. Moreover, we reviewed the literature on their multivariate type structures (MTV-MIL-101), whereby a pairwise combination of different metals is involved in the framework. Finally, the recent applications of MIL-101 in adsorption, catalysis, photocatalysis, membranes preparation, sensor design, and drug delivery were involved. Nevertheless, since we are interested in other framework isomers, a section discussing the various polymorphs of MIL-101 was also included in this review. This section went through the differences between MIL-101, MIL-88, MIL-53, and MIL-47 to get more insights for the third and fourth objectives.

The first phase also paved the road for the second objective. During discussions, some misconceptions and scientific gaps were recognized, such as the debate around Szilágyi's findings in applying the post-synthetic cation-exchange technique to prepare mixed-metal MIL-101 structures. Hence, for our second objective, we tried to settle this dispute. We investigated the experimental procedure of Szilágyi as reported and at extended conditions of time and different metal precursors. At this point, our results came against those of Szilágyi, in particular, and PSE, in general. The achievement of a MIL-101/α-Fe$_2$O$_3$ mixture instead of a mixed-metal MOF would direct us towards the direct synthesis technique. However, other studies that considered PSE for the synthesis of mixed-metal MOFs reported the sensitivity of the process to the applied reaction conditions. Accordingly, our experiments were conducted using DMF as the refluxing solvent instead of water. Also, we changed the reaction temperature and duration to match the conditions applied during the MIL-101(Fe) analogue synthesis (110 °C – 20 h). These selective changes were fruitful, turning the situation in favor of PSE, and mixed-metal MIL-101(Cr/Fe) was achieved.

For the third objective, and by utilizing the facilities in our lab, the flexible MIL-88B(Fe) structure was synthesized via the microwave-assisted technique at a high power input of 850 W. However, full control over the cooling step was not allowed considering the safety instructions programmed to the microwave reactor. Adopting the microwave-assisted technique allowed achieving the hexagonal diamond-like crystals of MIL-88B(Fe), expressing a particle-size range of a few microns. Besides, such a synthesis technique provided a much shorter reaction time, whereby the MIL-88B crystals were obtained within 15 min instead of several hours in the case of solvothermal synthesis. Nevertheless, further microscopic investigations revealed the presence of some short spindle-like crystals. MIL-88B(Fe), as an oxygen-rich material along with its high iron content, offers unique properties for its application as a catalyst for energetic systems. Thus, it was integrated with ammonium perchlorate in a composite, seeking better performance. The AP/MOF composite resulted in a 66% enhanced heat output of 1218 J g^{-1} at a lower decomposition temperature around 382 °C. The MOF contributed to the composite decomposition, resulting in higher heat output. Besides, it exhibits a catalytic effect through the exclusive formation of α-Fe$_2$O$_3$ particles in the nano range. Such nanoparticles support the catalytic ability of the composite and facilitate the decomposition of more AP present in the sample. Besides, MIL-88B(Fe) decreased AP decomposition activation energy by 23% and 25% using Kissinger and Kissinger–Akahira–Sunose (KAS) models, respectively.

Finally, in the fourth part, we focused on the vanadium-based metal-organic framework (MIL-47). The distinctive structure of MIL-47 stands midway between MIL-53 with its known flexibility and the robustness of the MIL-101 structure. The as-synthesized MIL-47

comprises the V-OH bonds, whereby the vanadium ions are in the trivalent oxidation state, showing a flexible structure exactly similar to MIL-53. However, upon its thermal activation, the MOF pores are evacuated, but the metal centers oxidize to V=O, and the structure loses its flexibility, expressing the robust structure of MIL-101. The synthesis of MIL-47 is usually reported from vanadium(III) chloride (VCl_3). However, our objective is to attempt the synthesis of MIL-47 from V_2O_5 as a better alternative. Using the solvothermal approach, the synthesis took place at 180 °C for 20 h, yielding MIL-47 microrods. The potential use of this vanadium MOF in anticorrosion applications was investigated. The obtained MOF crystals were incorporated in an epoxy coating over an aluminum alloy AA2024 substrate. The results showed that the MOF/epoxy coating provided extended corrosion prevention over 60 days for the AA2024 alloy against a chloride-rich environment.

Furthermore, our studies in the field of energetic materials were not limited to the MIL-88B (Fe) MOFs. Outside the scope of this thesis, we took part in the synthesis of energetic metal-organic frameworks (EMOFs) and their employment in various thermite mixtures (appendix **??**). A bimetallic energetic MOF [$Cu_4Na(Mtta)_5(CH_3CN)$, EMOF-1] was selected and synthesized via a rapid microwave-assisted strategy. This study introduced new thermite compositions based on EMOF-1, with low ignition temperature, stable propulsive force, and high reactivity. The results revealed that these new EMOF-based thermite mixtures exhibited superior combustion characteristics of one and a half to two-folds the average heat of combustion compared to conventional aluminum-based ones, at a lower ignition temperature. In this sense, the combustion reaction proceeds faster, easier (reduced activation energy), the ignition temperatures are noticeably lowered, and the heat released has considerably improved. In addition, they exhibited stable force with a longer burning time. Among them, EMOF-1/KIO_4 thermite exhibits the highest heat release (4.7 kJ g^{-1}), while EMOF-1/NH_4NO_3 thermite shows the lowest onset reaction temperature (224 °C). EMOF-1/$KClO_4$ yields the highest average force (8.4 N), calculated pressure (1365 kPa), pressurization rate (0.32 kPa μs^{-1}), and the longest burning time was assigned to EMOF-1/$K_2S_2O_8$ (40 ms).

Also, we contributed to the study of the anticorrosion performance of a Ce/Melamine coordination polymer (CMCP, appendix A). The synthesis of CMCP took place via a simple mixed-solvothermal approach. Besides, the structure of the resulting coordination polymer was studied thoroughly, whereby the results confirmed the coordination of cerium(III) ions with melamine through the amino groups (-NH_2) groups of the linker instead of the N atoms of the triazine ring. In addition, the molecular structure of CMCP was determined through computational calculations. Moreover, the potentiodynamic polarization results, along with the electrochemical impedance spectroscopy (EIS), confirmed that CMCP inhibits corrosion

and protects the aluminum alloy AA2024 in artificial seawater (3.5% NaCl) better than any of its constituents solely. The presence of cerium as cerium(III) in the CMCP structure plays the fundamental role of inhibition, whereby the inhibition mechanism occurs by cathodic oxidation of Ce(III) to Ce(IV) and cyclic reduction of Ce(IV) to Ce(III) by melamine within CMCP. As a result, CMCP offers more long-lasting corrosion protection than Ce(III) alone as melamine regenerates Ce(III) often during immersion, as confirmed by the 15 days extended immersion tests.

CHAPTER 9   CONCLUSIONS AND RECOMMENDATIONS

In this chapter, we will summarize the conclusions from the discussed publications in the previous chapters, followed by the limitations in our studies, and finally the recommendations for the points we missed or would complete our research.

Conclusions

Among the tremendous number of research focusing on metal-organic frameworks, here we are introducing our share for the scientific community. In this thesis, we are targeting the synthesis of MOFs for different applications. In our research, we are focusing on the preparation and characterization of different MIL-type metal-organic frameworks. Among the huge number of structures belonging to this type, we are focusing on three of the most-closely related ones, namely the MIL-101, MIL-88, and MIL-54/MIL-47 frameworks. These structures are all built from the same dicarboxylic linker (i.e., BDC or TPA linker). Nevertheless, they can be built for multiple trivalent metal ions (commonly, transition metals or 3d-elements, as well as Al, Ga, and In). To do so, different synthesis technique were employed like the hydrothermal/solvothermal and the microwave-assisted methods. Moreover, our research was not limited to monometallic MOFs (i.e., frameworks based on single metal basis). It was extended to include synthesis of bimetallic structure (mixed-metal MOFs).

The first part of this work includes a profound review on MIL-101 metal-organic framework. Previous reviews on the same subject were limited to the chromium-type MOF. In contrast, other metal analogues were not discussed, perpetuating a gap in the diversity of MIL-101 structures. Moreover, mixed-metal MTV-MIL-101s are even more subject to variability, and their reproducible synthesis is considered very challenging. In this regard, we gathered the recent attempts to tackle these objectives. Throughout this review the following aspects and conclusions were presented:

1- MIL-101 represents one of the first few evidence on the applicability of the priori design in the field of metal-organic frameworks. It were computationally designed and studied before its synthesis.

2- MIL-101 framework is still one of the highly researched MOFs so far. It possesses many distinguished properties, promoting it as the main candidate in several applications.

3- The chromium-type MIL-101, i.e., MIL-101(Cr), was first synthesized hydrothermally in an acidic medium (using HF), confirming the designed structure.

4- Hydrothermal synthesis in a fluoride-free environment recommended nitric acid (HNO_3) to be the second-best choice. Acid-free synthesis was also reported to be successful. However, employing TMAOH in the synthesis results in a pure crystals with a high yield reaching 88%.

5- Other synthesis techniques can be also utilized such as the microwave-assisted technique, the mechanochemical method, and the dry-gel route, resulting in smaller crystals.

6- Various trivalent metal ions like Fe, Al, V, Ti, Sc, and Mn, along with multiple functionalized linkers were also employed in constructing the MIL-101 framework. Most of these analogues are synthesized hydothermally, using the metal-chloride salt as the metal source and DMF as the reaction solvent.

7- The direct preparation of the aluminum analogue is limited to the amino-functionalized derivative, NH_2-MIL-101(Al). However, the unfunctionalized form, MIL-101(Al), was reported to be obtained indirectly via the deamination of the amino-functionalized one. In addition, the successful synthesis of the manganese analogue, MIL-101(Mn), is doubted based on the characterization of the obtained product.

8- The MIL-101 analogues offer a wider range of applications, since chromium is avoided even in its trivalent state. However, they are of lower chemical stability. The vanadium and titanium analogues are air- and moisture-sensitive, while the iron and aluminum ones are water-sensitive. The scandium and manganese analogues needs further investigations to ensure their successful synthesis.

9- The polymorphism of the MIL-101 structure was also reviewed, discussing the different structures and properties of these framework isomers (e.g., MIL-88, MOF-235, MIL-53, and MIL-47).

10- Multivariate MIL-101 frameworks or mixed-metal structures can be achieved through post-synthetic exchange or direct synthesis. Nevertheless, the direct synthesis of mixed-metal MIL-101s is reported to be more promising.

11- The progress in the MIL-101(Cr/Fe) synthesis is far more pronounced than MIL-101(Fe/Al). However, attempts are still working on such objective.

12- The MIL-101 MOF, made of different metal bases and various functionalized linkers, is still one of the top structures studied to serve multiple applications like adsorption, catalysis, photocatalysis, sensing, and drug delivery.

The second phase of this research investigated one of the highly-debated points mentioned in the first part, which is the achievement of multivariate metal-organic framework MTV-MIL-101(Cr/Fe) via post-synthetic Cation Exchange technique. The scientific community has doubted the validity of Szilágyi's findings and the applicability of the SACS method

in achieving the mixed-metal MIL-101(Cr/Fe). In this regard, we followed their reported experimental approach to confirm their results. Besides, we tested other metal precursor $(Fe(NO_3)_3 \cdot 9H_2O)$, different reaction solvent (DMF) and time. The following findings were concluded from this phase of the research:

1- Using an aqueous solution, as a cation exchange medium, does not allow for the substitution of the Cr^{3+} ions in the MIL-101 structure. Such a medium favors the formation of the hematite phase (α-Fe_2O_3) instead of the substitution of the metal ions within the framework.

2- Increasing the metal-ion concentrations, replacing the metal chloride source with the metal nitrate, or extending the reaction duration to 7 days instead of 3 days yields the same MOF/metal-oxide mixture rather than undergoing the cation-exchange process, as long as water is still present in the medium.

3- By reconsidering the reaction conditions to match those those applied during hydrothermal synthesis of MIL-101(Fe), and using DMF as a complex forming solvent, mixed-metal MIL-101(Cr/Fe) was successfully achieved.

4- Hence, the post-synthetic exchange route can be applied and compete with the direct synthesis technique to obtain the mixed-metal MIL-101(Cr/Fe). However, the SACS technique is only applicable at low concentrations of metal ions. At higher concentrations, the hematite phase was also detected.

In the third part of this research, one of the MIL-101 framework isomer, the flexible MIL-88B, was synthesized and its potential application in advanced energetic systems was evaluated. For this purpose, the iron-based MOF was selected and synthesized via the microwave-assisted technique, followed by the incorporation of these MOF crystals in an ammonium perchlorate matrix. The following conclusions can be drawn:

1- The microwave-assisted synthesis of the iron-based MIL-88B metal-organic framework at a high-power input of 850 W results in uniform hexagonal bipyramidal diamond-shaped crystals in the range of a few microns.

2- Further microscopic investigations revealed the presence of smaller spindle-like crystals obtained as a result of the rapid heating step during the synthesis.

3- The MIL-88B(Fe) structure showed high thermal stability above 300 °C and high Fe and O_2 content of 24% and 29%, respectively.

4- The thermal decomposition of the MOF crystals yields an α-Fe_2O_3 -nanocatalyst as a final product.

5- Ammonium perchlorate solely has a decomposition enthalpy of 733 J g^{-1}, while MIL-88B(Fe)

offered an increase in AP decomposition enthalpy by 66%. Also, the main exothermic decomposition temperature was decreased by 71 °C.

6- MIL-88B(Fe) resulted in a decrease in the AP activation energy by 23% and 25% according to the Kissinger and KAS models, respectively.

In the fourth and final phase of this work, another flexible framework isomer (i.e., MIL-47) was synthesized for its potential application in anticorrosion coating. To fulfill this objective, MIL-47(V) was synthesized solvothermally, using V_2O_5 as the metal precursor. In addition, the obtained MOF crystals were employed in an epoxy coating to work as a active barrier coating for AA2024 in chloride-rich environment. The conclusions of this work can be summarized as follows:

1- V_2O_5, as a readily abundant and thermodynamically-stable vanadium precursor of a low-cost, can be utilized as the metal-ion source in the solvothermal synthesis of MIL-47(V).

2- The synthesis took place in DMF at a lower reaction temperature and at a shorter duration than those usually reported (180 °C for 20 h, instead of 220 °C for 72 h), yielding MIL-47(V) microrods.

3- The obtained MOF products were pure without any metal-oxide contamination.

4- The applied MOF/epoxy coating was found to be uniform with a constant thickness of 10 ± 2 μm, revealing a homogeneous distribution of the MOF crystals within the thermoset epoxy matrix.

5- Compared to the neat-epoxy coating, the inclusion of small loading of the MOF particles (10 wt%) increases the hydrophilicity of the coating. However, they can extend the lifetime protection of the metal surface 3 folds.

6- According to the results of the EIS experiments, the MOF/epoxy coating would have the same behavior as the neat epoxy one for the first three weeks, whereby the corrosive species diffuse into the coating. Nevertheless, the MIL-47as crystals would then interact with these diffusing molecules releasing vanadate ions and developing a protective film at the intermetallic particles. Such a protective film provides extended cathodic protection up to 60 days.

In summary, this research provides interesting information for the MOF community, focusing on the synthesis, characterization, post-synthetic modifications, applications of such distinctive materials. It fills some gaps in the selected MIL-type MOF (i.e., MIL-101, MIL-88, and MIL-47). However, more investigations are required to get the complete picture of these structures, and the chemistry behind their unique properties. In addition, not only did we study the monometallic frameworks, we explored the synthesis of some of their bimetallic

structures via different synthesis techniques, which is one of the most challenging topics nowadays.

Future Research

This research provides insights about the synthesis of different MIL-type metal-organic frameworks of monometallic and bimetallic bases for various applications. However, there are some aspects that have not been explored in this research and are recommended in future studies:

1- Based on our discussion in the MIL-101 review, further studies concerning the synthesis of the manganese and scandium analogues are still required. Hence, investigations on the synthesis of these analogues are highly encouraged.

2- In the first phase of this research, mixed-metal MIL-101(Cr/Fe) of 31%wt Fe was proved to be obtainable via the post-exchange method. However, using highly concentrated solutions of ferric chloride in DMF resulted in the formation of hematite particles. Instead, a series of low concentrated solutions can be employed multiple times seeking a higher substitution percentage.

3- Modifying the reaction conditions to match those applied during the synthesis of MIL-101 (Fe) was one of the main approaches during the cation exchange process. In the same manner, it would be very helpful to investigate other synthesis technique like heating via the microwave-assisted technique. Using such a technique can reduce the reaction time to a few minutes rather than the 24-h employed in our process.

4- Following the same path, investigations on the possible achievement of MIL-101(Cr/Al) shall be performed both in aqueous solutions and DMF, as in the case of MIL-101(Cr/Fe). Moreover, other tetravalent and divalent metal ions were reported to be incorporated in the MIL-101 structure via direct synthesis such as: Ce^{4+} and Mg^{2+}. The synthesis of these mixed-metal structures shall be attempted via post-synthetic exchange method.

5- The synthesis of the mixed-metal MIL-101(Cr/Fe) shall be performed via the direct synthesis approach, and the products should be compared to those obtained from the post-synthetic exchange one. Both products should applied in gas-adsorption application (e.g., CO_2 adsorption).

6- For the second phase, the three frameworks isomers MIL-101(Fe), MIL-88B(Fe), and MIL-53(Fe) should be employed in the ammonium perchlorate matrix for comparison purpose, and their effect on the decomposition temperature of AP should be evaluated seeking the best performance.

7- Nickel oxide was reported to have a better impact on the AP decomposition compared to iron oxide. Also, MIL-88B(Fe/Ni) was reported to be synthesized solvothermally. Hence, the such mixed-metal MOF MIL-88B(Fe/Ni) should be synthesized following the reported procedure, and the effect of the obtained product on AP decomposition should be evaluated.

8- Moreover, the synthesis of MIL-88B(Fe/Ni) should be attempted by the microwave-assisted technique, seeking smaller crystal size for a better performance.

9- In the last phase of our work, the unfunctionalized MIL-47(V) was employed in a thermoset epoxy matrix as a barrier coating, and its anticorrosion performance was evaluated. The use of the amino-functionalized MIL-47 , NH_2-MIL-47(V), is expected to show a better performance since the attached amino group can take part in the epoxy-ring opening, offering a more-interconnected coating.

REFERENCES

[1] G. Férey, "Metal-organic frameworks: the young child of the porous solids family," in *From Zeolites to Porous MOF Materials - The 40th Anniversary of International Zeolite Conference*, ser. Studies in Surface Science and Catalysis, R. Xu, Z. Gao, J. Chen, and W. Yan, Eds. Elsevier, 2007, vol. 170, pp. 66–84. [Online]. Available: https://doi.org/10.1016/S0167-2991(07)80826-3

[2] G. Maurin, C. Serre, A. Cooper, and G. Férey, "The new age of mofs and of their porous-related solids," *Chemical Society Reviews*, vol. 46, no. 11, pp. 3104–3107, 2017.

[3] O. M. Yaghi, M. J. Kalmutzi, and C. S. Diercks, *Introduction to Reticular Chemistry: Metal-Organic Frameworks and Covalent Organic Frameworks*, 1st ed. Weinheim, Germany: John Wiley & Sons, 2019.

[4] T. D. Hamilton, D.-K. Bučar, and L. R. MacGillivray, "A metal–organic framework with three cavities based on three-coloured square tiling derived from a cyclobutane constructed in the solid state," *New Journal of Chemistry*, vol. 34, no. 11, pp. 2400–2402, 2010.

[5] Z. Wang, J. Huang, J. Mao, Q. Guo, Z. Chen, and Y. Lai, "Metal-organic framework/graphene composites: Preparation and applications in electrocatalysis and photocatalysis: A review," *Journal of Materials Chemistry A*, 2020.

[6] M. Schröder, *Functional metal-organic frameworks: gas storage, separation and catalysis*. Springer, 2010, vol. 293.

[7] D. Farrusseng, *Metal-organic frameworks: applications from catalysis to gas storage*, 1st ed. Weinheim, Germany: John Wiley & Sons, 2011.

[8] J. Lee, O. K. Farha, J. Roberts, K. A. Scheidt, S. T. Nguyen, and J. T. Hupp, "Metal–organic framework materials as catalysts," *Chemical Society Reviews*, vol. 38, no. 5, pp. 1450–1459, 2009.

[9] M. Lismont, L. Dreesen, and S. Wuttke, "Metal-organic framework nanoparticles in photodynamic therapy: current status and perspectives," *Advanced Functional Materials*, vol. 27, no. 14, p. 1606314, 2017.

[10] S. Li and F. Huo, "Metal–organic framework composites: from fundamentals to applications," *Nanoscale*, vol. 7, no. 17, pp. 7482–7501, 2015.

[11] J. Liu and C. Wöll, "Surface-supported metal–organic framework thin films: fabrication methods, applications, and challenges," *Chemical Society Reviews*, vol. 46, no. 19, pp. 5730–5770, 2017.

[12] S. Qiu, M. Xue, and G. Zhu, "Metal–organic framework membranes: from synthesis to separation application," *Chemical Society Reviews*, vol. 43, no. 16, pp. 6116–6140, 2014.

[13] G. Férey, C. Mellot-Draznieks, C. Serre, F. Millange, J. Dutour, S. Surblé, and I. Margiolaki, "A chromium terephthalate-based solid with unusually large pore volumes and surface area," *Science*, vol. 309, no. 5743, pp. 2040–2042, 2005. [Online]. Available: https://doi.org/10.1126/science.1116275

[14] O. M. Yaghi, G. Li, and H. Li, "Selective binding and removal of guests in a microporous metal–organic framework," *Nature*, vol. 378, no. 6558, pp. 703–706, 1995.

[15] H. Li, M. Eddaoudi, M. O'Keeffe, and O. M. Yaghi, "Design and synthesis of an exceptionally stable and highly porous metal-organic framework," *nature*, vol. 402, no. 6759, pp. 276–279, 1999.

[16] S. R. Batten, N. R. Champness, X.-M. Chen, J. Garcia-Martinez, S. Kitagawa, L. Öhrström, M. O'Keeffe, M. P. Suh, and J. Reedijk, "Coordination polymers, metal–organic frameworks and the need for terminology guidelines," *CrystEngComm*, vol. 14, no. 9, pp. 3001–3004, 2012. [Online]. Available: https://doi.org/10.1039/C2CE06488J

[17] S. R. Batten, N. R. Champness, X.-M. Chen, J. Garcia-Martinez, S. Kitagawa, L. Öhrström, M. O'Keeffe, M. P. Suh, and J. Reedijk, "Terminology of metal–organic frameworks and coordination polymers (IUPAC Recommendations 2013)," *Pure and Applied Chemistry*, vol. 85, no. 8, pp. 1715–1724, 2013. [Online]. Available: https://doi.org/10.1351/PAC-REC-12-11-20

[18] S. M. Cohen, "Modifying mofs: new chemistry, new materials," *Chemical Science*, vol. 1, no. 1, pp. 32–36, 2010.

[19] S. Kitagawa *et al.*, "Metal–organic frameworks (mofs)," *Chemical Society Reviews*, vol. 43, no. 16, pp. 5415–5418, 2014.

[20] M. J. Kalmutzki, N. Hanikel, and O. M. Yaghi, "Secondary building units as the turning point in the development of the reticular chemistry of mofs," *Science advances*, vol. 4, no. 10, p. eaat9180, 2018.

[21] C. Janiak and J. K. Vieth, "Mofs, mils and more: concepts, properties and applications for porous coordination networks (pcns)," *New Journal of Chemistry*, vol. 34, no. 11, pp. 2366–2388, 2010.

[22] P. Siman, C. A. Trickett, H. Furukawa, and O. M. Yaghi, "l-aspartate links for stable sodium metal–organic frameworks," *Chemical Communications*, vol. 51, no. 98, pp. 17 463–17 466, 2015.

[23] L. Valenzano, B. Civalleri, S. Chavan, G. T. Palomino, C. O. Areán, and S. Bordiga, "Computational and experimental studies on the adsorption of co, n2, and co2 on mg-mof-74," *The Journal of Physical Chemistry C*, vol. 114, no. 25, pp. 11 185–11 191, 2010.

[24] G. Férey, M. Latroche, C. Serre, F. Millange, T. Loiseau, and A. Percheron-Guégan, "Hydrogen adsorption in the nanoporous metal-benzenedicarboxylate m (oh)(o 2 c–c 6 h 4–co 2)(m= al 3+, cr 3+), mil-53," *Chemical communications*, no. 24, pp. 2976–2977, 2003. [Online]. Available: https://doi.org/10.1039/B308903G

[25] J.-J. Du, X. Zhang, X.-P. Zhou, and D. Li, "Robust heterometallic mof catalysts for the cyanosilylation of aldehydes," *Inorganic Chemistry Frontiers*, vol. 5, no. 11, pp. 2772–2776, 2018.

[26] N. Dhakar, *Metal and Metal Oxide Nanosponges: Synthesis and Applications*, 02 2019, pp. 143–171.

[27] J. C. Tan, T. D. Bennett, and A. K. Cheetham, "Chemical structure, network topology, and porosity effects on the mechanical properties of zeolitic imidazolate frameworks," *Proceedings of the National Academy of Sciences*, vol. 107, no. 22, pp. 9938–9943, 2010.

[28] Y.-R. Lee, J. Kim, and W.-S. Ahn, "Synthesis of metal-organic frameworks: A mini review," *Korean Journal of Chemical Engineering*, vol. 30, no. 9, pp. 1667–1680, 2013. [Online]. Available: https://doi.org/10.1007/s11814-013-0140-6

[29] Y. Bian, N. Xiong, and G. Zhu, "Technology for the remediation of water pollution: A review on the fabrication of metal organic frameworks," *Processes*, vol. 6, no. 8, p. 122, 2018.

[30] N. A. Khan and S. H. Jhung, "Synthesis of metal-organic frameworks (mofs) with microwave or ultrasound: Rapid reaction, phase-selectivity, and size reduction," *Coordination Chemistry Reviews*, vol. 285, pp. 11–23, 2015. [Online]. Available: https://doi.org/10.1016/j.ccr.2014.10.008

[31] J. Klinowski, F. A. A. Paz, P. Silva, and J. Rocha, "Microwave-assisted synthesis of metal–organic frameworks," *Dalton Transactions*, vol. 40, no. 2, pp. 321–330, 2011. [Online]. Available: https://doi.org/10.1039/C0DT00708K

[32] J.-S. Choi, W.-J. Son, J. Kim, and W.-S. Ahn, "Metal–organic framework mof-5 prepared by microwave heating: Factors to be considered," *Microporous and Mesoporous Materials*, vol. 116, no. 1-3, pp. 727–731, 2008.

[33] E. G. Avvakumov, E. G. Avvakumov, G. Avvakumov, M. Senna, and N. Kosova, *Soft mechanochemical synthesis: a basis for new chemical technologies.* Springer Science & Business Media, 2001.

[34] M. Klimakow, P. Klobes, A. F. Thünemann, K. Rademann, and F. Emmerling, "Mechanochemical synthesis of metal- organic frameworks: a fast and facile approach toward quantitative yields and high specific surface areas," *Chemistry of Materials*, vol. 22, no. 18, pp. 5216–5221, 2010. [Online]. Available: https://doi.org/10.1021/cm1012119

[35] T. Friščić, "New opportunities for materials synthesis using mechanochemistry," *Journal of Materials Chemistry*, vol. 20, no. 36, pp. 7599–7605, 2010. [Online]. Available: https://doi.org/10.1039/C0JM00872A

[36] W.-J. Son, J. Kim, J. Kim, and W.-S. Ahn, "Sonochemical synthesis of mof-5," *Chemical Communications*, no. 47, pp. 6336–6338, 2008.

[37] A. Dhakshinamoorthy, A. M. Asiri, and H. Garcia, "Mixed-metal or mixed-linker metal organic frameworks as heterogeneous catalysts," *Catalysis Science & Technology*, vol. 6, no. 14, pp. 5238–5261, 2016.

[38] B. Tu, Q. Pang, E. Ning, W. Yan, Y. Qi, D. Wu, and Q. Li, "Heterogeneity within a mesoporous metal–organic framework with three distinct metal-containing building units," *Journal of the American Chemical Society*, vol. 137, no. 42, pp. 13 456–13 459, 2015.

[39] H. Furukawa, U. Müller, and O. M. Yaghi, ""heterogeneity within order" in metal–organic frameworks," *Angewandte Chemie International Edition*, vol. 54, no. 11, pp. 3417–3430, 2015. [Online]. Available: https://doi.org/10.1002/anie.201410252

[40] W. Chen and C. Wu, "Synthesis, functionalization, and applications of metal–organic frameworks in biomedicine," *Dalton Transactions*, vol. 47, no. 7, pp. 2114–2133, 2018.

[41] P. Falcaro, A. J. Hill, K. M. Nairn, J. Jasieniak, J. I. Mardel, T. J. Bastow, S. C. Mayo, M. Gimona, D. Gomez, H. J. Whitfield *et al.*, "A new method to position and functionalize metal-organic framework crystals," *Nature communications*, vol. 2, no. 1, pp. 1–8, 2011.

[42] T. D. Bennett and A. K. Cheetham, "Amorphous metal–organic frameworks," *Accounts of chemical research*, vol. 47, no. 5, pp. 1555–1562, 2014. [Online]. Available: https://doi.org/10.1021/ar5000314

[43] T. D. Bennett and S. Horike, "Liquid, glass and amorphous solid states of coordination polymers and metal–organic frameworks," *Nature Reviews Materials*, vol. 3, no. 11, pp. 431–440, 2018. [Online]. Available: https://doi.org/10.1038/s41578-018-0054-3

[44] S. Horike, S. S. Nagarkar, T. Ogawa, and S. Kitagawa, "A new dimension for coordination polymers and metal–organic frameworks: towards functional glasses and liquids," *Angewandte Chemie International Edition*, vol. 59, no. 17, pp. 6652–6664, 2020. [Online]. Available: https://doi.org/10.1002/anie.201911384

[45] J. H. Lee, S. Jeoung, Y. G. Chung, and H. R. Moon, "Elucidation of flexible metal-organic frameworks: Research progresses and recent developments," *Coordination Chemistry Reviews*, vol. 389, pp. 161–188, 2019. [Online]. Available: https://doi.org/10.1016/j.ccr.2019.03.008

[46] J. D. Evans, V. Bon, I. Senkovska, H.-C. Lee, and S. Kaskel, "Four-dimensional metal-organic frameworks," *Nature Communications*, vol. 11, no. 1, pp. 1–11, 2020. [Online]. Available: https://doi.org/10.1038/s41467-020-16527-8

[47] C. Orellana-Tavra, E. F. Baxter, T. Tian, T. D. Bennett, N. K. Slater, A. K. Cheetham, and D. Fairen-Jimenez, "Amorphous metal–organic frameworks for drug delivery," *Chemical communications*, vol. 51, no. 73, pp. 13 878–13 881, 2015. [Online]. Available: http://dx.doi.org/10.1039/C5CC05237H

[48] X. Wu, H. Yue, Y. Zhang, X. Gao, X. Li, L. Wang, Y. Cao, M. Hou, H. An, L. Zhang *et al.*, "Packaging and delivering enzymes by amorphous metal-organic frameworks," *Nature communications*, vol. 10, no. 1, pp. 1–8, 2019. [Online]. Available: https://doi.org/10.1038/s41467-019-13153-x

[49] K. Barthelet, J. Marrot, D. Riou, and G. Férey, "A breathing hybrid organic–inorganic solid with very large pores and high magnetic characteristics,"

Angewandte Chemie, vol. 114, no. 2, pp. 291–294, 2002. [Online]. Available: https://doi.org/10.1002/1521-3773(20020118)41:2<281::AID-ANIE281>3.0.CO;2-Y

[50] C. Serre, F. Millange, C. Thouvenot, M. Nogues, G. Marsolier, D. Louër, and G. Férey, "Very large breathing effect in the first nanoporous chromium (iii)-based solids: Mil-53 or criii (oh)⊙{O2C- C6H4- CO2}⊙{HO2C- C6H4- CO2H} x⊙h2o y," *Journal of the American chemical society*, vol. 124, no. 45, pp. 13 519–13 526, 2002. [Online]. Available: https://doi.org/10.1021/ja0276974

[51] K. Barthelet, D. Riou, and G. Férey, "[v iii (h 2 o)] 3 o (o 2 cc 6 h 4 co 2) 3 · (cl, 9h 2 o)(mil-59): a rare example of vanadocarboxylate with a magnetically frustrated three-dimensional hybrid framework," *Chemical Communications*, no. 14, pp. 1492–1493, 2002. [Online]. Available: https://doi.org/10.1039/B202749F

[52] C. Serre, F. Millange, S. Surblé, and G. Férey, "A route to the synthesis of trivalent transition-metal porous carboxylates with trimeric secondary building units," *Angewandte Chemie International Edition*, vol. 43, no. 46, pp. 6285–6289, 2004. [Online]. Available: https://doi.org/10.1002/anie.200454250

[53] G. Férey, C. Serre, C. Mellot-Draznieks, F. Millange, S. Surblé, J. Dutour, and I. Margiolaki, "A hybrid solid with giant pores prepared by a combination of targeted chemistry, simulation, and powder diffraction," *Angewandte Chemie*, vol. 116, no. 46, pp. 6456–6461, 2004. [Online]. Available: https://doi.org/10.1002/anie.200460592

[54] S. Surblé, C. Serre, C. Mellot-Draznieks, F. Millange, and G. Férey, "A new isoreticular class of metal-organic-frameworks with the mil-88 topology," *Chemical communications*, no. 3, pp. 284–286, 2006. [Online]. Available: http://dx.doi.org/10.1039/B512169H

[55] C. Serre, F. Pelle, N. Gardant, and G. Ferey, "Synthesis and characterization of mil-79 and mil-80: two new luminescent open-framework rare-earth dicarboxylates with unusual 1d inorganic subnetworks," *Chemistry of materials*, vol. 16, no. 7, pp. 1177–1182, 2004. [Online]. Available: https://doi.org/10.1021/cm035045o

[56] K. Barthelet, J. Marrot, G. Férey, and D. Riou, "V iii (oh){O 2 C–C 6 H 4–CO 2}.(ho 2 c–c 6 h 4–co 2 h) x (dmf) y (h 2 o) z (or mil-68), a new vanadocarboxylate with a large pore hybrid topology: reticular synthesis with infinite inorganic building blocks?" *Chemical Communications*, no. 5, pp. 520–521, 2004. [Online]. Available: https://doi.org/10.1039/B312589K

[57] K. Barthelet, D. Riou, M. Nogues, and G. Ferey, "Synthesis, structure, and magnetic properties of two new vanadocarboxylates with three-dimensional hybrid frameworks," *Inorganic chemistry*, vol. 42, no. 5, pp. 1739–1743, 2003. [Online]. Available: https://doi.org/10.1021/ic026175m

[58] K. Barthelet, K. Adil, F. Millange, C. Serre, D. Riou, and G. Férey, "Synthesis, structure determination and magnetic behaviour of the first porous hybrid oxyfluorinated vanado (iii) carboxylate: Mil-71 or v iii 2 (oh) 2 f 2 {O 2 CC 6 H 4-CO 2} · h 2 o," *Journal of Materials Chemistry*, vol. 13, no. 9, pp. 2208–2212, 2003. [Online]. Available: https://doi.org/10.1039/B306852H

[59] J. K. Schnobrich, K. Koh, K. N. Sura, and A. J. Matzger, "A framework for predicting surface areas in microporous coordination polymers," *Langmuir*, vol. 26, no. 8, pp. 5808–5814, 2010. [Online]. Available: https://doi.org/10.1021/la9037292

[60] K. Koh, A. G. Wong-Foy, and A. J. Matzger, "A porous coordination copolymer with over 5000 m2/g bet surface area," *Journal of the American chemical society*, vol. 131, no. 12, pp. 4184–4185, 2009. [Online]. Available: https://doi.org/10.1021/ja809985t

[61] H. Furukawa, N. Ko, Y. B. Go, N. Aratani, S. B. Choi, E. Choi, A. Ö. Yazaydin, R. Q. Snurr, M. O'Keeffe, J. Kim *et al.*, "Ultrahigh porosity in metal-organic frameworks," *Science*, vol. 329, no. 5990, pp. 424–428, 2010. [Online]. Available: https://doi.org/10.1126/science.1192160

[62] O. K. Farha, I. Eryazici, N. C. Jeong, B. G. Hauser, C. E. Wilmer, A. A. Sarjeant, R. Q. Snurr, S. T. Nguyen, A. O. Yazaydın, and J. T. Hupp, "Metal–organic framework materials with ultrahigh surface areas: is the sky the limit?" *Journal of the American Chemical Society*, vol. 134, no. 36, pp. 15 016–15 021, 2012. [Online]. Available: https://doi.org/10.1021/ja3055639

[63] I. M. Hönicke, I. Senkovska, V. Bon, I. A. Baburin, N. Bönisch, S. Raschke, J. D. Evans, and S. Kaskel, "Balancing mechanical stability and ultrahigh porosity in crystalline framework materials," *Angewandte Chemie International Edition*, vol. 57, no. 42, pp. 13 780–13 783, 2018. [Online]. Available: https://doi.org/10.1002/anie.201808240

[64] A. P. Nelson, O. K. Farha, K. L. Mulfort, and J. T. Hupp, "Supercritical processing as a route to high internal surface areas and permanent microporosity in metal- organic framework materials," *Journal of the American Chemical Society*, vol. 131, no. 2, pp. 458–460, 2009. [Online]. Available: https://doi.org/10.1021/ja808853q

[65] J. E. Mondloch, O. Karagiaridi, O. K. Farha, and J. T. Hupp, "Activation of metal–organic framework materials," *CrystEngComm*, vol. 15, no. 45, pp. 9258–9264, 2013. [Online]. Available: https://doi.org/10.1039/C3CE41232F

[66] A. J. Howarth, A. W. Peters, N. A. Vermeulen, T. C. Wang, J. T. Hupp, and O. K. Farha, "Best practices for the synthesis, activation, and characterization of metal–organic frameworks," *Chemistry of Materials*, vol. 29, no. 1, pp. 26–39, 2017. [Online]. Available: https://doi.org/10.1021/acs.chemmater.6b02626

[67] O. K. Farha, A. Ö. Yazaydın, I. Eryazici, C. D. Malliakas, B. G. Hauser, M. G. Kanatzidis, S. T. Nguyen, R. Q. Snurr, and J. T. Hupp, "De novo synthesis of a metal–organic framework material featuring ultrahigh surface area and gas storage capacities," *Nature chemistry*, vol. 2, no. 11, pp. 944–948, 2010. [Online]. Available: https://doi.org/10.1038/nchem.834

[68] S. Bhattacharjee, C. Chen, and W.-S. Ahn, "Chromium terephthalate metal–organic framework mil-101: synthesis, functionalization, and applications for adsorption and catalysis," *RSC advances*, vol. 4, no. 94, pp. 52 500–52 525, 2014. [Online]. Available: https://doi.org/10.1039/C4RA11259H

[69] C. Mellot-Draznieks and G. Ferey, "Assembling molecular species into 3d frameworks: Computational design and structure solution of hybrid materials," *Progress in solid state chemistry*, vol. 33, no. 2-4, pp. 187–197, 2005. [Online]. Available: https://doi.org/10.1016/j.progsolidstchem.2005.11.047

[70] T. Zhao, F. Jeremias, I. Boldog, B. Nguyen, S. K. Henninger, and C. Janiak, "High-yield, fluoride-free and large-scale synthesis of mil-101 (cr)," *Dalton transactions*, vol. 44, no. 38, pp. 16 791–16 801, 2015. [Online]. Available: https://doi.org/10.1039/C5DT02625C

[71] A. Herbst and C. Janiak, "Mof catalysts in biomass upgrading towards value-added fine chemicals," *CrystEngComm*, vol. 19, no. 29, pp. 4092–4117, 2017. [Online]. Available: https://doi.org/10.1039/C6CE01782G

[72] C. Vaitsis, G. Sourkouni, and C. Argirusis, "Metal organic frameworks (mofs) and ultrasound: a review," *Ultrasonics sonochemistry*, vol. 52, pp. 106–119, 2019. [Online]. Available: https://doi.org/10.1016/j.ultsonch.2018.11.004

[73] V. Safarifard and A. Morsali, "Applications of ultrasound to the synthesis of nanoscale metal–organic coordination polymers," *Coordination Chemistry Reviews*, vol. 292, pp. 1–14, 2015. [Online]. Available: https://doi.org/10.1016/j.ccr.2015.02.014

[74] B. Szczęśniak, S. Borysiuk, J. Choma, and M. Jaroniec, "Mechanochemical synthesis of highly porous materials," *Materials Horizons*, vol. 7, no. 6, pp. 1457–1473, 2020. [Online]. Available: https://doi.org/10.1039/D0MH00081G

[75] D. Chen, J. Zhao, P. Zhang, and S. Dai, "Mechanochemical synthesis of metal–organic frameworks," *Polyhedron*, vol. 162, pp. 59–64, 2019. [Online]. Available: https://doi.org/10.1016/j.poly.2019.01.024

[76] T. Friščić, "Supramolecular concepts and new techniques in mechanochemistry: cocrystals, cages, rotaxanes, open metal–organic frameworks," *Chemical Society Reviews*, vol. 41, no. 9, pp. 3493–3510, 2012. [Online]. Available: https://doi.org/10.1039/C2CS15332G

[77] N. Stock and S. Biswas, "Synthesis of metal-organic frameworks (mofs): routes to various mof topologies, morphologies, and composites," *Chemical reviews*, vol. 112, no. 2, pp. 933–969, 2012. [Online]. Available: https://doi.org/10.1021/cr200304e

[78] M. Rubio-Martinez, C. Avci-Camur, A. W. Thornton, I. Imaz, D. Maspoch, and M. R. Hill, "New synthetic routes towards mof production at scale," *Chemical Society Reviews*, vol. 46, no. 11, pp. 3453–3480, 2017. [Online]. Available: https://doi.org/10.1039/C7CS00109F

[79] O. S. Bushuyev, G. R. Peterson, P. Brown, A. Maiti, R. H. Gee, B. L. Weeks, and L. J. Hope-Weeks, "Metal-organic frameworks (mofs) as safer, structurally reinforced energetics," *Chem. Eur. J*, vol. 19, pp. 1706–1711, 2013. [Online]. Available: https://doi.org/10.1002/chem.201203610

[80] S. Li, Y. Wang, C. Qi, X. Zhao, J. Zhang, S. Zhang, and S. Pang, "3d energetic metal–organic frameworks: synthesis and properties of high energy materials," *Angewandte Chemie International Edition*, vol. 52, no. 52, pp. 14 031–14 035, 2013. [Online]. Available: https://doi.org/10.1002/anie.201307118

[81] S. Yu, F. Pan, S. Yang, H. Ding, Z. Jiang, B. Wang, Z. Li, and X. Cao, "Enhanced pervaporation performance of mil-101 (cr) filled polysiloxane hybrid membranes in desulfurization of model gasoline," *Chemical Engineering Science*, vol. 135, pp. 479–488, 2015. [Online]. Available: https://doi.org/10.1016/j.ces.2014.11.058

[82] X. Sun, Q. Xia, Z. Zhao, Y. Li, and Z. Li, "Synthesis and adsorption performance of mil-101 (cr)/graphite oxide composites with high capacities of n-hexane,"

Chemical engineering journal, vol. 239, pp. 226–232, 2014. [Online]. Available: https://doi.org/10.1016/j.cej.2013.11.024

[83] O. Lebedev, F. Millange, C. Serre, G. Van Tendeloo, and G. Férey, "First direct imaging of giant pores of the metal- organic framework mil-101," *Chemistry of materials*, vol. 17, no. 26, pp. 6525–6527, 2005. [Online]. Available: https://doi.org/10.1021/cm051870o

[84] N. A. Khan, I. J. Kang, H. Y. Seok, and S. H. Jhung, "Facile synthesis of nano-sized metal-organic frameworks, chromium-benzenedicarboxylate, mil-101," *Chemical engineering journal*, vol. 166, no. 3, pp. 1152–1157, 2011. [Online]. Available: https://doi.org/10.1016/j.cej.2010.11.098

[85] M. Latroche, S. Surblé, C. Serre, C. Mellot-Draznieks, P. L. Llewellyn, J.-H. Lee, J.-S. Chang, S. H. Jhung, and G. Férey, "Hydrogen storage in the giant-pore metal–organic frameworks mil-100 and mil-101," *Angewandte Chemie*, vol. 118, no. 48, pp. 8407–8411, 2006. [Online]. Available: https://doi.org/10.1002/anie.200600105

[86] G. Akiyama, R. Matsuda, H. Sato, M. Takata, and S. Kitagawa, "Cellulose hydrolysis by a new porous coordination polymer decorated with sulfonic acid functional groups," *Advanced Materials*, vol. 23, no. 29, pp. 3294–3297, 2011. [Online]. Available: https://doi.org/10.1002/adma.201101356

[87] G. Akiyama, R. Matsuda, H. Sato, A. Hori, M. Takata, and S. Kitagawa, "Effect of functional groups in mil-101 on water sorption behavior," *Microporous and Mesoporous Materials*, vol. 157, pp. 89–93, 2012. [Online]. Available: https://doi.org/10.1016/j.micromeso.2012.01.015

[88] M. Lammert, S. Bernt, F. Vermoortele, D. E. De Vos, and N. Stock, "Single-and mixed-linker cr-mil-101 derivatives: a high-throughput investigation," *Inorganic chemistry*, vol. 52, no. 15, pp. 8521–8528, 2013. [Online]. Available: https://doi.org/10.1021/ic4005328

[89] J. Yang, Q. Zhao, J. Li, and J. Dong, "Synthesis of metal–organic framework mil-101 in tmaoh-cr (no3) 3-h2bdc-h2o and its hydrogen-storage behavior," *Microporous and Mesoporous Materials*, vol. 130, no. 1-3, pp. 174–179, 2010. [Online]. Available: https://doi.org/10.1016/j.micromeso.2009.11.001

[90] P. D. Du, H. T. M. Thanh, T. C. To, H. S. Thang, M. X. Tinh, T. N. Tuyen, T. T. Hoa, and D. Q. Khieu, "Metal-organic framework mil-101: synthesis and

photocatalytic degradation of remazol black b dye," *Journal of Nanomaterials*, vol. 2019, 2019. [Online]. Available: https://doi.org/10.1155/2019/6061275

[91] V. T. T. Chau and H. Van Duc, "A study on hydrothermal synthesis of metal–organic framework mil-101," *Hue University Journal of Science: Natural Science*, vol. 126, no. 1C, pp. 21–28, 2017. [Online]. Available: https://doi.org/10.26459/hueuni-jns.v126i1C.4417

[92] M. Shafiei, M. S. Alivand, A. Rashidi, A. Samimi, and D. Mohebbi-Kalhori, "Synthesis and adsorption performance of a modified micro-mesoporous mil-101 (cr) for vocs removal at ambient conditions," *Chemical Engineering Journal*, vol. 341, pp. 164–174, 2018. [Online]. Available: https://doi.org/10.1016/j.cej.2018.02.027

[93] N. A. Khan, J. W. Jun, and S. H. Jhung, "Effect of water concentration and acidity on the synthesis of porous chromium benzenedicarboxylates," 2010. [Online]. Available: https://doi.org/10.1002/ejic.200901064

[94] R. Seetharaj, P. Vandana, P. Arya, and S. Mathew, "Dependence of solvents, ph, molar ratio and temperature in tuning metal organic framework architecture," *Arabian journal of chemistry*, vol. 12, no. 3, pp. 295–315, 2019. [Online]. Available: https://doi.org/10.1016/j.arabjc.2016.01.003

[95] T. Hu, H. Lv, S. Shan, Q. Jia, H. Su, N. Tian, and S. He, "Porous structured mil-101 synthesized with different mineralizers for adsorptive removal of oxytetracycline from aqueous solution," *RSC advances*, vol. 6, no. 77, pp. 73 741–73 747, 2016. [Online]. Available: https://doi.org/10.1039/C6RA11684A

[96] M. S. Alivand, N. H. M. H. Tehrani, M. Shafiei-Alavijeh, A. Rashidi, M. Kooti, A. Pourreza, and S. Fakhraie, "Synthesis of a modified hf-free mil-101 (cr) nanoadsorbent with enhanced h2s/ch4, co2/ch4, and co2/n2 selectivity," *Journal of Environmental Chemical Engineering*, vol. 7, no. 2, p. 102946, 2019. [Online]. Available: https://doi.org/10.1016/j.jece.2019.102946

[97] L. Bromberg, Y. Diao, H. Wu, S. A. Speakman, and T. A. Hatton, "Chromium (iii) terephthalate metal organic framework (mil-101): Hf-free synthesis, structure, polyoxometalate composites, and catalytic properties," *Chemistry of Materials*, vol. 24, no. 9, pp. 1664–1675, 2012. [Online]. Available: https://doi.org/10.1021/cm2034382

[98] C.-Y. Huang, M. Song, Z.-Y. Gu, H.-F. Wang, and X.-P. Yan, "Probing the adsorption characteristic of metal–organic framework mil-101 for volatile organic compounds by

quartz crystal microbalance," *Environmental science & technology*, vol. 45, no. 10, pp. 4490–4496, 2011. [Online]. Available: https://doi.org/10.1021/es200256q

[99] D. Jiang, A. D. Burrows, and K. J. Edler, "Size-controlled synthesis of mil-101 (cr) nanoparticles with enhanced selectivity for co 2 over n 2," *CrystEngComm*, vol. 13, no. 23, pp. 6916–6919, 2011. [Online]. Available: https://doi.org/10.1039/C1CE06274C

[100] R. S. Forgan, "Modulated self-assembly of metal–organic frameworks," *Chemical science*, vol. 11, no. 18, pp. 4546–4562, 2020. [Online]. Available: https://doi.org/10.1039/D0SC01356K

[101] L. Yang, T. Zhao, I. Boldog, C. Janiak, X.-Y. Yang, Q. Li, Y.-J. Zhou, Y. Xia, D.-W. Lai, and Y.-J. Liu, "Benzoic acid as a selector–modulator in the synthesis of mil-88b (cr) and nano-mil-101 (cr)," *Dalton Transactions*, vol. 48, no. 3, pp. 989–996, 2019. [Online]. Available: https://doi.org/10.1039/C8DT04186E

[102] Z. Liang, M. Marshall, C. H. Ng, and A. L. Chaffee, "Comparison of conventional and hf-free-synthesized mil-101 for co2 adsorption separation and their water stabilities," *Energy & fuels*, vol. 27, no. 12, pp. 7612–7618, 2013. [Online]. Available: https://doi.org/10.1021/ef402212t

[103] P. B. Rallapalli, M. C. Raj, S. Senthilkumar, R. S. Somani, and H. C. Bajaj, "Hf-free synthesis of mil-101 (cr) and its hydrogen adsorption studies," *Environmental Progress & Sustainable Energy*, vol. 35, no. 2, pp. 461–468, 2016. [Online]. Available: https://doi.org/10.1002/ep.12239

[104] N. A. Khan and S. H. Jhung, "Phase-transition and phase-selective synthesis of porous chromium-benzenedicarboxylates," *Crystal growth & design*, vol. 10, no. 4, pp. 1860–1865, 2010. [Online]. Available: https://doi.org/10.1021/cg901562d

[105] E. Haque, N. A. Khan, J. E. Lee, and S. H. Jhung, "Facile purification of porous metal terephthalates with ultrasonic treatment in the presence of amides," *Chemistry–A European Journal*, vol. 15, no. 43, pp. 11 730–11 736, 2009. [Online]. Available: https://doi.org/10.1002/chem.200902036

[106] D.-Y. Hong, Y. K. Hwang, C. Serre, G. Ferey, and J.-S. Chang, "Porous chromium terephthalate mil-101 with coordinatively unsaturated sites: surface functionalization, encapsulation, sorption and catalysis," *Advanced Functional Materials*, vol. 19, no. 10, pp. 1537–1552, 2009. [Online]. Available: https://doi.org/10.1002/adfm.200801130

[107] S.-J. Lee, J. W. Yoon, Y.-K. Seo, M.-B. Kim, S.-K. Lee, U.-H. Lee, Y. K. Hwang, Y.-S. Bae, and J.-S. Chang, "Effect of purification conditions on gas storage and separations in a chromium-based metal–organic framework mil-101," *Microporous and mesoporous materials*, vol. 193, pp. 160–165, 2014. [Online]. Available: https://doi.org/10.1016/j.micromeso.2014.03.003

[108] G. Yang and S.-J. Park, "Conventional and microwave hydrothermal synthesis and application of functional materials: A review," *Materials*, vol. 12, no. 7, p. 1177, 2019. [Online]. Available: https://doi.org/10.3390/ma12071177

[109] B. Tan, Y. Luo, X. Liang, S. Wang, X. Gao, Z. Zhang, and Y. Fang, "Mixed-solvothermal synthesis of mil-101 (cr) and its water adsorption/desorption performance," *Industrial & Engineering Chemistry Research*, vol. 58, no. 8, pp. 2983–2990, 2019. [Online]. Available: https://doi.org/10.1021/acs.iecr.8b05243

[110] P. L. Llewellyn, S. Bourrelly, C. Serre, A. Vimont, M. Daturi, L. Hamon, G. De Weireld, J.-S. Chang, D.-Y. Hong, Y. Kyu Hwang *et al.*, "High uptakes of co2 and ch4 in mesoporous metal-organic frameworks mil-100 and mil-101," *Langmuir*, vol. 24, no. 14, pp. 7245–7250, 2008. [Online]. Available: https://doi.org/10.1021/la800227x

[111] S. H. Jhung, J.-H. Lee, J. W. Yoon, C. Serre, G. Férey, and J.-S. Chang, "Microwave synthesis of chromium terephthalate mil-101 and its benzene sorption ability," *Advanced Materials*, vol. 19, no. 1, pp. 121–124, 2007. [Online]. Available: https://doi.org/10.1002/adma.200601604

[112] Z. Zhao, X. Li, S. Huang, Q. Xia, and Z. Li, "Adsorption and diffusion of benzene on chromium-based metal organic framework mil-101 synthesized by microwave irradiation," *Industrial & Engineering Chemistry Research*, vol. 50, no. 4, pp. 2254–2261, 2011. [Online]. Available: https://doi.org/10.1021/ie101414n

[113] F. Soltanolkottabi, M. R. Talaie, S. Aghamiri, and S. Tangestaninejad, "Introducing a dual-step procedure comprising microwave and electrical heating stages for the morphology-controlled synthesis of chromium-benzene dicarboxylate, mil-101 (cr), applicable for co2 adsorption," *Journal of environmental management*, vol. 250, p. 109416, 2019. [Online]. Available: https://doi.org/10.1016/j.jenvman.2019.109416

[114] K. Leng, Y. Sun, X. Li, S. Sun, and W. Xu, "Rapid synthesis of metal–organic frameworks mil-101 (cr) without the addition of solvent and hydrofluoric acid," *Crystal Growth & Design*, vol. 16, no. 3, pp. 1168–1171, 2016. [Online]. Available: https://doi.org/10.1021/acs.cgd.5b01696

[115] M. J. Collins Jr, "Future trends in microwave synthesis," *Future medicinal chemistry*, vol. 2, no. 2, pp. 151–155, 2010. [Online]. Available: https://doi.org/10.4155/fmc.09.133

[116] M. Nüchter, B. Ondruschka, W. Bonrath, and A. Gum, "Microwave assisted synthesis–a critical technology overview," *Green chemistry*, vol. 6, no. 3, pp. 128–141, 2004. [Online]. Available: https://doi.org/10.1039/B310502D

[117] B. A. Roberts and C. R. Strauss, "Toward rapid,"green", predictable microwave-assisted synthesis," *Accounts of chemical research*, vol. 38, no. 8, pp. 653–661, 2005. [Online]. Available: https://doi.org/10.1021/ar040278m

[118] A. Demessence, P. Horcajada, C. Serre, C. Boissière, D. Grosso, C. Sanchez, and G. Férey, "Elaboration and properties of hierarchically structured optical thin films of mil-101 (cr)," *Chemical communications*, no. 46, pp. 7149–7151, 2009. [Online]. Available: https://doi.org/10.1039/B915011K

[119] Z. Zhang, S. Huang, S. Xian, H. Xi, and Z. Li, "Adsorption equilibrium and kinetics of co2 on chromium terephthalate mil-101," *Energy & Fuels*, vol. 25, no. 2, pp. 835–842, 2011. [Online]. Available: https://doi.org/10.1021/ef101548g

[120] S. Xian, X. Li, F. Xu, Q. Xia, and Z. Li, "Adsorption isotherms, kinetics, and desorption of 1, 2-dichloroethane on chromium-based metal organic framework mil-101," *Separation Science and Technology*, vol. 48, no. 10, pp. 1479–1489, 2013. [Online]. Available: https://doi.org/10.1080/01496395.2012.738756

[121] L. H. Wee, F. Bonino, C. Lamberti, S. Bordiga, and J. A. Martens, "Cr-mil-101 encapsulated keggin phosphotungstic acid as active nanomaterial for catalysing the alcoholysis of styrene oxide," *Green Chemistry*, vol. 16, no. 3, pp. 1351–1357, 2014. [Online]. Available: https://doi.org/10.1039/C3GC41988F

[122] X. Sun, J. Miao, J. Xiao, Q. Xia, and Z. Zhao, "Heterogeneity of adsorption sites and adsorption kinetics of n-hexane on metal–organic framework mil-101 (cr)," *Chinese Journal of Chemical Engineering*, vol. 22, no. 9, pp. 962–967, 2014. [Online]. Available: https://doi.org/10.1016/j.cjche.2014.06.031

[123] I. Thomas-Hillman, A. Laybourn, C. Dodds, and S. W. Kingman, "Realising the environmental benefits of metal–organic frameworks: recent advances in microwave synthesis," *Journal of Materials Chemistry A*, vol. 6, no. 25, pp. 11 564–11 581, 2018. [Online]. Available: https://doi.org/10.1039/C8TA02919A

[124] B. Ranu and A. Stolle, *Ball milling towards green synthesis: applications, projects, challenges.* Royal Society of Chemistry, 2014. [Online]. Available: "http://dx.doi.org/10.1039/9781782621980"

[125] S. Głowniak, B. Szczęśniak, J. Choma, and M. Jaroniec, "Mechanochemistry: Toward green synthesis of metal–organic frameworks," *Materials Today*, 2021. [Online]. Available: https://doi.org/10.1016/j.mattod.2021.01.008

[126] W.-H. Huang, X.-J. Luan, X. Zhou, J. Chen, Y.-Y. Wang, and Q.-Z. Shi, "The influence of ligand configuration, solvent size and solvent polarity on the porous shape and void volume in a series of isomeric or isomorphic porous mofs," *CrystEngComm*, vol. 15, no. 47, pp. 10 389–10 398, 2013. [Online]. Available: https://doi.org/10.1039/C3CE41801D

[127] Y.-C. He, J. Guo, H.-M. Zhang, J.-F. Ma, and Y.-Y. Liu, "Tuning the void volume in a series of isomorphic porous metal–organic frameworks by varying the solvent size and length of organic ligands," *CrystEngComm*, vol. 16, no. 24, pp. 5450–5457, 2014. [Online]. Available: https://doi.org/10.1039/C4CE00347K

[128] S. Bauer, C. Serre, T. Devic, P. Horcajada, J. Marrot, G. Férey, and N. Stock, "High-throughput assisted rationalization of the formation of metal organic frameworks in the iron (iii) aminoterephthalate solvothermal system," *Inorganic chemistry*, vol. 47, no. 17, pp. 7568–7576, 2008. [Online]. Available: https://doi.org/10.1021/ic800538r

[129] K. M. Taylor-Pashow, J. Della Rocca, Z. Xie, S. Tran, and W. Lin, "Postsynthetic modifications of iron-carboxylate nanoscale metal- organic frameworks for imaging and drug delivery," *Journal of the American Chemical Society*, vol. 131, no. 40, pp. 14 261–14 263, 2009. [Online]. Available: https://doi.org/10.1021/ja906198y

[130] N. V. Maksimchuk, K. A. Kovalenko, V. P. Fedin, and O. A. Kholdeeva, "Cyclohexane selective oxidation over metal–organic frameworks of mil-101 family: superior catalytic activity and selectivity," *Chemical Communications*, vol. 48, no. 54, pp. 6812–6814, 2012. [Online]. Available: https://doi.org/10.1039/C2CC31877F

[131] I. Y. Skobelev, A. B. Sorokin, K. A. Kovalenko, V. P. Fedin, and O. A. Kholdeeva, "Solvent-free allylic oxidation of alkenes with o2 mediated by fe-and cr-mil-101," *Journal of Catalysis*, vol. 298, pp. 61–69, 2013. [Online]. Available: https://doi.org/10.1016/j.jcat.2012.11.003

[132] M. Ma, A. Bétard, I. Weber, N. S. Al-Hokbany, R. A. Fischer, and N. Metzler-Nolte, "Iron-based metal–organic frameworks mil-88b and nh2-mil-88b: high quality microwave synthesis and solvent-induced lattice "breathing"," *Crystal growth & design*, vol. 13, no. 6, pp. 2286–2291, 2013. [Online]. Available: https://doi.org/10.1021/cg301738p

[133] A. Arenas-Vivo, D. Avila, and P. Horcajada, "Phase-selective microwave assisted synthesis of iron (iii) aminoterephthalate mofs," *Materials*, vol. 13, no. 6, p. 1469, 2020. [Online]. Available: https://doi.org/10.3390/ma13061469

[134] P. Horcajada, H. Chevreau, D. Heurtaux, F. Benyettou, F. Salles, T. Devic, A. Garcia-Marquez, C. Yu, H. Lavrard, C. L. Dutson, E. Magnier, G. Maurin, E. Elkaïm, and C. Serre, "Extended and functionalized porous iron(iii) tri- or dicarboxylates with mil-100/101 topologies," *Chemical Communications*, vol. 50, no. 52, pp. 6872–6874, 2014. [Online]. Available: http://dx.doi.org/10.1039/C4CC02175D

[135] M. K. Knyazeva, A. V. Shkolin, A. A. Fomkin, A. Y. Tsivadze, O. V. Solovtsova, N. P. Platonova, A. L. Pulin, I. E. Men'shchikov, A. A. Shiryaev, V. V. Vysotskii, and M. R. Kiselev, "Synthesis and structural-energy characteristics of fe-bdc metal-organic frameworks," *Protection of Metals and Physical Chemistry of Surfaces*, vol. 54, no. 6, pp. 1004–1009, 2018. [Online]. Available: https://doi.org/10.1134/S2070205118060151

[136] M. Yang, J. Tang, Q. Ma, N. Zheng, and L. Tan, "High activity fe-mil-101 solid acid catalyst for acetalization of aldehydes with methanol and enamination of β-dicarbonyl compounds," *Journal of Porous Materials*, vol. 22, no. 5, pp. 1345–1350, 2015. [Online]. Available: https://doi.org/10.1007/s10934-015-0011-0

[137] M. Hartmann and M. Fischer, "Amino-functionalized basic catalysts with mil-101 structure," *Microporous and mesoporous materials*, vol. 164, pp. 38–43, 2012. [Online]. Available: https://doi.org/10.1016/j.micromeso.2012.06.044

[138] K. Leus, T. Bogaerts, J. De Decker, H. Depauw, K. Hendrickx, H. Vrielinck, V. Van Speybroeck, and P. Van Der Voort, "Systematic study of the chemical and hydrothermal stability of selected "stable" metal organic frameworks," *Microporous and Mesoporous Materials*, vol. 226, pp. 110–116, 2016. [Online]. Available: https://doi.org/10.1016/j.micromeso.2015.11.055

[139] P. Küsgens, M. Rose, I. Senkovska, H. Fröde, A. Henschel, S. Siegle, and S. Kaskel, "Characterization of metal-organic frameworks by water adsorption," *Microporous*

and Mesoporous Materials, vol. 120, no. 3, pp. 325–330, 2009. [Online]. Available: https://doi.org/10.1016/j.micromeso.2008.11.020

[140] S. Zhang, Y. Zhang, F. Baig, and T.-F. Liu, "Synthesis and applications of stable iron-based metal–organic framework materials," *Crystal Growth & Design*, vol. 21, no. 5, pp. 3100–3122, 2021. [Online]. Available: https://doi.org/10.1021/acs.cgd.0c01500

[141] S. Li, S. Sun, H. Wu, C. Wei, and Y. Hu, "Effects of electron-donating groups on the photocatalytic reaction of mofs," *Catalysis Science & Technology*, vol. 8, no. 6, pp. 1696–1703, 2018. [Online]. Available: https://doi.org/10.1039/C7CY02622F

[142] P. Lemoine, A. Bekaert, J. Brion, and B. Viossat, "Crystal structure of hexakis (μ2-acetato)-tris (acetonitrile-κn)-μ3-oxotrialuminum (iii) tetrachloroaluminate,[al3 (c2h3o2) 6 (c2h3n) 3o][alcl4]," *Zeitschrift für Kristallographie-New Crystal Structures*, vol. 221, no. 1-4, pp. 309–310, 2006. [Online]. Available: https://doi.org/10.1524/ncrs. 2006.0087

[143] H. Hatop, M. Ferbinteanu, H. W. Roesky, F. Cimpoesu, M. Schiefer, H.-G. Schmidt, and M. Noltemeyer, "Lightest member of the basic carboxylate structural pattern:[al3 (μ3-o)(μ-o2ccf3) 6 (thf) 3][(me3si) 3cal (o2ccf3) 3]$\odot$ c7h8," *Inorganic chemistry*, vol. 41, no. 4, pp. 1022–1025, 2002. [Online]. Available: https://doi.org/10.1021/ic010880y

[144] L. Hamon, C. Serre, T. Devic, T. Loiseau, F. Millange, é. Férey, and G. D. Weireld, "Comparative study of hydrogen sulfide adsorption in the mil-53 (al, cr, fe), mil-47 (v), mil-100 (cr), and mil-101 (cr) metal- organic frameworks at room temperature," *Journal of the American Chemical Society*, vol. 131, no. 25, pp. 8775–8777, 2009. [Online]. Available: https://doi.org/10.1021/ja901587t

[145] A. García Márquez, A. Demessence, A. E. Platero-Prats, D. Heurtaux, P. Horcajada, C. Serre, J.-S. Chang, G. Férey, V. A. de la Peña-O'Shea, C. Boissière *et al.*, "Green microwave synthesis of mil-100 (al, cr, fe) nanoparticles for thin-film elaboration," *European Journal of Inorganic Chemistry*, vol. 2012, no. 32, pp. 5165–5174, 2012. [Online]. Available: https://doi.org/10.1002/ejic.201200710

[146] T. Loiseau, C. Volkringer, M. Haouas, F. Taulelle, and G. Férey, "Crystal chemistry of aluminium carboxylates: From molecular species towards porous infinite three-dimensional networks," *Comptes Rendus Chimie*, vol. 18, no. 12, pp. 1350–1369, 2015. [Online]. Available: https://doi.org/10.1016/j.crci.2015.08.006

[147] A. Samokhvalov, "Aluminum metal–organic frameworks for sorption in solution: a review," *Coordination Chemistry Reviews*, vol. 374, pp. 236–253, 2018. [Online]. Available: https://doi.org/10.1016/j.ccr.2018.06.011

[148] T. Wu, N. Prasetya, and K. Li, "Recent advances in aluminium-based metal-organic frameworks (mof) and its membrane applications," *Journal of Membrane Science*, p. 118493, 2020. [Online]. Available: https://doi.org/10.1016/j.memsci.2020.118493

[149] C. Volkringer, D. Popov, T. Loiseau, G. Férey, M. Burghammer, C. Riekel, M. Haouas, and F. Taulelle, "Synthesis, single-crystal x-ray microdiffraction, and nmr characterizations of the giant pore metal-organic framework aluminum trimesate mil-100," *Chemistry of Materials*, vol. 21, no. 24, pp. 5695–5697, 2009. [Online]. Available: https://doi.org/10.1021/cm901983a

[150] T. Ahnfeldt, N. Guillou, D. Gunzelmann, I. Margiolaki, T. Loiseau, G. Férey, J. Senker, and N. Stock, "[al4 (oh) 2 (och3) 4 (h2n-bdc) 3]· x h2o: A 12-connected porous metal–organic framework with an unprecedented aluminum-containing brick," *Angewandte Chemie International Edition*, vol. 48, no. 28, pp. 5163–5166, 2009. [Online]. Available: https://doi.org/10.1002/anie.200901409

[151] P. Serra-Crespo, E. V. Ramos-Fernandez, J. Gascon, and F. Kapteijn, "Synthesis and characterization of an amino functionalized mil-101 (al): separation and catalytic properties," *Chemistry of Materials*, vol. 23, no. 10, pp. 2565–2572, 2011. [Online]. Available: https://doi.org/10.1021/cm103644b

[152] S. Couck, J. F. Denayer, G. V. Baron, T. Rémy, J. Gascon, and F. Kapteijn, "An amine-functionalized mil-53 metal- organic framework with large separation power for co2 and ch4," *Journal of the American Chemical Society*, vol. 131, no. 18, pp. 6326–6327, 2009. [Online]. Available: https://doi.org/10.1021/ja900555r

[153] S. Couck, T. Rémy, G. V. Baron, J. Gascon, F. Kapteijn, and J. F. Denayer, "A pulse chromatographic study of the adsorption properties of the amino-mil-53 (al) metal–organic framework," *Physical Chemistry Chemical Physics*, vol. 12, no. 32, pp. 9413–9418, 2010. [Online]. Available: https://doi.org/10.1039/B927115E

[154] A. Boutin, S. Couck, F.-X. Coudert, P. Serra-Crespo, J. Gascon, F. Kapteijn, A. H. Fuchs, and J. F. Denayer, "Thermodynamic analysis of the breathing of amino-functionalized mil-53 (al) upon co2 adsorption," *Microporous and Mesoporous Materials*, vol. 140, no. 1-3, pp. 108–113, 2011. [Online]. Available: https://doi.org/10.1039/B927115E

[155] P. Á. Szilágyi, P. Serra-Crespo, J. Gascon, H. Geerlings, and B. Dam, "The impact of post-synthetic linker functionalization of mofs on methane storage: The role of defects," *Frontiers in Energy Research*, vol. 4, p. 9, 2016. [Online]. Available: https://doi.org/10.3389/fenrg.2016.00009

[156] Y. Dong, T. Hu, M. Pudukudy, H. Su, L. Jiang, S. Shan, and Q. Jia, "Influence of microwave-assisted synthesis on the structural and textural properties of mesoporous mil-101 (fe) and nh2-mil-101 (fe) for enhanced tetracycline adsorption," *Materials Chemistry and Physics*, vol. 251, p. 123060, 2020. [Online]. Available: https://doi.org/10.1016/j.matchemphys.2020.123060

[157] A. Chołuj, N. I. Nikishkin, and M. J. Chmielewski, "Facile post-synthetic deamination of mofs and the synthesis of the missing parent compound of the mil-101 family," *Chemical Communications*, vol. 53, no. 73, pp. 10 196–10 199, 2017. [Online]. Available: https://doi.org/10.1039/C7CC06054H

[158] A. Buragohain, P. Van Der Voort, and S. Biswas, "Facile synthesis and gas adsorption behavior of new functionalized al-mil-101-x (x=–ch3,–no2,–och3,–c6h4,–f2,–(ch3) 2,–(och3) 2) materials," *Microporous and Mesoporous Materials*, vol. 215, pp. 91–97, 2015. [Online]. Available: https://doi.org/10.1016/j.micromeso.2015.05.029

[159] E. Stavitski, M. Goesten, J. Juan-Alcañiz, A. Martinez-Joaristi, P. Serra-Crespo, A. V. Petukhov, J. Gascon, and F. Kapteijn, "Kinetic control of metal–organic framework crystallization investigated by time-resolved in situ x-ray scattering," *Angewandte Chemie*, vol. 123, no. 41, pp. 9798–9802, 2011. [Online]. Available: https://doi.org/10.1002/anie.201101757

[160] M. G. Goesten, E. Stavitski, J. Juan-Alcaniz, A. Martinez-Joaristi, A. V. Petukhov, F. Kapteijn, and J. Gascon, "Small-angle x-ray scattering documents the growth of metal-organic frameworks," *Catalysis today*, vol. 205, pp. 120–127, 2013. [Online]. Available: https://doi.org/10.1016/j.cattod.2012.08.044

[161] M. G. Goesten, P. C. Magusin, E. A. Pidko, B. Mezari, E. J. Hensen, F. Kapteijn, and J. Gascon, "Molecular promoting of aluminum metal–organic framework topology mil-101 by n, n-dimethylformamide," *Inorganic chemistry*, vol. 53, no. 2, pp. 882–887, 2014. [Online]. Available: https://doi.org/10.1021/ic402198a

[162] M. Haouas, C. Volkringer, T. Loiseau, G. Ferey, and F. Taulelle, "In situ nmr, ex situ xrd and sem study of the hydrothermal crystallization of nanoporous aluminum

trimesates mil-96, mil-100, and mil-110," *Chemistry of Materials*, vol. 24, no. 13, pp. 2462–2471, 2012. [Online]. Available: https://doi.org/10.1021/cm300439e

[163] G. A. Lawrance, *Introduction to coordination chemistry*, 1st ed. Wiltshire, UK: John Wiley & Sons, 2013.

[164] S. Biswas, S. Couck, M. Grzywa, J. F. Denayer, D. Volkmer, and P. Van Der Voort, "Vanadium analogues of nonfunctionalized and amino-functionalized mofs with mil-101 topology–synthesis, characterization, and gas sorption properties," *European Journal of Inorganic Chemistry*, vol. 2012, no. 15, pp. 2481–2486, 2012. [Online]. Available: https://doi.org/10.1002/ejic.201200106

[165] A. Lieb, H. Leclerc, T. Devic, C. Serre, I. Margiolaki, F. Mahjoubi, J. S. Lee, A. Vimont, M. Daturi, and J.-S. Chang, "Mil-100 (v)–a mesoporous vanadium metal organic framework with accessible metal sites," *Microporous and mesoporous materials*, vol. 157, pp. 18–23, 2012. [Online]. Available: https://doi.org/10.1016/j.micromeso.2011.12.001

[166] P. Van Der Voort, K. Leus, Y.-Y. Liu, M. Vandichel, V. Van Speybroeck, M. Waroquier, and S. Biswas, "Vanadium metal–organic frameworks: structures and applications," *New Journal of Chemistry*, vol. 38, no. 5, pp. 1853–1867, 2014. [Online]. Available: https://doi.org/10.1039/C3NJ01130E

[167] Q. Xu, L. Fang, Y. Fu, Q. Xiao, F. Zhang, and W. Zhu, "Synthesis, characterization, and co2 adsorption properties of metal–organic framework nh2–mil–101 (v)," *Materials Letters*, vol. 264, p. 127402, 2020. [Online]. Available: https://doi.org/10.1016/j.matlet.2020.127402

[168] F. Farzaneh and Y. Sadeghi, "Immobilized v-mil-101 on modified fe3o4 nanoparticles as heterogeneous catalyst for epoxidation of allyl alcohols and alkenes," *Journal of Molecular Catalysis A: Chemical*, vol. 398, pp. 275–281, 2015. [Online]. Available: https://doi.org/10.1016/j.molcata.2014.12.004

[169] Y. Liao, C. Li, X. Lou, X. Hu, Y. Ning, F. Yuan, B. Chen, M. Shen, and B. Hu, "Carbon-coated li3v2 (po4) 3 derived from metal-organic framework as cathode for lithium-ion batteries with high stability," *Electrochimica Acta*, vol. 271, pp. 608–616, 2018. [Online]. Available: https://doi.org/10.1016/j.electacta.2018.03.100

[170] F. Carson, J. Su, A. E. Platero-Prats, W. Wan, Y. Yun, L. Samain, and X. Zou, "Framework isomerism in vanadium metal–organic frameworks: Mil-88b (v) and

mil-101 (v)," *Crystal growth & design*, vol. 13, no. 11, pp. 5036–5044, 2013. [Online]. Available: https://doi.org/10.1021/cg4012058

[171] J. A. Mason, L. E. Darago, W. W. Lukens Jr, and J. R. Long, "Synthesis and o2 reactivity of a titanium (iii) metal–organic framework," *Inorganic chemistry*, vol. 54, no. 20, pp. 10 096–10 104, 2015. [Online]. Available: https://doi.org/10.1021/acs.inorgchem.5b02046

[172] H. L. Nguyen, "The chemistry of titanium-based metal–organic frameworks," *New Journal of Chemistry*, vol. 41, no. 23, pp. 14 030–14 043, 2017. [Online]. Available: https://doi.org/10.1039/C7NJ03153J

[173] A. M. Antonio, J. Rosenthal, and E. D. Bloch, "Electrochemically mediated syntheses of titanium (iii)-based metal–organic frameworks," *Journal of the American Chemical Society*, vol. 141, no. 29, pp. 11 383–11 387, 2019. [Online]. Available: https://doi.org/10.1021/jacs.9b05035

[174] S. Yuan, L. Feng, K. Wang, J. Pang, M. Bosch, C. Lollar, Y. Sun, J. Qin, X. Yang, P. Zhang *et al.*, "Stable metal–organic frameworks: design, synthesis, and applications," *Advanced Materials*, vol. 30, no. 37, p. 1704303, 2018. [Online]. Available: https://doi.org/10.1002/adma.201704303

[175] P. D. Dietzel, R. Blom, and H. Fjellvåg, "A scandium coordination polymer constructed from trimeric octahedral building blocks and 2, 5-dihydroxyterephthalate," *Dalton Transactions*, no. 17, pp. 2055–2057, 2006. [Online]. Available: https://doi.org/10.1039/B516365J

[176] I. A. Ibarra, X. Lin, S. Yang, A. J. Blake, G. S. Walker, S. A. Barnett, D. R. Allan, N. R. Champness, P. Hubberstey, and M. Schröder, "Structures and h2 adsorption properties of porous scandium metal–organic frameworks," *Chemistry–A European Journal*, vol. 16, no. 46, pp. 13 671–13 679, 2010. [Online]. Available: https://doi.org/10.1002/chem.201000926

[177] J. P. Mowat, S. R. Miller, A. M. Slawin, V. R. Seymour, S. E. Ashbrook, and P. A. Wright, "Synthesis, characterisation and adsorption properties of microporous scandium carboxylates with rigid and flexible frameworks," *Microporous and mesoporous materials*, vol. 142, no. 1, pp. 322–333, 2011. [Online]. Available: https://doi.org/10.1016/j.micromeso.2010.12.016

[178] Y.-T. Li, K.-H. Cui, J. Li, J.-Q. Zhu, X. Wang, and Y.-Q. Tian, "The giant pore metal-organic frameworks of scandium carboxylate with mil-100 and mil-101 structures," *Chinese Journal of Inorganic Chemistry*, vol. 27, no. 5, pp. 951–956, 2011. [Online]. Available: http://www.wjhxxb.cn/wjhxxbcn/ch/reader/create_pdf. aspx?file_no=20110525&flag=1&journal_id=wjhxxbcn&year_id=2011

[179] L. Mitchell, B. Gonzalez-Santiago, J. P. Mowat, M. E. Gunn, P. Williamson, N. Acerbi, M. L. Clarke, and P. A. Wright, "Remarkable lewis acid catalytic performance of the scandium trimesate metal organic framework mil-100 (sc) for c–c and c [double bond, length as m-dash] n bond-forming reactions," *Catalysis Science & Technology*, vol. 3, no. 3, pp. 606–617, 2013. [Online]. Available: https://doi.org/10.1039/C2CY20577G

[180] B. R. James, J. A. Boissonnault, A. G. Wong-Foy, A. J. Matzger, and M. S. Sanford, "Structure activity relationships in metal–organic framework catalysts for the continuous flow synthesis of propylene carbonate from co 2 and propylene oxide," *RSC advances*, vol. 8, no. 4, pp. 2132–2137, 2018. [Online]. Available: https://doi.org/10.1039/C7RA13245J

[181] B. Cordero, V. Gómez, A. E. Platero-Prats, M. Revés, J. Echeverría, E. Cremades, F. Barragán, and S. Alvarez, "Covalent radii revisited," *Dalton Transactions*, no. 21, pp. 2832–2838, 2008. [Online]. Available: https://doi.org/10.1039/B801115J

[182] V. I. Isaeva, M. N. Timofeeva, V. N. Panchenko, I. A. Lukoyanov, V. V. Chernyshev, G. I. Kapustin, N. A. Davshan, and L. M. Kustov, "Design of novel catalysts for synthesis of 1, 5-benzodiazepines from 1, 2-phenylenediamine and ketones: Nh2-mil-101 (al) as integrated structural scaffold for catalytic materials based on calix [4] arenes," *Journal of Catalysis*, vol. 369, pp. 60–71, 2019. [Online]. Available: https://doi.org/10.1016/j.jcat.2018.10.035

[183] T. Wittmann, R. Siegel, N. Reimer, W. Milius, N. Stock, and J. Senker, "Enhancing the water stability of al-mil-101-nh2 via postsynthetic modification," *Chemistry–A European Journal*, vol. 21, no. 1, pp. 314–323, 2015. [Online]. Available: https://doi.org/10.1002/chem.201404654

[184] J. Shin, M. Kim, J. Cirera, S. Chen, G. J. Halder, T. A. Yersak, F. Paesani, S. M. Cohen, and Y. S. Meng, "Mil-101 (fe) as a lithium-ion battery electrode material: a relaxation and intercalation mechanism during lithium insertion," *Journal of Materials Chemistry A*, vol. 3, no. 8, pp. 4738–4744, 2015. [Online]. Available: http://doi.org/10.1039/C4TA06694D

[185] Y. Lin, C. Kong, and L. Chen, "Direct synthesis of amine-functionalized mil-101 (cr) nanoparticles and application for co 2 capture," *RSC advances*, vol. 2, no. 16, pp. 6417–6419, 2012. [Online]. Available: https://doi.org/10.1039/C2RA20641B

[186] K. S. Sing, "Reporting physisorption data for gas/solid systems with special reference to the determination of surface area and porosity (recommendations 1984)," *Pure and applied chemistry*, vol. 57, no. 4, pp. 603–619, 1985. [Online]. Available: https://doi.org/10.1351/pac198557040603

[187] M. Thommes, K. Kaneko, A. V. Neimark, J. P. Olivier, F. Rodriguez-Reinoso, J. Rouquerol, and K. S. Sing, "Physisorption of gases, with special reference to the evaluation of surface area and pore size distribution (iupac technical report)," *Pure and applied chemistry*, vol. 87, no. 9-10, pp. 1051–1069, 2015. [Online]. Available: https://doi.org/10.1515/pac-2014-1117

[188] R. Bardestani, G. S. Patience, and S. Kaliaguine, "Experimental methods in chemical engineering: specific surface area and pore size distribution measurements—bet, bjh, and dft," *The Canadian Journal of Chemical Engineering*, vol. 97, no. 11, pp. 2781–2791, 2019. [Online]. Available: https://doi.org/10.1002/cjce.23632

[189] G. Mouchaham, S. Wang, and C. Serre, "The stability of metal–organic frameworks," *Metal-Organic Frameworks: Applications in Separations and Catalysis*, pp. 1–28, 2018. [Online]. Available: https://doi.org/10.1002/9783527809097.ch1

[190] C. Healy, K. M. Patil, B. H. Wilson, L. Hermanspahn, N. C. Harvey-Reid, B. I. Howard, C. Kleinjan, J. Kolien, F. Payet, S. G. Telfer *et al.*, "The thermal stability of metal-organic frameworks," *Coordination Chemistry Reviews*, vol. 419, p. 213388, 2020. [Online]. Available: https://doi.org/10.1016/j.ccr.2020.213388

[191] A. Vimont, J.-M. Goupil, J.-C. Lavalley, M. Daturi, S. Surblé, C. Serre, F. Millange, G. Férey, and N. Audebrand, "Investigation of acid sites in a zeotypic giant pores chromium (iii) carboxylate," *Journal of the American Chemical Society*, vol. 128, no. 10, pp. 3218–3227, 2006. [Online]. Available: https://doi.org/10.1021/ja056906s

[192] P. Horcajada, C. Serre, M. Vallet-Regí, M. Sebban, F. Taulelle, and G. Férey, "Metal–organic frameworks as efficient materials for drug delivery," *Angewandte chemie*, vol. 118, no. 36, pp. 6120–6124, 2006. [Online]. Available: https://doi.org/10.1002/anie.200601878

[193] P. Chowdhury, C. Bikkina, and S. Gumma, "Gas adsorption properties of the chromium-based metal organic framework mil-101," *The Journal of Physical Chemistry C*, vol. 113, no. 16, pp. 6616–6621, 2009. [Online]. Available: https://doi.org/10.1021/jp811418r

[194] C.-X. Yang and X.-P. Yan, "Metal–organic framework mil-101 (cr) for high-performance liquid chromatographic separation of substituted aromatics," *Analytical chemistry*, vol. 83, no. 18, pp. 7144–7150, 2011. [Online]. Available: https://doi.org/10.1021/ac201517c

[195] A. A. Voskanyan, C.-Y. V. Li, K.-Y. Chan, and L. Gao, "Combustion synthesis of cr 2 o 3 octahedra with a chromium-containing metal–organic framework as a sacrificial template," *CrystEngComm*, vol. 17, no. 13, pp. 2620–2623, 2015. [Online]. Available: https://doi.org/10.1039/C4CE02529F

[196] S. Mutyala, M. Jonnalagadda, H. Mitta, and R. Gundeboyina, "Co2 capture and adsorption kinetic study of amine-modified mil-101 (cr)," *Chemical Engineering Research and Design*, vol. 143, pp. 241–248, 2019. [Online]. Available: https://doi.org/10.1016/j.cherd.2019.01.020

[197] D. Zhang, F. Ye, Y. Guan, Y. Wang, and E. J. Hensen, "Hydrogenation of γ-valerolactone in ethanol over pd nanoparticles supported on sulfonic acid functionalized mil-101," *RSC advances*, vol. 4, no. 74, pp. 39 558–39 564, 2014. [Online]. Available: https://doi.org/10.1039/C4RA05250A

[198] I. J. Kang, N. A. Khan, E. Haque, and S. H. Jhung, "Chemical and thermal stability of isotypic metal–organic frameworks: effect of metal ions," *Chemistry–A European Journal*, vol. 17, no. 23, pp. 6437–6442, 2011. [Online]. Available: https://doi.org/10.1002/chem.201100316

[199] J. Ren, N. M. Musyoka, H. W. Langmi, T. Segakweng, B. C. North, M. Mathe, and X. Kang, "Modulated synthesis of chromium-based metal-organic framework (mil-101) with enhanced hydrogen uptake," *international journal of hydrogen energy*, vol. 39, no. 23, pp. 12 018–12 023, 2014. [Online]. Available: https://doi.org/10.1016/j.ijhydene.2014.06.019

[200] Y.-K. Seo, J. W. Yoon, J. S. Lee, Y. K. Hwang, C.-H. Jun, J.-S. Chang, S. Wuttke, P. Bazin, A. Vimont, M. Daturi *et al.*, "Energy-efficient dehumidification over hierachically porous metal–organic frameworks as advanced water adsorbents,"

Advanced materials, vol. 24, no. 6, pp. 806–810, 2012. [Online]. Available: https://doi.org/10.1002/adma.201104084

[201] J. J. Low, A. I. Benin, P. Jakubczak, J. F. Abrahamian, S. A. Faheem, and R. R. Willis, "Virtual high throughput screening confirmed experimentally: porous coordination polymer hydration," *Journal of the American Chemical Society*, vol. 131, no. 43, pp. 15 834–15 842, 2009. [Online]. Available: https://doi.org/10.1021/ja9061344

[202] L. Pukdeejorhor, K. Adpakpang, P. Ponchai, S. Wannapaiboon, S. Ittisanronnachai, M. Ogawa, S. Horike, and S. Bureekaew, "Polymorphism of mixed metal cr/fe terephthalate metal–organic frameworks utilizing a microwave synthetic method," *Crystal Growth & Design*, vol. 19, no. 10, pp. 5581–5591, 2019. [Online]. Available: https://doi.org/10.1021/acs.cgd.9b00508

[203] C. A. Lucchesi and W. Lewis, "Latent heat of sublimation of terephthalic acid from differential thermal analysis data," *Journal of Chemical & Engineering Data*, vol. 13, no. 3, pp. 389–391, 1968. [Online]. Available: https://doi.org/10.1021/je60038a026

[204] E. Haque, J. H. Jeong, and S. H. Jhung, "Synthesis of isostructural porous metal-benzenedicarboxylates: Effect of metal ions on the kinetics of synthesis," *CrystEngComm*, vol. 12, no. 10, pp. 2749–2754, 2010. [Online]. Available: https://doi.org/10.1039/B927113A

[205] H. Reinsch and N. Stock, "Formation and characterisation of mn-mil-100," *CrystEngComm*, vol. 15, no. 3, pp. 544–550, 2013. [Online]. Available: https://doi.org/10.1039/C2CE26436F

[206] B. Zhang, S. Hao, D. Xiao, J. Wu, and Y. Huang, "Templated formation of porous mn2o3 octahedra from mn-mil-100 for lithium-ion battery anode materials," *Materials & Design*, vol. 98, pp. 319–323, 2016. [Online]. Available: https://doi.org/10.1016/j.matdes.2016.03.041

[207] M. R. Mian, U. Afrin, M. S. Fataftah, K. B. Idrees, T. Islamoglu, D. E. Freedman, and O. K. Farha, "Control of the porosity in manganese trimer-based metal–organic frameworks by linker functionalization," *Inorganic chemistry*, vol. 59, no. 12, pp. 8444–8450, 2020. [Online]. Available: https://doi.org/10.1021/acs.inorgchem.0c00885

[208] M. Songolzadeh, M. Soleimani, and M. T. Ravanchi, "Multi-response optimization of mil-101 synthesis for selectively adsorbing n-compounds from fuels," *Petroleum*

Science, vol. 16, no. 6, pp. 1442–1454, 2019. [Online]. Available: https://doi.org/10.1007/s12182-019-0351-5

[209] W. Beckmann, *Crystallization: basic concepts and industrial applications.* Weinheim, Germany: John Wiley & Sons, 2013.

[210] R. Hilfiker, *Polymorphism: in the pharmaceutical industry.* Weinheim, Germany: John Wiley & Sons, 2006.

[211] C. Serre, C. Mellot-Draznieks, S. Surblé, N. Audebrand, Y. Filinchuk, and G. Férey, "Role of solvent-host interactions that lead to very large swelling of hybrid frameworks," *Science*, vol. 315, no. 5820, pp. 1828–1831, 2007. [Online]. Available: https://doi.org/10.1126/science.11379755

[212] C. Mellot-Draznieks, C. Serre, S. Surblé, N. Audebrand, and G. Férey, "Very large swelling in hybrid frameworks: a combined computational and powder diffraction study," *Journal of the American Chemical Society*, vol. 127, no. 46, pp. 16 273–16 278, 2005. [Online]. Available: https://doi.org/10.1021/ja054900x

[213] F. Millange, M. I. Medina, N. Guillou, G. Férey, K. M. Golden, and R. I. Walton, "Time-resolved in situ diffraction study of the solvothermal crystallization of some prototypical metal–organic frameworks," *Angewandte Chemie*, vol. 122, no. 4, pp. 775–778, 2010. [Online]. Available: https://doi.org/10.1002/anie.200905627

[214] A. C. Sudik, A. P. Côté, and O. M. Yaghi, "Metal-organic frameworks based on trigonal prismatic building blocks and the new "acs" topology," *Inorganic chemistry*, vol. 44, no. 9, pp. 2998–3000, 2005. [Online]. Available: https://doi.org/10.1021/ic050064g

[215] D. Kolokolov, H. Jobic, A. Stepanov, M. Plazanet, M. Zbiri, J. Ollivier, V. Guillerm, T. Devic, C. Serre, and G. Férey, "Comparison of the dynamics of mil-53 (cr) and mil-47 (v) frameworks using neutron scattering and dft methods," *The European Physical Journal Special Topics*, vol. 189, no. 1, pp. 263–271, 2010. [Online]. Available: https://doi.org/10.1140/epjst/e2010-01331-y

[216] A. Schoedel, M. Li, D. Li, M. O'Keeffe, and O. M. Yaghi, "Structures of metal–organic frameworks with rod secondary building units," *Chemical reviews*, vol. 116, no. 19, pp. 12 466–12 535, 2016. [Online]. Available: https://doi.org/10.1021/acs.chemrev.6b00346

[217] T. Loiseau, C. Serre, C. Huguenard, G. Fink, F. Taulelle, M. Henry, T. Bataille, and G. Férey, "A rationale for the large breathing of the porous aluminum terephthalate

(mil-53) upon hydration," *Chemistry–A European Journal*, vol. 10, no. 6, pp. 1373–1382, 2004. [Online]. Available: https://doi.org/10.1002/chem.200305413

[218] F. Millange, N. Guillou, R. I. Walton, J.-M. Grenèche, I. Margiolaki, and G. Férey, "Effect of the nature of the metal on the breathing steps in mofs with dynamic frameworks," *Chemical communications*, no. 39, pp. 4732–4734, 2008. [Online]. Available: https://doi.org/10.1039/B809419E

[219] C. Volkringer, T. Loiseau, N. Guillou, G. Férey, E. Elkaïm, and A. Vimont, "Xrd and ir structural investigations of a particular breathing effect in the mof-type gallium terephthalate mil-53 (ga)," *Dalton Transactions*, no. 12, pp. 2241–2249, 2009. [Online]. Available: https://doi.org/10.1039/B817563B

[220] E. V. Anokhina, M. Vougo-Zanda, X. Wang, and A. J. Jacobson, "In (oh) bdc⊙ 0.75 bdch2 (bdc= benzenedicarboxylate), a hybrid inorganic- organic vernier structure," *Journal of the American Chemical Society*, vol. 127, no. 43, pp. 15 000–15 001, 2005. [Online]. Available: https://doi.org/10.1021/ja055757a

[221] M. Hosseini, D. E. Vanpoucke, P. Giannozzi, M. Berahman, and N. Hadipour, "Investigation of structural, electronic and magnetic properties of breathing metal–organic framework mil-47 (mn): a first principles approach," *RSC Advances*, vol. 10, no. 8, pp. 4786–4794, 2020. [Online]. Available: https://doi.org/10.1039/C9RA09196C

[222] A. Perea-Cachero, J. Sánchez-Laínez, B. Zornoza, E. Romero-Pascual, C. Téllez, and J. Coronas, "Nanosheets of mil-53 (al) applied in membranes with improved co 2/n 2 and co 2/ch 4 selectivities," *Dalton Transactions*, vol. 48, no. 10, pp. 3392–3403, 2019. [Online]. Available: https://doi.org/10.1039/C8DT03774D

[223] D. Wang, R. Huang, W. Liu, D. Sun, and Z. Li, "Fe-based mofs for photocatalytic co2 reduction: role of coordination unsaturated sites and dual excitation pathways," *Acs Catalysis*, vol. 4, no. 12, pp. 4254–4260, 2014. [Online]. Available: https://doi.org/10.1021/cs501169t

[224] A. Schoedel and M. J. Zaworotko, "[m 3 (μ 3-o)(o 2 cr) 6] and related trigonal prisms: versatile molecular building blocks for crystal engineering of metal–organic material platforms," *Chemical Science*, vol. 5, no. 4, pp. 1269–1282, 2014. [Online]. Available: https://doi.org/10.1039/C4SC00171K

[225] M. Barona and R. Q. Snurr, "Exploring the tunability of trimetallic mof nodes for partial oxidation of methane to methanol," *ACS Applied Materials*

& Interfaces, vol. 12, no. 25, pp. 28 217–28 231, 2020. [Online]. Available: https://doi.org/10.1021/acsami.0c06241

[226] P. Á. Szilágyi, P. Serra-Crespo, I. Dugulan, J. Gascon, H. Geerlings, and B. Dam, "Post-synthetic cation exchange in the robust metal–organic framework mil-101 (cr)," *CrystEngComm*, vol. 15, no. 47, pp. 10 175–10 178, 2013. [Online]. Available: https://doi.org/10.1039/C3CE42006J

[227] X. Xia, Y. Xu, Y. Chen, Y. Liu, Y. Lu, and L. Shao, "Fabrication of mil-101 (cr/al) with flower-like morphology and its catalytic performance," *Applied Catalysis A: General*, vol. 559, pp. 138–145, 2018. [Online]. Available: https://doi.org/10.1016/j.apcata.2018.04.020

[228] M. Kim, J. F. Cahill, H. Fei, K. A. Prather, and S. M. Cohen, "Postsynthetic ligand and cation exchange in robust metal–organic frameworks," *Journal of the American Chemical Society*, vol. 134, no. 43, pp. 18 082–18 088, 2012. [Online]. Available: https://doi.org/10.1021/ja3079219

[229] T. A. Vu, G. H. Le, C. D. Dao, L. Q. Dang, K. T. Nguyen, P. T. Dang, H. T. Tran, Q. T. Duong, T. V. Nguyen, and G. D. Lee, "Isomorphous substitution of cr by fe in mil-101 framework and its application as a novel heterogeneous photo-fenton catalyst for reactive dye degradation," *RSC Advances*, vol. 4, no. 78, pp. 41 185–41 194, 2014. [Online]. Available: https://doi.org/10.1039/C4RA06522K

[230] T. Tanasaro, K. Adpakpang, S. Ittisanronnachai, K. Faungnawakij, T. Butburee, S. Wannapaiboon, M. Ogawa, and S. Bureekaew, "Control of polymorphism of metal–organic frameworks using mixed-metal approach," *Crystal Growth & Design*, vol. 18, no. 1, pp. 16–21, 2018. [Online]. Available: https://doi.org/10.1021/acs.cgd.7b01193

[231] C. Vallés-García, E. Gkaniatsou, A. Santiago-Portillo, M. Giménez-Marqués, M. Álvaro, J.-M. Greneche, N. Steunou, C. Sicard, S. Navalón, C. Serre *et al.*, "Design of stable mixed-metal mil-101 (cr/fe) materials with enhanced catalytic activity for the prins reaction," *Journal of Materials Chemistry A*, vol. 8, no. 33, pp. 17 002–17 011, 2020. [Online]. Available: https://doi.org/10.1039/D0TA02991B

[232] S. Li, T. Lei, F. Jiang, M. Liu, Y. Wang, S. Wang, and X. Yang, "Tuning the morphology and adsorption capacity of al-mil-101 analogues with fe3+ for phosphorus removal from water," *Journal of colloid and interface science*, vol. 560, pp. 321–329, 2020. [Online]. Available: https://doi.org/10.1016/j.jcis.2019.10.077

[233] Y. Hu, J. Zhang, H. Huo, Z. Wang, X. Xu, Y. Yang, K. Lin, and R. Fan, "One-pot synthesis of bimetallic metal–organic frameworks (mofs) as acid–base bifunctional catalysts for tandem reaction," *Catalysis Science & Technology*, vol. 10, no. 2, pp. 315–322, 2020. [Online]. Available: https://doi.org/10.1039/C9CY01940E

[234] K. E. Dekrafft, C. Wang, and W. Lin, "Metal-organic framework templated synthesis of fe2o3/tio2 nanocomposite for hydrogen production," *Advanced materials*, vol. 24, no. 15, pp. 2014–2018, 2012. [Online]. Available: https://doi.org/10.1002/adma.201200330

[235] N. Chang, H. Zhang, M.-S. Shi, J. Li, C.-J. Yin, H.-T. Wang, and L. Wang, "Regulation of the adsorption affinity of metal-organic framework mil-101 via a tio2 coating strategy for high capacity adsorption and efficient photocatalysis," *Microporous and Mesoporous Materials*, vol. 266, pp. 47–55, 2018. [Online]. Available: https://doi.org/10.1016/j.micromeso.2018.02.051

[236] J. Geng, J. Ma, F. Li, S. Ma, D. Zhang, and X. Ning, "Atomic layer deposition of cu2o on nh2-mil-101 (fe) for enhanced photocatalytic performance and decreased electron/hole recombination," *Ceramics International*, vol. 47, no. 10, pp. 13 291–13 300, 2021. [Online]. Available: https://doi.org/10.1016/j.ceramint.2020.09.239

[237] L. Ni, Y. Zhu, J. Ma, and Y. Wang, "Novel strategy for membrane biofouling control in mbr with cds/mil-101 modified pvdf membrane by in situ visible light irradiation," *Water Research*, vol. 188, p. 116554, 2021. [Online]. Available: https://doi.org/10.1016/j.watres.2020.116554

[238] J. Wang, Y. Muhammad, Z. Gao, S. J. Shah, S. Nie, L. Kuang, Z. Zhao, Z. Qiao, and Z. Zhao, "Implanting polyethylene glycol into mil-101 (cr) as hydrophobic barrier for enhancing toluene adsorption under highly humid environment," *Chemical Engineering Journal*, vol. 404, p. 126562, 2021. [Online]. Available: https://doi.org/10.1016/j.cej.2020.126562

[239] T. K. Vo, T. P. Trinh, V. C. Nguyen, and J. Kim, "Facile synthesis of graphite oxide/mil-101 (cr) hybrid composites for enhanced adsorption performance towards industrial toxic dyes," *Journal of Industrial and Engineering Chemistry*, vol. 95, pp. 224–234, 2021. [Online]. Available: https://doi.org/10.1016/j.jiec.2020.12.023

[240] C. Du, Z. Zhang, G. Yu, H. Wu, H. Chen, L. Zhou, Y. Zhang, Y. Su, S. Tan, L. Yang *et al.*, "A review of metal organic framework (mofs)-based materials for antibiotics

removal via adsorption and photocatalysis," *Chemosphere*, p. 129501, 2021. [Online]. Available: https://doi.org/10.1016/j.chemosphere.2020.129501

[241] X. Guo, C. Kang, H. Huang, Y. Chang, and C. Zhong, "Exploration of functional mofs for efficient removal of fluoroquinolone antibiotics from water," *Microporous and Mesoporous Materials*, vol. 286, pp. 84–91, 2019. [Online]. Available: https://doi.org/10.1016/j.micromeso.2019.05.025

[242] J. M. Park and S. H. Jhung, "A remarkable adsorbent for removal of bisphenol s from water: Aminated metal-organic framework, mil-101-nh2," *Chemical Engineering Journal*, vol. 396, p. 125224, 2020. [Online]. Available: https://doi.org/10.1016/j.cej.2020.125224

[243] W. Zhang, R.-Z. Zhang, Y. Yin, and J.-M. Yang, "Superior selective adsorption of anionic organic dyes by mil-101 analogs: Regulation of adsorption driving forces by free amino groups in pore channels," *Journal of Molecular Liquids*, vol. 302, p. 112616, 2020. [Online]. Available: https://doi.org/10.1016/j.molliq.2020.112616

[244] H. Jalayeri, P. Aprea, D. Caputo, A. Peluso, and F. Pepe, "Synthesis of amino-functionalized mil-101 (cr) mof for hexavalent chromium adsorption from aqueous solutions," *Environmental Nanotechnology, Monitoring & Management*, vol. 14, p. 100300, 2020. [Online]. Available: https://doi.org/10.1016/j.enmm.2020.100300

[245] F. Ahmadijokani, S. Tajahmadi, M. Rezakazemi, A. A. Sehat, H. Molavi, T. M. Aminabhavi, and M. Arjmand, "Aluminum-based metal-organic frameworks for adsorptive removal of anti-cancer (methotrexate) drug from aqueous solutions," *Journal of Environmental Management*, vol. 277, p. 111448, 2021. [Online]. Available: https://doi.org/10.1016/j.jenvman.2020.111448

[246] L. Liu, Y. Fang, Y. Meng, X. Wang, F. Ma, C. Zhang, and H. Dong, "Efficient adsorbent for recovering uranium from seawater prepared by grafting amidoxime groups on chloromethylated mil-101 (cr) via diaminomaleonitrile intermediate," *Desalination*, vol. 478, p. 114300, 2020. [Online]. Available: https://doi.org/10.1016/j.desal.2019.114300

[247] J. Jin, Z. Yang, W. Xiong, Y. Zhou, R. Xu, Y. Zhang, J. Cao, X. Li, and C. Zhou, "Cu and co nanoparticles co-doped mil-101 as a novel adsorbent for efficient removal of tetracycline from aqueous solutions," *Science of the Total Environment*, vol. 650, pp. 408–418, 2019. [Online]. Available: https://doi.org/10.1016/j.scitotenv.2018.08.434

[248] A. Hamedi, M. B. Zarandi, and M. R. Nateghi, "Highly efficient removal of dye pollutants by mil-101 (fe) metal-organic framework loaded magnetic particles mediated by poly l-dopa," *Journal of Environmental Chemical Engineering*, vol. 7, no. 1, p. 102882, 2019. [Online]. Available: https://doi.org/10.1016/j.jece.2019.102882

[249] X. Hou, J. Shi, N. Wang, Z. Wen, M. Sun, J. Qu, and Q. Hu, "Removal of antibiotic tetracycline by metal-organic framework mil-101 (cr) loaded nano zero-valent iron," *Journal of Molecular Liquids*, vol. 313, p. 113512, 2020. [Online]. Available: https://doi.org/10.1016/j.molliq.2020.113512

[250] B. Wang, Y. Yang, Y. Lu, W. Wang, Q. Wang, X. Dong, and J. Zhao, "Rapid and efficient removal of acetochlor from environmental water using cr-mil-101 sorbent modified with 3, 5-bis (trifluoromethyl) phenyl isocyanate," *Science of The Total Environment*, vol. 710, p. 135512, 2020. [Online]. Available: https://doi.org/10.1016/j.scitotenv.2019.135512

[251] N. A. Khan and S. H. Jhung, "Phytic acid-encapsulated mil-101 (cr): Remarkable adsorbent for the removal of both neutral indole and basic quinoline from model liquid fuel," *Chemical Engineering Journal*, vol. 375, p. 121948, 2019. [Online]. Available: https://doi.org/10.1016/j.cej.2019.121948

[252] J. Wang, Y. Liu, X. Guo, H. Qu, R. Chang, and J. Ma, "Efficient adsorption of dyes using polyethyleneimine-modified nh2-mil-101 (al) and its sustainable application as a flame retardant for an epoxy resin," *ACS omega*, vol. 5, no. 50, pp. 32 286–32 294, 2020. [Online]. Available: https://doi.org/10.1021/acsomega.0c04118

[253] H. Su, J. Lv, L. Yang, L. Feng, Y. Liu, Z. Du, and L. Zhang, "Rapid and selective adsorption of a typical aromatic organophosphorus flame retardant on mil-101-based metal–organic frameworks," *RSC Advances*, vol. 10, no. 4, pp. 2198–2208, 2020. [Online]. Available: https://doi.org/10.1039/C9RA09062B

[254] W. Wu, T. Yao, Y. Xiang, H. Zou, and Y. Zhou, "Efficient removal of methyl orange by a flower-like tio 2/mil-101 (cr) composite nanomaterial," *Dalton Transactions*, vol. 49, no. 17, pp. 5722–5729, 2020. [Online]. Available: https://doi.org/10.1039/D0DT00778A

[255] M. Lefèvre, E. Proietti, F. Jaouen, and J.-P. Dodelet, "Iron-based catalysts with improved oxygen reduction activity in polymer electrolyte fuel cells," *science*, vol. 324, no. 5923, pp. 71–74, 2009. [Online]. Available: https://doi.org/10.1126/science.1170051

[256] F. Afsahi and S. Kaliaguine, "Non-precious electrocatalysts synthesized from metal–organic frameworks," *Journal of Materials Chemistry A*, vol. 2, no. 31, pp. 12 270–12 279, 2014. [Online]. Available: https://doi.org/10.1039/C4TA02010C

[257] T. Tan, P. Tao, X. Li, S. Imhanria, J. Deng, and W. Wang, "Nitrogen-modified metal-organic framework-based carbon: An effective non-precious electrocatalyst for oxygen reduction reaction," *Catalysis Communications*, vol. 146, p. 106135, 2020. [Online]. Available: https://doi.org/10.1016/j.catcom.2020.106135

[258] Y. Luo, J. Zhang, M. Kiani, Y. Chen, J. Chen, G. Wang, S. H. Chan, and R. Wang, "Synthesis of mof-derived nonprecious catalyst with high electrocatalytic activity for oxygen reduction reaction," *Industrial & Engineering Chemistry Research*, vol. 57, no. 36, pp. 12 087–12 095, 2018. [Online]. Available: https://doi.org/10.1021/acs.iecr.8b02744

[259] H. Su, S. Zhou, X. Zhang, H. Sun, H. Zhang, Y. Xiao, K. Yu, Z. Dong, X. Dai, and X. Huang, "Metal–organic frameworks-derived core–shell fe 3 o 4/fe 3 n@ graphite carbon nanocomposites as excellent non-precious metal electrocatalyst for oxygen reduction," *Dalton Transactions*, vol. 47, no. 46, pp. 16 567–16 577, 2018. [Online]. Available: https://doi.org/10.1039/C8DT02250J

[260] S. Gao, B. Fan, R. Feng, C. Ye, X. Wei, J. Liu, and X. Bu, "N-doped-carbon-coated fe3o4 from metal-organic framework as efficient electrocatalyst for orr," *Nano Energy*, vol. 40, pp. 462–470, 2017. [Online]. Available: https://doi.org/10.1016/j.nanoen.2017.08.044

[261] Y. Cheng, J. Guo, Y. Huang, Z. Liao, and Z. Xiang, "Ultrastable hydrogen evolution electrocatalyst derived from phosphide postmodified metal-organic frameworks," *Nano Energy*, vol. 35, pp. 115–120, 2017. [Online]. Available: https://doi.org/10.1016/j.nanoen.2017.03.028

[262] Y. Guo, C. Feng, S. Qiao, S. Wang, T. Chen, L. Zhang, Y. Zhao, and J. Wang, "Magnetic fe 3 o 4-encapsulated van@ mil-101 (fe) with mixed-valence sites and mesoporous structures as efficient bifunctional water splitting photocatalysts," *Nanoscale*, vol. 12, no. 23, pp. 12 551–12 560, 2020. [Online]. Available: https://doi.org/10.1039/D0NR02230F

[263] F. Yin, G. Li, and H. Wang, "Hydrothermal synthesis of α-mno2/mil-101 (cr) composite and its bifunctional electrocatalytic activity for oxygen reduction/evolution

reactions," *Catalysis Communications*, vol. 54, pp. 17–21, 2014. [Online]. Available: https://doi.org/10.1016/j.catcom.2014.05.006

[264] J. Han, D. Wang, Y. Du, S. Xi, Z. Chen, S. Yin, T. Zhou, and R. Xu, "Polyoxometalate immobilized in mil-101 (cr) as an efficient catalyst for water oxidation," *Applied Catalysis A: General*, vol. 521, pp. 83–89, 2016. [Online]. Available: https://doi.org/10.1016/j.apcata.2015.10.015

[265] D. M. Fernandes, A. D. Barbosa, J. Pires, S. S. Balula, L. Cunha-Silva, and C. Freire, "Novel composite material polyoxovanadate@ mil-101 (cr): a highly efficient electrocatalyst for ascorbic acid oxidation," *ACS applied materials & interfaces*, vol. 5, no. 24, pp. 13 382–13 390, 2013. [Online]. Available: https://doi.org/10.1021/am4042564

[266] Y. Wang, W. Guo, and X. Li, "Activation of persulfates by ferrocene–mil-101 (fe) heterogeneous catalyst for degradation of bisphenol a," *RSC advances*, vol. 8, no. 64, pp. 36 477–36 483, 2018. [Online]. Available: https://doi.org/10.1039/C8RA07007E

[267] R. S. Andriamitantsoa, J. Wang, W. Dong, H. Gao, and G. Wang, "So 3 h-functionalized metal organic frameworks: an efficient heterogeneous catalyst for the synthesis of quinoxaline and derivatives," *RSC advances*, vol. 6, no. 41, pp. 35 135–35 143, 2016. [Online]. Available: https://doi.org/10.1039/C6RA02575G

[268] S. Wang, S. Hou, C. Wu, Y. Zhao, and X. Ma, "Rucl3 anchored onto post-synthetic modification mil-101 (cr)-nh2 as heterogeneous catalyst for hydrogenation of co2 to formic acid," *Chinese Chemical Letters*, vol. 30, no. 2, pp. 398–402, 2019. [Online]. Available: https://doi.org/10.1016/j.cclet.2018.06.021

[269] M. Saikia, D. Bhuyan, and L. Saikia, "Keggin type phosphotungstic acid encapsulated chromium (iii) terephthalate metal organic framework as active catalyst for biginelli condensation," *Applied Catalysis A: General*, vol. 505, pp. 501–506, 2015. [Online]. Available: https://doi.org/10.1016/j.apcata.2015.05.021

[270] A. M. Andani, T. Tabatabaie, S. Farhadi, and B. Ramavandi, "Mil-101 (cr)–cobalt ferrite magnetic nanocomposite: synthesis, characterization and applications for the sonocatalytic degradation of organic dye pollutants," *RSC Advances*, vol. 10, no. 54, pp. 32 845–32 855, 2020. [Online]. Available: https://doi.org/10.1039/D0RA04945J

[271] C. Zhao, P. Dong, Z. Liu, G. Wu, S. Wang, Y. Wang, and F. Liu, "Facile synthesis of fe 3 o 4/mil-101 nanocomposite as an efficient heterogeneous catalyst for degradation

of pollutants in fenton-like system," *RSC advances*, vol. 7, no. 39, pp. 24 453–24 461, 2017. [Online]. Available: https://doi.org/10.1039/C7RA01883E

[272] F. Zhang, Y. Jin, Y. Fu, Y. Zhong, W. Zhu, A. A. Ibrahim, and M. S. El-Shall, "Palladium nanoparticles incorporated within sulfonic acid-functionalized mil-101 (cr) for efficient catalytic conversion of vanillin," *Journal of Materials Chemistry A*, vol. 3, no. 33, pp. 17 008–17 015, 2015. [Online]. Available: https://doi.org/10.1039/C5TA03524D

[273] K. Mori and H. Yamashita, "Design and architecture of nanostructured heterogeneous catalysts for co 2 hydrogenation to formic acid/formate," *CO2 Hydrogenation Catalysis*, pp. 179–205, 2021. [Online]. Available: https://doi.org/10.1002/9783527824113.ch7

[274] L. Xu, T. Cui, J. Zhu, X. Wang, and M. Ji, "Pdag alloy nanoparticles immobilized on functionalized mil-101-nh 2: effect of organic amines on hydrogenation of carbon dioxide into formic acid," *New Journal of Chemistry*, vol. 45, no. 14, pp. 6293–6300, 2021. [Online]. Available: https://doi.org/10.1039/D1NJ00460C

[275] H. Alamgholiloo, S. Rostamnia, A. Hassankhani, X. Liu, A. Eftekhari, A. Hasanzadeh, K. Zhang, H. Karimi-Maleh, S. Khaksar, R. S. Varma *et al.*, "Formation and stabilization of colloidal ultra-small palladium nanoparticles on diamine-modified cr-mil-101: Synergic boost to hydrogen production from formic acid," *Journal of colloid and interface science*, vol. 567, pp. 126–135, 2020. [Online]. Available: https://doi.org/10.1016/j.jcis.2020.01.087

[276] H. Dai, N. Cao, L. Yang, J. Su, W. Luo, and G. Cheng, "Agpd nanoparticles supported on mil-101 as high performance catalysts for catalytic dehydrogenation of formic acid," *Journal of Materials Chemistry A*, vol. 2, no. 29, pp. 11 060–11 064, 2014. [Online]. Available: https://doi.org/10.1039/C4TA02066A

[277] P. Zhao, N. Cao, W. Luo, and G. Cheng, "Nanoscale mil-101 supported rhni nanoparticles: an efficient catalyst for hydrogen generation from hydrous hydrazine," *Journal of Materials Chemistry A*, vol. 3, no. 23, pp. 12 468–12 475, 2015. [Online]. Available: https://doi.org/10.1039/C5TA02201K

[278] I. B. Baguc, I. E. Ertas, M. Yurderi, A. Bulut, M. Zahmakiran, and M. Kaya, "Nanocrystalline metal organic framework (mil-101) stabilized copper nanoparticles: Highly efficient nanocatalyst for the hydrolytic dehydrogenation of methylamine borane," *Inorganica Chimica Acta*, vol. 483, pp. 431–439, 2018. [Online]. Available: https://doi.org/10.1016/j.ica.2018.08.056

[279] D. A. Islam, A. Chakraborty, and H. Acharya, "Fluorescent silver nanoclusters (ag ncs) in the metal–organic framework mil-101 (fe) for the catalytic hydrogenation of 4-nitroaniline," *New Journal of Chemistry*, vol. 40, no. 8, pp. 6745–6751, 2016. [Online]. Available: https://doi.org/10.1039/C6NJ00296J

[280] M. Zahid, J. Li, A. Ismail, F. Zaera, and Y. Zhu, "Platinum and cobalt intermetallic nanoparticles confined within mil-101 (cr) for enhanced selective hydrogenation of the carbonyl bond in α, β-unsaturated aldehydes: synergistic effects of electronically modified pt sites and lewis acid sites," *Catalysis Science & Technology*, vol. 11, no. 7, pp. 2433–2445, 2021. [Online]. Available: https://doi.org/10.1039/D0CY02082F

[281] M. Saikia, V. Kaichev, and L. Saikia, "Gold nanoparticles supported on nanoscale amine-functionalized mil-101 (cr) as a highly active catalyst for epoxidation of styrene," *RSC advances*, vol. 6, no. 108, pp. 106 856–106 865, 2016. [Online]. Available: https://doi.org/10.1039/C6RA24458K

[282] M. Trivedi, A. Kumar, G. Singh, A. Kumar, N. P. Rath *et al.*, "Metal–organic framework mil-101 supported bimetallic pd–cu nanocrystals as efficient catalysts for chromium reduction and conversion of carbon dioxide at room temperature," *New Journal of Chemistry*, vol. 40, no. 4, pp. 3109–3118, 2016. [Online]. Available: https://doi.org/10.1039/C5NJ02630J

[283] O. Grad, M. Mihet, G. Blanita, M. Dan, L. Barbu-Tudoran, and M. D. Lazar, "Mil-101-al2o3 as catalytic support in the methanation of co2–comparative study between ni/mil-101 and ni/mil-101-al2o3 catalysts," *Catalysis Today*, vol. 366, pp. 114–122, 2021. [Online]. Available: https://doi.org/10.1016/j.cattod.2020.05.003

[284] E. V. Ramos-Fernandez, M. Garcia-Domingos, J. Juan-Alcañiz, J. Gascon, and F. Kapteijn, "Mofs meet monoliths: hierarchical structuring metal organic framework catalysts," *Applied Catalysis A: General*, vol. 391, no. 1-2, pp. 261–267, 2011. [Online]. Available: https://doi.org/10.1016/j.apcata.2010.05.019

[285] H. M. Hassan, M. A. Betiha, S. K. Mohamed, E. El-Sharkawy, and E. A. Ahmed, "Salen-zr (iv) complex grafted into amine-tagged mil-101 (cr) as a robust multifunctional catalyst for biodiesel production and organic transformation reactions," *Applied Surface Science*, vol. 412, pp. 394–404, 2017. [Online]. Available: https://doi.org/10.1016/j.apsusc.2017.03.247

[286] M. Bahadori, S. Tangestaninejad, M. Moghadam, V. Mirkhani, A. Mechler, I. Mohammadpoor-Baltork, and F. Zadehahmadi, "Metal organic framework-

supported n-heterocyclic carbene palladium complex: a highly efficient and reusable heterogeneous catalyst for suzuki-miyaura cc coupling reaction," *Microporous and Mesoporous Materials*, vol. 253, pp. 102–111, 2017. [Online]. Available: https://doi.org/10.1016/j.micromeso.2017.06.048

[287] Y. Huang, L. Xie, K. Zhuo, H. Zhou, and Y. Zhang, "Simultaneous catalytic reduction of p-nitrophenol and hydrogen production on mil-101 (fe)-based composites," *New Journal of Chemistry*, vol. 45, no. 6, pp. 3120–3127, 2021. [Online]. Available: https://doi.org/10.1039/D0NJ05874B

[288] S. K. Loeb, P. J. Alvarez, J. A. Brame, E. L. Cates, W. Choi, J. Crittenden, D. D. Dionysiou, Q. Li, G. Li-Puma, X. Quan *et al.*, "The technology horizon for photocatalytic water treatment: sunrise or sunset?" 2018. [Online]. Available: https://doi.org/10.1021/acs.est.8b05041

[289] M. Fouad, M. G. Alalm, H. K. El-Etriby, D. C. Boffito, S. Ookawara, T. Ohno, and M. Fujii, "Visible-light-driven photocatalytic disinfection of raw surface waters (300–5000 cfu/ml) using reusable coated ru/wo3/zro2," *Journal of Hazardous Materials*, vol. 402, p. 123514, 2021. [Online]. Available: https://doi.org/10.1016/j.jhazmat.2020.123514

[290] D. Awfa, M. Ateia, M. Fujii, and C. Yoshimura, "Photocatalytic degradation of organic micropollutants: Inhibition mechanisms by different fractions of natural organic matter," *Water research*, vol. 174, p. 115643, 2020. [Online]. Available: https://doi.org/10.1016/j.watres.2020.115643

[291] A. Kumar, M. Khan, J. He, and I. M. Lo, "Recent developments and challenges in practical application of visible–light–driven tio2–based heterojunctions for ppcp degradation: a critical review," *Water research*, vol. 170, p. 115356, 2020. [Online]. Available: https://doi.org/10.1016/j.watres.2019.115356

[292] J. Lim, H. Kim, J. Park, G.-H. Moon, J. J. M. Vequizo, A. Yamakata, J. Lee, and W. Choi, "How g-c3n4 works and is different from tio2 as an environmental photocatalyst: mechanistic view," *Environmental science & technology*, vol. 54, no. 1, pp. 497–506, 2019. [Online]. Available: https://doi.org/10.1021/acs.est.9b05044

[293] A. Serrà, L. Philippe, F. Perreault, and S. Garcia-Segura, "Photocatalytic treatment of natural waters. reality or hype? the case of cyanotoxins remediation," *Water Research*, p. 116543, 2020. [Online]. Available: https://doi.org/10.1016/j.watres.2020.116543

[294] J. Xie, D. Jiang, M. Chen, D. Li, J. Zhu, X. Lü, and C. Yan, "Preparation and characterization of monodisperse ce-doped tio2 microspheres with visible light photocatalytic activity," *Colloids and Surfaces A: Physicochemical and Engineering Aspects*, vol. 372, no. 1-3, pp. 107–114, 2010. [Online]. Available: https://doi.org/10.1016/j.colsurfa.2010.09.037

[295] D. Ding, Z. Jiang, Q. Ouyang, L. Wang, Y. Zhang, and L. Zan, "Enhanced photocatalytic activity and mechanism insight of mnox/mil-101," *Journal of the Taiwan Institute of Chemical Engineers*, vol. 82, pp. 226–232, 2018. [Online]. Available: https://doi.org/10.1016/j.jtice.2017.09.013

[296] M. Wen, K. Mori, T. Kamegawa, and H. Yamashita, "Amine-functionalized mil-101 (cr) with imbedded platinum nanoparticles as a durable photocatalyst for hydrogen production from water," *Chemical Communications*, vol. 50, no. 79, pp. 11 645–11 648, 2014. [Online]. Available: https://doi.org/10.1039/C4CC02994A

[297] Y. Tang, X. Yin, M. Mu, Y. Jiang, X. Li, H. Zhang, and T. Ouyang, "Anatase tio2@ mil-101 (cr) nanocomposite for photocatalytic degradation of bisphenol a," *Colloids and Surfaces A: Physicochemical and Engineering Aspects*, vol. 596, p. 124745, 2020. [Online]. Available: https://doi.org/10.1016/j.colsurfa.2020.124745

[298] Y. Zhang, M. Xiong, A. Sun, Z. Shi, B. Zhu, D. K. Macharia, F. Li, Z. Chen, J. Liu, and L. Zhang, "Mil-101 (fe) nanodot-induced improvement of adsorption and photocatalytic activity of carbon fiber/tio2-based weavable photocatalyst for removing pharmaceutical pollutants," *Journal of Cleaner Production*, vol. 290, p. 125782, 2021. [Online]. Available: https://doi.org/10.1016/j.jclepro.2021.125782

[299] Y. Xu, M. Lv, H. Yang, Q. Chen, X. Liu, and F. Wei, "Bivo 4/mil-101 composite having the synergistically enhanced visible light photocatalytic activity," *RSC advances*, vol. 5, no. 54, pp. 43 473–43 479, 2015. [Online]. Available: https://doi.org/10.1039/C4RA11383G

[300] S. Abdpour, E. Kowsari, B. Bazri, M. R. A. Moghaddam, S. S. Tafreshi, N. H. de Leeuw, I. Simon, L. Schmolke, D. Dietrich, S. Ramakrishna *et al.*, "Amino-functionalized mil-101 (cr) photodegradation enhancement by sulfur-enriched copper sulfide nanoparticles: An experimental and dft study," *Journal of Molecular Liquids*, vol. 319, p. 114341, 2020. [Online]. Available: https://doi.org/10.1016/j.molliq.2020.114341

[301] X.-Y. Dao, X.-F. Xie, J.-H. Guo, X.-Y. Zhang, Y.-S. Kang, and W.-Y. Sun, "Boosting photocatalytic co2 reduction efficiency by heterostructures of nh2-mil-101

(fe)/g-c3n4," *ACS Applied Energy Materials*, vol. 3, no. 4, pp. 3946–3954, 2020. [Online]. Available: https://doi.org/10.1021/acsaem.0c00352

[302] J. Gong, W. Zhang, T. Sen, Y. Yu, Y. Liu, J. Zhang, and L. Wang, "Metal–organic framework mil-101 (fe) nanoparticles decorated with ag nanoparticles for regulating the photocatalytic phenol oxidation pathway for cr (vi) reduction," *ACS Applied Nano Materials*, vol. 4, no. 5, pp. 4513–4521, 2021. [Online]. Available: https://doi.org/10.1021/acsanm.1c00119

[303] Y. Gong, B. Yang, H. Zhang, and X. Zhao, "A gc 3 n 4/mil-101 (fe) heterostructure composite for highly efficient bpa degradation with persulfate under visible light irradiation," *Journal of Materials Chemistry A*, vol. 6, no. 46, pp. 23 703–23 711, 2018. [Online]. Available: https://doi.org/10.1039/C8TA07915C

[304] C. Huang, J. Wang, M. Li, X. Lei, and Q. Wu, "Construction of a novel z-scheme v2o5/nh2-mil-101 (fe) composite photocatalyst with enhanced photocatalytic degradation of tetracycline," *Solid State Sciences*, vol. 117, p. 106611, 2021. [Online]. Available: https://doi.org/10.1016/j.solidstatesciences.2021.106611

[305] Y. Wang, Y. Zhang, Z. Jiang, G. Jiang, Z. Zhao, Q. Wu, Y. Liu, Q. Xu, A. Duan, and C. Xu, "Controlled fabrication and enhanced visible-light photocatalytic hydrogen production of au@ cds/mil-101 heterostructure," *Applied Catalysis B: Environmental*, vol. 185, pp. 307–314, 2016. [Online]. Available: https://doi.org/10.1016/j.apcatb.2015.12.020

[306] D. Ding, Z. Jiang, J. Jin, J. Li, D. Ji, Y. Zhang, and L. Zan, "Impregnation of semiconductor cds nps in mofs cavities via double solvent method for effective photocatalytic co2 conversion," *Journal of catalysis*, vol. 375, pp. 21–31, 2019. [Online]. Available: https://doi.org/10.1016/j.jcat.2019.05.015

[307] Z. Li, Y. Zhao, Q. Guan, Q. Liu, S. Khan, L. Zhang, X. Wang, L. Chen, X. Yang, and M. Huo, "Novel direct dual z-scheme agbr (ag)/mil-101 (cr)/cufe2o4 for efficient conversion of nitrate to nitrogen," *Applied Surface Science*, vol. 508, p. 145225, 2020. [Online]. Available: https://doi.org/10.1016/j.apsusc.2019.145225

[308] B. Lv, J. Jiao, Y. Liu, L. Liu, J. Zhang, Y. Li, J. Wang, and J. Tang, "Heterostructure nagdf4: Yb, er anchored on mil-101 for promoting photoelectronic response and photocatalytic activity," *Nanoscale*, vol. 11, no. 47, pp. 22 730–22 733, 2019. [Online]. Available: https://doi.org/10.1039/C9NR08571H

[309] F. Zhao, Y. Liu, S. B. Hammouda, B. Doshi, N. Guijarro, X. Min, C.-J. Tang, M. Sillanpää, K. Sivula, and S. Wang, "Mil-101 (fe)/g-c3n4 for enhanced visible-light-driven photocatalysis toward simultaneous reduction of cr (vi) and oxidation of bisphenol a in aqueous media," *Applied Catalysis B: Environmental*, vol. 272, p. 119033, 2020. [Online]. Available: https://doi.org/10.1016/j.apcatb.2020.119033

[310] S. Su, Z. Xing, S. Zhang, M. Du, Y. Wang, Z. Li, P. Chen, Q. Zhu, and W. Zhou, "Ultrathin mesoporous g-c3n4/nh2-mil-101 (fe) octahedron heterojunctions as efficient photo-fenton-like system for enhanced photo-thermal effect and promoted visible-light-driven photocatalytic performance," *Applied Surface Science*, vol. 537, p. 147890, 2021. [Online]. Available: https://doi.org/10.1016/j.apsusc.2020.147890

[311] X. Y. Chen, O. G. Nik, D. Rodrigue, and S. Kaliaguine, "Mixed matrix membranes of aminosilanes grafted fau/emt zeolite and cross-linked polyimide for co2/ch4 separation," *Polymer*, vol. 53, no. 15, pp. 3269–3280, 2012. [Online]. Available: https://doi.org/10.1016/j.polymer.2012.03.017

[312] N. Tien-Binh, D. Rodrigue, and S. Kaliaguine, "In-situ cross interface linking of pim-1 polymer and uio-66-nh2 for outstanding gas separation and physical aging control," *Journal of membrane science*, vol. 548, pp. 429–438, 2018. [Online]. Available: https://doi.org/10.1016/j.memsci.2017.11.054

[313] P. Sharma and V. K. Shahi, "Assembly of mil-101 (cr)-sulphonated poly (ether sulfone) membrane matrix for selective electrodialytic separation of pb2+ from mono-/bi-valent ions," *Chemical Engineering Journal*, vol. 382, p. 122688, 2020. [Online]. Available: https://doi.org/10.1016/j.cej.2019.122688

[314] M. Fang, G. Zhang, Y. Liu, R. Xiong, W. Wu, F. Yang, L. Liu, J. Chen, and J. Li, "Exploiting giant-pore systems of nanosized mil-101 in pdms matrix for facilitated reverse-selective hydrocarbon transport," *ACS applied materials & interfaces*, vol. 12, no. 1, pp. 1511–1522, 2019. [Online]. Available: https://doi.org/10.1021/acsami.9b17516

[315] H. Rajati, A. H. Navarchian, and S. Tangestaninejad, "Preparation and characterization of mixed matrix membranes based on matrimid/pvdf blend and mil-101 (cr) as filler for co2/ch4 separation," *Chemical Engineering Science*, vol. 185, pp. 92–104, 2018. [Online]. Available: https://doi.org/10.1016/j.ces.2018.04.006

[316] C. Song, R. Li, Z. Fan, Q. Liu, B. Zhang, and Y. Kitamura, "Co2/n2 separation performance of pebax/mil-101 and pebax/nh2-mil-101 mixed matrix membranes and

intensification via sub-ambient operation," *Separation and Purification Technology*, vol. 238, p. 116500, 2020. [Online]. Available: https://doi.org/10.1016/j.seppur.2020.116500

[317] M. A. Rodrigues, J. de Souza Ribeiro, E. de Souza Costa, J. L. de Miranda, and H. C. Ferraz, "Nanostructured membranes containing uio-66 (zr) and mil-101 (cr) for o2/n2 and co2/n2 separation," *Separation and Purification Technology*, vol. 192, pp. 491–500, 2018. [Online]. Available: https://doi.org/10.1016/j.seppur.2017.10.024

[318] N. Song, Y. Sun, X. Xie, D. Wang, F. Shao, L. Yu, and L. Dong, "Doping mil-101 (cr)@ go in polyamide nanocomposite membranes with improved water flux," *Desalination*, vol. 492, p. 114601, 2020. [Online]. Available: https://doi.org/10.1016/j.desal.2020.114601

[319] A.-S. Zhang, S.-H. Li, A. Ahmad, H. Mao, L.-H. Xu, and Z.-P. Zhao, "Coordinate covalent grafted ils-modified mil-101/peba membrane for pervaporation: Adsorption simulation and separation characteristics," *Journal of Membrane Science*, vol. 619, p. 118807, 2021. [Online]. Available: https://doi.org/10.1016/j.memsci.2020.118807

[320] M. Khdhayyer, A. F. Bushell, P. M. Budd, M. P. Attfield, D. Jiang, A. D. Burrows, E. Esposito, P. Bernardo, M. Monteleone, A. Fuoco *et al.*, "Mixed matrix membranes based on mil-101 metal–organic frameworks in polymer of intrinsic microporosity pim-1," *Separation and Purification Technology*, vol. 212, pp. 545–554, 2019. [Online]. Available: https://doi.org/10.1016/j.seppur.2018.11.055

[321] A. D. Pournara, G. D. Tarlas, G. S. Papaefstathiou, and M. J. Manos, "Chemically modified electrodes with mofs for the determination of inorganic and organic analytes via voltammetric techniques: a critical review," *Inorganic Chemistry Frontiers*, vol. 6, no. 12, pp. 3440–3455, 2019. [Online]. Available: https://doi.org/10.1039/C9QI00965E

[322] H. Wang, W. P. Lustig, and J. Li, "Sensing and capture of toxic and hazardous gases and vapors by metal–organic frameworks," *Chemical Society Reviews*, vol. 47, no. 13, pp. 4729–4756, 2018. [Online]. Available: https://doi.org/10.1039/C7CS00885F

[323] J.-M. Yang and Y.-K. Kou, "Sulfo-modified mil-101 with immobilized carbon quantum dots as a fluorescence sensing platform for highly sensitive detection of dnp," *Inorganica Chimica Acta*, vol. 519, p. 120276, 2021. [Online]. Available: https://doi.org/10.1016/j.ica.2021.120276

[324] A. Mousavi, R. Zare-Dorabei, and S. H. Mosavi, "A novel hybrid fluorescence probe sensor based on metal–organic framework@ carbon quantum dots for the highly

selective detection of 6-mercaptopurine," *Analytical Methods*, vol. 12, no. 44, pp. 5397–5406, 2020. [Online]. Available: https://doi.org/10.1039/D0AY01592J

[325] E. Haghighi and S. Zeinali, "Formaldehyde detection using quartz crystal microbalance (qcm) nanosensor coated by nanoporous mil-101 (cr) film," *Microporous and Mesoporous Materials*, vol. 300, p. 110065, 2020. [Online]. Available: https://doi.org/10.1016/j.micromeso.2020.110065

[326] E. Haghighi and S. Zeinali, "Nanoporous mil-101 (cr) as a sensing layer coated on a quartz crystal microbalance (qcm) nanosensor to detect volatile organic compounds (vocs)," *RSC advances*, vol. 9, no. 42, pp. 24 460–24 470, 2019. [Online]. Available: https://doi.org/10.1039/C9RA04152D

[327] J. Guo, S. Wu, Y. Wang, and M. Zhao, "A label-free fluorescence biosensor based on a bifunctional mil-101 (fe) nanozyme for sensitive detection of choline and acetylcholine at nanomolar level," *Sensors and Actuators B: Chemical*, vol. 312, p. 128021, 2020. [Online]. Available: https://doi.org/10.1016/j.snb.2020.128021

[328] K. Zhang, K. Dai, R. Bai, Y. Ma, Y. Deng, D. Li, X. Zhang, R. Hu, and Y. Yang, "A competitive microcystin-lr immunosensor based on au nps@ metal-organic framework (mil-101)," *Chinese Chemical Letters*, vol. 30, no. 3, pp. 664–667, 2019. [Online]. Available: https://doi.org/10.1016/j.cclet.2018.10.021

[329] T. Gan, J. Li, L. Xu, Y. Yao, and Y. Liu, "Construction of a voltammetric sensor based on mil-101 hollow cages for electrocatalytic oxidation and sensitive determination of nitrofurazone," *Journal of Electroanalytical Chemistry*, vol. 848, p. 113287, 2019. [Online]. Available: https://doi.org/10.1016/j.jelechem.2019.113287

[330] J. Zhang, L. Sun, C. Chen, M. Liu, W. Dong, W. Guo, and S. Ruan, "High performance humidity sensor based on metal organic framework mil-101 (cr) nanoparticles," *Journal of Alloys and Compounds*, vol. 695, pp. 520–525, 2017. [Online]. Available: https://doi.org/10.1016/j.jallcom.2016.11.129

[331] J. Gordon, H. Kazemian, and S. Rohani, "Mil-53 (fe), mil-101, and sba-15 porous materials: potential platforms for drug delivery," *Materials Science and Engineering: C*, vol. 47, pp. 172–179, 2015. [Online]. Available: https://doi.org/10.1016/j.msec.2014.11.046

[332] M. Almáši, V. Zeleňák, P. Palotai, E. Beňová, and A. Zeleňáková, "Metal-organic framework mil-101 (fe)-nh2 functionalized with different long-chain polyamines as

drug delivery system," *Inorganic Chemistry Communications*, vol. 93, pp. 115–120, 2018. [Online]. Available: https://doi.org/10.1016/j.inoche.2018.05.007

[333] A. Cabrera-García, E. Checa-Chavarria, E. Rivero-Buceta, V. Moreno, E. Fernández, and P. Botella, "Amino modified metal-organic frameworks as ph-responsive nanoplatforms for safe delivery of camptothecin," *Journal of colloid and interface science*, vol. 541, pp. 163–174, 2019. [Online]. Available: https://doi.org/10.1016/j.jcis.2019.01.042

[334] C.-H. Liu, H.-C. Chiu, H.-L. Sung, J.-Y. Yeh, K. C.-W. Wu, and S.-H. Liu, "Acute oral toxicity and repeated dose 28-day oral toxicity studies of mil-101 nanoparticles," *Regulatory Toxicology and Pharmacology*, vol. 107, p. 104426, 2019. [Online]. Available: https://doi.org/10.1016/j.yrtph.2019.104426

[335] H. García and S. Navalón, *Metal-Organic Frameworks: Applications in Separations and Catalysis*, 1st ed. Weinheim, Germany: John Wiley & Sons, 2018.

[336] R. Boddula, M. I. Ahamed, A. M. Asiri *et al.*, *Applications of metal-organic frameworks and their derived materials*, 1st ed. New Jersey, USA: John Wiley & Sons, 2020.

[337] W. Xuan, C. Zhu, Y. Liu, and Y. Cui, "Mesoporous metal–organic framework materials," *Chemical Society Reviews*, vol. 41, no. 5, pp. 1677–1695, 2012. [Online]. Available: https://doi.org/10.1039/C1CS15196G

[338] H. Furukawa, K. E. Cordova, M. O'Keeffe, and O. M. Yaghi, "The chemistry and applications of metal-organic frameworks," *Science*, vol. 341, no. 6149, 2013. [Online]. Available: https://doi.org/10.1126/science.1230444

[339] M. Y. Zorainy, M. I. G. Alkalla, S. Kaliaguine, and D. C. C. Boffito, "Revisiting the mil-101 metal-organic framework: design, synthesis, modifications, advances, and recent applications," *Journal of Materials Chemistry A*, 2021. [Online]. Available: https://doi.org/10.1039/D1TA06238G

[340] A. Sonnauer, F. Hoffmann, M. Fröba, L. Kienle, V. Duppel, M. Thommes, C. Serre, G. Férey, and N. Stock, "Giant pores in a chromium 2, 6-naphthalenedicarboxylate open-framework structure with mil-101 topology," *Angewandte Chemie*, vol. 121, no. 21, pp. 3849–3852, 2009. [Online]. Available: https://doi.org/10.1002/anie.200805980

[341] S. Abednatanzi, P. G. Derakhshandeh, H. Depauw, F.-X. Coudert, H. Vrielinck, P. Van Der Voort, and K. Leus, "Mixed-metal metal–organic frameworks,"

Chemical Society Reviews, vol. 48, no. 9, pp. 2535–2565, 2019. [Online]. Available: https://doi.org/10.1039/C8CS00337H

[342] M. Wen, Y. Kuwahara, K. Mori, D. Zhang, H. Li, and H. Yamashita, "Synthesis of ce ions doped metal–organic framework for promoting catalytic h 2 production from ammonia borane under visible light irradiation," *Journal of Materials Chemistry A*, vol. 3, no. 27, pp. 14 134–14 141, 2015. [Online]. Available: https://doi.org/10.1039/C5TA02320C

[343] Z. Zhou, L. Mei, C. Ma, F. Xu, J. Xiao, Q. Xia, and Z. Li, "A novel bimetallic mil-101 (cr, mg) with high co2 adsorption capacity and co2/n2 selectivity," *Chemical Engineering Science*, vol. 147, pp. 109–117, 2016. [Online]. Available: https://doi.org/10.1016/j.ces.2016.03.035

[344] H. Deng, C. J. Doonan, H. Furukawa, R. B. Ferreira, J. Towne, C. B. Knobler, B. Wang, and O. M. Yaghi, "Multiple functional groups of varying ratios in metal-organic frameworks," *Science*, vol. 327, no. 5967, pp. 846–850, 2010. [Online]. Available: https://doi.org/10.1126/science.1181761

[345] X. Kong, H. Deng, F. Yan, J. Kim, J. A. Swisher, B. Smit, O. M. Yaghi, and J. A. Reimer, "Mapping of functional groups in metal-organic frameworks," *Science*, vol. 341, no. 6148, pp. 882–885, 2013. [Online]. Available: https://doi.org/10.1126/science.1238339

[346] M. Y. Masoomi, A. Morsali, A. Dhakshinamoorthy, and H. Garcia, "Mixed-metal mofs: unique opportunities in metal–organic framework (mof) functionality and design," *Angewandte Chemie*, vol. 131, no. 43, pp. 15 330–15 347, 2019. [Online]. Available: https://doi.org/10.1002/anie.201902229

[347] C. K. Brozek and M. Dinca, "Ti3+-, v2+/3+-, cr2+/3+-, mn2+-, and fe2+-substituted mof-5 and redox reactivity in cr-and fe-mof-5," *Journal of the American Chemical Society*, vol. 135, no. 34, pp. 12 886–12 891, 2013. [Online]. Available: https://doi.org/10.1021/ja4064475

[348] J.-H. Liao, W.-T. Chen, C.-S. Tsai, and C.-C. Wang, "Characterization, adsorption properties, metal ion-exchange and crystal-to-crystal transformation of cd 3 [(cd 4 cl) 3 (btt) 8 (h 2 o) 12] 2 framework, where btt 3-= 1, 3, 5-benzenetristetrazolate," *CrystEngComm*, vol. 15, no. 17, pp. 3377–3384, 2013. [Online]. Available: https://doi.org/10.1039/C3CE27063G

[349] S. Qiu, Y. Wang, J. Wan, J. Han, Y. Ma, and S. Wang, "Enhancing water stability of mil-101 (cr) by doping ni (ii)," *Applied Surface Science*, vol. 525, p. 146511, 2020. [Online]. Available: https://doi.org/10.1016/j.apsusc.2020.146511

[350] R. Fazaeli, H. Aliyan, M. Moghadam, and M. Masoudinia, "Nano-rod catalysts: Building mof bottles (mil-101 family as heterogeneous single-site catalysts) around vanadium oxide ships," *Journal of Molecular Catalysis A: Chemical*, vol. 374, pp. 46–52, 2013. [Online]. Available: https://doi.org/10.1016/j.molcata.2013.03.020

[351] L. Gao, C.-Y. V. Li, H. Yung, and K.-Y. Chan, "A functionalized mil-101 (cr) metal–organic framework for enhanced hydrogen release from ammonia borane at low temperature," *Chemical Communications*, vol. 49, no. 90, pp. 10 629–10 631, 2013. [Online]. Available: https://doi.org/10.1039/C3CC45719B

[352] W. M. Haynes, *CRC handbook of chemistry and physics*, 97th ed. New York, USA: CRC press, 2016.

[353] M. A. J. Kouhbanani, N. Beheshtkhoo, S. Taghizadeh, A. M. Amani, and V. Alimardani, "One-step green synthesis and characterization of iron oxide nanoparticles using aqueous leaf extract of teucrium polium and their catalytic application in dye degradation," *Advances in Natural Sciences: Nanoscience and Nanotechnology*, vol. 10, no. 1, p. 015007, 2019. [Online]. Available: https://doi.org/10.1088/2043-6254/aafe74

[354] L. Pauling and S. B. Hendricks, "The crystal structures of hematite and corundum," *Journal of the American Chemical Society*, vol. 47, no. 3, pp. 781–790, 1925. [Online]. Available: https://doi.org/10.1021/ja01680a027

[355] R. Blake, R. Hessevick, T. Zoltai, and L. W. Finger, "Refinement of the hematite structure," *American Mineralogist: Journal of Earth and Planetary Materials*, vol. 51, no. 1-2, pp. 123–129, 1966.

[356] D. L. A. de Faria and F. N. Lópes, "Heated goethite and natural hematite: can raman spectroscopy be used to differentiate them?" *Vibrational Spectroscopy*, vol. 45, no. 2, pp. 117–121, 2007. [Online]. Available: https://doi.org/10.1016/j.vibspec.2007.07.003

[357] H. T. M. Thanh, N. T. T. Tu, N. P. Hung, T. N. Tuyen, T. X. Mau, and D. Q. Khieu, "Magnetic iron oxide modified mil-101 composite as an efficient visible-light-driven photocatalyst for methylene blue degradation," *Journal*

of Porous Materials, vol. 26, no. 6, pp. 1699–1712, 2019. [Online]. Available: https://doi.org/10.1007/s10934-019-00767-1

[358] A. Jarrah and S. Farhadi, "K 6 p 2 w 18 o 62 encapsulated into magnetic fe 3 o 4/mil-101 (cr) metal–organic framework: a novel magnetically recoverable nanoporous adsorbent for ultrafast treatment of aqueous organic pollutants solutions," *RSC Advances*, vol. 8, no. 66, pp. 37 976–37 992, 2018. [Online]. Available: https://doi.org/10.1039/C8RA06287K

[359] E. A. Berdonosova, K. A. Kovalenko, E. V. Polyakova, S. N. Klyamkin, and V. P. Fedin, "Influence of anion composition on gas sorption features of cr-mil-101 metal–organic framework," *The Journal of Physical Chemistry C*, vol. 119, no. 23, pp. 13 098–13 104, 2015. [Online]. Available: https://doi.org/10.1021/acs.jpcc.5b02861

[360] A. Rufus, N. Sreeju, and D. Philip, "Synthesis of biogenic hematite (α-fe 2 o 3) nanoparticles for antibacterial and nanofluid applications," *RSC advances*, vol. 6, no. 96, pp. 94 206–94 217, 2016. [Online]. Available: https://doi.org/10.1039/C6RA20240C

[361] K. Supattarasakda, K. Petcharoen, T. Permpool, A. Sirivat, and W. Lerdwijitjarud, "Control of hematite nanoparticle size and shape by the chemical precipitation method," *Powder technology*, vol. 249, pp. 353–359, 2013. [Online]. Available: https://doi.org/10.1016/j.powtec.2013.08.042

[362] J. Tu, X. Zeng, F. Xu, X. Wu, Y. Tian, X. Hou, and Z. Long, "Microwave-induced fast incorporation of titanium into uio-66 metal–organic frameworks for enhanced photocatalytic properties," *Chemical Communications*, vol. 53, no. 23, pp. 3361–3364, 2017. [Online]. Available: https://doi.org/10.1039/C7CC00076F

[363] R. Dai, W. Sun, L.-P. Lv, M. Wu, H. Liu, G. Wang, and Y. Wang, "Bimetal-organic-framework derivation of ball-cactus-like ni-sn-p@ c-cnt as long-cycle anode for lithium ion battery," *Small*, vol. 13, no. 27, p. 1700521, 2017. [Online]. Available: https://doi.org/10.1002/smll.201700521

[364] E. C. Sklute, S. Kashyap, M. D. Dyar, J. F. Holden, T. Tague, P. Wang, and S. J. Jaret, "Spectral and morphological characteristics of synthetic nanophase iron (oxyhydr) oxides," *Physics and chemistry of minerals*, vol. 45, no. 1, pp. 1–26, 2018. [Online]. Available: https://doi.org/10.1007/s00269-017-0897-y

[365] D. L. De Faria, S. Venâncio Silva, and M. De Oliveira, "Raman microspectroscopy of some iron oxides and oxyhydroxides," *Journal of Raman spectroscopy*, vol. 28, no. 11, pp. 873–878, 1997. [Online]. Available: https://doi.org/10.1002/(SICI) 1097-4555(199711)28:11

[366] Z. Li, T. Zhang, and K. Li, "One-step synthesis of mesoporous two-line ferrihydrite for effective elimination of arsenic contaminants from natural water," *Dalton Transactions*, vol. 40, no. 9, pp. 2062–2066, 2011. [Online]. Available: https://doi.org/10.1039/C0DT01138J

[367] M. Compeán-Jasso, F. Ruiz, J. Martínez, and A. Herrera-Gómez, "Magnetic properties of magnetite nanoparticles synthesized by forced hydrolysis," *Materials Letters*, vol. 62, no. 27, pp. 4248–4250, 2008. [Online]. Available: https://doi.org/10.1016/j.matlet.2008.06.053

[368] H. Guo and A. S. Barnard, "Naturally occurring iron oxide nanoparticles: morphology, surface chemistry and environmental stability," *Journal of Materials Chemistry A*, vol. 1, no. 1, pp. 27–42, 2013. [Online]. Available: https://doi.org/10.1039/C2TA00523A

[369] R. M. Cornell and U. Schwertmann, *The iron oxides: structure, properties, reactions, occurrences and uses*, 2nd ed. Weinheim,Germany: John Wiley & Sons, 2003.

[370] E. Elsayed, P. Anderson, A.-D. Raya, S. Mahmoud, and A. Elsayed, "Mil-101 (cr)/calcium chloride composites for enhanced adsorption cooling and water desalination," *Journal of Solid State Chemistry*, vol. 277, pp. 123–132, 2019. [Online]. Available: https://doi.org/10.1016/j.jssc.2019.05.026

[371] M. Sheikh Alivand, N. H. M. Hossein Tehrani, M. Shafiei-alavijeh, A. Rashidi, M. Kooti, A. Pourreza, and S. Fakhraie, "Synthesis of a modified hf-free mil-101(cr) nanoadsorbent with enhanced h2s/ch4, co2/ch4, and co2/n2 selectivity," *Journal of Environmental Chemical Engineering*, vol. 7, no. 2, p. 102946, 2019. [Online]. Available: https://doi.org/10.1016/j.jece.2019.102946

[372] M. Asiabi, A. Mehdinia, and A. Jabbari, "Electrospun biocompatible chitosan/mil-101 (fe) composite nanofibers for solid-phase extraction of 9-tetrahydrocannabinol in whole blood samples using box-behnken experimental design," *Journal of Chromatography A*, vol. 1479, pp. 71–80, 2017. [Online]. Available: https://doi.org/10.1016/j.chroma.2016.12.024

[373] Y. Liu, Y. Xie, M. Dai, Q. Gong, and Z. Dang, "Ag/agcl/mil-101 (fe) catalyzed degradation of methylene blue under visible light irradation," *Materials*, vol. 12, no. 9, p. 1453, 2019. [Online]. Available: https://doi.org/10.3390/ma12091453

[374] M. Alhamami, H. Doan, and C.-H. Cheng, "A review on breathing behaviors of metal-organic-frameworks (mofs) for gas adsorption," *Materials*, vol. 7, no. 4, pp. 3198–3250, 2014. [Online]. Available: https://doi.org/10.3390/ma7043198

[375] H. Li, K. Wang, Y. Sun, C. T. Lollar, J. Li, and H.-C. Zhou, "Recent advances in gas storage and separation using metal–organic frameworks," *Materials Today*, vol. 21, no. 2, pp. 108–121, 2018. [Online]. Available: https://doi.org/10.1016/j.mattod.2017.07.006

[376] B. Li, H.-M. Wen, Y. Yu, Y. Cui, W. Zhou, B. Chen, and G. Qian, "Nanospace within metal–organic frameworks for gas storage and separation," *Materials Today Nano*, vol. 2, pp. 21–49, 2018. [Online]. Available: https://doi.org/10.1016/j.mtnano.2018.09.003

[377] J.-R. Li, R. J. Kuppler, and H.-C. Zhou, "Selective gas adsorption and separation in metal–organic frameworks," *Chemical Society Reviews*, vol. 38, no. 5, pp. 1477–1504, 2009. [Online]. Available: https://doi.org/10.1039/B802426J

[378] X. Zhao, Y. Wang, D.-S. Li, X. Bu, and P. Feng, "Metal–organic frameworks for separation," *Advanced Materials*, vol. 30, no. 37, p. 1705189, 2018. [Online]. Available: https://doi.org/10.1002/adma.201705189

[379] A. Bavykina, N. Kolobov, I. S. Khan, J. A. Bau, A. Ramirez, and J. Gascon, "Metal–organic frameworks in heterogeneous catalysis: recent progress, new trends, and future perspectives," *Chemical Reviews*, vol. 120, no. 16, pp. 8468–8535, 2020. [Online]. Available: https://doi.org/10.1021/acs.chemrev.9b00685

[380] V. Remya and M. Kurian, "Synthesis and catalytic applications of metal–organic frameworks: a review on recent literature," *International Nano Letters*, vol. 9, no. 1, pp. 17–29, 2019. [Online]. Available: https://doi.org/10.1007/s40089-018-0255-1

[381] L. Öhrström and F. M. A. Noa, *Metal-organic frameworks (ACS in Focus)*. American Chemical Society, 2021. [Online]. Available: https://doi.org/10.1021/acs.infocus.7e4004

[382] Z. Chang, D.-H. Yang, J. Xu, T.-L. Hu, and X.-H. Bu, "Flexible metal–organic frameworks: recent advances and potential applications," *Advanced*

Materials, vol. 27, no. 36, pp. 5432–5441, 2015. [Online]. Available: https://doi.org/10.1002/adma.201501523

[383] A. Li, R. B. Perez, S. Wiggin, S. C. Ward, P. A. Wood, and D. Fairen-Jimenez, "The launch of a freely accessible mof cif collection from the csd," *Matter*, vol. 4, no. 4, pp. 1105–1106, 2021. [Online]. Available: https://doi.org/10.1016/j.matt.2021.03.006

[384] M. Ma, H. Noei, B. Mienert, J. Niesel, E. Bill, M. Muhler, R. A. Fischer, Y. Wang, U. Schatzschneider, and N. Metzler-Nolte, "Iron metal–organic frameworks mil-88b and nh2-mil-88b for the loading and delivery of the gasotransmitter carbon monoxide," *Chemistry–A European Journal*, vol. 19, no. 21, pp. 6785–6790, 2013. [Online]. Available: https://doi.org/10.1002/chem.201201743

[385] X. Cai, J. Lin, and M. Pang, "Facile synthesis of highly uniform fe-mil-88b particles," *Crystal Growth & Design*, vol. 16, no. 7, pp. 3565–3568, 2016. [Online]. Available: https://doi.org/10.1021/acs.cgd.6b00313

[386] X. Liao, F. Wang, F. Wang, Y. Cai, Y. Yao, B.-T. Teng, Q. Hao, and L. Shuxiang, "Synthesis of (100) surface oriented mil-88a-fe with rod-like structure and its enhanced fenton-like performance for phenol removal," *Applied Catalysis B: Environmental*, vol. 259, p. 118064, 2019. [Online]. Available: https://doi.org/10.1016/j.apcatb.2019.118064

[387] S. Hou, Y.-n. Wu, L. Feng, W. Chen, Y. Wang, C. Morlay, and F. Li, "Green synthesis and evaluation of an iron-based metal–organic framework mil-88b for efficient decontamination of arsenate from water," *Dalton transactions*, vol. 47, no. 7, pp. 2222–2231, 2018. [Online]. Available: https://doi.org/10.1039/C7DT03775A

[388] V. Sintya, A. Saefumillah, and A. Zulys, "Development study of iron-based metal organic frameworks (fe-based mofs) as a binding agent in diffusive gradient in thin film method (dgt) for phosphate adsorption," in *IOP Conference Series: Materials Science and Engineering*, vol. 902, no. 1. IOP Publishing, 2020, p. 012026. [Online]. Available: https://doi.org/10.1088/1757-899x/902/1/012026

[389] A. Kumari, Mehilal, S. Jain, M. Jain, and B. Bhattacharya, "Nano-ammonium perchlorate: preparation, characterization, and evaluation in composite propellant formulation," *Journal of Energetic Materials*, vol. 31, no. 3, pp. 192–202, 2013. [Online]. Available: https://doi.org/10.1080/07370652.2012.694576

[390] S. Jain, M. Mehilal, S. Nandagopal, P. Singh, K. Radhakrishnan, and B. Bhattacharya, "Size and shape of ammonium perchlorate and their influence on properties of

composite propellant," *Defence Science Journal*, vol. 59, no. 3, p. 294, 2009. [Online]. Available: https://doi.org/10.14429/dsj.59.1523

[391] P. A. Figueiredo and F. M. Brójo, "Theoretical analysis of ammonium-perchlorate based composite propellants containing small size particles of boron," *Energy Procedia*, vol. 136, pp. 202–207, 2017. [Online]. Available: https://doi.org/10.1016/j.egypro.2017.10.320

[392] A. Manash and P. Kumar, "Comparison of burn rate and thermal decomposition of ap as oxidizer and pvc and htpb as fuel binder based composite solid propellants," *Defence Technology*, vol. 15, no. 2, pp. 227–232, 2019. [Online]. Available: https://doi.org/10.1016/j.dt.2018.08.010

[393] W. Cai, P. Thakre, and V. Yang, "A model of ap/htpb composite propellant combustion in rocket-motor environments," *Combustion Science and Technology*, vol. 180, no. 12, pp. 2143–2169, 2008. [Online]. Available: https://doi.org/10.1080/00102200802414915

[394] J. L. Arroyo, P. Povea, R. Faundez, M. B. Camarada, C. Cerda-Cavieres, G. Abarca, J. M. Manriquez, and C. Morales-Verdejo, "Influence iron-iron distance on the thermal decomposition of ammonium perchlorate. new catalysts for the highly efficient combustion of solid rocket propellant," *Journal of Organometallic Chemistry*, vol. 905, p. 121020, 2020. [Online]. Available: https://doi.org/10.1016/j.jorganchem.2019.121020

[395] G. P. Li, L. H. Shen, B. M. Zheng, M. Xia, and Y. J. Luo, "The preparation and properties of ap-based nano-limit growth energetic materials," in *Advanced Materials Research*, vol. 924. Trans Tech Publ, 2014, pp. 105–109. [Online]. Available: https://doi.org/10.4028/www.scientific.net/AMR.924.105

[396] W. Pang, L. T. De Luca, X. Fan, F. Maggi, H. Xu, W. Xie, and X. Shi, "Effects of different nano-sized metal oxide catalysts on the properties of composite solid propellants," *Combustion Science and Technology*, vol. 188, no. 3, pp. 315–328, 2016. [Online]. Available: https://doi.org/10.1080/00102202.2015.1083986

[397] S. Chaturvedi and P. N. Dave, "A review on the use of nanometals as catalysts for the thermal decomposition of ammonium perchlorate," *Journal of Saudi Chemical Society*, vol. 17, no. 2, pp. 135–149, 2013. [Online]. Available: https://doi.org/10.1016/j.jscs.2011.05.009

[398] S. Elbasuney and M. Yehia, "Ammonium perchlorate encapsulated with tio 2 nanocomposite for catalyzed combustion reactions," *Journal of Inorganic and*

Organometallic Polymers and Materials, vol. 29, no. 4, pp. 1349–1357, 2019. [Online]. Available: https://doi.org/10.1007/s10904-019-01099-y

[399] S. Elbasuney and M. Yehia, "Thermal decomposition of ammonium perchlorate catalyzed with cuo nanoparticles," *Defence Technology*, vol. 15, no. 6, pp. 868–874, 2019. [Online]. Available: https://doi.org/10.1016/j.dt.2019.03.004

[400] M. Zou, X. Jiang, L. Lu, and X. Wang, "Nano or micro? a mechanism on thermal decomposition of ammonium perchlorate catalyzed by cobalt oxalate," *Journal of hazardous materials*, vol. 225, pp. 124–130, 2012. [Online]. Available: https://doi.org/10.1016/j.jhazmat.2012.05.010

[401] S. S. Joshi, P. R. Patil, and V. Krishnamurthy, "Thermal decomposition of ammonium perchlorate in the presence of nanosized ferric oxide." *Defence Science Journal*, vol. 58, no. 6, 2008. [Online]. Available: https://doi.org/10.14429/dsj.58.1699

[402] S. Elbasuney and M. Yehia, "Ferric oxide colloid: A novel nano-catalyst for solid propellants," *Journal of Inorganic and Organometallic Polymers and Materials*, vol. 30, no. 3, pp. 706–713, 2020. [Online]. Available: https://doi.org/10.1007/s10904-019-01339-1

[403] S. Chaturvedi and P. N. Dave, "Nano-metal oxide: potential catalyst on thermal decomposition of ammonium perchlorate," *Journal of Experimental Nanoscience*, vol. 7, no. 2, pp. 205–231, 2012. [Online]. Available: https://doi.org/10.1080/17458080.2010.517571

[404] A. Yurdusen and Y. Yurum, "A controlled synthesis strategy to enhance the co2 adsorption capacity of mil-88b type mof crystallites by the crucial role of narrow micropores," *Industrial & Engineering Chemistry Research*, vol. 58, no. 31, pp. 14 058–14 072, 2019. [Online]. Available: http://doi.org/10.1021/acs.iecr.9b01653

[405] S. Xiong, X. Lin, S. Liu, S. Weng, S. Jiang, Y. Jiao, Y. Xu, and J. Cheng, "Metal-organic framework derived α-fe2o3 nano-octahedron with oxygen vacancies for realizing outstanding energy storage performance," *Vacuum*, vol. 182, p. 109692, 2020. [Online]. Available: https://doi.org/10.1016/j.vacuum.2020.109692

[406] A. Banerjee, V. Aravindan, S. Bhatnagar, D. Mhamane, S. Madhavi, and S. Ogale, "Superior lithium storage properties of α-fe2o3 nano-assembled spindles," *Nano Energy*, vol. 2, no. 5, pp. 890–896, 2013. [Online]. Available: https://doi.org/10.1016/j.nanoen.2013.03.006

[407] Y. Pang, Z. Li, X. Jiao, D. Chen, and C. Li, "Metal-organic framework derived porous α-fe2o3/c nano-shuttles for enhanced visible-light photocatalysis," *ChemistrySelect*, vol. 5, no. 3, pp. 1047–1053, 2020. [Online]. Available: https://doi.org/10.1002/slct.201904021

[408] A. Khawam and D. R. Flanagan, "Basics and applications of solid-state kinetics: a pharmaceutical perspective," *Journal of pharmaceutical sciences*, vol. 95, no. 3, pp. 472–498, 2006. [Online]. Available: https://doi.org/10.1002/jps.20559

[409] D. Trache, A. Abdelaziz, and B. Siouani, "A simple and linear isoconversional method to determine the pre-exponential factors and the mathematical reaction mechanism functions," *Journal of Thermal Analysis and Calorimetry*, vol. 128, no. 1, pp. 335–348, 2017. [Online]. Available: https://doi.org/10.1007/s10973-016-5962-0

[410] S. Vyazovkin, A. K. Burnham, J. M. Criado, L. A. Pérez-Maqueda, C. Popescu, and N. Sbirrazzuoli, "Ictac kinetics committee recommendations for performing kinetic computations on thermal analysis data," *Thermochimica acta*, vol. 520, no. 1-2, pp. 1–19, 2011. [Online]. Available: https://doi.org/10.1016/j.tca.2011.03.034

[411] D. Trache, K. Khimeche, A. Mezroua, and M. Benziane, "Physicochemical properties of microcrystalline nitrocellulose from alfa grass fibres and its thermal stability," *Journal of Thermal Analysis and Calorimetry*, vol. 124, no. 3, pp. 1485–1496, 2016. [Online]. Available: https://doi.org/10.1007/s10973-016-5293-1

[412] T. Akahira, "Trans. joint convention of four electrical institutes," *Res. Rep. Chiba Inst. Technol.*, vol. 16, pp. 22–31, 1971.

[413] A. Dhakshinamoorthy, M. Alvaro, H. Chevreau, P. Horcajada, T. Devic, C. Serre, and H. Garcia, "Iron (iii) metal–organic frameworks as solid lewis acids for the isomerization of α-pinene oxide," *Catalysis Science & Technology*, vol. 2, no. 2, pp. 324–330, 2012. [Online]. Available: https://doi.org/10.1039/C2CY00376G

[414] E. Rahmani and M. Rahmani, "Alkylation of benzene over fe-based metal organic frameworks (mofs) at low temperature condition," *Microporous and Mesoporous Materials*, vol. 249, pp. 118–127, 2017. [Online]. Available: https://doi.org/10.1016/j.micromeso.2017.04.058

[415] K. S. Walton and R. Q. Snurr, "Applicability of the bet method for determining surface areas of microporous metal- organic frameworks," *Journal of the American*

Chemical Society, vol. 129, no. 27, pp. 8552–8556, 2007. [Online]. Available: https://doi.org/10.1021/ja071174k

[416] Y.-S. Bae, A. O. Yazaydın, and R. Q. Snurr, "Evaluation of the bet method for determining surface areas of mofs and zeolites that contain ultra-micropores," *Langmuir*, vol. 26, no. 8, pp. 5475–5483, 2010. [Online]. Available: https://doi.org/10.1021/la100449z

[417] J. Rouquerol, P. Llewellyn, F. Rouquerol *et al.*, "Is the bet equation applicable to microporous adsorbents," *Stud. Surf. Sci. Catal*, vol. 160, no. 07, pp. 49–56, 2007. [Online]. Available: https://doi.org/10.1021/la100449z

[418] A. Schneemann, V. Bon, I. Schwedler, I. Senkovska, S. Kaskel, and R. A. Fischer, "Flexible metal–organic frameworks," *Chemical Society Reviews*, vol. 43, no. 16, pp. 6062–6096, 2014. [Online]. Available: https://doi.org/10.1039/C4CS00101J

[419] G.-T. Vuong, M.-H. Pham, and T.-O. Do, "Synthesis and engineering porosity of a mixed metal fe2ni mil-88b metal–organic framework," *Dalton Transactions*, vol. 42, no. 2, pp. 550–557, 2012. [Online]. Available: https://doi.org/10.1039/C2DT32073H

[420] J. Wang, J. Wan, Y. Ma, Y. Wang, M. Pu, and Z. Guan, "Metal–organic frameworks mil-88a with suitable synthesis conditions and optimal dosage for effective catalytic degradation of orange g through persulfate activation," *RSC advances*, vol. 6, no. 113, pp. 112 502–112 511, 2016. [Online]. Available: https://doi.org/10.1039/C6RA24429G

[421] B. Wu, J. Fu, Y. Zhou, S. Luo, Y. Zhao, G. Quan, X. Pan, and C. Wu, "Tailored core–shell dual metal–organic frameworks as a versatile nanomotor for effective synergistic antitumor therapy," *Acta Pharmaceutica Sinica B*, vol. 10, no. 11, pp. 2198–2211, 2020. [Online]. Available: https://doi.org/10.1016/j.apsb.2020.07.025

[422] A. Yurduşen, A. Yürüm, and Y. Yürüm, "Engineering mil-88b crystallites for enhanced h2 uptake capacity: The role of ultramicropores," *International Journal of Energy Research*, vol. 44, no. 4, pp. 2875–2888, 2020. [Online]. Available: https://doi.org/10.1002/er.5104

[423] L. Liu, D. Zhang, Y. Zhu, and Y. Han, "Bulk and local structures of metal–organic frameworks unravelled by high-resolution electron microscopy," *Communications Chemistry*, vol. 3, no. 1, pp. 1–14, 2020. [Online]. Available: https://doi.org/10.1038/s42004-020-00361-6

[424] G. A. Bodkhe, B. S. Hedau, M. A. Deshmukh, H. K. Patil, S. M. Shirsat, D. M. Phase, K. K. Pandey, and M. D. Shirsat, "Selective and sensitive detection of lead pb (ii) ions: Au/swnt nanocomposite-embedded mof-199," *Journal of Materials Science*, vol. 56, no. 1, pp. 474–487, 2021. [Online]. Available: https://doi.org/10.1007/s10853-020-05285-z

[425] G. Férey and C. Serre, "Large breathing effects in three-dimensional porous hybrid matter: facts, analyses, rules and consequences," *Chemical Society Reviews*, vol. 38, no. 5, pp. 1380–1399, 2009. [Online]. Available: https://doi.org/10.1039/B804302G

[426] C. Xu, R. Fang, R. Luque, L. Chen, and Y. Li, "Functional metal–organic frameworks for catalytic applications," *Coordination chemistry reviews*, vol. 388, pp. 268–292, 2019. [Online]. Available: https://doi.org/10.1016/j.ccr.2019.03.005

[427] C. Petit, "Present and future of mof research in the field of adsorption and molecular separation," *Current opinion in chemical engineering*, vol. 20, pp. 132–142, 2018. [Online]. Available: https://doi.org/10.1016/j.coche.2018.04.004

[428] J. Caro, "Quo vadis, mof?" *Chemie Ingenieur Technik*, vol. 90, no. 11, pp. 1759–1768, 2018. [Online]. Available: https://doi.org/10.1002/cite.201800034

[429] P. Kumar, A. Deep, and K.-H. Kim, "Metal organic frameworks for sensing applications," *TrAC Trends in Analytical Chemistry*, vol. 73, pp. 39–53, 2015. [Online]. Available: https://doi.org/10.1016/j.trac.2015.04.009

[430] C.-Y. Sun, C. Qin, X.-L. Wang, and Z.-M. Su, "Metal-organic frameworks as potential drug delivery systems," *Expert opinion on drug delivery*, vol. 10, no. 1, pp. 89–101, 2013. [Online]. Available: https://doi.org/10.1517/17425247.2013.741583

[431] W. Chen, L. Du, and C. Wu, "Chapter 7 - hydrothermal synthesis of mofs," in *Metal-Organic Frameworks for Biomedical Applications*, M. Mozafari, Ed. Woodhead Publishing, 2020, pp. 141–157. [Online]. Available: https://doi.org/10.1016/B978-0-12-816984-1.00009-3

[432] N. L. Rosi, J. Kim, M. Eddaoudi, B. Chen, M. O'Keeffe, and O. M. Yaghi, "Rod packings and metal- organic frameworks constructed from rod-shaped secondary building units," *Journal of the American Chemical Society*, vol. 127, no. 5, pp. 1504–1518, 2005. [Online]. Available: https://doi.org/10.1021/ja045123o

[433] Y.-X. Tan, Y.-P. He, Y. Zhang, Y.-J. Zheng, and J. Zhang, "Solvent controlled assembly of four mn (ii)-2, 5-thiophenedicarboxylate frameworks with rod-packing

architectures and magnetic properties," *CrystEngComm*, vol. 15, no. 30, pp. 6009–6014, 2013. [Online]. Available: https://doi.org/10.1039/C3CE40677F

[434] P. G. Yot, Q. Ma, J. Haines, Q. Yang, A. Ghoufi, T. Devic, C. Serre, V. Dmitriev, G. Férey, C. Zhong *et al.*, "Large breathing of the mof mil-47 (v iv) under mechanical pressure: a joint experimental–modelling exploration," *Chemical Science*, vol. 3, no. 4, pp. 1100–1104, 2012. [Online]. Available: https://doi.org/10.1039/C2SC00745B

[435] X. Wang, J. Eckert, L. Liu, and A. J. Jacobson, "Breathing and twisting: an investigation of framework deformation and guest packing in single crystals of a microporous vanadium benzenedicarboxylate," *Inorganic chemistry*, vol. 50, no. 5, pp. 2028–2036, 2011. [Online]. Available: https://doi.org/10.1021/ic1025087

[436] H. Leclerc, T. Devic, S. Devautour-Vinot, P. Bazin, N. Audebrand, G. Férey, M. Daturi, A. Vimont, and G. Clet, "Influence of the oxidation state of the metal center on the flexibility and adsorption properties of a porous metal organic framework: Mil-47 (v)," *The Journal of Physical Chemistry C*, vol. 115, no. 40, pp. 19 828–19 840, 2011. [Online]. Available: https://doi.org/10.1021/jp206655y

[437] G. Zhan and H. C. Zeng, "Alternative synthetic approaches for metal–organic frameworks: transformation from solid matters," *Chemical Communications*, vol. 53, no. 1, pp. 72–81, 2017. [Online]. Available: https://doi.org/10.1039/C6CC07094A

[438] J. Reboul, S. Furukawa, N. Horike, M. Tsotsalas, K. Hirai, H. Uehara, M. Kondo, N. Louvain, O. Sakata, and S. Kitagawa, "Mesoscopic architectures of porous coordination polymers fabricated by pseudomorphic replication," *Nature materials*, vol. 11, no. 8, pp. 717–723, 2012. [Online]. Available: https://doi.org/10.1038/nmat3359

[439] S. Biswas, D. E. Vanpoucke, T. Verstraelen, M. Vandichel, S. Couck, K. Leus, Y.-Y. Liu, M. Waroquier, V. Van Speybroeck, J. F. Denayer *et al.*, "New functionalized metal–organic frameworks mil-47-x (x=- cl,- br,- ch3,- cf3,- oh,-och3): synthesis, characterization, and co2 adsorption properties," *The Journal of Physical Chemistry C*, vol. 117, no. 44, pp. 22 784–22 796, 2013. [Online]. Available: https://doi.org/10.1021/jp406835n

[440] N. A. Khan, J. W. Jun, J. H. Jeong, and S. H. Jhung, "Remarkable adsorptive performance of a metal–organic framework, vanadium-benzenedicarboxylate (mil-47), for benzothiophene," *Chemical Communications*, vol. 47, no. 4, pp. 1306–1308, 2011. [Online]. Available: https://doi.org/10.1039/C0CC04759G

[441] L. Alaerts, C. E. Kirschhock, M. Maes, M. A. Van Der Veen, V. Finsy, A. Depla, J. A. Martens, G. V. Baron, P. A. Jacobs, J. F. Denayer *et al.*, "Selective adsorption and separation of xylene isomers and ethylbenzene with the microporous vanadium (iv) terephthalate mil-47," *Angewandte Chemie International Edition*, vol. 46, no. 23, pp. 4293–4297, 2007. [Online]. Available: https://doi.org/10.1002/anie.200700056

[442] K. Leus, M. Vandichel, Y.-Y. Liu, I. Muylaert, J. Musschoot, S. Pyl, H. Vrielinck, F. Callens, G. B. Marin, C. Detavernier *et al.*, "The coordinatively saturated vanadium mil-47 as a low leaching heterogeneous catalyst in the oxidation of cyclohexene," *Journal of Catalysis*, vol. 285, no. 1, pp. 196–207, 2012. [Online]. Available: https://doi.org/10.1016/j.jcat.2011.09.014

[443] B. Niu, B. Yao, M. Zhu, H. Guo, S. Ying, and Z. Chen, "Carbon paste electrode modified with fern leave-like mil-47 (as) for electrochemical simultaneous detection of pb (ii), cu (ii) and hg (ii)," *Journal of Electroanalytical Chemistry*, vol. 886, p. 115121, 2021. [Online]. Available: https://doi.org/10.1016/j.jelechem.2021.115121

[444] X. Wang, L. Liu, and A. J. Jacobson, "Intercalation of organic molecules into vanadium (iv) benzenedicarboxylate: adsorbate structure and selective absorption of organosulfur compounds," *Angewandte Chemie*, vol. 118, no. 39, pp. 6649–6653, 2006. [Online]. Available: https://doi.org/10.1002/anie.200602556

[445] W. Kaveevivitchai, X. Wang, L. Liu, and A. J. Jacobson, "Two distinct redox intercalation reactions of hydroquinone with porous vanadium benzenedicarboxylate mil-47," *Inorganic chemistry*, vol. 54, no. 4, pp. 1822–1828, 2015. [Online]. Available: https://doi.org/10.1021/ic502730y

[446] J. Reboul, K. Yoshida, S. Furukawa, and S. Kitagawa, "Reductive coordination replication of v 2 o 5 sacrificial macrostructures into vanadium-based porous coordination polymers," *CrystEngComm*, vol. 17, no. 2, pp. 323–330, 2015. [Online]. Available: https://doi.org/10.1039/C4CE01501K

[447] C. Vargel, "Chapter a.3 - the advantages of aluminium," in *Corrosion of Aluminium*, 2nd ed., C. Vargel, Ed. Amsterdam: Elsevier, 2020, pp. 9–16. [Online]. Available: https://doi.org/10.1016/B978-0-08-099925-8.00003-X

[448] J. R. Kissell, S. G. Pantelakis, and G. N. Haidemenopoulos, *Aluminum and Aluminum Alloys*. John Wiley Sons, Ltd, 2004, ch. 9, pp. 321–463. [Online]. Available: https://doi.org/10.1002/0471465186.ch9

[449] C. Verma, L. O. Olasunkanmi, E. D. Akpan, M. Quraishi, O. Dagdag, M. El Gouri, E.-S. M. Sherif, and E. E. Ebenso, "Epoxy resins as anticorrosive polymeric materials: A review," *Reactive and Functional Polymers*, p. 104741, 2020. [Online]. Available: https://doi.org/10.1016/j.reactfunctpolym.2020.104741

[450] F. Seidi, M. Jouyandeh, M. Taghizadeh, A. Taghizadeh, H. Vahabi, S. Habibzadeh, K. Formela, and M. R. Saeb, "Metal-organic framework (mof)/epoxy coatings: A review," *Materials*, vol. 13, no. 12, p. 2881, 2020. [Online]. Available: https://doi.org/10.3390/ma13122881

[451] M. Zhang, L. Ma, L. Wang, Y. Sun, and Y. Liu, "Insights into the use of metal–organic framework as high-performance anticorrosion coatings," *ACS applied materials & interfaces*, vol. 10, no. 3, pp. 2259–2263, 2018. [Online]. Available: https://doi.org/10.1021/acsami.7b18713

[452] Y. J. Tarzanagh, D. Seifzadeh, Z. Rajabalizadeh, A. Habibi-Yangjeh, A. Khodayari, and S. Sohrabnezhad, "Sol-gel/mof nanocomposite for effective protection of 2024 aluminum alloy against corrosion," *Surface and Coatings Technology*, vol. 380, p. 125038, 2019. [Online]. Available: https://doi.org/10.1016/j.surfcoat.2019.125038

[453] S. Duan, B. Dou, X. Lin, S. Zhao, W. Emori, J. Pan, H. Hu, and H. Xiao, "Influence of active nanofiller zif-8 metal-organic framework (mof) by microemulsion method on anticorrosion of epoxy coatings," *Colloids and Surfaces A: Physicochemical and Engineering Aspects*, vol. 624, p. 126836, 2021. [Online]. Available: https://doi.org/10.1016/j.colsurfa.2021.126836

[454] N. Keshmiri, P. Najmi, M. Ramezanzadeh, and B. Ramezanzadeh, "Designing an eco-friendly lanthanide-based metal organic framework (mof) assembled graphene-oxide with superior active anti-corrosion performance in epoxy composite," *Journal of Cleaner Production*, vol. 319, p. 128732, 2021. [Online]. Available: https://doi.org/10.1016/j.jclepro.2021.128732

[455] S. M. Lashgari, H. Yari, M. Mahdavian, B. Ramezanzadeh, G. Bahlakeh, and M. Ramezanzadeh, "Application of nanoporous cobalt-based zif-67 metal-organic framework (mof) for construction of an epoxy-composite coating with superior anti-corrosion properties," *Corrosion Science*, vol. 178, p. 109099, 2021. [Online]. Available: https://doi.org/10.1016/j.corsci.2020.109099

[456] S. M. Lashgari, H. Yari, M. Mahdavian, B. Ramezanzadeh, G. Bahlakeh, and M. Ramezanzadeh, "Synthesis of graphene oxide nanosheets decorated by nanoporous

zeolite-imidazole (zif-67) based metal-organic framework with controlled-release corrosion inhibitor performance: Experimental and detailed dft-d theoretical explorations," *Journal of Hazardous Materials*, vol. 404, p. 124068, 2021. [Online]. Available: https://doi.org/10.1016/j.jhazmat.2020.124068

[457] M. Ramezanzadeh, B. Ramezanzadeh, M. Mahdavian, and G. Bahlakeh, "Development of metal-organic framework (mof) decorated graphene oxide nanoplatforms for anti-corrosion epoxy coatings," *Carbon*, vol. 161, pp. 231–251, 2020. [Online]. Available: https://doi.org/10.1016/j.carbon.2020.01.082

[458] M. Ramezanzadeh, B. Ramezanzadeh, G. Bahlakeh, A. Tati, and M. Mahdavian, "Development of an active/barrier bi-functional anti-corrosion system based on the epoxy nanocomposite loaded with highly-coordinated functionalized zirconium-based nanoporous metal-organic framework (zr-mof)," *Chemical Engineering Journal*, vol. 408, p. 127361, 2021. [Online]. Available: https://doi.org/10.1016/j.cej.2020.127361

[459] N. Wang, Y. Zhang, J. Chen, J. Zhang, and Q. Fang, "Dopamine modified metal-organic frameworks on anti-corrosion properties of waterborne epoxy coatings," *Progress in Organic Coatings*, vol. 109, pp. 126–134, 2017. [Online]. Available: https://doi.org/10.1016/j.porgcoat.2017.04.024

[460] A. Morozan and F. Jaouen, "Metal organic frameworks for electrochemical applications," *Energy & environmental science*, vol. 5, no. 11, pp. 9269–9290, 2012. [Online]. Available: https://doi.org/10.1039/C2EE22989G

[461] Y. Fang, X. Li, F. Li, X. Lin, M. Tian, X. Long, X. An, Y. Fu, J. Jin, and J. Ma, "Self-assembly of cobalt-centered metal organic framework and multiwalled carbon nanotubes hybrids as a highly active and corrosion-resistant bifunctional oxygen catalyst," *Journal of Power Sources*, vol. 326, pp. 50–59, 2016. [Online]. Available: https://doi.org/10.1016/j.jpowsour.2016.06.114

[462] S. E.-d. H. Etaiw, A. E.-A. S. Fouda, and M. M. El-bendary, "Cluster type molecule as novel corrosion inhibitor for steel in hcl solution," *Protection of Metals and Physical Chemistry of Surfaces*, vol. 49, no. 1, pp. 113–123, 2013. [Online]. Available: http://doi.org/10.1134/S2070205113010061

[463] M. Jouyandeh, F. Tikhani, M. Shabanian, F. Movahedi, S. Moghari, V. Akbari, X. Gabrion, P. Laheurte, H. Vahabi, and M. R. Saeb, "Synthesis, characterization, and high potential of 3d metal–organic framework (mof) nanoparticles for curing

with epoxy," *Journal of Alloys and Compounds*, vol. 829, p. 154547, 2020. [Online]. Available: https://doi.org/10.1016/j.jallcom.2020.154547

[464] M. Zorainy, D. C. Boffito, M. Gobara, A. Baraka, I. Naeem, and H. Tantawy, "Synthesis of a novel ce (iii)/melamine coordination polymer and its application for corrosion protection of aa2024 in nacl solution," *RSC Advances*, vol. 11, no. 11, pp. 6330–6345, 2021. [Online]. Available: https://doi.org/10.1039/D0RA08587A

[465] M. Gobara, A. Baraka, R. Akid, and M. Zorainy, "Corrosion protection mechanism of ce 4+/organic inhibitor for aa2024 in 3.5% nacl," *RSC Advances*, vol. 10, no. 4, pp. 2227–2240, 2020. [Online]. Available: https://doi.org/10.1039/C9RA09552G

[466] J. Ketelaar, "Crystal structure and shape of colloidal particles of vanadium pentoxide," *Nature*, vol. 137, no. 3460, pp. 316–316, 1936. [Online]. Available: https://doi.org/10.1038/137316a0

[467] M. Gobara, H. Kamel, R. Akid, and A. Baraka, "Corrosion behaviour of aa2024 coated with an acid-soluble collagen/hybrid silica sol–gel matrix," *Progress in Organic Coatings*, vol. 89, pp. 57–66, 2015. [Online]. Available: https://doi.org/10.1016/j.porgcoat.2015.07.026

[468] A. S. Hamdy, I. Doench, and H. Möhwald, "Intelligent self-healing corrosion resistant vanadia coating for aa2024," *Thin Solid Films*, vol. 520, no. 5, pp. 1668–1678, 2011. [Online]. Available: https://doi.org/10.1016/j.tsf.2011.05.080

[469] G. Chen, M. Gao, and R. Wei, "Microconstituent-induced pitting corrosion in aluminum alloy 2024-t3," *corrosion*, vol. 52, no. 01, 1996. [Online]. Available: https://doi.org/10.5006/1.3292099

[470] D. Ho, N. Brack, J. Scully, T. Markley, M. Forsyth, and B. Hinton, "Cerium dibutylphosphate as a corrosion inhibitor for aa2024-t3 aluminum alloys," *Journal of the Electrochemical Society*, vol. 153, no. 9, p. B392, 2006. [Online]. Available: https://doi.org/10.1149/1.2217260

[471] R. Akid, M. Gobara, and H. Wang, "Corrosion protection performance of novel hybrid polyaniline/sol–gel coatings on an aluminium 2024 alloy in neutral, alkaline and acidic solutions," *Electrochimica Acta*, vol. 56, no. 5, pp. 2483–2492, 2011. [Online]. Available: https://doi.org/10.1016/j.electacta.2010.12.032

[472] B. Chambers and S. Taylor, "The high throughput assessment of aluminium alloy corrosion using fluorometric methods. part ii–a combinatorial study of corrosion

inhibitors and synergistic combinations," *Corrosion science*, vol. 49, no. 3, pp. 1597–1609, 2007. [Online]. Available: https://doi.org/10.1016/j.corsci.2006.08.006

[473] O. A. Lopez-Garrity, *Corrosion inhibition mechanisms of aluminum alloy 2024-T3 by selected non-chromate inhibitors.* The Ohio State University, 2013. [Online]. Available: https://www.proquest.com/dissertations-theses/corrosion-inhibition-mechanisms-aluminum-alloy/docview/1647138206/se-2?accountid=40695

[474] R. Buchheit, R. Grant, P. Hlava, B. McKenzie, and G. Zender, "Local dissolution phenomena associated with s phase (al2cumg) particles in aluminum alloy 2024-t3," *Journal of the electrochemical society*, vol. 144, no. 8, p. 2621, 1997. [Online]. Available: https://doi.org/10.1149/1.1837874

[475] K. A. Yasakau, M. L. Zheludkevich, S. V. Lamaka, and M. G. Ferreira, "Mechanism of corrosion inhibition of aa2024 by rare-earth compounds," *The Journal of Physical Chemistry B*, vol. 110, no. 11, pp. 5515–5528, 2006. [Online]. Available: https://doi.org/10.1021/jp0560664

[476] F. Salles, S. Bourrelly, H. Jobic, T. Devic, V. Guillerm, P. Llewellyn, C. Serre, G. Ferey, and G. Maurin, "Molecular insight into the adsorption and diffusion of water in the versatile hydrophilic/hydrophobic flexible mil-53 (cr) mof," *The Journal of Physical Chemistry C*, vol. 115, no. 21, pp. 10 764–10 776, 2011. [Online]. Available: https://doi.org/10.1021/jp202147m

[477] M. A. Amin and M. M. Ibrahim, "Corrosion and corrosion control of mild steel in concentrated h2so4 solutions by a newly synthesized glycine derivative," *Corrosion Science*, vol. 53, no. 3, pp. 873–885, 2011. [Online]. Available: https://doi.org/10.1016/j.corsci.2010.10.022

[478] R. Jindal, V. Raja, M. A. Gibson, M. J. Styles, T. J. Bastow, and C. Hutchinson, "Effect of annealing below the crystallization temperature on the corrosion behavior of al–ni–y metallic glasses," *Corrosion science*, vol. 84, pp. 54–65, 2014. [Online]. Available: https://doi.org/10.1016/j.corsci.2014.03.015

[479] C. Fan, Y. Liu, X. Yin, J. Shi, and K. Dilger, "Electrochemical behavior and interfacial delamination of a polymer-coated galvanized steel system in acid media," *ACS omega*, vol. 6, no. 31, pp. 20 331–20 340, 2021. [Online]. Available: https://doi.org/10.1021/acsomega.1c02270

[480] W. Zhang, Y.-C. Wu, and H.-J. Li, "Apostichopus japonicus polysaccharide as efficient sustainable inhibitor for mild steel against hydrochloric acid corrosion," *Journal of Molecular Liquids*, vol. 321, p. 114923, 2021. [Online]. Available: https://doi.org/10.1016/j.molliq.2020.114923

[481] K. D. Ralston, S. Chrisanti, T. L. Young, and R. G. Buchheit, "Corrosion inhibition of aluminum alloy 2024-t3 by aqueous vanadium species," *Journal of The Electrochemical Society*, vol. 155, no. 7, p. C350, 2008. [Online]. Available: https://doi.org/10.1149/1.2907772

[482] M. Iannuzzi and G. S. Frankel, "Mechanisms of corrosion inhibition of aa2024-t3 by vanadates," *Corrosion Science*, vol. 49, no. 5, pp. 2371–2391, 2007. [Online]. Available: https://doi.org/10.1016/j.corsci.2006.10.027

[483] T. Zheng, J. Liu, L. Wang, J. Wang, and G. Jia, "Corrosion inhibition of aa2024-t3 in alkaline solution by disodium-n-dodecyliminodiacetate: Experimental and theoretical studies," *Colloids and Surfaces A: Physicochemical and Engineering Aspects*, p. 126989, 2021. [Online]. Available: https://doi.org/10.1016/j.colsurfa.2021.126989

[484] C. Li, X. Guo, and G. S. Frankel, "Corrosion inhibition of aa2024-t3 by a coating containing dual-ph sensitive, corrosion inhibitor loaded microspheres," *Corrosion Science*, vol. 192, p. 109835, 2021. [Online]. Available: https://doi.org/10.1016/j.corsci.2021.109835

[485] D. S. Kharitonov, J. Sommertune, C. Örnek, J. Ryl, I. I. Kurilo, P. M. Claesson, and J. Pan, "Corrosion inhibition of aluminium alloy aa6063-t5 by vanadates: Local surface chemical events elucidated by confocal raman microspectroscopy," *Corrosion Science*, vol. 148, pp. 237–250, 2019. [Online]. Available: https://doi.org/10.1016/j.corsci.2018.12.011

[486] "Chapter 2 - vanadium and its compounds," in *Vanadium: Extraction, Manufacturing, and Applications*, B. Yang, J. He, G. Zhang, and J. Guo, Eds. Elsevier, 2021, pp. 9–32. [Online]. Available: https://doi.org/10.1016/B978-0-12-818898-9.00002-4

[487] D. C. Crans and A. S. Tracey, *The Chemistry of Vanadium in Aqueous and Nonaqueous Solution.* American Chemical Society, 1998, ch. 1, pp. 2–29. [Online]. Available: https://doi.org/10.1021/bk-1998-0711.ch001

[488] A. Bouali, N. M. André, M. S. Campos, M. Serdechnova, J. F. dos Santos, S. Amancio-Filho, and M. L. Zheludkevich, "Influence of ldh conversion coatings

on the adhesion and corrosion protection of friction spot-joined aa2024-t3/cf-pps," *Journal of Materials Science & Technology*, vol. 67, pp. 197–210, 2021. [Online]. Available: https://doi.org/10.1016/j.jmst.2020.06.038

[489] A. E. Hoffman, L. Vanduyfhuys, I. Nevjestic, J. Wieme, S. M. Rogge, H. Depauw, P. Van Der Voort, H. Vrielinck, and V. Van Speybroeck, "Elucidating the vibrational fingerprint of the flexible metal–organic framework mil-53 (al) using a combined experimental/computational approach," *The Journal of Physical Chemistry C*, vol. 122, no. 5, pp. 2734–2746, 2018. [Online]. Available: https://doi.org/10.1021/acs.jpcc.7b11031

[490] H. Zhang, X. Xiao, X. Lu, G. Chai, Y. Sun, Y. Zhan, and G. Xu, "A cost-effective method to fabricate vo2 (m) nanoparticles and films with excellent thermochromic properties," *Journal of Alloys and Compounds*, vol. 636, pp. 106–112, 2015. [Online]. Available: https://doi.org/10.1016/j.jallcom.2015.01.277

[491] D. S. Bhaskaram, R. Cheruku, and G. Govindaraj, "Reduced graphene oxide wrapped v 2 o 5 nanoparticles: green synthesis and electrical properties," *Journal of Materials Science: Materials in Electronics*, vol. 27, no. 10, pp. 10 855–10 863, 2016. [Online]. Available: https://doi.org/10.1007/s10854-016-5194-x

[492] C. O'Dwyer, V. Lavayen, S. B. Newcomb, M. A. Santa Ana, E. Benavente, G. Gonzalez, and C. S. Torres, "Vanadate conformation variations in vanadium pentoxide nanostructures," *Journal of the Electrochemical Society*, vol. 154, no. 8, p. K29, 2007. [Online]. Available: https://doi.org/10.1149/1.2746556

[493] C. Londoño-Calderón, C. Vargas-Hernández, and J. Jurado, "Desorption influence of water on structural, electrical properties and molecular order of vanadium pentoxide xerogel films," *Revista mexicana de física*, vol. 56, no. 5, pp. 411–415, 2010. [Online]. Available: http://www.scielo.org.mx/scielo.php?script=sci_arttext&pid=S0035-001X2010000500009&nrm=iso

[494] C. Vargel, *Corrosion of aluminium.* Elsevier, 2020.

[495] J. K. Wessel, *The handbook of advanced materials: enabling new designs.* John Wiley & Sons, 2004.

[496] S. Papavinasam, *Evaluation and Selection of Corrosion Inhibitors.* John Wiley Sons, Ltd, 2000, ch. 67, pp. 1169–1178.

[497] A. E.-A. S. Fouda, S. E.-D. H. Etaiw, M. M. El-bendary, and M. M. Maher, "Metal-organic frameworks based on silver (i) and nitrogen donors as new corrosion inhibitors for copper in hcl solution," *Journal of Molecular Liquids*, vol. 213, pp. 228–234, 2016. [Online]. Available: https://doi.org/10.1016/j.molliq.2015.11.001

[498] T. Manh, P. Hien, Q. Nguyen, T. Quyen, B. Hinton, and N. Nam, "Corrosion inhibition of steel in naturally-aerated chloride solution by rare-earth 4-hydroxycinnamate compound," *Journal of the Taiwan Institute of Chemical Engineers*, vol. 103, pp. 177–189, 2019. [Online]. Available: https://doi.org/10.1016/j.jtice.2019.07.012

[499] Y. Peng, A. E. Hughes, J. I. Mardel, G. B. Deacon, P. C. Junk, M. Forsyth, B. R. Hinton, and A. E. Somers, "Leaching behavior and corrosion inhibition of a rare earth carboxylate incorporated epoxy coating system," *ACS applied materials & interfaces*, vol. 11, no. 39, pp. 36 154–36 168, 2019. [Online]. Available: https://doi.org/10.1021/acsami.9b13722

[500] Y. Cui, Y. Wang, Z. Cui, W. Qi, J. Wang, P. Ju, Y. Zhao, B. Liu, T. Zhang, and F. Wang, "Influence of rare earth element (y) on microstructure and corrosion behavior of hot extrusion az91 magnesium alloy," *Materials*, vol. 13, no. 16, p. 3651, 2020. [Online]. Available: https://doi.org/10.3390/ma13163651

[501] S. Kozhukharov and C. Girginov, "Recent trends of the use of rare earth elements for efficient environmentally compliant corrosion protection of aluminum and its alloys," in *Nanoscience and nanotechnology in security and protection against CBRN threats.* Springer, 2020, pp. 437–445. [Online]. Available: https://doi.org/10.1007/978-94-024-2018-0_35

[502] A. Hughes, J. Mol, and I. Cole, "The cost and availability of rare earth-based corrosion inhibitors," in *Rare Earth-Based Corrosion Inhibitors.* Elsevier, 2014, pp. 291–305. [Online]. Available: https://doi.org/10.1533/9780857093585.291

[503] S. E.-d. H. Etaiw, A. E.-A. S. Fouda, S. N. Abdou, and M. M. El-bendary, "Structure, characterization and inhibition activity of new metal–organic framework," *Corrosion science*, vol. 53, no. 11, pp. 3657–3665, 2011. [Online]. Available: https://doi.org/10.1016/j.corsci.2011.07.007

[504] S. E.-d. H. Etaiw, A. E.-A. S. Fouda, S. A. Amer, and M. M. El-bendary, "Structure, characterization and anti-corrosion activity of the new metal–organic framework [ag (qox)(4-ab)]," *Journal of Inorganic and Organometallic*

Polymers and Materials, vol. 21, no. 2, pp. 327–335, 2011. [Online]. Available: https://doi.org/10.1007/s10904-011-9467-9

[505] A. M. Alshima'a, A. Hefnawy, V. Langer, M. A. Khatab, L. Öhrstrom, and M. A. Abu-Youssef, "Synthesis, x-ray structure and anti-corrosion activity of two silver (i) pyrazino complexes," *Polyhedron*, vol. 28, no. 13, pp. 2794–2802, 2009. [Online]. Available: https://doi.org/10.1016/j.poly.2009.05.064

[506] T. Matsuda, K. B. Kashi, K. Fushimi, and V. J. Gelling, "Corrosion protection of epoxy coating with ph sensitive microcapsules encapsulating cerium nitrate," *Corrosion Science*, vol. 148, pp. 188–197, 2019. [Online]. Available: https://doi.org/10.1016/j.corsci.2018.12.012

[507] T. Hu, H. Shi, D. Hou, T. Wei, S. Fan, F. Liu, and E.-H. Han, "A localized approach to study corrosion inhibition of intermetallic phases of aa 2024-t3 by cerium malate," *Applied Surface Science*, vol. 467, pp. 1011–1032, 2019. [Online]. Available: https://doi.org/10.1016/j.apsusc.2018.10.243

[508] H. Boudellioua, Y. Hamlaoui, L. Tifouti, and F. Pedraza, "Effects of polyethylene glycol (peg) on the corrosion inhibition of mild steel by cerium nitrate in chloride solution," *Applied Surface Science*, vol. 473, pp. 449–460, 2019. [Online]. Available: https://doi.org/10.1016/j.apsusc.2018.12.164

[509] S. Taylor and B. Chambers, "Identification and characterization of nonchromate corrosion inhibitor synergies using high-throughput methods," *Corrosion*, vol. 64, no. 3, pp. 255–270, 2008. [Online]. Available: https://doi.org/10.5006/1.3278470

[510] A. B. Wiles, D. Bozzuto, C. L. Cahill, and R. D. Pike, "Copper (i) and (ii) complexes of melamine," *Polyhedron*, vol. 25, no. 3, pp. 776–782, 2006. [Online]. Available: https://doi.org/10.1016/j.poly.2005.08.022

[511] M. Yin, X. Chen, Y. Wan, W. Zhang, L. Feng, L. Zhang, and H. Wang, "Doping carbon nitride quantum dots into melamine-silver matrix: an efficient photocatalyst with tunable morphology and photocatalysis for h2o2 evolution under visible light," *ChemCatChem*, vol. 12, no. 5, pp. 1512–1518, 2020. [Online]. Available: https://doi.org/10.1002/cctc.20190

[512] A. Baraka, H. Hatem, M. S. El-Geundi, H. Tantawy, K. Karaghiosoff, M. Gobara, A. Elbeih, M. Shoaib, M. A. Elsayed, and M. M. Kotb, "A new cationic silver (i)/melamine coordination polymer,[ag2 (melamine)] n2n+: Synthesis,

characterization and potential use for aqueous contaminant anion exchange," *Journal of Solid State Chemistry*, vol. 274, pp. 168–175, 2019. [Online]. Available: https://doi.org/10.1016/j.jssc.2019.03.038

[513] X. Zhang, J. Zhou, Y. Zheng, and D. Chen, "Co0. 85se nanoparticles encapsulated by nitrogen-enriched hierarchically porous carbon for high-performance lithium-ion batteries," *ACS applied materials & interfaces*, vol. 12, no. 8, pp. 9236–9247, 2020. [Online]. Available: https://doi.org/10.1021/acsami.9b20866

[514] J. Liu, N. Qi, B. Zhou, and Z. Chen, "Exceptionally high co2 capture in an amorphous polymer with ultramicropores studied by positron annihilation," *ACS applied materials & interfaces*, vol. 11, no. 34, pp. 30 747–30 755, 2019. [Online]. Available: https://doi.org/10.1021/acsami.9b07015

[515] Y.-H. Li, D. Sun, G.-G. Luo, F.-J. Liu, H.-J. Hao, Y.-M. Wen, Y. Zhao, R.-B. Huang, and L.-S. Zheng, "Two ag (i) coordination polymers derived from melamine and dicarboxylates: Syntheses, crystal structures and thermal stabilities," *Journal of Molecular Structure*, vol. 1000, no. 1-3, pp. 85–91, 2011. [Online]. Available: https://doi.org/10.1016/j.molstruc.2011.05.056

[516] K. G. Chattaraj and S. Paul, "Inclusion of theobromine modifies uric acid aggregation with possible changes in melamine–uric acid clusters responsible for kidney stones," *The Journal of Physical Chemistry B*, vol. 123, no. 49, pp. 10 483–10 504, 2019. [Online]. Available: https://doi.org/10.1021/acs.jpcb.9b08487

[517] K. Wang, Z. Geng, Y. Yin, X. Ma, and Z. Wang, "Morphology effect on the luminescent property and antibacterial activity of coordination polymer particles with identical crystal structures," *CrystEngComm*, vol. 13, no. 16, pp. 5100–5104, 2011. [Online]. Available: https://doi.org/10.1039/C1CE05202K

[518] B. M. Alsmadi and P. Fox, "Semi-quantitative analysis of changes in soil coatings by scanning electron microscope and energy dispersive x-ray mapping," *Colloids and Surfaces A: Physicochemical and Engineering Aspects*, vol. 194, no. 1-3, pp. 249–261, 2001. [Online]. Available: https://doi.org/10.1016/S0927-7757(01)00814-7

[519] B. Woods, K. P. Kirkbride, C. Lennard, and J. Robertson, "Soil examination for a forensic trace evidence laboratory–part 2: elemental analysis," *Forensic science international*, vol. 245, pp. 195–201, 2014. [Online]. Available: https://doi.org/10.1016/j.forsciint.2014.10.018

[520] M. Gobara, A. Saleh, and I. Naeem, "Synthesis, characterization and application of acrylate-based poly ionic liquid for corrosion protection of c1020 steel in hydrochloric acid solution," *Materials Research Express*, vol. 7, no. 1, p. 016517, 2019. [Online]. Available: https://doi.org/10.1088/2053-1591/ab6000

[521] J. R. Scully, "Polarization resistance method for determination of instantaneous corrosion rates," *Corrosion*, vol. 56, no. 02, 2000.

[522] F. Mansfeld, "The polarization resistance technique for measuring corrosion currents," in *Advances in corrosion science and technology*. Springer, 1976, pp. 163–262. [Online]. Available: https://doi.org/10.1007/978-1-4684-8986-6_3

[523] F. Mansfeld, "Tafel slopes and corrosion rates from polarization resistance measurements," *Corrosion*, vol. 29, no. 10, pp. 397–402, 1973. [Online]. Available: https://doi.org/10.5006/0010-9312-29.10.397

[524] A. R. H. Zadeh, I. Danaee, and M. H. Maddahy, "Thermodynamic and adsorption behaviour of medicinal nitramine as a corrosion inhibitor for aisi steel alloy in hcl solution," *Journal of Materials Science & Technology*, vol. 29, no. 9, pp. 884–892, 2013. [Online]. Available: https://doi.org/10.1016/j.jmst.2013.06.006

[525] B. Schrader, *Infrared and Raman spectroscopy: methods and applications*. John Wiley & Sons, 2008.

[526] D. W. Mayo, F. A. Miller, and R. W. Hannah, *Course notes on the interpretation of infrared and Raman spectra*. John Wiley & Sons, 2004. [Online]. Available: https://doi.org/10.1002/0471690082

[527] W. Sawodny, K. Niedenzu, and J. W. Dawson, "Vibrational spectrum and assignment of normal vibrations of melamine," *The Journal of Chemical Physics*, vol. 45, no. 8, pp. 3155–3156, 1966. [Online]. Available: https://doi.org/10.1063/1.1728077

[528] M. K. Marchewka, "Infrared and raman spectra of melaminium bis (4-hydroxybenzenesulfonate) dihydrate," *Acta chimica slovenica*, vol. 50, no. 2, pp. 239–250, 2003.

[529] H. Tanak and M. K. Marchewka, "Ft-ir, ft-raman, and dft computational studies of melaminium nitrate molecular–ionic crystal," *Journal of Molecular Structure*, vol. 1034, pp. 363–373, 2013. [Online]. Available: https://doi.org/10.1016/j.molstruc.2012.10.046

[530] I. R. M. Ramos, A. Malkin, and F. M. Lyng, "Current advances in the application of raman spectroscopy for molecular diagnosis of cervical cancer," *BioMed research international*, vol. 2015, 2015. [Online]. Available: https://doi.org/10.1155/2015/561242

[531] X. Chen, Y. Hu, J. Gao, Y. Zhang, and S. Li, "Interaction of melamine molecules with silver nanoparticles explored by surface-enhanced raman scattering and density functional theory calculations," *Applied spectroscopy*, vol. 67, no. 5, pp. 491–497, 2013. [Online]. Available: https://doi.org/10.1366/12-06838

[532] M. Marchewka, "Infrared and raman spectra of the new melaminium salt: 2, 4, 6-triamino-1, 3, 5-triazin-1-ium hydrogenphthalate," *Materials Letters*, vol. 58, no. 6, pp. 843–848, 2004. [Online]. Available: https://doi.org/10.1016/j.matlet.2003.07.022

[533] L. He, Y. Liu, M. Lin, J. Awika, D. R. Ledoux, H. Li, and A. Mustapha, "A new approach to measure melamine, cyanuric acid, and melamine cyanurate using surface enhanced raman spectroscopy coupled with gold nanosubstrates," *Sensing and Instrumentation for Food Quality and Safety*, vol. 2, no. 1, pp. 66–71, 2008. [Online]. Available: https://doi.org/10.1007/s11694-008-9038-0

[534] X.-F. Zhang, M.-Q. Zou, X.-H. Qi, F. Liu, X.-H. Zhu, and B.-H. Zhao, "Detection of melamine in liquid milk using surface-enhanced raman scattering spectroscopy," *Journal of Raman Spectroscopy*, vol. 41, no. 12, pp. 1655–1660, 2010. [Online]. Available: https://doi.org/10.1002/jrs.2629

[535] M. Marchewka, "Infrared and raman spectra of melaminium chloride hemihydrate," *Materials Science and Engineering: B*, vol. 95, no. 3, pp. 214–221, 2002. [Online]. Available: https://doi.org/10.1016/S0921-5107(02)00235-0

[536] S. Debrus, M. Marchewka, M. Drozd, and H. Ratajczak, "Vibrational, calorimetric and nonlinear optical studies of melaminium-bis (trichloroacetate) monohydrate molecular–ionic crystal," *Optical Materials*, vol. 29, no. 8, pp. 1058–1062, 2007. [Online]. Available: https://doi.org/10.1016/j.optmat.2006.04.004

[537] A. Mebel *et al.*, "Ir spectroscopy and theoretical vibrational calculation of the melamine molecule," *Journal of the Chemical Society, Faraday Transactions*, vol. 93, no. 19, pp. 3445–3451, 1997. [Online]. Available: https://doi.org/10.1039/A701732D

[538] A. P. Kotula, C. R. Snyder, and K. B. Migler, "Determining conformational order and crystallinity in polycaprolactone via raman spectroscopy," *Polymer*, vol. 117, pp. 1–10, 2017. [Online]. Available: https://doi.org/10.1016/j.polymer.2017.04.006

[539] N. E. Mircescu, M. Oltean, V. Chiş, and N. Leopold, "Ftir, ft-raman, sers and dft study on melamine," *Vibrational Spectroscopy*, vol. 62, pp. 165–171, 2012. [Online]. Available: https://doi.org/10.1016/j.vibspec.2012.04.008

[540] M. Muniz-Miranda, "Surface enhanced raman scattering and normal coordinate analysis of 1, 10-phenanthroline adsorbed on silver sols," *The Journal of Physical Chemistry A*, vol. 104, no. 33, pp. 7803–7810, 2000. [Online]. Available: https://doi.org/10.1021/jp001578y

[541] R. Flouty, E. Abi-Aad, S. Siffert, and A. Aboukaïs, "Formation of cereous sulphate phase upon interaction of so 2 with ceria at room temperature," *Journal of thermal analysis and calorimetry*, vol. 73, no. 3, pp. 727–734, 2003. [Online]. Available: https://doi.org/10.1023/A:1025818127541

[542] R. Jayasree, V. Nayar, and V. Jordanovska, "Infrared and polarized raman spectra of tetramethyl ammonium cerium (iii) bis (sulfate) trihydrate," *Journal of Solid State Chemistry*, vol. 127, no. 1, pp. 51–55, 1996. [Online]. Available: https://doi.org/10.1006/jssc.1996.0355

[543] G. Socrates, *Infrared and Raman characteristic group frequencies: tables and charts*, 3rd ed.   John Wiley & Sons, 2004.

[544] J. A. Jacob, S. Naumov, T. Mukherjee, and S. Kapoor, "Preparation, characterization, surface modification and redox reactions of silver nanoparticles in the presence of tryptophan," *Colloids and Surfaces B: Biointerfaces*, vol. 87, no. 2, pp. 498–504, 2011. [Online]. Available: https://doi.org/10.1016/j.colsurfb.2011.06.017

[545] S. Jawaid, F. N. Talpur, H. I. Afridi, S. M. Nizamani, A. A. Khaskheli, and S. Naz, "Quick determination of melamine in infant powder and liquid milk by fourier transform infrared spectroscopy," *Analytical Methods*, vol. 6, no. 14, pp. 5269–5273, 2014. [Online]. Available: https://doi.org/10.1039/C4AY00558A

[546] P. Bairi, B. Roy, and A. K. Nandi, "ph and anion sensitive silver (i) coordinated melamine hydrogel with dye absorbing properties: metastability at low melamine concentration," *Journal of Materials Chemistry*, vol. 21, no. 32, pp. 11 747–11 749, 2011. [Online]. Available: https://doi.org/10.1039/C1JM11994J

[547] H. Ma, X. Jia, L. Chen, P. Zhu, W. Guo, X. Guo, Y. Wang, S. Li, G. Zou, G. Zhang *et al.*, "High-pressure pyrolysis study of c3n6h6: a route to preparing bulk c3n4,"

Journal of Physics: Condensed Matter, vol. 14, no. 44, p. 11269, 2002. [Online]. Available: https://doi.org/10.1088/0953-8984/14/44/466

[548] R. S. Bhosale, M. Al Kobaisi, S. V. Bhosale, S. Bhargava, and S. V. Bhosale, "Flower-like supramolecular self-assembly of phosphonic acid appended naphthalene diimide and melamine," *Scientific reports*, vol. 5, no. 1, pp. 1–11, 2015. [Online]. Available: https://doi.org/10.1038/srep14609

[549] C. Hu, Y. Xiao, Y. Zhao, N. Chen, Z. Zhang, M. Cao, and L. Qu, "Highly nitrogen-doped carbon capsules: scalable preparation and high-performance applications in fuel cells and lithium ion batteries," *Nanoscale*, vol. 5, no. 7, pp. 2726–2733, 2013. [Online]. Available: https://doi.org/10.1039/C3NR34002C

[550] Y. Liu, J. Zuo, X. Ren, and L. Yong, "Synthesis and character of cerium oxide (ceo 2) nanoparticles by the precipitation method," *Metalurgija*, vol. 53, no. 4, pp. 463–465, 2014.

[551] F. Lundvall, D. Wragg, P. Dietzel, and H. Fjellvåg, "Two new cu (ii) and la (iii) 2d coordination polymers, synthesis and in situ structural analysis by x-ray diffraction," *Dalton Transactions*, vol. 45, no. 32, pp. 12 827–12 834, 2016. [Online]. Available: https://doi.org/10.1039/C6DT02195F

[552] M. Zheludkevich, R. Serra, M. Montemor, K. Yasakau, I. M. Salvado, and M. Ferreira, "Nanostructured sol–gel coatings doped with cerium nitrate as pre-treatments for aa2024-t3: corrosion protection performance," *Electrochimica Acta*, vol. 51, no. 2, pp. 208–217, 2005. [Online]. Available: https://doi.org/10.1016/j.electacta.2005.04.021

[553] N. K. Gupta, C. Verma, M. Quraishi, and A. Mukherjee, "Schiff's bases derived from l-lysine and aromatic aldehydes as green corrosion inhibitors for mild steel: experimental and theoretical studies," *Journal of Molecular Liquids*, vol. 215, pp. 47–57, 2016. [Online]. Available: https://doi.org/10.1016/j.molliq.2015.12.027

[554] A. N. Grassino, J. Halambek, S. Djaković, S. R. Brnčić, M. Dent, and Z. Grabarić, "Utilization of tomato peel waste from canning factory as a potential source for pectin production and application as tin corrosion inhibitor," *Food Hydrocolloids*, vol. 52, pp. 265–274, 2016. [Online]. Available: https://doi.org/10.1016/j.foodhyd.2015.06.02

[555] E. Matter, S. Kozhukharov, M. Machkova, and V. Kozhukharov, "Comparison between the inhibition efficiencies of ce (iii) and ce (iv) ammonium nitrates against corrosion of aa2024 aluminum alloy in solutions of low chloride

concentration," *Corrosion Science*, vol. 62, pp. 22–33, 2012. [Online]. Available: https://doi.org/10.1016/j.corsci.2012.03.039

[556] H. Al-Shafey, O. El Azabawy, and E. Ismail, "Ethoxylated melamine as corrosion inhibitor for carbon steel in 1m hcl," *Journal of dispersion science and technology*, vol. 32, no. 7, pp. 995–1001, 2011. [Online]. Available: https://doi.org/10.1080/01932691.2010.497427

[557] P. Rodič and I. Milošev, "Corrosion inhibition of pure aluminium and alloys aa2024-t3 and aa7075-t6 by cerium (iii) and cerium (iv) salts," *Journal of The Electrochemical Society*, vol. 163, no. 3, p. C85, 2015. [Online]. Available: https://doi.org/10.1149/2.0431603jes

[558] H. Shi, E.-H. Han, and F. Liu, "Corrosion protection of aluminium alloy 2024-t3 in 0.05 m nacl by cerium cinnamate," *corrosion science*, vol. 53, no. 7, pp. 2374–2384, 2011. [Online]. Available: https://doi.org/10.1016/j.corsci.2011.03.012

[559] T. Hu, H. Shi, T. Wei, F. Liu, S. Fan, and E.-H. Han, "Cerium tartrate as a corrosion inhibitor for aa 2024-t3," *Corrosion Science*, vol. 95, pp. 152–161, 2015. [Online]. Available: https://doi.org/10.1016/j.corsci.2015.03.010

[560] B. Jegdić, B. Bobić, and S. Linić, "Corrosion behaviour of aa2024 aluminium alloy in different tempers in nacl solution and with the cecl3 corrosion inhibitor," *Materials and Corrosion*, vol. 71, no. 3, pp. 352–364, 2020. [Online]. Available: https://doi.org/10.1002/maco.201911219

[561] A. Singh and M. Quraishi, "The extract of jamun (syzygium cumini) seed as green corrosion inhibitor for acid media," *Research on Chemical Intermediates*, vol. 41, no. 5, pp. 2901–2914, 2015. [Online]. Available: https://doi.org/10.1007/s11164-013-1398-3

[562] A. Yurt, S. Ulutas, and H. Dal, "Electrochemical and theoretical investigation on the corrosion of aluminium in acidic solution containing some schiff bases," *Applied Surface Science*, vol. 253, no. 2, pp. 919–925, 2006. [Online]. Available: https://doi.org/10.1016/j.apsusc.2006.01.026

[563] S. Cao, D. Liu, H. Ding, J. Wang, H. Lu, and J. Gui, "Task-specific ionic liquids as corrosion inhibitors on carbon steel in 0.5 m hcl solution: an experimental and theoretical study," *Corrosion Science*, vol. 153, pp. 301–313, 2019. [Online]. Available: https://doi.org/10.1016/j.corsci.2019.03.035

[564] G. Burstein and R. Cinderey, "The potential of freshly generated metal surfaces determined from the guillotined electrode—a new technique," *Corrosion science*, vol. 32, no. 11, pp. 1195–1211, 1991. [Online]. Available: https://doi.org/10.1016/0010-938X(91)90132-9

[565] H. Elgahawi, M. Gobara, A. Baraka, and W. Elthalabawy, "Eco-friendly corrosion inhibition of aa2024 in 3.5% nacl using the extract of linum usitatissimum seeds," *Journal of Bio-and Tribo-Corrosion*, vol. 3, no. 4, pp. 1–13, 2017. [Online]. Available: https://doi.org/10.1007/s40735-017-0116-x

[566] S. Elbasuney, M. Gobara, M. Zoriany, A. Maraden, and I. Naeem, "The significant role of stabilized colloidal zro2 nanoparticles for corrosion protection of aa2024," *Environmental Nanotechnology, Monitoring & Management*, vol. 12, p. 100242, 2019. [Online]. Available: https://doi.org/10.1016/j.enmm.2019.100242

[567] E. Hür, G. Bereket, and Y. Şahin, "Corrosion inhibition of stainless steel by polyaniline, poly (2-chloroaniline), and poly (aniline-co-2-chloroaniline) in hcl," *Progress in organic coatings*, vol. 57, no. 2, pp. 149–158, 2006. [Online]. Available: https://doi.org/10.1016/j.porgcoat.2006.08.004

[568] X. Li, S. Deng, and H. Fu, "Sodium molybdate as a corrosion inhibitor for aluminium in h3po4 solution," *Corrosion Science*, vol. 53, no. 9, pp. 2748–2753, 2011. [Online]. Available: https://doi.org/10.1016/j.corsci.2011.05.002

[569] A. Balaskas, M. Curioni, and G. Thompson, "Corrosion protection mechanism of 2-mercaptobenzothiazole and its potential synergistic effect with cerium ions for treatment of aa 2024-t3," *Journal of Electroanalytical Chemistry*, vol. 863, p. 114081, 2020. [Online]. Available: https://doi.org/10.1016/j.jelechem.2020.114081

[570] V. Thangarasu, B. Balaji, and A. Ramanathan, "Experimental investigation of tribo-corrosion and engine characteristics of aegle marmelos correa biodiesel and its diesel blends on direct injection diesel engine," *Energy*, vol. 171, pp. 879–892, 2019. [Online]. Available: https://doi.org/10.1016/j.energy.2019.01.079

[571] Z. Chen, Z. Li, X. Ma, Y. Wang, Q. Zhou, and S. Zhang, "A new dmf-derived ionic liquid with ultra-high conductivity for high-capacitance electrolyte in electric double-layer capacitor," *Electrochimica Acta*, vol. 319, pp. 843–848, 2019. [Online]. Available: https://doi.org/10.1016/j.electacta.2019.07.015

[572] G. Bierwagen, D. Tallman, J. Li, L. He, and C. Jeffcoate, "Eis studies of coated metals in accelerated exposure," *Progress in organic coatings*, vol. 46, no. 2, pp. 149–158, 2003. [Online]. Available: https://doi.org/10.1016/S0300-9440(02)00222-9

[573] B. Valdez, S. Kiyota, M. Stoytcheva, R. Zlatev, and J. Bastidas, "Cerium-based conversion coatings to improve the corrosion resistance of aluminium alloy 6061-t6," *Corrosion Science*, vol. 87, pp. 141–149, 2014. [Online]. Available: https://doi.org/10.1016/j.corsci.2014.06.023

[574] O. Gharbi, D. Jiang, D. Feenstra, S. Kairy, Y. Wu, C. Hutchinson, and N. Birbilis, "On the corrosion of additively manufactured aluminium alloy aa2024 prepared by selective laser melting," *Corrosion Science*, vol. 143, pp. 93–106, 2018. [Online]. Available: https://doi.org/10.1016/j.corsci.2018.08.019

[575] L. Coelho, D. Cossement, and M.-G. Olivier, "Benzotriazole and cerium chloride as corrosion inhibitors for aa2024-t3: An eis investigation supported by svet and tof-sims analysis," *Corrosion Science*, vol. 130, pp. 177–189, 2018. [Online]. Available: https://doi.org/10.1016/j.corsci.2017.11.004

[576] A. D. King, N. Birbilis, and J. R. Scully, "Accurate electrochemical measurement of magnesium corrosion rates; a combined impedance, mass-loss and hydrogen collection study," *Electrochimica Acta*, vol. 121, pp. 394–406, 2014. [Online]. Available: https://doi.org/10.1016/j.electacta.2013.12.124

[577] V. Palanivel, Y. Huang, and W. J. van Ooij, "Effects of addition of corrosion inhibitors to silane films on the performance of aa2024-t3 in a 0.5 m nacl solution," *Progress in Organic Coatings*, vol. 53, no. 2, pp. 153–168, 2005. [Online]. Available: https://doi.org/10.1016/j.porgcoat.2003.07.008

[578] A.-E. A. Hermas, A. M. Elnady, and R. M. Ali, "Corrosion inhibition of stainless steel in sulfuric acid solution containing sulfide ions," *Anti-Corrosion Methods and Materials*, 2019. [Online]. Available: https://doi.org/10.1108/ACMM-10-2018-2016

[579] I. Obot, I. B. Onyeachu, N. Wazzan, and A. H. Al-Amri, "Theoretical and experimental investigation of two alkyl carboxylates as corrosion inhibitors for steel in acidic medium," *Journal of Molecular Liquids*, vol. 279, pp. 190–207, 2019. [Online]. Available: https://doi.org/10.1016/j.molliq.2019.01.116

[580] Q. Liu, Y.-R. Xu, A.-J. Wang, and J.-J. Feng, "One-step melamine-assisted synthesis of graphene-supported aupt@ au nanocrystals for enhanced catalytic reduction of

p-nitrophenol," *RSC advances*, vol. 5, no. 116, pp. 96 028–96 033, 2015. [Online]. Available: https://doi.org/10.1039/C5RA21645A

[581] A. B. Prevot, V. Maurino, D. Fabbri, A. M. Braun, and M. C. Gonzalez, "Degradation of melamine in aqueous systems by vacuum uv-(vuv-) photolysis. an alternative to photocatalysis," *Catalysis Today*, vol. 340, pp. 286–293, 2020. [Online]. Available: https://doi.org/10.1016/j.cattod.2018.11.045

[582] D. Feng, Y. Wu, X. Tan, Q. Chen, J. Yan, M. Liu, C. Ai, Y. Luo, F. Du, S. Liu *et al.*, "Sensitive detection of melamine by an electrochemiluminescence sensor based on tris (bipyridine) ruthenium (ii)-functionalized metal-organic frameworks," *Sensors and Actuators B: Chemical*, vol. 265, pp. 378–386, 2018. [Online]. Available: https://doi.org/10.1016/j.snb.2018.03.046

APPENDIX A   ARTICLE 5 - SYNTHESIS OF A NOVEL CE(III)/MELAMINE COORDINATION POLYMER AND ITS APPLICATION FOR CORROSION PROTECTION OF AA2024 IN NACL SOLUTION

Mahmoud Zorainy,[1,2] Daria C. Boffito,[2] Mohamed Gobara,[1] Ahmed Baraka,[1] Ibrahim Naeem,[1] and Hesham Tantawy[1]

Published in February 2021, in *RSC Advances.*

Abstract

We present the synthesis of a new cerium(III)-melamine coordination polymer (CMCP) by a mixed-solvothermal method and its characterization. Characterization techniques included Raman, Fourier Transformation Infra-Red (FTIR), X-Ray Diffraction (XRD) and Scanning Electron Microscope (SEM), in which the change in the electronic environment and the crystallinity were tracked. The characterization results confirm the coordination of cerium(III) with melamine through $-NH_2$ groups, instead of the N atoms of the triazine ring, for which we propose a mechanism of interaction. In addition, Biovia Materials Studio package was applied to determine and investigate the molecular structure of the CMCP. All simulations were done using COMPASS force-field theory and atom-based method for summation of electrostatic and van de Waals forces. The application of the CMCP for the corrosion inhibition of AA2024 in 3.5% NaCl solution was tested using the potentiodynamic polarization and electrochemical impedance spectroscopy (EIS) techniques. The results point out that the presence of cerium as cerium(III) in the CMCP structure plays the fundamental role of inhibition, whereby the inhibition mechanism occurs by cathodic oxidation of Ce(III) to Ce(IV) and cyclic reduction of Ce(IV) to Ce(III) by melamine part of CMCP.

Introduction

Corrosion inhibition crosscuts several industrial applications, including metals and alloys for pipelines, plant elements and other metallic assets, concrete for the construction industry, heritage artifacts,... etc. Aluminium has been widely used in numerous engineering applications due to its many advantages such as recycling, low density, wide range of alloys and ease of surface treatments.[494] AA2xxx is an aluminium alloy series with copper ($\approx$ 3.8 - 4.9%) main alloying element. AA2024 is widely used in aircraft applications due to a combination of high strength to weight ratio, high fatigue resistance and toughness.[495] However, this

---

[1]Chemical Engineering Department, Military Technical College, Cairo (Egypt)
[2]Chemical Engineering Department, Polytechnique Montréal, Montréal, QC H3C 3A7 (Canada)

alloy does not have suitable corrosion resistance in atmospheric conditions; consequently, it is used with cladding and/or coating which usually comprises an inhibitor. Using inhibitors is a cost effective technique during operation and maintenance where using economical materials with inhibitor is much cheaper than using an expensive corrosion resistant material without inhibitor.[496]

Generally, metal corrosion is inhibited, reduced or controlled by adsorption-blocking and/or electrochemical action.[460] Inhibitors working via the adsorption-blocking mechanism form a protective layer by physisorption at the metal/electrolyte interphase or as an insoluble complex barrier constructed by chemisorption, which prevents direct contact between the metal surface and the corrosive medium. Most of these inhibitors are organic materials designed to comprise aromaticity, heteroatoms such as nitrogen, oxygen and/or sulfur and/or conjugation. Indeed, the interaction is most favored with the metal when the inhibitor has a planar conjugated structure with a high π electron density.[497]

Chromate inhibitor/treatments had been effectively used to control the corrosion of AA2024 for many decades. Although, the prices of chromate treatment are cheap with respect to other inhibitors, there is a pressing demand to phase it out due to its carcinogenic effect. This adverse impact governs its concentration limits and finally it would be banned in many countries. Recently, researchers have investigated to replace chromate inhibitors with many eco-friendly inhibitors. Rare earth elements and coordination polymers (CPs) are considered as a suitable replacement candidate.[498–501] The bonding of rare earth element to an organic matrix would confer the material the advantages of both organic and inorganic inhibitor. Although, the high prices of rear earth elements due to the high demands of other technology, cerium would have suitable stable price due to the fact that its applications in other technologies are well established.[502]

Recently, coordination polymers have been considered for corrosion inhibition, whereby the adsorption mechanism plays the leading role. For example, Etaiw *et al.* proposed $Ag(CN)_4$ (quinoxaline)$_2$ to inhibit the corrosion of carbon steel in 1 M HCl and found that nitrogen heteroatoms are responsible for the strong adsorption of the material to the metal surface.[503] The same authors repeated the same type of experiments with Ag(quinoxaline) (4-aminobenzoic acid) as an inhibitor and found that inhibition is ascribed to adsorption as well.[504]

On the other hand, Massoud *et al.* suggested that the inhibition by CPs acts through both anodic and cathodic processes, with a dominant anodic inhibitory effect, when they investigated the use of two silver pyrazine MOFs, $[Ag_2(ampyz)(NO_3)_2]_n$ and $[Ag(2,3\text{-pyzdic})(NO_3)]_n$ as corrosion inhibitors for mild steel in acidic medium.[505]

However, the literature data concerning the use of coordinated polymers (CPs) and metal-organic frameworks (MOFs) for corrosion inhibition are relatively scarce, and they all lead to the same conclusion that inhibition occurs by an adsorption-blocking mechanism.[459, 461, 462] Indeed, CPs and MOFs include a countless number of different compounds where the organic linker confers them different functional groups, electron donor heteroatoms and p-orbital characters.[460] On the other hand, and to the best of our knowledge, the corrosion inhibition by CPs or MOFs through electrochemical action has not been reported yet.

The use of a CP or a MOF for inhibition through electrochemical action requires a moiety in the structure that is suitable for a redox reaction, i.e., a moiety that undergoes oxidation/reduction must be present with suitable potential with respect to the metal it protects. Cerium is well known for being used as a corrosion inhibitor.[506–508] In a corrosive media, Ce(III) plays the crucial role in the protection mechanism, whereby it precipitates on the cathodic sites as insoluble oxides and/or hydroxide hindering the reduction reactions.[507–509] Therefore, we speculated that bonding Ce(III) to melamine as a ligand could form an effective material for metal corrosion inhibition.

Melamine (2,4,6-triamino-s-triazine) is considered as a poor ligand as it has a strong network structure due to extensive hydrogen bonding throughout the material, which causes very low solubility in common solvents, except for hot water. Hence literature data on the coordination of neat melamine is poor and mostly concerns its coordination with Ag metal to either purify water or perform ion exchange in aqueous media.[510–512] Differently, there are many examples concerning the coordination chemistry of either functionalized melamine (hexamethylolmelamine [513], Schiff base networks [514]), or its coordination with other organic monomers such as succinic and adipic acid [515], uric acid.[516] However, pure melamine/metal coordination should occur under proper synthetic conditions involving, for instance, an acidic environment.

In this study, we aimed at coordinating Ce(III) in the form of CP, whereby melamine was used as the coordinating ligand. This work is original for several reasons: it presents the synthesis of this novel CP, cerium/melamine coordination polymer (CMCP) and its characterization using FTIR, Raman, CHNO/S elemental analysis, XRD, and SEM-EDX. Also, it discusses the potential use of CMCP in the corrosion protection of AA2024 in aerated 3.5% NaCl solution. The electrochemical inhibition was studied through two techniques: potentiodynamic polarization (PDP), and electrochemical impedance spectroscopy (EIS). The results of corrosion inhibition by CMCP are compared with those of blank, melamine, and cerium(III) inhibitors. In addition, SEM/EDX mapping was applied to give a better understanding of the inhibition behavior. This work presents the capability of corrosion inhibition

by CPs as a promising valuable application in addition to other vital applications such as catalysis, gas storage, ion exchange, optics, and drug delivery.[517]

Materials and methods

Synthesis of cerium/melamine coordination polymer (CMCP)

Cerium(III) sulfate (0.142 g) was dissolved in deionized water (5 ml), and melamine (0.126 g) solubilization was aided by an over-the-counter microwave furnace in acetic acid (15 ml, closed vial). The Ce(III)/water solution was added to the melamine/acetic acid solution, and the vial was tightly closed and put in a pre-heated oven (70 °C) for a mixed-solvothermal reaction. After about 30 minutes, the white CMCP solid precipitate settled at the bottom of the vial. The precipitate was separated from the reaction solution and was thoroughly washed several times alternating acetic acid and water, and then left to dry at ambient conditions. After that, it was stored in a clean vial until characterization and the corrosion inhibition experiments.

CMCP characterizations

Dry amounts of CMCP, cerium(III) sulfate $Ce_2(SO_4)_3$, and melamine were characterized by Raman spectroscopy in the 400 cm^{-1} - 4000 cm^{-1} range using a dispersive Raman microscope (Model Senterra, Bruker, Germany, at laser wavelength 532 nm). In addition, dry amounts of CMCP and its precursors, $Ce_2(SO_4)_3$ and melamine, were thoroughly mixed separately with KBr and then were pressed to form transparent discs. The FTIR spectra of these discs were recorded in the 400 cm^{-1} - 4000 cm^{-1} range with an automatic signal gain that collected 500 scans at a 4 cm^{-1} resolution with a JASCO Model 4100 spectrometer (Japan). The background spectrum was recorded from the clean empty cell at ambient temperature and was taken into consideration during the analyses. To reveal the crystalline nature of CMCP, powder XRD patterns of CMCP and melamine were recorded in the 2θ range from 20 ° to 60 ° with a CuKα radiation at 40 kV and 30 mA at a scanning speed of 4 degree per min with a sampling angle interval of 0.04 degree using an X-ray diffractometer (XRD, Shimadzu XD-l).

The surface morphology of the CMCP powder sample was investigated using a scanning electron microscope (SEM, Carl Zeiss EVO-10) equipped with an energy-dispersive X-ray spectroscopy (EDX) analyzer. The semi-quantitative elemental analysis for the prepared CMCP crystals was conducted using EDX.[518, 519]

Aluminum alloy specimen preparation

A sheet of aluminium alloy AA2024 [composition, as determined by wt%: Cu (3.8-4.9), Mg (1.2-1.8), Si (0.50), Fe (0.50), Mn (0.3-0.9), Cr (0.10), Zn (0.25), Ti (0.15), and Al (balance)] was obtained from Q-panel™. The sheet was pressed-cut into coupons where each had the dimensions $3.0 \times 2.5 \times 0.1 \text{ cm}^3$. Coupons were degreased and cleaned using ethanol, followed by rinsing with deionized water before drying for about an hour at room temperature. After dryness, the coupons were stored in a desiccator until the use in corrosion experiments. In this study, saline corrosive electrolyte (3.5% aqueous NaCl, Sigma Aldrich) is used, which is the typical salt concentration in sea water. Many researchers have widely used such electrolyte to evaluate the corrosion resistance of aluminium alloys. This aggressive Cl^--containing electrolyte is able to damage the passive aluminium oxide layer and significantly cause a localized corrosion attack. In addition, this solution is used as the corrosive electrolyte for AA2xxx series in many corrosion evaluation standards such as ASTM G44 and G47.

Electrochemical characterization studies

A potentiostat/galvanostat with three-electrode type cell was the setup to perform the electrochemical corrosion experiments with a Gamry™, model reference 600. For all the experiments, the ratio of corrosive solution volume to sample surface area was adjusted to 50 ml cm^{-2}.

For each experiment, a freshly prepared AA2024 coupon constituted the working electrode, saturated calomel was the reference electrode, and platinum the auxiliary electrode. The measurements were conducted according to ASTM standard G59 where the potentiodynamic polarization experiments were performed after immersion of the working electrode for at least 30 minutes in the corrosive solution. The potentiodynamic polarization curves were obtained in the potential range of -250 to +250 mV with respect to open-circuit potential (OCP) at a scan rate of 0.5 mV s^{-1}. The inhibition efficiency (IE) was calculated using the following relation:[520]

$$IE = \frac{I_{corr}^\circ - I_{corr}}{I_{corr}^\circ} \times 100 \tag{A.1}$$

where: I_{corr}° is the corrosion current density of blank sample and I_{corr} is the corrosion current density of inhibited sample.

The polarization resistance (R_p) was also determined to evaluate the corrosion resistance of AA2024 in presence and absence of inhibitor. R_p was calculated from both anodic and

cathodic slopes (β_a and β_c) of Tafel extrapolation curve according to the following equation: [521–523]

$$I = \frac{\beta_a \beta_c}{2.3(\beta_a + \beta_c)} \frac{1}{R_p} \tag{A.2}$$

Moreover, the corresponding protection efficiency (PE%) was calculated according to the following equation:

$$PE\% = \frac{(R_p - R_p^\circ) \times 100}{R_p} \tag{A.3}$$

where: R_p and R_p° are the polarization resistances of metal substrate in the electrolyte with and without the additives respectively.

The EIS tests were performed at room temperature by a three-electrode assembly. A saturated calomel electrode was used as a reference electrode, platinum as a counter electrode, and freshly prepared AA2024 was the working electrode. The EIS tests were performed using a Gamry reference 600 instruments in a frequency range of 10^5 to 10^{-2} Hz with an amplitude of 10 mV peak-to-peak, using AC signal at OCP. The inhibition efficiency (η) was calculated using the following relation:[524]

$$\eta = \frac{R_{total} - R_{total}^\circ}{R_{total}} \times 100 \tag{A.4}$$

where R_{total}° and R_{total} (Ω cm^2) are the total real resistance in the absence and the presence of inhibitor, respectively.

Fitting the EIS experimental data to equivalent electrical circuits was conducted by applying a nonlinear least square fitting technique using Gamry™ Echem Analyst software version 5.68. The quality of fitting was accepted when the goodness of fitting was not more than 1×10^{-3}.

Results and discussion

CMCP characterization

In a first exploratory step, Raman and FTIR spectroscopies identified the structure of the samples based on the electronic environment of the precursors and products. In a second step, XRD and then SEM-EDX inspected the coordination within CMCP and its morphology.

The Raman spectrum (Figure A.1) can be divided into three regions. The first region is the low wavenumber region (below 300 cm^{-1}), which corresponds to lattice vibrations and is considered key in the case of crystalline materials.[525] Hence, the presence of peaks in this region for melamine and CMCP indicates that these materials are crystalline. The disappearance and/or change of lattice vibration peaks upon the formation of CMCP from melamine indicates that crystal is changed by any means.[526] From the figure, the main lattice vibration bands for melamine are present at 57, 93, 123, and 153 cm^{-1}.[527–529] Once CMCP is formed, on the other hand, only one very strong sharp peak appears at 87 cm^{-1}. Since lattice vibrations are unique for a given crystalline substance, this peak can be sought as identification of the formation of CMCP.[526] In general, the observed dramatic change in the lattice vibrations region of the product, CMCP, with respect to that of melamine, indicates that we obtained a crystalline CMCP. In addition, the lack of lattice vibration peaks of melamine in the CMCP spectrum would indicate complete conversion and a pure product.
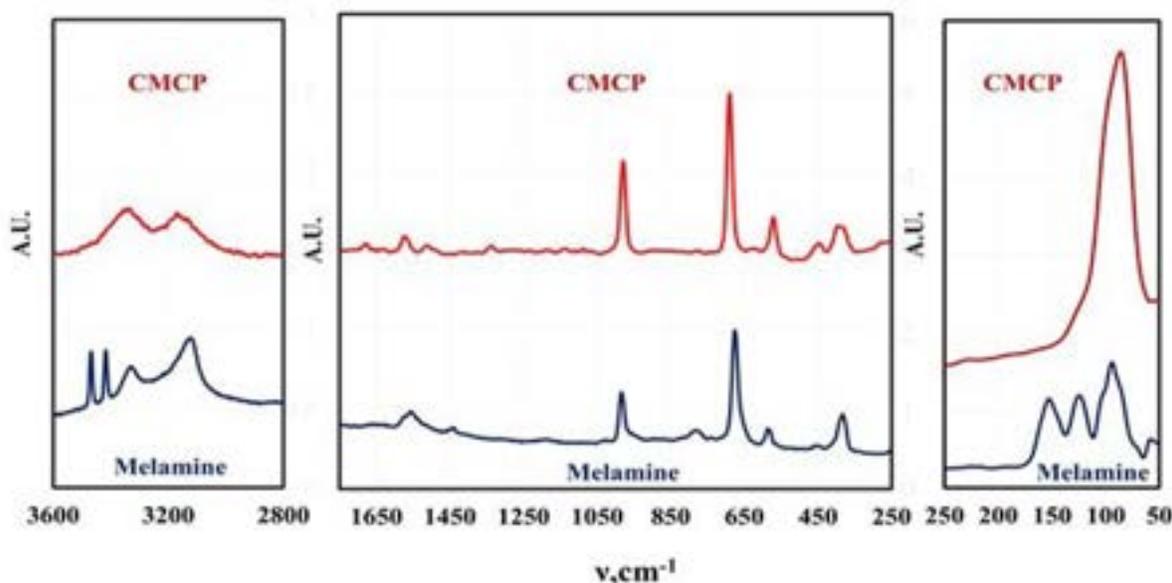

Figure A.1 Raman spectra of (a) melamine and (b) CMCP.

The second region is the fingerprint region, which lies in the 400-1800 cm^{-1} range.[530, 531] Typical Raman peaks of melamine appears at 380, 582, 676, 780 and 984 cm^{-1}.[527, 529, 531, 532], The most intense one at 676 cm^{-1} is assigned to the ring breathing II mode and involves in-plane deformation of the triazine ring. [533, 534]The second intense peak at 984 cm^{-1} arises from the ring breathing mode I of the triazine ring.[533] Peaks appearing at 380, 582, and 780 cm^{-1} correspond to the triazine ring as follows: quadrant out-of-plane, ring bending, and out of plane C-N bend, respectively.[535, 536] The weak peak at 1438 cm^{-1}

and the broad weak peak around 1560 cm^{-1} belong to ring vibrations and side-chain C-N stretching, respectively.[527, 535, 537]

Regarding the Raman spectrum of CMCP, it is evident that the melamine fingerprint peaks are collectively still present with some shifts. Furthermore, in this region, these peaks became more intense relative to those of melamine. This indicates that the triazine ring kept its aromatic structure and became even more ordered in the CMCP crystal.[538] Moreover, the emergence of a new weak peak in the CMCP spectrum at 1678 cm^{-1} may be attributed to a new mode of NH$_2$ bending upon complexing.[531, 535, 539] The previous discussion leads to the conclusion of coordination of cerium with the amino groups, not with N-triazine and the observed shifts in peaks' positions of CMCP to those of melamine may occur merely because of the coordination of NH$_2$-melamine molecules with cerium, which changes the electronic environment of the triazine ring. Besides, the observed strong blue-shift of the peak at 675 cm^{-1} (ring bending deformations of melamine) to 690 cm^{-1} (CMCP) confirms the presence of successive Ce(III)-melamine molecule bonding as the coordination weakens the original triazine ring bond strength.[540] The last region comprises mainly the N-H vibrations. The melamine spectrum shows four typical peaks: sharp twin peaks at 3468 and 3417 cm^{-1}, with two other peaks at 3328 and 3210 cm^{-1}. These peaks are attributed to the asymmetric and symmetric N-H stretching.[535, 536] The splitting of the N-H vibrations may be caused by the strong hydrogen bonding between the melamine molecules.[527] On the other hand, CMCP has only two broad peaks at 3337 and 3165 cm^{-1}, and this could be attributed to the distortion of N-H groups of melamine molecules in the CMCP crystal. There are probably no conditions for the strong coupling giving NH bands caused by intermolecular hydrogen bonds N-H. . . N type, like in the crystal of melamine alone.[535] The significant change in this part of the spectrum of the product confirms the difference of orientation of melamine molecules in the product rather than of the pure melamine.

The Raman spectrum also confirms that CMCP does not contain Ce-oxides, as no corresponding peaks are observed. In addition, there are no peaks from sulfate species bands between 990-1035 cm^{-1} and 1100-1180 cm^{-1} [541, 542], which points to the purity of CMCP. Moreover, when a ligand coordinates to a metal atom, new modes of vibration that are not present in the free ligand may become infrared or Raman active.[543] Additionally, the N-H stretching frequency should shift, indicating a change of the n-electron density on nitrogen [544], which will be investigated thereafter.

The FTIR analysis of melamine and CMCP is reported in Figure A.2. Melamine spectrum presents the known characteristic peaks: NH$_2$ stretching (3438 and 3386 cm^{-1}), asymmetric NH$_2$ stretching (3243 cm^{-1}), symmetric NH$_2$ stretching (3111 cm^{-1}), NH$_2$ deformation

(1614 cm^{-1}), quadrant stretching of the 1,3,5-s-triazine ring (1515 cm^{-1}), semicircle stretching of the 1,3,5-s-triazine ring (1425 cm^{-1}), C-N stretching of primary amines (1020 cm^{-1}) and out-of-plane ring bending (811 cm^{-1}).[545]
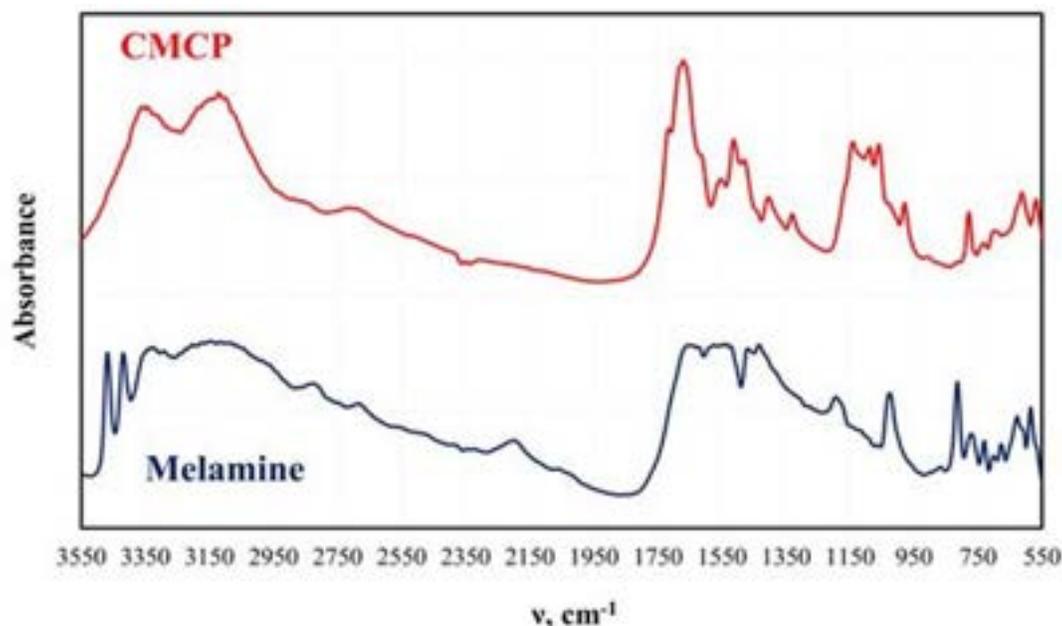

Figure A.2 FTIR spectra of melamine and CMCP.

On the other hand, the CMCP spectrum shows noticeable differences from that of melamine, which strongly suggests the coordination of cerium ion with melamine pendent-amines, and these are: the absence of NH$_2$ stretching, the shift of both symmetric NH$_2$ stretching and asymmetric NH$_2$ stretching to lower wavenumbers 3333 and 3113 cm^{-1} respectively, and the shift of NH$_2$ deformation to a higher wavenumber 1662 cm^{-1}. At the same time, the quadrant stretching of the 1,3,5 in the triazine ring are the sites that should preferably coordinate with Ce(III) [546], in our case, the coordination in CMCP occurred through pendent amine groups under the applied acidic condition (through optimization of acetic acid to water ratio). The proposed mechanism for this coordination presupposes that the hydrogen bonds between melamine molecules break down, and melamine molecules dissolve as melamium ions, whereby the protonation of the N-triazine atoms occur. As a consequence, the amino groups, conserving free lone pairs, can coordinate with Ce(III).[546]

Figure A.3 shows the PXRD patterns of melamine and CMCP. For melamine, all recorded diffraction peaks are as references: $2\theta=$ 22.37 °, 22.51 °, 26.89 °, 27.55 °, 29.25 °, 30.31 °, and 38.75 °.[547–549] The pattern of CMCP clearly displays strong and narrow peaks, indicating the good crystallinity of the CMCP. The peaks are at $2\theta =$ 7.27 °, 15.98 °, 17.53 °, 25.28 °, 26.23 °, and 27.23 °. This set is different from that of melamine and indicates the successful

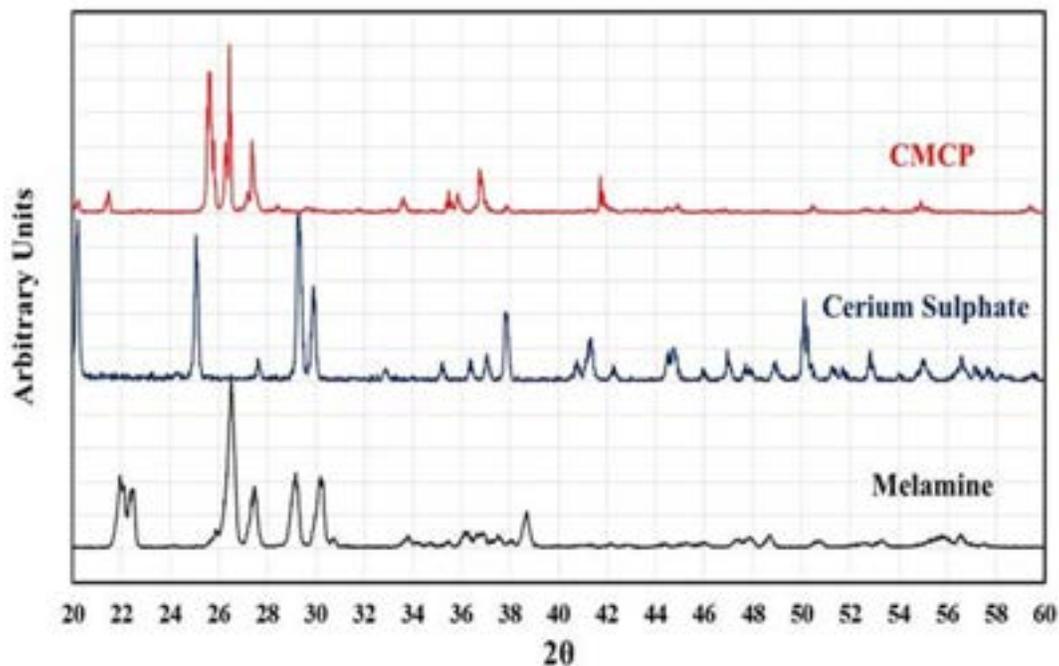preparation of the crystalline CMCP. In addition, there are no peaks of CeO_2.[550]

Figure A.3 PXRD patterns of CMCP, cerium sulfate $(Ce_2(SO_4)_3)$, and melamine.

Figure A.4 displays the SEM image of CMCP particles. It is evident that the particles are rhombus-like thick flakes. The results of the EDX and the CHNO/S elemental analysis (Table A.1) are very similar and lead to the conclusion that the Ce(III) coordination number is eight.
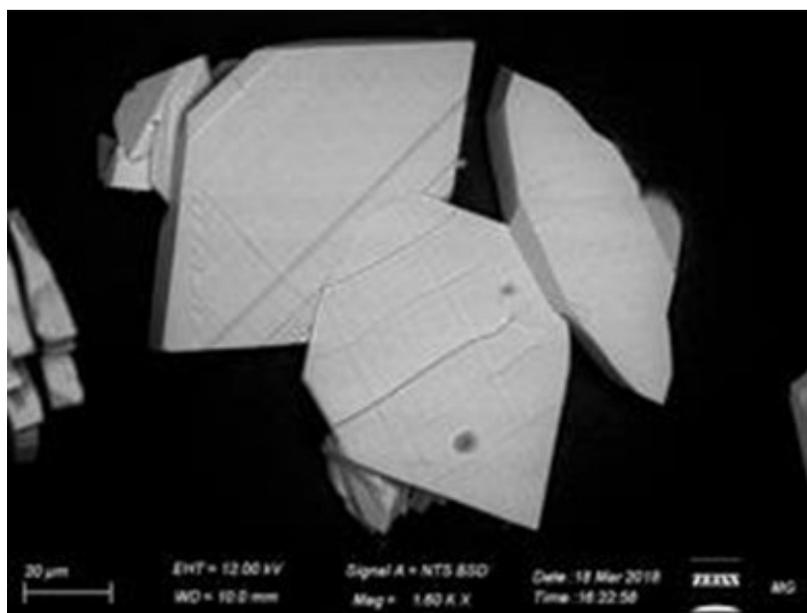

Figure A.4 SEM image of the rhombic CMCP particles.

Table A.1 The relative percentage for the CMCP elemental analysis

Element	Atoms% (EDX)	Atoms% (EA)
H	—	
C	16.29	11.42
N	32.53	22.85
O	37.85	34.28
S	9.23	8.57
Ce	4.12	—

According to the results of EDX, CHNO/S elemental analysis and FTIR, we proposed that the crystal superstructure of CMCP is of general formula $[Ce_2^{III}(M)_2(SO_4)_3(H_2O)_2 \cdot 2H_2O]_n$, where Ce(III) ions are linearly coordinated to two lateral tetradentate sulfate ions forming a 1D-linear chain, while the third tetradentate sulfate ion bridges between two Ce(III) ions from two adjacent chains forming a double-strand (or stair-like) 1D-linear chain. Each Ce(III) ion is also coordinated to one water molecule plus one melamine molecule through the nitrogen of the amino group forming a coordination sphere of eight. Last, there are two free water molecules per each two Ce(III) ions located in the crystal cavities. As a result, water molecules can easily diffuse between the layers and between the chains of the layers leading to dissolution of the material.[505, 551]

To visualize the molecular structure of the developed material and to investigate the mechanism of assembling these 1D linear chains into the observed 3D structure, we used conformers and Forcite modules available in Biovia Materials Studio 2017 package. All simulations were done using COMPASS forcefield theory and atom-based method for summation of electrostatic and van de Waals forces. The charges were assigned using QEq method (QEq_charged 1.1) using formal charges as initial guess values and convergence limit of 1.0×10^{-6} e. Geometry optimization were performed using Smart algorithm with convergence limits of 0.001 kcal mol^{-1} Å^{-1} and 1.0×10^{-5} Å for force and displacement respectively. The free water molecules in the structure were ignored in simulations. To construct a preliminary molecular structure for the developed material, we started by drawing the coordination sphere of Ce(III) and running conformers module to search for the best conformer with minimum energy. Then, we continued to construct a double strand chain by connecting eight geometry optimized coordination spheres and ran geometry optimization using Forcite module to minimize the energy of the structure. The results of this simulation are displayed in Figure A.5.
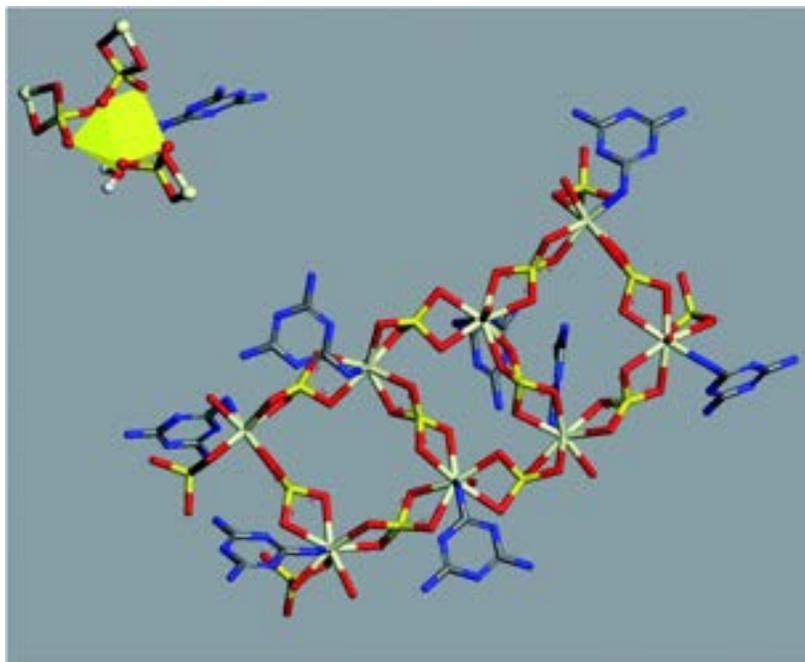
Figure A.5 Optimized molecular structure of Ce(III) coordination sphere (top left) and double-strand chain (centre) (hydrogen atoms were omitted for clarity).

Further simulation was performed to investigate the way of assembling the chains into 3D structure. Two double-strand chains were inserted at close proximity (5 Å separation) and geometry optimization were carried out again to find out the best way of packing and ordering of these chains and to search for the formed hydrogen bonds as well. The image in Figure A.6 shows that the two stair-like chains are connected to each other through numerous hydrogen bonds between N(H)-O, O(H)-N, O(H)-O and N(H)-NH in the range of 2.01-3.3 Å. These hydrogen bonds in addition to the hydrogen bonds formed by the free water molecules present in the residual cavities of the structure are responsible for assembling and packing the 1D stair-like chains into 2D layers which are further assembled by the same mechanism into the observed 3D flakes. The rupture of some layers, each of which has a thickness of about 1.2 μm in Figure A.7a, after exposing the particle to an SEM electron beam for about 2 minutes, supports this 3D-topology formation mechanism. After a prolonged exposure of about 7 minutes to the SEM electron beam, two facial layers (seems to be sheets-stacked) detached from each other (Figure A.7b and c). Therefore, the electron beam energy is sufficient to heat up the sample inducing thermal stresses and/or water molecules removal resulting in rupture of some H-bonds and separation of the stacked layers.
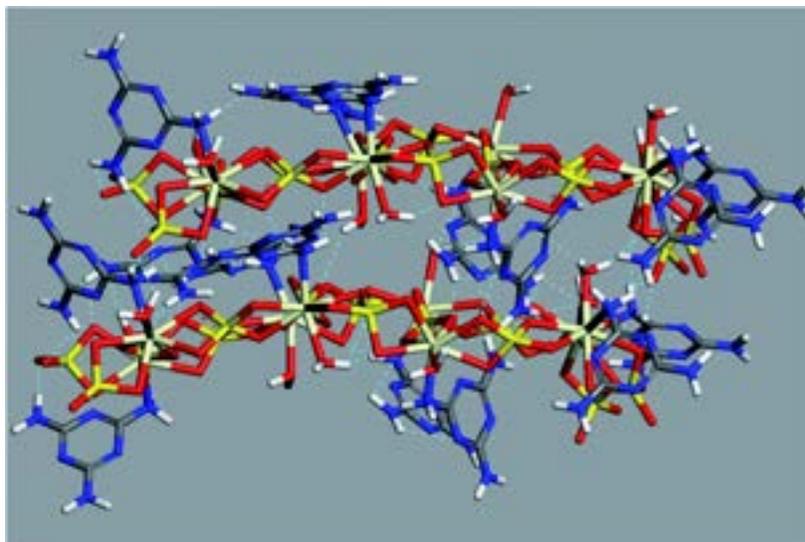
Figure A.6 Optimized geometry and hydrogen bonding scheme of two adjacent double-strand chains (without inclusion of free water molecules).
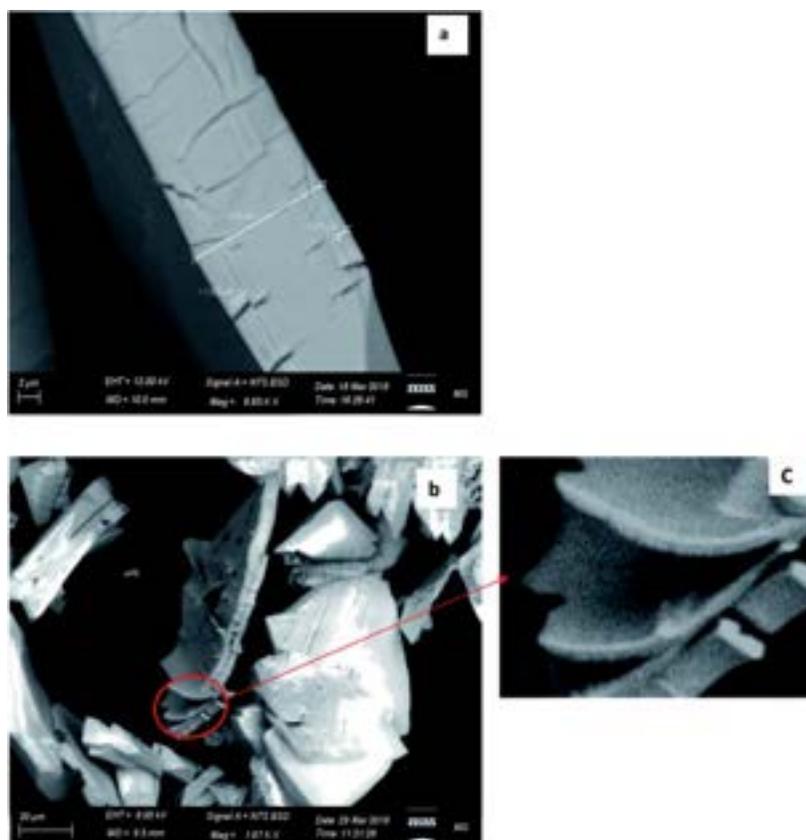

Figure A.7 Detailed SEM images of CMCP. (a) Expressing the thickness of a single rhombus-shaped particle. (b) and (c) The exfoliation of the CMCP sheets via the SEM electron beam.

Corrosion measurements of AA2024 in 3.5% NaCl

The inhibition effect of CMCP on AA2024 corrosion in 3.5% NaCl solution was investigated by potentiodynamic polarization and electrochemical impedance spectroscopy techniques as given below. As a matter of comparison, the corrosion performance of a blank, melamine, Ce(III) sulfate (Ce), and CMCP containing solutions were also considered.

The AA2024 samples were separately immersed in NaCl solutions containing 10 ppm of the different inhibitors: blank, melamine, Ce, and CMCP. The immersion time and bath temperature were 1 h and 25 °C, respectively. The polarization curves of the different samples were obtained, and the associated corrosion kinetics parameters of Tafel extrapolations (E_{corr}, β_c, β_a, I_{corr}, and IE%) were determined. Figure A.8 displays the polarization diagrams of the different samples and demonstrates the anodic and cathodic polarization behavior of AA2024.
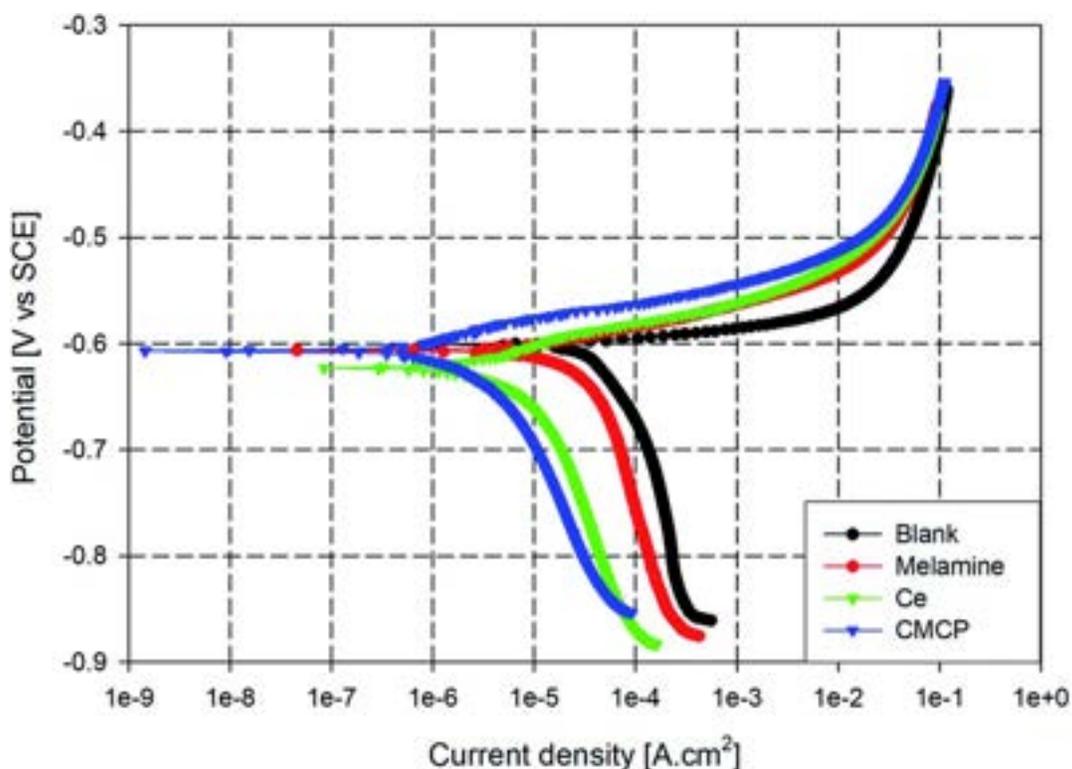

Figure A.8 Tafel plots of AA2024 in 3.5% NaCl with different inhibitors at room temperature. Ce = Ce(III) sulfate, CMCP = cerium(III)-melamine coordination polymer.

It can be noticed that the corrosion potentials of M, Ce, and CMCP seem to be in the same range as the blank sample, however, nobler. The anodic branch is very similar for all the samples, which corresponds to the oxidation of aluminum. Also, the anodic current density immediately increases sharply in the anodic polarization direction beyond the cor-

rosion potential in all samples, and no passive region is observed. This behavior with low anodic overpotentials indicates that these samples would show localized corrosion during an immersion course in 3.5% NaCl solution, i.e., pitting.

On the other hand, all curves are consistent with a cathodic process whereby oxygen controls the reduction reaction. Also, all the four samples exhibited a similar cathodic polarization response in the given condition, which indicates that all the samples have typically the same cathodic reaction but with different rates. Moreover, adding melamine insignificantly decrease the cathodic polarization of AA2024, whereas Ce and CMCP significantly suppressed the cathodic reaction. The parallel cathodic branch of CMCP and Ce samples with the blank sample indicates that CMCP inhibited the cathodic reaction but did not alter it. These data point out that the CMCP acts as a cathodic inhibitor for AA2024 in a 3.5% NaCl solution.[552–554]

Although the used CMCP contains the same amount of cerium as Ce and the same amount of melamine as M, it exhibits higher corrosion protection. The actual role of cerium in the corrosion inhibition process mainly depends on the oxidation state of cerium ion (i.e., Ce^{3+} or Ce^{4+}). Literature data report that the only presence of Ce(III) ion can provide corrosion protection.[555] On the other hand, melamine molecule contains six nitrogen atoms, which could enact an adsorptive-blocking mechanism of the aluminum substrate.[556] However, the excessive hydrogen bonding in melamine structure makes its dissolution difficult.

Table A.2 lists the electrochemical kinetic parameters of the Tafel extrapolations (E_{corr}, β_c, β_a, I_{corr}, and IE%). The anodic and cathodic slopes (β_a and β_c) are in the same range (Table A.2). Likewise, E_{corr} (the corrosion potentials) are close to each other. The clear difference lies in the corrosion current density (I_{corr}), whereby the CMCP and Ce samples are an order of magnitude lower than other samples, and the CMCP is the lowest. Although CMCP contains a lower concentration of Ce(III) than the Ce sample, it offers better corrosion protection.

Table A.2 Corrosion kinetic parameters of AA2024 with varying concentrations for different corrosion inhibitors. Ce = cerium(III) sulfate, CMCP = cerium(III)-melamine coordination polymer

Sample	β_a [mV per decade]	β_c [mV per decade]	E_{corr} [mV]	$I_{corr} \times 10^5$ [A cm^{-2}]	IE%	R_p
Blank	19±3.1	242±3.5	-601±5.9	5.6±1.2	—	90.047
Melamine	26±2.3	265±4.4	-603±5.1	2.9±2.1	48.2	290.49
Ce	27±m1.1	232±3.6	-619±3.8	0.73±1.8	86.9	933.79
CMCP	35±2.2	195±2.6	-605±4.5	0.24±1.0	95.7	2748.16

Moreover, Table A.2 shows the values of polarization resistance (R_p) and the corresponding protection efficiency (PE%) for all tested samples where CMCP sample shows the highest corrosion resistance.

On comparing the inhibition efficiency of CMCP to other previous work that used cerium inhibitor, it turns out that the corrosion inhibition percent of CMCP seems to be better than cerium(III) and (IV) treatment for protection of AA2024. Rodič *et al.* used different cerium salts (chloride, nitrate, acetate and sulphate) as inhibitor for AA2024 in less aggressive corrosive solution (0.1 M NaCl).[557] Also, the corrosion current density of CMCP is in the same order of that of cerium tartrate, cerium cinnamate treatment and cerium chloride for the same alloy (1.75×10^{-6} A cm^{-2}) in 0.05 M NaCl solution.[558–560] In our work, it can be noted that the corrosion current density of AA2024 inhibited with CMCP is slightly better than that of the synergistic effect of using cerium and melamine due to the intimate presence of cerium and melamine within same molecular structure.[465]

To better understand the corrosion performance of CMCP and to emphasize the importance of the coexistence of cerium and melamine in the same molecular structure, electrochemical impedance spectroscopy (EIS) measurements were performed. Again, as a matter of comparison, EIS was measured for blank, melamine, Ce, and CMCP samples.

Generally, AA2024 is susceptible to pitting corrosion in chloride-containing electrolytes due to inhomogeneity of the alloy surface. This heterogeneity comes from intermetallic particles (IMP), which are different in the corrosion potential with respect to the aluminium matrix. The pitting shape and size vary according to the size and nature of the IMP.[469]
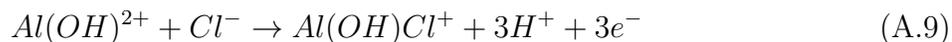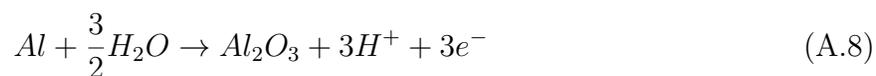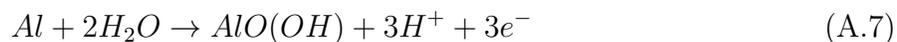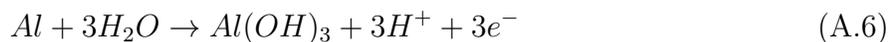
IMP covers ≈3% of the AA2024 surface area, and it can be classified into three categories according to size: hardening precipitates, dispersoid particles, and inclusions. The later type not only (size >1 μm) contribute to the mechanical properties of the alloy, but also have an adverse impact on the corrosion protection.[472, 473] Particularly, IMP containing Cu (such

as Al$_2$CuMg, AlCuMnFe, and AlCu$_2$) decreases the corrosion resistance of AA2024.[474, 475]

The reduction reaction in this aerated neutral electrolyte is the oxygen reduction:

$$\frac{1}{2}O_2 + H_2O + 2e^- \rightarrow 2OH^- \tag{A.5}$$

While Al undergoes a series of oxidation reactions in this chloride-containing solution, forming an aluminium hydroxyl chloride complex that easily dissolves in the solution.

$$Al + 3H_2O \rightarrow Al(OH)_3 + 3H^+ + 3e^- \tag{A.6}$$

$$Al + 2H_2O \rightarrow AlO(OH) + 3H^+ + 3e^- \tag{A.7}$$

$$Al + \frac{3}{2}H_2O \rightarrow Al_2O_3 + 3H^+ + 3e^- \tag{A.8}$$

$$Al(OH)^{2+} + Cl^- \rightarrow Al(OH)Cl^+ + 3H^+ + 3e^- \tag{A.9}$$

The presence of IMP increases the area of oxygen reduction and the corrosion process takes place in the IMP neighbouring area, forming pitting.

Nyquist plots of AA2024 in a 3.5% NaCl solution after 24 h at open circuit potential, either in the absence or presence of various additives, are reported in Figure A.9. All the plots are imperfect semicircles with different diameters. This deviation from perfectness may be due to the frequency dispersion and/or the inhomogeneity of the surface.[477, 561] In a Nyquist plot, the greater the real diameter of the Nyquist' loop, the higher the corrosion resistance, where this radius represents the total resistance, including the charge transfer resistance (R_{ct}) of the corrosion process.
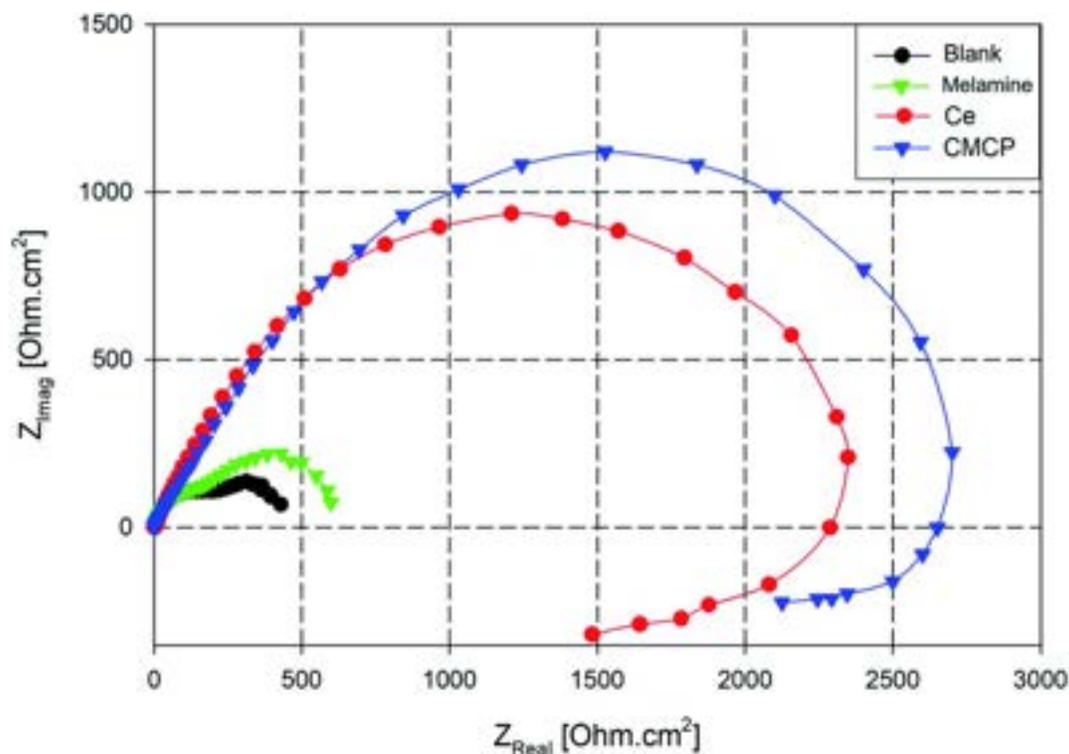
Figure A.9 Nyquist plots AA2024 in 3.5% NaCl solution with different additives. Ce = Ce(III) sulfate, CMCP = cerium(III)-melamine coordination polymer.

In Figure A.9, the blank sample exhibits the smallest diameter in the Nyquist plot, and the melamine's diameter is slightly greater, i.e., it acts slightly better as a corrosion inhibitor. In contrast, the CMCP and Ce samples have superior corrosion protection.

Also, the impedance plots of the blank and melamine have two semicircles; a capacitive loop that covers the high range of frequency and another loop at the low-frequency range. For aluminium alloys, this loop at the high-frequency range is attributed to formation of an oxide layer.[562, 563] Aluminium surface is immediately oxidized by O_2 in air or aqueous solutions.[564] However, the other one (time constant) at low frequency usually associates with the dissolution of aluminium i.e. evolution of corrosion products.[552,565] These results are in good agreement with the potentiodynamic polarization results and the visual inspection where dark spots appeared on the surfaces of both samples after 72 h of immersion as indication of dissolution of AA2024.[566]

While the Nyquist plot CMCP and Ce samples show two impeded capacitive loops at high and mid frequency range, in addition to an inductive loop at low frequency range. The presence of an inductive loop at a low frequency may be attributed to redox activity [471,567] and/or adsorption/desorption process of intermediates taking place on the surface of the substrate.[568, 569] The capacitive loop at high frequency range represents the inhibitive

and/or the oxide film, however, the other loop represents the double-layer capacitance and the charge transfer resistance.

EIS is a semi-quantitative technique that offers measuring and predicting the protection efficiency of a metal in a corrosive electrolyte.[570–572] The quantitative analysis of the EIS technique was applied by fitting the experimental data into an equivalent circuit. The equivalent circuit illustrated in Figure A.10a is used to fit the experimental data of both blank and melamine samples in the NaCl solution. While, equivalent circuit depicted in Figure A.10b is used for CMCP and Ce samples. The circuit, Figure A.10a, composes of ohmic electrolyte resistance (R_s), in series with a first constant phase element for the oxide film (CPE_{ox}), in parallel with a second resistance (R_1) representing resistance of the oxide film, and in series with a second circuit correlated to the interaction at the metal/electrolyte interface. This interaction is represented by the double-layer capacitance (CPE_{dl}) and the charge transfer resistance (R_{ct}). A constant phase element (CPE) are used instead of pure capacitance due to defects such as surface roughness, heterogeneous appearance.[573] In addition to the above components, circuit in Figure A.10b contains resistance (R_3) and an inductor (L) representing the redox reaction and/or adsorbed intermediates on a fresh substrate.
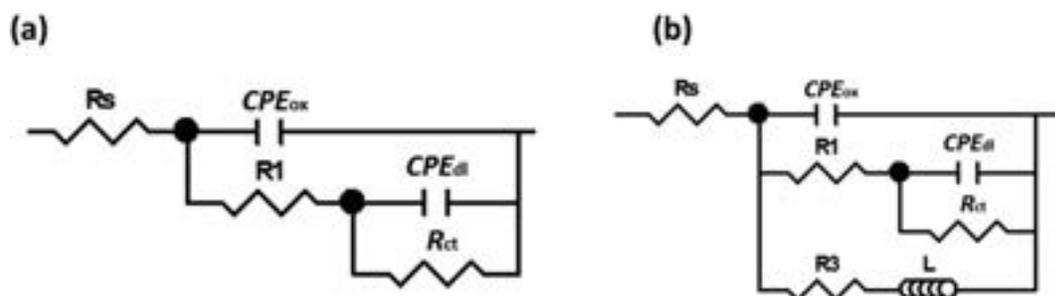

Figure A.10 Equivalent circuits used for modelling of impedance data for (a) blank and melamine (b) CMCP and Ce samples in 3.5% NaCl solution at room temperature.

The fitting results of the experimental EIS data are listed in Table A.3. It is clear from the table that the charge transfer resistance values of Ce and CMCP samples are much greater than that of blank and melamine samples.

Table A.3 Fitting results for the EIS measurements of AA2024 performed in 3.5% NaCl with different additives

Sample	R_s	CPE_{ox}			CPE_{dl}				
		Y	n	R_1	Y	n	R_{ct}	R_3	L
	$[\Omega cm^2]$	$[\mu\Omega^{-1}cm^{-2}S^n]$		$[\Omega cm^2]$	$[\mu\Omega^{-1}cm^{-2}S^n]$		$[k\Omega cm^2]$	$[\Omega cm^2]$	$[kHcm^{-2}]$
Blank	5.2	1362.1	0.87	185.1	86.3	0.90	0.26	—	—
Melamine	7.4	113.4	0.89	192.3	9.9	0.93	0.42	—	—
Ce	8.1	194.5	0.91	128.6	6.4	0.94	2.11	241.3	17.6
CMCP	8.9	121.5	0.93	201.5	5.2	0.95	2.58	521.1	22.7

Morphology of the corrosion of AA2024 in 3.5% NaCl

An SEM equipped with EDX imaged the morphology of the samples after 72 h of immersion in 3.5% NaCl electrolyte (Figure A.11). The back-scatter image shows severe pitting covering the whole surface. It can be noticed from the images that there are two types of pitting on the sample surface; small (red arrow) and large (the one in the center). The former can be attributed to IMP that detached from the surface in an earlier stage of immersion, forming a honeycomb-like shape.[552, 574] The latter seems to propagate in the area adjacent to IMP containing Cu, as the EDX analysis indicates.
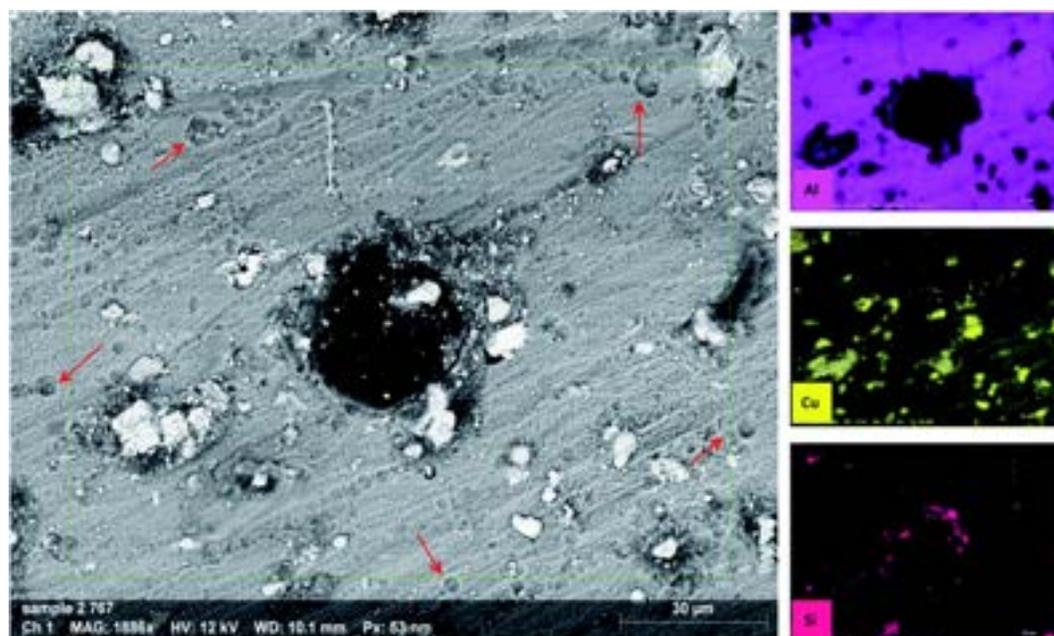

Figure A.11 SEM images and EDX analysis of AA2024 tested in 3.5% NaCl after 72 h at room temperature.

Figure A.12 displays the SEM images of AA2024 in the 3.5% NaCl solution with 10 ppm

melamine. The surface exhibits many pits of different sizes covering the whole surface. This result proves that melamine alone cannot protect the alloy from corrosion at the tested conditions, in agreement with the electrochemical measurements.
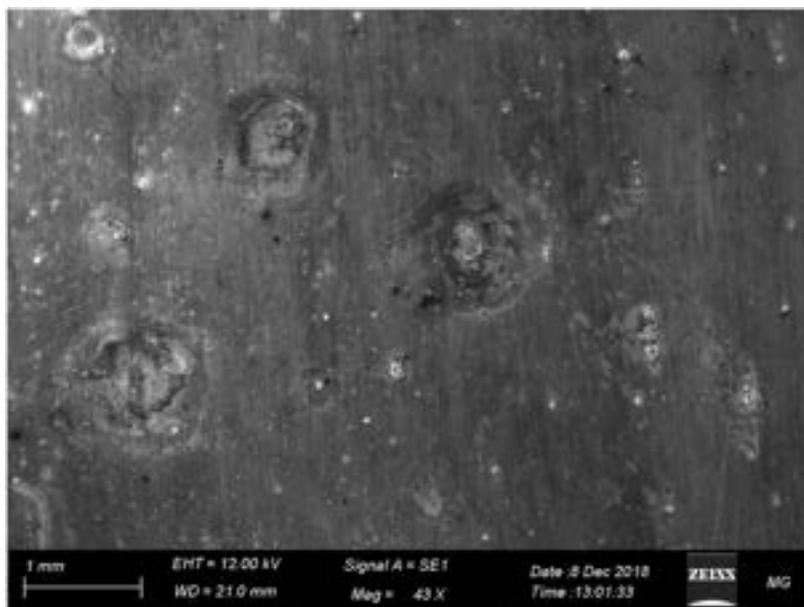

Figure A.12 SEM images of AA2024 tested in 3.5% NaCl after 72 h melamine at room temperature.

Ce(III) sulfate showed better corrosion protection of AA2024 in 3.5% NaCl solution than melamine (Figure A.13), where neither pitting nor corrosion products appeared after 72 h of immersion in the corrosive solution. These findings seem to be consistent with other data, which found that Ce(III) can protect AA2024 in 3.5% NaCl.[470, 555, 575]
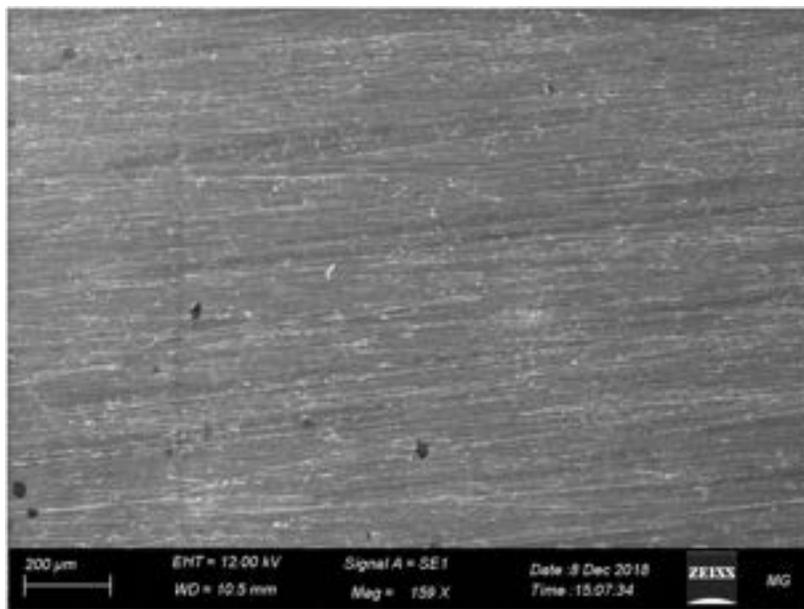
Figure A.13 SEM images of AA2024 tested in 3.5% NaCl after 72 h with Ce(III) at room temperature.

Figure A.14 reports the SEM image of AA2024 after 72 h of immersion in the 3.5% NaCl solution in the presence of 10 ppm CMCP. It is clear from images, at both low and high magnification, that there is no sign of corrosion on the surface of the sample. Besides, the high-resolution image demonstrates an intermetallic particle, around which there is no sign of corrosion. The EDX mapping also shows that the IMP contains copper, silica, and iron, where it is, generally, nobler than the aluminum matrix. The EDX clearly shows that cerium, oxygen, and carbon cover the IMP, where the source of carbon, in this case, is melamine. Therefore, the EDX analysis manifests the electrochemical measurements.
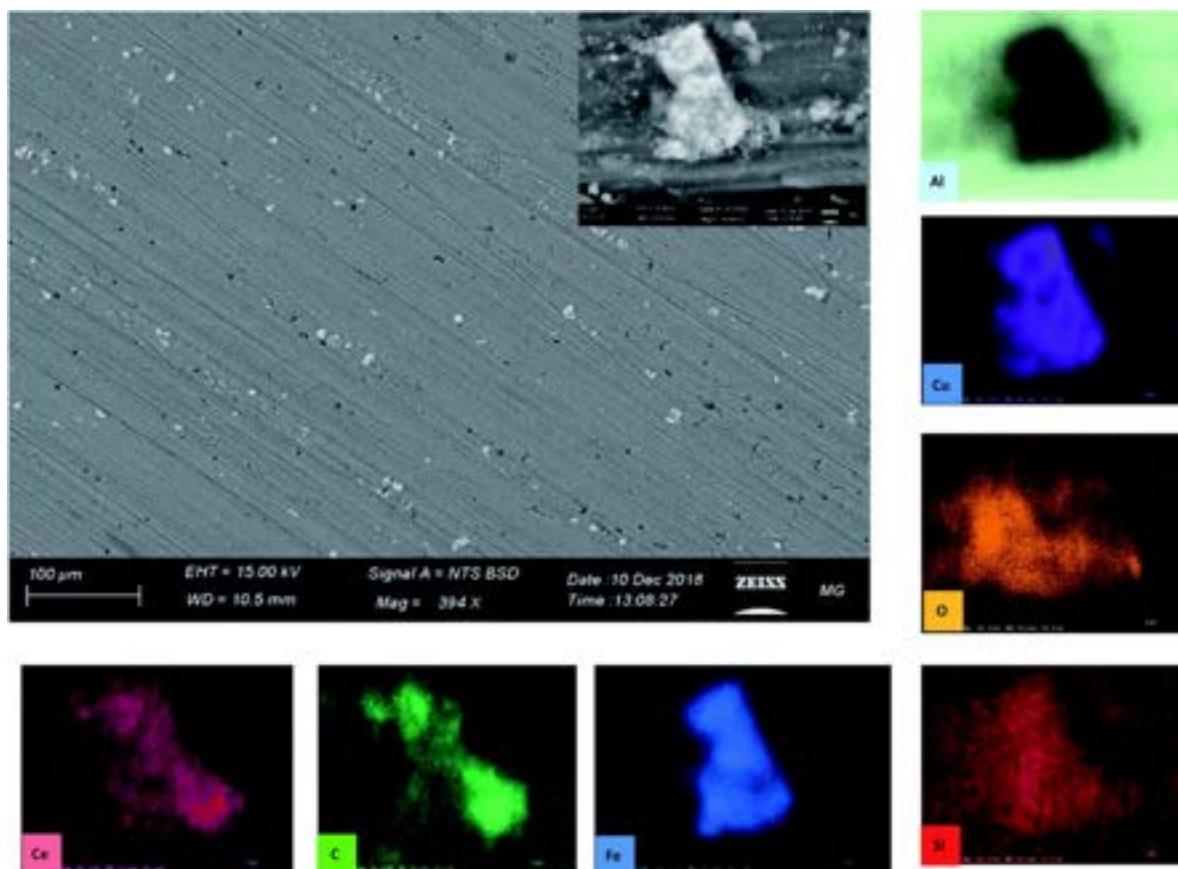
Figure A.14 SEM images of AA2024 tested in 3.5% NaCl after 72 h with CMCP at room temperature.

In conclusion, CMCP offers corrosion inhibition for AA2024 by forming a film that covers the cathodic sites, which decreases the oxygen reduction reaction and consequently decreases the susceptibility to pitting corrosion.

Extended time (15 days) corrosion measurements of AA2024 in 3.5% NaCl

The data above shows that both Ce and CMCP offer comparable corrosion prevention for AA2024 in artificial seawater. Nevertheless, upon an extended time of immersion, CMCP exhibits a more stable behavior than that of Ce(III) (Figure A.15). Neither Ce nor CMCP sample change its corrosion behavior during the immersion period. However, they lose some of their impedance. The polarization resistance, R_p, can be estimated as the impedance (frequency $\rightarrow$ 0) at -Z$_{Imag}$ = 0.96 [576], Indeed Ce(III) loses nearly $\approx$ 20% of the polarization resistance, while CMCP loses nearly $\approx$ 9%. These results indicate that CMCP can offer more stable corrosion protection than that of Ce sample.
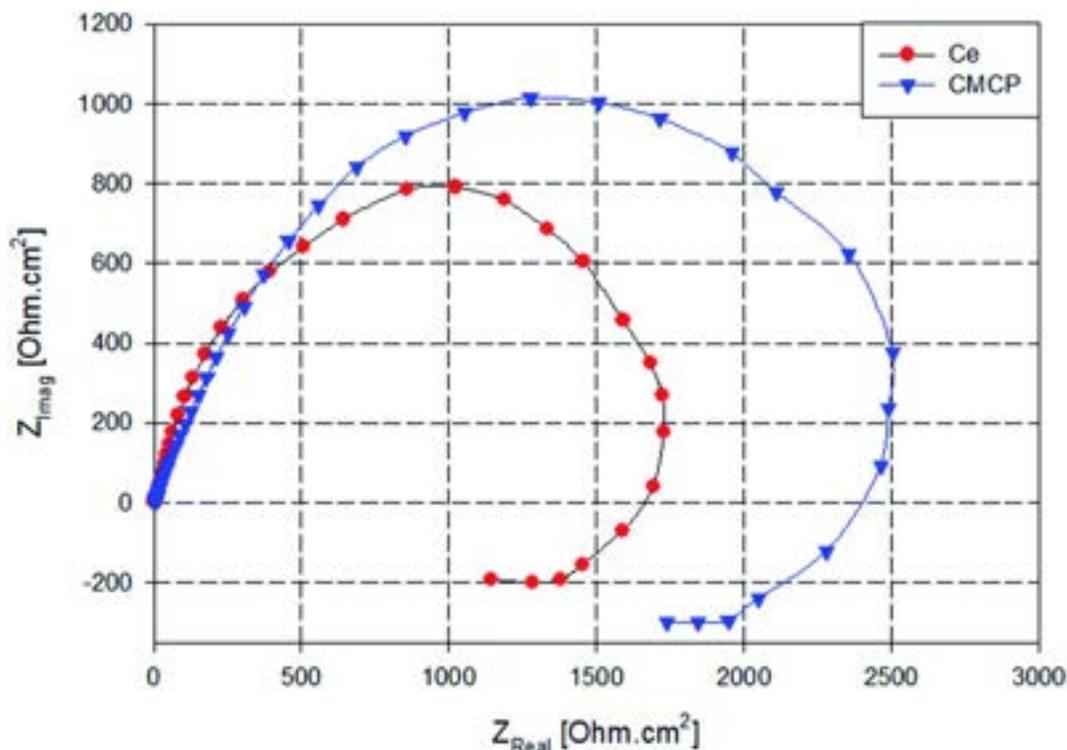
Figure A.15 Nyquist plots of AA2024 with Ce and CMCP in 3.5% NaCl solution after 15 days of immersion.

CMCP can offer corrosion prevention to the AA2024 via the following assumed mechanism; the aluminium matrix (anode) is oxidized following eqn A.6 and A.7.[577] The Ce(III) within the CMCP (stair-like chains) reacts with the hydroxide ions to form a thin hydroxide layer of Ce(III) (eqn A.10). The presence of H_2O_2 as an intermediate of oxygen reduction (eqn (A.11)) would interact with Ce(III) to precipitate Ce(IV) at the cathodic sites (the intermetallic particles) according to eqn A.12.[555, 577] Generally, Ce(III) can be oxidized to Ce(IV) at high pH as a result of the OH⁻ ions (eqn A.5 and A.11). In this case, the CMCP would hinder the cathodic reaction (oxygen reduction) taking place at the cathodic sets, consequently, decreasing the corrosion rate of the aluminium alloy.[465] This proposed mechanism is in good agreement with the PDP results, where the results indicated that the type of corrosion inhibitor is predominantly a cathodic inhibitor.

$$Ce^{3+} + 3OH^- \rightarrow Ce(OH)_3 \tag{A.10}$$

$$O_2 + H_2O + 2e^- \rightarrow H_2O_2 + OH^- \tag{A.11}$$

$$2Ce^{3+} + H_2O_2 \rightarrow 2Ce^{4+} + 2OH^- \tag{A.12}$$

Melamine in the molecular structure of the CMCP offers different types of protecting actions, as follows: (i) it is adsorbed on the metal substrate via nitrogen atoms due to the lone-pairs to coordinate to the metal surface.[578, 579] (ii) It improves the interaction of such a large molecule (coordination polymer), as it acts as a structure-director.[580] (III) It reduces Ce(IV) to Ce(III), where melamine should be oxidized subsequently.[581, 582] In the last case, melamine often regenerates Ce(III) during the immersion, thus extending the period of corrosion protection (Figure A.15).

Conclusions

Cerium(III)-melamine coordination polymer (CMCP) was synthesized via one-pot mixed-solvothermal technique. Raman, FTIR, and PXRD techniques were applied to investigate the prepared coordination of cerium(III) with melamine. It was found that the coordination occurs through -NH$_2$ groups rather than the N-triazine ring, which is distinctive. The morphology study clarifies that CMCP particles has a rhombic shape induced by a coordination number of eight around the cerium atom. The results were in a good agreement with the computational calculations conducted by Material studio software. The CMCP structure is composed of 1D stair-like chains assembled into 2D layers, which in turn stacked into 3D flakes mainly via H-bonding of the free water molecules located inside the residual voids of the structure. Importantly, water molecules can easily diffuse between the layers and between the chains of the layers leading to dissolution of the material. The electrochemical measurements confirmed that CMCP inhibits corrosion and protects the aluminium alloy AA2024 in artificial seawater (3.5% NaCl) better than any of its constituents solely. The mechanism through which inhibition comprises a synergistic action by the presence of both cerium(III) ion and melamine side by side within the same structure, which induces a see-saw redox process of cerium (continuous back-forth: Ce(III) to Ce(IV)). Moreover, CMCP offers more stable corrosion protection then Ce(III) alone as melamine regenerates Ce(III) often during immersion as confirmed by the 15 days extended immersion tests.